AMERICAN INSTITUTE OF STEEL CONSTRUCTION

AISC

FOUNDED 1921

ECCS
CECM
E K S

# CONNECTIONS VII
# 7th International Workshop on
# Connections in Steel Structures

Technical Committee 10
Structural Connections

N° 133 | **2012**

Dan Dubina | Daniel Mihai Grecea (Eds.)

Connections VII

7<sup>th</sup> International Workshop on
Connections in Steel Structures

May 30 – June 2, 2012
Timisoara, Romania

ECCS TC10
Structural Connections

# Connections VII
# 7th International Workshop on
# Connections in Steel Structures

1st Edition, 2013

Editors:
**Dan Dubina**
**Daniel Grecea**

# FOREWORD

This book presents the proceedings of the Seventh International Workshop on Connections in Steel Structures. The workshop was held at the Hotel Timisoara in Timisoara, Romania during the period 30 May - 1 June, 2012 under the auspices of the European Convention for Constructional Steelwork and the American Institute of Steel Construction.

The six preceding international workshops were held in Cachan, France, in 1987; Pittsburgh, Pennsylvania, USA in 1991; Trento, Italy, in 1995; Roanoke, Virginia, USA, in 2000; in Amsterdam, The Netherlands, in 2004; and in Chicago, Illinois, USA, in 2008. Proceedings for the six preceding workshops were published by Elsevier Applied Science Publishers (1988), the American Institute of Steel Construction (1992), Pergamon/Elsevier Science (1996), the American Institute of Steel Construction (2002), Bouwen met Staal, the Netherlands (2005), and the American Institute of Steel Construction (2008).

The idea of holding this seventh workshop was strongly supported by the American Institute of Steel Construction (AISC) and the European Convention for Constructional Steel (ECCS). Financial support for the workshop was provided by ECCS and the Politehnica University of Timisoara.

The European Convention for Constructional Steelwork was the official host of this workshop. Outstanding work by the hosts from the Department of Steel Structures and Structural Mechanics at the Politehnica University of Timisoara made the workshop possible. The stewardship of Professors Dan Dubina and Daniel Grecea in particular are particularly appreciated. In addition, the participation of the individuals who served as session chairs contributed significantly to the smooth running of all three days of the workshop.

Finally, the support and technical contributions of the 64 participants from 20 countries who presented 44 technical papers must be acknowledged. Without their commitment to research, design, and construction of structural steel connections worldwide, none of this would have been possible. It is expected that the continued commitment of these participants and others to come in the future, will result in another successful workshop in a North American location in 2016.

July 2012

Frans S. K. Bijlaard,                              Charles J. Carter,
European Convention for Constructional       American Institute of Steel Construction,
Steelwork,                                         Vice President and Chief Structural Engineer
Chairman of TC10 – Connections

# PREFACE

This is the 7th International Workshop on Connections in Steel Structures (*Connections VII*), jointly organized by European Convention of Constructional Steelworks (ECCS) and The American Institute of Steel Construction (AISC) since 1987, starting with the first edition in Paris (Cachan, France), followed by *Connections II* in 1991 (Pittsburgh, Pennsylvania, USA), *Connections III* in 1995 (Trento, Italy), *Connections IV* in 2000 (Roanoke, Virginia, USA), *Connections V* in 2004 (Amsterdam, The Netherlands), while *Connections VI* was organized in 2008 in Chicago, USA.

The success of previous 6 series *"Connections"* workshops was confirmed, not only by the number of outstanding scientists and professional engineers, mainly coming from Europe and USA, but also from other areas, who have contributed along the years, with their papers and know-how, to a fruitful scientific and professional exchange of experience. The six volumes of Proceedings, containing the contributions of participants to those workshops, include 289 scientific papers, all of very high quality, as well as the Concluding Reports based on the Summary Reports presented by the Chairmen of Technical Sessions. The recommendations issued at the end of each workshop have been afterwards considered as valuable references in codification and practice in Europe and USA, and not only.

The 7th Workshop was organized in 2012, May 30th – June 2nd, in the historical city of Timisoara, located the *Banat* County, Romania, by the "Politehnica" University and the Romanian Academy, under the supervision of ECCS and AISC. This time, 44 papers, by 110 authors have been presented and debated by 64 participants coming from Europe and USA, but also from Canada, Brazil, Chili, China and Australia. Six general topics were covered by these contributions i.e.:

1. Structural design and design codes (chair : C.J. Carter (American Institute of Steel Construction, USA), F.S.K. Bijlaard (Delft University of Technology, The Netherlands))
2. Methods of analysis (chair: R. Trambley (École Polytechnique of Montréal, Canada), L. Simoes da Silva (University of Coimbra, Portugal))
3. Connections for seismic effects (chair: F. Charney (Virginia Polytechnic Institute, USA), V. Piluso (University of Salerno, Italy))
4. Connections with hollow structural sections (chair: J.A. Packer (University of Toronto, Canada), J.P. Jaspart (University of Liege, Belgium))
5. Bolting and special connection topics (chair: L. Lima (State University of Rio de Janeiro, Brazil), F. Wald (Czech Technical University, Czech Republic))
6. Bracing and truss connections (chair: G.A. Rassati (University of Cincinnati, USA), D. Grecea (Politehnica University of Timisoara, Romania))

At the end, a *Concluding Panel*, chaired by Prof. Riccardo Zandonini (ECCS) and Dr. Reidar Bjorhovde (AISC) summarized and concluded on the main contributions collected during oral presentations and free discussions.

In the Opening Session of the Workshop, the Silver Medal of European Convention of Constructional Steelwork was awarded by Professor Luis Da Silva, Chairman of ECCS Technical Management Board, to Professor Frans Bijlaard, chairman of Technical Committee No. 10 – Connections, along the previous three Workshops – 4th, Roanoke, USA, 2000, 5th Amsterdam, Europe, 2004, 6th Chicago, USA, 2008, including this one in Timisoara.

We are expressing our gratitude to the authors of the papers, as well as to all contributors to Connections VII. Thanks are due to the Chairmanship of ECCS and AISC, and to the Technical Committees of the two bodies involved in the organization and promoting of series of workshops on *Connections*, particularly to Prof. Frans Bijlaard, Chaiman of ECCS-TC10 and Dr. Charles Carter, Vice President and Chief Structural Engineer at the AISC.

The support of Joana Albuquerque, of CMM – *Associação Portuguesa de Construção Metálica e Mista*, to the editing of this Volume, as well as to Professor Stefan Kilyeni, of EOU - *Editura Orizonturi Universitare*, of Timisoara, for printing has to be acknowledged, too.

Editors

Prof. Dan Dubina      Prof. Daniel Grecea
Chairman      Scientific secretary
of Connections VII Workshop      of Connections VII Workshop

Timisoara, Romania, December 2012

# TABLE OF CONTENTS

# RECENT CHANGES IN U.S. CONNECTION DESIGN PRACTICE

Charles J. Carter, S.E., P.E., Ph.D.
*Vice President and Chief Structural Engineer*
*at the American Institute of Steel Construction in Chicago, IL, USA*
*carter@aisc.org*

Cynthia J. Duncan
*Director of Engineering at the American Institute of Steel Construction in Chicago, IL, USA*
*duncan@aisc.org*

## ABSTRACT

The 2010 AISC Specification for Structural Steel Buildings (AISC 360-10) is the basis upon which the 14th edition AISC Steel Construction Manual was written. These documents reflect changes in connection design requirements and practices. This paper summarizes the most relevant changes in connection design requirements and practices made in these latest versions of these documents.

## 1. BASIC BOLT STRENGTH INCREASED

U.S. practice in the design of bolted joints for shear has long been based upon a reduction in the basic shear strength to account for conditions in which the shear distribution in the joint is not uniform. As a matter of simplicity, this reduction has been applied to all bolted joints so that the bolt shear strength is not usually affected by the number of bolts in the joint.

Prior to the 2010 AISC Specification, a 20% reduction was included in the basic strength for joint lengths up to 50 in. (1 270 mm). Above that dimension, an additional 20% reduction was required in the calculations.

A re-evaluation of existing data and common joint lengths in modern construction led to a change in the 2010 AISC Specification. A similar approach is used, but the initial reduction is taken as 10% and the length at which an additional reduction (of 17%) is taken at 38 in. (965 mm). This new approach is illustrated and compared to the old approach in Figure 1.

In theory, the non-uniform distribution is present only in end-loaded joints (see Figure 2). However, the reduction is applied to all joints as a matter of simplicity, and also to account for restraint and behavior that is customarily ignored in many connection design approaches.
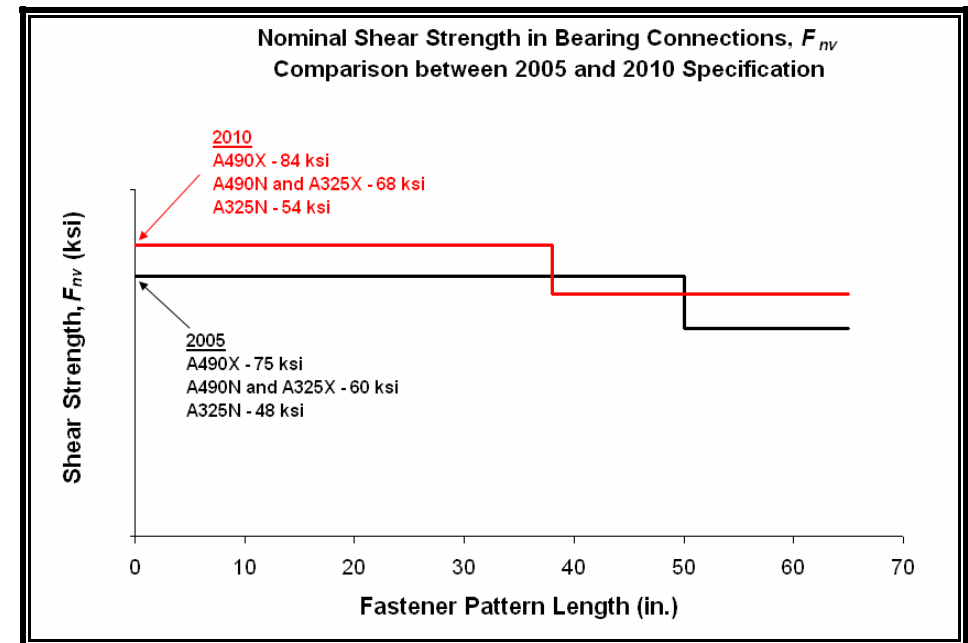


Figure 1. Comparison of Bolt Shear Strengths in 2005 and 2010 AISC Specifications
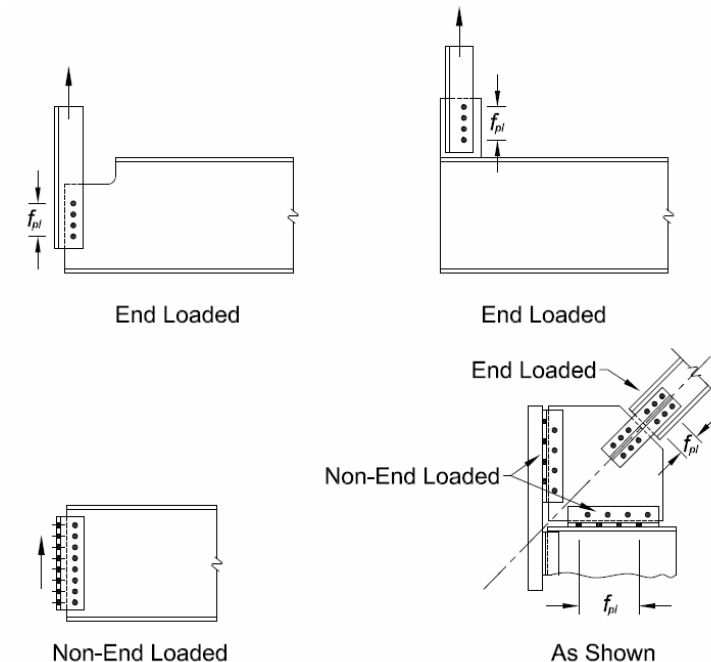


Figure 2. Examples of end-loaded and non-end-loaded joints

## 2. BOLT STRENGTH GROUPINGS ESTABLISHED

ASTM A325 and A490 bolts are the usual fasteners contemplated in bolted joints in U.S. practice. The twist-off-type tension-control configurations of these products have become prevalent in the U.S. marketplace, and so ASTM standards have been developed to define them: ASTM F1852 is similar to A325, and ASTM F2280 is similar to A490. When added to the other grades, such as ASTM A354 and A449 that exist in the U.S. marketplace, and also counting all of the metric equivalents that exist for these standards, there are a number of fastener options and many have similar or identical strength levels for design.

To simplify the provisions used in the AISC Specification, these products have been grouped as shown in Table 1.

Table 1. Bolt strength levels as grouped in 2010 AISC Specification

| Group | ASTM | Basic Strength | | | | | |
|---|---|---|---|---|---|---|---|
| | | Tension | | Shear | | | |
| | | | | N | | X | |
| | | ksi | MPa | ksi | MPa | ksi | MPa |
| A | A325, A325M, F1852, A354 gr. BC, A449 | 90 | 620 | 54 | 372 | 68 | 457 |
| B | A490, F2280, A354 gr. BD | 113 | 780 | 68 | 457 | 84 | 579 |

One unintended item of confusion has been discovered: Group A and B tension and shear strength levels do not have anything to do with the faying surface classifications Class A and Class B used in slip-critical connection design.

## 3. SLIP-CRITICAL CONNECTION DESIGN SIMPLIFIED AND IMPROVED

Up until the 2005 AISC Specification, the designer was asked to decide if slip was to be prevented as a matter of serviceability or strength. Dubiously buried in the background of this decision was the reality that the actual checks were calibrated to give similar results in common cases, making the choice confusing at best.

In 2005, changes were made that created different levels of design between serviceability and strength. However, the strength-level slip checks caused concern in the industry because some joints previously designed for serviceability slip were now required to be designed with more bolts at the strength-level slip resistance. These included connections with oversized holes or slotted holes parallel to the direction of the load

Large-scale (see Figure 3) and other research (Borello et al., 2009; Dusicka and Iwai, 2007, and Grondin et al., 2007) was undertaken almost immediately, and much was learned about slip behavior and joint design requirements. The results affected the design method, allowing significant simplification and better addressing behavior. The serviceability-strength dichotomy was eliminated, slip coefficients were changed, requirements for when fillers are used in the joint were added, among other refinements.



Figure 3. Test specimen used in AISC slip-critical joint research

The new equation for calculation of slip resistance is given as:

$$R_n = \mu \cdot D_u \cdot h_f \cdot T_b \cdot N_s$$

The variables $T_b$ and $N_s$ are unchanged. They represent the bolt pretension and number of slip planes, respectively.

A resistance factor for LRFD or safety factor for ASD is required:
- for standard holes and short-slotted holes perpendicular to the direction of the load, $\phi$ = 1.0 and $\Omega$ = 1.50;
- for oversized and short-slotted holes parallel to the load the direction of the load, $\phi$ = 0.85 and $\Omega$ = 1.76;
- for long-slotted holes, $\phi$ = 0.70 and $\Omega$ = 2.14.

The value of the slip coefficient, "$\mu$" was changed from 0.35 to 0.30 primarily because of the wide variability of the slip resistance of Class A "clean mill scale" surfaces. The slip coefficient for Class B surfaces was maintained as $\mu$ = 0.50 for Class B "blast-cleaned" surfaces and blast-cleaned surfaces with Class B coatings.

A reduction applicable to joints in which multiple fillers are used was added; alternatively, additional bolts can be added to develop the fillers. The filler factor, $h_f$, is determined as follows:
- Where bolts have been added to distribute loads in the fillers, $h_f$ =1.0
- Where bolts have not been added to distribute loads in the fillers, $h_f$ =1.0 for one filler between connected parts; $h_f$ = 0.85 for two or more fillers between connected parts.

It also is worth noting that prior to the 2010 AISC Specification fillers greater than ¾ in. (19 mm) thick had to be developed. This is no longer the case. A reduction factor still applies to the bolt shear strength when fillers are not developed, but the 2010 Specification recognizes that the reduction factor need not exceed 0.85 regardless of the thickness of the filler.

## 4. BASE METAL DESIGN AT WELDS

Table J2.5 in the 2010 AISC Specification summarizes the available strengths for welds and base metal and weld metal in welded joints. Base metal strength at welds is now based upon the rupture strength rather than the yield strength. Previously, the design was based upon yielding in the base metal, which has come to be viewed as conservative and incorrect, since the weld itself adjacent to the base metal is designed for a rupture limit state.

## 5. DIRECTIONAL STRENGTH INCREASE EXTENDED TO OUT-OF-PLANE LOADING

Prior to 2010, the AISC Specification included the words "in plane" when provisions were provided for the directional strength increase for fillet welds. That is, the provisions were limited to loading in the plane of the weld or weld group. Common usage of the provisions in practice, however, extended these provisions to out-of-plane loading as well. Research (Kanvinde et al., 2009) was conducted to evaluate that practice and showed that the restriction (words "in plane") could be eliminated. Accordingly, they do not appear in the 2010 AISC Specification.

## 6. WELD GROUP SIZE UNIFORMITY REQUIREMENTS WERE ADDED

Fillet welds used in groups generally are all of the same size, but not always. Provisions in Section Sections J2.4 (a) and (c) in the 2010 AISC Specification are based upon a load-deformation behavior that is affected by the weld size (Muir, 2008). Accordingly, these provisions have been clarified to reflect that they are based upon fillet weld groups in which the size of the weld is uniform. When the weld group is not of uniform size, Section J2.4(b) can be used to accounts for size variations.

## 7. PRYING ACTION FORMULAS IMPROVED WITH SIMPLE CHANGE

Treatment of prying action in the AISC Manual and other sources traditionally have been based upon the use of $F_y$ in the calculations. At the same time, it has long been known that the resulting predictions of the equations for prying action are significantly conservative (Thornton, 1992; Swanson, 2002). To address this in a simple manner, the AISC Manual now uses $F_u$ in place of $F_y$ for prying action checks.

## 8. SINGLE-PLATE CONNECTION ECCENTRICITY CALCULATIONS REVISED

Changes in the bolt shear strength values necessitated a change in the 14th Edition AISC *Steel Construction Manual* procedures for single-plate connections. In the 13th Edition AISC Manual, the 20% bolt shear strength reduction was used as a convenient way to simplify the design of single-plate connections. That is, we knew the effect of most eccentricities was less than the 20% reduction, and we also knew that shear connections are not end-loaded and didn't need the 20% reduction. It was accepted on this basis that most eccentricities in these connections could be ignored.

The changes to the 2010 AISC Specification cut the margin on bolt strength to a 10% reduction, which no longer was enough to offset the impact of eccentricity in the connection design. As a result, eccentricity requirements re-appeared in the single-plate connection design procedures in the 14th Edition AISC Manual. Table 2 illustrates the eccentricities that are used in the design of single plate connections.

Table 2. Bolt strength levels as grouped in 2010 AISC Specification

| $n$ | Hole Type | $e$, in. | Max. $t_p$ or $t_w$, in. |
|---|---|---|---|
| 2 to 5 | SSLT | a/2 | None |
| | STD | a/2 | $d_b$/2 + 1/16 |
| 6 to 12 | SSLT | a/2 | $d_b$/2 + 1/16 |
| | STD | a | $d_b$/2 - 1/16 |

### REFERENCES

[1] AISC, 2010, *Specification for Structural Steel Buildings* (ANSI/AISC 360-11), AISC, Chicago, IL.

[2] AISC, 2011, *Steel Construction Manual*, AISC Chicago, IL.

[3] Borello, D.B., Denavit, M.D., and Hajjar, J.F., 2009, "Behavior of Bolted Steel Slip-Critical Connections with Fillers," Report No. NSEL-017, Department of Civil and Environmental Engineering, University of Illinois at Urbana-Champaign, Urbana, IL.

[4] Dusika, P. and Iwai, R., 2007, "Development of Linked Column Frame Lateral Load Resisting System," 2nd Progress Report for AISC and Oregon Iron Works, Portland State University, Portland, OR.

[5] Grondin, G, Jin, M. and Josi, G., 2007, "Slip Critical Bolted Connections A Reliability Analysis for the Design at the Ultimate Limit State," Preliminary Report prepared for AISC, University of Alberta, Edmonton, Alberta, CA.

[6] Kanvinde, A.M., Grondin, G.Y., Gomez, I.R., and Kwan, Y.K., "Experimental Investigation of Fillet Welded Joints Subjected to Out-of-Plane Eccentric Loads," *Engineering Journal,* American Institute of Steel Construction, 3rd Quarter, 2009.

[7] Muir, L.S., "Deformational Compatibility in Weld Groups." ECCS / AISC Workshop Connections in Steel Structures VI. June 23-24, 2008. Chicago, IL.

[8] Swanson, J.A., 2002, "Ultimate Strength Prying Models for Bolted T-Stub Connections," *Engineering Journal*, AISC, Vol. 39, No. 3, 3rd Quarter, pp. 136-147, AISC, Chicago, IL.

[9] Thornton, W.A., 1992, "Strength and Serviceability of Hanger Connections," *Engineering Journal*, AISC, Vol., 29, No. 4, 4th Quarter, pp. 145-149, AISC, Chicago, IL.

# COMPARATIVE DESIGN OF CERTAIN STEEL CONNECTIONS ACCORDING TO USA AND EUROPEAN PROVISIONS

Anna Marinopoulou
*Phd. Structural Engineer - CCS S.A., Greece*
*annamar @ccs.gr*

Euripidis Kardaras
*Structural Engineer, Greece*
*e-akarda @otenet.gr*

Ioannis Palamas
*Phd. Structural Engineer - CCS S.A., Greece*
*jpalamas @ccs.gr*

## ABSTRACT

The main subject of this research is the comparative presentation of different practices used in America and Europe for the design of commonly used connections, and their complete design in accordance with the provisions of the respective codes. The work focuses on the comparative presentation of the European and U.S. design codes on structural steel connections and specifically on the beam to column moment connections. Beam to column moment connections of multi story buildings are designed and checked in accordance with European and U.S. standards. Included is the design in accordance with EC3 and AISC, where either the connection configuration is identical in both cases (EC3 and AISC) or it is different practices applied in U.S. and Europe. In each case the corresponding failure ratios are calculated and conclusions concerning the most economical design are deducted.

## 1. INTRODUCTION

Beam-to-column moment connections of multi-storey steel building frames are examined. Hot-rolled sections of the European and the American industry are implemented in the examples presented herein. Specifically, a joint of IPE 450 beam section to HE 500A column section, IPE 600 beam section to HE 500A column section and W27x94 beam section to W14x311 column section are considered. For gravity and wind loads, the joints are designed with the internal forces that have been computed from the analysis. On the other hand, for the seismic applications – according to the European and the American standards – the joints are designed with the beam over-strength, as it is explained in detail further down.

## 2. CONNECTION OVER-STRENGTH DEMANDS ACCORDING TO EAK 2000 (Greek seismic code) AND AISC341

The exterior joint of a frame of a multi-storey building shown in Fig. 1, is examined. The design shear force for the connection is:

$$V_f = V_0 + V_m \tag{1}$$

The design bending moment of the connection is:

$$M_f = M_{pr} + V_f \times L_p^{'} \tag{2}$$

$$V_0 = \frac{q \times L'}{2} \qquad V_m = \frac{2M_{pr}}{L'} \qquad M_{pr} = c \times f_{yb} \times Z_{xb}$$
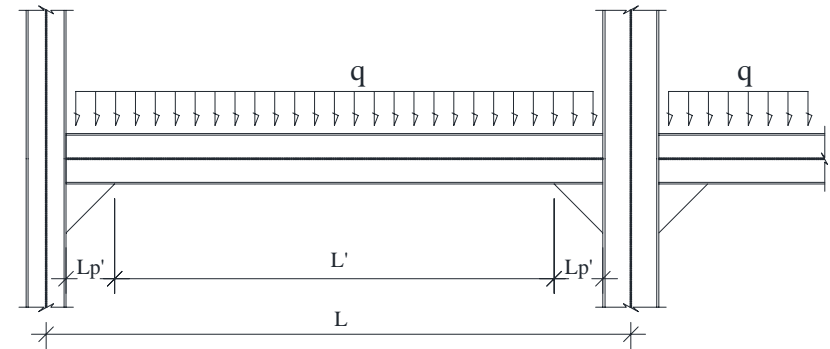


Figure 1. Frame of a multi-storey building (part elevation)

Where q: the uniformly distributed permanent and live loads compatible with seismic design, $L'$: the distance between the plastic hinges of the beam, $L_p^{'}$: the distance from the point where the plastic hinge occurs to the face of the column, c: over-strength factor, specified in the codes for connection of dissipative zones (beams) to the rest of the frame (columns). These non-dissipative connections should have sufficient over-strength to allow for the development of cyclic yielding in the dissipative parts. In this capacity design the possibility that the actual yield stress of steel is higher than the nominal value is taken into account by this material over-strength factor. $f_{yb}$: the nominal yield stress of the steel material of the beam and $Z_{xb}$: the plastic modulus of beam section.

According to EAK 2000 [2]: c =1.2 irrespective of steel grade (i.e. the same for all grades of steel).

According to AISC 341 [4, 5, 7]: c = 1.10 x $R_y$ where 1.10: factor which takes into account mainly the strain hardening of the material and $R_y$: the ratio of the expected yield stress to the specified minimum yield stress. This ratio is taken 1.10 for steel grade with yield stress $f_y$ = 50 ksi = 345 MPa and 1.50 for steel grade with $f_y$ = 36 ksi = 248 MPa. Thus c = 1.21 for steel grade with $f_y$ = 50 ksi (corresponding to the steel grade S355) and c = 1.65 for steel grade with $f_y$ = 36 ksi (approximately corresponding to the steel grade S235).

In the calculations of the following paragraphs, where certain numerical examples are examined (concerning seismic design), in case in which hot-rolled American sections are used, the corresponding American over-strength factors, described in AISC 341, are used, while in cases where hot-rolled European sections are used, then the corresponding factor 1.20, described in the Greek seismic code, is utilised. According to the European provisions, the design forces of the joint (shear force and bending moment) are significantly less for beams of steel grade S235 than those for beams of steel grade S355. For this reason, it is often quite wise to use beams from S235 steel grade (whereas the column section could be of S355 grade) in order to decrease the design forces of the joint. On the contrary, according to AISC 341, the difference in the design forces of a joint with beams of steel grade with $f_y = 36$ ksi and $f_y = 50$ ksi is insignificant. Thus, usually, the same steel grade for beams and columns is specified. This is derived quite easily by comparing the product 1.10 x $R_y$ x $f_y$ for both steel grades (for yield stress $f_y = 36$ ksi it is 1.65 x 36 = 59.4 ksi, while for $f_y = 50$ ksi it will be 1.21 x 50 = 60.5 ksi ≈59.4 ksi).

## 3. CONNECTION DESIGN ACCORDING TO EC3 / EAK 2000 AND AISC 341 SEISMIC PROVISIONS/ AISC Steel Construction Manual

### 3.1. Beam IPE 600 to column HE 500A for seismic design
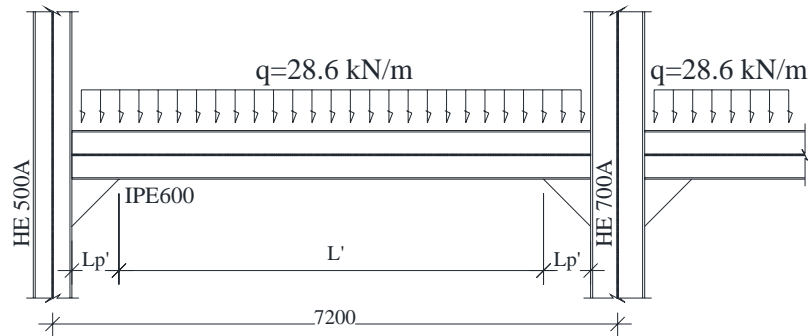


Figure 2. Frame of a multi-storey building

The exterior joint of Fig. 2 is investigated. For this beam IPE 600 / S235 – to – column HE 500A / S355 connection, the permanent and live loads compatible with seismic loading are taken 28.60 kN/m.

American connection (according to AISC):
The distance between the beam plastic hinges is:

$$L' = 7.2 - 2 \times 0.35 - 0.5 \times 0.49 - 0.5 \times 0.69 = 5.90 \ m \ .$$

The design shear force is:

$$V_f = V_0 + V_m = 28.60 \times \frac{5.90}{2} + 2 \times \frac{1.20 \times 0.235 \times 3512}{5.90} = 84 + 336 \cong 420 \ kN$$

The design bending moment of the connection is:

$$M_f = M_{pr} + V_f \times L'_p = 1.20 \times 0.235 \times 3512 + 420 \times 0.35 \cong 1137 \ kNm$$

European connection (according to EN):
The distance between the beam plastic hinges is now:

$$L' = 7.20 - 2 \times 0.83 - 0.5 \times 0.49 - 0.5 \times 0.69 = 4.95 \ m$$

different from the one calculated for the American connection, because of the larger length of stiffening. The design shear force according to EAK 2000 is:

$$V_f = V_0 + V_m = 28.60 \times \frac{4.95}{2} + 2 \times \frac{1.20 \times 0.235 \times 3512}{4.95} \cong 471 \ kN$$

and thus the hogging design bending moment is:

$$M_f = M_{pr} + V_f \times L'_p = 1.20 \times 0.235 \times 3512 + 471 \times 0.83 \cong 1382 \ kNm$$

For the positive design bending moment, we have:

$$V_f = V_m - V_0 = 401 - 71 = 330 \ kN$$

The positive design bending moment will be:

$$M_f = M_{pr} + V_f \times L'_p = 1.20 \times 0.235 \times 3512 + 330 \times 0.83 \cong 1264 \ kNm$$

American configuration (Fig. 3(α)) [3, 4, 5, 6]:
End plate: 35 x 240 x 970 (mm)
Material: S235 ($f_y$ = 235 MPa and $f_u$ = 360 Mpa)
Bolts: 2 x 8, 1" A490N – $d_{bolt}$ = 1 in. (corresponding european bolts M24 – Grade 10.9).
Beam web welds: double-sided fillet 8 mm. Flange welds: full penetration groove weld.
Height of triangular stiffener: 185 mm. Length of triangular stiffener: 320 mm
Thickness of triangular stiffener: 15 mm



(a) USA

Figure 3. Beam IPE 600 to column HE 500A connection
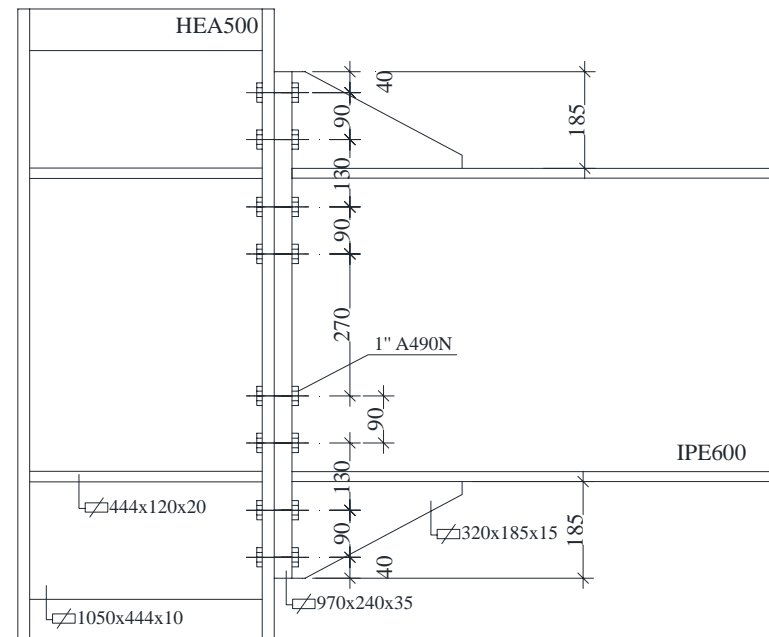
__American configuration__ (Fig. 4(α)) [3, 4, 6]:

End plate: 20 x 240 x 760 (mm)

Material: S235 ($f_y$ = 235 MPa and $f_u$ = 360 Mpa)

Bolts: 2 x 5, ¾ " A325N – $d_{bolt}$ = 3/4 in. (corresponding European bolts M20 – Grade 8.8)

Web welds: double-sided fillet 6 mm. Flange welds: double-sided fillet 10 mm.
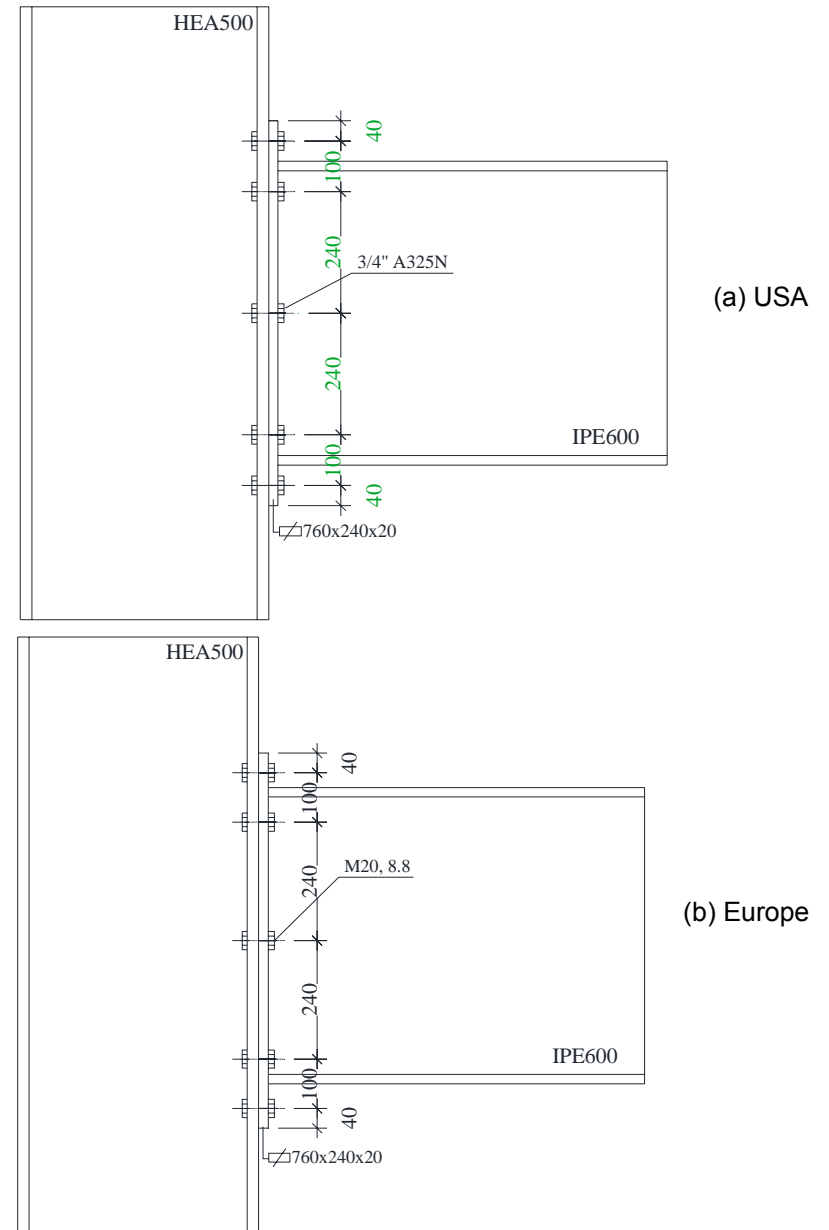


Figure 4. Beam IPE 600 to column HE 500A connection

__European configuration__ (Fig. 3(b)) [1]:

End plate: 30 x 240 x 1550 (mm)

Material: S235 ($f_y$ = 235 MPa and $f_u$ = 360 Mpa)

Bolts: 2 x 11, M27 – 10.9

Web welds: double-sided fillet 8 mm. Flange welds: double-sided fillet 12 mm.

Height and length of stiffening: 800 mm

Thickness of stiffening flange: 30 mm

Table 1. Failure ratios

| Check | AISC | EN (hogging moment) | EN (positive moment) |
|---|---|---|---|
| Bending resistance | 0.67 | 0.96 | 1.01  1.00 |

### 3.2. Beam IPE 600 to column HE 500A for gravity and wind loading

Design shear force (factored force): V = 210 kN

Design bending moment (factored force): M = 296 kNm

**European configuration** (Fig. 4(b)) [1]:
End plate: 20 x 240 x 760 (mm)
MAterial: S235 ($f_y$ = 235 MPa and $f_u$ = 360 Mpa)
Bolts: 2 x 5, M20 – 8.8
Web welds: double-sided fillet 6 mm. Flange welds: double-sided fillet 10 mm.

Table 2. Failure ratios

| Check | AISC | EN |
|---|---|---|
| Bending resistance | 0.72 | 0.86 |

### 3.3. Beam IPE 450 to column HE 500A for seismic design

The exterior joint of Fig. 5 is investigated. For this beam IPE 450 / S235 – to – column HE 500A / S355, the permanent and live loads for seismic loading are equal to 28.60 kN/m.

<u>American connection (according to AISC):</u>

Because there is no stiffening at the joint, it is assumed that the plastic hinges occur at a distance equal to 20 cm from the column flange ( $t_p + d_b/3 = 0.04 + 0.45/3 \cong 0.20\ m$ ).

The distance between the beam plastic hinges is:

$$L' = 7.2 - 2 \times 0.20 - 0.5 \times 0.49 - 0.5 \times 0.69 = 6.20\ m \,.$$

The design shear force is:

$$V_f = V_0 + V_m = 28.60 \times \frac{6.20}{2} + 2 \times \frac{1.20 \times 0.235 \times 1702}{6.20} = 243\ kN$$

The design bending moment is:

$$M_f = M_{pr} + V_f \times L'_p = 1.20 \times 0.235 \times 1702 + 243 \times 0.20 = 529\ kNm$$
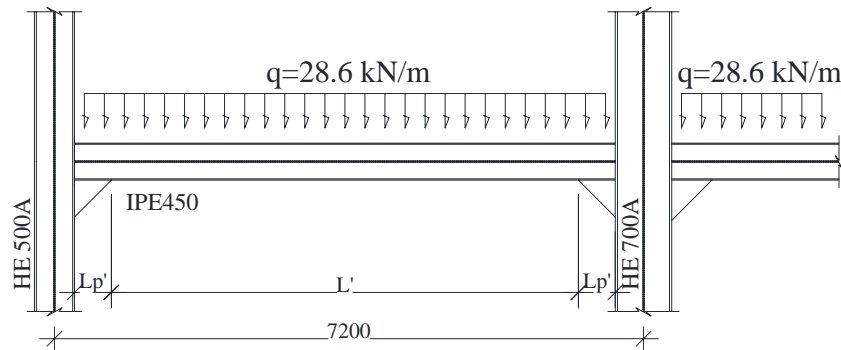


Figure 5. Frame of a multi-storey building

<u>European connection (according to EN):</u>

The plastic hinges occur at the end of stiffening: $L' = 7.20 - 0.75 - 0.85 = 5.60\ m$ .

The design shear force is:

$$V_f = V_0 + V_m = 28.60 \times \frac{5.60}{2} + 2 \times \frac{1.20 \times 0.235 \times 1702}{5.60} = 251\ kN \,.$$

The hogging design bending moment is:

$$M_f = M_{pr} + V_f \times L'_p = 1.20 \times 0.235 \times 1702 + 251 \times 0.50 = 605\ kNm \,.$$

For the positive design bending moment, we have:

$$V_f = V_m - V_0 = 171 - 80 = 91\ kN$$

and $M_f = M_{pr} + V_f \times L'_p = 1.20 \times 0.235 \times 1702 + 91 \times 0.50 = 525\ kNm$ .

<u>American configuration</u> (Fig. 6(α)) [3, 4, 5, 6]:
End plate: 40 x 230 x 670 (mm), material: S235 ($f_y$ = 235 MPa and $f_u$ = 360 Mpa).
Bolts: 2 x 4, 1 & 1/8 ” A490N – $d_{bolt}$ = 1 & 1/8 in. (corresponding European bolts: between M27 and M30 – Grade 10.9).
Beam web welds: double-sided fillet 6 mm. Flange welds: full penetration groove weld.

<u>European configuration</u> (Fig. 6(b)) [1]:
End plate: 40 x 230 x 970 (mm), material: S235 ($f_y$ = 235 MPa and $f_u$ = 360 Mpa).
Bolts: 2 x 7, M27 – 10.9.
Web welds: double-sided fillet 6 mm. Flange welds: double-sided fillet 10 mm.
Height and length of stiffening: 450 mm. Thickness of stiffening flange: 25 mm

Table 3. Failure ratios

| Check | AISC | EN (hogging moment) | EN (positive moment) |
|---|---|---|---|
| Bending resistance | 0.72 | 0.96 | 0.93 |



(a) USA

www.steelconstruct.com

Figure 6. Beam IPE 450 to column HE 500A connection

### 3.4. Beam IPE 450 to column HE 500A for gravity and wind loading

Application for gravity and wind loading
Design shear force: V = 194 kN
Design bending moment: M = 252 kNm



(a) USA



Figure 7. Beam IPE 450 to column HE 500A connection

<u>American configuration</u> (Fig. 7(α)) [3, 5, 6]:

End plate: 25 x 210 x 620 (mm), material: S235 ($f_y$ = 235 MPa and $f_u$ = 360 Mpa).
Bolts: 2 x 5, ¾ " A490N – $d_{bolt}$ = ¾ in. (corresponding European bolts M20 – Grade 10.9).
Beam web welds: double-sided fillet 6 mm. Flange welds: double-sided fillet 10 mm.

<u>European configuration</u> (Fig. 7(b)) [1]:

End plate: 20 x 210 x 620 (mm), material: S235 ($f_y$ = 235 MPa and $f_u$ = 360 Mpa).
Bolts: 2 x 5, M20 – 10.9.
Web welds: double-sided fillet 6 mm. Flange welds: double-sided fillet 10 mm.

Table 4. Failure ratios

| Check | AISC | EN |
|---|---|---|
| Bending resistance | 0.69 | 0.85 |

### 3.5. Beam W27x94 to column W14x311 for seismic design



Figure 8. Frame of a multi-storey building

www.steelconstruct.com

The exterior joint of a frame of a multi-storey building of Fig. 8 is investigated. The beam span is 28 ft, i.e. approximately 8.54 m. The column section is W14x311 and the beam section is W27x94, steel grade Gr50 with yield stress $f_y$ = 50 ksi (345 MPa) and tensile stress $f_u$ = 65 ksi (450 MPa). The permanent and live loads compatible with seismic loading are considered to be 18.6 kN/m.

<u>American connection 1</u> (extended end plate according to AISC):

The distance between the plastic hinges of the beam is:

$$L' = 8.54 - 2 \times 0.4 - 2 \times 0.5 \times 0.435 = 7.30 \ m.$$

The design shear force is:

$$V_f = V_0 + V_m = 18.6 \times \frac{7.30}{2} + 2 \times \frac{1.21 \times 0.345 \times 4556}{7.30} = 589 \ kN.$$

The design bending moment is:

$$M_f = M_{pr} + V_f \times L'_p = 1.21 \times 0.345 \times 4556 + 589 \times 0.40 = 2138 \ kNm.$$

<u>American connection 2</u> (flange plated moment connection according to AISC) [7]:

The outer joint of the previous example is considered again. According to AISC, a flange plated moment connection is utilized. This type of connection is widely used in USA. The bending moment is undertaken by the flange plates and it is transferred through them to the column. The shear force is undertaken by the web shear plate (shear tab).

After formation of plastic hinges, we consider yielding of the beam. For this reason, thick flange plates are used in order to resist and transfer the design bending moment. Bolts are allowed to slip which contributes to absorption of a significant amount of seismic energy. The plastic hinge is assumed to occur at the point of the last bolt row of the flange plates. The most distant bolt row is at a distance of 720 mm from the column flange. Therefore, the distance between the plastic hinges of the beam is equal to $L' = 8.54 - 2 \times 0.72 - 0.435 = 6.66 \ m$. The design shear force is:

$$V_f = V_0 + V_m = 18.6 \times \frac{6.66}{2} + \frac{2 \times 1.21 \times 0.345 \times 4556}{6.66} = 633 \ kN.$$

The design bending moment is:

$$M_f = M_{pr} + V_f \times L'_p = 1.21 \times 0.345 \times 4556 + 633 \times 0.72 = 2357 \ kNm$$

<u>European connection</u> (<u>according to EN</u>):

The plastic hinges occur at the end of the stiffening. The distance between the plastic hinges of the beam is $L' = 8.54 - 2 \times 0.84 - 0.435 = 6.42 \ m$. The design shear force is:

$$V_f = V_0 + V_m = 18.6 \times \frac{6.42}{2} + \frac{2 \times 1.21 \times 0.345 \times 4556}{6.42} = 652 \ kN$$

The hogging bending design moment is:

$$M_f = M_{pr} + V_f \times L'_p = 1.21 \times 0.345 \times 4556 + 652 \times 0.84 = 2450 \ kNm$$

In order to calculate the positive bending design moment, we have:

$$V_f = V_m - V_0 = 533 \ kN \quad \text{and}$$

$$M_f = M_{pr} + V_f \times L'_p = 1.21 \times 0.345 \times 4556 + 533 \times 0.84 = 2350 \ kNm$$
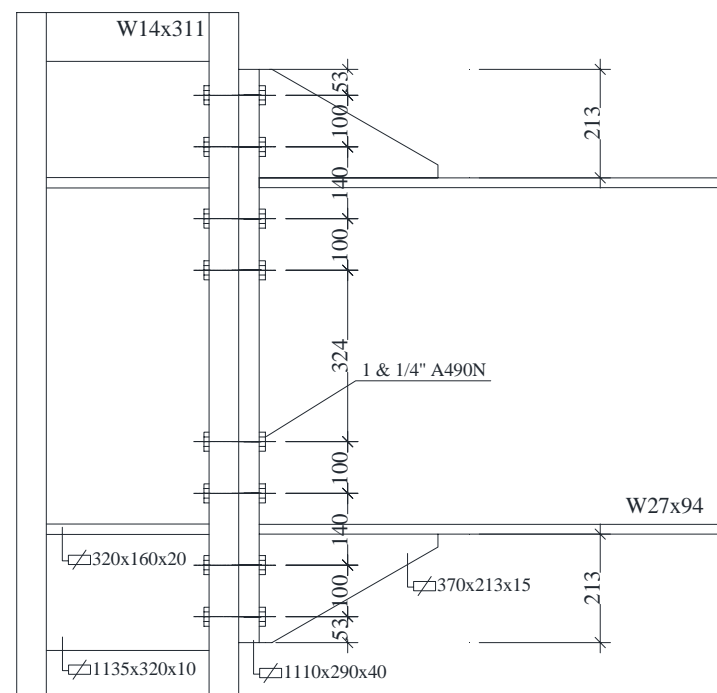


(a) USA 1
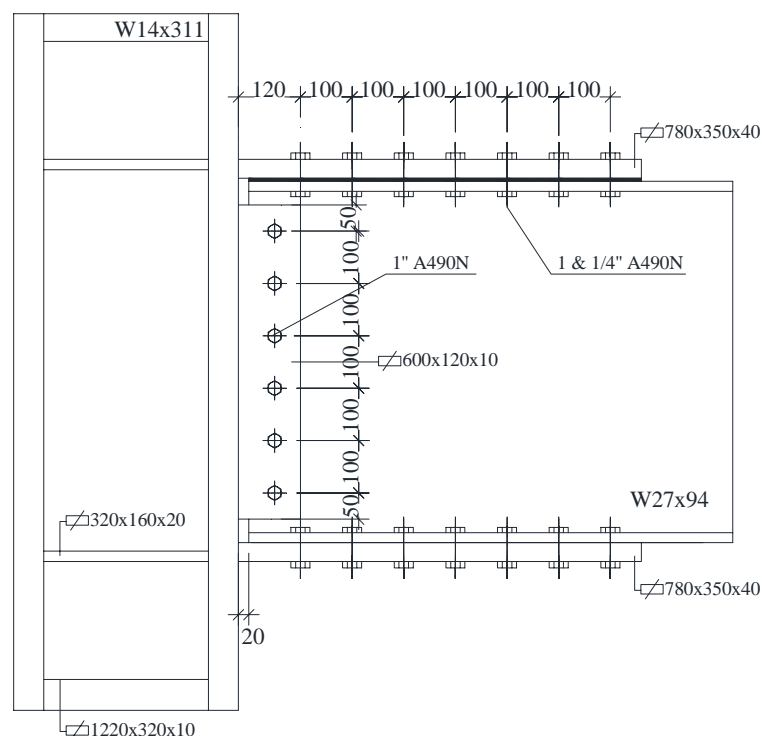


(a) USA 2
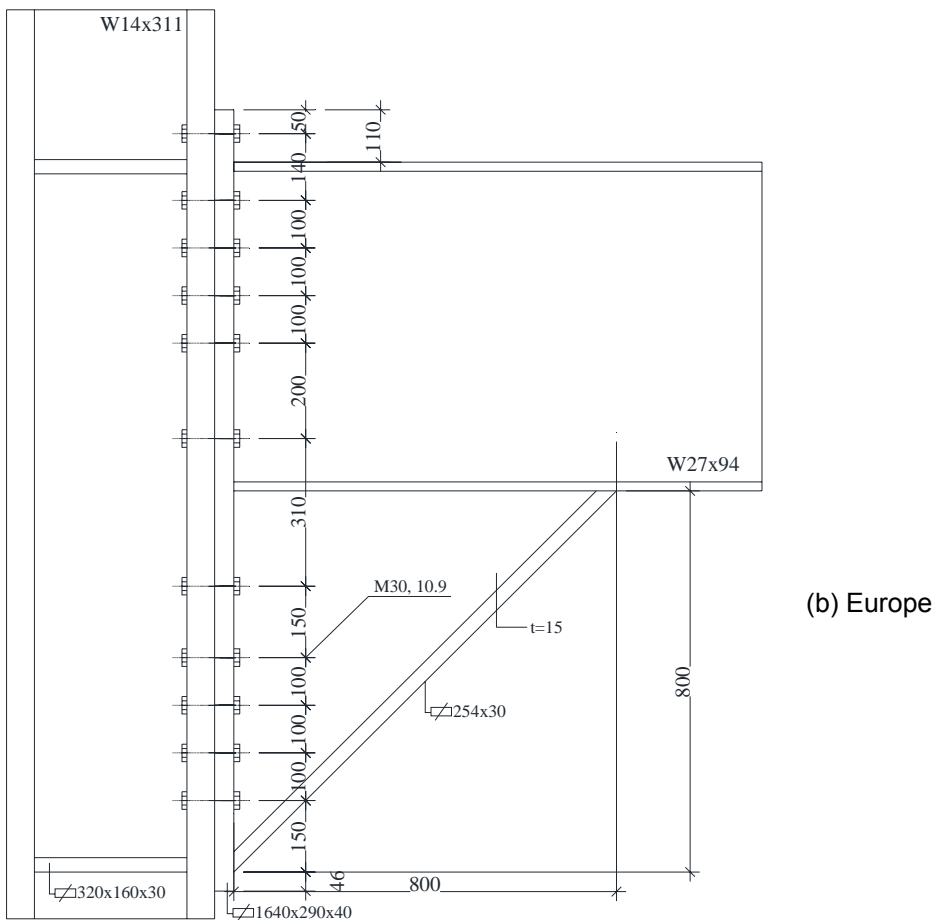
**(b) Europe**

Figure 9. Beam W27x94 to column W14x311connection

American configuration 1 (Fig. 9(α)) [3, 4, 5, 6]:

End plate: 40 x 290 x 1110 (mm), material: Grade 50 ($f_y$ = 345 MPa καί $f_u$ = 450 Mpa).
Bolts: 2 x 8, 1 ¼ " A490N – $d_{bolt}$ = 1 ¼ in. (corresponding European bolts: between M30 and M33 – Grade 10.9).
Web welds: double-sided fillet 8 mm. Flange welds: full penetration groove weld.
Height of stiffening: 213 mm. Length of stiffening: 370 mm. Thickness of stiffening: 15 mm.

American configuration 2 (Fig. 9(bβ)) [3, 4, 5, 6, 8]:

Shear plate (shear tab): 10 x 120 x 600 (mm), material: Grade 50.
Bolts: 6, 1" A490N – $d_{bolt}$ = 1 in. (corresponding European bolts M24 – Grade 10.9).
Shear tab-to-column flange welds: double-sided fillet 6 mm.
Flange plates: 40 x 350 x 780 (mm), material: Grade 50.
Bolts: 2 x 7, 1 & ¼" A490N – $d_{bolt}$ = 1 & ¼" in. (corresponding European: between M30 and M33 - 10.9).
Flange plates-to-column flange welds: full penetration groove weld.

European configuration (Fig. 9(c)) [1]:

End plate: 40 x 290 x 1640 (mm), material: Grade 50.
Bolts: 2 x 11, M30 – 10.9
Web welds: double-sided fillet 8 mm. Flange welds: double-sided fillet 12 mm.
Height and length of stiffening: 800 mm. Thickness of stiffening flange: 30 mm.

Table 5. Failure ratios

| Check | AISC (1) | AISC (2) | EN (hogging moment) | EN (positive moment) |
|---|---|---|---|---|
| Bending resistance | 0.66 | 1.00 | 0.92 | 1.01 ≈ 1.00 |

### 3.6. Beam W27x94 to column W14x311 for gravity and wind loading

Design shear force: V = 580 kN
Design bending moment: M = 1000 kNm

American configuration (Fig. 10(α)) [3, 6, 7]:

Shear plate (shear tab): 10 x 120 x 600 (mm), material: Grade 50 ($f_y$ = 345 MPa and $f_u$ = 450 Mpa).
Bolts: 6, 1" A490N – $d_{bolt}$ = 1 in. (corresponding European bolts M24 – Grade 10.9).
Shear tab-to-column flange welds: double-sided fillet 6 mm.
Flange plates: 20 x 300 x 550 (mm), material: Grade 50.
Bolts: 2 x 6, 1" A490N – $d_{bolt}$ = 1 in. (corresponding european M24, 10.9).
Flange plates-to-column flange welds: full penetration groove weld.
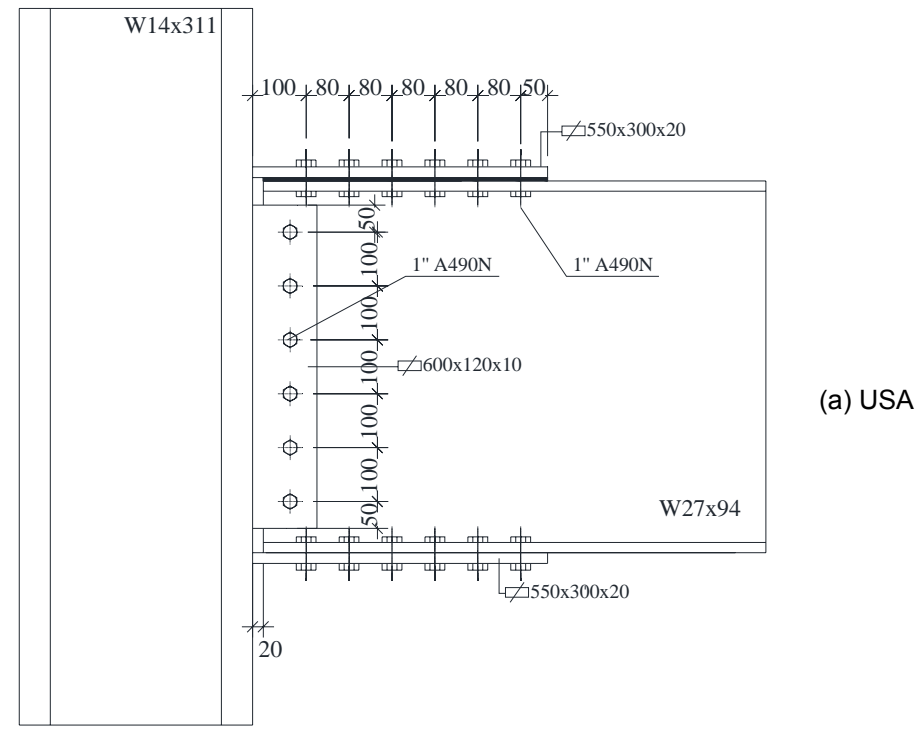


**(a) USA**
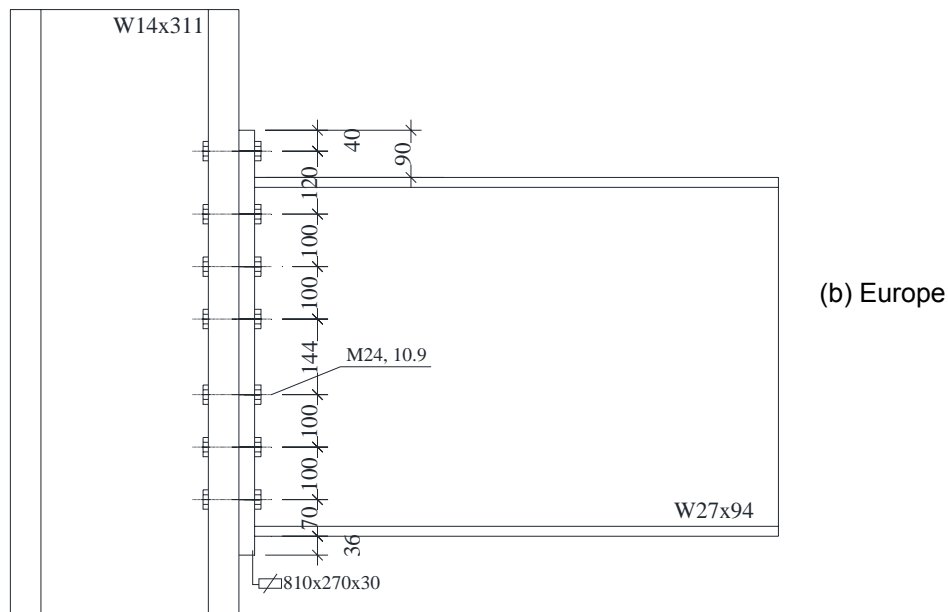
Figure 10. Beam W27x94 to column W14x311 connection

(b) Europe

W14x311

W27x94

M24, 10.9

810x270x30

European configuration (Fig. 10(b)) [1]:

End plate: 30 x 270 x 810 (mm), material: S355 ($f_y$ = 355 MPa and $f_u$ = 510 Mpa).
Bolts: 2 x 7, M24 – 10.9.
Web welds: double-sided fillet 8 mm. Flange welds: double-sided fillet 12 mm.

Table 6. Failure ratios

| Check | AISC | EN |
|---|---|---|
| Bending resistance | 0.93 | 0.91 |

## 4. CONCLUSIONS

The present investigation concludes that for the joints with end plate moment connection for gravity and wind loading, the design of the connection according to AISC and EN is quite similar. On the other hand, for end plate moment connections under seismic loading, the design was quite different in order to reflect the different practices followed in Europe and America. According to the American practice, the end plate connection (with or without stiffening) is symmetrical top and bottom, while according to the European practice the connection is not symmetrical and a triangular stiffening is added only at the bottom flange. This inevitably leads to a larger height of stiffening. Consequently, the length of the stiffening is also large, which means greater design bending moment for the connection (due to the additional moment due to shear force), and hence more bolts in general. Thus, the European connection, as used in practice, is found to be 40% more expensive (in material) compared to the American corresponding connection. It is, besides, worthy to say that the American

configuration presents less architectural problems due to the smaller stiffening at bottom flange (the stiffening at top flange is almost always covered by the concrete slab). Apart from the connection with end plate, an alternative connection configuration according to the American practice is presented. It is a connection where bolted flange plates are used. This type of connection is very popular in USA, much more than the one with end plate. This type of connection is designed for gravity and wind loading and for seismic loading also. It is proved to be more expensive in material compared to the corresponding American beam-to-column end plate connection, but it is more convenient for the erection.

This paper presents a comparison between the different practices followed in USA and Europe in the design of beam-to-column moment connections of multi-storey buildings, through specific numerical examples. Of course, it is not complete and it is considered to be just an initial investigation and assessment. More examples with the same types of connections as well as different practices also could further be examined. Moreover, it would be useful to investigate the individual checks that each standard code demands, in order that conclusions about the conservatism of the corresponding codes in the design of moment connections in USA and Europe could be drawn. Finally, this paper could also be extended further in the investigation of different types of connections other than moment connections.

## REFERENCES

[1] Eurocode 3: Design of steel structures – Part 1-8: Design of joints.
[2] EAK 2000, Greek seismic design code
[3] Steel Construction Manual, American Institute of Steel Construction, 13th Edition.
[4] AISC 341-05. Seismic Provisions for Structural Steel Buildings.
[5] AISC Steel Design Guide 4. Extended End Plate Moment Connections. 2nd edition.
[6] AISC Steel Design Guide 13. Stiffening of W-flange columns at Moment Connections: Wind and Seismic Applications.
[7] Akbar R. Tamboli. "Handbook of Structural Steel Connection Design and Details", 2nd edition. McGraw Hill, 2010.
[8] Robert Englekirk. "Steel Structures, Controlling Behavior through Design", John Wiley and Sons, 1994.
[9] Instant 2010 – Struconnect, Computer Control Systems, S.A.

# RESISTANCE TABLES FOR STANDARDIZED JOINTS IN ACCORDANCE WITH EN 1993-1-8

Klaus Weynand & Ralf Oerder
*Feldmann + Weynand GmbH, Aachen, Germany*
*k.weynand@fw-ing.de; r.oerder@ fw-ing.de*

Jean-François Demonceau
*Department ArGenCo, University of Liège, Belgium*
*jfdemonceau@ulg.ac.be*

## ABSTRACT

Publications containing resistance tables for joints in steel structures have been published in the last decades in various European countries. However, most of those publications provide joint resistances according to the design rules of national standards or according to the ENV version of Eurocode 3. The present paper refers to two new publications containing resistance tables in accordance with the new EN Eurocode 3 Part 1.8. One of these two publications is devoted to joints with open sections including simple joints and moment resistant joints. One specific type of connection is the end-plate connection with four bolts in a horizontal row. This connection type is not directly covered by EC 3. The paper describes briefly the design model for this specific type of connection which is fully in accordance with the design methods of EC 3. The second publication is of particular interest for practitioners because it is the first design tool dealing with hollow section joints in lattice structures. The paper discusses the practical impact of such resistance tables and it reports on some observations using the EC 3 design rules for hollow section joints.

## 1. INTRODUCTION

Many papers have been published to report on the background of design models to determine the structural properties of joints in steel structures according to Eurocode 3 (EC3). Also design tools, for example resistance tables, were published. However, most of those publications provide joint resistances in accordance with the design rules of national standards or the ENV version of EC3. The present paper reports on some practical issues of two new publications (Weynand and Oerder, 2012 and Weynand *et al.*, 2011) containing resistance tables in accordance with the new EN 1993 Part 1.8.

The first publication is devoted to simple joints and moment resistant joints of open sections. One type of connection is the end-plate connection with four bolts in a horizontal row. This connection type is not directly covered by EC3. For the design of such connections it was necessary to extend the existing design model. In the present paper the extended model is briefly described. The model, which is fully in accordance with the design methods of EC3, refers to the so-called T-stub approach. Therefore this approach is also summarised.

The second publication is the first design tool for the design of hollow section joints. These design tools, consisting of design resistance tables and a computer program, cover most commonly used types of joints in lattice structures.

## 2. MOMENT RESISTANT JOINTS OF OPEN SECTIONS

### 2.1. End plate connection with four bolts in a row

In Eurocode 3 Part 1-8 (EN 1993-1-8, 2005) rules for bolted end plate connections are regulated only for two bolts in each horizontal row. Especially when wide flange H-sections are used it is sometimes more economical to use four bolts in one row instead of two. The theoretical model, the so-called T-stub approach, is general and can be potentially applied to connections with four bolts per row.

### 2.2. T-stub approach

Four bolts per row instead of two significantly influence the following components:
- end-plate in bending and
- column flange in bending.

The design rules for these components are founded on the so-called "T-stub approach". This approach substitutes a tensile part of the connection by a T-stub of appropriate effective length $l_{eff}$, with the flanged bolted to a presumably infinitely rigid foundation and subject to a uniformly distributed tension force acting in the web plate (Figure 1).
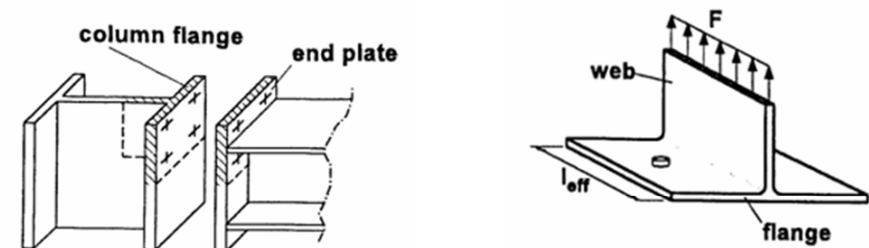


Figure 1. T-stub idealization and T-stub on a rigid foundation

In this approach, three different failure modes can appear:
1. Onset of a yield lines mechanism in the plate before the strength of the bolts is exhausted (Mode 1);
2. Mixed failure involving yield lines – but not a full plastic mechanism – in the plate and exhaustion of the bolt strength (Mode 2), and
3. Bolt fracture without prying forces, as a result of a very large stiffness of the plate (Mode 3).

The design resistance of a T-stub flange depending on the failure mode is given in the following:

$$\text{Mode 1:}\quad F_{Rd,1} = \frac{(8n - 2e_W)M_{pl,1,Rd}}{2mn - e_W(m+n)}$$

Mode 2: $F_{Rd,2} = \dfrac{2M_{pl,2,Rd} + n\sum F_{t,Rd}}{m+n}$

Mode 3: $F_{Rd,3} = \sum F_{t,Rd}$

with:

$m$      defined in Figure 2;

$n$      $= e_{min}$ as defined in Figure 1, but $n \leq 1,25m$

$e_w$      $d_w / 4$ (see Figure 2);

$\sum F_{t,Rd}$    is the sum of the design resistances of the bolts connecting the T-stub to the foundation;

$M_{pl,1,Rd}$   $= 0,25 l_{eff,1} t_f^2 f_y / \gamma_{M0}$;

$M_{pl,2,Rd}$   $= 0,25 l_{eff,2} t_f^2 f_y / \gamma_{M0}$;

$t_f , f_y$      the thickness and yield strength of the T-stub flange;

$l_{eff,1}$      minimum effective length associated to circular or non-circular patterns (see 1.1.3.);

$l_{eff,2}$      minimum effective length associated to non-circular patterns (see 1.1.3.).

As these formulas are only valid for joints with two bolts per row, new formulas for four bolts per row will be derived in 2.3.
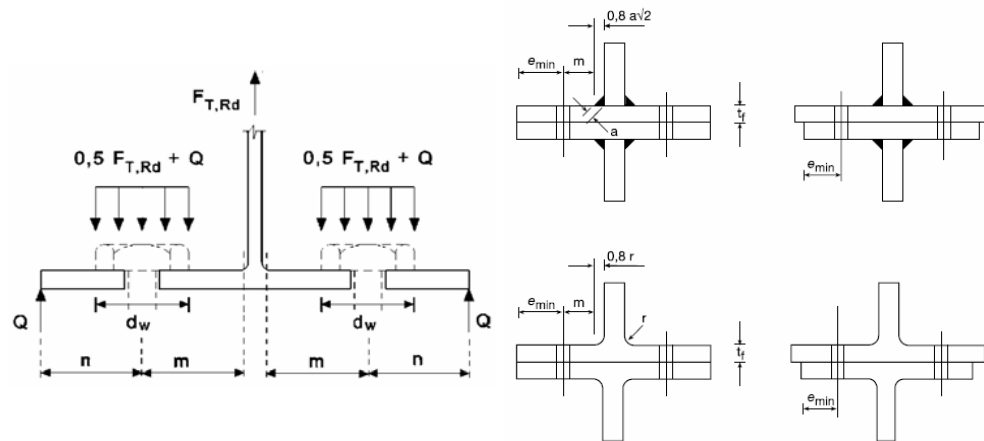


Figure 2. T-stub parameters (with two bolts)

Also the derivation of the effective lengths for joints with four bolts in a row is requested. Tables with analytical formulas are given in Eurocode 3 (EN 1993-1-8 (2005), for end-plate or column flange with two bolts per row. These effective lengths will be different if the considered bolt row is an external or inner one. Examples for formulae to predict these effective lengths are reported in 1.1.3.

## 2.3. Extension of the T-stub approach to connections with four bolts per row

### 2.3.1. General

To extend the T-stub approach to connections with four bolts in a row, both the basic formulae checking all possible failure modes as well as the determination of the effective length need to be adopted. Preliminary studies have been reported by Weynand *et al.*, 2008. A more complete description of the extend design model was present by Demonceau *et al.*, 2011.

### 2.3.2. Possible failure modes for T-stubs with four bolts

For both, T-stubs with two and T-stubs with four bolts in a row, three failure modes can appear, which are explained in the following.

Mode 1: This failure mode represents a yielding line within the T-stub in the zone between the web and the bolts which are closest to the web, as illustrated in Figure 3. The resistance of this failure mode is calculated with the same formula as for a T-stub with two bolts:

$$F_{Rd,1} = \frac{(8n - 2e_w)M_{pl,1,Rd}}{2mn - e_w(m+n)}$$

with $n = p_2 + e_2$ (see Figure 3) but $n \leq 1,25m$, $n_1 = p_2$, $n_2 = e_2$ but $n_2 \leq 1,25m + n_1$.
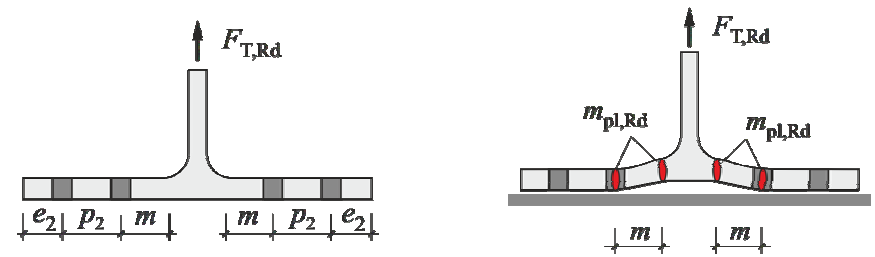


Figure 3. Failure mode 1 – Yield line plastic mechanism

Mode 2: In this failure mode two yielding lines appear. One in the T-stub web and one in the bolts closest to the web, see Figure 1. The formula for T-stubs with two bolts cannot be directly extended to the present configuration, because this failure mode is influenced by the presence of the "outer" bolts, i.e. the bolts which are the closest to the flange boundaries.

Therefore to cover this failure mode new formulas were developed. Two different situations are taken into account for T-stubs with four bolts:

Failure mode "2p": this failure mode corresponds to a non-circular pattern of the yielding lines along with the existence of prying forces Q at the T-stub boundaries:

$$F_{Rd,2,p} = \frac{2M_{pl,2,Rd} + \dfrac{\sum F_{t,Rd}}{2}\left(\dfrac{n_1^2 + 2n_2^2 + 2n_1 n_2}{n_1 + n_2}\right)}{(m + n_1 + n_2)}$$

     www.steelconstruct.com

Failure mode "2np": this failure mode corresponds to a circular or non-circular pattern for the yielding lines without prying forces at the T-stub boundaries:

$$F_{Rd,2,np} = \frac{2M_{pl,1,Rd} + \dfrac{\sum F_{t,Rd}}{2} n_1}{(m+n_1)}$$

Finally:

$$F_{Rd,2} = \min(F_{Rd,2,p}; F_{Rd,2,np})$$
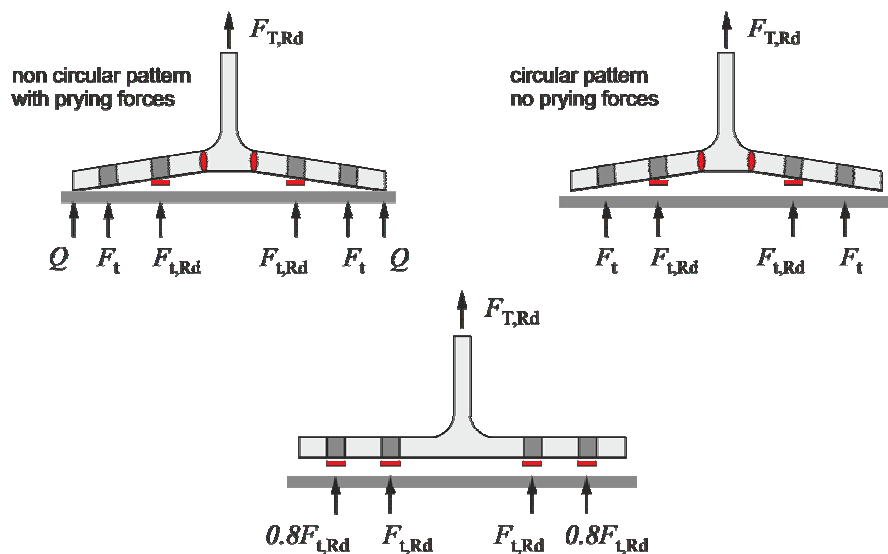


Figure 4. Mode 2 (yield lines + bolt failure) and mode 3 (failure of the 4 bolts)

Mode 3: This failure mode is similar to the one of the T-stub with two bolts. In order to derive these formulae, the T-stub flange is assumed to be a rigid body (i.e. these formulas are derived from a rigid-plastic theory). The latter may be fully justified for T-stubs with 2 bolts per row while it could possibly lead to unsafe results for T-stub with 4 bolts. When the bolts which are closest to the web reach $F_{t,Rd}$, due to the flexibility of the T-stub flange, the axial load in the other bolts could be estimated to at least 80% of $F_{t,Rd}$ (see Petersen, 1993 and Demonceau, 2011). Because of that the formula for the resistance is equal to:

$$F_{Rd,3} = \frac{\sum F_{t,Rd}}{2}(1+0.8) = 0,9 \sum F_{t,Rd}$$

### 2.3.3. Determination of the effective lengths

Because of the presence of four bolts per row new formulas for the determination of the effective lengths need to be developed. Finally, there are quite a lot of formulae to check all possible yield line patterns. The present paper does not give enough room to present the complete set of formulae. However, as an example, the formulae for effective lengths of circular and non-circular patterns of an external bolt row in the extended part of an end-plate are given hereafter.

For non-circular patterns $l_{eff,nc} = \min(l_{eff,20}; l_{eff,21}; \dots l_{eff,29})$ with $l_{eff,20}$ to $l_{eff,29}$ defined in Figure 5. For circular patterns $l_{eff,c} = \min(l_{eff,14}; l_{eff,15}; \dots l_{eff,19})$ with $l_{eff,14}$ to $l_{eff,19}$ defined in Figure 6.
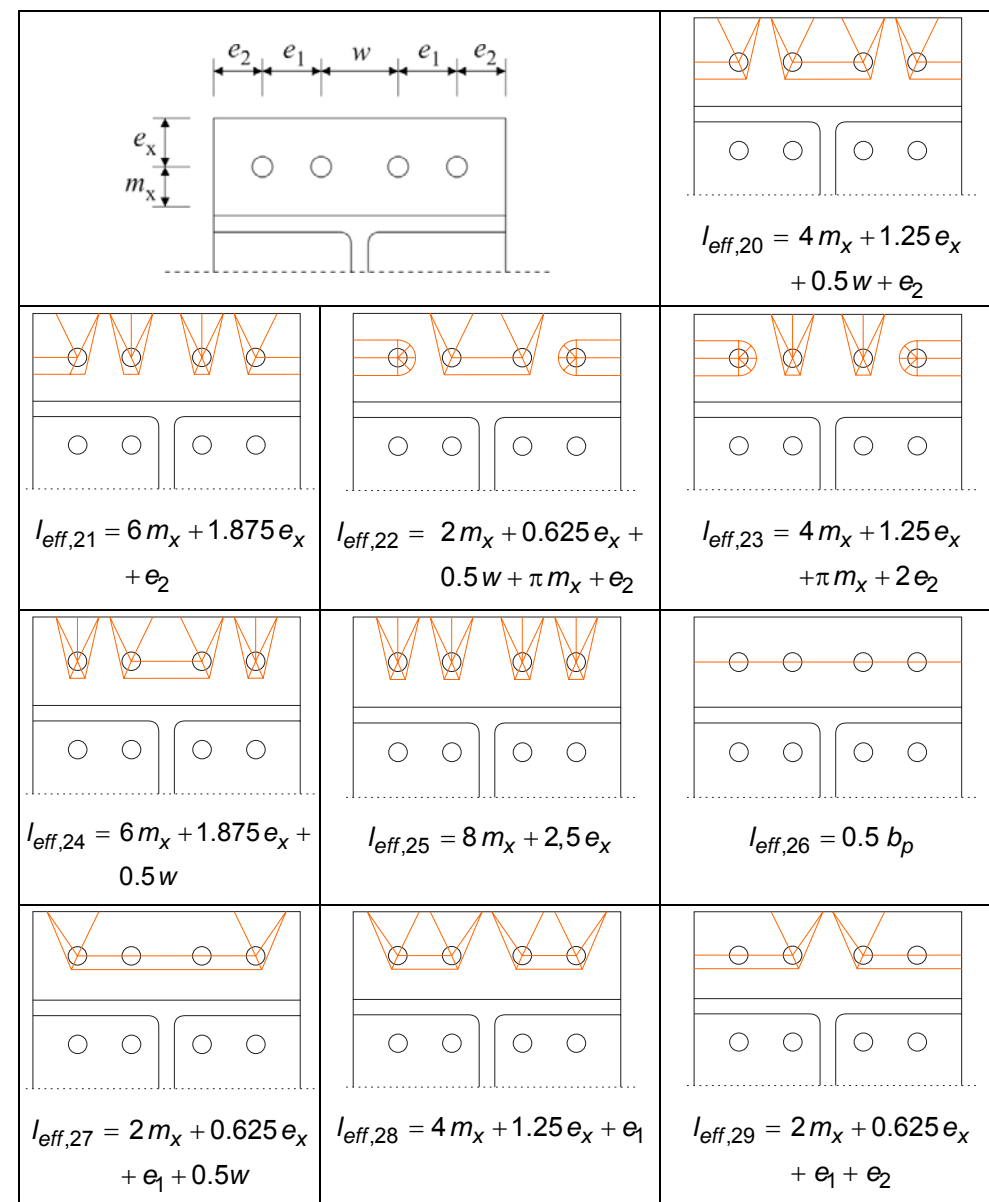


Figure 5. Non-circular yielding patterns for the external bolt row

    www.steelconstruct.com

$$l_{eff,14} = 3\pi m_x + w \qquad l_{eff,15} = 3\pi m_x + 2e_2 \qquad l_{eff,16} = \pi m_x + 2(e_1 + e_2)$$

$$l_{eff,17} = 2(\pi m_x + e_1) \qquad l_{eff,18} = \pi m_x + 2e_1 + w \qquad l_{eff,19} = 4\pi m_x$$
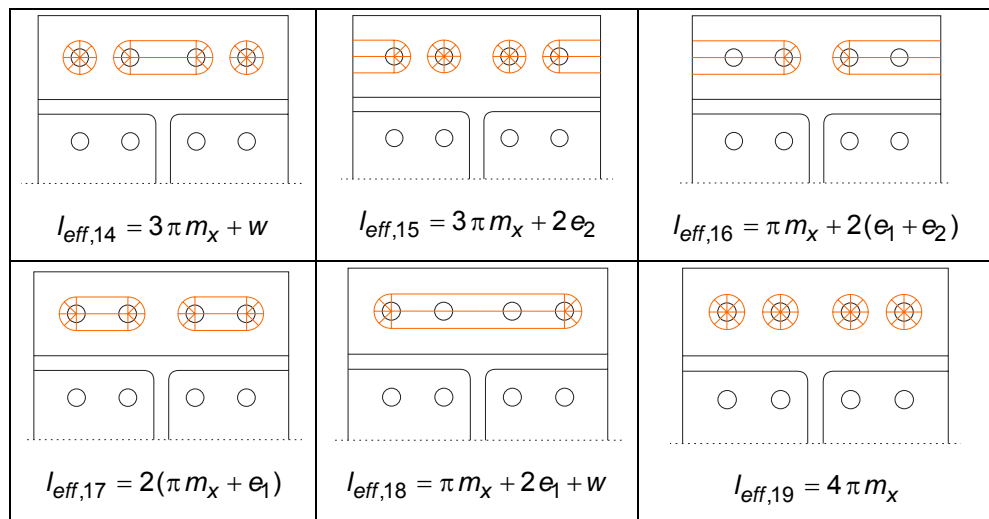
Figure 6. Circular yielding patterns for the external bolt row

## 3. SIMPLE JOINTS OF OPEN SECTIONS

### 3.1. Double web cleated connections

The ECCS publication "European Recommendations for the Design of Simple Joints in Steel Structures" (Jaspart *et al.*, 2009) provides detailed rules for the design of simple joints. Explicit rules are given for header plate connections and for fin plate connections respectively. Detailed formulae for connections with web cleats are not given. They must be deduced from those rules given for header plate and fin plate connections. Following this approach, this is quite clear and easy for most of the components which can be identified for a web cleated connection. However, the transfer of the component "header plate in bending" needs some further considerations.

For the check "header plate in bending", the header plate is modelled as a simple single-span beam with elastic stress distribution over its rectangular cross section. This model is not applicable for web cleats. In a double web cleated connection, the eccentricity of the bolts connected to the supporting member lead to a moment $M_y$, see Figure 7, resulting in compression forces in the upper part and horizontal tension forces in the lower part of the cleat. It is assumed that the compression forces will be carried by contact of the cleats to the web of the beam (Figure 8). The width of the compression zone $b_{com}$ is derived by assuming an angle $\alpha = 60°$. The height of the compression zone $h_{com}$ results from the criterion that the compression force should not exceed the yield strength of the plates (Figure 9).

The tension forces are taken by additional (horizontal) forces in the bolts of the leg connected to the supporting member (Figure 9), leading to a reduction in the vertical component of the shear force in the bolt.

The centre of compression is assumed mid height of the compression zone. An elastic distribution of the resulting horizontal forces is assumed. Hence, horizontal

forces in the bolts increase linear (Figure 9). With these assumptions and an initial guess for the height of the compression zone $h_{com}$, all forces may be determined and a more accurate value of $h_{com}$ can be found by a short iteration.

Because of the short distance from the compression zone to the supporting element side, the horizontal forces are directly absorbed by the bolts at the supporting element side (Figure 8). Torsion in the cleat and additional tying forces in the bolts on the supported element side do not arise.
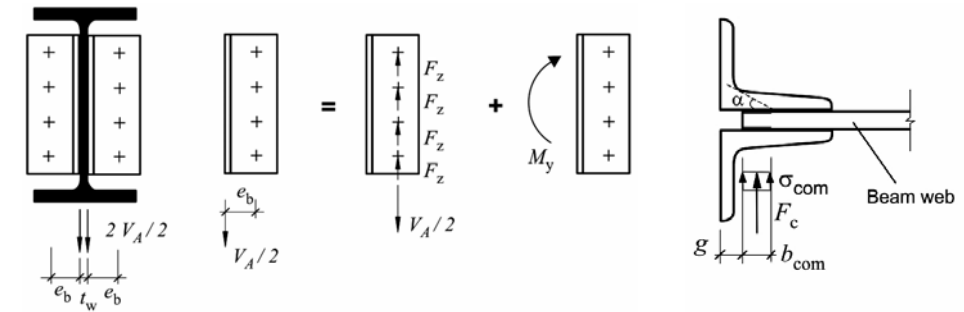


Figure 7. Forces at supporting member side



Figure 8. Compression zone
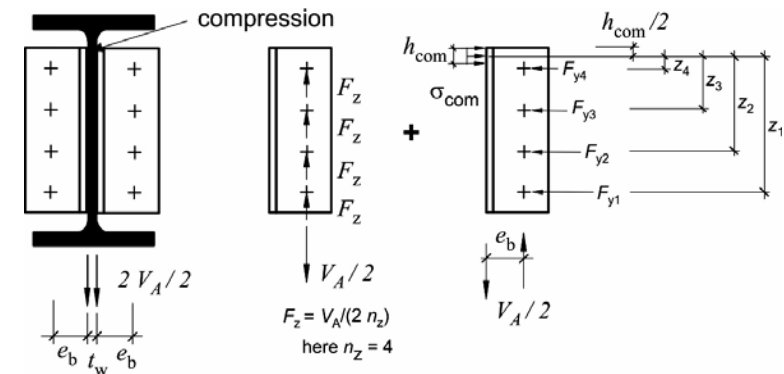


Figure 9. Forces on the supporting element side

### 3.2. Double web cleated connections with long legs

In order to avoid notched beams, a configuration with double web cleated connections with long legs may be used as shown in Figure 10. To check the "bending in the cleat" connected to the supporting member, for such a configuration, a compression zone as shown in Figure 8 may not be assumed. Hence, the cleat can rotate more freely and the moment $M_y$, see Figure 7, must be carried by the bolt pattern of the cleat legs on the supporting member. Resulting forces are shown in Figure 10. If these "bolts in shear" are the decisive component of the joint, the presence of the horizontal forces due to $M_y$ will obviously lead to a reduction of the shear resistance of the joint.
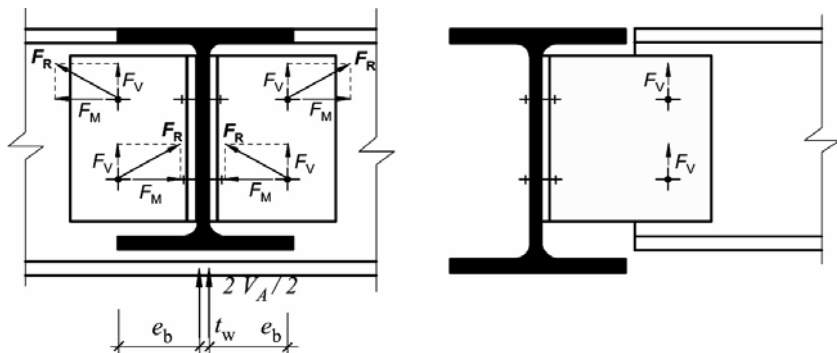
Figure 10. Forces on the supporting element side

## 4 HOLLOW SECTION JOINTS

To facilitate the use of hollow sections, an initiative has been launched to develop new design tools for the daily design practice resulting in a new publication (Weynand *et al.*, 2011). It will enable the engineer to perform design checks of joints connecting hollow sections in an easy, safe and economic manner.

Two different kinds of design tools are provided. A set of design resistance tables for standardised joints with predefined dimensions are published in a book. The resistance tables have been checked and approved by the German building authorities. In addition, software for the verification of joints with individual dimensions is available. Both, the book and the software, are available in English and German language.

With these design tools it is possible to determine the structural characteristics of hollow section joints under static loading. Joints made in typical lattice girder steel constructions and simple frames made of hollow sections are covered. The design tools for hollow section joints are strictly based on the design rules given in EC 3 including its latest corrigenda (ECCS TC 10, 2011) and the German National Annexes. Beside the design resistance, also the relevant failure mode is given.

### 4.1. Observations using the Eurocode 3 rules

Some observations resulting from an intensive and systematic use of the design rules of EN 1993-1-8 chapter 7 (hollow section joints) while developing and checking the design tools are presented hereafter.

### 4.4.1. T, X, and Y joints between RHS or CHS braces and RHS chords

In Table 7.11 of EN 1993-1-8 design axial resistances of welded T, X and Y joints between RHS or CHS braces an RHS chords are provided, see Figure 11.

For this type of joint different failure modes have to be checked. They are dependent on the width ratio $\beta = b_1/b_0$. For $\beta \leq 0.85$ the failure mode "chord face failure" is governing, while for $\beta \geq 0.85$ other failure modes have to be checked. To show the effect of the switch from one failure mode to another, Figure 12 shows resistance values for an Y joints (chord RHS 150x20, brace RHS 120x12.5, S 355, $\Theta = 37°$, $N_{0,Ed} = 0$), where $b_1$ varies between 120 mm and 135 mm, so that $\beta$

varies between 0.8 to 0.9. Relevant failure modes are indicated. A significant drop of the resistance becomes obvious at the point $\beta = 0.85$ as in the first case failure mode "chord face failure" and in the latter "brace failure" is governing.



Figure 11. Design axial resistance of welded T, X and Y joints between RHS or CHS braces an RHS chords



Figure 12. Design resistances for an Y joint

## 4.1.2. T joints between transverse plates to RHS members

Design rules for T joints between transverse plates and RHS members can be found in Table 7.13 of EN 1993-1-8. The latest corrigendum proposed by ECCS TC 10 and CIDECT (ECCS TC 10, 2011) is already taken into account in the calculations (Note: A check of chord face failure had been added).

For this type of joint, similar steps (drops or increases) in the resistance function as shown in section 0 can be found. Again, different failure modes have to be checked and they are dependent on the width ratio $\beta = b_1/b_0$ . To show the effect of the switch from one failure mode to another, Figure 13 shows resistance values for a T joint (RHS 300x20, plate 240x25 mm, S 355, $N_{0,Ed} = 7800$ kN ), where $b_1$ varies between 240 mm and 270 mm, so that $\beta$ varies between 0.8 to 0.9. Relevant failure modes are indicated. In this specific configuration the resistance curve shows two steps. The first step is an sudden increase when the governing failure mode "chord face failure" changes to "brace failure", the second step is a drop from "punching shear failure" to "chord web failure". However, in this particular example, the second step is not relevant, because the governing failure mode is "brace failure".

## 4.1.3. Summary

These examples indicate that the limiting conditions of $\beta$ in tables 7.11 and 7.13 in EN 1993-1-8 seem not to reflect the mechanical behaviour of such joints. A "step" in curve of a resistance over a specific joint parameter should not occur. It would be desirable if, in a future revision of EN 1993-1-8, such inconsistencies could be eliminated.
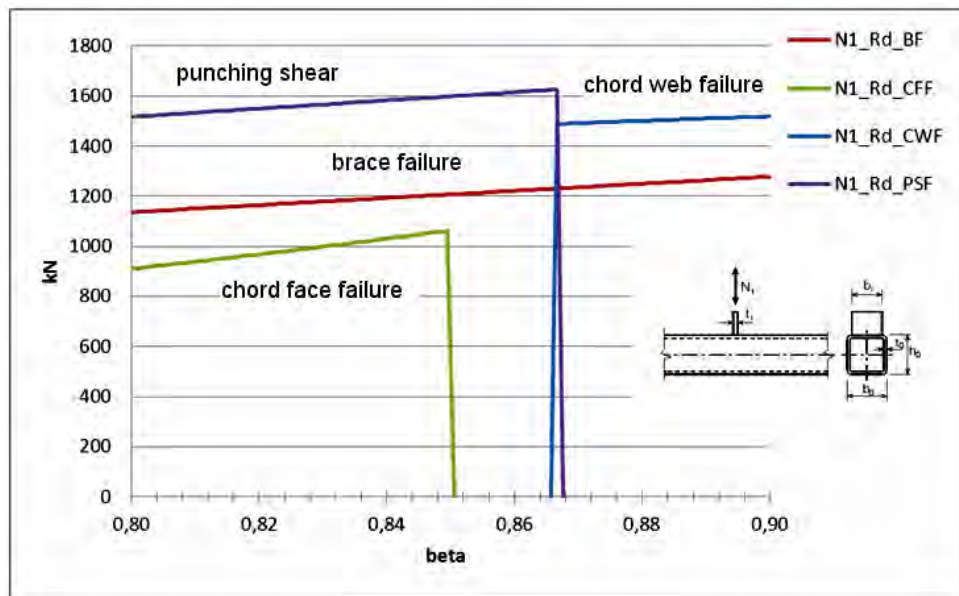


Figure 13. Design resistance

## REFERENCES

[1] Demonceau, J.-F; Jaspart, J.-P.; Weynand, K.; Oerder, R. Müller, C (2011): "Connections with Four Bolts per Horizontal Row - Application of Eurocode 3", Eurosteel 2011, August 31 - September 2, Budapest, Hungary

[2] ECCS TC 10 (2011), CIDECT comments to EN 1993-1-8 and corrigendum (EN) 1993‑1‑8:2005/AC), ECCS TC 10 Doc 723

[3] EN 1993-1-8 (2005), "Eurocode 3: Design of steel structures – Part 1-8: Design of joints". CEN - European committee for standardization

[4] Jaspart, J.-P.; Demonceau, J.-F; Renkin, S.; Guillaume, M.-L. (2009). "European Recommendations for the Design of Simple Joints in Steel Structures", ECCS Technical Committee 10, Publ. Nº 126, http://www.steelconstruct.com

[5] Jaspart, J.-P. (1997). "Contribution to recent advances in the field of steel joints. Column bases and further configurations for beam-to-column joints and beam splices". Thèse d'agrégé de l'enseignement supérieur, Liège University

[6] Petersen, Ch. (1993): "Stahlbau: Grundlagen der Berechnung und baulichen Ausbildung von Stahlbauten", Vieweg-Verlag, Braunschweig

[7] Weynand, K.; Kuck, J.; Oerder, R.; Herion, S.; Fleischer, O.; Rode, M. (2011), "Design Tools for Hollow Section Joints", published by V & M Tubes, Düsseldorf, www.vmtubes.com/cop

[8] Weynand, K.; Oerder, R. (2012), "Typisierte Anschlüsse im Stahlhochbau", 3rd edition, Stahlbau Verlags- und Service GmbH, Düsseldorf (in preparation)

[9] Weynand, K.; Klinkhammer, R.; Ungermann, D.; Schneider, S.; Oberegge, O.; Hockelmann, H.-P.; Ritterbusch, N. (2008): "Application of the EC3 design rules to end-plate connections with 4 bolts in one row", AISC/ECCS International Workshop on Connections VI, Ed. by Bjorhovde, Bijlaard, Geschinder, Chicaco, USA

[10] Weynand, K., Oerder, R. (2012), CoP - The Connection Program, Program for the design of steel and composite joints according to Eurocode, http://cop.fw-ing.de

# ON THE BEARING RESISTANCE OF BOLTED CONNECTIONS

Primož Može, Darko Beg
*University of Ljubljana, Faculty of Civil and Geodetic Engineering*
*primoz.moze@fgg.uni-lj.si, darko.beg@fgg.uni-lj.si*

## ABSTRACT

The paper presents 48 tests on the connections with bolts in bearing. Single bolts connections as well as the connections with up to six bolts positioned in the direction of loading were testes in order to obtain the evidence on bolt bearing deformation capacity and resistance. Several connection configurations including connection with bolts in single shear were tested. The bolt bearing resistance and the connection resistance are compared to Eurocode 3 design rules. Moreover, the numerical parametric study on 114 single bolt connections is presented. The results of the study are compared to the Eurocode bearing resistance formula, as well as to the new bearing resistance formula that is based on the results of high strength steel bolt bearing connections.

## 1. INTRODUCTION

In recent years the authors of this paper have studied the bolt bearing connections made of high strength steel (Može & Beg, 2010, 2011). The study revealed that the bearing resistance formula as defined in Eurocode (CEN, 2005) lacks interpretation for certain cases. It is defined by mean bearing stress in order to limit deformations and it is referred as an ultimate check. However, Eurocode does not prescribe the limit deformation. Since even a significant hole elongation is not an ultimate limit state in a strict sense, Eurocode formula is conservative if compared to the maximum bearing resistance. Such conservativeness of the Eurocode bearing formula was shown by several researchers. The current definition of bolt bearing resistance is appropriate, if the bolt bearing deformation capacity is known. Unfortunately, these data are not available (see Table 6.1 in EN 1993-1-8). Eurocode also defines the resistance of a group of fasteners (Chapter 3.7 in 1993-1-8) as the sum of the bearing resistances of the individual fasteners under certain conditions. Obviously the summation should be considered at the same bearing deformation level, but Eurocode gives only the maximum bearing resistance and not also the bearing deformation level. Moreover, it also does not provide the distribution of bearing forces on bolts in connection with several bolts. It is usually assumed that the distribution is uniform. On the contrary, the tests of high strength steel connections have shown that it may be very unequal. Due to the conservativeness of the Eurocode bearing formula or due to unequal distribution of bearing forces, an overload may result in the failure of bolts that are considered as non-ductile failures.

An extensive test programme of bolt bearing connections of different configurations was performed in order to provide answers to the open issues. Due to the limitations of the tests, the finite element simulations are necessary to complete the test results, to obtain additional data and to expand the connection database.

## 2. TEST PROGRAMME

The test programme covered tension splices with up to six bolts positioned in the loading direction (42 tests) as well as splices with two bolts in a row, positioned perpendicular to loading direction (6 tests). The connection geometries are given in Table 1. Besides the connections with bolts in double shear, also the connections with bolts in single shear (denoted by letter *s*) were tested. The selected plate thicknesses for the fabrication of the connections were 8, 12 and 16 mm in grade S235. Special attention was devoted to the actual material strengths in order to obtain tensile splices with similar strengths of the inner and outer plates. The standard tensile tests showed that all used steels were very ductile with ultimate-to-yield stress ratio higher than 1.4 and with strain at fracture exceeding 35 %. The ultimate tensile strength was in the range of 400 MPa to 450 MPa for all steel plates. The packing plate was installed between the outer plates of the connections with bolts in double shear.

Table 1. Connection geometries. The number in the name after M stands for the number of bolts in a connection (exp. M508 – 5 bolts)

| Name | $e_1/d_0$ | $p_1/d_0$ | $e_2/d_0$ | $p_2/d_0$ | $d_0$ [mm] | b [mm] | t [mm] | Bolt | Name | $e_1/d_0$ | $p_1/d_0$ | $e_2/d_0$ | $p_2/d_0$ | $d_0$ [mm] | b [mm] | t [mm] | Bolt |
|---|---|---|---|---|---|---|---|---|---|---|---|---|---|---|---|---|---|
| M101 | 1.23 | | 1.23 | | 26 | 64 | 12 | M24 | M404 | 1.23 | 2 | 2 | | 22 | 88 | 16 | M20 |
| M102 | 1.5 | | 1.23 | | 26 | 64 | 12 | M24 | M405 | 1.23 | 3 | 3.86 | | 22 | 170 | 16 | M20 |
| M103 | 2 | | 1.23 | | 26 | 64 | 12 | M24 | M405h | As M405, holes shifted so that end bolt activates first | | | | | | | |
| M104 | 1 | | 1.5 | | 26 | 78 | 12 | M24 | M405s | 1.23 | 3 | 3.86 | | 22 | 170 | 8 | M20 |
| M105 | 1.23 | | 1.5 | | 26 | 78 | 12 | M24 | M405t | 1.23 | 3 | 3.86 | | 22 | 170 | 16 | M20 |
| M106 | 1.5 | | 1.5 | | 26 | 78 | 12 | M24 | M406 | 1.23 | 3 | 2 | | 22 | 88 | 16 | M20 |
| M107 | 2 | | 1.5 | | 26 | 78 | 12 | M24 | M407 | 1.5 | 3 | 3.86 | | 22 | 170 | 16 | M20 |
| M108 | 2.5 | | 1.5 | | 26 | 78 | 12 | M24 | M408* | 2 | 3 | 3.86 | | 22 | 170 | 16 | M20 |
| M109 | 1 | | 1.5 | | 18 | 54 | 12 | M16 | M409* | 2.5 | 3 | 3.86 | | 22 | 170 | 16 | M20 |
| M110 | 1.22 | | 1.5 | | 18 | 54 | 12 | M16 | M501 | 1.5 | 2 | 3.86 | | 22 | 170 | 16 | M20 |
| M111 | 1.5 | | 1.5 | | 18 | 54 | 12 | M16 | M502 | 1.5 | 2 | 2.41 | | 22 | 106 | 16 | M20 |
| M112 | 2 | | 1.5 | | 18 | 54 | 12 | M16 | M502s | 1.5 | 2 | 3.86 | | 22 | 170 | 8 | M20 |
| M113 | 2.5 | | 1.5 | | 18 | 54 | 12 | M16 | M504 | 1.23 | 3 | 3.86 | | 22 | 170 | 16 | M20 |
| M201 | 1.5 | | 2.41 | 2.41 | 22 | 159 | 12 | M20 | M504t | 1.23 | 3 | 3.86 | | 22 | 170 | 16 | M20 |
| M202 | 2.5 | | 2.41 | 2.41 | 22 | 159 | 12 | M20 | M505 | 1.23 | 3 | 2.41 | | 22 | 106 | 16 | M20 |
| M203 | 1.5 | | 1.23 | 3.68 | 22 | 135 | 12 | M20 | M505t | 1.23 | 3 | 2.41 | | 22 | 106 | 16 | M20 |
| M204 | 2.5 | | 1.23 | 3.68 | 22 | 135 | 12 | M20 | M506 | 3 | 3 | 3.86 | | 22 | 170 | 16 | M20 |
| M205 | 1.5 | | 1.5 | 3 | 22 | 132 | 12 | M20 | M506s | 3 | 3 | 3.86 | | 22 | 170 | 8 | M20 |
| M206 | 2.5 | | 1.5 | 3 | 22 | 132 | 12 | M20 | M507 | 1.23 | 4 | 3.86 | | 22 | 170 | 16 | M20 |
| M401 | 2 | 2 | 3.86 | | 22 | 170 | 16 | M20 | M508 | 2 | 4 | 3.86 | | 22 | 170 | 16 | M20 |
| M402 | 3 | 2 | 3.86 | | 22 | 170 | 16 | M20 | M508h | As M508, holes shifted so that 2nd bolt activates first | | | | | | | |
| M403 | 4 | 2 | 3.86 | | 22 | 170 | 16 | M20 | M602 | 1.23 | 3 | 3,86 | | 22 | 170 | 16 | M20 |
| M403h | As M403, holes shifted so that end bolt activates first | | | | | | | | M602t | 1.23 | 3 | 3,86 | | 22 | 170 | 16 | M20 |
| M403s | 4 | 2 | 3.86 | | 22 | 170 | 8 | M20 | M602th | As M602t, holes shifted so that last bolt activates first | | | | | | | |
| | | | | | | | | | * 3 bolts | | | | | | | | |

They had the same thickness as the inner plate. The outer plates and the packing plates were welded together to form a fork into which the inner plate and bolts with washers were inserted, forming the splice connection. The fork (two outer plates) was denoted by MF and the inner plate was denoted by M. Bolts M16, M20 and M24, all 10.9, in standard holes were used. They were not under investigation, thus they were designed accordingly.

Two options of the connections with bolts in double shear were considered. In the first the thickness of both outer plates was equal to the thickness of the inner plate (equal axial strength and stiffness of inner and outer plates). In the second option the thickness of the outer plates was twice larger than the thickness of the inner plate. The second option is denoted by letter *t*. All connections with one and two bolts had cover plates that were twice stiffer and stronger than the inner plate. The functional fabrication tolerances were simulated at specimens designated by letter *h*, where bolt holes were shifted by 4 mm (twice the bolt hole clearance). Thus, only one bolt was carrying the bearing load for the first 4 mm of hole elongation and after that the remaining bolts activated. The geometry of the specimens was designed to cover different failure types and different distributions of bearing forces between bolts. The range of pitches, end and edge distances were selected according to EN 1993-1-8 from the minimum allowed distances to the most common ones. For the connections with more than 3 bolts the edge distance $e_2$ was limited to 85 mm due to the strength of the material and the capacity of the testing machine. The tests were carried out at a prescribed displacement rate of 2 mm/min on a testing machine with the capacity of 1 MN. A relative displacement between the inner and the cover plates was measured by two inductive displacement transducers (IDT). In five tests, the bolts were instrumented with a strain gauge embedded in a hole along the bolt shank (on bolt head side) to measure the axial deformation of the bolt. All measuring devices were connected to an external universal recording unit. The bolts were hand tightened to achieve firm contact between plates and to ensure that the load was transferred primarily by the bearing and not by friction.

## 3. TEST RESULTS

Table 2 gives information about connections' experimental resistance, type of failure and resistances calculated according to EN 1993-1-8 (bearing, net cross-section and block tear resistance).

The most typical failure modes were observed at single bolt connections (see Figure 1). The failure, commonly referred to as shear failure, was observed at the connections with edge distance $e_2$ at least equal to or larger than end distance $e_1$, while the end distance was $e_1 \leq 1.5d_0$. This failure was characterized by large hole elongation, a distinctive response curve with long yield plateau and a fracture in the shear plane. The hole elongation was the result of plastic transformation of the material in front of the bolt due to high bearing pressures. The failure of M106 resembles the splitting failure, where the plate in front of the bolts splits or bursts out due to high tension stress in the direction perpendicular to the loading on the free edge of the plate in front of the bolt. Another typical failure was net cross-section failure. The hole elongation mainly developed due to necking of the net cross-section.

Table 2. Test results and various resistances according to Eurocode

| Name | | Experiment | | | EN 1993-1-8 | | | | | | | |
| --- | --- | --- | --- | --- | --- | --- | --- | --- | --- | --- | --- | --- |
| | | Failure type | $F_{max}$ [kN] | Average force per bolt [kN] | edge bolt | | inner bolt | | $F_b$ [kN] | $F_{net}$ [kN] | $V_{eff}$ [kN] | Critical check |
| | | | | | $k_{1\ b}$ | $F_b$ [kN] | $k_{1\ b}$ | $F_b$ [kN] | | | | |
| single bolt connections | M101 | shear | 151 | 151 | 0.72 | 88 | | | 88 | 174 | | bearing |
| | M102 | net | 192 | 192 | 0.87 | 107 | | | 107 | 174 | | bearing |
| | M103 | net | 202 | 202 | 1.16 | 143 | | | 143 | 174 | | bearing |
| | M104 | shear | 125 | 125 | 0.83 | 102 | | | 102 | 239 | | bearing |
| | M105 | shear | 164 | 164 | 1.03 | 126 | | | 126 | 239 | | bearing |
| | M106 | shear | 197 | 197 | 1.25 | 153 | | | 153 | 239 | | bearing |
| | M107 | net/bearing | 283 | 283 | 1.67 | 204 | | | 204 | 239 | | bearing |
| | M108 | net | 279 | 279 | 2.08 | 255 | | | 255 | 239 | | net |
| | M109 | shear | 84 | 84 | 0.83 | 68 | | | 68 | 165 | | bearing |
| | M110 | shear | 104 | 104 | 1.02 | 83 | | | 83 | 165 | | bearing |
| | M111 | shear | 129 | 129 | 1.25 | 102 | | | 102 | 165 | | bearing |
| | M112 | net/bearing | 182 | 182 | 1.67 | 136 | | | 136 | 165 | | bearing |
| | M113 | net | 188 | 188 | 2.08 | 170 | | | 170 | 165 | | net |
| 2 bolts perpendicular to loading | M201 | block shear | 359 | 180 | 0.84 | 85 | | | 171 | 528 | 254 | bearing |
| | M202 | block shear | 493 | 246 | 1.40 | 142 | | | 285 | 528 | 349 | bearing |
| | M203 | block shear (single) | 348 | 174 | 0.87 | 89 | | | 177 | 418 | 259 | bearing |
| | M204 | partial net | 455 | 228 | 1.45 | 148 | | | 295 | 418 | 354 | bearing |
| | M205 | shear | 353 | 176 | 1.25 | 128 | | | 255 | 404 | 320 | bearing |
| | M206 | net | 469 | 235 | 2.08 | 213 | | | 425 | 404 | 415 | net |
| 4 bolts (except M408, M409 – 3 bolts) | M401 | end split | 861 | 215 | 1.67 | 224 | 1.04 | 140 | 727 | 894 | | bearing |
| | M402 | net | 902 | 225 | 2.50 | 336 | 1.04 | 140 | 951 | 894 | | net |
| | M403 | net | 941 | 235 | 2.50 | 319 | 1.04 | 133 | 904 | 850 | | net |
| | M403h | net | 1000 | 250 | 2.50 | 358 | 1.04 | 149 | 1015 | 955 | | net |
| | M403s | curling | 429 | 107 | 2.50 | 168 | 1.04 | 70 | 475 | 447 | | net |
| | M404 | net | 431 | 108 | 1.02 | 137 | 1.04 | 140 | 554 | 399 | | net |
| | M405 | end split | 965 | 241 | 1.02 | 147 | 1.88 | 269 | 831 | 955 | | bearing |
| | M405h | end split | 898 | 224 | 1.02 | 147 | 1.88 | 269 | 831 | 955 | | bearing |
| | M405s | end split/curling | 449 | 112 | 1.02 | 69 | 1.88 | 126 | 389 | 447 | | bearing |
| | M405t | net | 989 | 247 | 1.02 | 147 | 1.88 | 269 | 953 | 955 | | bearing |
| | M406 | net | 428 | 107 | 1.02 | 137 | 1.88 | 252 | 778 | 399 | | net |
| | M407 | end split/net | 1000 | 250 | 1.25 | 179 | 1.88 | 269 | 896 | 955 | | bearing |
| | M408 | end split | 877 | 292 | 1.67 | 239 | 1.88 | 269 | 747 | 955 | | bearing |
| | M409 | net | 925 | 308 | 2.08 | 266 | 1.88 | 239 | 771 | 850 | | bearing |
| 5 bolts | M501 | end split/net | 933 | 187 | 1.25 | 160 | 1.04 | 133 | 718 | 850 | | bearing |
| | M502 | net | 598 | 120 | 1.25 | 176 | 1.04 | 147 | 792 | 532 | | net |
| | M502s | net | 449 | 90 | 1.25 | 90 | 1.04 | 75 | 403 | 477 | | bearing |
| | M504 | net | 943 | 189 | 1.02 | 131 | 1.88 | 239 | 979 | 850 | | net |
| | M504t | net | 1000 | 200 | 1.02 | 147 | 1.88 | 269 | 1222 | 955 | | net |
| | M505 | net | 537 | 107 | 1.02 | 137 | 1.88 | 252 | 1030 | 507 | | net |
| | M505t | net | 621 | 124 | 1.02 | 147 | 1.88 | 269 | 1222 | 542 | | net |
| | M506 | net | 926 | 185 | 2.50 | 336 | 1.88 | 252 | 1426 | 894 | | net |
| | M506s | net | 469 | 94 | 2.50 | 168 | 1.88 | 126 | 713 | 447 | | net |
| | M507 | end split/net | 930 | 186 | 1.02 | 137 | 2.50 | 336 | 1281 | 894 | | net |
| | M508 | net | 934 | 187 | 1.67 | 224 | 2.50 | 336 | 1454 | 894 | | net |
| | M508h | net | 930 | 186 | 1.67 | 224 | 2.50 | 336 | 1454 | 894 | | net |
| 6 bolts | M602 | net | 915 | 153 | 1.02 | 137 | 1.88 | 252 | 1281 | 894 | | net |
| | M602t | net | 1041 | 174 | 1.02 | 147 | 1.88 | 269 | 1491 | 955 | | net |
| | M602th | net | 1000 | 167 | 1.02 | 147 | 1.88 | 269 | 1491 | 955 | | net |

*the capacity of the testing machine was reached

www.steelconstruct.com

shear failure | shear/splitting failure | from shear to cross-section failure | net cross-section failure

block shear | sigle bolt tear out | end splitting failure (only 3 bolts!)

necking of the net cross-section | curling of the plate
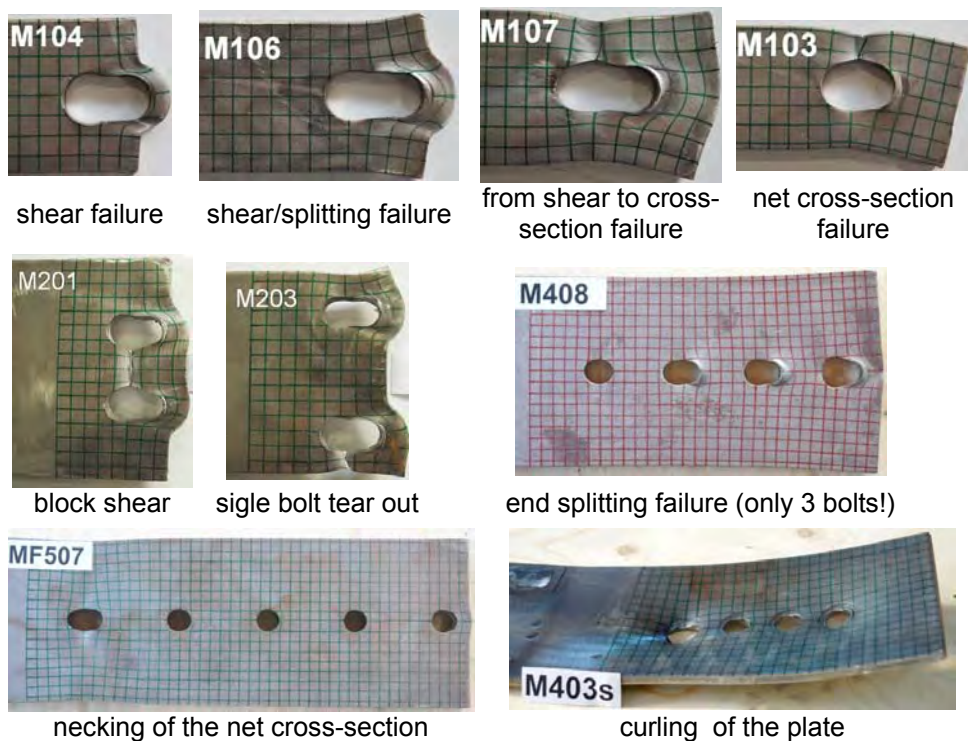
Figure 1. Failure modes

The transition from the shear failure to the net cross-section failure was very sharp, similarly as at the high strength steel connections. The failures at the transition between failure modes almost reach the net cross-section resistance, which is the maximum possible resistance for a defined width of the connection, and are typified with the highest hole elongation due to the bearing pressures and the necking of the net cross-section.

The specific failure of the connections with 2 bolts positioned perpendicular to loading is block shear failure (also referred to as block tear failure). The common type of block shear was observed at M201 (Figure 1) and M202 with both bolts tearing from the plate. M203 (Figure 1) and M204 fractured at the shorter edge of the net cross-section, showing resistance lower than net cross-section resistance and developing deformations also in the shear plane. Thus, they present a special case of the block shear failure of a single bolt, similar to the block shear of eccentrically connected angle (see Figure 3.8 in EN 1993-1-8).

The connections with more than 3 bolts positioned in a row in the direction of loading performed as expected. The bearing deformation capacity ensured the distribution of bearing forces on all bolts without significant reduction of the resistance. The connections noted with letter *h* were designed to transfer the load with a single bolt bearing for the deformation of 4 mm (twice the hole clearance) before all the remaining bolts started to bear. If the resistance of the plate in bearing was underestimated in a way that it was smaller than the shear resistance of the bolt, the bolt would

fracture in shear at low loading, before the load was distributed among all bolts. The response curves of the connections with several bolts (see Figure 2) differ from those of single bolt connections (see Figure 6). The first part of the curve is distinctively linear with a constant slope. It is followed by a short plateau, gaining plastic stiffness, and continues with a gradually decreasing slope to the displacement equalling up to 1.5 times the bolt diameter (if the net cross-section failure does not prevail). The fracture opened quickly after the maximum resistance had been achieved. Figure 2 also suggests that $d_0/6$ may correspond to an acceptable hole elongation in the serviceability limit state. The same limit was discussed for high strength steel connections (Može & Beg, 2010). The reduction of the ultimate resistance at this displacement is in relation to ratio $f_u / f_y$.
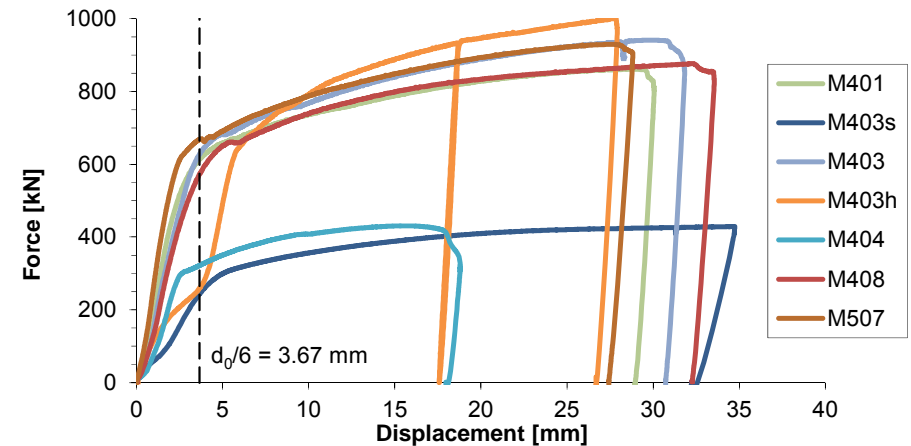


Figure 2. The response curves for selected connections

In case of net cross-section failure all hole elongations remain equal to the point, where the net cross-section fully yields. From that point on, the displacement is increasing mainly on account of necking, while the bearing pressure on bolts increases until the ultimate strength of the net cross-section is reached. The hole elongations outside the net cross-section do not need to increase much. Therefore, the deformation at the maximum resistance is less than 1.5 $d$ for M404 in Figure 2.

In case of end bolt tear out (end splitting failure) all hole elongations have to remain equal until the splitting fracture. This situation results in an increase of bearing pressures on all bolts. If the end distance $e_1$ is much smaller than the pitch $p_1$, unequal distribution of bearing forces between bolts occurs (different bearing pressure stiffness, equal displacement). This situation could result in accidental bolt fracture, since equal distribution of bearing forces is assumed in the design. Fortunately, mild steel grades have high $f_u / f_y$ ratio that acts as a fuse. With a proper design of the connection it triggers yielding of the net cross-section and thus allows high accumulation of plastic deformations in the net cross-section, preventing the splitting failure. The statement is correct only if the strain hardening of the plate in bearing is higher than in tension (in the net cross-section). This was confirmed in the tests (see MF507 in Figure 1). The connection M507 had small end distance $e_1 = 1.23 \, d_0$,

but large pitch $p_1 = 4 \, d_0$. It can be clearly seen in Figure 1 that yielding of the net cross-section prevented the tearing out of the end bolt.
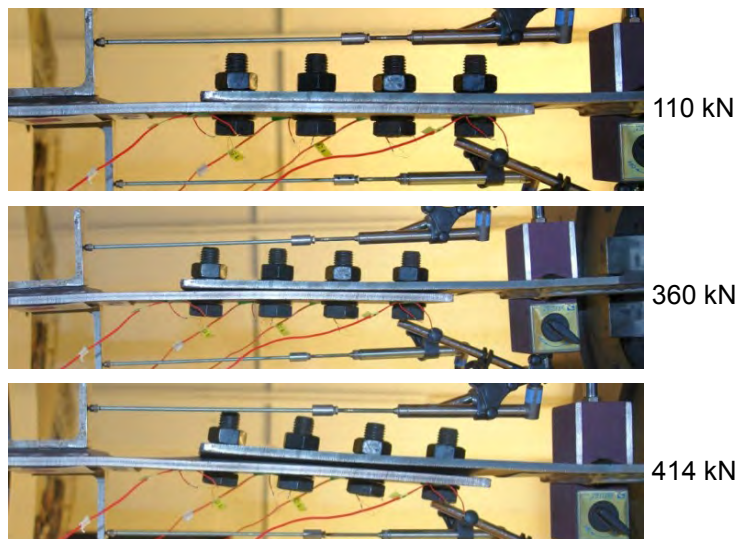


Figure 3. M405s at different level of resistance

110 kN

360 kN

414 kN



Figure 4. M403s at 424 kN

Four tests were performed on connections with four or five bolts in single shear. Soon after the force was applied to the connection, the plates bended and the bolts rotated to allow load transfer from one plate to another along the shortest path. Therefore, the bolts were subjected also to tension not only to bearing. There was no eccentricity due to clamping of the connection. Figure 3 illustrates the connection M405s at different levels of resistance. The test of M403s was stopped due to excessive curling of the plates. Figure 4 presents the connection M403s just before unloading at 424 kN (curling failure), not reaching the maximum resistance or fracture (Figure 2). Nevertheless, the connections reached their full capacity as their twin connection with bolts in double shear.

On the horizontal axis of Figure 5 a the bearing forces per bolt according to Eurocode are plotted. The vertical axis illustrates the average bearing force as a result of the test (see Table 2). The connections where the net cross-section is the critical check are not included. The results are very scattered with low correlation coefficient equalling 0.45. Most of the results are on the safe side (above the dotted line), except the bearing forces on the inner bolt (all for the end splitting failure). Figure 5b compares the Eurocode critical check (net cross-section, block tear and sum of bearing resistances) to the experimental resistance. Eurocode values of resistances are always higher than the experimental ones. The sum of bearing resistances per bolt was calculated differently, for two connection configuration. For the basic configuration two edge bolts were assumed and for the configuration with stiff outer plates (denoted by letter $t$) one bolt was considered as the edge bolt and the remaining as inner bolts.



a)

b)
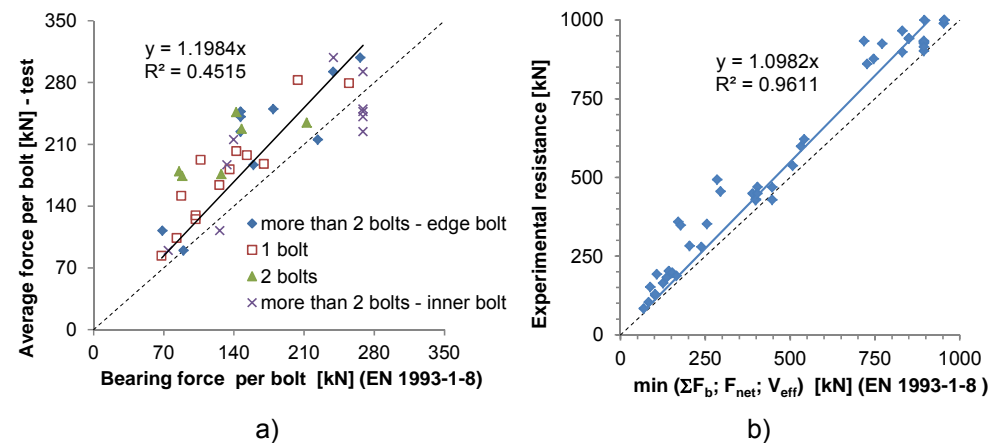
Figure 5. Test results versus resistances according to EN 1993-1-8

## 4. NUMERICAL ANALYSIS

### 4.1. Comparison to experiments results

Single bolt connections were modelled in the finite element environment ABAQUS v6.10 . They were modelled by deformable steel plate and rigid tube that presented the bolt. A "hard" surface-to-surface contact formulation in the normal direction was defined between the bolt shank and the bolt hole on the plate. The plate was meshed by linear brick finite elements with eight nodes and with incompatible modes (C3D8I). These elements were selected due to their enhanced bending behaviour. Moreover, they also preserve constant volume at large deformations. Additionally, 6-node linear triangular prisms C3D6 were used only to complete the mesh. The structural steel was modelled as an elastic–plastic material, where plasticity was considered as a polygonal approximation of the stress–strain curve, obtained from the standard tensile tests.
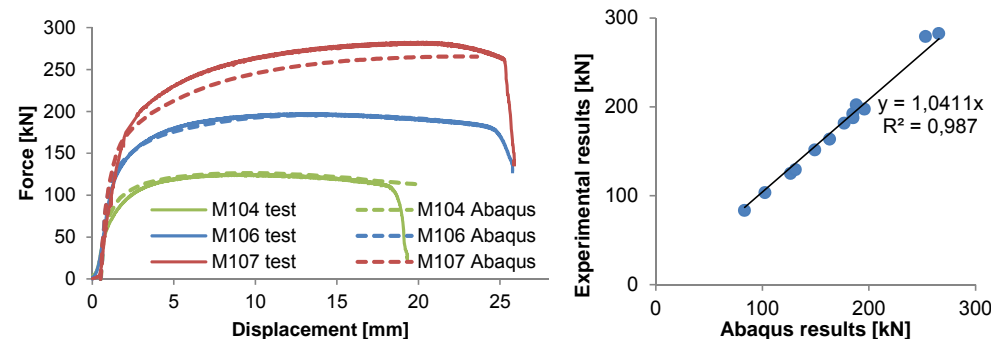


Figure 6. Comparison of numerical response curves and experimental ones

Figure 7. Comparison of numerical and experimental results

www.steelconstruct.com

For the application in the FE model the engineering material curves were then translated to the form of logarithmic strain and true (Cauchy) stress. Young's modulus was taken as $E$ = 210000 MPa and Poisson's ratio as $\nu$ = 0.3.

The tests of single bolt connections were numerically simulated in order to obtain reliable numerical results. As a consequence, the models could be used for the parametric study. In Figure 6 the experimental and numeric response curves for single bolt connections with different failure mechanisms are presented. M104, M106 and M107 have constant edge distance $e_2$, while end distance $e_1$ is increasing. It may be observed that the numerical results are in great agreement with the experimental ones. A difference is noticeable at M107 that failed in net cross-section. Similar observations are observed at the response curves for the remaining connections. Figure 7 compares maximum resistances between the numerical simulations and the tests. The correlation coefficient is 0.987 the regression coefficient 1.04. If the connections with net cross-section failures are excluded, the correlation coefficient is 0.997 and the regression coefficient drops to 1.001. It may be concluded that the results obtained by the presented numerical model are reliable.

## 4.2. Numerical parametric study

The numerical parametric study was performed in order to obtain the bolt bearing forces for single bolt connections. The study included 114 connections. The geometries of the connections in the study as well as the normalized maximum resistance $F_{max}$ and the displacement at $F_{max}$ are presented in Table 3.

The varying parameters were bolt diameter, plate thickness, end distance $e_1$ and edge distance $e_2$. For the selected normalized end distances $e_1/d_0$ = 1.2, 1.5, 2, 3 the normalized edge distance $e_2/d_0$ was varied. The minimum selected edge distance was the distance where the bolt bearing force was approximately equal to the net cross-section resistance. For the edge distances $e_2$ lower than the minimum selected, the net cross-section resistance check is critical (see Figure 8b – the net cross-section is fully yielded). The edge distance was increased until the bolt bearing force converged to the upper limit (see Figure 8a, c). The maximum resistance in Table 3 is normalized by tensile strength, plate thickness and bolt diameter. The displacement at $F_{max}$ presents the bolt hole elongation.

The results seem to be highly reliable for $e_1/d_0 \leq 2$. This may be concluded from the comparison of the numerical simulations to the experiments presented in the previous chapter. For the end distance $e_1/d_0$ = 3 and the edge distances $e_2/d_0 \geq 3$ the analysis stopped at the plateau, reaching its maximum force. The problem presented the 12 mm thick plates with bolt M24 for $e_1/d_0$ = 3 and $e_2/d_0 \geq 3$. For these connections the analysis stopped before reaching the maximum force due to convergence difficulties. The whole study was repeated with the material model that included damage initiation and damage evolution, but the results did not change much. It is expected that the bearing pressure has an upper limit due to tearing of the material in front of the bolt. Therefore, for the connections with large end and edge dimensions ($e_1 \gg d_0$ and $e_2 \gg d_0$) the bearing pressure is limited by fracture of the material or bolt shear failure. According to this study it appears that the bearing stress limit is about $3f_u$.

Table 3. The results of the numerical parametric study

| S235 $f_y$ = 313 Mpa $f_u$ = 425 Mpa | | Normalized max. bearing force $F_{max}/(d\,t\,f_u)$ | | | | | | Displacement at max. bearing force [mm] | | | | | |
|---|---|---|---|---|---|---|---|---|---|---|---|---|---|
| | | M16 $d$ = 16 mm. $d_0$ = 18 mm | | | M24 $d$ = 24 mm. $d_0$ = 26 mm | | | M16 $d$ = 16 mm. $d_0$ = 18 mm | | | M24 $d$ = 24 mm. $d_0$ = 26 mm | | |
| $e_1/d_0$ | $e_2/d_0$ | plate thickness $t$ [mm] | | | | | | plate thickness $t$ [mm] | | | | | |
| | | 8 | 12 | 16 | 8 | 12 | 20 | 8 | 12 | 16 | 8 | 12 | 20 |
| **1.2** | 1.2 | 1.26 | 1.26 | 1.26 | 1.22 | 1.23 | 1.54 | 7.3 | 7.3 | 7.3 | 10.7 | 11.1 | 11.0 |
| | 1.5 | 1.29 | 1.29 | 1.30 | 1.26 | 1.26 | 1.58 | 7.6 | 7.4 | 7.5 | 11.1 | 10.8 | 10.8 |
| | 2 | 1.36 | 1.37 | 1.37 | 1.32 | 1.33 | 1.66 | 7.8 | 7.7 | 7.7 | 10.6 | 10.3 | 10.8 |
| | 3 | 1.39 | 1.39 | 1.40 | 1.35 | 1.35 | 1.70 | 6.9 | 7.0 | 8.0 | 10.3 | 10.2 | 10.1 |
| | 5 | 1.39 | 1.40 | 1.40 | 1.35 | 1.35 | 1.70 | 7.3 | 7.6 | 7.5 | 9.9 | 10.2 | 9.9 |
| **1.5** | 1.25 | 1.67 | 1.66 | 1.66 | 1.62 | 1.63 | 2.03 | 10.5 | 11.4 | 11.2 | 14.8 | 16.2 | 15.4 |
| | 1.5 | 1.65 | 1.65 | 1.65 | 1.60 | 1.61 | 2.01 | 9.1 | 9.1 | 9.2 | 14.3 | 13.3 | 14.3 |
| | 2 | 1.71 | 1.71 | 1.72 | 1.67 | 1.67 | 2.09 | 9.2 | 9.5 | 9.5 | 13.6 | 13.8 | 14.7 |
| | 3 | 1.79 | 1.79 | 1.80 | 1.74 | 1.74 | 2.18 | 9.6 | 9.6 | 9.8 | 13.2 | 13.9 | 13.2 |
| | 5 | 1.80 | 1.80 | 1.80 | 1.75 | 1.74 | 2.19 | 9.8 | 9.8 | 9.9 | 13.0 | 13.9 | 13.2 |
| **2** | 1.5 | 2.21 | 2.21 | 2.20 | 2.16 | 2.15 | 2.69 | 14.1 | 13.9 | 13.6 | 21.2 | 21.4 | 22.1 |
| | 2 | 2.21 | 2.21 | 2.20 | 2.16 | 2.16 | 2.69 | 11.9 | 11.9 | 12.0 | 18.4 | 18.9 | 18.2 |
| | 3 | 2.33 | 2.33 | 2.32 | 2.28 | 2.26 | 2.84 | 14.7 | 14.4 | 14.3 | 20.4 | 17.6 | 20.1 |
| | 5 | 2.38 | 2.38 | 2.37 | 2.32 | 2.32 | 2.89 | 13.2 | 13.2 | 13.1 | 19.5 | 19.0 | 18.5 |
| **3** | 1.5 | 2.29 | 2.32 | 2.35 | 2.19 | 2.21 | 2.81 | 10.2 | 10.9 | 11.6 | 13.2 | 13.8 | 15.5 |
| | 2 | 3.02 | 3.03 | 3.02 | 2.95 | *2.76* | 3.71 | 20.2 | 22.1 | 23.5 | 26.4 | *17.1* | 30.0 |
| | 3 | 3.09 | 3.09 | 3.09 | 3.00 | 2.80 | 3.76 | 18.7 | 20.9 | 22.4 | 24.5 | 16.2 | 26.8 |
| | 5 | 3.21 | 3.20 | 3.22 | 3.14 | *2.83* | 3.95 | 18.5 | 19.3 | 22.2 | 25.7 | *15.7* | 29.5 |
| | 7 | 3.23 | 3.22 | 3.24 | 3.16 | *2.84* | 3.96 | 18.4 | 19.8 | 22.4 | 25.5 | *15.6* | 29.2 |
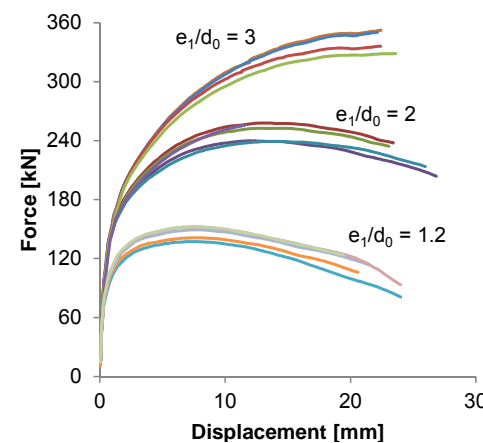


a) response curves for M16, t = 16 mm    b) connection M16, t = 8 mm, $e_1/d_0$ = 2, $e_2/d_0$ 1.5 at max. resistance
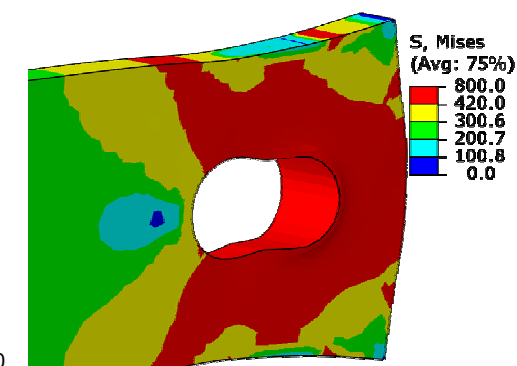
www.steelconstruct.com
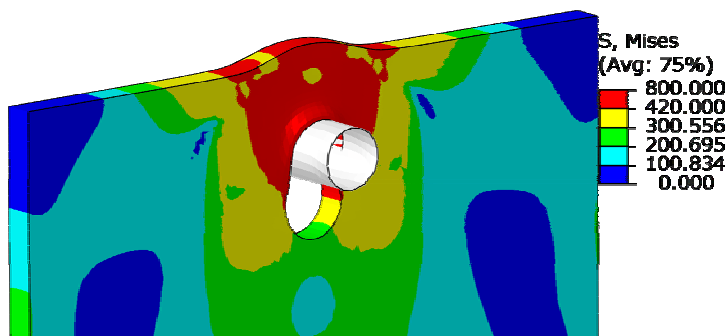
c) connection M16, t = 8 mm, $e_1/d_0 = 2$, $e_2/d_0$ 5 at max. resistance

Figure 8. The response curves of the connections with bolt M16 and 16 mm thick plate a) and Mises stress field for two selected connections

## 5. NEW DESIGN RULE

The ultimate bearing stress is presented as $k_1 k_2 f_u$, where coefficients $k_i$ are linear functions of end to edge distance ratio $e_1/e_2$ and normalized edge distance $e_2/d_0$. Written in mathematical language, it follows:

$$F_{b,new} = \max\left(k_1 k_2; k_{max}\right) \cdot d \cdot t \cdot f_u = \max\left(k_1 k_2; 2.9\right) \cdot d \cdot t \cdot f_u \qquad (1)$$

$$k_1 = \min\left(k_{11}\frac{e_1}{e_2}; k_{12}\right) = \min\left(1.3\frac{e_1}{e_2}; 1.9\right) \qquad (2)$$

$$k_2 = k_{21}\frac{e_2}{d_0} + k_{22} = 0.9\frac{e_2}{d_0} - \frac{1}{4} \qquad (3)$$

The formulation on the new formula is based on the results of the tests of single bolt connections made of steel S690 (Može & Beg, 2010). The main assumption is that the resistance of the shear planes ($A_{shear} f_u/\sqrt{3}$) in front of the bolt and the net cross-section resistance ($A_{net} f_u$) are equal. Thus, net cross-section failure becomes a function of the ratio $e_1/e_2$ and the edge distance $e_2$ and it occurs when the ratio $e_1/e_2 = 1.43$ for $e_2/d_0 = 1.2$ and converges to the ratio $e_1/e_2$ equalling 1.7 for large edge distances. This is considered in coefficient $k_1$. The upper limit of $k_1 = 1.9$ defines net cross-section failures ($e_1/e_2 = k_{12}/k_{11} = 1.9/1.3 = 1.46$). The addition to the formula presented in Može and Beg (2010) is the upper limit $k_{max} = 2.9$ of the product $k_1 k_2$. Some further test are planned to confirm this upper limit. Figure 9 illustrates the results of the new formula without an upper limit and limited to $k_{max} = 2.9$. Figure 9b compares the bearing resistance calculated according to the presented rule (filled triangles) and to Eurocode (circles) to the numerical results. It can be seen that the presented rule has higher correlation coefficient equalling 0.99 and quite lower regression coefficient.
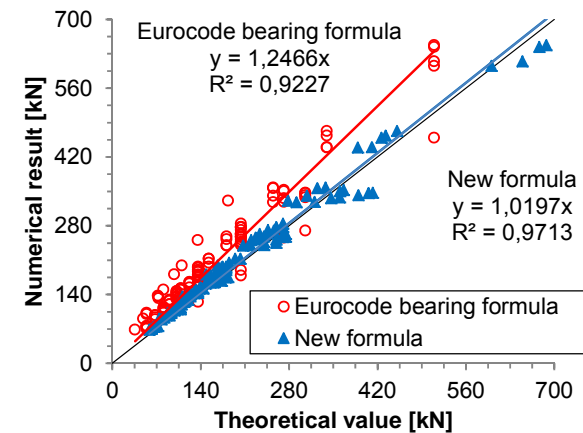


a) without upper limit of the new formula
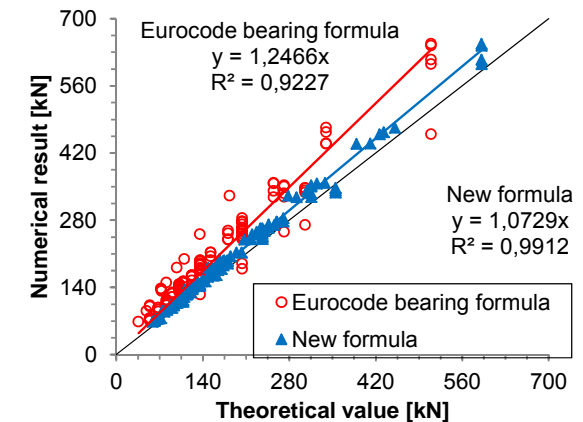


b) the new formula is limited to $k_{max} = 2.9$

Figure 9. The Eurocode bearing formula and the new formula compared to the numerical results

## REFERENCES

[1] CEN. (2005). Eurocode 3: Design of steel structures - Part 1-8: Design of joints. In EN 1993-1-8. Brussels: European Committee for Standardisation.

[2] Može, P., & Beg, D. (2010). High strength steel tension splices with one or two bolts. Journal of Constructional Steel Research, 66(8-9), 1000-1010.

[3] Može, P., & Beg, D. (2011). Investigation of high strength steel connections with several bolts in double shear. Journal of Constructional Steel Research, 67(3), 333-347.

    www.steelconstruct.com

# COLUMN-BASE PLATE JOINTS UNDER MONOTONIC LOADS: THEORETICAL AND EXPERIMENTAL ANALYSIS

Massimo Latour; Vincenzo Piluso; Gianvittorio Rizzano
*DICIV - Department of Civil Engineering, University of Salerno, Italy*
*mlatour@unisa.it; v.piluso@unisa.it; g.rizzano@unisa.it*

## ABSTRACT

In this work, within a research program aimed to set up a cyclic rotational model of base plate joints by using a mechanical model based on the so-called component approach, the evaluation of the accuracy of the component approach for predicting the monotonic behaviour of base plate joints up to failure is carried out as the first step of the planned research activity. In particular, the accuracy in predicting stiffness, resistance and overall moment-rotation curve of base plate joints by the component method given in Eurocode 3 is evaluated by means of experimental tests, recently carried out at Salerno University. Specimens have been preliminarily tested in elastic range under different values of the column axial load and, successively, tested to collapse.

The comparison between the predictions coming from the component method and the experimental tests has been extended considering not only the authors own tests, but also a significant number of available tests collected from the technical literature in order to widen the variability range of the geometrical and mechanical parameters affecting the behaviour of base plate joints.

## 1. INTRODUCTION

In the last years, following the introduction in Eurocode 3 of detailed procedures for predicting the joint rotational behaviour, the attention of researchers towards advanced modelling of steel framed structures has gradually increased. In particular, with reference to seismic design issues, more and more interest has been devoted to the study of the cyclic rotational behaviour of steel members and connections in order to develop reliable models to be successfully used in the nonlinear analysis of steel framed structures subjected to earthquakes. In addition, within the framework of most recent probabilistic approaches aimed at the evaluation of seismic reliability of structures, significant research activity has been also carried out aiming to the improvement of structural models for non-linear dynamic analyses to reduce the epistemic uncertainties due to the prediction of the cyclic behaviour of dissipative zones.

It is well known that accurate seismic non-linear analyses require an appropriate modelling of the hysteretic cyclic behaviour of steel members and connections. These models must be able to grasp with satisfactory accuracy the main phenomena characterizing the cyclic response under seismic actions, such as strength and stiffness degradation and pinching phenomena.

Regarding connections, the modelling of the rotational behaviour under monotonic loading conditions has been extensively studied both with reference to beam-to-column connections and with reference to column-base joints leading to the development of the so-called component method codified in Eurocode 3. The main advantage of the component method is its ability to allow the prediction of the rotational behaviour of different joint typologies by means of a unified approach, starting from an appropriate identification and modelling of all the sources of strength and deformability, i.e. all the components. Even though the method has been codified dealing mainly with the prediction of the stiffness and strength of the components starting from the values of their geometrical and mechanical properties, the possibility of predicting also the component ductility has been recently pointed out by several authors (Piluso *et al.*, 2001; Girão *et al.*, 2004). Therefore, it can be stated that the modelling of the whole moment-rotation curve up to collapse can also be obtained, provided that rules for predicting the ultimate deformation of the joint components are available, at least with reference to the weakest joint component which governs the ductility supply of connections.

Regarding the prediction of the joint cyclic behaviour, additional studies and experimental tests are still needed in order to develop accurate and reliable models. In particular, with reference to beam-to-column joints, some works have been recently developed towards the extension of the component method to the prediction of the cyclic behaviour (Nogueiro *et al.*, 2007; Latour *et al.*, 2008, 2011). These studies have shown that a reliable modelling of the cyclic behaviour of connections, accounting for the strength and stiffness degradation and the pinching effects, is possible, provided that an accurate modelling of the extensional (force versus displacement) behaviour of each joint component is available.

It is evident that an accurate modelling of steel frames subjected to seismic actions requires not only a reliable modelling of the cyclic behaviour of beam-to-column joints, but also an accurate modelling of the cyclic behaviour of column-base joints. Unfortunately, with reference to the cyclic behaviour of column-base joints, predicting models based on the component approach are nowadays not available in the technical literature. Therefore, within this framework, the main purpose of the research activity planned at Salerno University is the investigation and modelling of the cyclic behaviour of the base plate joints. In particular, the whole research program on this topic involves the development of the following steps:

- Step 1: theoretical and experimental study of the monotonic behaviour of base plate joints aiming to evaluate the degree of accuracy of Eurocode 3 approach for predicting the stiffness and strength of column-base connections;
- Step 2: extension of the method for predicting the ductility of beam-to-column joints, developed by the authors, to the case of base plate joints;
- Step 3: definition of new criteria for designing full-strength base plate joints with adequate overstrength to account for overstrength due material strain hardening and overstrength due to the uncertainties deriving from random material variability;
- Step 4: modelling of the cyclic behaviour of base plate joints by the component approach and definition of practical rules for designing dissipative column-base joints.

In this paper, the results gained during the first step of the research program are presented and discussed. In particular, the accuracy of the component method suggested by Eurocode 3 for predicting the stiffness and strength of column-base connections is analysed on the base of the experimental test results of Salerno University and those coming from a wide collection of tests available in the literature.

## 2. EUROCODE 3 MODEL FOR PREDICTING THE MOMENT-ROTATION CURVE

The prediction of the behaviour of base plate joint is more complex than that of beam-to-column joints due to several factors, such as the bond between the anchor bars and the concrete base material, the behaviour of the bedding mortar layer and the complex evaluation of the stiffness and resistance of the concrete below the compressed flange, due to the contact phenomena between the base plate and the concrete. In addition, also the loading process plays an important role in the behaviour of base plate joints. In the technical literature, two different types of loading process are usually adopted: the first one is characterized by a proportional loading process where the vertical load and the bending moment are proportionally increased, so that the eccentricity is constant during the loading process; conversely, the second one is characterized by a load process where the vertical load is applied in a first loading phase and, subsequently, the application of an increasing bending moment is carried out up to failure. In this case, the eccentricity is continuously increasing giving rise to an additional non-linearity source in the joint behaviour.

The application of the component method requires the development of three steps:
- Identification of the deformability and strength of components;
- Mechanical characterization of each joint component;
- Assembling of the overall joint mechanical model.

In past, several studies have been carried out to develop reliable procedures for evaluating the strength and stiffness of column-base joints (Wald, 1995; Vandegans, 1997; Steenhuis, 1998).

With reference to the procedure proposed by Eurocode 3, the sources of deformability and resistance, for a usual base plate joint of "Exposed" typology, are: the concrete in compression, the base plate in bending, the anchor bars in tension and the column flange and web in compression. This latter component is involved only in the resistance evaluation and does not provide a contribution to the joint deformability.

In case of column-base joints subjected to centred axial load, Eurocode 3 suggests to consider three compressed T-stubs located according to the column flanges and web (Figure 1a). Conversely, in case of column-base joints subjected to axial load and bending moment, a simplified approach is proposed by the code suggesting to neglect the contribution due to the web T-stub. Starting from the translational and rotational equilibrium conditions, the joint flexural resistance $M_{j,Rd}$ can be expressed as a function of the load eccentricity $e$ as follows:

low eccentricity $e < z_{c,r}$
$$M_{j,Rd} = \min\left\{\frac{F_{cl,Rd}z}{z_{c,r}/e - 1} \; ; \; \frac{F_{cr,Rd}z}{z_{c,l}/e + 1}\right\} \quad (1)$$

high eccentricity $e > z_{c,r}$
$$M_{j,Rd} = \min\left\{\frac{F_{tl,Rd}z}{1 - z_{c,r}/e} \; ; \; \frac{F_{cr,Rd}z}{z_{t,l}/e + 1}\right\} \quad (2)$$

where $F_{cl,Rd}$ is the resistance in compression of the left T-stub, $F_{cr,Rd}$ is the resistance in compression of the right T-stub, $F_{tl,Rd}$ is the resistance in tension of the left T-stub, $F_{tr,Rd}$ is the resistance in tension of the right T-stub, $z_{cl}$, $z_{cr}$, $z_{tl}$ are the distances from the column axis of the components depicted in Figure 2 and $z$ is the lever arm equal to $z_{cl}+z_{cr}$, in case of small eccentricity, and equal to $z_{tl}+z_{cr}$, in case of big eccentricity.

The resistance of the base plate in tension $F_{tl,Rd}$ can be modelled by means of an equivalent T-stub according to the well known Eurocode 3 formulations. In particular, in case of stiff base plates allowing the development of prying forces, it corresponds to the minimum value of the resistances corresponding to type 1, 2 and 3 collapse mechanisms; conversely, when the base plate is not stiff enough, it is equal to the minimum resistance given by type 1* and 3 collapse mechanisms. Therefore, the resistance of the base plate in tension can be evaluated by means of the following relationships:

with prying forces
$$F_{t,Rd} = \min\left\{\frac{(8n - 2e_w)M_{pl,1,Rd}}{2mn - e_w(m+n)}; \frac{2M_{pl,2,Rd} + n\sum F_{t,Rd}}{m+n}; \sum F_{t,Rd}\right\} \quad (3)$$

without prying forces
$$F_{t,Rd} = \min\left\{\frac{2M_{pl,1,Rd}}{m}; \sum F_{t,Rd}\right\} \quad (4)$$

where $M_{pl,1,Rd}$ is the plastic bending moment of the base plate corresponding to type 1 collapse mechanism, $M_{pl,2,Rd}$ is the plastic bending moment corresponding to type 2 collapse mechanism, $F_{t,Rd,}$ is the design resistance in tension of the anchor bars, $m$ is the distance between the plastic hinge and the bolt axis, $n$ is the extension of the contact area and $e_w$ is the washer diameter.



(a)                    (b)
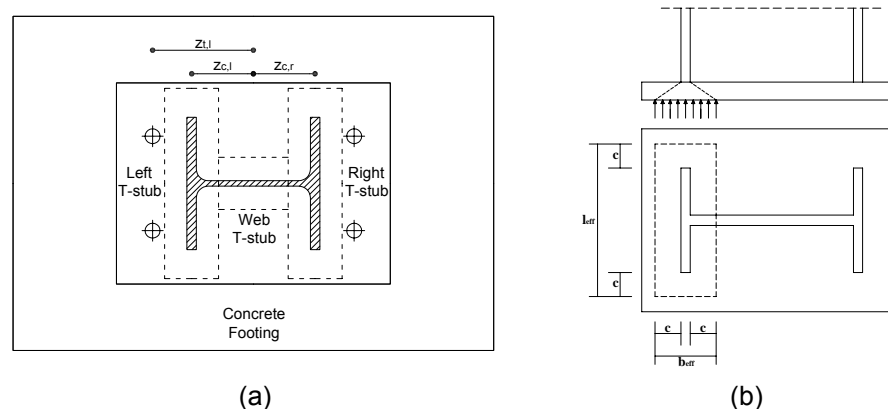
Figure 1. Eurocode 3 model

The resistance of the components in compression $F_{cl,Rd}$, $F_{cr,Rd}$ is given by the minimum value between the crash resistance of the concrete and the crash resistance of the column flange and web, as follow:

$$F_{c,Rd} = \min\left\{f_{jd}b_{eff}l_{eff}; \frac{M_{c,Rd}}{(h_c - t_{cf})}\right\} \quad (5)$$

where $f_{jd}$ is the resistance in compression of concrete under concentrated axial loads provided by Eurocode 2 as a function of the quality of the bedding mortar and of the

confinement effect due to the unloaded concrete, $b_{eff}$ and $l_{eff}$ are the effective width and length of the compressed T-stub flange (Figure 1b), $M_{c,Rd}$ is the column plastic moment accounting for the interaction with shear and axial stresses, according to Eurocode 3, $h_c$ is the column section height and $t_{cf}$ is the column flange thickness.

The rotational stiffness, according to Eurocode 3, is evaluated by means of the following relations as a function of the eccentricity (Figure 2):

$$low\ eccentricity\ e < z_{c,r} \qquad S_j = \frac{Ez^2}{\mu\left(\frac{1}{k_{c,l}} + \frac{1}{k_{c,r}}\right)} \frac{e}{e - e_k} \quad \text{where} \quad e_k = \frac{z_{c,r}k_{c,r} - z_{c,l}k_{c,l}}{k_{c,r} + k_{c,l}} \qquad (6)$$

$$high\ eccentricity\ e > z_{c,r} \qquad S_j = \frac{Ez^2}{\mu\left(\frac{1}{k_{t,l}} + \frac{1}{k_{c,r}}\right)} \frac{e}{e - e_k} \quad \text{where} \quad e_k = \frac{z_{c,r}k_{c,r} - z_{t,l}k_{t,l}}{k_{c,r} + k_{t,l}} \qquad (7)$$

where $k_{c,l}$ and $k_{c,r}$ are the stiffnesses of the components in compression, $k_{t,l}$ is the stiffness of the component in tension resulting from the axial stiffness of the base plate and that of the anchor bars, $\mu$ is a coefficient accounting for the stiffness reduction in plastic range assuming a value greater than 1 when the bending moment is greater than 2/3 of joint moment resistance. In particular, the stiffness of the components in tension and in compression are given by:

$$k_c = \frac{E_c\sqrt{b_{eff}l_{eff}}}{1.275E} \qquad (8)$$
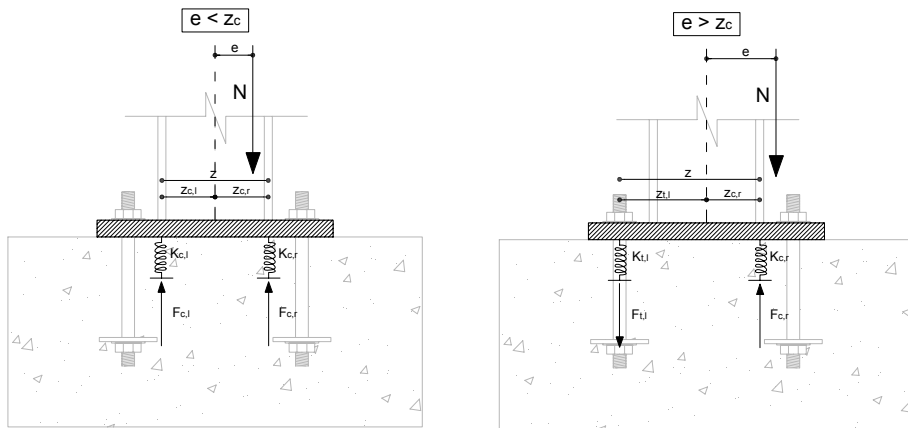


Figure 2. Mechanical model for base plate joints provided by Eurocode 3

$$with\ prying\ forces \qquad k_t = \left(\frac{m^3}{0,85 l_{eff,bp}t_{bp}^3} + \frac{L_b}{1,6A_b}\right)^{-1} \qquad (9)$$

$$without\ prying\ forces \qquad k_t = \left(\frac{m^3}{0,425 l_{eff,bp}t_{bp}^3} + \frac{L_b}{2A_b}\right)^{-1} \qquad (10)$$

where $E_c$ is the concrete modulus of elasticity, $l_{eff,bp}$ is the effective base of the T-stub in tension, $A_b$ is the anchor bar section, $L_b$ is the effective length of the anchor bar equal to the sum of the thickness of the half nut, washer, base plate, layer of mortar and eight times the diameter of the anchor bar itself.

## 3. EXPERIMENTAL TESTS

### 3.1. Test set-up

New experimental tests have been carried out at the Materials and Structures Laboratory of Salerno University by means of a specifically developed test set-up. The vertical column has been connected to a concrete base by means of a base plate joint. The concrete base is fixed to the strong floor of the laboratory by means of a reacting system constituted by two steel beams connected to the strong floor with four high resistance DYWIDAG bars properly preloaded in order to avoid the concrete base rotation (Figure 3).

The vertical axial load has been applied to the column by means of a MOOG hydraulic actuator (maximum load equal to 2000 kN) located on the top of the column and contrasted by a self-balanced system constituted by a rigid steel beam connected to the concrete base by means of two high resistance DYWIDAG bars (Figure 3). The horizontal load has been applied by means of an hydraulic actuator MTS model 243 (maximum load ±250 kN, stroke ±125 mm). The tests have been conducted under displacement control for monotonic loading conditions.

Each specimen has been initially subjected to several tests in elastic range aiming to the evaluation of rotational stiffness for different values of the applied axial load. In particular, such tests have been performed applying seven values of the axial load N equal to 1%, 2%, 3%, 4%, 10%, 15% and 20% of the column squash load. The values of the rotational stiffness have been evaluated as the secant stiffness corresponding to three values of the top displacement of the column equal to $\delta$ = 1.5, 3 and 4.5 mm which correspond to joint rotation values equal to 0.13%, 0.26% and 0.39%, respectively. Successively, a monotonic test up to failure has been carried out to investigate the whole moment-rotation curve.

During the tests, the displacement and the force of both actuators have been monitored and, in order to monitor the displacements of each joint component, 6 LVDT have been arranged according to the scheme depicted in Figure 4.

In particular, the arrangement of the transducers was selected aiming to the evaluation of the deformability of the equivalent T-stub in tension, the deformability of the concrete in compression and the elongation of the anchor bars.

Up-to-now 3 monotonic tests on the base plate joints have been carried out. The specimens are composed by HE240B and HE160A column profiles connected to a 1400x600x600 mm concrete base by means of base plates with thickness equal to 15 and 25 mm. In addition, 3 cyclic tests have been planned and are ongoing. All the steel elements, columns and plates, are made of S275 steel grade while the concrete base is made of C20/25 class. The connections between the base plate and the concrete base have been made by means of M20 threaded bars of 8.8 class. The anchor bars have been fixed to the concrete base by means of their insertion into a M24 hole having a length equal to 400 mm and their casting with a two-component resin FISV360S provided by Fischer. The bars have been successively tightened with a torque wrench applying a tightening torque corresponding to a normal stress in the bolt shank equal to 80% of the yield stress.

Figure 3. Test equipment



Figure 4. Location of LVDT transducers

The contact between the base plate and concrete was guaranteed by means of epoxy expansive mortar, Mapefill-R type, obtaining a mortar thickness equal to about 25 mm. The specimens geometrical characteristics are summarized in Table 1, with reference to the notation shown in Figure 5, where, in addition, $t_{bp}$ is the base plate thickness.

Table 1. Geometrical properties of specimens

| Specimen | bars | $t_{bp}$ [mm] | B [mm] | L [mm] | $B_0$ [mm] | $L_0$ [mm] | $e_1$ [mm] | $e_2$ [mm] | $s_f$ [mm] | $s_w$ [mm] |
|---|---|---|---|---|---|---|---|---|---|---|
| HE 240 B-15 | 6 | 15 | 340 | 500 | 90 | 380 | 80 | 60 | 10 | 8 |
| HE 240 B-25 | 6 | 25 | 340 | 540 | 80 | 440 | 90 | 50 | 10 | 8 |
| HE 160 A-15 | 4 | 15 | 280 | 335 | 160 | 245 | 60 | 45 | 8 | 6 |
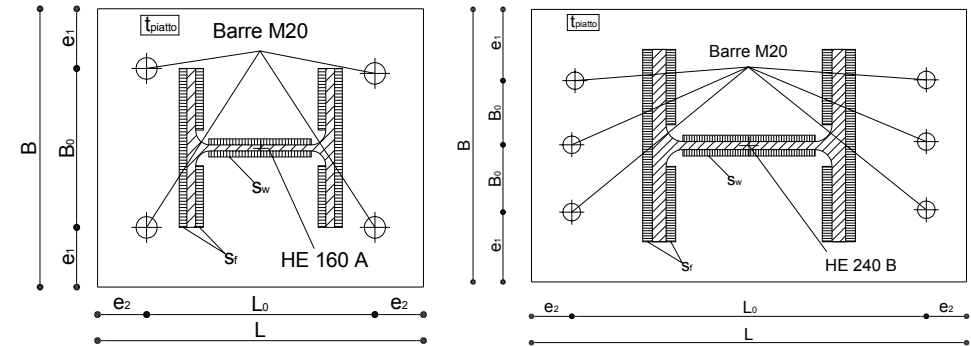


Figure 5. Definition of geometrical properties of specimens

### 3.2. Experimental results and comparison with Eurocode 3 predictions

The specimens have been designed on the basis of the formulations proposed by Eurocode 3. In particular, the base plate joints have been designed as partial-strength joints by imposing a predefined ratio between the base plate joint resistance and the column flexural strength, varying in the range 50%-100%. In particular, specimens HE240B-15 and HE240B-25 have been designed with a partial-strength degree equal, respectively, to 50% and 60%. The specimen HE 160A-15 has been tested applying, in the first loading phase, an axial load equal to 34 kN up to the rotation of 75 mrad (referred as HE16A-15-34 in the following). Successfully, it has been unloaded and then reloaded up to failure with an axial load equal to 233 kN (referred as HE160A-15-233 in the following). For this specimen, the degree of partial strength, evaluated according to Eurocode 3, is equal to 80% in the first loading phase and equal to 100% in the final phase.

Specimens HE 240B-15, HE240B-25 and HE160A-15-34 have been designed so that the weakest joint component is the base plate, while the test HE160A-15-233 has been designed by balancing the resistance of the component on the tensile side and that on the compressed side. Regarding the failure mechanisms, the experimental tests evidenced the good accuracy provided by Eurocode 3 model. In fact, in all the tests, according to the prediction, collapse has occurred due to the fracture of the base plate at the heat affected zone. Only in case of specimen HE-160A-15-233, the premature instability of the column compressed flange anticipated the fracture of the base plate.

www.steelconstruct.com
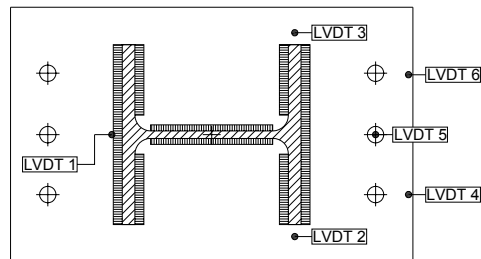
In Figure 6, the M-φ curves provided by the experimental tests are compared with those predicted by means of the application of Eurocode 3 model. A first quantitative comparison is also given in Table 2 where the ratios between the areas under the experimental curves and those under the corresponding predicted curves are evaluated. For each experimental test two values of the above ratio are shown in Table 2: the first one is evaluated considering the whole M-φ curve up to the collapse, the second one considering only the portion of the M-φ curve up to the achievement of the plastic moment. It can be observed that up to the achievement of the plastic moment, the error is equal to about 20% in average and it is mainly due to overestimation of the initial stiffness. The comparison up to failure points out that the model provides a safe side prediction, consistent with the aim of code provisions which simplify the complex non-linear response by adopting a perfectly plastic branch, so that the capture of the hardening phase is out of the scope of the codified approach.
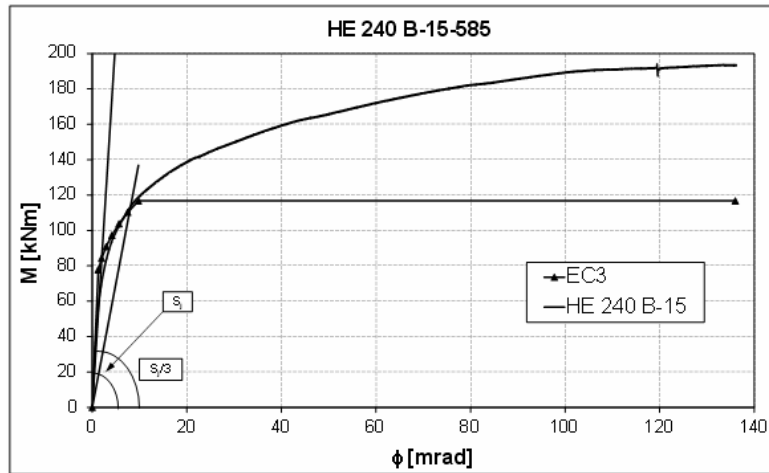


*HE 240 B - $t_{bp}$= 15 mm – N=585 kN*
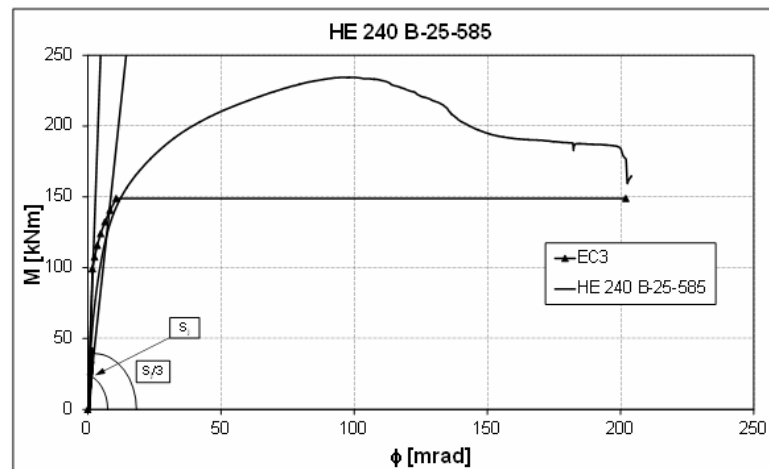


*HE 240 B - $t_{bp}$= 25 mm – N=585 kN*
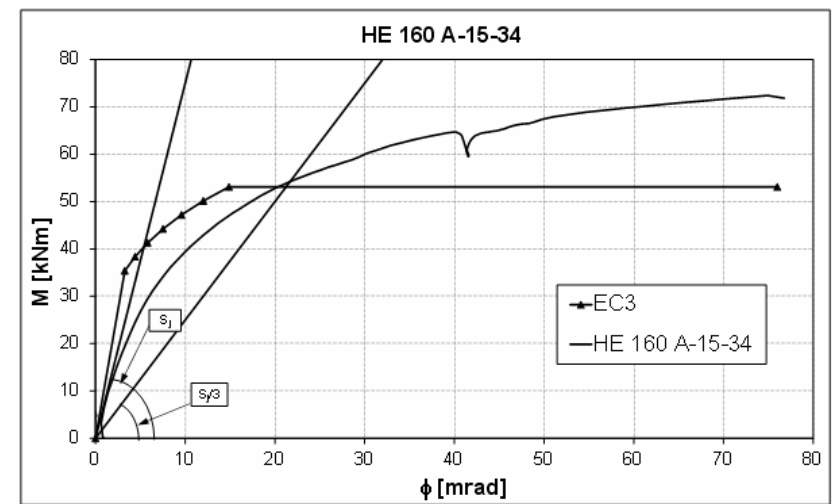


*HE 160 A - $t_{bp}$= 15 mm – N=34 kN*
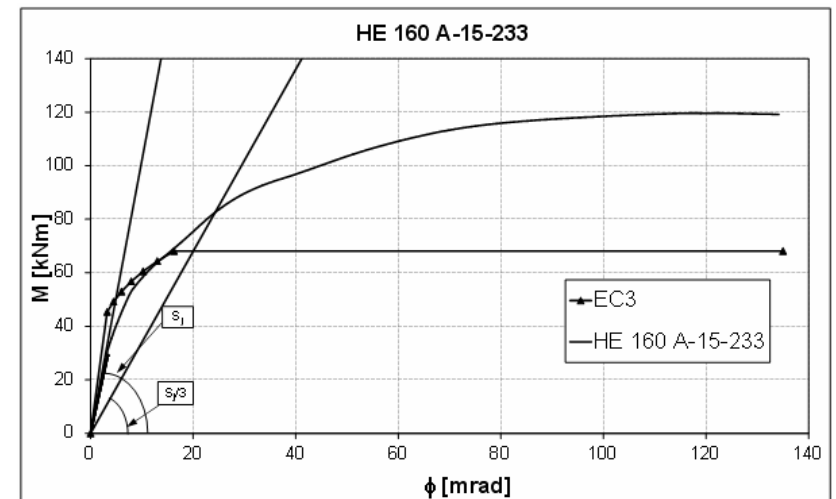


*HE 160 A - $t_{bp}$= 15 mm – N=233 kN*

Figure 6. Experimental results and comparisons with Eurocode 3 model

Table 2. Comparison between experimental results and model predictions in terms of dissipated energy

| Specimen | $E_{pl,EC3}/E_{pl,exp}$ | $E_{u,EC3}/E_{u,exp}$ |
|---|---|---|
| HE240B-15 | 1.11 | 0.75 |
| HE240B-25 | 1.34 | 0.80 |
| HE160A-15-33 | 1.31 | 0.87 |
| HE160A-15-233 | 1.10 | 0.60 |
| **average** | **1.21** | **0.76** |

## 4. ACCURACY OF EUROCODE 3 APPROACH

In order to widen the investigation dealing with the accuracy of Eurocode 3 model, a more extensive comparison with experimental results collected from the technical literature has been performed. In particular, considering only those experimental tests for which all the parameters needed for the application of Eurocode 3 approach are clearly specified, a set of 25 experimental tests have been identified (Wald et al., 1995; Vandegans, 1997; Picard et al., 1984; Latour et al., 2009). All the tests deal with base plate connections with a number of bolts in the tension zone ranging from 1 to 3. The considered set includes column-base joints with anchor bars both outside and inside the column flanges. The column profiles are double T profiles, whose height ranges between 100 and 220 mm, and tubular profiles whose size is equal to 150 mm. The anchors bars are made both with "washer plate" and "end hooks" and are characterized by diameter ranging between M20 and M24 with resistance classes equal to 4.6, 8.8 and 10.9. The range of plate thickness is quite large varying between 10 and 30 mm.

For each experimental test, the flexural resistance and the initial stiffness have been evaluated both for proportional and for non-proportional loading processes. In cases of non-proportional loading, the evaluation of the initial stiffness has been performed considering the eccentricity corresponding to 2/3 of the ultimate moment. In Tables 3-4 and in Figure 7 the experimental values of stiffness and moment resistance are compared with those predicted by means of Eurocode 3. Regarding the evaluation of the experimental value of the flexural resistance, according to Eurocode 3 approach, a conventional value has been considered as described in Figure 8.

The comparison with the experimental tests shows that the Eurocode 3 model provides sufficient accuracy in predicting flexural resistance, giving an average value of the ratio predicted/experimental value equal to 0.89, with a standard deviation equal to 0.24. Conversely, the stiffness prediction is less accurate providing a moderate overestimation. Such drawback is also pointed out by the results of the tests carried out at different values of eccentricity.

Table 3. Comparison experimental versus Eurocode 3 prediction for resistance

| Specimen | $M_{EC3}$ [kNm] | $M_{exp}$ [kNm] | $\frac{M_{EC3}}{M_{exp}}$ | Specimen | $M_{EC3}$ [kNm] | $M_{exp}$ [kNm] | $\frac{M_{EC3}}{M_{exp}}$ | Specimen | $M_{EC3}$ [kNm] | $M_{exp}$ [kNm] | $\frac{M_{EC3}}{M_{exp}}$ |
|---|---|---|---|---|---|---|---|---|---|---|---|
| W7-4.20-110 | 60,4 | 82,3 | 0,73 | Pic.Beau. 1F | 15,0 | 17,0 | 0,88 | Pic.Beau. 13F | 47,3 | 50,0 | 0,95 |
| W8-4.20-0 | 44,9 | 55,0 | 0,82 | Pic.Beau. 2F | 15,0 | 18,0 | 0,83 | Pic.Beau. 14CF | 72,0 | 95,0 | 0,76 |
| W9-4.20-0 | 44,9 | 55,0 | 0,82 | Pic.Beau. 3F | 15,0 | 18,0 | 0,83 | Pic.Beau. 15CF | 71,8 | 105,0 | 0,68 |
| S220-010 | 41,4 | 58,3 | 0,71 | Pic.Beau. 5CF | 27,9 | 45,0 | 0,62 | HE 240 B-15 | 116,7 | 116,0 | 1,01 |
| S220-040 | 66,0 | 56,6 | 1,17 | Pic.Beau. 8F | 46,4 | 39,0 | 1,19 | HE 160 A-15-34 | 53,1 | 54,2 | 0,98 |
| S220-150 | 74,4 | 112,0 | 0,66 | Pic.Beau. 9F | 46,4 | 38,0 | 1,22 | HE 160 A-15-233 | 68,1 | 83,0 | 0,82 |
| S220-190 | 59,8 | 68,0 | 0,88 | Pic.Beau. 10CF | 69,2 | 71,2 | 0,97 | HE 240 B-25 | 148,9 | 129,0 | 1,15 |
| S140-010 | 23,5 | 40,0 | 0,59 | Pic.Beau. 11CF | 69,2 | 71,2 | 0,97 | | | | |
| S140-100 | 31,7 | 32,0 | 0,99 | Pic.Beau. 12F | 47,3 | 50,0 | 0,95 | | | | |

**Legend:** W (Wald et al., 1995); S (Vandegans, 1997);
Pic.Beau. (Picard and Beaulieu, 1984);
HE (Latour et al. 2009)

**Mean value 0.89**
**Standard deviation 0.24**

Table 4. Comparison experimental versus Eurocode 3 prediction for stiffness

| Specimen | $S_{EC3}$ [kNm] | $S_{exp}$ [kNm] | $\frac{S_{j,EC3}}{S_{j,exp}}$ | Specimen | $S_{EC3}$ [kNm] | $S_{exp}$ [kNm] | $\frac{S_{j,EC3}}{S_{j,exp}}$ | Specimen | $S_{EC3}$ [kNm] | $S_{exp}$ [kNm] | $\frac{S_{j,EC3}}{S_{j,exp}}$ |
|---|---|---|---|---|---|---|---|---|---|---|---|
| W7-4.20-110 | 27849 | 24093 | 1,16 | Pic.Beau. 1F | 1868 | 1733 | 1,08 | Pic.Beau. 13F | 18707 | 10523 | 1,78 |
| W8-4.20-0 | 15255 | 11500 | 1,33 | Pic.Beau. 2F | 1868 | 1733 | 1,08 | Pic.Beau 14CF | 30346 | 26092 | 1,16 |
| W9-4.20-0 | 15255 | 11500 | 1,33 | Pic.Beau. 3F | 1868 | 1733 | 1,08 | Pic.Beau. 15CF | 30260 | 26092 | 1,16 |
| S220-010 | 3862 | 5061 | 0,76 | Pic.Beau. 5CF | 4924 | 8626 | 0,57 | HE 240 B-15-585 | 68416 | 59193 | 1,16 |
| S220-040 | 18664 | 19991 | 0,93 | Pic.Beau. 8F | 18656 | 12484 | 1,49 | HE 160 A-15-34 | 11336 | 7494 | 1,51 |
| S220-150 | 85300 | 70404 | 1,21 | Pic.Beau. 9F | 18656 | 12120 | 1,54 | HE 160 A-15-233 | 20723 | 10437 | 1,99 |
| S220-190 | 83693 | 53000 | 1,58 | Pic.Beau. 10CF | 41663 | 26092 | 1,60 | HE 240 B-25-585 | 80508 | 43851 | 1,84 |
| S140-010 | 1897 | 1131 | 1,68 | Pic.Beau. 11CF | 41663 | 26092 | 1,60 | | | | |
| S140-100 | 25540 | 18132 | 1,41 | Pic.Beau. 12F | 18707 | 10523 | 1,78 | | | | |

**Legend:** W (Wald et al., 1995); S (Vandegans, 1997);
Pic.Beau. (Picard and Beaulieu, 1984);
HE (Latour et al. 2009)

**Mean value 1.35**
**Standard deviation 0.35**

The comparison between the results of experimental tests and the Eurocode 3 predictions for different values of the eccentricity evaluated according to Eqs. (6-7) is shown in Figure 9.

It can be noted that all the tests show an overestimation of the stiffness which is particularly significant in case of small eccentricity.
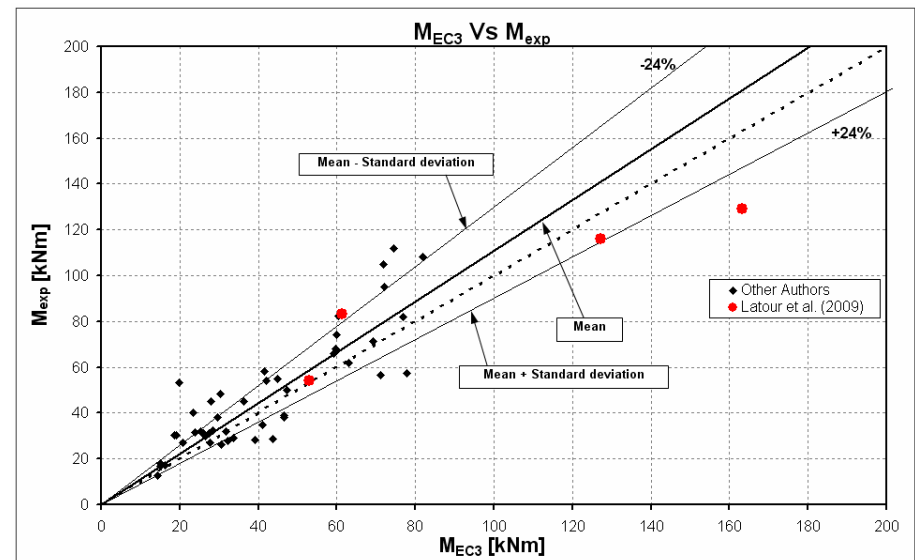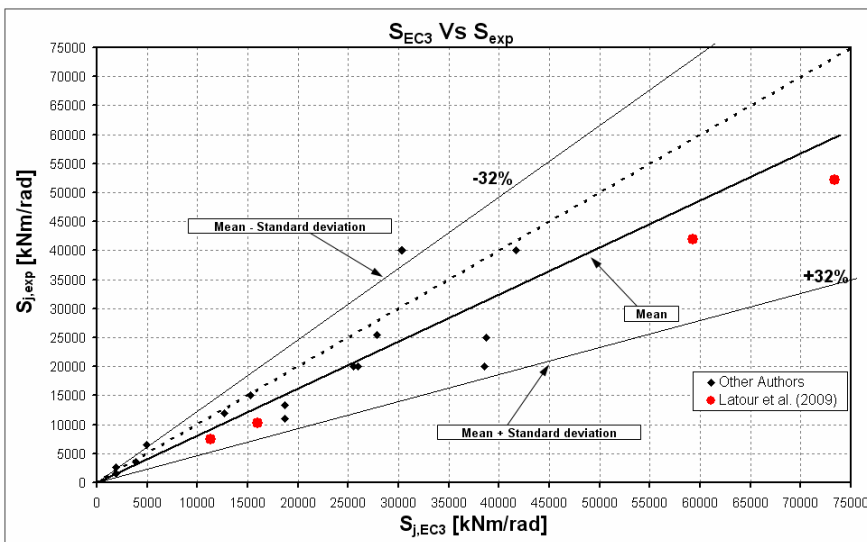
Figure 7. Comparison between experimental results and the EC3 prediction
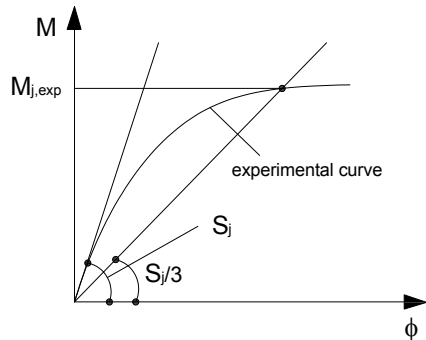


Figure 8. Evaluation of the experimental flexural resistance
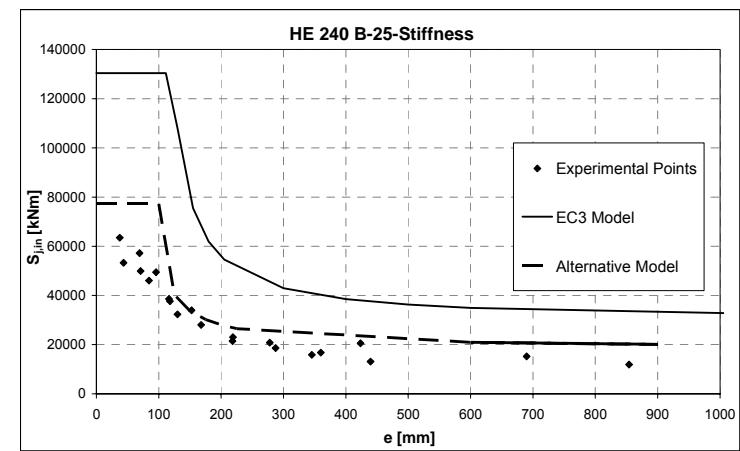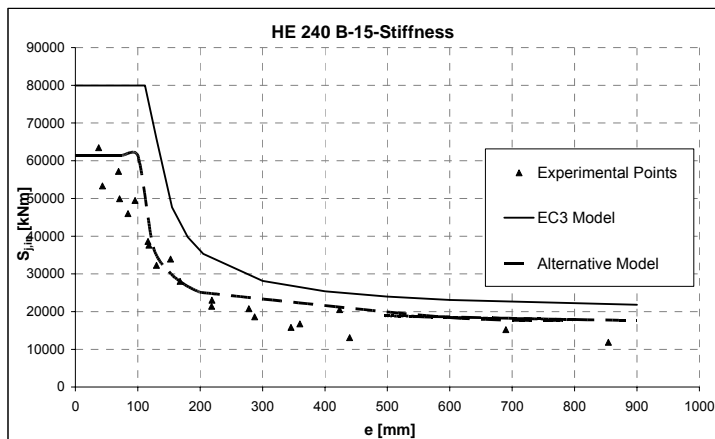




Figure 9. Accuracy of the predicting models

## 5. ALTERNATIVE MODEL FOR EVALUATING THE INITIAL STIFFNESS

The accuracy provided by Eurocode 3 in predicting the column-base joint stiffness can be generally considered satisfactory provided that the attention is focused mainly on the ultimate behaviour. Conversely, when structural deformability is mainly of concern, a more accurate prediction of the base joint rotational stiffness can be useful. To this scope, some simplifications introduced by Eurocode 3 for an easier application, can be removed. In particular, the definition of an effective width to be specifically applied in stiffness calculation and, therefore, different from that used by Eurocode 3 for resistance evaluation could allow a further improvement of the stiffness prediction.

Regarding the component "concrete in compression", according to the approach suggested by Steenhuis et al. (2008), the extension of the concrete zone subjected to compression in elastic range can be evaluated considering an equivalence between the behaviour, in terms of maximum deformation, of a flexible plate supported by springs with that of a rigid plate. From this analysis, the spreading of the action transmitted by the compressed column flange, which defines the effective width and length of the concrete in compression (Figure 1), provides a value of the parameter $c$ in elastic range equal to $1.25\ t_{bp}$.

In addition, with reference to the base plate in tension, according to an approach already suggested for beam-to-column joints (Faella et al., 1999), two different issues need to be considered: the first one regards the definition of the effective width in elastic range which can be defined assuming a 45° spreading of the concentrated bolt action starting from the bolt head edge, the second one regards the influence of bolt preloading, due to tightening, which can be accounted for by means of the following relationships:

$$k_t = 0.5\,\frac{\psi\,\dfrac{b_{eff,bp}\cdot t_{bp}^3}{m^3}}{\eta+(1-\eta)\psi} \qquad \text{with} \qquad \psi = 0.57\left(\frac{t_{bp}}{d_b\cdot\sqrt{\alpha}}\right)^{-1.28} \tag{11}$$

where η is the bolt preloading level expressed as a fraction of that leading to a bolt tensile stress equal to 80% of the yield stress, $d_b$ is the bolt diameter and $α=m/d_b$.

The results of the comparison between the values of the stiffness predicted by means of the proposed approach and those provided by the experimental tests are given in Table 5. It can be observed that the introduction of a more appropriate evaluation of effective width both in compression and in tension allows to improve the predictions leading to an average value of the ratio predicted/experimental value of the base plate stiffness equal to 1.09, while the standard deviation is almost unchanged.

Table 5. Comparison between experimental stiffness and the proposed approach

| Specimen | $S_{EC3}$ [kNm] | $S_{exp}$ [kNm] | $\frac{S_{j,EC3}}{S_{j,exp}}$ | Specimen | $S_{EC3}$ [kNm] | $S_{exp}$ [kNm] | $\frac{S_{j,EC3}}{S_{j,exp}}$ | Specimen | $S_{EC3}$ [kNm] | $S_{exp}$ [kNm] | $\frac{S_{j,EC3}}{S_{j,exp}}$ |
|---|---|---|---|---|---|---|---|---|---|---|---|
| W7-4.20-110 | 20533 | 24093 | 0,85 | Pic.Beau. 1F | 1326 | 1733 | 0,77 | Pic.Beau. 13F | 18441 | 10523 | 1,75 |
| W8-4.20-0 | 14010 | 11500 | 1,22 | Pic.Beau. 2F | 1326 | 1733 | 0,77 | Pic.Beau. 14CF | 28529 | 26092 | 1,09 |
| W9-4.20-0 | 14010 | 11500 | 1,22 | Pic.Beau. 3F | 1326 | 1733 | 0,77 | Pic.Beau. 15CF | 28458 | 26092 | 1,09 |
| S220-010 | 2317 | 5061 | 0,46 | Pic.Beau. 5CF | 3379 | 8626 | 0,39 | HE 240 B-15-585 | 55505 | 59193 | 0,94 |
| S220-040 | 9660 | 19991 | 0,48 | Pic.Beau. 8F | 18461 | 12484 | 1,48 | HE 160 A-15-34 | 10131 | 7494 | 1,35 |
| S220-150 | 63017 | 70404 | 0,90 | Pic.Beau. 9F | 18461 | 12120 | 1,52 | HE 160 A-15233 | 12945 | 10437 | 1,24 |
| S220-190 | 60369 | 53000 | 1,14 | Pic.Beau. 10CF | 37634 | 26092 | 1,44 | HE 240 B-25-585 | 41452 | 43851 | 0,95 |
| S140-010 | 1543 | 1131 | 1,36 | Pic.Beau. 11CF | 37634 | 26092 | 1,44 | | | | |
| S140-100 | 17861 | 18132 | 0,99 | Pic.Beau. 12F | 18441 | 10523 | 1,75 | | | | |

**Legend:** W (Wald et al., 1995); S (Vandegans, 1997);
Pic.Beau. (Picard and Beaulieu, 1984);
HE (Latour et al. 2009)

**Mean value 1.09**
**Standard deviation 0.38**

## CONCLUSIONS

The results of the first part of a research program aimed at the theoretical and experimental prediction of the cyclic behaviour of base plate joints have been presented. In particular, the analysis of the experimental tests carried out at the University of Salerno and of those collected from the technical literature has pointed out the degree of accuracy of Eurocode 3 component method for predicting the stiffness and resistance of column-base connections. An improvement of the approach for the stiffness predictions has been also obtained by means of a better definition of the effective width in elastic range, both in compression and in tension, according to models already proposed in the technical literature.

## ACKNOWLEDGMENTS

## REFERENCES

[1] DeWolf J.T., Sarisley E.F. (1980). "Column Base Plates with Axial Loads and Moments", *Journal of the Structural Division*, ASCE

[1] Girão Coelho A. (2004). "Characterization of the ductility of bolted extended end plate beam-to-column steel connections". PhD dissertation, University of Coimbra, Coimbra, Portugal.

[2] Jaspart J.P., Vandegans D. (1998). "Application of the Component Method to Column Bases", *Journal of Constructional Steel Research*. N°48 pp.89-106.

[3] Latour M., Piluso V., Rizzano G. (2008). "Cyclic Model of Beam-to-Column Joints". Proceedings of Eurosteel 2008, Graz.

[4] Latour M. and Rizzano G. (2009). "Comportamento teorico-sperimentale di giunti di base in strutture in acciaio". Proceedings of XXII Italian Conference on Steel Structures, 2009, Padova.

[5] Latour, M., Piluso, V. & Rizzano , G., (2011). "Cyclic Modeling of Bolted Beam-to-Column Connections: Component Approach". Journal of Earthquake Engineering, 15(4), pp.537-63.

[6] Nogueiro P., Simões da Silva L., Bento R., Simoes R. (2007). "Calibration of Model Parameters for the Cyclic Response of End-Plate Beam-to-Column Steel-Concrete Composite Joints", Submitted for Publication to International Journal of Steel and Composite Structures.

[7] Picard A., Beaulieu (1984). "Behaviour of a Simple Column Base Connection", *Canadian Journal of Civil Engineering*, Vol.12, (pp.126-136).

[8] Piluso V., Faella C., Rizzano G. (2001), "Ultimate behavior of bolted TStubs.I: Theoretical model". *Journal of Structural Engineering*, ASCE,127(6), (pp.686-693).

[9] Steenhuis C.M. (1998). "Assembly procedure for base plates", report 98-CON-R0447, TNO Building and Construction Research, Delft, the Netherlands.

[10] Steenhuis C.M., Wald F., Sokol Z., Stark J.W.B. (2008). "Concrete in compression and base plate in bending", HERON, Vol. 53, N. 1/2.

[11] Vandegans D. (1997). "Column Bases: Experimentation and Application of Analytical Models", Research Centre of the Belgian Metalworking Industry, MT 196, p.80, Brussels,Belgium.

[12] Wald F. (1995): "Patky Sloupù - Column Bases", CVUT Praha, 1995, p. 137.

www.steelconstruct.com

# BEHAVIOUR OF TRAPEZOIDAL SHEAR PANELS IN STEEL JOINTS

Eduardo Bayo[1]; Alfonso Loureiro[2]; Manuel Lopez[2]; Beatriz Gil[1]

[1] *Department of Structural Analysis and Design, University of Navarra, Spain*
*ebayo@unav.es; bgilr@unav.es*

[2] *Escuela Politecnica Superior, University of Coruña, Spain*
*lourerio@cdf.udc.es; manuellopez@cdf.udc.es*

## ABSTRACT

Previous research has stressed the need for a correct definition of the column panel zone deformations under static conditions due to its influence on the overall sway behaviour of the frame. An increase in frame drift due to panel zone shear deformation may render the frame unserviceable. This may even happen for commonly considered rigid joints. Modelling of the panel is also important for the avoidance of local failure of the columns under ultimate limit state conditions.

The shear behaviour of rectangular column shear panels has been investigated thoroughly and different formula has been proposed to characterize their strength and resistance. Modern codes including Eurocode 3 (EN 1993-1-8, 2005) have included these research advances so that they may be used in common practice. However the case of trapezoidal column panels, formed by beams of different depths at each side of the column, has not been researched as much. Steel connections with beams of unequal size are not currently included in design codes.

This paper deals with the experimental results obtained of the shear behaviour of trapezoidal panels arising from steel joints using commercial sections. Also finite element modelling is carried out to compare results. Current modelling procedures are tested and the results compared with those coming from the experiments and numerical simulation.

## 1. INTRODUCTION

The characterization of steel joint behaviour and properties have been a matter of research for a number of years, and all the accumulated knowledge has been compiled to a large extent in currently available steel design codes.

One important aspect is the behaviour of the column panel subjected to the shear forces arising from the moments of the adjacent beams as well as the shear forces acting on the columns. Krawinkler et al (1975) reported the importance that panel shear deformations have on the frame behaviour under lateral loads, and proposed a formulation for the stiffness and resistance of shear panels of beam to column connections with beams of equal depths. An alternative formulation has been proposed in the Eurocode 3, part 1.8 (2005). These and other proposed methods allow introducing the flexibility of the joints in both the elastic and inelastic range in order to assess the frame response.

The lines connecting the flanges of beams of unequal depths define a trapezoid within the panel column zone. Hoogenbroom and Blaauwendraad (2000) and Curtis and Greiner (1996) have proposed analytical and computational methods to characterize the shear behaviour of isolated quadrilateral panels. Recently, Hashemi and Jazany (2012) have investigated the connection detailing of joints of unequal beam depths under seismic loads. One of their conclusions is that inclined stiffeners connecting the lower flanges of the beams perform better than the horizontal ones. Jordao (2008) studied the performance of this type of joints for high strength steel without the use of web stiffeners. As a consequence the stress field at the panel zone becomes rather complex due to the fact that the compression, tension and shear zones are all coupled together. The common failure mode of the experiments carried out was web buckling due to compression. Within the context of Eurocode 3, Jordao et al (2008) also proposed modelling and design recommendations based on modified transformation parameters. A suitable modelling of the joint for global analysis can be achieved by considering the cruciform element proposed by Bayo el al (2006, 2012).

Work remains to be done to better characterize the complex behaviour of steel joints with beams of unequal depths and trapezoidal panels. The study involves a wide large number of variables and intervening factors. Hopefully, future work and results will make it possible to include the design of this kind of joints in design codes. In this paper we present some experimental work and numerical (finite element) results in the hope that they will provide some additional insight into this broad and interesting problem.

The moment rotation diagrams depend on a large number of material, geometrical and loading variables. In this work we concentrate on the shear stiffness and resistance of the trapezoidal panel zone and the additional contribution provided by the elements surrounding the panel such as the column flanges and the beam adjacent to the joint. These elements play a major role in the joint post-elastic reserve shear strength and stiffness. Consequently, stiffeners are included to avoid the effects of other components such as the column web in tension and compression, and the column flange in bending and to prevent as much as possible their interaction with the shear component. For the same reason, only fully welded connections are considered in this investigation. The moments acting at both sides of the joint are the most important contribution to the panel shear force, and they are usually considered as the load variables characterizing the strength and stiffness of the joint. However, the beneficial effect of the column shear should also be considered (particularly in the case of short columns) in the joint stiffness and strength as proposed by Krawinkler at al (1975). The deformation is defined in terms of the average shear distortion of the panel zone (PZ), and it is measured in this investigation by means of two inclinometers located on the middle section of the panel. Also the deformations on both sides of the joint will be considered. The aim is to understand the mechanisms of deformation and characterize the moment rotation curves due to the panel shear for this type of joints.

## 2. EXPERIMENTAL WORK AND FINITE ELEMENT MODELS

The experimental work has been carried out in two different experiments with beams of unequal beam depths. The overall scheme is illustrated in Figure 1. The column is pinned at both ends and actuation is applied at points A and B. Those two points

are placed exactly 1 meter away from the column flanges. The beam and column sizes are shown in Table 1. A picture of the experimental set up is depicted in Figure 2.

Table 1. Experimental beam and column configurations.

| Test | Column | Deep Beam | Shallow Beam | Depth Ratio | Loading Point | Type of Loading |
|------|--------|-----------|--------------|-------------|---------------|-----------------|
| E1A | HEA 240 | HEB 300 | HEB 160 | 1.88 | A | Elastic |
| E1B | HEA 240 | HEB 300 | HEB 160 | 1.88 | B | Failure |
| E2A | HEA 240 | HEB 300 | HEB 180 | 1.67 | A | Elastic |
| E2B | HEA 240 | HEB 300 | HEB 180 | 1.67 | B | Failure |
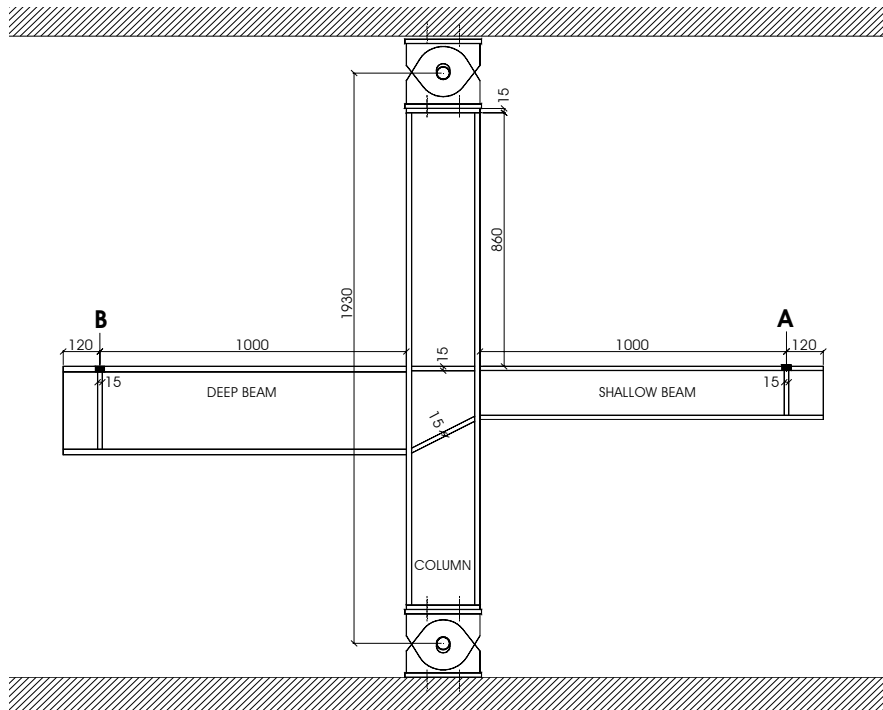


Figure 1. Experimental setup

The top horizontal and the inclined stiffeners were welded as depicted in Figures 1 and 2 to avoid, as mentioned above, any type of failure other than that produced by shear. The stiffeners were 15 mm thick and in all cases were rigid enough to provide the necessary resistance to prevent either tension or compression failure of the column webs, as well as out of plane bending of the column flanges. The type of steel used for all the parts was S275. Coupons were extracted from both the columns and stiffeners to obtain the true properties of the material. Table 2 shows those properties that were subsequently used in the finite element analyses.

The panel was instrumented with 4 strain gages placed at the corners of the panel as shown in Figure 3. They served to monitor the yielding sequence and the levels of shear distortion. Five inclinometers were used as shown in Figure 3 to obtain the rotations. Two were placed vertically at the beams adjacent to the joint.

Two more were placed vertically at the top and bottom of the web panel to capture the possible different rotations at those levels. A fifth one was placed in the middle of the panel to capture the rotation of the column due to bending. This rotation is subtracted from those at the beams to obtain the rotation due to the shear deformations.



Figure 2. Experiment E1 during the loading process

Table 2. Steel properties obtained from coupons.

| Part | $\sigma_y$ (MPa) | $\sigma_u$ (MPa) | E (MPa) |
|------|------------------|------------------|---------|
| HEA 240 | 330 | 493 | 207000 |
| HEA 240 | 328 | 494 | 211000 |
| HEA 240 | 326 | 496 | 209000 |
| HEA 240 | 329 | 490 | 210000 |
| Stiffeners | 300 | 446 | 213000 |
| Stiffeners | 309 | 449 | 211000 |
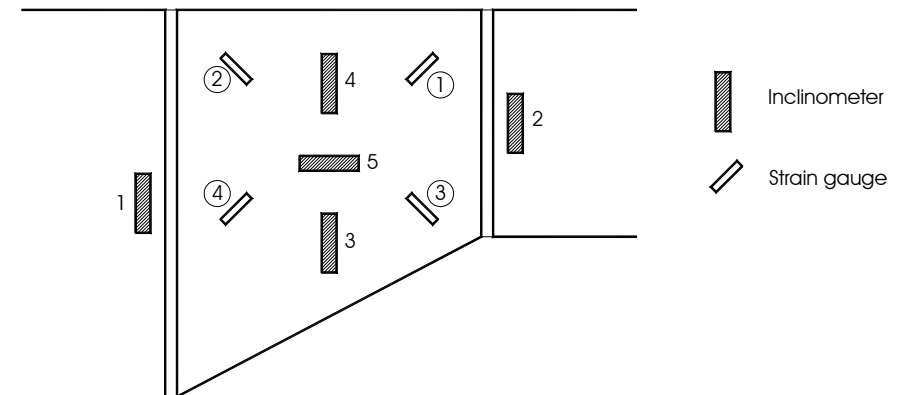


Figure 4. Placement of strain gauges and inclinometers.

The finite element analysis was performed using Abacus®. Solid elements with reduced integration (to avoid shear locking) and hourglass control (C3D8R) were adopted. Figure 4 illustrates part of the model. The material behaviour was introduced by means of the true stress-strain data obtained from the coupons. Static nonlinear material and geometric analyses with force control were performed. The Von Misses yield criterion was selected to define the inelastic response.
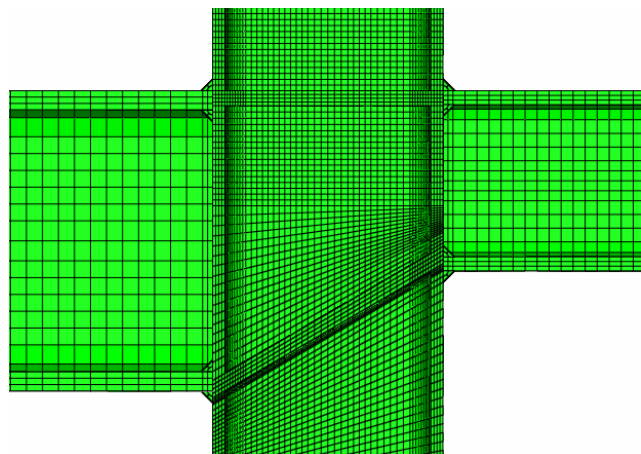


Figure 4. Detail of the finite element model

## 3. DESCRIPTION OF RESULTS

The first test E1A consisted in loading the experiment E1 at the tip of the shallow beam (point A). The aim was to obtain the elastic stiffness of the trapezoidal panel under the shear coming from loading the shallow beam. The maximum load applied was 30 kN, and afterwards it was unloaded. A previous finite element analysis had predicted pure elastic behaviour up to that loading level. The shear stress distribution within the panel obtained from the finite element analysis is illustrated in Figure 5a, which corresponds to the level of strains given by the strain gauges shown in Figure 5b.

It may be seen that the stress distribution is very uniform over the upper rectangular part of the panel. The readings of the inclinometers 3 and 4 were similar, and the inclinometers 1 and 2 showed that the rotation at the shallow beam was approximately double the size of the rotation of the deep beam.

The following test, E1B, consisted in loading the experiment E1 at the tip of the deep beam (point B) until failure, which occurred at a load of 230 kN. The shear stress distributions within the panel coming from the finite element analysis during the elastic and inelastic parts of the response are illustrated in Figure 6a and 6b respectively. It may be seen how even in the elastic range the shear stress field now extends more towards the bottom of the panel becoming more trapezoidal in shape.

The readings of the inclinometers 3 and 4 were similar in the elastic range and departed from each other as the inelastic response progressed. The rotation of the lower part of the panel became 35% higher than that of the higher part right before failure. The failure was produced by the cracking of the panel at the upper right corner (right next to strain gauge 1). The angles at the shallow beam were similar to those

of the deep beam during the elastic part of the response. However, within the inelastic response the angles at the shallow beam became much larger than those of the deep beam reaching almost 40% more right before failure.

The test, E2A, consisted in loading the experiment E2 at the tip of the shallow beam. The qualitative behaviour of this test was similar to that of E1A. The maximum load applied was 37 kN, and afterwards it was unloaded. Again, a previous finite element analysis had predicted pure elastic behaviour up to that loading level. The shear stress distribution within the panel obtained from the finite element analysis is illustrated in Figure 7a, which corresponds with the level of strains given by the strain gauges and shown in Figure 7b. The readings of the inclinometers 3 and 4 were similar, and the rotation at the shallow beam was approximately 60% higher than the rotation of the deep beam.
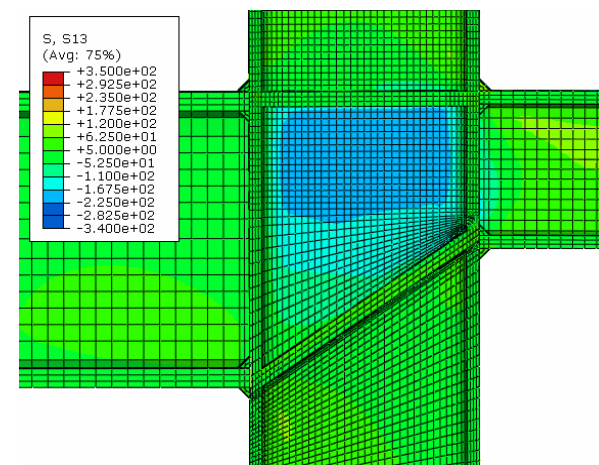


Figure 5a. Shear stress contours in E1A
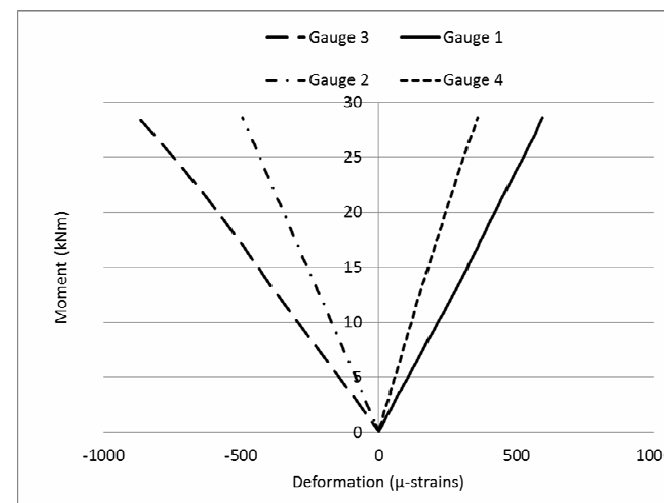


Figure 5b. Strains gauges in E1B
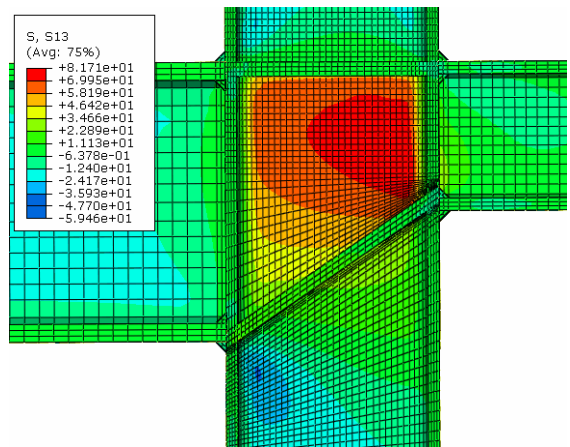
Figure 6a. Elastic shear stress levels in E1B
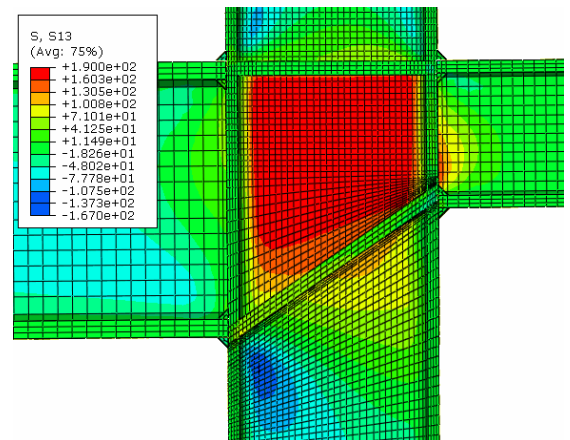


Figure 6b. Plastic shear stress levels in E1B
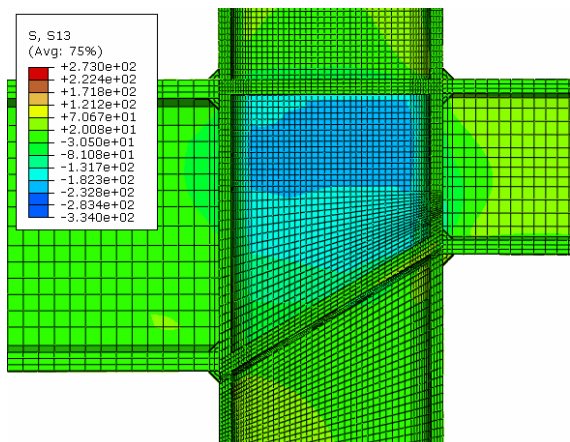


Figure 7a.  Shear stress levels in E2A
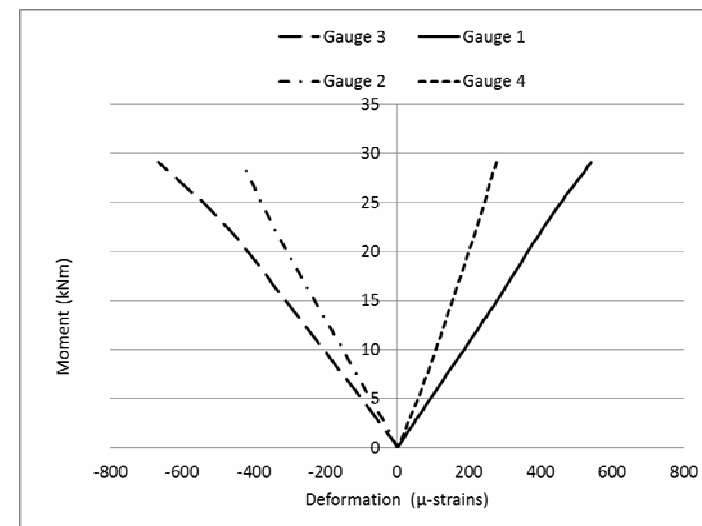


Figure 7b. Strains at gauges in E2A

The final test, E2B, consisted in loading the experiment E2 at the tip of the deep beam (point B) until failure, which occurred at a load of 265 kN. The shear stress distributions within the panel coming from the finite element analysis during the elastic and inelastic parts of the response are illustrated in Figures 8a and 8b respectively. The readings of the inclinometers 3 and 4 were similar in the elastic range and departed from each other as the inelastic response progressed. The rotation of the lower part of the panel became 20% higher than that of the higher part right before failure. The angles at the shallow beam were similar to those of the deep beam during the elastic part of the response. However, within the inelastic response the angles at the shallow beam became much larger than those of the deep beam reaching a difference of 40% right before failure.
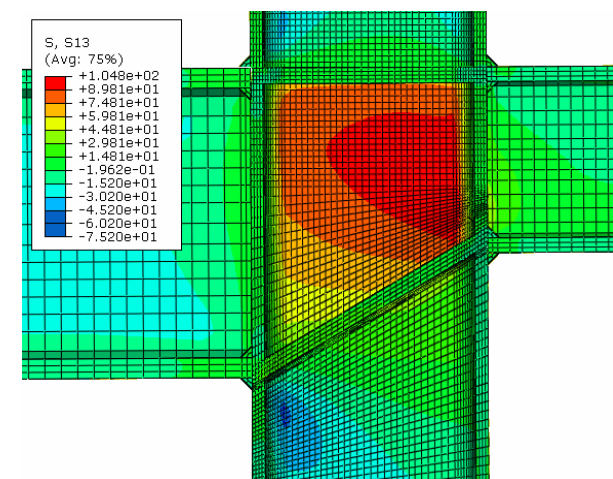


Figure 8a. Elastic shear stress levels in E2B
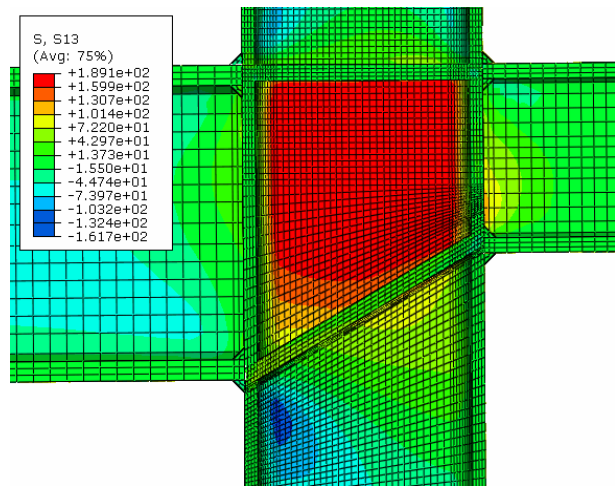
Figure 8b. Plastic shear stress levels in E2B

The deformed panel and deformed shape of the experiment before failure are shown in Figures Figure 9a and 9b, respectively.



Figure 9a. Panel inelastic deformation



Figure 9b. Deformed shape before failure

The plastic shear stress levels of the column panel as well as the final deformed shape of the specimen can be seen in Figure 10. It is worth noting how the shallow beam gets much more inclined that the deep beam due to the deformation of the trapezoidal panel as an articulated quadrilateral mechanism.
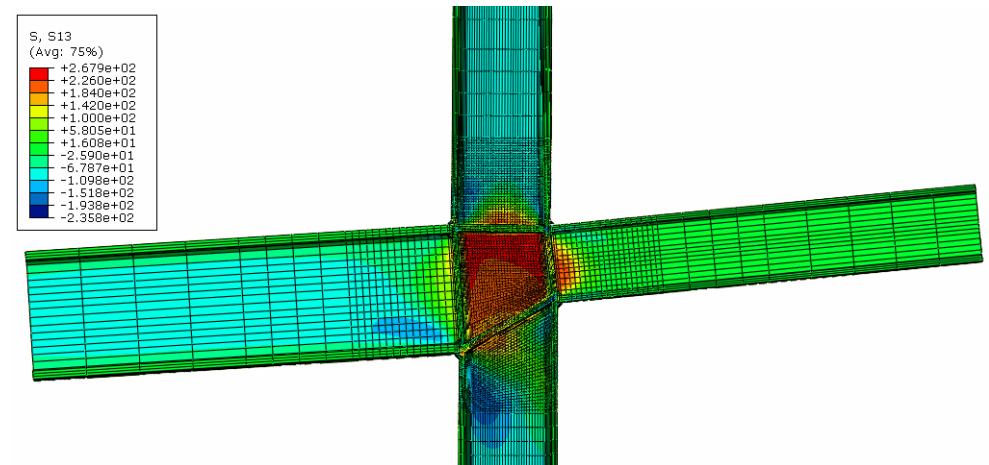


Figure 10. Final stage of stress and deformation in test E2B.

## 4. MOMENT ROTATION CURVES: STIFFNESS AND RESISTANCE

From the previous discussion we observe that there are three distinct rotations and therefore three degrees of freedom (DOF) in the elastic range: left connection, right connection and centre of panel; and only one DOF in the inelastic range corresponding to an articulated quadrilateral mechanism.

We compare in this section the moment rotation curves obtained from the experiments, the finite element analysis, the Eurocode 3 and the method proposed by Krawinkler et al (1975). Since the last two do not include trapezoidal panels they are applied to each connection (left and right) as if the panel were rectangular for the corresponding beam depth. The comparison is established in terms of the moment at the connection versus the average shear rotation of the panel, as well as the other possible rotations at each side of the joint (additional DOFs). The rotation of the panel that has been measured using the following relation:

Average rotation of the panel = (inclin(3) + inclin(4)) / 2 – inclin(5)

Inclinometer 3 and 4 measure the total rotation at the top and bottom part on the panel along the centre line (see Figure 3), and the reading of inclinometer 5 is subtracted to take into account the flexural rotation of the column at the joint level.

Figures 11a and 11b show the moment rotations curves corresponding to the tests E1A and E2A, respectively. The tests only provide the initial stiffness since they are only loaded in the linear elastic range, and the plot is hidden underneath the finite element one. Figures 12a and 12b show the moment rotations curves corresponding to the tests E1B and E2B, respectively.
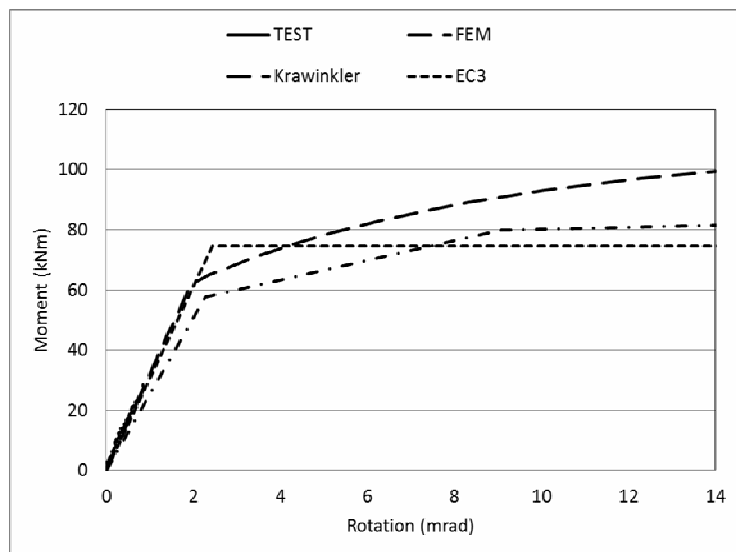
Figure 11a. Moment-rotation for test E1A
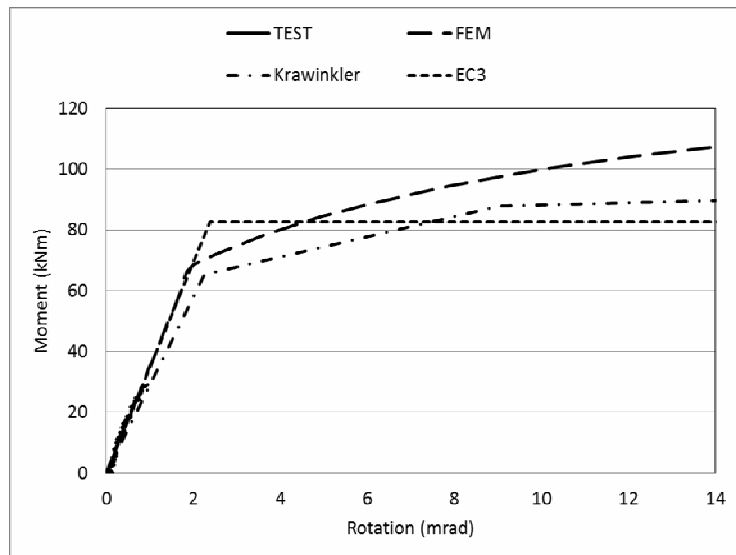


Figure 11b. Moment-rotation for test E2A

It may be seen that the predictions of the finite element model in terms of stiffness and resistance are good when considering the rotation at the centre of the panel. The differences at the knee level may be due to the uncertainty in the modelling of the welding material properties. EC3 provides a good prediction of the stiffness but a poor prediction of the resistance, even when including the additional resistance provided by the column flanges. Krawinkler's model underestimates both the stiffness and resistance, although the latter is better approximated than EC3.

Table 3 compares the values of the stiffness obtained by the different methods, as well as the relative errors, when considering the rotation of <u>the central section of the panel</u> as the reference for the rotations (first DOF).
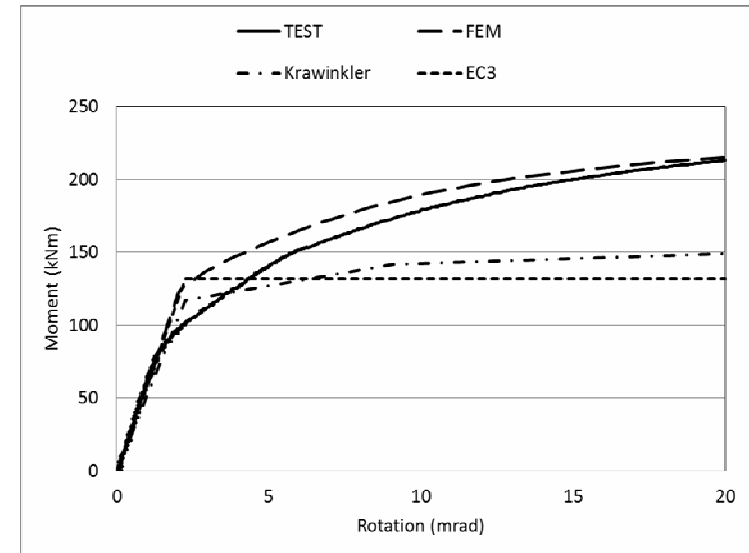


Figure 12a. Moment-rotation for test E1B
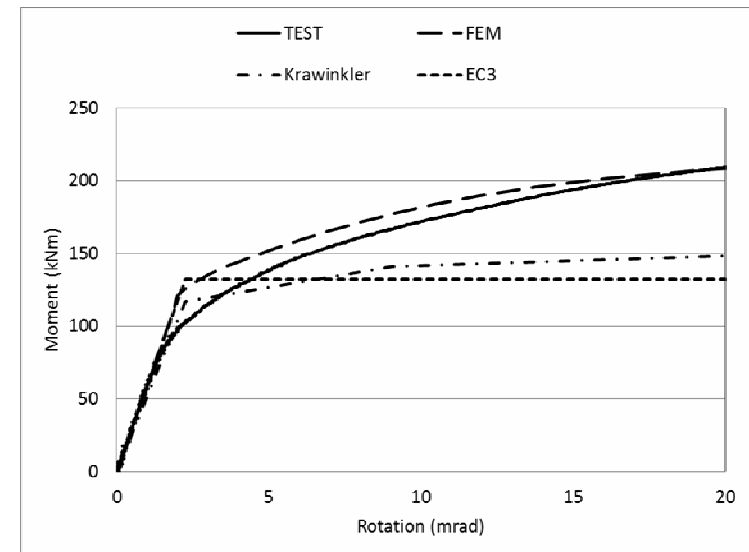


Figure 12b. Moment-rotation for test E2B

It is worth mentioning that the Eurocode does not account for the effect of the shear in the column, $V_c$. If that effect had been included, the stiffness values would have been those shown in Table 3 and the prediction would have been stiffer with higher errors.

www.steelconstruct.com

Table 3. Comparison of rotational stiffness (kNm/mrad)
considering the central section of the panel.

|  | Test | FEM | Error (%) | EC3 | Error (%) | EC3 with Vc | Error (%) | Krawinkler | Error (%) |
|---|---|---|---|---|---|---|---|---|---|
| E1A | 32.2 | 32.1 | -0.6 | 30.6 | -5.3 | 33.4 | 3.6 | 25.4 | -21.2 |
| E1B | 61.8 | 60.2 | -2.6 | 58.4 | -5.6 | 70.5 | 14.0 | 51.7 | -16.4 |
| E2A | 35.4 | 34.9 | -1.2 | 34.5 | -2.5 | 38.5 | 8.7 | 28.9 | -18.3 |
| E2B | 60.1 | 59.4 | -1.2 | 58.4 | -2.7 | 69.2 | 15.2 | 51.7 | -13.9 |

Results get worse when considering the deep section of the panel as the reference for the rotations (second DOF). Table 4 shows the differences and EC3 becomes less accurate and provides stiffness values that are non-conservative.

Table 4. Comparison of rotational stiffness (kNm/mrad)
considering the deep section of the panel

|  | FEM | EC3 | Error (%) | EC3 with Vc | Error (%) | Krawinkler | Error (%) |
|---|---|---|---|---|---|---|---|
| E1B | 55.9 | 58.4 | 4.5 | 70.5 | 26.1 | 51.7 | -7.5 |
| E2B | 53.2 | 58.4 | 9.8 | 70.5 | 32.5 | 51.7 | -2.8 |

The worst comes when considering the shallow section of the panel as the reference for the rotations. Table 5 shows that the errors introduced by both the EC3 and Krawinkler are considerable and non-conservative.

Table 5. Comparison of rotational stiffness (kNm/mrad)
considering the shallow section of the panel

|  | FEM | EC3 | Error (%) | EC3 with Vc | Error (%) | Krawinkler | Error (%) |
|---|---|---|---|---|---|---|---|
| E1A | 17.9 | 30.6 | 71.0 | 33.4 | 86.6 | 25.4 | 41.9 |
| E2A | 20.7 | 34.5 | 66.7 | 38.5 | 86.0 | 28.9 | 39.6 |

## 5. CONCLUSIONS

In this paper we have investigated the shear performance of trapezoidal shear panels appearing in joints with unequal beam depths. Tests and FE simulations have been performed. The main conclusions can be summarized as follows:

1. The shear deformation zone corresponds to the upper rectangle when loading the shallow beam, and the whole trapezoid when loading the deep beam. Consequently the initial stiffness values of the left and right connections are different.

2. Three independent DOF are identified in the elastic range: the rotations corresponding to the left, right and central sections of the panel. Only one DOF appears in the plastic range, which corresponds to an articulated quadrilateral mechanism. These DOF should be considered at the time of defining the joint stiffness for frame analyses.

3. The FE analysis predicts the stiffness and resistance with good accuracy. EC3 approximates reasonably well the initial stiffness of the left and right connections

when using the dimensions of beam attached to the corresponding connection and the middle section of the panel as the reference for the rotations. However, the estimation gets worse for the deep beam and becomes very poor when considering the rotation of the shallow beam.

4. The column shear should be included in the stiffness formulation.

5. More research is needed to better model the stiffness, resistance and post-elastic behaviour of this type of joints and include them in the codes.

## ACKNOWLEDGMENT

## REFERENCES

[1] Bayo, E., Cabrero, J.M., Gil, B. (2006). "An effective component based method to model semi-rigid connections for the global analysis of steel and composite structures". *Engineering Structures*, vol. 28 (pp. 97-108).

[2] Bayo, E., Gracia, J., Gil, B., Goñi, R. (2012). "An efficient cruciform element to model semirigid composite connections for frame analysis". *Journal of Constructional Steel Research,* vol. 72, (pp. 97–104).

[3] Curtis, H., Greiner, G. (1996). "A stress-based quadrilateral shear panel". *Finite element analysis and design*, vol. 21, (pp. 159-178).

[4] EN 1993-1-8-2005. European Committee for Standardization – CEN. Eurocode 3: Design of steel structures. Part 1.8: Design of joints, Brussels.

[5] Hashemi, B.H., Jazany, R.A. (2012). "Study of connection detailing on SMRF seismic behaviour fro unequal beam depths". *Journal of Constructional Steel Research*, vol. 68 (pp. 150-164).

[6] Hoogenbroom, P., Blaauwendraad, J. (2000). "Quadrilateral shear panel". *Engineering Structures*, vol. 22 (pp. 1690-1698).

[7] Jordao, S. (2008) "Comportamento de juntas soldadas em no interno com vigas de diferentes Alturas e aco de alta resistencia". PhD. Thesis. Departamento de Engenharia Civil. University of Coimbra. Portugal.

[8] Jordao, S., Simoes da Silva, L., Simoes, R. (2008) "Design rules proposal for high strength steel: internal nodes with beams of different heights". *Eurosteel 2008*. Graz, Austria.

[9] Krawinkler, H., Bertero, V., Popov, E. (1975). "Shear behaviour of steel frame joints". *Journal of the Structural Division*, vol. 101, (pp. 2317-2336).

www.steelconstruct.com

# STRUCTURAL ASSESSMENT OF THE TENSION CAPACITY OF CARBON & STAINLESS STEEL PLATES WITH STAGGERED BOLTS

João de Jesus dos Santos, André Tenchini da Silva
*PGECIV – Post Graduate Program in Civil Engineering, UERJ, Brazil*
*paraduc@yahoo.com.br, andretsilva@gmail.com*

Luciano Rodrigues Ornelas de Lima, Pedro Colmar Gonçalves da Silva Vellasco,
Sebastião Arhur Lopes de Andrade, José Guilherme Santos da Silva
*Structural Engineering Department, UERJ, Brazil*
*luciano@eng.uerj.br, vellasco@eng.uerj.br, andrade@civ.puc-rio.br,*
*jgss@eng.uerj.br*

## ABSTRACT

The current stainless steel design codes like the Eurocode 3, part 1.4, (2006), are still largely based in analogies with the carbon steel structural behaviour. The net section rupture represents one of the ultimate limit states usually verified for structural elements submitted to tension normal stress. The present paper presents an investigation aiming to evaluate the tension capacity of carbon and stainless steel bolted structural elements. The results are discussed and compared in terms of the stress distribution, force-displacement curves, among others. The assessment of the results was made by comparisons to the Eurocode 3 (2003) provisions for carbon and stainless steels. The investigation indicated that when stainless steel is used in certain structural engineering applications like joints under tension forces, the current design criteria based on deformation limits need to be re-evaluated specially due to the differences in the yield to ultimate deformation and stress ratios.

## 1. INTRODUCTION

Stainless steel have been used in various types of constructions due to its main characteristics associated to high corrosion resistance, durability, fire resistance, ease of maintenance, appearance and aesthetics (Gardner & Badoo, 2006). Stainless steel is indicated, as a structural element in construction due multiple reasons. Its high ductility allows its use in structures subjected to cyclic loadings, enabling the dissipation of the energy before the structural collapse. Despite these facts, current stainless steel design codes like the Eurocode 3, part 1.4, (2003), are still largely based in carbon steel structural analogies.

The search for a broader understanding of the actual behaviour of stainless steel joints motivated investigations in various research centres like: Burgan et al. (2000), Gardner and Nethercot (2004) and Bouchair et al (2008). The motivation was the search for the most cost-effective structure resulting from an optimum joint design, as well as an improvement of the joint fabrication and assembly costs. Experimental studies indicated that different types of collapses, especially due to serviceability limitations, were observed in stainless steel joints with thin and thick plates under shear. These paper presents an investigation aiming to evaluate the tension capacity of carbon and stainless steel bolted structural elements. The results are discussed and compared in terms of the stress distribution, force-displacement curves, among others. The assessment of the results was made by comparisons to the Eurocode 3 (2003) provisions for carbon and stainless steels.

## 2. EUROCODE 3 DESIGN CODE PROVISIONS

The current investigation uses the European code for stainless steel elements - Eurocode 3, pt 1.4 (2003). In this design standard, the failure modes for a plate with staggered holes under tension axial forces are governed by two ultimate limit states: the gross area yield and the net area tension rupture. The presence of staggered holes in the transversal section, Figure 1, difficult an immediate identification of the plate critical net section. This process is not new since in 1922, Cochrane (1922), performed one of the first attempts to characterize staggered bolted connection failure modes by using the eq. (1). This expression adds a term to the original net width to obtain the final net section area and it is present in major steel design codes all over the world.

$$b_n = b - d_b + \frac{s^2}{4p} \tag{1}$$

In the previous equation $b$ is the plate width, $d_b$ is the bolt diameter, $s$ and $p$ represent the staggered centre to centre hole distances measured parallel and perpendicular to the member axis. The Eurocode 3, part 1.4, (2003), establishes the guidelines for the stainless steel plate design submitted to axial tension forces. As cited before, the structural failure is associated to the smallest tension axial force obtained considering two limit states: gross cross-section plastic resistance given by eq. (2), or the ultimate net cross-section tension rupture expressed by eq. (3).

$$N_{pl,Rd} = \frac{A_g \cdot f_y}{\gamma_{M0}} \tag{2}$$

where $N_{pl,Rd}$ is the tension design plastic resistance, $A_g$ is the plate gross area, $f_y$ is the steel yielding stress, $\gamma_{M0}$ is the partial safety factor, in this case equal to 1.

$$N_{u,Rd} = \frac{k_r \cdot A_n \cdot f_u}{\gamma_{M2}} \quad \text{with} \quad k_r = \left(1 + 3r\left(d_0 / u - 0.3\right)\right) \tag{3}$$

where $A_n$ is the net cross-section plate area, $f_u$ is the steel tension rupture stress, $k_r$ is obtained from eq. (4), $\gamma_{M2}$ is the partial safety factor, equal to 1.25, $r$ is the ratio between the number of bolts at the cross-section and the total joint bolt number, $d_0$ is the hole diameter, $u = 2.e_2$ but $u \leq p_2$ where $e_2$ is the edge distance measured from the bolt hole centre to its adjacent edge, in the direction perpendicular to the load direction and $p_2$ is the hole centre-to-centre distance perpendicular to the load axis.

The tension plate design has also some additional provisions: in bolted joints, the hole width should be considered 2 mm larger than the nominal bolt diameter,

perpendicular to the applied force direction; in the case of staggered holes, when a diagonal direction to the load axis or zigzag is considered, the net width should be calculated first deducing from the initial gross width, all the holes present in it, and after that adding for each staggered holes a value equal to $s^2/4p$, where $s$ and $g$, correspond to the considered longitudinal and traverse hole spacing; the bolted joint critical net width is the smallest evaluated net width for all the possible net ruptures.

### 3. EXPERIMENTAL INVESTIGATIONS

An innovative experimental program was used to evaluate the tension capacity of carbon and stainless steel plates with staggered bolts. The experiments involved bolted cover plate joints made of stainless steel A304 and carbon steel USI300 (Santos, 2008). All the geometrical properties for the tests are presented in Table 1. The bolted joints were made of two 3 mm thick stainless and carbon steel plates and two 15 mm thick carbon steel plates used to transfer load to the 3mm plate with a 5 mm gap. The horizontal bolt pitch, $s$, was modified in each test and the vertical bolt pitch, $p$, were 55 mm (see Figure 1). The bolted cover plate joint tests were carried out on a 600kN Universal Lousenhausen test machine, see Figure 2(a). The strains measurements were performed using linear strain gauges located in both stainless steel plates named SG in Figure 1.
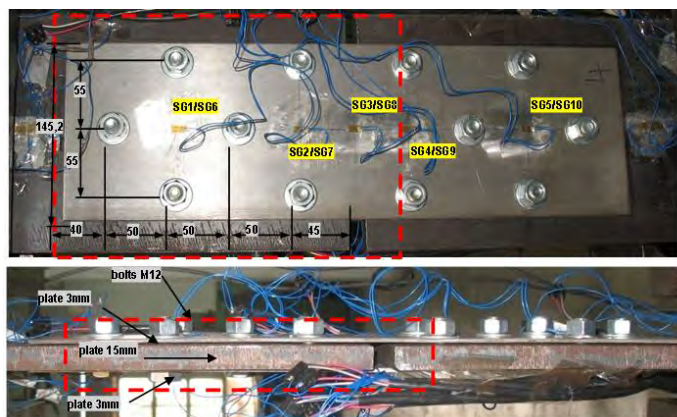


Figure 1. Cover plate joint detail and strain gauges location

Table 1. Summary of experimental tests (Santos, 2008)

| ID | s (mm) | p (mm) | e₁ (mm) | e₂ (mm) | d₀ (mm) | STEEL | t_base (mm) | bolts |
|---|---|---|---|---|---|---|---|---|
| E3_CARB_S50 | 50 | 55 | 40 | 17.6 | 14.7 | carbon | 15 | 6 |
| E4_CARB_S30 | 30 | 55 | 40 | 17.6 | 14.7 | carbon | 15 | 6 |
| E5_STAIN_S50 | 50 | 55 | 40 | 17.6 | 14.7 | stainless | 15 | 6 |
| E6_CARB_S30_P10 | 30 | 55 | 40 | 17.6 | 14.7 | carbon | 10 | 6 |
| E7_STAIN_S30 | 30 | 55 | 40 | 17.6 | 14.7 | stainless | 15 | 6 |
| E8_CARB_S50_P8 | 50 | 55 | 40 | 17.6 | 14.7 | carbon | 8 | 6 |
| E9_STAIN_S23 | 23 | 55 | 40 | 17.6 | 14.7 | stainless | 15 | 6 |

The tensile coupons tests curves presented a nonlinear expected behaviour, mainly for the stainless steel – see Figure 2(c). The stainless steel yield stress was determined using a straight line parallel to the initial stiffness at a 0.2% deformation, leading to a value equal to 350.6 MPa while the ultimate tension stress was 710.7 MPa. For the carbon steel, these values were equal to 386.8 MPa and 478.7 MPa for the yield and ultimate stress, respectively. Figure 2(c) also present the results of a well known true stress versus true strain curve. This curve was used in the finite element modelling due to the large strain and stresses associated to the investigated problem.



a) universal test machine, 600kN



b) cover plate joint detail
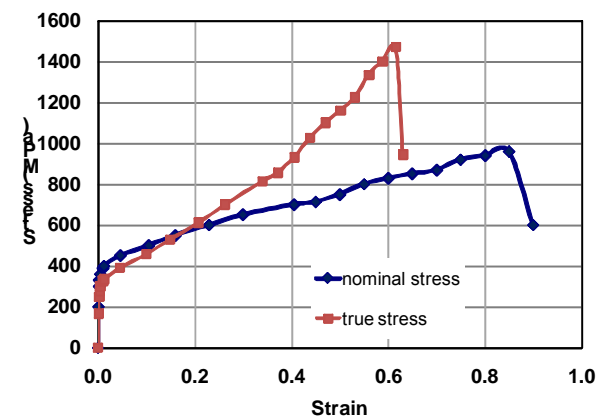


c) Stress versus strain curves for the stainless steel A304

Figure 2. Santos *et al.* (2008) test layout

Figure 3 presents the comparison between the results from tests E3_CARB_S50 and E5_STAIN_S50 in terms of the load *versus* axial displacement curves. In this figure, it may be depicted out the experimental ultimate loads of 310.0 kN and 469.4 kN for E3_CARB_S50 and E5_STAIN_S50 tests, respectively. According to the Eurocode 3, (2003), eq. (2) and (3), for the E3_CARB_S50 test, the design resistances were 337.0 kN for gross cross-section plastic resistance and 298.7 kN for ultimate net cross-section tension rupture (section with three holes). While for the E5_STAIN_S50 test, these values were 305.5 kN and 810.8 kN (net section with three holes), respectively. The partial

safety factor was taken equal to 1.0. Figure 3 also indicates that in both tests, the test rupture occurred in the section represented by two holes near to joint symmetry axis. For the carbon steel test E3_CARB_S50, the theoretical and experimental values presented a good agreement but the stainless steel test E5_STAIN_S50 presented a larger difference in terms of the ultimate design equation and test loads.

Figure 3 also presents the results for tests: E4_CARB_S30 and E7_STAIN_S30. The ultimate loads were 303.6 kN and 545.8 kN for E4_CARB_S30 and E7_STAIN_S30 tests. According to the Eurocode 3 (2003), eq. (2) and (3), for the E4_CARB_S30 test, the design resistances were 337.0 kN for gross cross-section plastic resistance and 291.7 kN for ultimate net cross-section tension rupture (section with three holes). For the E5_STAIN_S50 test, these values were 305.5 kN and 791.9 kN (net section with three holes), respectively. Figure 4 indicates that in both tests, the rupture occurred in the section with two holes near to joint symmetry axis. Again the carbon steel test E3_CARB_S50 theoretical and experimental values presented a good agreement while the stainless steel test E5_STAIN_S50, still shown a non-negligible difference of the ultimate design equation and test loads.
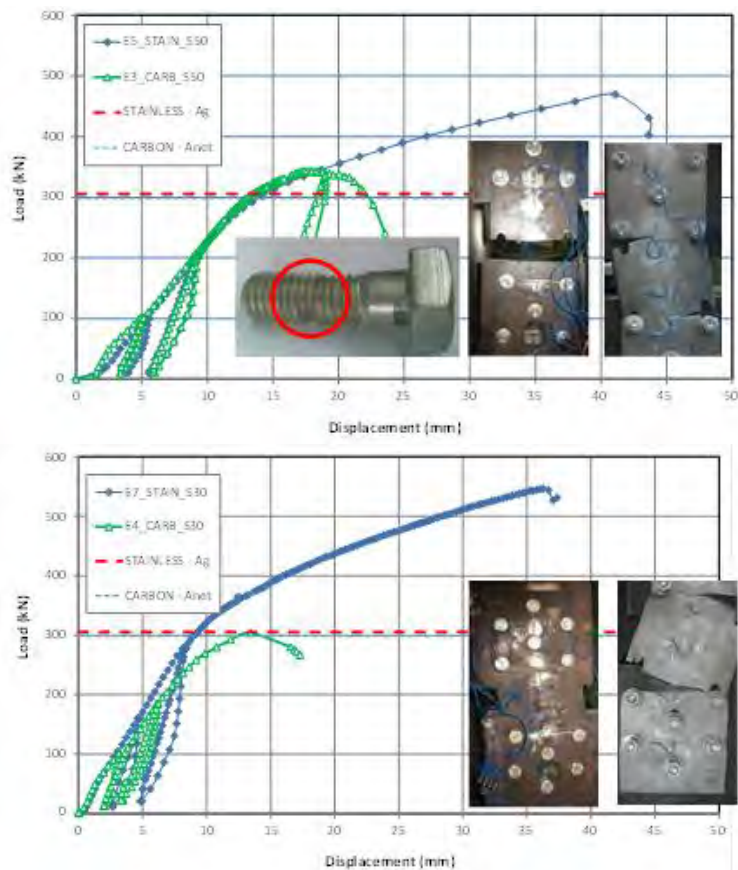
Considering the difference between the failure modes for the two stainless steel joints presented before, another test, E9_STAIN_S23, was made to investigate this issue where the horizontal bolt pitch was taken equal to 23mm. This value was considered increase the difference between the load failure in sections with two and three bolts, respectively. According to Eurocode 3 (2003), for this test, the design resistances were 305.4 kN for gross cross-section plastic resistance and 787.7 kN for ultimate net cross-section tension rupture (section with three holes). Figure 4 presents the load *versus* displacement for this test where the ultimate load was equal to 526.5 kN. It can also be observed that the joint rupture occurred in the net section passing through three bolts, in agreement with the Eurocode 3 (2003). Despite this fact, the design equation and the tests collapse loads still had some difference.
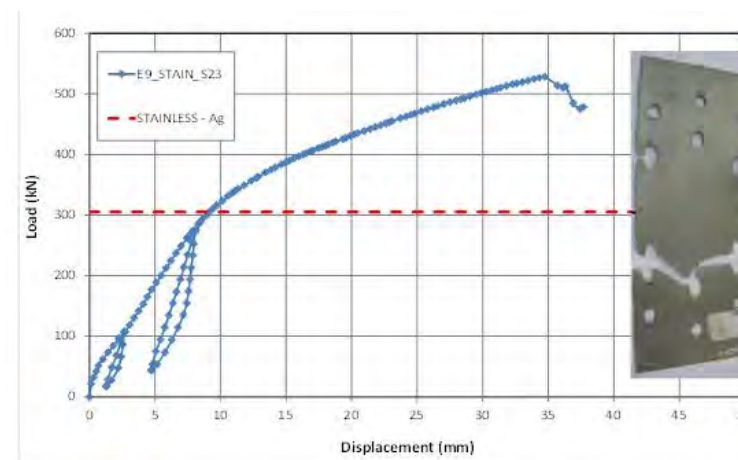


Figure 4. Load *versus* displacement - E9_STAIN_S23 (Santos, 2008)

A summary of these results is presented in Table 2. It may be concluded that for carbon steel joints, a good agreement was observed comparing the theoretical and experimental results. Alternatively, for the stainless steel joints, larger differences were found in terms of ultimate (rupture) loads.

Table 2. Summary of experimental tests (Santos, 2008)

| ID | Experimental Failure Mode | Experimental Ultimate Load (kN) | EC3 Failure Mode | EC3 Ultimate Load (kN) | % $\frac{EXP}{EC3}$ |
|---|---|---|---|---|---|
| E3_CARB_S50 | 2H | 310.0 | 3H | 298.3 | 3.9 |
| E4_CARB_S30 | 2H | 296.0 | 3H | 282.5 | 4.8 |
| E5_INOX_S50 | 2H | 480.0 | AB | 302.9 | 58.5 |
| E6_CARB_S30_P10 | 3H | 309.5 | 3H | 282.5 | 9.6 |
| E7_INOX_S30 | 2H | 459.0 | AB | 302.9 | 51.5 |
| E8_CARB_S50_P8 | 2H | 326.0 | 2H | 282.5 | 13.3 |
| E9_INOX_S23 | 3H | 436.0 | AB | 302.9 | 43.9 |
| 2H: two hole net rupture; 3H: three hole net rupture and AB: gross section yielding | | | | | |



Figure 3. Load versus displacement - E3_CARBON_S50 & E5_STAIN_S50 and E4_CARBON_S30 & E7_STAIN_S30 (Santos, 2008).

www.steelconstruct.com

Another key issue was also studied in the current study and involved the assessment of the influence of the load application plate thickness, adopted initially equal to 15mm (E3_CARB_S50 and E4_CARB_S30). Two other tests were performed, E6_CARB_S30_P10 (load plate thickness equal to 10 mm) and E8_CARB_S50_P8 (load plate thickness equal to 8 mm). Comparing the E3, E8 and E4 tests with E6, Figure 5, it may be concluded that the load application plate thickness significantly alters the joint response in terms of ultimate load and associated failure mode.
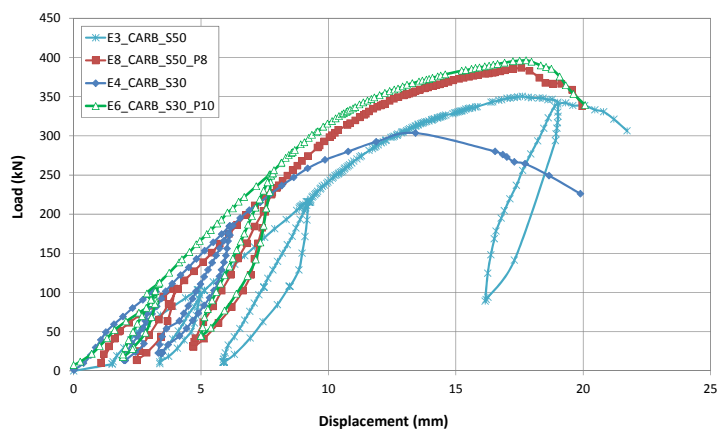


Figure 5. Load versus displacement – load plate thickness variation (Santos, 2008)

## 4. Numerical Investigation

Finite element numerical analyses provide a relatively inexpensive and time efficient alternative to physical experiments. Despite this fact, due to their nature, these numerical simulations have to be properly calibrated against experimental test results (Silva, 2008). If the validity of FE analysis is assured, it is possible to investigate the structural behaviour against a wide range of parameters with the FE model. A finite element model was used to investigate the tension capacity of cover plate joints developed with the aid of the Ansys 11 (2008) FE package. The numerical model adopted solid elements (SOLID45) defined by eight nodes with three degrees of freedom per node: translations in the nodal x, y and z directions.

Contact elements (CONTA174 and TARGE170) presented in the Ansys 11 (2008) Elements Library, were considered between the plates and between the holes and the bolt shanks. The load was applied by means of axial displacements in the load plate such as presented in Figure 6. In this figure, it is also possible to observe that the bolt head and nuts were simulated through UZ displacements restraints at the hole adjacent area. The numerical model was calibrated against experiments made by Santos (2008). Figure 7 presents a typical mesh configuration of the complete model. It is emphasized here that only half of the model was considered using symmetry conditions sufficient to characterize the joint ultimate limits states.

The adopted material properties were: Young's modulus of 210 GPa (see Figure 2) and a Poisson's coefficient of 0.3. As previously mentioned, stainless steel true stress versus true strain curves with a nonlinear behaviour were adopted using data from the tensile coupons tests - Figure 2(c). A full nonlinear analysis was performed for the developed numerical model. The material non-linearity was considered
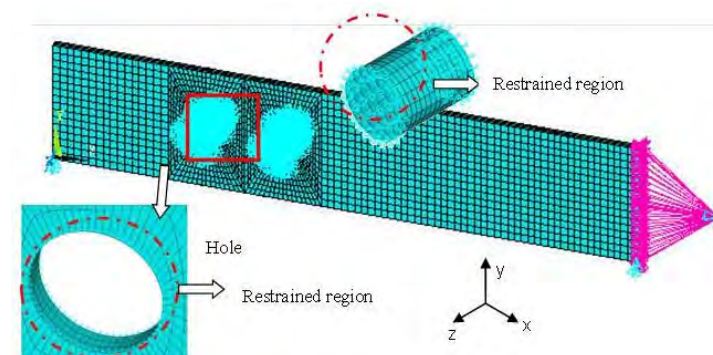


Figure 6. Finite element model and contact elements (Silva, 2008)
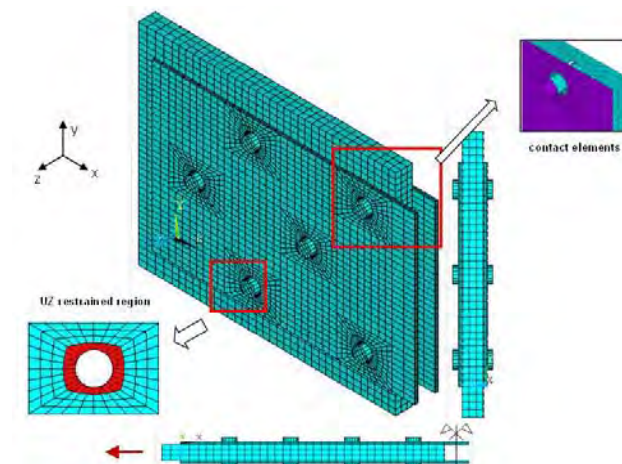


Figure 7. Finite element model and contact elements (Silva, 2008)

using a *von Mises* yield criterion associated to a multi-linear stress-strain relationship and isotropic hardening response. The geometrical non-linearity was introduced in the model by using an Updated Lagrangean formulation. This procedure represents the full structural assessment of the analysed bolted joints, and may be summarized in several outputs, namely the stress distribution (that detects, among other data, first yield), or the force *versus* displacement curve for any node within the connection.

Figure 8 presents the load *versus* displacements curves for each individual test, where it can be observed that the ultimate load of experiments E5_INOX_S50, E7_INOX_S30 e E9_INOX_S23 were: 389 kN, 389 kN and 385 kN, respectively. All the numerical model loads were situated in an interval between the experimental loads and the Eurocode 3 part 1.4 (2003) estimated values. Figure 9 depicts the *von Mises* stress distributions for the three numerical models, where could be noticed that all models presented high stress concentrations in the region between the bolt holes and the plate edge. In the numerical model corresponding to E5_INOX_S50 test the stress distribution indicates a possible rupture in the stainless steel plate net area passing through two bolt holes, failure mode that also occurred in the experiment. In the numerical model corresponding to E7_INOX_S30, the section in

which the net area rupture occurs is not clear, i.e. it could be located in the plate region passing through two or three bolt holes. In the numerical model corresponding to E9_INOX_S23 test the stress distribution indicates a possible rupture in the stainless steel plate net area passing through three bolt holes, failure mode that also was identified in the experiment.
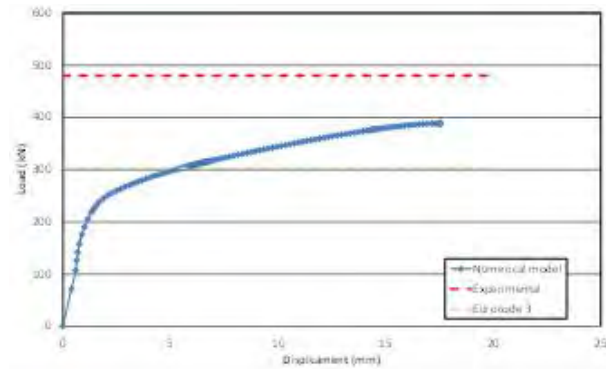


a) E5_INOX_S50 specimen
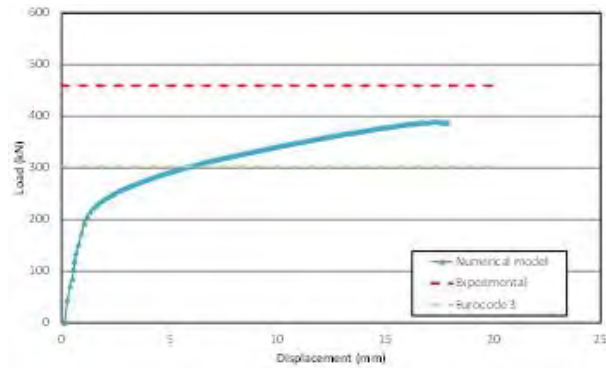


b) E7_INOX_S30 specimen
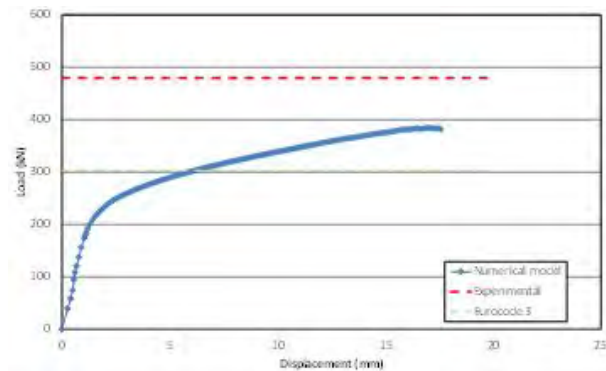


c) E9_INOX_S23 specimen

Figure 8. Stainless steel load *versus* displacement curves (Silva, 2008)



a) Test – E5_INOX_S50     b) Test – E7_INOX_S30     c) Test – E9_INOX_S23
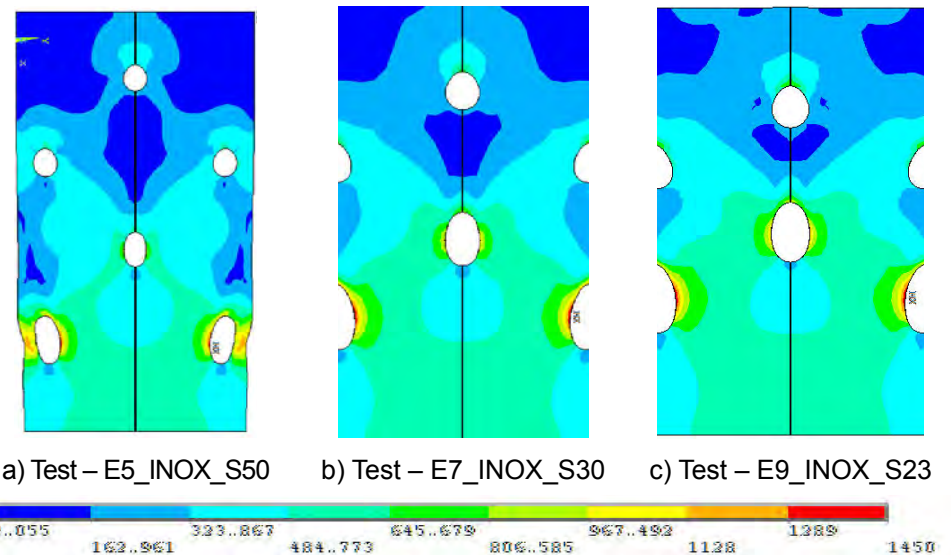
Figure 9. Von Mises stress distribution (in MPa) at the ultimate load

In order to validate the proposed numerical model, a series of comparisons will be presented in terms of load versus strain curves for specific points that were measured in the experimental programme. Figure 10 presents numerical and experimental strain comparisons for the E5_INOX_S50 specimen, measured in the region close to the joint centre line. It can be observed that a similar response was found in the numerical and experimental curves, for strain gauges 2(4) and 3(8). However, the numerical model presented, in the plastic range, a stiffness value lower than their experimental counterparts. Figure 11 depicts load vs. strain curves for the E7_INOX_S30 test where it can be observed that the numerical results were not as good as the previous tests, presenting a lower stiffness and achieving larger strains than its experimental counterparts. Alternatively, the results of E9_INOX_S23 tests, Figure 12, indicated a good similarity between the numerical and test evidences.
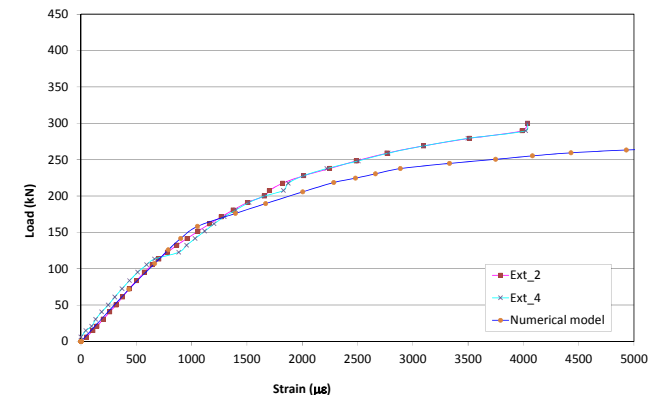


a) Strain gauges 2 and 4
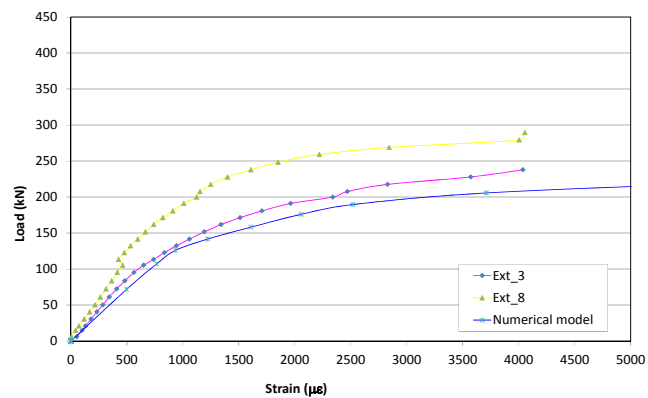
b) Strain gauges 3 and 8

Figure 10. Load vs strain (experimental and numerical) - E5_INOX_50 (Silva, 2008)



a) Strain gauges 2 and 4



a) Strain gauges 2 and 4



b) Strain gauges 3 and 8

Figure 12. Load vs strain (experimental and numerical) - E9_INOX_23 (Silva, 2008)

The plate section at which the stainless steel net area rupture failure mode occurred was determined with the aid of Figure 13 where load vs. strain curves are
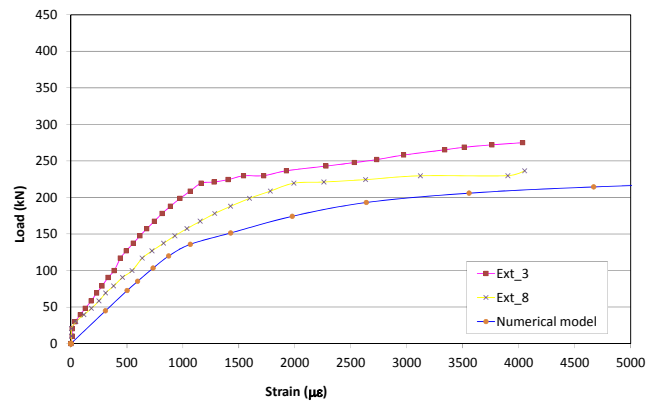


b) Strain gauges 3 and 8

Figure 11. Load vs strain (experimental and numerical) - E7_INOX_30 (Silva, 2008)
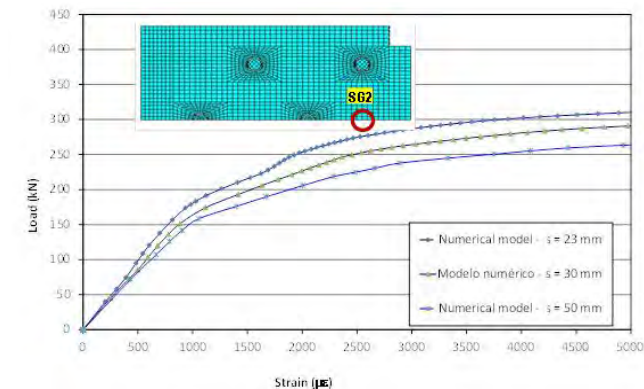
Figure 13. Load *versus* strain curves for all the numerical models (Silva, 2008)

illustrated for a point locates at the plate cross section with two bolt holes at the horizontal symmetry axes. From this graph it can be observed that as the horizontal distance between two bolt holes increases the magnitude of the stresses on the bolt present in adjacent section diminishes. For example, for a 250 kN load level, the left curve is associated to a strain level lower than the others highlighting the net area rupture failure passing in a plate section with three bolt holes. On the other hand, for this load level, E5_INOX_S50 numerical model, highlights that the failure mode is associated to the net area rupture failure passing in a section with two bolt holes.

## 5. FINAL CONSIDERATIONS

This paper presented an experimental and numerical programme to investigate the structural response of the carbon steel and stainless steel plates with staggered bolts under tension. Initially the experimental results were compared to theoretical results according to Eurocode 3, (2003), provisions. For carbon steel tests, a good agreement was reached between the design equation and the experiments, fact that was not corroborated in the stainless steel tests where large difference were observed, mainly in terms of the ultimate load. A possible explanation for these discrepancies could be related to the fact that the great majority of stainless steel structural design codes are still based on carbon steel analogies. At this point it is interesting to observe that the stainless steel codes need to be improved in order to correct evaluate the stainless steel structural elements behaviour. A finite element numerical model was also developed with the aid of the Ansys 11 (2008) and considered material and geometrical nonlinearities through the *von Mises* yield criterion and the Updated Lagrangian Formulation, respectively. The numerical model calibration was made against Santos (2008) experiments where the optimum mesh and element sizes were determined, Silva (2008).

Table 3 presents a comparison between the numerical results and the Eurocode 3 provisions (2003), for the already mentioned stainless steel tests (Santos, 2008). Differences of about 28% were found when the Eurocode 3 (2003) and the numerical models were compared. The numerical ultimate loads were less than their experimental counterparts for all the investigated specimens. This can be explained by the fact that the developed numerical models represent the joints in an idealized form, without imperfections or residual stresses. Another reason for these differences can be attributed to the fact that the stainless steel stress *versus* strain curve adopted in the finite element model was obtained through a serie of coupons that are influenced by the rolling direction. The problem related to the numerical and experimental assessment of stainless and carbon bolted tensioned members is certainly much more complicated and it is influenced by several other design parameters. Further research in this area is currently being carried out, in order to consider imperfections, residual stresses and the coupons rolling directions.
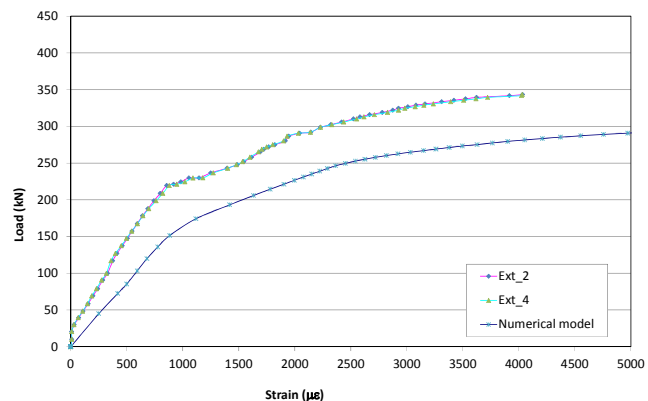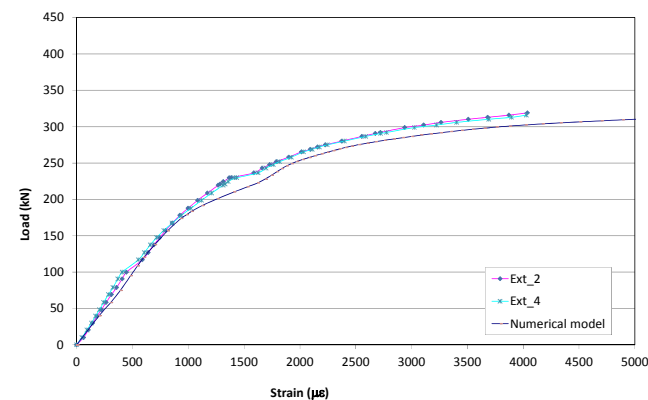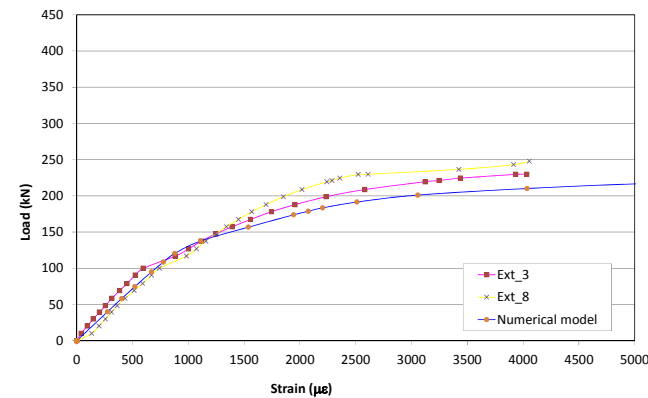
On the other hand, differences varying from entre 12% up to 19% were found when the numerical and the experimental values were compared. These differences were also partly due to the natural conservatism present in most of the design standard Eurocode 3, part 1.4, (2003). This conservatism is largely due to the lack of experimental evidence regarding stainless steel response still present in literature. The investigation indicated that when stainless steel is used in certain structural engineering applications like joints under shear forces, the current design criteria based on deformation limits need to be re-evaluated specially due to the differences in the yield to ultimate deformation and stress ratios.

Table 3. Summary of experimental tests (Silva, 2008)

| Experimental tests | Experimental failure mode | Experimental ultimate load (kN) | Numerical failure mode | Numerical ultimate load (kN) | Difference Numerical x Experimental (%) | Difference Numerical x EC3 (%) |
|---|---|---|---|---|---|---|
| E5-INOX-S50 | 2F | 480.0 | 2F | 389 | 19.0 | 28.8 |
| E7-INOX-S30 | 2F | 459.0 | 2F / 3F | 389 | 15.2 | 28.8 |
| E9-INOX-S23 | 3F | 436.0 | 3F | 385 | 11.6 | 27.5 |

## ACKNOWLEDGMENTS

## REFERENCES

[1] Ansys, Inc. Theory Reference (version 11.0), 2008.
[2] Bouchair, J., Averseng, A., Abidelah, Analysis of the behaviour of stainless steel bolted connections, LaMI, Civil Engineering, Blaise Pascal University, rue des Meuniers, BP 206, 63174 Aubière cedex, France, 2008
[3] Burgan B. A, Baddoo, N. R., Gilsenan, K. A., Structural design of stainless steel members - comparison between Eurocode 3, Part 1.4 and test results. Journal of Constructional Steel Research; 54(1):51–73, 2000.
[4] Cochrane, V. H., 1922, Rules for Rivet Hole Deduction in Tension Members, Engineering News-Record, vol. 80, November.
[5] Eurocode 3, ENV 1993-1-1, 2003: Design of steel structures - Structures – Part 1-1: General rules and rules for buildings. CEN, European Committee for Standardisation, Brussels, 2003.
[6] Eurocode 3, ENV 1993-1-4, 2003: Design of steel structures – Part 1.4: General rules – Supplementary rules for stainless steel, CEN – European Committee for Standardisation 2003.
[7] Gardner L, Baddoo N. R., Fire testing and design of stainless steel structures. Journal of Constructional Steel Research; 62: 532-43, 2006.
[8] Gardner, L., Nethercot, D. A., Experiments on stainless steel hollow sections — Part 1: Material and cross-sectional behaviour. Journal of Constructional Steel Research ;60:1291–318.cap 3, 2004.
[9] Santos, J. de J. dos, 2008, Comportamento Estrutural de Elementos em Aço Inoxidável, MSc in Civil Engineering, State University of Rio de Janeiro, UERJ, Rio de Janeiro, Brazil (in portuguese).
[10] Silva, A. T. da, 2008, Comportamento de Peças Tracionadas em Esruturas de Aço-Carbono e Aço Inoxidável, Graduate Project, Structural Engineering Department, State University of Rio de Janeiro, UERJ, Rio de Janeiro, Brazil (in portuguese).

# BLOCK SHEAR CAPACITY OF BOLTED CONNECTIONS IN HOT-ROLLED STEEL PLATES

Lip H. Teh and Veysel Yazici
*School of Civil, Mining and Environmental Engineering, University of Wollongong, Australia*
*lteh@uow.edu.au*

## ABSTRACT

This paper extends the research previously conducted at the University of Wollongong on block shear failure of bolted connections in cold-reduced steel sheets with low ductility to hot-rolled steel plates. It examines the applicability of the basic approach employed for cold-reduced sheet steel bolted connections, which makes use of the so-called active shear planes, to hot-rolled steel plate connections. The active shear planes lie midway between the gross and the net shear planes defined in the steel structures specifications. The paper shows that shear yielding leading to the block shear failure of a bolted connection in a hot-rolled steel gusset plate is typically accompanied by full strain hardening. The paper proposes a design equation that provides more accurate and consistent results compared to the American, Australian, Canadian and European code equations in determining the block shear capacities of bolted connections in hot-rolled steel gusset plates. A resistance factor of 0.85 is recommended in order to achieve a target reliability index of 4.0 or greater.

## 1. INTRODUCTION

Block shear failure is recognised as a strength limit state of bolted connections in the AISC Specification for Structural Steel Buildings (AISC 2010a), Eurocode 3 Part 1.8 (ECS 2005), Canadian and Australian steel structures standards (CSA 2009, SA 2012). However, since it was discovered by Birkemoe & Gilmor (1978) and first incorporated into the AISC specification (AISC 1978), the design provisions for determining the block shear capacity of a bolted connection have continued to change and even oscillate between certain equations, as described by Teh & Clements (2012) and summarised in Table 1. The reasons are at least two folds.

The first reason is that there was the uncertainty concerning the possible mechanisms even for conventional block shear failures. Some versions of the AISC specification (AISC 1978, 1989) assume the simultaneous shear and tensile rupture mechanism, while others provide for the shear yielding and tensile rupture mechanism and for the shear rupture and tensile yielding mechanism (AISC 1986, 1993). The latest version incorporates the simultaneous shear and tensile rupture mechanism, and the shear yielding and tensile rupture mechanism (AISC 2010a).

The more important reason, however, is the inconsistent definitions of the shear failure planes used in the code equations for determining the block shear capacity. The gross shear area is used when the failure mechanism is shear yielding and tensile rupture, while the net shear area is used for the shear rupture and tensile yielding mechanism or simultaneous shear and tensile rupture mechanism. Such a procedure is awkward since shear yielding must precede shear rupture, and often leads to anomalies since a lower load is required to fail the connection by simultaneous shear and tensile ruptures.

Table 1. AISC's block shear design equations over the years

| Year | Equation |
|---|---|
| 1978 | $R_n = F_u A_{nt} + 0.6 F_u A_{nv}$ |
| 1986 | $R_n = \max\left( F_u A_{nt} + 0.6 F_y A_{gv}; \quad F_y A_{gt} + 0.6 F_u A_{nv} \right)$ |
| 1989 | $R_n = F_u A_{nt} + 0.6 F_u A_{nv}$ |
| 1993 | If $F_u A_{nt} \geq 0.6 F_u A_{nv}$ : $R_n = F_u A_{nt} + 0.6 F_y A_{gv}$ <br> If $F_u A_{nt} \leq 0.6 F_u A_{nv}$ : $R_n = F_y A_{gt} + 0.6 F_u A_{nv}$ |
| 1999 | If $F_u A_{nt} \geq 0.6 F_u A_{nv}$ : $R_n = \min\left( F_u A_{nt} + 0.6 F_u A_{nv}; \quad F_u A_{nt} + 0.6 F_y A_{gv} \right)$ <br> If $F_u A_{nt} \leq 0.6 F_u A_{nv}$ : $R_n = \min\left( F_u A_{nt} + 0.6 F_u A_{nv}; \quad F_y A_{gt} + 0.6 F_u A_{nv} \right)$ |
| 2005 2010a | $R_n = \min\left( F_u A_{nt} + 0.6 F_u A_{nv}; \quad F_u A_{nt} + 0.6 F_y A_{gv} \right)$ |

The uncertainty and the inconsistency mentioned in the preceding paragraphs have been discussed by Teh & Clements (2012) and Clements & Teh (2012), who verified their theoretical expositions and proposed design equation against laboratory test results of bolted connections in cold-reduced steel sheets having low ductility. Teh & Clements (2012) found the use of the shear yield stress only in computing the shear resistance to block shear failure to be reasonably accurate.

This paper presents a modification to the block shear equation proposed by Teh & Clements (2012) to suit bolted connections in hot-rolled steel gusset plates, and verifies the resulting equation against laboratory test results obtained by various researchers around the world. All the steel materials used in the laboratory tests had much greater ductility compared to the cold-reduced sheet steels used by Teh & Clements (2012). For the purpose of the present work, the physical reasoning presented by Teh & Clements (2012) will be described in order to accentuate the feasible mechanism for a conventional block shear failure.

## 2. FEASIBLE MECHANISM FOR CONVENTIONAL BLOCK SHEAR FAILURE

Consider the connected end of a flat member shown in Figure 1 that is subjected to a concentric load and is restrained from out-of-plane failure modes. Leaving out the pure net section tension failure mode and the bearing failure mode from the present discussion, there are essentially only two possible failure modes for the connected end. If the connection shear length (which is denoted by $e_n$ in Figure 1) is relatively short, it will fail by "shear out" of each bolt, as shown in Figure 2.

As the connection shear length $e_n$ increases, or as the bolt spacing $p_2$ decreases, or both, any of which results in an increase of the aspect ratio (defined as $e_n/p_2$ for the connection depicted in Figure 1), a condition would be reached such that it is conceivable for the connected end to undergo block shear failure by simultaneous shear and tensile ruptures. The aspect ratio at which the hypothetical mechanism

of simultaneous shear and tensile ruptures could occur is termed the threshold ratio in the present work.
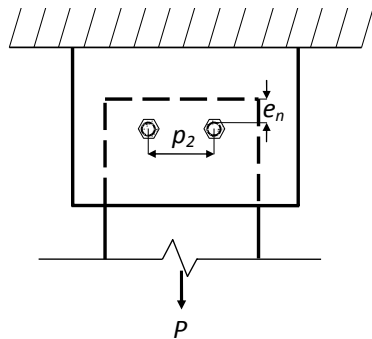


Figure 1. A two-bolt connection



Figure 2. Shear-out of individual bolts



Figure 3. Shear-out deformations gave way to block shear failure

However, once yielding around the perimeter of the block takes place and the block displaces as a whole, the tensile strains in the net section between bolt holes increase much more rapidly than the shear strains so that the block eventually fails by shear yielding and tensile rupture. Even at an aspect ratio that is slightly lower than the threshold ratio, a block shear failure by shear yielding and tensile rupture is still possible as shown in Figure 3, where the shear-out deformations were over-run by the shear yielding and tensile rupture mechanism. The change-over in the failure mode took place when yielding started in the tensile net section between the two bolt holes, where tensile rupture eventually took place.

As the aspect ratio increases beyond the threshold ratio, block shear failure can only be due to shear yielding and tensile rupture since the tensile strains are always more critical than the shear strains.

Obviously, at an aspect ratio that is sufficiently lower than the threshold ratio, the shear-out failure mode governs. There is therefore no aspect ratio at which a conventional block shear failure occurs by the shear rupture and tensile yielding mechanism.

In summary, a conventional block shear failure can only occur by the shear yielding and tensile rupture mechanism. However, shear yielding leading to a block shear failure may occur with significant strain hardening, depending on the ductility of the steel material. The greater the elongation at fracture exhibited by the tension coupon, the greater the scope for strain hardening along the shear yielding planes before fracture takes place in the tensile net section.

## 3. RELEVANT EQUATIONS FOR BLOCK SHEAR CAPACITY

Having established that a conventional block shear failure invariably fails by the shear yielding and tensile rupture mechanism, as borne out by laboratory test results, the present work is primarily concerned with the equations that are based on such a mechanism. There are four equations to consider.

The first equation is found in the AISC specification (AISC 2010a) and the Australian steel structures standard (SA 2012)

$$R_n = F_u A_{nt} + 0.6 F_y A_{gv} \qquad (1)$$

in which $F_u$ is the material tensile strength, $F_y$ is the yield stress, $A_{nt}$ is the net tensile area, and $A_{gv}$ is the gross shear area. The implied block is depicted in Figure 4(a), which shows that the shear yielding planes assumed in Equation (1) lie at the outer perimeter of the block.

The second equation to consider is found in the European steel structures code (ECS 2005)

$$R_n = F_u A_{nt} + \frac{F_y A_{nv}}{\sqrt{3}} \approx F_u A_{nt} + 0.577 F_y A_{nv} \qquad (2)$$

in which $A_{nv}$ is the net shear area indicated in Figure 4(b). This approach ignores the fact that the planes coinciding with the centrelines of the bolt holes in the direction of loading do not have maximum shear stresses due to the bolt bearing condition.

The third equation is given in the Canadian steel structures standard (CSA 2009) based on the research results of Driver et al. (2006)

$$R_n = F_u A_{nt} + 0.3 \left( F_y + F_u \right) A_{gv} \qquad (3)$$

in which the mean between the yield stress and the tensile strength is used to simulate the contribution of strain hardening to the shear resistance. The definition of the shear yielding planes is the same as that used in the AISC specification.

The fourth equation results from a modification to the block shear equation for cold-reduced sheet steels with low ductility and little strain hardening proposed by Teh & Clements (2012)

$$R_n = F_u A_{nt} + 0.6 \left( \frac{a F_y + b F_u}{a + b} \right) A_{av} \qquad (4a)$$
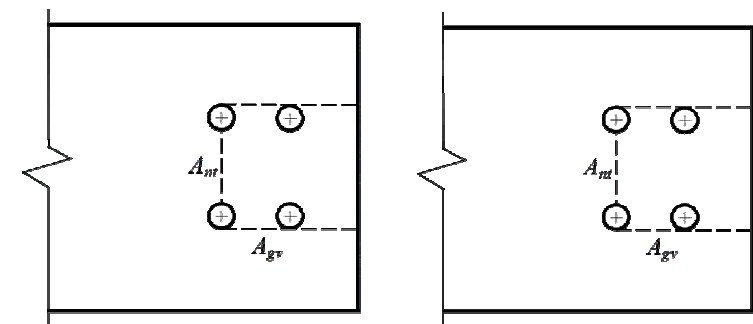


a) Gross shear planes    b) Net shear planes

Figure 4. Gross and net shear failure planes

www.steelconstruct.com

in which $A_{av}$ is the active shear area defined in Figure 5. The variable $n_r$ denotes the number of bolt rows. The coefficients $a$ and $b$ are used to determine the extent of strain hardening in the shear yielding planes. The greater the value of $b$ relative to $a$, the greater the extent of strain hardening. A zero value of $a$ indicates full strain hardening, while a zero value of $b$ indicates no strain hardening. The appropriate values are discussed in the next section.

The active shear area $A_{av}$ was used by Teh & Clements (2012) based partially on the experimental evidence of Franchuk et al. (2003) shown in Fig. 3 of their paper. The location of the active shear planes, which lie midway between the gross and the net shear planes, has subsequently been confirmed by Clements & Teh (2012) through nonlinear contact finite element analysis. Maximum shear stresses do not take place in both the gross and the net shear planes, but between them irrespective of whether the block shear failure occurs by shear yielding or shear rupture.



$$L_{av} = L_{gv} - \left(\frac{n_r - 1}{2} + \frac{1}{4}\right)d_h$$

$$\approx L_{gv} - \frac{n_r d_h}{2}$$

$$A_{av} = 2L_{av}t$$
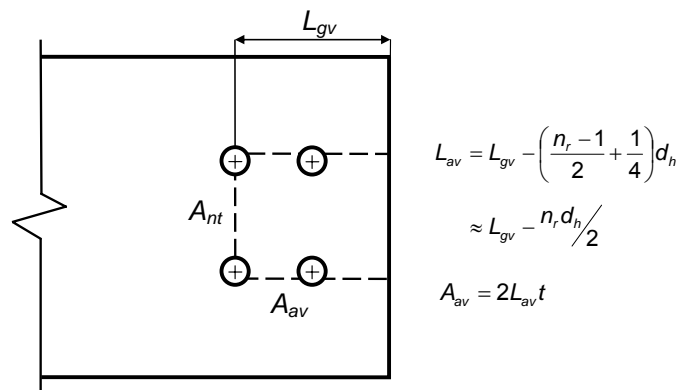
Figure 5. Active shear planes

## 4. COMPARISONS OF ALTERNATIVE EQUATIONS

Equations (1) through (4) are verified against the laboratory test results of bolted connections in hot-rolled steel gusset plates failing by block shear obtained by various researchers around the world. The steel materials used in the tests had much higher strain hardening capability compared to the high strength sheet steels tested by Teh & Clements (2012), with the ratio of tensile strength $F_u$ to yield stress $F_y$ being as high as 1.75. The uniform elongations at fracture of such steels were 3 to 6 times those of the sheet steels tested by Teh & Clements (2012), the latter having low uniform elongations at fracture between 6 and 8 percent only.

Based on the conclusion of Driver et al. (2006) in comparing the same test results against Equation (3), which makes use of the mean between $F_y$ and $F_u$ in conjunction with the gross shear area $A_{gv}$, it was surmised that full or almost full strain hardening had been achieved along the shear yielding planes in most of the tested hot-rolled steel specimens. Therefore, Equation (4a) becomes, with $a = 0$ and $b = 1$:

$$R_n = F_u A_{nt} + 0.6 F_u A_{av} \qquad (4b)$$

It should be noted that, unlike the AISC specifications (1978, 2010a), the use of the tensile strength $F_u$ in Equation (4b) for computing the shear resistance does not represent the block shear failure by shear (and tensile) rupture.

Table 2 shows the *average* professional factors of the alternative equations for each set of laboratory test results. The variable $N$ denotes the number of specimens failing by block shear in each set.

It can be seen from Table 2 that Equation (2) specified in the European steel structures code (ECS 2005) is excessively conservative even on the basis of the average professional factors. Equation (3) specified in the Canadian steel structures standard (CSA 2009), on the other hand, is over-optimistic for many of the tested specimens (see also Table 3).

Table 2. Average professional factors

| | N | (1) AISC 2010a | (2) ECS 2005 | (3) CSA 2009 | (4b) Proposed |
|---|---|---|---|---|---|
| Udagawa & Yamada (1998) | 73 | 1.04 | 1.38 | 0.94 | 1.03 |
| Aalberg & Larsen (1999) | 8 | 1.01 | 1.41 | 0.91 | 1.03 |
| Rabinovitch & Cheng (1993) | 5 | 1.01 | 1.36 | 0.93 | 1.01 |
| Huns et al. (2002) | 5 | 1.18 | 1.53 | 1.05 | 1.11 |
| Mullin (2002) | 5 | 1.14 | 1.44 | 1.00 | 1.01 |
| Hardash & Bjorhovde (1985) | 28 | 1.18 | 1.50 | 1.06 | 1.06 |

Based on the average professional factors, Equation (1) given in the AISC specification for the shear yielding and tensile rupture mechanism appears to be rather accurate. In fact, it would appear from Table 2 that Equation (1) was more accurate than Equation (4b) for the specimens tested by Aalberg & Larsen (1999).

However, examination of the individual professional factors reveals a very different outcome. Table 3 shows that, for every single specimen tested by Aalberg & Larsen (1999), Equation (4b) is consistently more accurate than Equation (1). The variable $n_r$ denotes the number of bolt rows in a specimen.

Table 3. Individual professional factors for specimens of Aalberg & Larsen (1999)

| | $n_r$ | (1) AISC 2010a | (2) ECS 2005 | (3) CSA 2009 | (4b) Proposed |
|---|---|---|---|---|---|
| T7 | 2 | 1.21 | 1.59 | 1.05 | 1.12 |
| T8 | 2 | 0.90 | 1.21 | 0.89 | 1.05 |
| T9 | 3 | 1.18 | 1.65 | 1.01 | 1.07 |
| T10 | 3 | 0.86 | 1.22 | 0.84 | 1.01 |
| T11 | 4 | 1.13 | 1.64 | 0.96 | 1.02 |
| T12 | 4 | 0.82 | 1.20 | 0.80 | 0.96 |
| T15 | 3 | 1.12 | 1.56 | 0.95 | 1.01 |
| T16 | 3 | 0.83 | 1.18 | 0.82 | 0.98 |
| | Mean | 1.01 | 1.41 | 0.91 | 1.03 |
| | COV | 0.169 | 0.154 | 0.100 | 0.049 |

Table 3 shows that, while the average professional factor of Equation (1) is close to unity (1.01), it underestimates the strength of specimen T7 by 17% (1/1.21 = 0.83) but overestimates that of specimen T12 by 22% (1/0.82 = 1.22). It can also be seen from the table that Equation (4b) is much more accurate and consistent than all the code equations, which can overestimate or underestimate the block shear capacity considerably.

Table 4 shows the results of using the complete block shear equation prescribed in the current AISC specification (AISC 2010a)

$$R_n = \min\left(F_u A_{nt} + 0.6 F_u A_{nv}; \quad F_u A_{nt} + 0.6 F_y A_{gv}\right) \quad (5)$$

Table 4. Average professional factors of AISC (2010a)

| | $N$ | $R_n = \min\left(F_u A_{nt} + 0.6 F_u A_{nv}; \quad F_u A_{nt} + 0.6 F_y A_{gv}\right)$ |
|---|---|---|
| Udagawa & Yamada (1998) | 73 | 1.18 |
| Aalberg & Larsen (1999) | 8 | 1.21 |
| Rabinovitch & Cheng (1993) | 5 | 1.22 |
| Huns et al. (2002) | 5 | 1.26 |
| Mullin (2002) | 5 | 1.14 |
| Hardash & Bjorhovde (1985) | 28 | 1.19 |

By comparing the results of Equation (5) shown in Table 4 against those of Equation (1) shown in Table 2, it becomes evident that the first term of Equation (5), which is based on the simultaneous shear and tensile rupture mechanism, virtually determines the block shear capacity of all specimens since it leads to the lower computed capacities. In any case, it can be seen that the current AISC block shear equation is over-conservative even on the basis of average professional factors.

## 5. RELIABILITY ANALYSIS AND RESISTANCE FACTOR

The reliability analysis methodology and the statistical parameters used in the present work have been adopted from Driver et al. (2006), who determined the required resistance factor $\phi$ using the equation proposed by Fisher et al. (1978)

$$\phi = \left(0.0062\beta^2 - 0.131\beta + 1.338\right) M_m F_m P_m e^{-p} \quad (6)$$

in which $\beta$ is the target reliability index, $M_m$ is the mean value of the material factor equal to 1.11 (Schmidt & Bartlett 2002), $F_m$ is the mean value of the fabrication factor equal to 1.00 (Hardash & Bjorhovde 1985), and $P_m$ is the mean value of the relevant professional factor computed for all the 124 specimens listed in Table 2.

The exponential term $p$ in Equation (6) is computed from

$$p = \alpha_R \beta \sqrt{V_m^2 + V_F^2 + V_P^2} \quad (7)$$

in which $\alpha_R$ is the separation variable equal to 0.55 (Ravindra & Galambos 1978), $V_M$ is the coefficient of variation of the material factor equal to 0.054 (Schmidt & Bartlett 2002), $V_F$ is the coefficient of variation of the fabrication factor equal to 0.05 (Hardash & Bjorhovde 1985), $V_P$ is the coefficient of variation of the relevant professional factor computed for all the 124 specimens listed in Table 2.

Table 5 shows the resulting reliability indices $\beta$ of the code and proposed equations if the resistance factor $\phi$ of 0.75 prescribed in the AISC specification (AISC 2010a) is used. The "acceptable" values for $\beta$ range from 4 to 5 (AISC 2010b).

It can be seen from Table 5 that the current AISC provision for the limit state of block shear failure is very conservative, resulting in a reliability index $\beta$ of 6.1. The resistance factor $\phi$ of 0.75 has remained the same since the first LRFD edition (AISC 1986), even though the block shear equations have changed as shown in Table 1.

The application of the resistance factor $\phi$ of 0.75 to the first LRFD block shear equation (AISC 1986) resulted in a reliability index $\beta$ of 4.5 for the same set of test results.

Table 5. Reliability analysis results of code and proposed equations

| | (5) AISC 2010a | (2) ECS 2005 | (3) CSA 2009 | (4b) Proposed |
|---|---|---|---|---|
| $P_m$ | 1.19 | 1.41 | 0.96 | 1.04 |
| $V_P$ | 0.051 | 0.093 | 0.074 | 0.058 |
| $\beta$; $\phi = 0.75$ | 6.1 | 6.7 | 4.2 | 5.0 |
| $\phi$; $\beta = 4.0$ | 0.99 | 1.10 | 0.78 | 0.86 |

Table 5 also shows the required resistance factor $\phi$ for each equation if the target reliability index $\beta$ is set to be 4.0 (AISC 2010b). Consistent with the finding of Driver et al. (2006), it was found that the required resistance factor $\phi$ for Equation (5) is close to unity. This outcome does not demonstrate the superiority of Equation (5), but merely indicates the conservatism of the existing resistance factor $\phi$ of 0.75 for bolted connections in gusset plates.

For the same level of procedural complexity, the design equation should be the one which is the most *consistently* accurate among available alternatives, as reflected in the individual professional factors. A good rule of thumb may be that the average professional factor should fall between 0.95 and 1.05, with a standard deviation not greater than 0.10. However, Equation (3), which satisfies this rule, overestimates the capacity of 33 specimens by more than 10% (and that of 5 specimens by 20% or more). Equation (4b), on the other hand, only overestimates the capacity of one specimen by more than 10% (20% for an outlier specimen for all equations).

While in theory the application of capacity factors $\phi$ equal to 0.78 and 0.86 to Equations (3) and (4), respectively, would result in the same reliability index $\beta$ equal to 4.0, it is evident from Table 3 and the facts in the preceding paragraph that Equation (3) leads to significantly more varied safety margins across connections of different configurations, notwithstanding the aim of the LRFD approach to achieve consistent reliability in structural design. The same is true for the other code equations. Sns. The implication is that, while the code equations may or may not be unsafe, they are (in conjunction with the corresponding capacity factors) too conservative for many if not most connections. Reliance on the use of an "appropriate" capacity factor as determined from a reliability analysis to compensate for a grossly inaccurate equation is not ideal for achieving efficient designs.

## 6. SUMMARY AND CONCLUSIONS

Among the various mechanisms for conventional block shear failures postulated in the literature and anticipated in the design codes, there is only one feasible mechanism, that which involves shear yielding and tensile rupture. The physical reasoning described by the authors explains why extensive published laboratory tests of hot-rolled steel bolted connections have never found a block shear failure caused by any other mechanisms anticipated in the steel design codes around the world.

The shear yielding planes in a block shear failure, termed the active shear planes, lie midway between the gross and the net shear planes assumed in the AISC specification for shear yielding and for shear rupture, respectively. In reality, the shear failure planes are unique and do not depend on the prevalent mechanism of block shear failure.

www.steelconstruct.com

The use of the net shear area in the European steel structures code in conjunction with the shear yield stress leads to excessive conservatism in determining the block shear capacity of hot-rolled steel bolted connections. This conservatism is somewhat tempered in the AISC specification by the use of the shear ultimate stress instead of the shear yield stress (when the net shear area is used to compute the shear rupture resistance component), but the resulting equation is still quite conservative with more than 25% underestimation in some individual cases. The significant conservatism of the current European and American code equations is also reflected in the reliability analysis results presented by the authors and Driver et al. (2006).

For bolted connections in hot-rolled steel plates, full or almost full strain hardening takes place along the shear yielding planes. This means that the shear ultimate stress rather than the shear yield stress should be used in computing the shear yielding resistance component in conjunction with the active shear area.

The use of the gross shear area in conjunction with the shear yield stress in the AISC specification for the shear yielding and tensile rupture mechanism led to overestimation and underestimation by 20% or more of the block shear capacity.

The use of the gross shear area in conjunction with the mean between the shear yield stress and the shear ultimate stress in the Canadian steel structures standard led to overestimation by up to 25% (1/0.80 = 1.25) of the tested capacity.

Reliability analyses can only ensure that the same reliability index is achieved for a group of different design equations, but cannot achieve a consistent safety margin across the components being designed when an inaccurate equation is used.

The proposed equation, which makes use of the active shear area in conjunction with the shear ultimate stress, has been demonstrated to provide the most consistent and accurate results in determining the block shear capacities of bolted connections in hot-rolled steel gusset plates tested by various researchers around the world. A resistance factor equal to 0.85 is recommended for use with the proposed equation to ensure a reliability index of 4.0 is achieved.

## ACKNOWLEDGMENT

## REFERENCES

[1] Aalberg, A., and Larsen, P.K. (1999) Strength and ductility of bolted connections in normal and high strength steels, Report N-7034, Dept. of Structural Engineering, Norwegian University of Science and Technology, Trondheim, Norway.

[2] ABAQUS (2009) ABAQUS Analysis User's Manual, Version 6.9, Dassault Systèmes, Providence RI.

[3] AISC (1978) Specification for the Design, Fabrication and Erection of Structural Steel for Buildings, American Institute of Steel Construction, Chicago IL.

[4] AISC (1986) Load and Resistance Factor Design Specification for Structural Steel Buildings, American Institute of Steel Construction, Chicago IL.

[5] AISC (1989) Allowable Stress Design Specification for Structural Steel Buildings, American Institute of Steel Construction, Chicago IL.

[6] AISC (1993, 1999) Load and Resistance Factor Design Specification for Structural Steel Buildings, American Institute of Steel Construction, Chicago IL.

[7] AISC (2005) Specification for Structural Steel Buildings, ANSI/AISC 360-05, American Institute of Steel Construction, Chicago IL.

[8] AISC (2010a) Specification for Structural Steel Buildings, ANSI/AISC 360-10, American Institute of Steel Construction, Chicago IL.

[9] AISC (2010b) Commentary on the Specification for Structural Steel Buildings, ANSI/AISC 360-10, American Institute of Steel Construction, Chicago IL.

[10] Birkemoe, P.C., and Gilmor, M.I. (1978) "Behavior of bearing-critical double-angle beam connections." *Engineering Journal*, AISC, 15 (3), 109–115.

[11] Clements, D.D.A., and Teh, L.H. (2012) "Active shear planes of bolted connections failing in block shear," accepted for publication in J. Struct. Eng., ASCE.

[12] CSA (2009) Design of steel structures, CSA-S16-09, Canadian Standards Association, Toronto, ON.

[13] Driver, R. G., Grondin, G.Y., and Kulak, G.L. (2006) "Unified block shear equation for achieving consistent reliability." *J. Construct. Steel Res.*, 62 (3), 210-222.

[14] ECS (2005) Eurocode 3: Design of steel structures, Part 1.8: Design of joints, EN 1993-1-8, European Committee for Standardisation, Brussels, Belgium.

[15] Fisher, J.W., Galambos, T.V., Kulak, G.L., and Ravindra, M.K. (1978) "Load and resistance factor design criteria for connectors." *J. Struct. Div.*, ASCE, 104 (ST9), 1427-1441.

[16] Franchuk, C.R., Driver, R.G., and Grondin, G. Y. (2003) "Experimental investigation of block shear failure in coped steel beams." *Can. J. Civ. Eng.*, 30, 871-881.

[17] Hardash, S. G., and Bjorhovde, R. (1985) "New design criteria for gusset plates in tension." *Engineering Journal*, AISC, 22 (2), 77-94.

[18] Huns, B. B. S., Grondin, G. Y., and Driver, R. G. (2006) "Tension and shear block failure of bolted gusset plates." *Can. J. Civ. Eng.*, 33, 395-408.

[19] Mullin, D. (2002) Unpublished test data, Dept. of Civil and Environmental Engineering, University of Alberta, Edmonton, Canada.

[20] Rabinovitch, J. S., and Cheng, J. J. R. (1993) Cyclic behaviour of steel gusset plate connections, Structural Engineering Report No. 191, Dept. of Civil and Environmental Engineering, University of Alberta, Edmonton, Canada.

[21] Ravindra, M. K., and Galambos, T. V. (1978) "Load and resistance factor design for steel." *J. Struct. Div.*, ASCE, 104 (ST9), 1337-1353.

[22] SA (2012) Amendment No. 1 to AS 4100-1998 Steel Structures, Standards Australia.

[23] Schmidt, B. J., and Bartlett, F. M. (2002) "Review of resistance factor for steel: Data collection." *Can. J. Civ. Eng.*, 29 (1), 98-108.

[24] Teh, L.H., and Clements, D.D.A. (2012) "Block shear capacity of bolted connections in cold-reduced steel sheets," *J. Struct. Eng.*, 138 (4), 459-467.

[25] Teh, L.H., and Gilbert, B.P. (2012) "Net section tension capacity of bolted connections in cold-reduced steel sheets," *J. Struct. Eng.*, 138 (3), 337-344.

[26] Udagawa, K., and Yamada, T. (1998) "Failure modes and ultimate tensile strength of steel plates jointed with high-strength bolts." *J. Struct. Const. Eng.*, AIJ, 505, 115–22.

# FINITE ELEMENT EVALUATION OF THE ROTATION CAPACITY OF PARTIAL STRENGTH STEEL JOINTS

Ana M. Girão Coelho (a.m.girao@clix.pt)
Institute of Computers and Systems Engineering of Coimbra (INESCC), Portugal

Frans S. K. Bijlaard (f.s.k.bijlaard@tudelft.nl)
Delft University of Technology, The Netherlands

## ABSTRACT

The paper presents a refined three-dimensional finite element analysis of partial strength bolted end plate beam-to-column bare steel joints. The joint configurations are drawn from a previous experimental study in order to compare the structural numerical behaviour with test results, with good prediction shown by the finite element model. Failure of the joint is confined to the end plate in all models and is predicted by means of micromechanical models based on void growth mechanisms and coalescence, which are able to predict ductile fracture as a function of multiaxial stresses and plastic strains. Parametric studies are carried out to investigate the structural behaviour with variations in beam depth and thickness of the end plate. Quantitative assessments of resistance and rotation capacity are undertaken.

## 1. INTRODUCTION

Conventional analysis and design of steel frameworks are usually carried out under the assumption of fully rigid or ideally pinned joints connecting the beams to the columns. Both assumptions do not account for the structural interaction between joints and members. At the research level, however, considerable progress has been made in the past years to explore the implication of joints on the overall frame performance. This type of analysis explicitly recognizes the joint properties that become an additional variable in the frame analysis and design. These are the principles of semi-continuous or partially-restrained construction that are adopted in modern design codes (AISC, 2010; CEN, 2005). This type of construction assumes that the joints transfer moments from the beam to the column and vice versa and allow rotation between the connected members as the load is resisted.

Ductility and rotation capacity are important features of a (partial strength) joint in semi-continuous framing. An accurate prediction of both performance measures is thus crucial. The analytical evaluation of these key properties in bolted end plate joints is an extremely complex and highly indeterminate problem, with a large number of parameters and phenomena affecting the structural behaviour. The finite element method provides a reliable alternative tool to solve such a complex problem.

Past studies have correlated finite element analyses and experimental tests and successfully found that finite element modelling can be used to predict the nonlinear behaviour of bolted end plate joints. These numerical results were mostly used to supplement test data and give a more accurate description of the loading paths in the connecting components of the joints. In order to model more practically realistic behaviour, certain failure criteria have to be defined. The use of micromechanical models based on void growth and coalescence seem like an attractive tool to evaluate conditions for ductile fracture initiation and, consequently, the joint deformation capacity (Lemaitre, 1985). These models are able to predict ductile fracture from fundamental mechanical principles, as a function of multiaxial stresses and plastic strains.

In this study, finite element analyses of bolted end plate joints are conducted and the stress and strain results are postprocessed to evaluate the potential for ductile fracture of different specimens. First, a refined three-dimensional finite element model is formulated using the commercial software LUSAS (FEA, 2011). The nonlinear finite element modelling techniques implemented in this research are consistent with experimentally verified techniques used in earlier studies by the authors (2006, 2010). The model accounts for material nonlinearities through classical metal plasticity theory based on the Von Mises yield criterion, associated flow and the assumption of isotropic hardening. Geometric nonlinearities are taken into account by means of a large strain, large displacement formulation. Contact conditions between all the components are also explicitly modelled. For parametric studies, first the beam depth is varied from 250 mm to 350 mm, while the end plate thickness is fixed to 10 mm. Second, the end plate thickness is varied from 7.5 mm to 12.5 mm. In all cases the bolts were M20.

This current work is part of a larger overall effort by the authors with the objective of improving design rules for joint design in the context of the component method (CEN, 2005). The overall effort includes the implementation, execution and application of a comprehensive set of numerical testing that will provide information for derivation of appropriate design rules for evaluation of the available joint rotation capacity.

## 2. FINITE ELEMENT MODEL

A three-dimensional model is proposed to generate the full nonlinear moment-rotation response of the partial strength joints. The general purpose finite element programme LUSAS (an implicit solver) is used for this numerical study. The experimental work and test results of Girão Coelho and co-workers (2004) are modelled for this purpose: single-sided bolted end plate joint that consists of HE340M column connected with a IPE300 beam ($M_{pl,beam}$ = 223 kNm) using 400$\times$150$\times$10 mm thick extended end plates and 6 M20 grade 8.8 (non-preloaded) bolts in 22 mm drilled holes. The tension bolt holes are positioned 90 mm centre to centre both vertically and horizontally. Bolts are located centrally into the holes. The model has a beam length of 500 mm. The column is continuous through the joint.

Only half of the joint is modelled because of symmetry of the model about the plane of the web. Because the column in the joint tests was designed to be very stiff and assumed to be fully restrained against any movement or rotation only the column flange connected to the end plate is modelled (as a rigid plate). Bolts are modelled as *equivalent bolts* (Girão Coelho et al, 2006) complying with the requirements for symmetry in the *xy* plane. The equivalent bolt is defined so that its geometrical stiffness is identical to that of the actual bolt, i.e. the elongation of the equivalent bolt represents half of the elongation behaviour of the actual bolt. These simplifications can be very useful in terms of finite element analyses, since the number of elements is significantly reduced.

Welded regions are not explicitly modelled. The welding that connects the beam end to the plate is modelled as part of the beam material, and then connected to the end plate by fully coupling all the degrees-of-freedom at the interface. Therefore, partial separation of the weld from the parent material is not possible.

The boundary and loading conditions adopted in the finite element analysis follow closely those used in the experiments.

## 2.1. Mesh Description

The end plate connection is generated with fully integrated (2×2×2 Gauss points) first order bricks to model the continuum. Node-to-node nonlinear contact friction elements simulate the interface between the end plate and the column flange and the bolts and end plate.

The mesh density was varied to determine the most efficient modelling scheme that also compared well with the experimental results. A mesh sensitivity study was conducted with respect to two parameters: degree of discretization in order to represent the bending-dominated problem and the number of elements through thickness to check the capability of representing the yielding lines. It was found that the finite element mesh depicted in Fig. 1 (16070 three-dimensional continuum elements) complies with the requirements for a reliable simulation and also satisfies the convergence requirements.
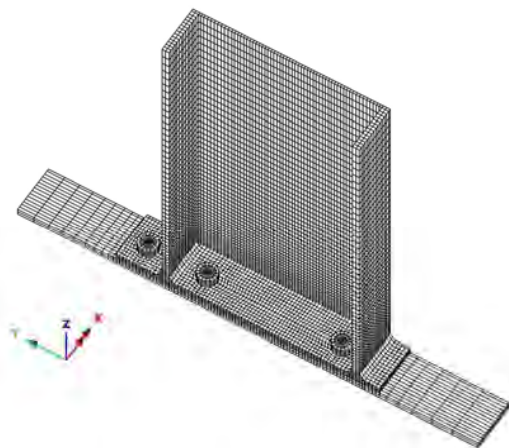


Fig. 1. Finite element mesh (e.g. FS1)

## 2.2. Boundary and Load Conditions

Appropriate boundary conditions that are consistent with the actual column restraints are applied. Displacements in the x, y and z directions are restrained at the bottom of the half rigid plate. Supports restraining movement in the z direction are also added to the back side of the rigid plate simulating the column flange. Displacements in the x direction are restrained along all surfaces on the centre line of the model. Also, complying with geometrical symmetry, the bottom surface bolt nodes are fixed in the z direction.

Contact between all parts is explicitly modelled with nonlinear contact elements. The contact areas are the bolt head-to-end plate and the end plate-to-column flange. The bolts clamp the end plate and the column flange together in order to resist the applied rotation. This mechanism has a major effect on the performance of the joint

and its response. The contact surfaces are defined and paired using a general contact formulation that involves a master-slave type algorithm (Crisfield, 1997). This formulation recognizes the surfaces that are in contact or interpenetrate or slip and imposes constraints on the nodes of the slave surface such that they do not penetrate the master surface. The sliding and sticking conditions are reproduced with the classic isotropic Coulomb friction law. Friction is ignored in the column flange-end plate interface.

The load is applied monotonically by imposing incremental vertical displacements at the cantilevered beam tip during the analysis to achieve the required range of joint bending moments.

## 2.3. Material Properties

Material nonlinearity is included in the model by specifying a stress-strain curve in terms of true stress and logarithmic strain because large deformations are anticipated. The elastoplastic material response is taken into account through dissociation of the elastic and plastic deformations. Plasticity is modelled with strain hardening. The yield condition is defined under the Von Mises yield criterion. A Prandtl-Reuss associative flow rule defines the direction plastic strain vector. Isotropic hardening is assumed. The constitutive model is integrated by means of the explicit forward Euler algorithm.

The full actual stress-strain relationship of the end plate and bolt materials is reproduced with a piecewise linear model, as shown in Fig. 2.
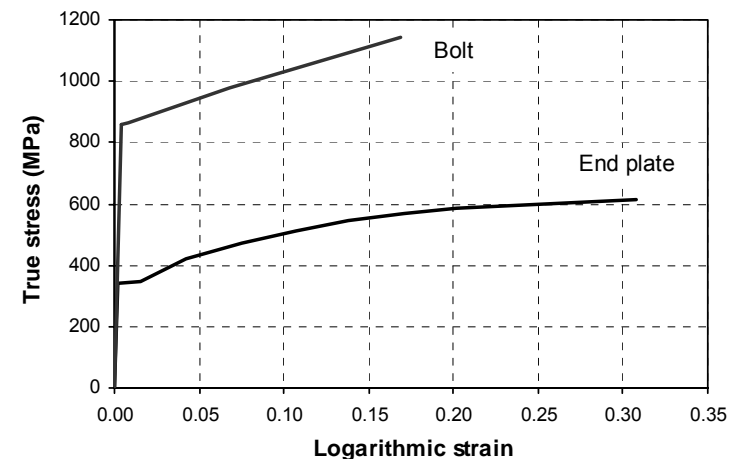


Fig. 2. Material stress-strain characteristics

## 2.4. Failure Criterion: Lemaitre Formulation

Fracture is a process of separation of a solid into pieces as a result of an imposed stress. It involves two basic stages: crack formation and propagation. The cracks may propagate slowly and when the stress is increased in cases where the materials have the ability to deform plastically. Most steel structures undergo large scale plasticity before actually fracturing. Failure usually occurs in a ductile manner. This is known as ductile fracture, in contrast with cleavage fracture, which is a brittle type of fracture.

Ductile fracture mechanisms involve microvoid nucleation from inclusions, growth and coalescence in a plastically deforming metal matrix (Anderson, 1995). Damage results in softening of the material and fracture proceeds from the competition between hardening and damage. When damage prevails over hardening, there is a strain

localization that eventually results in a crack. The stress triaxiality and the effective plastic strain play an important role in this process. This type of mechanism is best described by micromechanical models as opposed to traditional fracture mechanics in situations with geometrical concentrations of stresses and strains, as structural steel bolted joints. These models rely on combinations of local stresses and plastic strains to predict ductile crack initiation. Void nucleation and growth has been first recognized as the key micromechanism of fracture for ductile metals by McClintock (1968) and Rice and Tracey (1969) who also proposed failure criteria based on cavity growth. Since then, many models and criteria have been proposed in the literature. These approaches can be grouped in three main classes: (i) local fracture, (ii) porous metal plasticity and (iii) continuum damage mechanics. The latter is incorporated in the present study.

The continuum damage mechanic approach was initially proposed by Lemaitre (1985). Lemaitre proposed a model of isotropic ductile plastic damage based on a continuum damage variable, the effective stress concept and on thermodynamics. The model relies on the following basic assumptions: (i) isotropy (isotropic plasticity and isotropic damage), (ii) strain equivalence: the strain behaviour is modified by damage only through the effective stress, (iii) constant triaxiality ratio during loading (approximately constant principal directions of stresses) and (iv) in the range of very large strains, the material becomes almost perfectly plastic, with small stress variations. The rupture process is therefore strain-controlled. Beginning with these assumptions he derived an expression to predict the equivalent strain at failure $\varepsilon_f^*$, as follows:

$$\varepsilon_f^* = \varepsilon_f \left[ 2(1+\nu)/3 + 3(1-2\nu)\left(\sigma_m/\sigma_{eq}\right)^2 \right]^{-1} \tag{1}$$

whereby $\varepsilon_f$ is the strain at rupture from uniaxial tension tests, $\nu$ is the Poisson ratio, $\sigma_m$ is the mean normal stress and $\sigma_{eq}$ is the Von Mises equivalent stress. Fig. 3 plots the ratios $\varepsilon_f^*/\varepsilon_f$ vs. $\sigma_m/\sigma_{eq}$ (triaxiality ratio), complying with Eq. (1), for different values of the Poisson coefficient. The graph shows that there is significant influence of the stress triaxiality on the equivalent strain level at which fracture initiates.
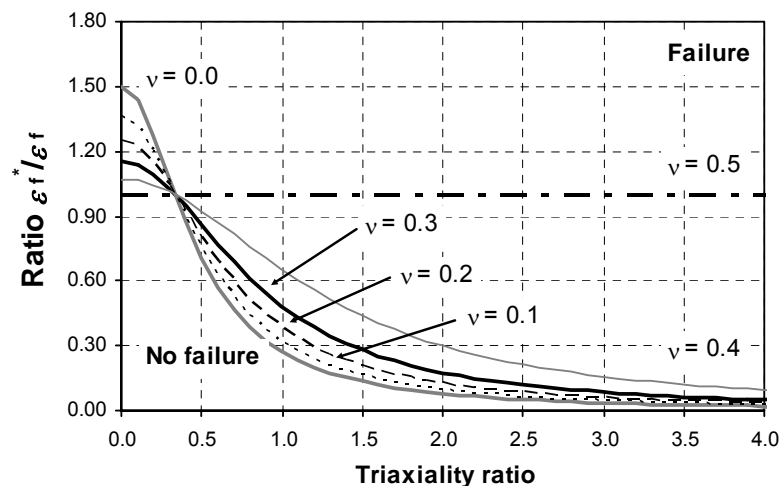


Fig. 3. Influence of triaxiality on strain to rupture according to the Lemaitre criterion

## 3. MODELLING VERIFICATION

Figs. 4 and 5 show comparisons of the numerical response with the experimental results of joint FS1, test b (Girão Coelho et al, 2004). The general response of the moment-rotation curve agrees well with the experimental data. This behaviour is generally characterized by an initial stiff phase that is followed by a second phase of much reduced stiffness. The numerical curve for test FS1 (Fig. 4) exhibits nonlinearity from the very beginning. The curve flattens out near failure, which occurs at a moment of 158.26 kNm and rotation of 69.5 mrad. These values are in line with the experimental predictions ($M_{max}$ = 161.17 kNm and $\phi_{Mmax}$ = 77.1 mrad).
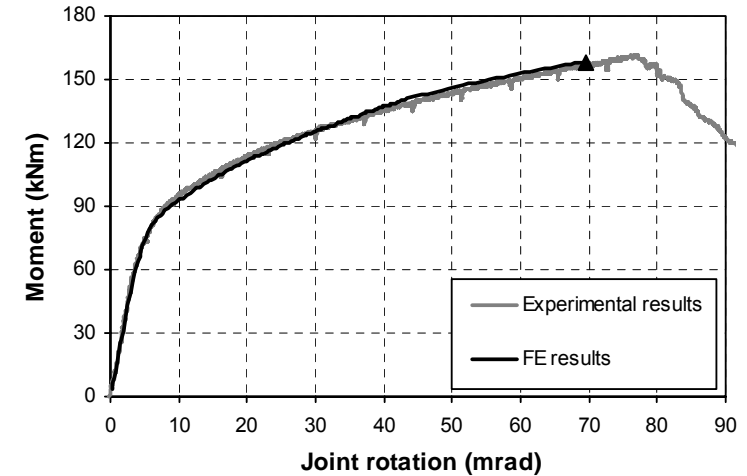


Fig. 4. Comparison of moment vs. joint rotation curves of specimen FS1
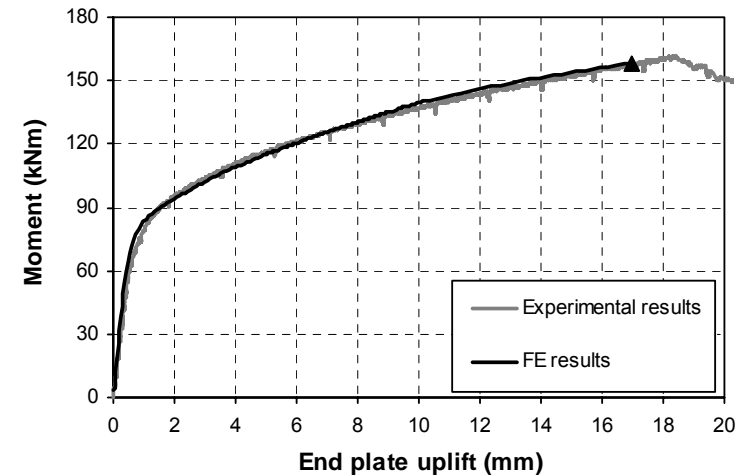


Fig. 5. Comparison of moment vs. end plate deformation curves of specimen FS1

The response of the end plate in the tension zone is similar to elastoplastic behaviour, with additional strength after reaching the yield moment that is most likely due to membrane action. This behaviour is depicted in Fig. 5 that plots the joint moment

against the end plate and column flange separation. This graph shows that the numerical response for the whole loading process is in good agreement with the test results.

Results of the analysis were postprocessed to compute the equivalent strain at failure and evaluate the rotation capacity of the joint. In this study, it was assumed that the fracture initiates when the end plate equivalent plastic strain reaches the ultimate plastic strain of materials based on the stress-strain characteristics plotted in Fig. 2 and Eq. (1).

The finite element predictions show that the high plastic strain concentrates at the end plate just above the beam tension flange, in the heat affected zone. This is also the region where the stress triaxiality ratio is largest. Ductile damage starts to accumulate in this critical region, close to the centre of the end plate, at a rotation of 27 mrad, as shown in Fig. 6. Fracture progressively extends along the end plate width and thickness as the load increases (see Fig. 7). At a joint rotation of 45 mrad, ductile



Fig. 6. Plastic strain distributions at $\phi$ = 27 mrad (detail of the tension zone)



Fig. 7. Plastic strain distributions at $\phi$ = 45 mrad (detail of the tension zone)

fracture has already propagated along the top surface of the end plate and through-thickness fracture initiates. This suggests that the process takes place nearly simultaneously over a large area, after which the entire section fails suddenly by ductile tearing. Thus, end plate through-thickness fracture condition is likely to be the limiting factor in the joint. This is consistent with experimental evidence. The rupture criterio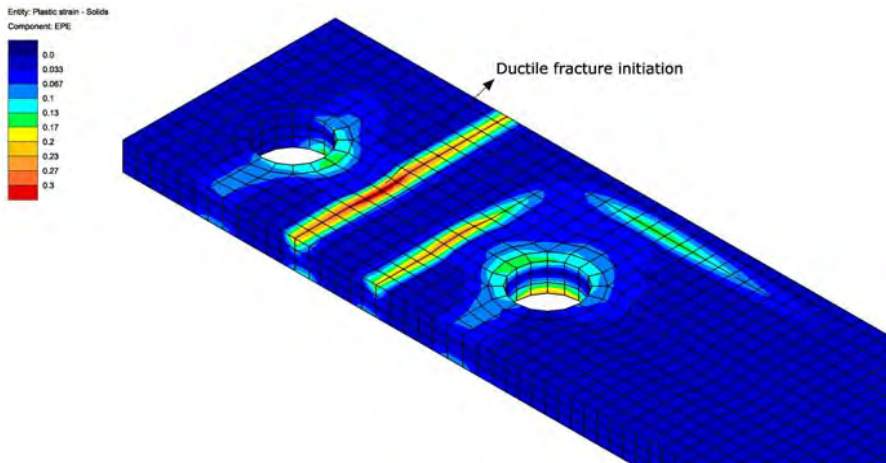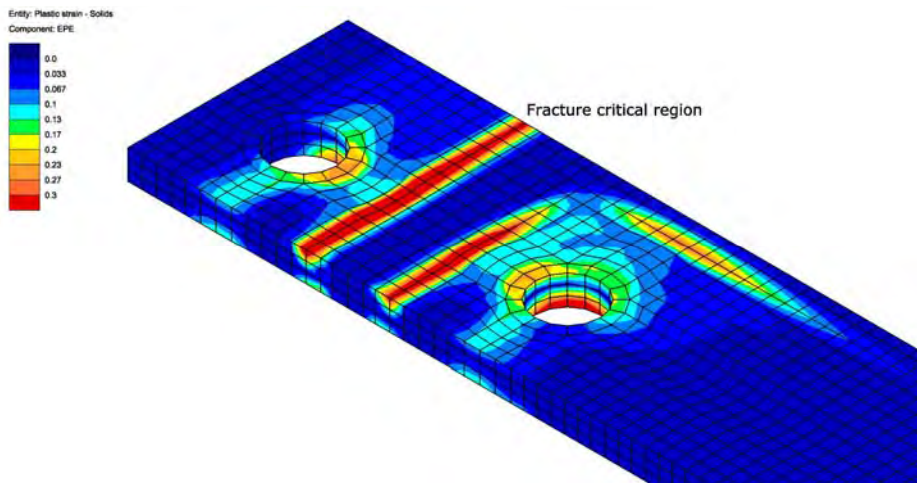n follows from these observations: the maximum joint deformation is reached when the ductile crack growths over an effective region of the end plate and propagates through the plate thickness (Fig. 8).

The numerical study shows that this particular joint develops a rotation of 69.5 mrad. The calculated failure rotation matches the actual response quite well (error 9.8%) and demonstrates the accuracy of the proposed methodology to predict the rotation capacity in specimens subjected to large scale yielding.
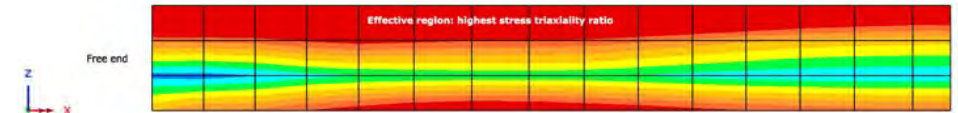


Fig. 8. Fracture critical region: detail of the effective end plate area

## 4. PARAMETRIC STUDIES

Using the capability of the predicting bolted joint response with the validated finite element modelling approach discussed above, it is possible to extend the experimental study to investigate various parameters which affect the joint response. A parametric study is presented here to evaluate the effect of beam depth ($h_b$) and end plate thickness ($t_{ep}$), which are considered to be influential factors for the joint ductility. Figs. 9 and 10 plot the moment-rotation characteristics of the models. Each of the figures focuses on illustrating the effect of each variable. These are discussed in the following subsections from a rotation capacity point of view.

### 4.1. Effect of the beam depth on rotation capacity

In order to quantify the effect of different beam depth, four models are built from the original joint, by varying the depth of the IPE 300 beam. The rotation capacity is reduced as a higher size beam is chosen. The modelling results are shown in Fig. 9 and Table 1 and suggest that the rotation capacity decreases linearly with the beam depth.

### 4.2. Effect of the end plate thickness on rotation capacity

The ratio between the end plate thickness and the bolt diameter is probably the most important geometrical parameter in determining the rotation capacity of a joint. In this study, the bolt diameter was kept constant. End plate thickness values of 7.5 mm, 10 mm and 12.5 mm are considered below. For these three models, the mode of failure is due to ductile cracking of the end plate. Brittle bolt failure is not observed.

The comparison results are shown in Fig. 10 and Table 1. It can be seen that when the end plate thickness is decreased, lower moment capacity and larger rotation capacity are achieved. The rotation capacity is improved by about 20% by changing the end plate thickness from 12.5 mm to 10 mm (25%). However, when the end plate thickness id decreased from 10 mm to 7.5 mm, the differences in rotation capacity are much smaller (7%). The results indicate that the response $t_{ep}$ vs. $\phi_{max}$ can be approximated by a quadratic function. Naturally, this trend requires further investigation due to the limited number of simulation studies examined in this paper.

www.steelconstruct.com
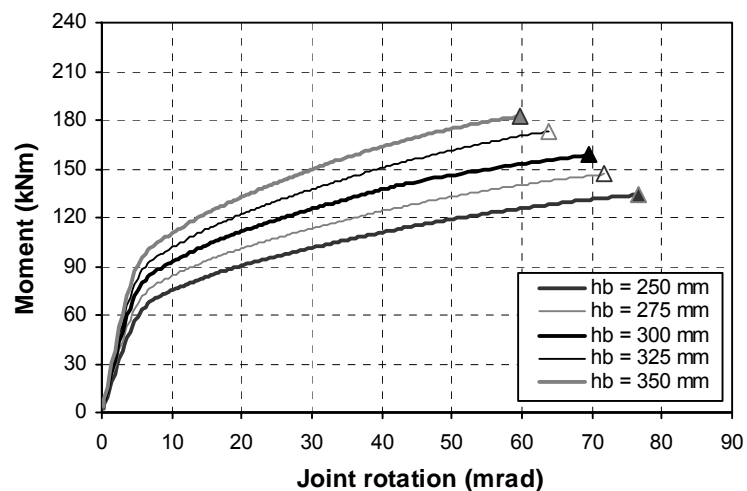
Fig. 9. Variation of moment-rotation curves with different beam depth
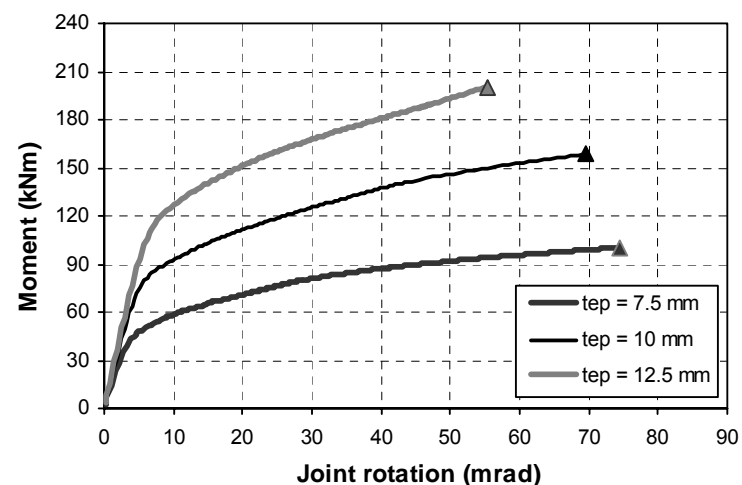


Fig. 10. Variation of moment-rotation curves with different thickness of end plate

Table 1. Modelling results

| Variable | | $M_{max}$ (kNm) | $\phi_{max}$ (mrad) |
|---|---|---|---|
| $h_b$ (mm) | 250 | 134.09 | 76.7 |
| | 275 | 146.63 | 71.7 |
| | *300* | *158.26* | *69.5* |
| | 325 | 172.97 | 63.8 |
| | 350 | 182.41 | 59.6 |
| $t_{ep}$ (mm) | 7.5 | 100.28 | 74.6 |
| | *10* | *158.26* | *69.5* |
| | 12.5 | 200.50 | 55.3 |

## 5. CONCLUDING REMARKS AND FURTHER RESEARCH WORK

The proposed three-dimensional finite element model is able to represent all the main features of the structural behaviour of partial strength bolted end plate joints. In particular, it offers a reliable alternative to large-scale laboratory testing to predict the rotation capacity and the ductility characteristics to fill in knowledge gaps in the available experimental data pertaining to the ultimate behaviour of these joint types.

Two different variables have been studied on their influence on the rotation capacity of the joint. The following conclusions are briefly summarized:
1. Reduced beam depth leads to increased rotation capacity.
2. Increased thickness of the end plate reduces the rotation capacity but improves the resistance of the joint.

The relationships between the rotation capacity and the beam depth and end plate thickness are under investigation to develop practical and accurate guidelines to quantitatively assess rotation capacity in bolted end plate joints.

## REFERENCES

[1] Anderson T.L. (1995). *Fracture mechanics: fundamentals and applications*, CRC Press, Boca Raton, Florida.
[2] AISC - American Institute of Steel Construction (2010). *Specification for structural steel buildings*, ANSI/AISC Standard No. 360-10, Chicago IL.
[3] CEN - European Committee for Standardization (2005). *EN* 1993 *Design of steel structures*, *Part* 1-8: *Design of joints*, Brussels.
[4] Crisfield M.A. (1997). *Non-linear finite element analysis of solids and structures*, *Vol.* 2: *Advanced topics*, John Wiley & Sons, Chichester.
[5] FEA (2011). *LUSAS: Finite element analysis system*, Version 14.5-4, Produced by FEA Ltd., Kinston-upon-Thames, Surrey.
[6] Girão Coelho A.M., Bijlaard F.S.K. and Simões da Silva L. (2004). "Experimental assessment of the ductility of extended end plate connections". *Engineering Structures*, Vol. 26 (pp. 1185-1206).
[7] Girão Coelho A.M., Simões da Silva L. and Bijlaard, F.S.K. (2006). "Finite-element modeling of the nonlinear behavior of bolted T-stub connections". *Journal of Structural Engineering ASCE*, Vol. 132, No. 6 (pp. 918-928).
[8] Girão Coelho A.M., Bijlaard F.S.K. (2010). "Finite element evaluation of the strength behaviour of high-strength steel column web in transverse compression". *Steel and Composite Structures*, Vol. 10, No. 5 (pp. 385-414).
[9] Lemaitre J. (1985). "A continuous damage mechanics model for ductile fracture". *Journal of Engineering Materials and Technology*, Vol. 107 (pp. 83-89).
[10] McClintock F.A. (1968). "A criterion for ductile fracture by the growth of holes". *Journal of Applied Mechanics – Trans. ASME* (pp. 363-371).
[11] Rice J.R. and Tracey D.M. (1969). "On the ductile enlargement of voids in triaxial stress fields". *Journal of the Mechanics and Physics of Solids*, Vol. 17 (pp. 201-217).

    www.steelconstruct.com

# SIMPLIFIED FORMULAS FOR ASSESSMENT OF STEEL JOINT FLEXIBILITY CHARACTERISTICS

Aleksander Kozłowski; Lucjan Ślęczka
*Rzeszów University of Technology, Poland*
*kozlowsk@prz.edu.pl, sleczka@prz.edu.pl*

## ABSTRACT

Code 1993-1-8 includes full design procedures, based on component method, allowing to asses design resistance $M_{j,Rd}$ and initial stiffness $S_{j,ini}$ of the most often used steel joints, as end-plate bolted connections. This method, despite of many simplifying assumptions, is still burdensome and time consuming and is addressed to final check of designed structure. In the pre-design phase, when designer is forced to change input data many times, there is a need to use design tools, like tables, graphs or simplified formulas, to quick asses joint properties for global analysis of the frame. Such simplified formulae for assessment of design moment resistance $M_{j,Rd}$ and initial stiffness $S_{j,ini}$ of steel joint has been presented in the paper. Comparison to results obtained using available software shows that simplified formulas present a good agreement (ca. 20 %).

## 1. INTRODUCTION

Current steel structures design codes, including EN 1993-1-1, require taking into account during global analysis actual properties of joints and connections. Joint main characteristics, as M-φ curve, can be taken from experimental tests or analytical models. Code EN 1993-1-8 includes full design procedures, based on component method, allowing to asses design resistance $M_{j,Rd}$ and initial stiffness $S_{j,ini}$ of the most often used steel joints, as end-plate bolted connections. This method, despite of many simplifying assumptions, is still burdensome and time consuming. It requires to input many geometrical and structural properties of design joints, which are not known to designers on this stage of design. It is enough to say, that hand calculation of multi-row bolted end-plate connections takes a dozen or so pages (Kozlowski, 2009).

Computer software in such a situation were widely developed to support design work. There are few computers programs allowing to obtain moment resistance and stiffness of steel joints: (CoP, CRSJAE, module "connections" in Autodesk ROBOT). Application of these programs are reasonable in the last stage of design, where structure design is nearly finished. In the pre-design phase, when designer is forced to change input data many times, there is a need to use design tools, like tables, graphs or simplified formulas, to quick asses joint properties for global analysis of the frame.

The aim of the paper is to propose such simplified formula for steel joint.

## 2. ANALYSIS OF EFFECTIVE LENGTH AND FAILURE MODES OF T-STUBS

Components of steel joint can be divided as component of:
- shell behaviour,
- plate behaviour.

The first group contains: column web in shear, column web in compression and column web in tension. In the second, there are: column flange in bending, end plate in bending, angle in tension. These components are modeled by T-stub. Resistance of plate components is calculated for three failure modes of T-stub (table 6.2 of EN 1993-1-8). Effective lengths for each component, for circular and non-circular modes are presented in Tables 6.4, 6.5 and 6.6 of EN 1993-1-8. Code requires to analyze all effective length and choose the smallest, what is the main reason of huge time consuming during calculation.

In the frame of diploma work (Kowal-Gaska, 2011) wide analysis of all possible effective lengths and failure modes were conducted, to eliminate this ones which are never or seldom possible. Conclusions from this work is as follows:
- for unstiffened column flange, circular failure modes are possible only when distance "e" (Figure 1) is 2,8 times bigger than bolt diameter, what is practically impossible, so as reliable non-circular effective length: $l_{eff,nc} = 4m + 1,25e$ should be taken,
- for bolt row in end plate above beam flange, always the smallest is non-circular length: $l_{eff,nc} = 0,5\ b_p$,
- for bolt row in end plate below beam flange decisive is effective length: $l_{eff,nc} = \alpha$. After analysis of many case, it was concluded that $\alpha = 5,8$ can be safely taken,
- for most of design cases, decisive are non-circular failure modes and final resistance of components should be calculated using:
  - for column flange: mode of failure 2,
  - for end plate: mode 1 for row above beam flange and mode 2 for rows below beam flange.

## 3. ANALYSIS OF RESISTANCE AND STIFFNESS OF BASIC JOINT COMPONENTS

### 3.1. Assumptions

Simplified formulas for assessing bending resistance and rotational stiffness requires some assumptions about geometry of analysed joints:
- As most often case in design, it was assumed cross section of beams made of IPE and cross section of columns made of HEB,
- The beam depth was limited to the range between 240 and 450 mm,
- The column depth was limited to the range between 140 and 300 mm,
- There were assumed following relations between geometrical dimensions of beam, column and end plate cross sections (Table 1):

Table 1. Assumed geometrical properties of analyzed joints

| Column | | |
|---|---|---|
| $b_c = h_c = 11 \, r_c = 13,5 \, t_{fc}$ | $t_{wc} = 0,6 \, t_{fc}$ | $r_c = 1,2 \, t_{fc}$ |
| End plate | | |
| $t_p = t_{fc}$ | $b_p = b_{fb} = 10 \, t_{fc}$ | $e_{min} = 1,5 \, d_0 = 1,65d = 2 \, t_{fc}$ |
| $d = 1,25 \, t_{fc}$ | $a_p = 0,7 \, t_{fb}$ | $n = e_{min} = 2 \, t_{fc}$ |
| Beam | | |
| $z = h_b = 2b_{fb}$ | $b_{fb} = 10 \, t_{fc}$ | $t_{fb} = 0,8 \, t_{fc}$ |
| $a_w = 0,7 \, t_{wb} = 0,6 \, t_{wc}$ | $t_{wb} = 0,9 \, t_{wc}$ | |

where:

$h_c$, $b_c$, $t_{fc}$, $t_{wc}$, $r_c$ – depth, width, thickness of flange, thickness of web and the root radius of column cross section,

$h_b$, $b_{fb}$, $t_{fb}$, $t_{wb}$ - depth, width, thickness of flange, thickness of web and the root radius of beam cross section,

$d$, $d_0$ – nominal bolt diameter, the hole diameter for a bolt,

$a_w$, $a_p$– thickness of the weld between beam web and end plate, thickness of the weld between beam flange and end plate, (Figure 1).
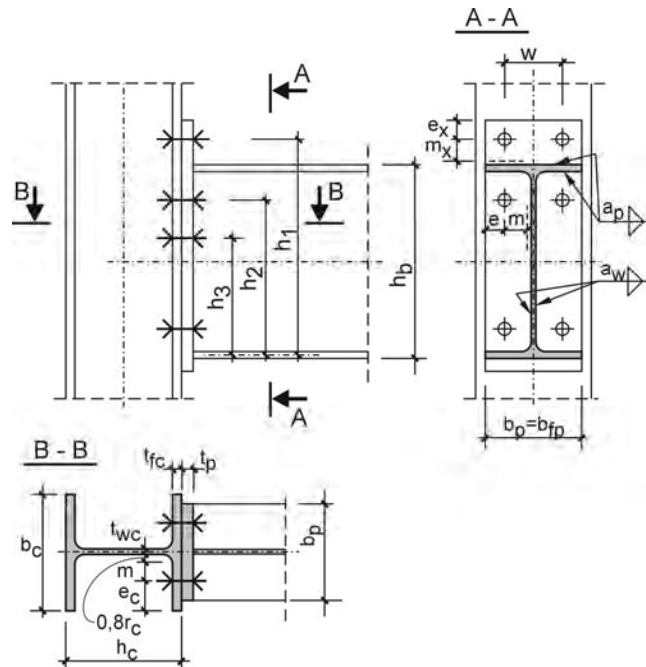


Figure 1. Geometrical configuration of beam-to-column joint

## 3.2. Resistance of basic components

Considering the case of single sided (external) joint, the transformation parameter β is equal to β=1,0. The values of partial safety factors according to Polish National Annex (EN 1993-1-8) were established as $\gamma_{MO}$=1,0 and $\gamma_{M2}$=1,25.

- Column web panel in shear (eq. (6.7) in EN 1993-1-8):

$$V_{wp,Rd} = \frac{0,9 f_y \, A_{vc}}{\sqrt{3} \, \gamma_{M0}}$$

It can be assumed that

$$A_{vc} = (h_c + 4t_{fc})t_{wc} = (13,5t_{fc} + 4t_{fc})0,6t_{fc} = 10,5t_{fc}^2$$

$$V_{wp,Rd} = \frac{0,9 f_y \, 10,5t_{fc}^2}{\sqrt{3}} = 5,5t_{fc}^2 \cdot f_y \qquad (1)$$

- Column web in transverse compression (eq. (6.9) in EN 1993-1-8)

$$F_{c,wc,Rd} = \frac{\omega \, k_{wc} \, b_{eff,c,wc} \, t_{wc} \, f_y}{\gamma_{M0}}$$

$$b_{eff,c,wc} = t_{fb} + 2\sqrt{2} \cdot a_p + 5(t_{fc} + r_c) + 2t_p = t_{fb} + 2\sqrt{2} \cdot 0,7t_{fb} + 5(t_{fc} + 1,2t_{tc}) + 2t_{fc} =$$
$$= 3t_{fb} + 13t_{fc} = 3 \cdot 0,8t_{fc} + 13t_{fc} = 15,4t_{fc}$$

Average value of $\omega$ is equal to $\omega \approx 0,7$ and $k_{wc}$ =1,0. Then:

$$F_{c,wc,Rd} = \frac{0,7 \cdot 1,0 \cdot 15,4t_{fc} \, t_{wc} \, f_y}{1,0} = 0,7 \cdot 15,4t_{fc} \cdot 0,6t_{fc} \cdot f_y = 6,5t_{fc}^2 \cdot f_y \qquad (2)$$

- Column flange in transverse bending (Figure 1)

$$m = \frac{b_c - 2e_c - t_{wc} - 2 \cdot 0,8r_c}{2} = \frac{13,5t_{fc} - 2e_c - 0,6t_{fc} - 2 \cdot 0,8 \cdot 1,2t_{fc}}{2} = 5,5t_{fc} - e_c$$

For the most popular bolts M20: d=20 and $d_0$=22

$$e_{min} = 1,5 \cdot d_0 = 1,65d = 1,65 \cdot 1,25t_{fc} = 2,1t_{fc}$$

$$e_c = e_{min} + 1,75t_{fc} = 2,1t_{fc} + 1,75t_{fc} = 3,85t_{fc}$$

(see Figure 1). Then

$$m = 5,5t_{fc} - e_c = 5,5t_{fc} - 3,85t_{fc} = 1,65t_{fc}$$

$$l_{eff} = 4m + 1,25e_c = 4 \cdot 1,65t_{fc} + 1,25 \cdot 3,85t_{fc} = 11,4t_{fc}$$

Considering mode 2 of failure (Table 6.2 in EN 1993-1-8):

$$F_{T2,Rd} = \frac{2M_{pl,2,Rd} + n \cdot \sum F_{t,Rd}}{m + n}$$

$$M_{pl,2,Rd} = 0,25 l_{eff} \, t_{fc}^2 \cdot \frac{f_y}{\gamma_{M0}} = 0,25 \cdot 11,4t_{fc} \, t_{fc}^2 \, f_y = 2,85t_{fc}^3 f_y$$

In case of bolts M16, M20 and M24:

$$A_s = 0,78A = 0,78\frac{\pi d^2}{4} = 0,61d^2$$

$$\sum F_{t,Rd} = 2 \cdot \frac{k_2 f_{ub} A_s}{\gamma_{M2}} = 2\frac{0,9 f_{ub} \cdot 0,61 d^2}{1,25} = 2\frac{0,9 f_{ub} \cdot 0,61(1,25 t_{fc})^2}{1,25} = 1,37 t_{fc}^2 f_{ub}$$

$$n = e_{min} = 2 t_{fc} < 1,25 m = 1,25 \cdot 1,65 t_{fc} = 2,1 t_{fc}$$

$$F_{T2,Rd} = \frac{2 M_{pl,2,Rd} + n \cdot \sum F_{t,Rd}}{m+n} = \frac{2 \cdot 2,85 t_{fc}^3 \cdot f_y + 2 t_{fc} \cdot 1,37 \cdot t_{fc}^2 \cdot f_{ub}}{1,65 t_{fc} + 2 t_{fc}} =$$

$$= 1,56 t_{fc}^2 f_y + 0,75 t_{fc}^2 f_{ub}$$

In case of steel grade S235 and bolt class 10.9: $f_{ub}=4,26 f_y$ and then

$$F_{t,fc,Rd} = F_{T2,Rd} = 1,56 t_{fc}^2 f_y + 0,75 t_{fc}^2 f_{ub} = 1,56 t_{fc}^2 f_y + 0,75 t_{fc}^2 \cdot 4,26 f_y = 4,8 t_{fc}^2 f_y$$

In case of steel grade S355 and bolt class 10.9: $f_{ub}=2,82 f_y$ and then

$$F_{t,fc,Rd} = F_{T2,Rd} = 1,56 t_{fc}^2 f_y + 0,75 t_{fc}^2 f_{ub} = 1,56 t_{fc}^2 f_y + 0,75 t_{fc}^2 \cdot 2,82 f_y = 3,7 t_{fc}^2 f_y \quad (3)$$

- End-plate in bending, (Figure 1)
  - Bolt-row outside tension flange of beam:

$$b_p = b_{fb} = 10 t_{fc} \; ; \; l_{eff} = 0,5 b_p = 5 t_{fc}$$

$$m = m_x = 1,5 d = 1,5 \cdot 1,25 t_{fc} = 1,9 t_{fc}$$

Considering mode 1 of failure (Table 6.1 in EN 1993-1-8):

$$M_{pl,1,Rd} = 0,25 l_{eff} t_p^2 \cdot \frac{f_y}{\gamma_{M0}} = 0,25 \cdot 5 t_{fc} t_{fc}^2 f_y = 1,25 t_{fc}^3 f_y$$

$$F_{t,ep,Rd} = F_{t,1,Rd} = \frac{4 M_{pl,1,Rd}}{m} = \frac{4 \cdot 1,25 t_{fc}^3 f_y}{1,9 t_{fc}} = 2,6 t_{fc}^2 f_y \quad (4)$$

  - First bolt-row below tension flange of beam:

$$m = \frac{b_p - 2e - t_{wb} - 2 \cdot 0,8 \cdot a_w \sqrt{2}}{2}$$

$$e = e_{min} = 2,1 t_{fc}$$

$$m = \frac{10 t_{fc} - 2 \cdot 2,1 t_{fc} - 0,9 t_{wc} - 2 \cdot 0,8 \cdot 0,6 t_{wc} \cdot \sqrt{2}}{2} =$$

$$= 2,9 t_{fc} - 1,13 t_{wc} = 2,9 t_{fc} - 1,13 \cdot 0,6 t_{fc} = 2,22 t_{fc}$$

$$\alpha_{śr} = 5,8 \; ; \; l_{eff} = \alpha m = 5,8 \cdot 2,22 t_{fc} = 12,9 t_{fc}$$

$$M_{pl,2,Rd} = 0,25 l_{eff} t_p^2 \cdot \frac{f_y}{\gamma_{M0}} = 0,25 \cdot 12,9 t_{fc} t_{fc}^2 f_y = 3,22 t_{fc}^3 f_y$$

$$n = e_{min} = 2,1 t_{fc}$$

$$F_{T2,Rd} = \frac{2 M_{pl,2,Rd} + n \cdot \sum F_{t,Rd}}{m+n} = \frac{2 \cdot 3,22 t_{fc}^3 \cdot f_y + 2,1 t_{fc} \cdot 1,37 \cdot t_{fc}^2 \cdot f_{ub}}{2,22 t_{fc} + 2,1 t_{fc}} =$$

$$= 1,49 t_{fc}^2 f_y + 0,67 t_{fc}^2 f_{ub}$$

In case of steel grade S235 and bolt class 10.9: $f_{ub}=4,26 f_y$ and then

$$F_{t,ep,Rd} = F_{T2,Rd} = 1,49 t_{fc}^2 f_y + 0,67 t_{fc}^2 f_{ub} = 1,49 t_{fc}^2 f_y + 0,67 t_{fc}^2 \cdot 4,26 f_y = 4,3 t_{fc}^2 f_y$$

In case of steel grade S355 and bolt class 10.9: $f_{ub}=2,82 f_y$ and then

$$F_{t,ep,Rd} = F_{T2,Rd} = 1,49 t_{fc}^2 f_y + 0,67 t_{fc}^2 f_{ub} = 1,49 t_{fc}^2 f_y + 0,67 t_{fc}^2 \cdot 2,82 f_y = 3,4 t_{fc}^2 f_y \quad (5)$$

  - Other inner bolt-rows:

$$l_{eff} = 4m + 1,25 e = 4 \cdot 2,22 t_{fc} + 1,25 \cdot 2,1 t_{fc} = 11,5 t_{fc}$$

$$M_{pl,2,Rd} = 0,25 \cdot l_{eff} \cdot t_p^2 \cdot \frac{f_y}{\gamma_{M0}} = 0,25 \cdot 11,5 t_{fc} \cdot t_{fc}^2 \cdot f_y = 2,88 t_{fc}^3 f_y$$

$$F_{T2,Rd} = \frac{2 M_{pl,2,Rd} + n \cdot \sum F_{t,Rd}}{m+n} = \frac{2 \cdot 2,88 t_{fc}^3 \cdot f_y + 2,1 t_{fc} \cdot 1,37 \cdot t_{fc}^2 \cdot f_{ub}}{2,22 t_{fc} + 2,1 t_{fc}} =$$

$$= 1,33 t_{fc}^2 f_y + 0,67 t_{fc}^2 f_{ub}$$

In case of steel grade S235 and bolt class 10.9: $f_{ub}=4,26 f_y$ and then

$$F_{t,ep,Rd} = F_{T2,Rd} = 1,33 t_{fc}^2 f_y + 0,67 t_{fc}^2 f_{ub} = 1,33 t_{fc}^2 f_y + 0,67 t_{fc}^2 \cdot 4,26 f_y = 4,2 t_{fc}^2 f_y$$

In case of steel grade S355 and bolt class 10.9: $f_{ub}=2,82 f_y$ and then

$$F_{t,ep,Rd} = F_{T2,Rd} = 1,33 t_{fc}^2 f_y + 0,67 t_{fc}^2 f_{ub} = 1,33 t_{fc}^2 f_y + 0,67 t_{fc}^2 \cdot 2,82 f_y = 3,2 t_{fc}^2 f_y \quad (6)$$

- Column web in transverse tension (eq. (6.15) in EN 1993-1-8)

$$F_{t,wc,Rd} = \frac{\omega l_{eff} t_{wc} f_y}{\gamma_{M0}} = 0,7 \cdot 11,4 t_{fc} \cdot 0,6 t_{fc} \cdot f_y = 4,8 t_{fc}^2 \cdot f_y \quad (7)$$

- Beam flange and web in compression (eq. (6.21) in EN 1993-1-8)

$$F_{c,fb,Rd} = \frac{M_{c,Rd}}{h - t_{fb}} \approx \frac{b_{fb} t_{fb} f_y (h - t_{fb})}{(h - t_{fb})\gamma_{M0}} = b_{fb} t_{fb} f_y = 10 t_{fc} \cdot 0,8 t_{fc} \cdot f_y = 8,0 t_{fc}^2 f_y \quad (8)$$

- Beam web in tension (eq. (6.22) in EN 1993-1-8)

$$F_{t,wb,Rd} = \frac{b_{eff,t,wb} t_{wb} f_y}{\gamma_{M0}} = b_{eff,t,wb} \cdot 0,9 t_{wc} \cdot f_y = b_{eff,t,wb} \cdot 0,9 \cdot 0,6 t_{fc} \cdot f_y =$$

$$= b_{eff,t,wb} \cdot 0,54 t_{fc} \cdot f_y$$

o In case of first bolt-row below tension flange of beam $b_{eff, t, wb}$ = 12,9 tfc

$$F_{t,wb,Rd} = 12,9t_{fc} \cdot 0,54t_{fc} \cdot f_y = 7,0t_{fc}f_y$$

o In case of next bolt-rows $b_{eff, t, wb}$ =11,9 tfc

$$F_{t,wb,Rd} = 11,5t_{fc} \cdot 0,54t_{fc} \cdot f_y = 6,2t_{fc}f_y \qquad (9)$$

Above calculations were related to single sided joints. In double sided joints, the transformation parameter β was assumed as β≈0. Reduction factor ω is equal to ω=1,0. So, for some components, values of resistance are changing:

$$V_{wp,Rd} = \infty , \; F_{c,wc,Rd} = 9,2t_{fc}^2 f_y \; \text{and} \; F_{t,wc,Rd} = 6,8t_{fc}^2 f_y .$$

### 3.3. Stiffness analysis of basic components

The stiffness coefficients (related to single sided joint) can be calculated as below:

• Column web panel in shear (Table 6.11 in EN 1993-1-8):

$$k_1 = \frac{0,38A_{vc}}{\beta \cdot z}$$

$$A_{vc} = 10,5t_{fc}^2 ; \; z = h_b = 2b_{fb} = 2 \cdot 10t_{fc} = 20t_{fc}$$

$$k_1 = \frac{0,38 \cdot 10t_{fc}^2}{1 \cdot 20t_{fc}} = 0,19t_{fc} \qquad (10)$$

(In case of double sided joint, when β≈0 component is inactive).

• Column web in transverse compression (Table 6.11 in EN 1993-1-8):

$$k_2 = \frac{0,7 \, b_{eff,c,wc} \, t_{wc}}{d_c}$$

$$d_c = h_c - 2(t_{fc} + r) = 13,5t_{fc} - 2(t_{fc} + 1,2t_{fc}) = 9,1t_{fc}$$

$$k_2 = \frac{0,7 \cdot 15,4t_{fc} \cdot 0,6t_{fc}}{9,1t_{fc}} = 0,71t_{fc} \qquad (11)$$

• Column web in transverse tension (Table 6.11 in EN 1993-1-8):

$$k_3 = \frac{0,7 \, b_{eff,t,wc} \, t_{wc}}{d_c} = \frac{0,7 \cdot 11,4 \cdot t_{fc} \cdot 0,6t_{fc}}{9,1t_{fc}} = 0,53t_{fc} \qquad (12)$$

• Column flange in transverse bending (Table 6.11 in EN 1993-1-8):

$$k_4 = \frac{0,9 l_{eff} \, t_p^3}{m^3} = \frac{0,9 \cdot 11,4t_{fc} \cdot t_{fc}^3}{(1,65t_{fc})^3} = 2,28t_{fc} \qquad (13)$$

• End-plate in bending (Table 6.11 in EN 1993-1-8):

$$k_5 = \frac{0,9 l_{eff} \, t_p^3}{m^3}$$

Table 2. Simplified formulas to assess resistance and stiffness coefficients in basic components

| Component | Bolt-row | Effective width/length | Resistance | | | Stiffness coefficients | |
| | | | Symbol | Formula | | | |
| | | | | Single-sided | Double sided | Symbol | Formula |
|---|---|---|---|---|---|---|---|
| Column web panel in shear | - | - | $V_{wp,Rd}$ | 5,5 $t^2f_y$ | ∞ | $k_1$ | 0,19 t |
| Column web in transverse compression | - | 15,4 t | $F_{c,wc,Rd}$ | 6,5 $t^2f_y$ | 9,2 $t^2f_y$ | $k_2$ | 0,71 t |
| Beam flange and web in compression | - | - | $F_{c,fb,Rd}$ | 8,0 $t^2f_y$ | | - | - |
| Column web in transverse tension | - | 11,4 t | $F_{t,wc,Rd}$ | 4,8 $t^2f_y$ | 6,8 $t^2f_y$ | $k_3$ | 0,53 t |
| Column flange in transverse bending | | 11,4 t | $F_{t,fc,Rd}$ | 4,8 $t^2f_y$ (3,7 $t^2f_y$) | | $k_4$ | 2,28 t |
| End-plate in bending | outside tension flange | 5 t | $F_{t,ep,Rd}$ | 2,6 $t^2f_y$ | | $k_5$ | 0,66 t |
| | below tension flange | 12,9 t | | 4,3 $t^2f_y$ (3,4 $t^2f_y$) | | | 1,06 t |
| | other | 11,5 t | | 4,2 $t^2f_y$ (3,2 $t^2f_y$) | | | 0,95 t |
| Beam web in tension | below tension flange | 12,9 t | $F_{t,wb,Rd}$ | 7,0 $t^2f_y$ | | - | - |
| | other | 11,5 t | | 6,2 $t^2f_y$ | | - | - |
| Bolts in tension | - | - | - | - | | $k_{10}$ | 0,51 t |
| Remarks: t = min ($t_{fc}$; $t_p$), Resistance of basic components is related to steel grade S235 (in parenthesis values for S355) | | | | | | | |

Bolt-row outside tension flange of beam:

$$k_5 = \frac{0,9 \cdot 5t_{fc} \cdot t_{fc}^3}{(1,9t_{fc})^3} = 0,66t_{fc} \qquad (14)$$

First bolt-row below tension flange of beam:

$$k_5 = \frac{0,9 \cdot 12,9t_{fc} \cdot t_{fc}^3}{(2,22t_{fc})^3} = 1,06t_{fc} \qquad (15)$$

www.steelconstruct.com

Other inner bolt-rows:

$$k_5 = \frac{0,9 \cdot 11,5 t_{fc} \cdot t_{fc}^3}{(2,22 t_{fc})^3} = 0,95 t_{fc} \qquad (16)$$

- Bolts in tension (Table 6.11 in EN 1993-1-8):

$$k_{10} = \frac{1,6 A_s}{L_b}$$

$$A_s = 0,78A = 0,78 \frac{\pi d^2}{4} = 0,61 d^2 = 0,61(1,25 t_{fc})^2 = 0,95 t_{fc}^2$$

$$L_b \approx 2 t_{fc} + t_{fc} = 3 t_{fc}$$

$$k_{10} = \frac{1,6 \cdot 0,95 t_{fc}^2}{3 t_{fc}} = 0,51 t_{fc} \qquad (17)$$

Table 2 gives the review of simplified formulas, which can be used to assess resistance and stiffness coefficients of steel joints basic components.

## 4. MOMENT RESISTANCE AND ROTATIONAL STIFFNESS OF STEEL JOINTS

Mechanical models representing different types of joints with distinguished components are shown in figures:
- single sided joints (Figure 2),
- double sided joints (Figure 3),
- beam splices with bolted end-plates (Figure 4).
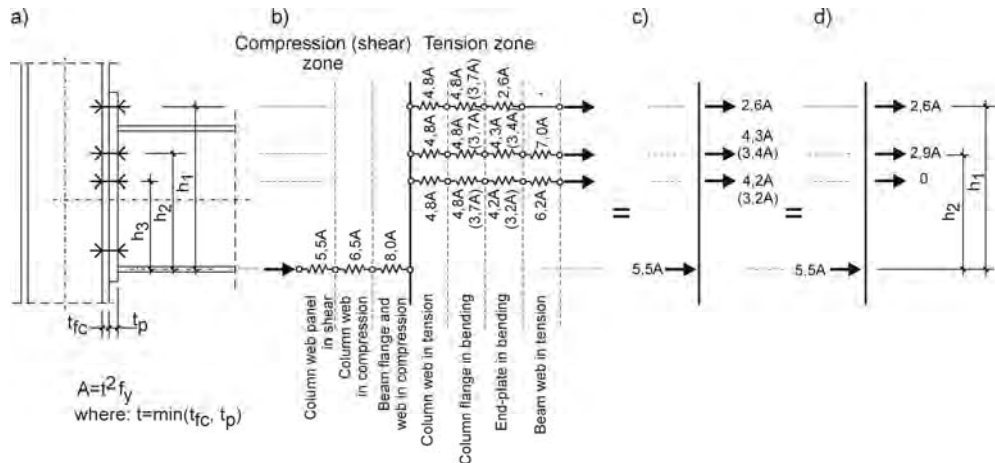


Figure 2. Single sided joint with extended end plate;
a) general view, b) mechanical model, c) effective design resistance of each bolt-rows, d) final model with reduced values according to resistance of compression (shear) zone
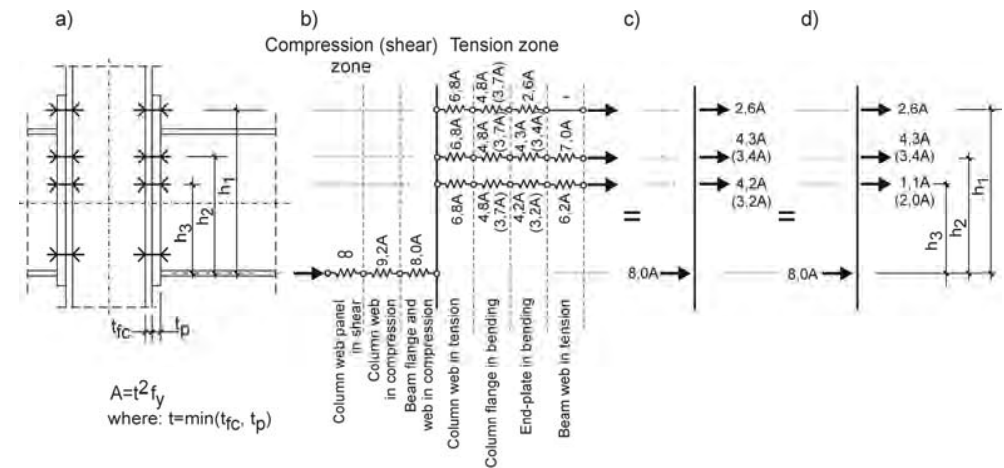


Figure 3. Double sided joint with extended end plate; a) general view, b) mechanical model, c) effective design resistance of each bolt-rows, d) final model with reduced values according to resistance of compression (shear) zone
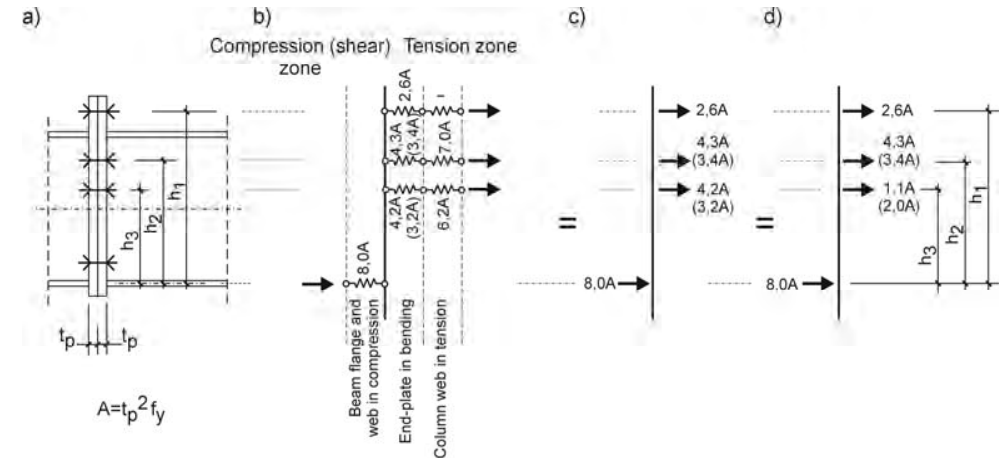


Figure 4. Beam splice with extended end plate; a) general view, b) mechanical model, c) effective design resistance of each bolt-rows, d) final model with reduced values according to resistance of compression (shear) zone

Each from above-mentioned figures show first view of joint (figures marked „a") and next show mechanical model with calculated values of each component (figures marked „b"). Such system in next step is replaced by simpler model, with only one component in every line, representing the smallest value of the tension (compression) resistance for an individual row (figures marked „c").

Final models (figures marked as "d") show effective design tension resistances, reduced according to the resistance of compression zone (the sum of tension resistances of bolt-row cannot exceed the resistance of compression zone).

The final models shown in Figure 2d, 3d and 4d can be easily used to assess design moment resistance, taking into account only the distances from bolt-rows to the centre of compression, thickness of column flange (or end plate) and yield strength.

Initial stiffness single sided joint with flush end plate can be calculated, assuming $z=0,9h_b$, as follows:

$$S_{j,ini} = \frac{E \cdot (0,9h_b)^2}{\sum \frac{1}{k}}$$

The only one bolt-row was taken into account (first below tension flange):

$$\sum \frac{1}{k} = \frac{1}{0,19t_{fc}} + \frac{1}{0,71t_{fc}} + \frac{1}{0,53t_{fc}} + \frac{1}{2,28t_{fc}} + \frac{1}{1,06t_{fc}} + \frac{1}{0,51t_{fc}} = \frac{11,90}{t_{fc}}$$

$$S_{j,ini} = \frac{210 \cdot 10^3 \cdot (0,9h_b)^2}{\frac{11,9}{t_{fc}}} \frac{1}{10^6} = \frac{h_b^2 t_{fc}}{70} \qquad (19)$$

In above formula input values (the depth of the beam $h_b$ and thickness of column flange $t_{fc}$) should be put on in [mm], then the result is calculated in [kNm/rad].

Initial stiffness of double sided joint with flush end plate:

$$\sum \frac{1}{k} = \frac{1}{0,71t_{fc}} + \frac{1}{0,53t_{fc}} + \frac{1}{2,28t_{fc}} + \frac{1}{1,06t_{fc}} + \frac{1}{0,51t_{fc}} = \frac{6,64}{t_{fc}}$$

$$S_{j,ini} = \frac{210 \cdot 10^3 \cdot (0,9h_b)^2 t_{fc}}{6,64} \frac{1}{10^6} = \frac{h_b^2 t_{fc}}{39} \qquad (20)$$

For extended end-plate connections, simplified method was applied. Instead of calculation concerning two bolt-rows (one in the extended part of the end-plate and one between the flanges of the beam) there was used modified value for a single bolt-row in the extended part of the end-plate, taken as twice to the corresponding value. The influence of the third bolt-row was neglected. In case of single sided joint:

$$\sum \frac{1}{k} = \frac{1}{0,19t_{fc}} + \frac{1}{0,71t_{fc}} + \frac{1}{2 \cdot 0,53t_{fc}} + \frac{1}{2 \cdot 2,28t_{fc}} + \frac{1}{2 \cdot 0,66} + \frac{1}{2 \cdot 0,51t_{fc}} = \frac{9,29}{t_{fc}}$$

$$S_{j,ini} = \frac{210 \cdot 10^3 \cdot (1,05h_b)^2 \cdot t_{fc}}{9,29} \frac{1}{10^6} = \frac{h_b^2 t_{fc}}{40} \qquad (21)$$

And in case of double sided joint with external end plate:

$$\sum \frac{1}{k} = \frac{1}{0,71t_{fc}} + \frac{1}{2 \cdot 0,53t_{fc}} + \frac{1}{2 \cdot 2,28t_{fc}} + \frac{1}{2 \cdot 0,66} + \frac{1}{2 \cdot 0,51t_{fc}} = \frac{4,24}{t_{fc}}$$

$$S_{j,ini} = \frac{210 \cdot 10^3 \cdot (1,05h_b)^2 \cdot t_{fc}}{4,24} \frac{1}{10^6} = \frac{h_b^2 t_{fc}}{18} \qquad (22)$$

Full list of developed formulas is presented w Table 4.

Table 4. List of simplified formulas to assess design moment resistance and initial rotational stiffness of steel joints

| Type of joint | Steel grade | Design moment resistance $M_{j,Rd}$ | Initial rotational stiffness $S_{j,ini}$ |
|---|---|---|---|
| Single sided with flush end plate | S235 | $(4,3h_2 + 1,2h_3)t^2 f_y$ | $\dfrac{h_b^2 t}{70}$ |
| | S355 | $(3,4h_2 + 2,1h_3)t^2 f_y$ | |
| Double sided with flush end plate | S235 | $(4,3h_2 + 3,7h_3)t^2 f_y$ | $\dfrac{h_b^2 t}{39}$ |
| | S355 | $(3,4h_2 + 3,2h_3)t^2 f_y$ | |
| Single sided with extended end plate | S235 | $(2,6h_1 + 2,9h_2)t^2 f_y$ | $\dfrac{h_b^2 t_{fc}}{40}$ |
| | S355 | | |
| Double sided with extended end plate | S235 | $(2,6h_1 + 4,3h_2 + 1,1h_3)t^2 f_y$ | $\dfrac{h_b^2 t}{18}$ |
| | S355 | $(2,6h_1 + 3,4h_2 + 2,0h_3)t^2 f_y$ | |
| Beam splice with bolted flush end-plates | S235 | $(4,3h_2 + 3,7h_3)t^2 f_y$ | $\dfrac{h_b^2 t}{23}$ |
| | S355 | $(3,4h_2 + 3,2h_3)t^2 f_y$ | |
| Beam splice with bolted extended end-plates | S235 | $(2,6h_1 + 4,3h_2 + 1,1h_3)t^2 f_y$ | $\dfrac{h_b^2 t}{11}$ |
| | S355 | $(2,6h_1 + 3,4h_2 + 2,0h_3)t^2 f_y$ | |

Remarks:

$h_1$, $h_2$, $h_3$ – the distances from bolt-rows (accordingly from one outside tension flange, below tension flange and other) to the centre of compression, (Figure 1), $t=min(t_{fc}, t_p)$

Design moment resistance is calculated in the same units, as input values, while rotational stiffness is calculated in [kNm/rad], on condition that input values are in [mm].

## 5. ACCURACY OF DEVELOPED FORMULAS

Accuracy of developed formulas (Table 4) was checked by confronting obtained values of structural properties of steel joints with "accurate" ones, from component method. There were used results of calculations included in (Bródka et al, 2009, Kozłowski et al, 2009, Kozłowski et al 2010, Giżejowski & Ziółko, 2010, Sprint). Additionally calculation of a few joints were performed by Cop software (Cop). Results of comparison applying to the bending resistance is shown in Figure 5, results of rotational stiffness comparison is shown in Figure 6.
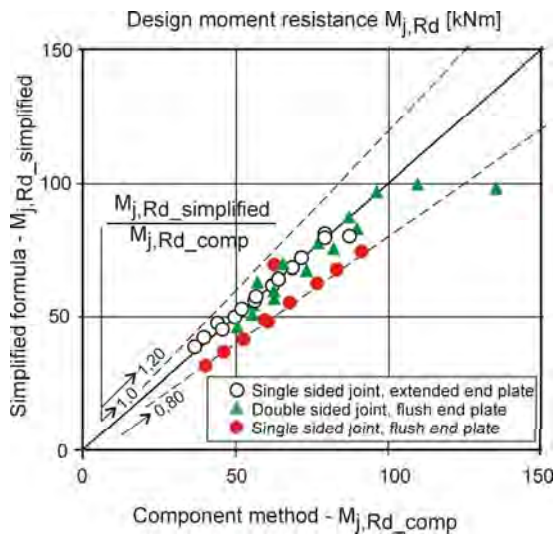
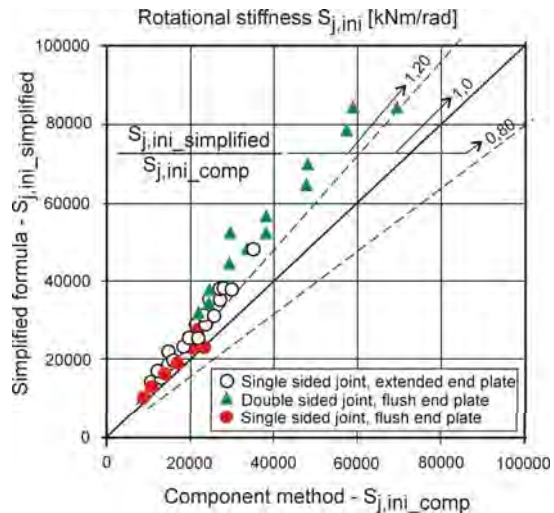Figure 5. Results of comparison applying to the bending resistance



Figure 6. Results of comparison applying to the rotational stiffness

## 6. CONCLUSIONS

With reference to the prediction of the bending resistance by component method, the use of simplified formulas shows good agreement. The range of error varies between -8% do +7% in case of single sided joints with extended end plate, -27% do +9% in case of double sided joints with flush end plate and -20% do +11% in case of single sided joints with flush end plate.

Rotational stiffness results obtained from simplified method differ from "exact" results from –20% to +40%.

Proposed formulas are addressed only to predesign stage and should help designers to establish structural properties of steel joints in easy way, to use them in global analysis of structure. Sensivity analysis of frames show limited influence of joint rotational stiffness on global behaviour of frames. Even 50% change in rotational stiffness does not significantly change values of internal forces in steel frames (Steenhuis et al, 1996 and Kozłowski 1998). So proposed formulas enables practitioners to assess structural properties of joint without complicated calculation.

It should be noted that full verification of the joint have to be carried out after the structure has been designed.

## REFERENCES

[1] Autodesk® Robot™ Structural Analysis Professional, http://www.autodesk.pl
[2] Bródka J., Kozłowski A., Ligocki I., Łaguna J., Ślęczka L., (2009) Design and calculations of steel joints and connections (in Polish), vol. 2, Polskie Wydawnictwo Techniczne, Rzeszów.
[3] CoP, The Connection Program, http://www.connectionprogram.com
[4] CRSJAE (1998) Computer program for calculation of resistance and stiffness of joints according to Eurocodes, Rzeszow University of Technology.
[5] EN 1993-1-1. European Committee for Standardization – CEN. Eurocode 3: Design of steel structures - Part 1-1: General rules and rules for buildings. Brussels.
[6] EN 1993-1-8. European Committee for Standardization – CEN. Eurocode 3: Design of steel structures - Part 1-8: Design of joints. Brussels.
[7] Giżejowski M., Ziółko J. (ed.), (2010) Building engineering, vol. 5. Steel building structures. Design according to Eurocodes with worked examples (in Polish). Arkady, Warszawa.
[8] Kowal-Gąska G., (2011) Analysis of the influence of joint geometric parameters on the behaviour of steel frame structures (in Polish). Diploma thesis. Rzeszów University of technology, Rzeszów.
[9] Kozłowski A., (1999), Shaping of the steel and composite skeletons with semi-rigid joints (in Polish). Publishing House of Rzeszów University of Technology. Rzeszów.
[10] Kozłowski A., Pisarek Z., Wierzbicki S., (2009), Design of end-plate connections according to PN-EN 1993-1-1 and PN-EN 1993-1-8 (in Polish), Inżynieria i Budownictwo, nr 4.
[11] Sprint. L'Eurocode 3 et les assemblages en acier. Aides de calcul pour assemblages rigides et semi-rigidies. Liege.
[12] Steenhuis M., Evers H., Gresnigt N., (1996) Conceptual design of joints in braced steel frames. IABSE Semi-Rigid Structural Connections Colloquium, Istanbul, pp 327- 336.

www.steelconstruct.com

# THE INFLUENCE OF TRUE BASE CONNECTION STIFFNESS ON THE COMPUTED DRIFT OF METAL BUILDING FRAMES

Finley Charney; Amber Verma; Maninder Bajwa; Cris Moen
*Department of Civil and Environmental Engineering, Virginia Tech, Blacksburg, VA U.S.A*
*fcharney@vt.edu*

## ABSTRACT

The connection at the base of the columns in gable frames used for metal buildings is usually modeled as pinned. However, this connection may have significant rotational stiffness, and including this stiffness in structural analysis may be beneficial. This paper describes the results of two projects related to assessment of the stiffness of the base connections. The first project, which is described in some detail, is the physical testing and related structural analysis of a metal building in Christiansburg, Virginia. The second project, which is described in less detail, is a series of analytical studies in which a computer program was developed which automatically creates a detailed finite element model of a typical connection and reports the moment-rotation behavior and the bearing stress distribution of the connection under gravity load followed by lateral load.

## 1. INTRODUCTION

Many metal buildings use gable frames for resistance to both gravity and lateral loads. These frames, usually with tapered columns and rafters, are supported at the bottom of the columns with steel base plates that are attached to the concrete foundation with anchor bolts. The column is usually continuously fillet welded to the base plate. In some cases there is a layer of grout between the base plate and the foundation. For the purpose of structural analysis it is usually assumed that the column to foundation connection is pinned, and as such does not resist any bending moment. However, the connection does have some rotational stiffness, and thus it will resist bending moment. While it is generally conservative to ignore this moment when designing for strength, it may be beneficial to include the connection stiffness in analysis for wind and seismic drift serviceability.

## 2. TESTING OF A METAL BUILDING

In order to assess the influence of the stiffness of the column base connection on the lateral-load response of metal buildings, an existing building was tested (Bajwa, 2010). This building, erected in Christiansburg Virginia in 2007, is 150 ft by 80 ft in plan. The building has five interior gable frames, spaced 25 ft apart. The three most interior frames are of one design, and the two most exterior frames are of a

different design. The building is 18 ft tall at the eave, and has a roof slope of 1/12. The wall and roof decking is attached with metal screws. In this paper only the interior frame is described. Bajwa (2010) provides a detailed description of the entire test building.

An elevation of the interior gable frames is shown in Figure 1. As may be observed, both the column and rafter are web-tapered. The column is 12 inches deep at the base, and 42 inches deep at the haunch. The rafter is 14 inches deep at mid-span, and 42 inches deep at the haunch. The thickness of the flange and web of the column is 0.375 inches and 0.1875 inches, respectively. The width of the column flange is 5 inches. The thickness of the flanges of the rafter varies from 0.375 inches at the haunch to 0.3125 inches at mid-span. The web thickness of the rafter is 0.1875 inches at the haunch, and 0.1345 inches at mid-span. The width of the rafter flanges ranges from 5.0 to 6.0 inches.

The column base plate is 13 inches long and 9 inches wide, with a thickness of 0.375 inches. The concrete slab supports the base plate. There is no grout between the base plate and slab. The plate is affixed to the slab with four 1.0 inch diameter anchor bolts, each with a length of 13 inches. The column is continuously fillet welded to the base plate. The base plate detail is shown in Figure 2.
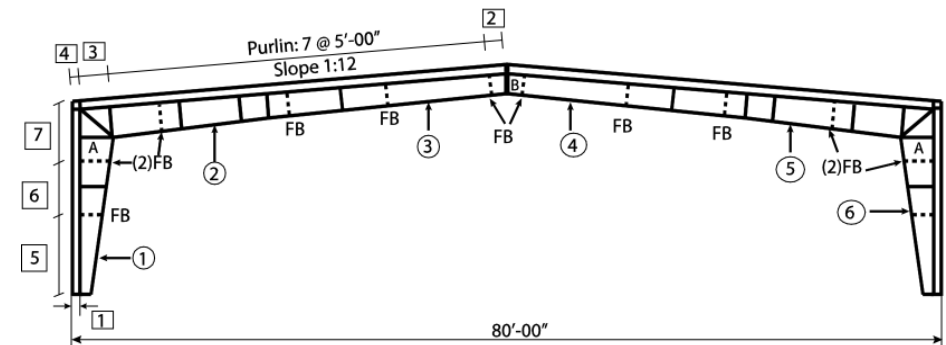


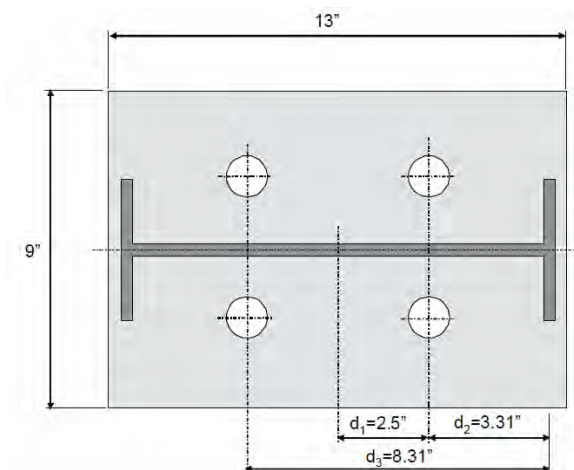Figure 1. Elevation of Interior Frame of Test Building



Figure 2. Column Base Plate Connection in Test Building

www.steelconstruct.com

The frame was tested by pulling on a single frame from the interior, as shown in Figure 3. The deflection at the eave height at each end of the tested frames and at the eave height at the ends of the adjacent frames was recorded using linear voltage displacement transducers. The rotation at the base of the columns of the tested frame was measured using inclinometers. Strain gages were positioned on the flanges of the columns near the base, and these were used to determine the applied moment at the base of the column.



Figure 3. Test Set Up

## 2.1. Preliminary Analysis

A detailed structural analysis was performed on the test structure prior to physical testing. One of the main goals of the analysis was to determine the influence of the rotational stiffness of the column base connection on the lateral drift at the eave of the frame. The frame itself was modeled with SAP2000 (CSI, 2010) using shell elements to represent the columns and rafters. While only one frame was analyzed, this was in fact a three-dimensional analysis because the flanges of the sections were explicitly modeled. Details of the modeling of the frames are reported in Bajwa (2010).

In this analysis, the column base connection stiffness was systematically varied from 1 in-kip/radian (representing a pinned connection) to $10^9$ in-kip/radian (representing a fixed connection). A simple rotational spring was used to represent the base stiffness. Both of the column base connections were assumed to have the same rotational stiffness. As discussed later, this assumption may not always be accurate.

The results of the analysis are shown in Figure 4. In this figure the computed drift is shown on the vertical axis, and the assumed base connection rotational stiffness is plotted on the horizontal axis. The three curves shown on the figure are for three different assumptions on how the frame is modeled. The curve with triangle symbols is from the finite element analysis (FEA). This is the most accurate analysis and is thereby used for further discussion.

As may be seen from FEA curve the lateral deflection is approximately 0.66 inches for a base stiffness of 1.0 in-kip/radian and reduces only slightly as the stiffness increases to about 1000 in-k/radian. Between a stiffness of 1000 and 1,000,000 in-k/radian there is a sharp reduction in deflection. At a rotational stiffness above 1,000,000 in-k/radian the displacement is again relatively constant, with a minimum value of about 0.28 inches.
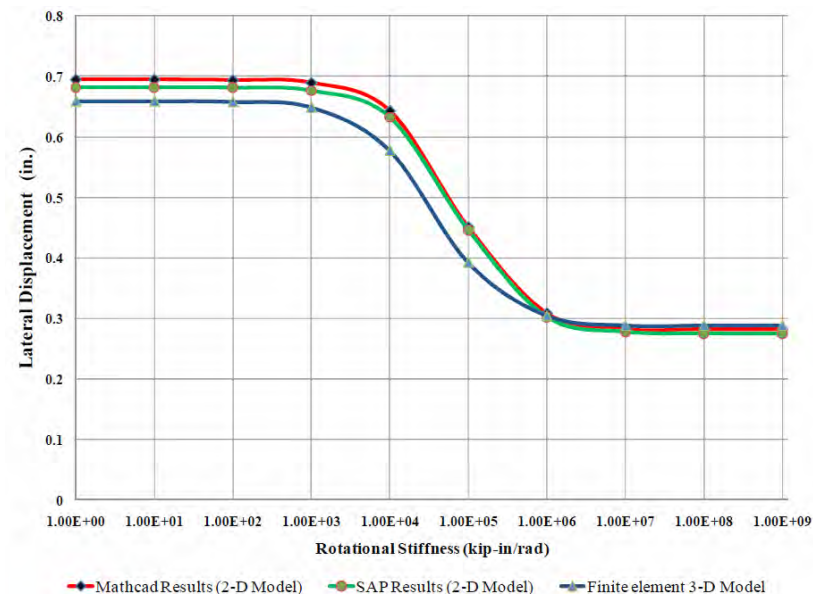


Figure 4. Variation in Lateral Displacement with Base Connection Stiffness

The curve shown in Figure 4 can be used to estimate the base connection's stiffness if the deflection at the eave is known. Conversely, the eave deflection can be determined if the connection's rotational stiffness is known.

To determine the deflection at the eave of the frame the base conditions for the finite element model were modeled explicitly, wherein the base plate and anchor bolts were physically represented. This refined connection replaced the rotational spring from the previous model.

In general, the rotational stiffness of the base connection depends on the following factors:

- Base plate size (plan dimensions)
- Base plate thickness
- Number and arrangement of anchor bolts
- Diameter and length of anchor bolts
- Pretension in anchor bolts
- Thickness and properties of grout
- Size and geometry of the column
- Detail for attaching column to base plate
- Magnitude of initial gravity load
- Magnitude of current lateral load

The dependence of the stiffness on load magnitude and direction is a nonlinear effect, and is due to the fact that a portion of the base plate will lift off of the foundation. This lift off and computed bearing stresses after lift off is shown in Figure 5. Lift off can be sudden or gradual, depending on the factors listed above. Note the bending deformation in the base plate in Figure 5a. While both of the column connections in a given (symmetric) gable frame will have the same initial stiffness, the lift off will occur first for the windward column, then (if at all) for the leeward column. In the extreme case the base plate could lift off completely on the windward side if the column goes into net tension, but this is not expected in serviceability calculations.
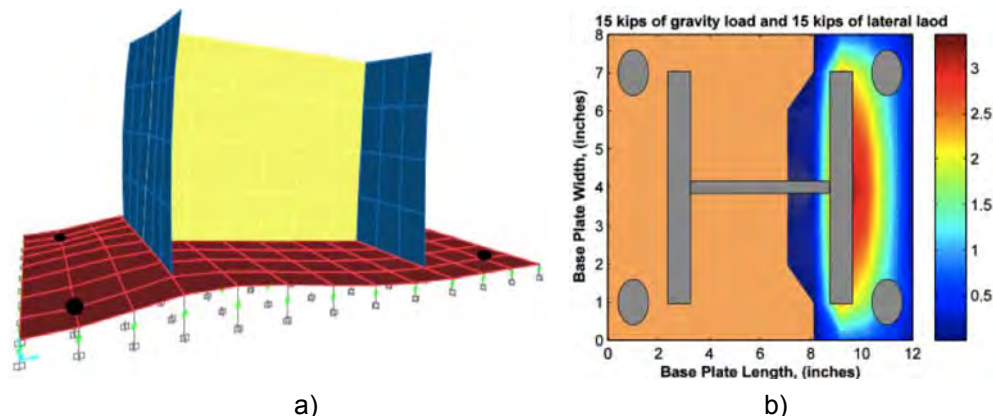


Figure 5. Lift off of Base Plate (a) and Bearing Stress, ksi, after Lift Off (b)

For the test building there was no grout below the base plate, and there was no pretension in the anchor bolts. The base plate was modeled using shell elements, and this plate was supported by an array of nonlinear springs. One spring was located at each node point, with edge and corner springs having, respectively, 1/2 and 1/4 of the stiffness of interior springs. The assumed force-deformation relationship for one of these springs is shown in Figure 6a. When in tension the springs have virtual zero stiffness (allowing uplift) and in compression the springs have a large stiffness, thereby preventing the base plate from pushing into the concrete slab.
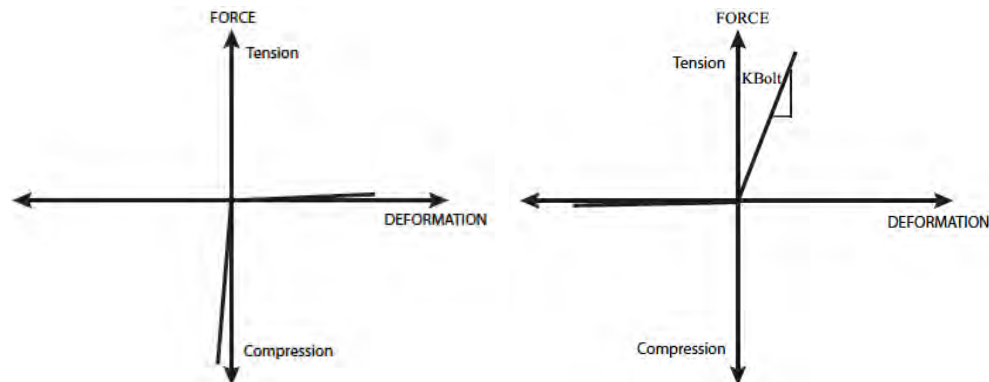


Figure 6. Force-Deformation Behavior for (a) Foundation Springs and (b) Anchor Bolts

Each anchor bolt is also represented by a nonlinear spring. The stiffness in tension is taken as $AE/L_{eff}$ where $A$ is the cross sectional area, $E$ is the modulus of elasticity, and $L_{eff}$ is the effective length. The effective length depends on the assumed bond stress distribution along the length of the bolt. If the bond stress is uniform the effective length is half of the actual length. If the bolt is unbonded and supported only at its embedded end (e.g. via an embedded bearing plate) the effective length is equal to the true length. When the anchor bolt is in compression the stiffness is taken as a very small value because through thickness deformations in the base plate would result in disengagement of the bolt. The force-deformation relationship used for the anchor bolts is shown in Figure 6b.

The results of the analysis are shown in Figure 7 for the case where the effective length of the anchor bolt was taken as 1/2 of the true length. Under a lateral load of 7.5 kips the computed displacement is 0.525 inches, and the resulting base connection stiffness is approximately 20,000 in-k/radian. This value would represent the average stiffness of the two base connections, where the windward side connection (column in tension under wind) would generally have a somewhat lower stiffness than the leeward side connection (column in compression under wind).
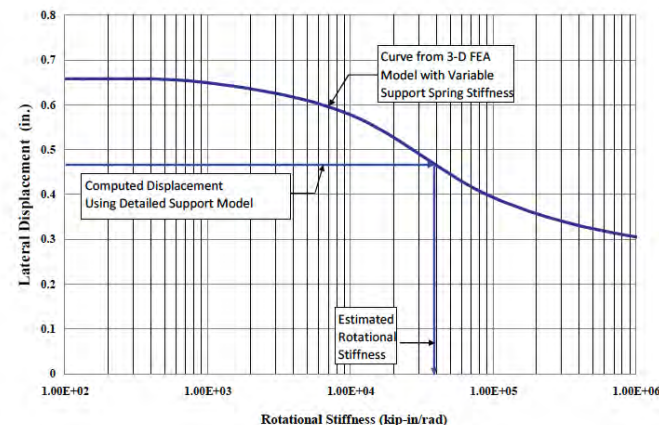


Figure 7. Results of Finite Element Analysis

It is of some interest to determine how variations in connection properties would influence the lateral displacement of the frame. Figure 8 shows the influence of both base plate thickness and anchor bolt stiffness. The top curve is for the base plate thickness of 3/8 inch, which is used in the test building. For this base plate thickness the stiffness of the anchor bolt has a definite influence on behavior when the bolt stiffness is less than about 5,000 kips/inch. However, the influence on anchor bolt stiffness is much greater when the base plate is thickened to 0.75 inches and again to 1.5 inches. For a 1.0 inch diameter anchor bolt the stiffness is 3,500 kips/inch, and it appears for the test building that doubling the thickness of the base plate from 3/8 to 3/4 inches would reduce the lateral drift by a factor of 2. This is a remarkable influence in behavior given the small additional cost related to the thicker plate.

The influence on initial dead load on the behavior of the test frame is shown in Figure 9. In this analysis the anchor bolt stiffness was kept constant at 3,500 kips/inch, and the dead load and the base plate thickness was varied. As may be observed the influence of dead load is small, and is more significant for thinner base plates.
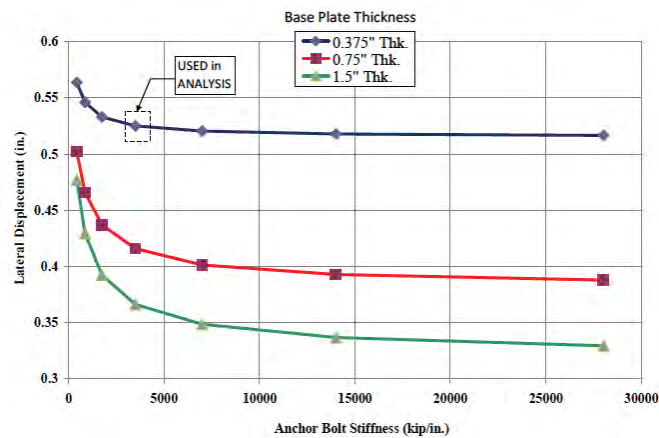
Figure 8. Influence of Base Plate Thickness and Anchor Bolt Stiffness on Drift



Figure 9. Influence of Dead Load Magnitude and Base Plate Thickness on Drift

## 2.2. Test Results

While not directly related to column base stiffness, it is interesting to note that the two columns in one frame shared almost equally in resisting the lateral load, and that only a small portion of the lateral load was shed to adjacent frames. This indicates that the roof diaphragm (the screwed on metal deck and supporting purlins) was ineffective as a load transfer mechanism. Additionally, the fact that the columns almost equally shared in loads indicates that the effect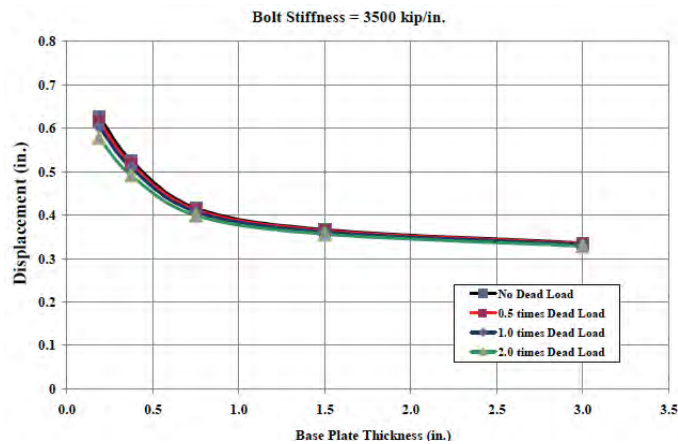ive rotational stiffness at the two column bases was nearly the same. This behavior is reasonable given the relatively light lateral load applied during tests, but could change as one of the columns begins to lift off.

Measurements from the strain gages on the columns and the inclinometers placed near the base of the columns gave estimates of column base stiffness that ranged considerably, but several of these values were in the range of 25,000 inch-kip per radian. A typical plot is shown in Figure 10. Note from this figure that the noise in the data acquisition system was rather large compared to the values being read. However the measured stiffness was in the range of that predicted from analysis (see Figure 7 above).
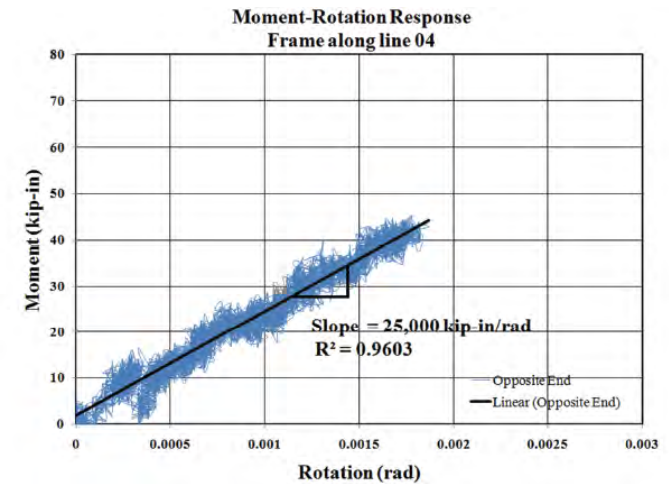


Figure 10. Moment-Rotation Plot from Frame Tests

## 3. SUMMARY AND CONCLUSIONS

The research reported herein indicates that the base connections in metal buildings can have a significant influence on computed behavior of gable frames under lateral loading. While several factors influence the stiffness of the connection, the most important factors appear to be the thickness of the base plate and the axial stiffness of the anchor bolts. The influence of other parameters such as anchor bolt location, presence of pretension, and presence of grout, is somewhat less important (Verma, 2012).

Determining a realistic rotational stiffness for a base plate connection is not trivial however, and generally requires a detailed finite element analysis of the type described in this paper. A utility for estimating the connection stiffness was developed by Verma (2012). This utility includes an easy-to-use graphical user interface, and uses either SAP2000 or OpenSEES (PEER, 2012) as the analytical engine. This tool is currently being used by the authors to provide a better understanding of the influence of column base stiffness on the performance of metal buildings under lateral load.

## ACKNOWLEDGEMENTS

## REFERENCES

[1] Bajwa, M. (2010), "Assessment of Analytical Procedures for Designing Metal Buildings for Wind Drift Serviceability", Master of Science Thesis, Department of Civil and Environmental Engineering, Virginia Tech, Blacksburg, VA.

[2] CSI (2010), "SAP 2000", Computers and Structures, Inc., Berkeley, CA.

[3] PEER (2012), OpenSEES Computer Program, Version 2.3, Pacific Earthquake Engineering Research Center, Berkeley, CA.

[4] Verma, A. (2012), "Influence of Column Base Fixity on Lateral Drift of Gable Frames", Master of Science Thesis, Department of Civil and Environmental Engineering, Virginia Tech, Blacksburg, VA.

# INFLUENCE OF CONNECTION TYPOLOGY ON THE SEISMIC BEHAVIOUR OF MR-FRAMES

*Rosario Montuori, Vincenzo Piluso, Marina Troisi*
*DICIV - Department of Civil Engineering, University of Salerno, Italy*
*r.montuori@unisa.it; v.piluso@unisa.it; m.troisi@unisa.it*

## ABSTRACT

The work herein presented is aimed at the investigation of the influence of beam-to-column connection typologies on the seismic response of MR-Frames. The investigated typologies are three partial strength connections whose structural detail has been designed by means of hierarchy criteria based on the component approach, aiming to obtain the same flexural resistance. They are characterized by different location of the weakest joint component, leading to different values of the joint rotational stiffness and of the plastic rotation supply. Moreover, the shape of the hysteresis loops with their stiffness and strength degradation, governing the connection dissipative capacity, is strongly affected by the weakest joint component as testified by the developed experimental tests.

In order to evaluate the seismic response of steel moment resisting frames, an appropriate modelling of structures is needed to accurately represent both strength and deformation characteristics, especially with reference to beam-to-column connections. In particular, in case of partial-strength beam-to-column joints, the dissipation of the earthquake input energy is obtained through the yielding of the connecting elements. In particular, beam-to-column joints are commonly modelled by means of rotational inelastic spring elements located at the ends of the beams whose moment-rotation curve is characterized by a cyclic behaviour accounting for both stiffness and strength degradation and pinching phenomenon. In this paper, the monotonic non-linear envelope and the cyclic moment-rotation diagram of these elements have been defined by using the Polygonal Hysteretic Model (PHM) of IDARC 2D. The parameters characterizing the cyclic hysteretic behaviour have been calibrated on the base of experimental results aiming to the best fitting. Successively, a blind prediction of the frame structural response by means of dynamic analyses has been carried out, based on the calibrated joint rotational response models, to investigate the influence of the joint structural detail on the seismic response of MR-Frames.

## 1. INTRODUCTION

According to the traditional seismic design, the seismic input energy dissipation in moment resisting frames is concentrated in some zones of structural members, namely dissipative zones, which are engaged in plastic range so that they have to be properly detailed in order to assure wide and stable hysteresis loops. Moreover, aiming at the design of dissipative structures, it is important to promote the plastic engagement of the greatest number of dissipative zones by properly controlling the failure mode. To this scope, as the plastic engagement of columns can lead to non dissipative collapse mechanisms, modern seismic codes, such as ANSI-AISC 341-10 (AISC, 2010) and Eurocode 8 (CEN 2005a), suggest the application of the column hierarchy criterion which imposes that, at each beam-to-column joint, the flexural strength of connected columns has to be sufficiently greater than the flexural strength of the connected beams. However, it is important to underline that the fulfillment of this design criterion is only able to prevent the development of storey mechanisms, but it is not sufficient to guarantee the formation of a collapse mechanism of global type (Mazzolani and Piluso, 1996; 1997).

The dissipative zones can be located at the beam ends or in the connecting elements, depending on the beam-to-column joint typology. In fact, beam-to-column connections can be designed either as full-strength joints, having sufficient overstrength with respect to the connected beam concentrating dissipative zones at the beams ends (Mazzolani and Piluso, 1996; Bruneau *et al.*, 1998, Faella et al., 2000), or as partial-strength joints, so that the seismic input energy is dissipated by means of the plastic engagement of properly selected joint components.

The use of rigid full-strength joints has been traditionally considered the best way to dissipate the seismic input energy, as a consequence, seismic codes provide specific design criteria for full-strength joints, but there are no detailed recommendations dealing with partial-strength connections.

After Kobe and Northridge seismic events, two strategies have been identified to improve the plastic rotation supply of welded connections. The first one consists in the improvement of the welding technique, usually strengthening the critical area subjected to fracture. The second one is based on the possibility of promoting the energy dissipation in the beam, reducing the bending resistant area of beams by properly cutting the flanges in a zone close to beam-to-column connections. This weakening approach is commonly called RBS (Reduced Beam Section) (Moore et al.,1999; FEMA 351, 2000; FEMA 352, 2000).

Eurocode 8 has opened the door to the use of partial-strength joints for dissipating the seismic input energy in the connecting elements of beam-to-column joints. It was recognized that semi-rigid partial strength connections can lead to dissipation and ductility capacity compatible with the seismic demand, provided that they are properly designed by means of an appropriate choice of the joint components where the dissipation has to occur.

Moreover, the use of partial-strength joints can be an effective tool to avoid the plastic engagement of columns without their over-sizing, leading to convenient structural solutions particularly in case of long span MR-Frames (Faella *et al.*, 1998).

In order to develop more accurate methodologies to assess the seismic performance of structures with partial-strength connections, the present paper is aimed at the evaluation of the influence of beam-to-column connection typologies on the seismic response of MR-Frames starting from the knowledge of the cyclic rotational behavior of beam-to-column joints.

## 2. EXAMINED BEAM-TO-COLUMN CONNECTIONS AND THEIR MODELLING

The study of semi-rigid steel joints can be carried out by means of the component approach (Jaspart, 1991; Faella *et al.*, 2000) which has been codified by Eurocode 3 (CEN, 2005b). With reference to beam-to-column joints, the component approach allows the prediction of the moment-rotation response, provided that all the sources of strength and deformability of the joint, i.e. all the components, are properly identified. However, Eurocode 3 provides information for evaluating only the monotonic behaviour of beam-to-column connections, but it does not give any indication concerning the modelling of the cyclic behaviour of the joint components. For this reason, a significant research activity dealing with the ultimate behaviour of the main components of beam-to-column connections under cyclic actions has been carried out (Faella et al., 1998, 2000; Kim and Engelhardt, 2002; Clemente et al., 2004; Piluso and Rizzano, 2008; Dubina et al., 2008, Hu et al., 2011). In particular, in a recent experimental program (Iannone et al., 2011) it has been pointed out that the energy dissipation provided by beam-to-column joints under cyclic loads can be obtained as the sum of the energy dissipation due to the single joint components, provided that they are properly identified and their cyclic force-displacement response is properly measured. This result is very important, because it testifies the applicability of the component approach even in the case of cyclic loading conditions.

In addition, the actual possibility of extending the component approach to the prediction of the cyclic response of beam-to-column joints has been investigated (Latour et al., 2011) leading to the definition of a mechanical model for predicting the cyclic response of bolted connections.

On the base of the component approach, it has been pointed out how the ultimate behaviour of bolted beam-to-column connections under cyclic actions can be governed by properly strengthening the components whose yielding has to be prevented (Iannone *et al.*, 2011). Therefore, the component approach can be also regarded as an effective design tool from the seismic point of view allowing the adoption of hierarchy criteria at the component level, as soon as the dissipative zone, i.e. the weakest joint component, has been properly selected and designed.

The beam-to-column typologies herein investigated are three partial-strength connections whose structural detail has been designed by means of hierarchy criteria, based on the component approach, aiming to obtain the same flexural resistance, but changing the weakest component. Therefore, they are characterized by different locations of the weakest joint component, leading to different values of the joint rotational stiffness and of the plastic rotation supply (Iannone et al., 2011).

The reason for investigating these beam-to-column joints is related to the availability of results dealing with their cyclic rotational response, tested as structural sub-assemblages at the Materials and Structures Laboratory of Salerno University. The structural details of the connections are depicted in Fig. 1 with the analysed MR-Frame.

In order to point out how the cyclic behaviour is governed by the location of the weakest joint component, the tested specimens have been designed aiming to obtain the same flexural strength, but different values of rotational stiffness and plastic rotation supply. The joint non-dimensional resistance $\overline{m}$, given by the ratio between the joint flexural resistance $M_{jRd}$ and the beam plastic moment $M_{bRd}$, is equal to 0.76 (Iannone et al., 2011).

Specimen EEP-CYC 02 was designed aiming to obtain the aforementioned value of the non-dimensional resistance and relying on the ductility supply of the end-plate, by properly designing its thickness and bolt location (Piluso et al., 2001). The first component to be designed is the weakest component, i.e. the end-plate, whose design resistance is obtained as the ratio between the desired joint flexural resistance and the lever arm. Successively, the other components are designed to have sufficient overstrength aiming to avoid their plastic engage.

Specimen EEP-DB-CYC 03 is an extended end-plate connection, whose design is aimed at the investigation of the energy dissipation capacity of beams. However, aiming to obtain the same flexural resistance of previous specimen, the RBS (Reduced Beam Section) strategy, called also "dog bone", has been adopted whose structural detail has been designed according to Moore et al. (1999).

Last specimen, TS-CYC 04, is a partial-strength joint with a couple of T-stubs bolted to the beam flanges and to the column flanges and designed to be the main source of plastic deformation capacity. The design goal is to avoid the plastic engage of the components related to the column web panel, the column web in compression/tension and the panel zone in shear. The main advantage of double split tee connections is due to their easy repair. In fact, if the panel zone is designed with adequate overstrength, it is possible to substitute only the end T-stubs after a seismic event. Also in this case the same flexural resistance of the other joints was imposed requiring, in addition, a plastic rotation supply of about 0.08 rad. The plastic deformation supply of the T-stub components has been predicted as suggested by Piluso et al. (2001).

In order to assess the seismic performance of steel moment resisting frames with partial-strength joints, it is preliminarily needed to set up an appropriate model to accurately represent the cyclic rotational behaviour of connections. In fact, the rotational behaviour of connections under cyclic actions is complicated by the development of strength and stiffness degradation and by pinching phenomena as the number of cycles increases.



EEP-CYC 02

    www.steelconstruct.com
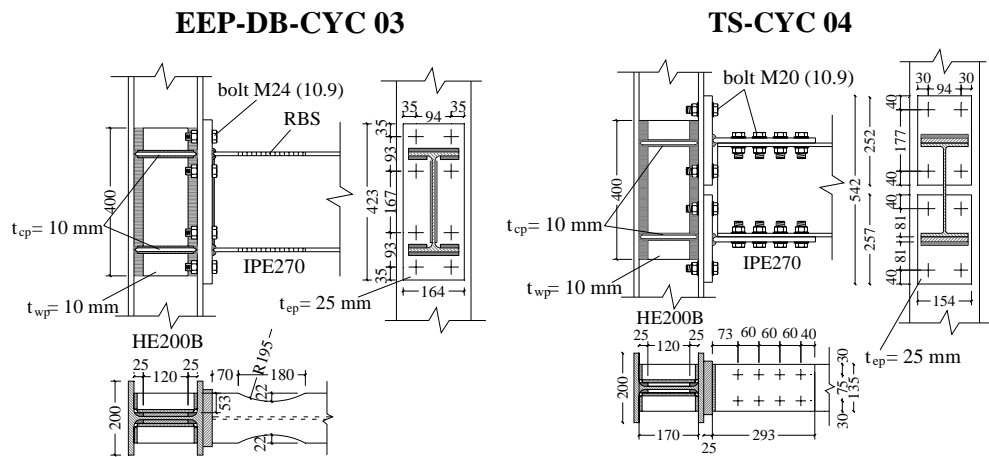
**EEP-DB-CYC 03**

**TS-CYC 04**
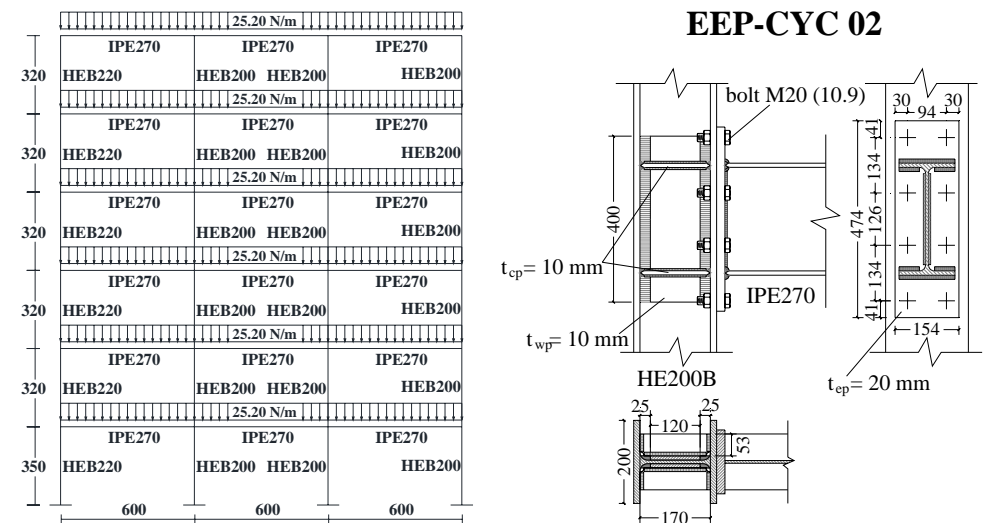


Figure 1. Analysed MR-Frame with structural details of examined connections

The rules describing these phenomena cannot be deduced by means of theoretical approaches; therefore, it is necessary to have sufficient experimental data aiming to develop adequately accurate semi-analytical models, in which the monotonic envelope is predicted by means of the use of mechanical models based on the component method, while the degradation rules are empirically derived by means of the available experimental results (Latour et al., 2011). As testified by the developed experimental tests, the cyclic response of connections in terms of shape of hysteresis loops, their stiffness and strength degradation and the resulting dissipation capacity are directly related to the components involved in plastic range, mainly the weakest component.

In this work, aiming to investigate the influence of the beam-to-column joint structural detail on the seismic response of MR-Frames, the non-linear cyclic rotational response of beam-to-column joints has been modelled by means of the spring elements included in IDARC 2D (Version 6.0) software. In particular, the rotational inelastic spring elements are located at the ends of the beams. The cyclic moment-rotation curve of such spring elements has been properly calibrated on the base of available experimental results to account for both stiffness and strength degradation and for pinching phenomenon. In order to derive the parameters governing the cyclic response of the spring elements, a cyclic push-over analysis under displacement control has been carried out with reference to a structural scheme, depicted in the top left corner of Fig. 2, whose feature is that its structural response is dependent on the cyclic response of the spring elements only. Therefore, it is possible to apply to such structural model a displacement time-history exactly reproducing that adopted in testing beam-to-column joint sub-assemblages and to compare the cyclic moment-rotation response of the spring element with the one obtained from experimental tests. Therefore, by properly modifying the parameters modelling strength and stiffness degradation and pinching phenomena, it has been possible to select, for each tested specimen, the connection model leading to the best fitting between the analytical model and the experimental test results.
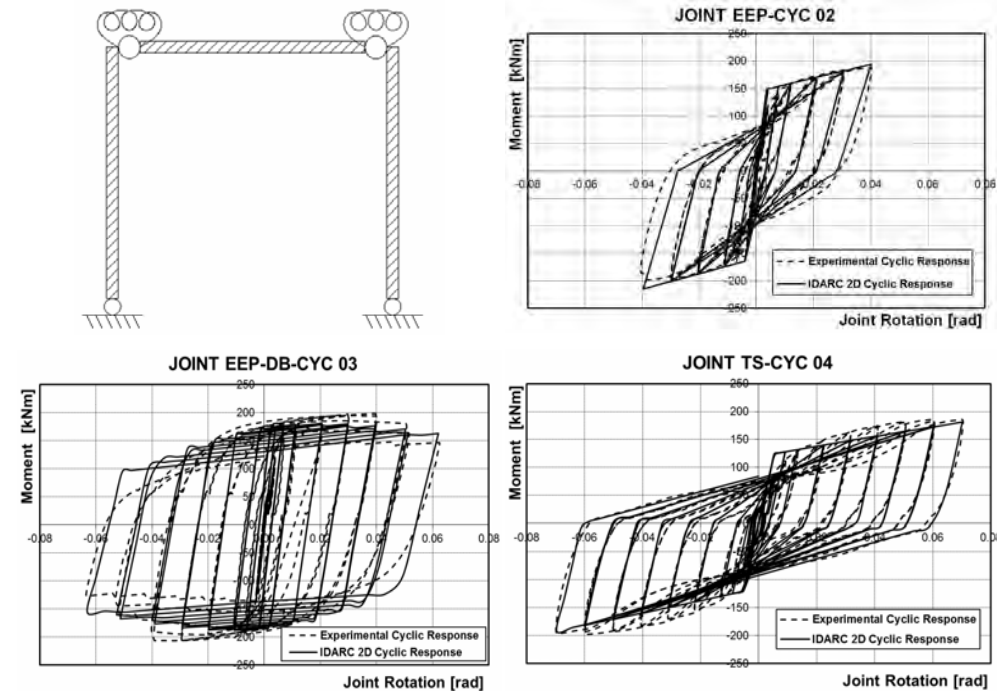


Figure 2. Comparison between the cyclic moment-rotation response of the spring elements and the experimental test results

The parameters of the trilinear envelope of the moment-rotation curve of the spring element, adopted in IDARC 2D model, are delivered in Table 1. In addition, the damage phenomena occurring under cyclic loading conditions have been accounted for by calibrating the corresponding parameters by imposing the equivalence in terms of dissipated energy between experimental test results and the IDARC 2D spring element response.

Table 1. Parameters of the spring elements adopted for connection modelling in IDARC 2D

| Connection | Initial Rotational Stiffness [kNmm/rad] | First Yielding Moment [kNmm] | Plastic Moment [kNmm] | Yield Rotation [rad] | Ultimate Rotation [rad] | Post Yield stiffness ratio as % of elastic |
|---|---|---|---|---|---|---|
| | [EI] | [PCP] | [PYP] | [UYP] | [UUP] | [EI3P] |
| **EEP-CYC 02** | 41411466 | +116463/-130074 | +157000/-173000 | +0.01/-0.01 | +0.1/-0.1 | +3.07/-3.52 |
| **EEP-DB-CYC 03** | 43420000 | +119200/-136667 | +180000/-190000 | +0.011/-0.011 | +0.1/-0.1 | +1.3/-0.8 |
| **TS-CYC 04** | 23196000 | +89817/-88344 | +140000/-140000 | +0.022/-0.022 | +0.1/-0.1 | +4/-5 |

www.steelconstruct.com

In particular, the adopted hysteretic model is the Polygonal Hysteretic Model (PHM), available in the library of IDARC 2D program, which can be combined with three different hysteretic rules: the Yield Oriented Model, the Bilinear Model and the Vertex Oriented Model.

The PHM is an extension of three-parameter Park model, while the hysteretic rules allow to account for the stiffness and strength degradation and for pinching. The parameters characterizing the cyclic hysteretic behaviour of the tested beam-to-column connections are reported in Table 2.

In particular, the stiffness degradation is defined by means of the parameter HC which locates the pivot point (HC = 200 corresponds to a stiffness degradation equal to zero); the strength degradation is defined by the parameters HBD and HBE which represent the measure of strength degradation related to ductility and to energy, respectively (HBD = 0.01 and HBE = 0.01 correspond to a strength degradation equal to zero); finally, the parameter HS defines the pinching (HS = 1.0 corresponds to the absence of pinching).

The general meaning of the parameters can be synthesized as follows: an increase in HC delays the amount of stiffness degradation; an increase in HBD and HBE accelerates the strength deterioration; an increase in HS reduces the amount of slip.

Table 2. Hysteretic parameters of spring elements for IDARC 2D input

| CONNECTIONS | CYCLIC MODEL | HC | HBD | HBE | HS |
|---|---|---|---|---|---|
| EEP-CYC 02 | PHM-Vertex Oriented | 5 | 0.01 | 0.01 | 1 |
| EEP-DB-CYC 03 | PHM-Yield Oriented | 15 | 0.01 | 0.10 | 1 |
| TS-CYC 04 | PHM-Vertex Oriented | 200 | 0.01 | 0.01 | 1 |

The comparison between the cyclic moment-rotation curve of the tested connections, depicted in Fig. 1, and the corresponding rotational response, predicted by means of the IDARC 2D structural model with the spring element modelling parameters given in Tables 1 and 2, is provided in Fig. 2. From these figures, a satisfactory degree of accuracy in the modelling of the beam-to-column joint cyclic behaviour can be observed.

## 3. ANALYSED MR-FRAME AND ITS STRUCTURAL MODELLING

The seismic response of semirigid steel frames has recently gained new attention from researchers (Elnashai et al., 1998; Grecea et al., 2004; Fragiacomo et al., 2004; Aksoylar et al., 2011). In particular, in this paper, the influence of the structural detail of beam-to-column joints on the seismic response of MR-Frames with partial-strength connections is investigated with reference to the three bay-six storey steel frame, depicted in the top left corner of Fig. 1 (Rizzano, 2006). This choice is justified considering that the tested joints were selected on the basis of the same MR-Frame.

Regarding the design loads, a uniform dead load ($G_k$) of 12.00 kN/m and a uniform live load ($Q_k$) of 6.00 kN/m are applied. The spans of the longitudinal frames are equal to 6.00 m, while the interstorey heights are equal to 3.20 m except for the first storey whose height is equal to 3.50 m.

The design vertical load is $q_d = 1.35G + 1.5Q = 25.20 \text{ kN/m}$. In order to withstand vertical loads, a design value of the beam plastic moment approximately equal to $q_d L^2/8$ has been chosen and IPE270 profiles made of S275 steel grade have been adopted for the beams.

The size of the columns are selected by adopting a design procedure assuring a global collapse mechanism (Mazzolani and Piluso, 1996, 1997; Faella et al., 1998). The whole design procedure has been carried out with reference to S275 steel grade.

However, in order to assure a frame structural response consistent with the joint rotational behaviour obtained from experimental tests and modelled as described in the previous Section, the values of column and beam material mechanical properties to be adopted in non-linear dynamic analyses are assumed to be equal to those measured in testing beam-to-column joint sub-assemblages and reported in Table 3.

Table 3. Columns and beams mechanical properties.

| Structural Element | $f_y$ [N/mm$^2$] | $f_u$ [N/mm$^2$] |
|---|---|---|
| Beam | 405 | 546 |
| Column | 430 | 523 |

Regarding beam and column elements, firstly, the moment-curvature monotonic envelope has been derived and a trilinear approximation has been considered. Successively, the non-linear moment-curvature diagram has been adopted in IDARC 2D computer program to provide the input parameters to model the cyclic response of members according to the so-called "Bilinear Model" characterized by an hysteretic behaviour with no stiffness degradation, no ductility-based strength decay, no hysteretic energy-based decay and no slip. However, it is useful to underline that this issue is not significant, because the use of partial-strength connections leads to the concentration of yielding at connections, so that only the connection modelling, discussed in the previous Section, is of primary importance.

In Table 4 the hysteretic parameters adopted for the structural elements are reported.

Table 4. Hysteretic parameters adopted for modelling structural elements in IDARC 2D

| Structural Element | CYCLIC MODEL | HC | HBD | HBE | HS |
|---|---|---|---|---|---|
| Beams | PHM-Bilinear Model | 200 | 0.01 | 0.01 | 1 |
| Columns | PHM-Bilinear Model | 200 | 0.01 | 0.01 | 1 |

## 4. INFLUENCE OF BEAM-TO-COLUMN JOINTS ON SEISMIC RESPONSE

The seismic performances of the examined MR-frame with the three structural details of beam-to-column connections are investigated by means of non-linear dynamic analyses, carried out by IDARC 2D program, for increasing levels of the seismic intensity measure. As the work on this topic is still ongoing, only the preliminary results are presented and discussed in this paper.

In these preliminary results, record-to-record variability is accounted for performing dynamic non-linear analyses, assuming 3% of critical damping, considering

three earthquake records selected from PEER database. The main data of the considered records (name of earthquake, date, component, spectral acceleration corresponding to the period of vibration of the considered Moment Resistant Steel Frames, PGA and length) are reported in Table 5.

Table 5. Main data of considered records

| Earthquake | Date | Component | Sa (T=1.6 sec) (g) | Sa (T=1.7 sec) (g) | PGA (g) | Length (sec) |
|---|---|---|---|---|---|---|
| Northridge | 17/01/1994 | N-S | 0.13 | 0.11 | 0.233 | 39.99 |
| Imperial Valley | 15/10/1979 | N-S | 0.27 | 0.30 | 0.370 | 28.35 |
| Kobe | 16/01/1995 | N-S | 0.22 | 0.29 | 0.251 | 40.95 |

Aiming to perform an incremental dynamic non linear analysis, all the records have been properly scaled to provide increasing values of the spectral acceleration $S_a(T_1)$ corresponding to the fundamental period of vibration of the structure equal to $T_1$=1.6 sec for connections EEP-CYC 02 and EEP-DB-CYC 03 and equal to $T_1$=1.7 sec for connection TS-CYC 04. In particular, the analyses have been repeated increasing the $S_a(T_1)/g$ value until the attainment of the experimental ultimate value of the plastic rotation supply of connections. Scaling the records at the same value of $S_a$ gives the possibility to reduce the variability of structural seismic response.

In particular, in the top left corner of Figure 3, the elastic spectra of the analysed records are given; in addition, the same figure provides also the IDA curves giving the maximum spring rotation versus the spectral acceleration. In these figures, the ultimate plastic rotation for each considered connection is also represented. The IDA analyses have been stopped when the available ductility has been exceeded at least for one spring element. In particular, it can be observed that for Imperial Valley earthquake, the maximum value of spectral acceleration is equal to 0.64g, 1.17g and 1.44g for MR-frames with connections EEP-CYC 02, EEP-DB-CYC 03 and TS-CYC 04, respectively; for Kobe earthquake the maximum value of spectral acceleration is equal to 0.56g, 1.96g and 1.31g for MR-frames with connections EEP-CYC 02, EEP-DB-CYC 03 and TS-CYC 04, respectively; finally, for Northridge earthquake the maximum value of spectral acceleration is equal to 0.64g, 1.48g and 0.75g for MR-frames with connections EEP-CYC 02, EEP-DB-CYC 03 and TS-CYC 04, respectively.

It is evident the dependence of the results on the considered earthquake. In particular, the MR-Frame with TS-CYC 04 connections behaves better than the one with EEP-DB-CYC 03 connections for the Imperial Valley earthquake, while EEP-DB-CYC 03 connections lead to the best behaviour in case of Kobe and Northridge earthquakes. The MR-Frame with EEP-CYC 02 connections always exhibits the worst behaviour. However, as this is due to the limited plastic rotation supply provided by this connection, it is useful to remember that, during the experimental test, as the displacement amplitude increased, the plastic engagement of the end-plate at the welded flange-to-end plate connection zone increased, leading to the formation of a crack along the whole width of the end-plate starting from the heat affected zone which progressively propagated along the thickness up to the

complete fracture of the endplate (Iannone et al., 2011). Even though this failure mode is consistent with the design purposes of type-1 collapse mechanism for the end-plate in bending, it provides a reduction of the plastic rotation supply under cyclic loads.
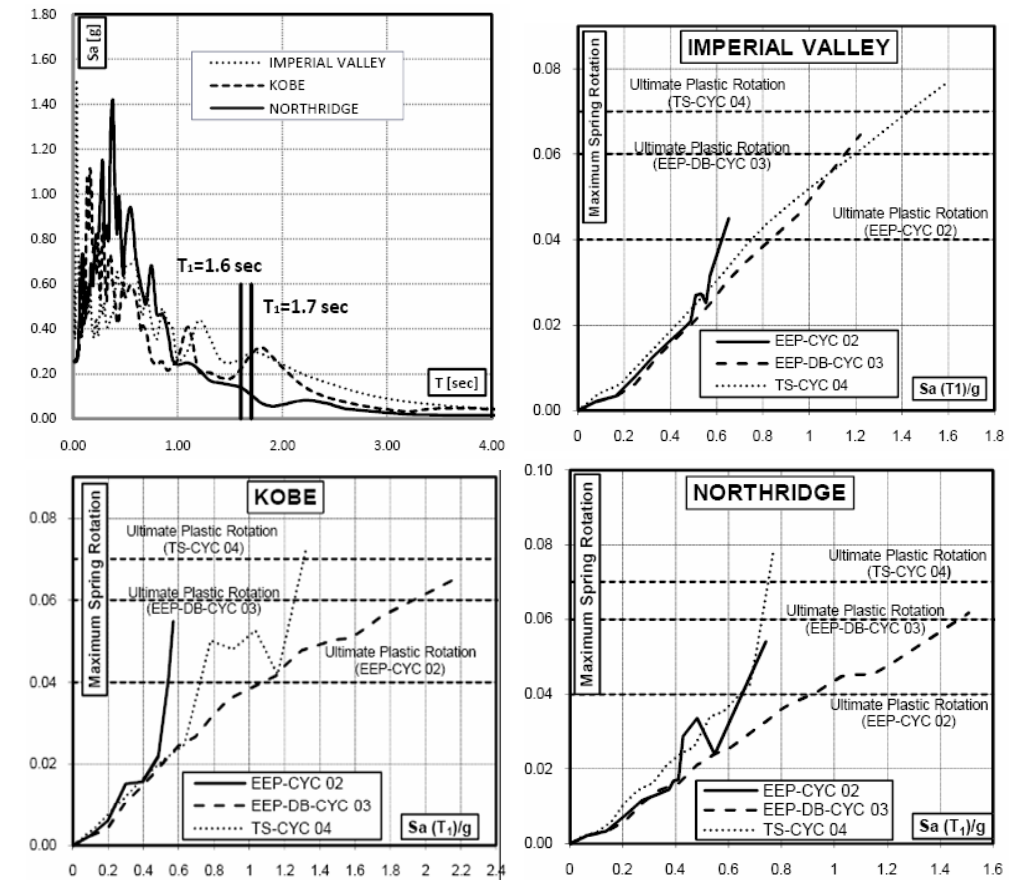


Figure 3. Response spectra of considered ground motions and maximum spring rotation versus spectral acceleration

In Figure 4 the maximum interstorey drift ratio (MIDR) and the roof drift angle (RDA, ratio between top displacement and building height) versus spectral acceleration are reported for the Imperial Valley earthquake. The behaviour of the three structures are similar; the differences are due again to the different ultimate plastic rotation of the connections. In particular, the MR-Frames with TS-CYC 04 connections exhibits a more regular increase of considered parameters with spectral acceleration.

In Figure 5 and 6 the same parameters are reported for Kobe and Northridge earthquakes respectively. Also in these cases the main differences among the three structures are due to the different ultimate plastic rotations of the spring elements.
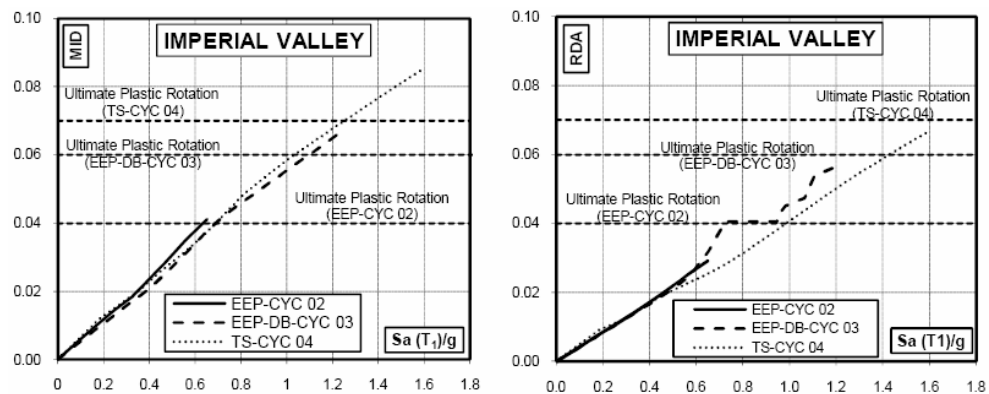
Figure 4. Maximum Interstorey Drift Ratio and Roof Drift Angle versus spectral acceleration for Imperial Valley earthquake
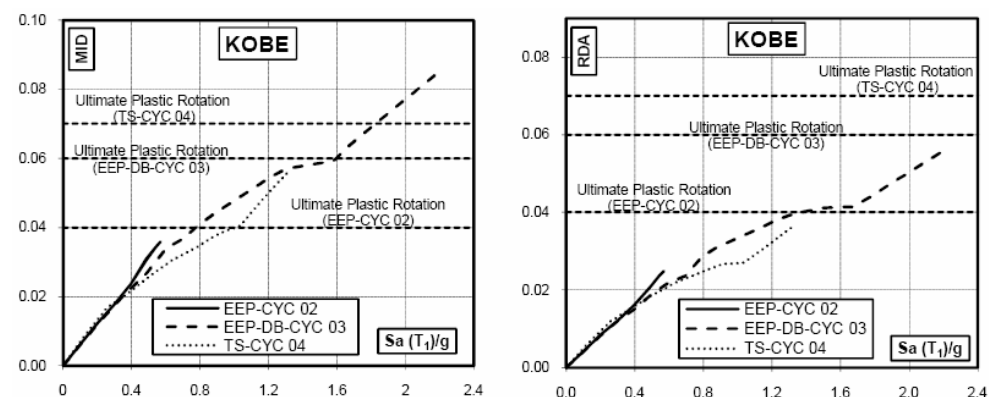


Figure 5. Maximum Interstorey Drift Ratio and Roof Drift Angle versus spectral acceleration for Kobe earthquake
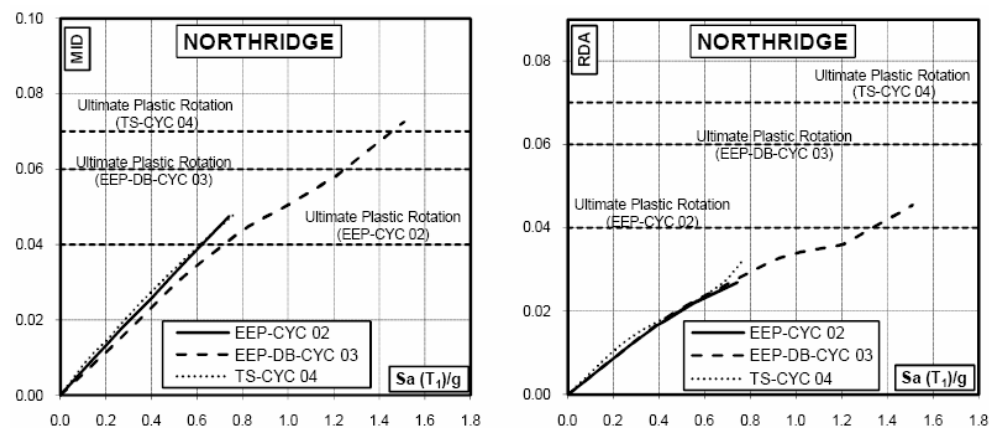


Figure 6. Maximum Interstorey Drift Ratio and Roof Drift Angle versus spectral acceleration for Northridge earthquake

## 5. CONCLUSIONS

Nowadays semi-rigid partial-strength connections, if well designed, can be considered to have ductility and dissipation capacity in order to satisfy the seismic demand. Therefore, in this paper the influence of beam-to-column connections on the seismic response of MR-Frames has been studied.

Starting from the knowledge of the cyclic rotational behaviour of beam-to-column joints, three different MR-Frames have been considered. Each structure is characterized by a different structural detail of beam-to-column connections. The cyclic behaviour of each joint has been modelled by means of the spring element of IDARC 2D computer program with the polygonal hysteretic model, either vertex oriented or yielded oriented depending of the shape of the hysteresis loops, whose parameters have been calibrated on the base of available experimental tests obtaining a good agreement between experimental and modelled behaviour.

The observation of the results obtained from IDA analyses shows that the behaviour of the analysed MR-Frames with EEP-CYC 02 connections, i.e. bolted end-plate connections, and TS-CYC 04 connections, i.e. bolted double split tee connections, is very similar to the one of the MR-Frame with EEP-DB-CYC 03 connections, i.e. RBS connections. In particular, for the Imperial Valley earthquake record the behaviour of the structure with bolted double split tee connections (TS-CYC 04) is the best one. Conversely, RBS connections have led to the best behaviour in case of Northridge and Kobe earthquakes.

However, it has to be underlined that the results herein presented are just the preliminary results of an ongoing research activity, so that general conclusions cannot be still provided. Only three ground motions have been considered up-to-now, so that in next future further IDA analyses, considering many earthquakes and different MR-Frames, have to be performed. In addition, also different modelling options regarding the cyclic response of beam-to-column joints will be investigated by means of other software with the aim of analysing the influence of this kind of epistemic uncertainty.

## REFERENCES

[1] ANSI-AISC 341-10 [2010] "Seismic Provisions for Structural Steel Buildings", American Institute of Steel Construction, Chicago, Illinois.

[2] Aksoylar, N.D., Elnashai, A.S. and Mahmoud, H. [2011] "The Design and Seismic Performance of Low-Rise Long-Span Frames with Semi-Rigid Connections", Journal of Constructional Steel Research, Vol. 67 (2011) pp. 114-126.

[3] Bruneau, M., Uang, C. M., and Whittaker, A. [1998] "Ductile Design of Steel Structures", McGraw Hill, New York.

[4] CEN [2005a] EN 1993-1 Eurocode 8: Design of Structures for Earthquake Resistance. Part 1: General Rules, Seismic Actions and Rules for Buildings, CEN, European Committee for Standardization.

[5] CEN [2005b] EN 1993-1-8 Eurocode 3: Design of Steel Structures. Part 1-8: Design of Joints, CEN, European Committee for Standardization.

[6] Clemente, I, Noè, S. and Rassati, G.A. [2004] "Experimental Behaviour of T-stub Connection Components for the Mechanical Modelling of Bare Steel and Composite Partially Restrained Beam-to-Column Connections", International Workshop on Connections in Steel Structures, Amsterdam, June 3-4, 2004.

[7] Dubina, D., Stratan, A., Muntean, N., Grecea, D. [2008] "Dual steel T-stub behaviour under monotonic and cyclic loading", International Workshop on Connections in Steel Structures, Chicago, June 25, 2008.

[8] Elnashai, A.S., Elghazouli, A.Y. and Denesh-Ashtiani, F.A. [1998] "Response of Semirigid Steel Frames to Cyclic and Earthquake Loads", Journal of Structural Engineering, ASCE, Vol. 124, N.8, August 1998, pp. 857-867.

[9] Faella, C., Piluso, V., and Rizzano, G. [1997] "A new method to design extended end plate connection and semirigid braced frames", *Journal of Constructional Steel Research* 41(1), 61-91.

[10] Faella, C., Montuori, R., Piluso, V., and Rizzano, G. [1998] "Failure mode control: economy of semi-rigid frames", Proc. of the XI European Conference on Earthquake Engineering, Paris.

[11] Faella, C., Piluso, V., and Rizzano, G. [1998] "Cyclic Behavior of bolted joints components" , *Journal of Constructional Steel Research* 46 (1-3), paper number 129.

[12] Faella, C., Piluso, V. and Rizzano, G. [2000] "Structural Steel Semirigid Connections", CRC Press, Boca Raton, Florida.

[13] FEMA 351 [2000] "Recommended seismic evaluation and upgrade criteria for existing welded steel moment-frame buildings", Federal Emergency Management Agency, Washington, D.C.

[14] FEMA 352 [2000] "Recommended post earthquake evaluation and repair criteria for steel moment-frame buildings", Federal Emergency Management Agency, Washington, D.C.

[15] Fragiacomo, M., Amadio, C. and Macorini, L. [2004] "Seismic Response of Steel Frames under Repeated Earthquake Ground Motions", Engineering Structures, Vol. 26 (2004) pp. 2021-2035.

[16] Grecea, D., Dinu, F., and Dubina, D. [2004] " Performance Criteria for MR Steel Frames in Seismic Zones", Journal of Constructional Steel Research, Vol. 60 (2004) pp. 739-749.

[17] Hu, J.W., Leon, R.T. and Park, T. [2011] "Mechanical Modeling of Bolted T-stub Connections under Cyclic Loads. Part I: Stiffness Modeling", Journal of Constructional Steel Research, Vol. 67, Issue 11, pp. 1710-1718.

[18] Iannone, F., Latour, M., Piluso, V. and Rizzano G. [2011] "Experimental Analysis of Bolted Steel Beam-to-Column Connections: Component Identification", *Journal of Earthquake Engineering* 15, 215-244.

[19] Jaspart, J. P. [1991] "Etude de la semi-rigide des noeuds Poutre-Colonne et son influence sur la resistence et la stabilite des ossature en acier", PhD Thesis, University of Liege, Belgium.

[20] Kim, K.D. and Engelhardt, M.D. [2002] "Monotonic and Cyclic Loading Models for Steel Panel Zones in Steel Moment Frames", Journal of Constructional Steel Research, Vol. 58, pp. 605-635.

[21] Latour, M., Piluso, V. and Rizzano, G. [2011] "Cyclic modeling of bolted beam-to-column connections: component approach", *Journal of Earthquake Engineering,* Vol. 15, pp. 537-563.

[22] Mazzolani, F. M. and Piluso, V. [1996] "Theory and Design of Seismic Resistant Steel Frames" (E & FN Spon).

[23] Mazzolani, F. M. and Piluso, V. [1997] "Plastic design of seismic resistant steel frames", *Earthquake Engineering and Structural Dynamics* 26, 167-191.

[24] Moore, K.S., Malley, J. O., and Engelhardt, M. D. [1999] "Design of Reduced Beam Section (RBS) Moment Frame Connections", AISC Structural Steel Educational Council, Moraga, CA.

[25] Piluso, V., Faella, C. and Rizzano, G. [2001] "Ultimate behavior of bolted T-stubs, I: theoretical model", *Journal of Structural Engineering* ASCE, 127 (6), 686-693.

[26] Piluso, V. and Rizzano, G. [2008] "Experimental Analysis and Modelling of Bolted T-stubs under Cyclic Loads", Journal of Constructional Steel Research, Vol. 64, Issue 6, pp. 655-669.

[27] Rizzano, G. [2006] "Seismic Design of Steel Frames with Partial Strength Joints", *Journal of Earthquake Engineering*, 10 (5), 725-747.

[28] Shen, J. and Astaneh-Asl, A. [2000] "Hysteresis Model of Bolted Angle Connections", Journal of Constructional Steel Research, Vol. 54 (2000), pp. 317-343

# INFLUENCE OF STEEL-TO-CONCRETE CONNECTION OF SEISMIC RESISTANT FRAME BEAMS LOADED IN BENDING OR SHEAR

Adrian Ciutina[1]; Dan Dubina[1,2]
*[1] Department of Steel Structures and Structural Mechanics,
Politehnica University of Timisoara, Romania
[2] Romanian Academy, Timisoara Branch, Romania
adrian.ciutina@ct.upt.ro; dan.dubina@ct.upt.ro*

Gelu Danku
*Technical University of Cluj-Napoca, North University Centre,
Faculty of Mineral Ressources and Environment
dnkgelu@yahoo.com*

## ABSTRACT

The study presents the results of the experimental research carried out at the CEMSIG Laboratory at the Politehnica University of Timisoara, investigating the influence of the steel-to-concrete connection for beams on the seismic response of moment resisting and eccentrically braced frames. The results focus on the differences resulted for the pure steel beam response (considered as reference), full composite beams and composite beams disconnected over the dissipative zones – beam ends and links respectively. The load applied is of monotonic and cyclic type.

## 1. INTRODUCTION

Both Moment Resisting Frames (MRF) and Eccentrically Braced Frames (EBF) are considered highly dissipative steel and composite steel and concrete structural solutions. The dual MRF+EBF configuration preserves the high dissipation capacity while combining the architectural freedom offered by moment frames with the increased lateral stiffness of the EBF although the dissipation of seismic input energy is different: in MRF by plastic hinges formed in bending at beam ends or beam-to-column connections while in case of EBF by bending and or shear of the link element (see Figure 1).
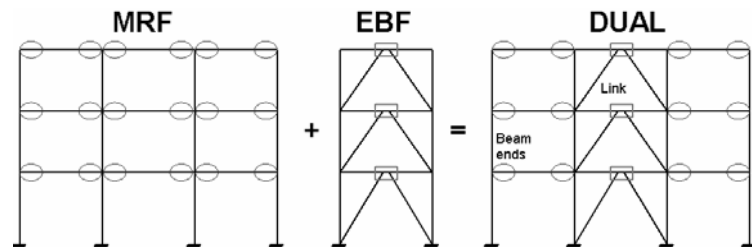


Figure 1. Dual MR+EB frame and characteristic dissipative zones.

The current seismic design practice in case of steel dual MR + EBF with steel and concrete composite beams is to disconnect the steel element from the slab in the dissipative zones (§7.6.2 of EN 1998-1, 2004). In consequence the design could be based only on the steel element capacity, with a symmetrical resistance response in bending (for the case of beam ends) or shear (for link elements).

However, although the connectors are suppresses over the potential plastic zones, the connection of the concrete slab in the non-dissipative zone may influence the real behaviour of the hinge, leading to an unsymmetrical plastic behaviour. The real behaviour of hinges could have implications on the final plastic mechanism of the frame as well as on the seismic design values for the behaviour and the overstrength factors.

## 2. EXPERIMENTAL PROGRAM

Taking into account the particular configuration of structure considered for investigation as a dual MR+EBF, the experimental tests considered separately the investigation on the ductile elements (see Figure 2), taken as subassemblies from a larger structure:
- investigations on the short links (through EBFs tests)
- investigations on beam-to-column joints of MRF.
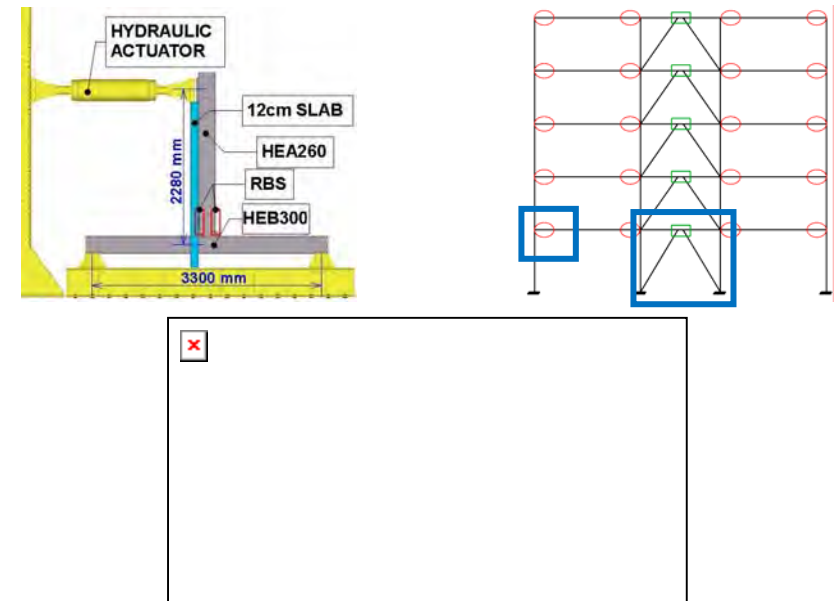


Figure 2. Identification of subassemblies and testing set-up for MR joints and EBF.

The MR joint and EBF specimens tested in laboratory were retrieved from a larger 2D structure (see Figure 2) with 5 storeys and 3 spans (2x5m + 1x4.5m) and designed in a Romanian high seismicity zone of 0.24 g (corresponding to the city of Bucharest). The initial design was performed for the pure steel structure according to Eurocode 8 and Eurocode 3 (EN 1993-1, 2004) requirements.

For the beam-to-column connection it was adopted the welded typology through full penetration welds (see Figure 3) and Reduced Beam Section (RBS). This solution

was considered from the condition of dissipating the energy only in the beam element and preventing the column or connection plastifications, according to the purpose of the study. The RBS design was performed according to EN1998-3, Annex B, section 5.3.4.
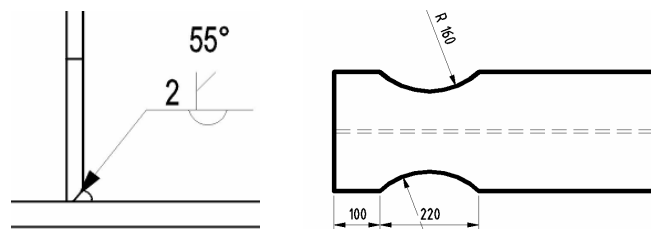


Figure 3. Beam-to-column weld and geometry of the reduced beam section.

In both experimental investigations, three beam configurations have been considered: (i) the simple steel beam – denoted by M; (ii) beam connected with the concrete slab by means of shear connectors (composite cross-section) on the entire span and (iii) composite beam with connectors suppressed in the potentially plastic region. Another parameter considered was the loading type: monotonic and cyclic respectively. The cyclic loading was applied according to the ECCS protocol (ECCS, 1986), with the yield characteristics determined on the basis of steel monotonic test.

In case of composite specimens the connection between steel beam and concrete slab (12 cm full slab) was realized through shear stud connectors of 19x100 mm. The design of the shear connection was done in accordance to the Eurocode 4 (EN 1994-1, 2004). The slab was reinforced by two layers of reinforced bars Φ12 mm disposed both transversally and longitudinally at 150mm. The effective widths of the slab considered for composite specimens was 1.2 m for EBF specimens and respectively 1.0m for beam-to-column joints.

## 2.1. Description of EBF specimens

Figure 4 shows the loading schema and the cross-section characteristics of the initial steel EBF. The dissipation of the seismic-input energy is realised through the short link of 300mm. The load is applied at the beam level through an actuator of +/- 100 kN. The tested specimens were pinned at the column base by mechanical hinges for reducing the top force needed for plastic hinge development.
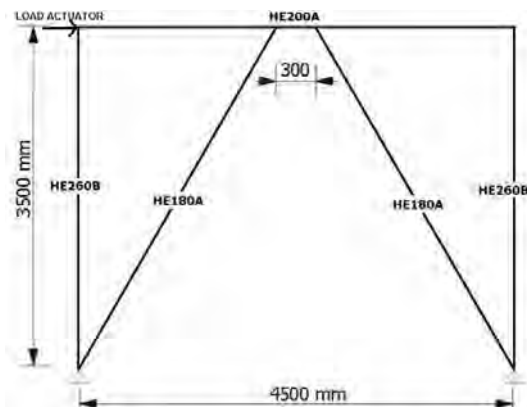


Figure 4. EBF specimens: static scheme, loading conditions and cross-sections.

Table 1 shows the characteristics of EBF specimens, in function of loading and steel beam to concrete slab interaction. Prior testing standard tensile (for steel) and compressive (for concrete) material sample testing was performed in order to confirm the material characteristics used in design: S235 for HEA 200 profile (beams), S355 for HEB 260 (columns) and HEA 180 for braces and respectively C20/25 class for concrete slab. Details on the material characteristics could be found elsewhere (Danku, 2011).

Table 1. Description of EBF specimens.

| No. | Specimen name | Beam type | Type of loading | Connectors over the link |
|-----|---------------|-----------|-----------------|--------------------------|
| 1 | EBF_M_LF-M* | steel | monotonic | No |
| 2 | EBF_M_LF-C | steel | cyclic | No |
| 3 | EBF_Comp_LF1 | composite | cyclic | No |
| 4 | EBF_Comp_LF2 | composite | cyclic | Yes |

Besides the load recording (at the level of actuator), LVDT transducers were used to monitor different displacements and deformations:
- global displacements of the frame;
- web panel distortion of the link;
- slip and displacements of the non-dissipative elements (base connections, columns and braces);
- deformation and rotation of beam-to-column joints (designed as bolted end-plate connections).

## 2.2. Description of RBS specimens

In case of MRF joint specimens, the column was disposed horizontally and pinned at ends while the beam (at half-story distances) while the beam was vertical and loaded at its tip (see Figure 2). A lateral-restraining frame was placed for keeping the in-plane behaviour of the specimens. The following characteristics were considered for beam-to-column specimens:
- column: HEB260 (S355), HEB300 (S460);
- beam: HEA260 (S235);
- beam-to-column typology: by direct welding and RBS;
- concrete slab of 12 cm C20/25, reinforced as described in paragraph 2.

The real material characteristics were found through material sample testing; S355 for beams (HEA 260) and S355 for columns (HEB 300). It should be mentioned the fact that in case of first four specimens for design the steel quality required for the beam was S235, but the delivered class was S355. For this reason, it was decided to repeat one steel and one composite specimen (denoted by RLD), by adjusting correspondingly the steel quality: the beam HEA 260 S355 was kept, but the column profiles were changed to HEB 300 on S460.

Table 2. Description of RBS specimens.

| No. | Specimen name | Beam type | Loading type | Connectors over RBS |
|-----|---------------|-----------|--------------|---------------------|
| 1 | DB-M | steel | monotonic | No |
| 2 | DB-C | steel | cyclic | No |
| 3 | DB-Comp1 | composite | cyclic | No |
| 4 | DB-Comp2 | composite | cyclic | Yes |
| 5 | DB-C RLD | steel | cyclic | No |
| 6 | DB-Comp RLD | composite | cyclic | Yes |

The load was recorded through a load cell integrated in the actuator, while LVDT transducers were installed for monitoring:

- beam top displacement;
- local rotations, deformations and distortions in the dissipative elements: RBS, web panel of the column and welds respectively;
- local slip in column pins.

## 3. EXPERIMENTAL RESULTS

### 3.1. EBF specimens

Figure 5 show the response curves for the EBF_M_LF-M specimen, monotonically loaded up to failure. The steel link element showed a very ductile behaviour by shear distortion up to values of 280 mrad. All the other elements (columns, braces) including connections remained within the elastic range. The loading was stopped at very large inelastic link deformations on the descending branch, at a drop of more than 20% of the maximum load, coincident with stroke limitation of the actuator.

For the same typology, the cyclic loading conducted to a significant drop in the link distortion to about 160 mrad while keeping the same resistance. It is also to be noted the stiffer behaviour as compared to monotonic curve. Another important difference was recorded in the failure of specimens: the monotonic load conducted to high distortions of the panel without cracking of the steel web while the cyclic loading torn the link web panel starting from the cycles of 6δy.


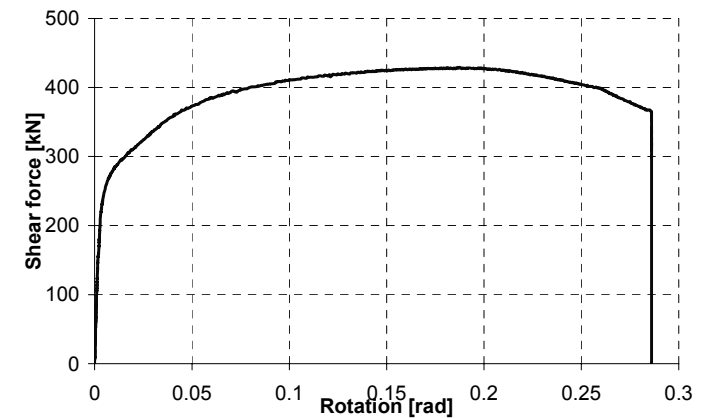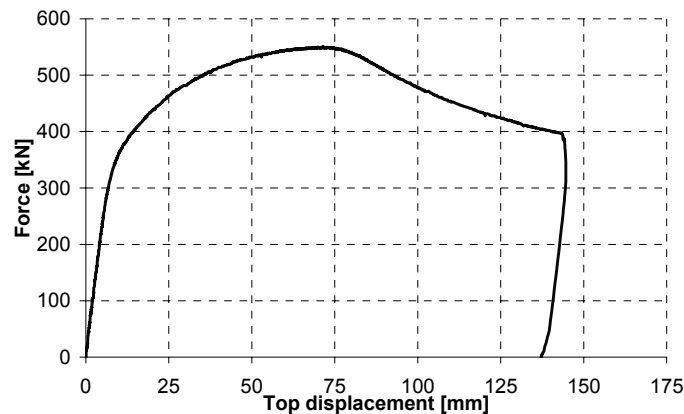


Figure 5. Global load – top displacement and shear force – link distortion response of EBF_M_LF-M specimen.





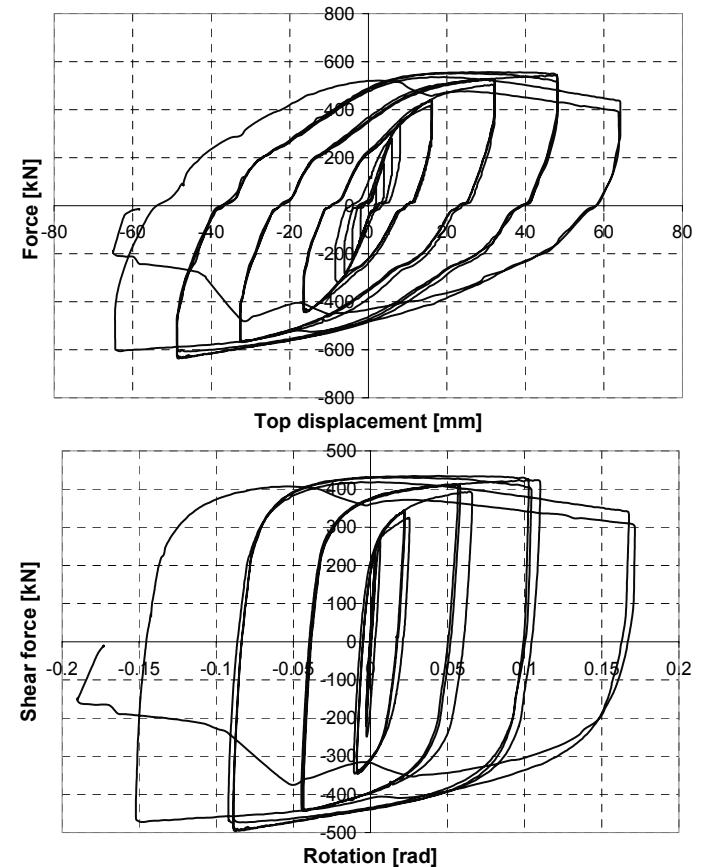Figure 6. Global load – top displacement and shear force – link distortion response of EBF_M_LF-C specimen.

www.steelconstruct.com

Figure 7. Failure of the link zone for the EBF_M_LF-C (left) and EBF_M_LF-C (right) specimens.



Figure 8. Damage of the fixed link and concrete slab for EBF_LF_Comp1 (left) and EBF_LF_Comp2 (right) specimens.

Figure 8 show the results of the two composite specimens under the form of shear force – link distortion curves. To be noted that shear force – distortion for LF-Comp 2 specimen is truncated due the deterioration of the displacement transducer's readings, affected by the highly-damaged concrete slab above the link. However, the behaviours of both specimens are found to have similar characteristics. Only small differences exist for the main response characteristics: resistance, rigidity and ductility. The values of ultimate link distortions up to 150 mrad in both situations (similar to the steel cyclically loaded specimen) are considered sufficient to withstand important values if inter-storey-drift deformations of 2 to 3%. However, several differences could be noted in regard to the steel specimen such as a smaller initial rigidity and higher resistance.

The failure conditions for link composite elements are shown in Figure 8. Both specimens experienced high damages in the link panel zone, practically reeling the web plate. Generally, the damage of the slab was local, with crack patterns developing at angles of 45 degrees from the position of the link. No relative deformations (horizontal or vertical) were recorded between the concrete slab and the steel flange. However, in the case of specimen with shear connectors placed over the link, the concrete slab was significantly more damaged.

Table 3 shows the synthetic results of the EBF specimens: initial rigidity, shear resistance and shear distortion. Figure 9 show the link responses of the three cyclic specimens under the form of envelope curves.
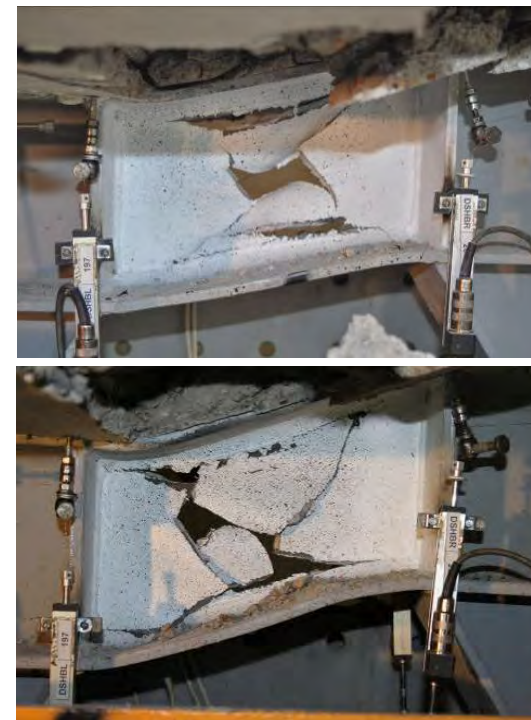
Table 3. Synthetic values resulted from EBF experimental tests.

| Specimen | Initial rigidity $S_{j,link}$ [kN/rad] | Max. shear resistance $V_{max}$ [kN] | Shear distortion $\gamma$ at $V_{max}$ [mrad] | Max. shear distortion $\gamma_{max}$ [mrad] |
|---|---|---|---|---|
| EBF_M_LF-M | 130460 | 429 | 187 | 286 |
| EBF_M_LF-C | 74644 | 495 | 87 | 171 |
| EBF_Comp_LF1 | 123414 | 598 | 105 | 156 |
| EBF_Comp_LF2 | 152488 | 587 | 74 | 150* |

\* Estimated value

Note: all values were computed on the maximum envelope curve (cycle 1).

The main difference in results regards the resistance of specimens: both composite elements show greater resistance (up to 20%) as compared to pure steel specimens. Also, the maximum resistances are comparable for full and partial composite specimens (Comp_LF2 and Comp_LF1 respectively), which means that the presence of connecters over the link plays only a secondary role in the global behaviour of composite beams. Another immediate notice is that all specimens exhibited high levels of link distortions, reaching practically the requirements of modern seismic norms (80-140 mrad) for high ductility structures. In what concerns the

initial stiffness, the computed values show that the cyclic envelope rigidity of composite specimens is about 30% higher than that of the corresponding steel element.

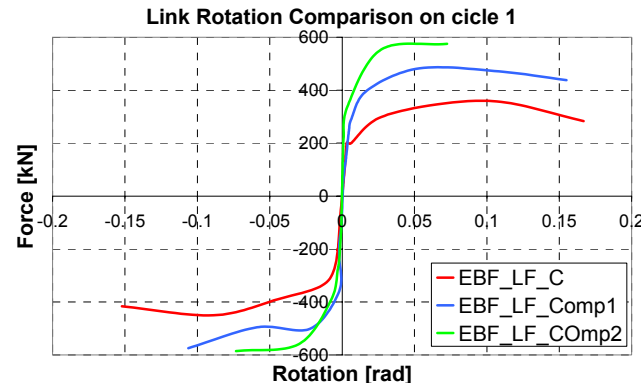**Link Rotation Comparison on cicle 1**



Figure 9. Influence of link connection on the concrete slab – envelope curves.

The link experimental study shows very clear that the presence of the slab over the link element will influence noticeably the behaviour of the frame, independently of the link connection with the concrete slab.

### 3.2. DB specimens

The investigation on moment resisting connections followed the same parameters as in case of link specimens: (i) influence of steel to concrete shear connection and (ii) influence of loading type: monotonic and cyclic. For all specimens the reduced beam section was considered near the beam.

Figure 10 shows the ductile behaviour of the steel DB-M specimen loaded by incremental monotonic force up to failure. As it could be noticed, the largest amount of rotation was recorded in the RBS but an important rotation part was shifted to other connection components, such as the column web panel. Due to the fact that for the level arms are different for the RBS location and column panel zone, the force-rotation curve was preferred to the characteristic moment-rotation relationship. The total RBS rotation could be considered as high, exceeding 80mrad for RBS solely. The plastification of the specimen was by buckling of the compressed flange of the RBS zone, but the specimen did not failed practically.

**Rotation of the node**
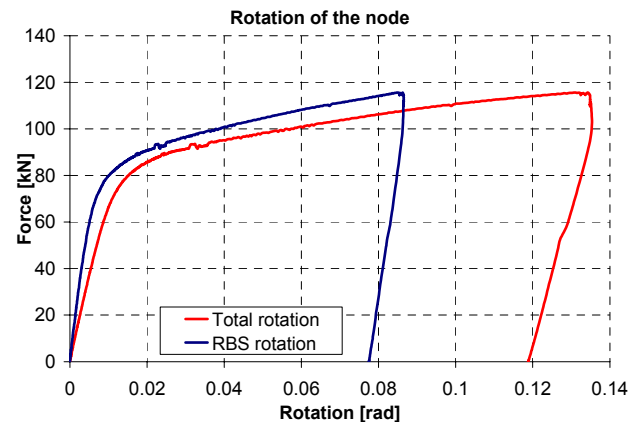




Figure 10. DB-M specimen: total vs. RBS rotation (left) and joint deformation (right).

In case of steel cyclically loaded specimen, (DB_C, see Figure 11), the total joint rotation of 80 mrad could be considered satisfactory, but this ductility is not due primarily to RBS zone but to the column web panel working in shears. Moreover, due to deficient execution, the specimen failed by welding fracture, after reaching the maximum available stroke in the actuator at an increment of 8xδy in the third cycle.





Figure 11. DB-C specimen: total rotation (left) and weld failure(right).

www.steelconstruct.com

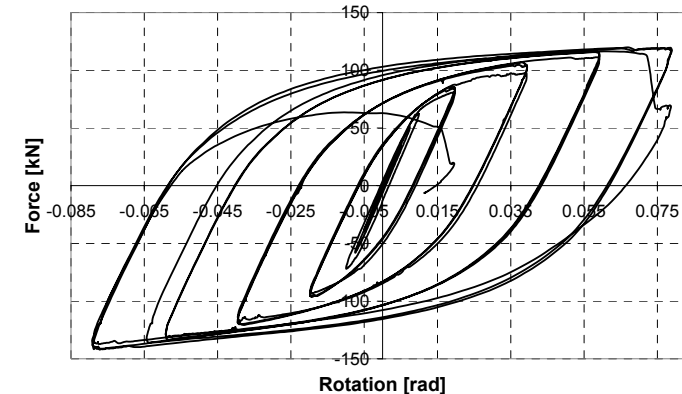In Figure 12 are shown the lateral force – total rotation curves for the composite DB-Comp specimens. High values of rotation were recorded in both cases (of the order of 60 mrad) for deformation increments of 6 and respectively 8 times the yield deformation. Similar resistances and rotation capacities could be noticed for both specimens, with logical increased negative forces for compressed concrete slab.
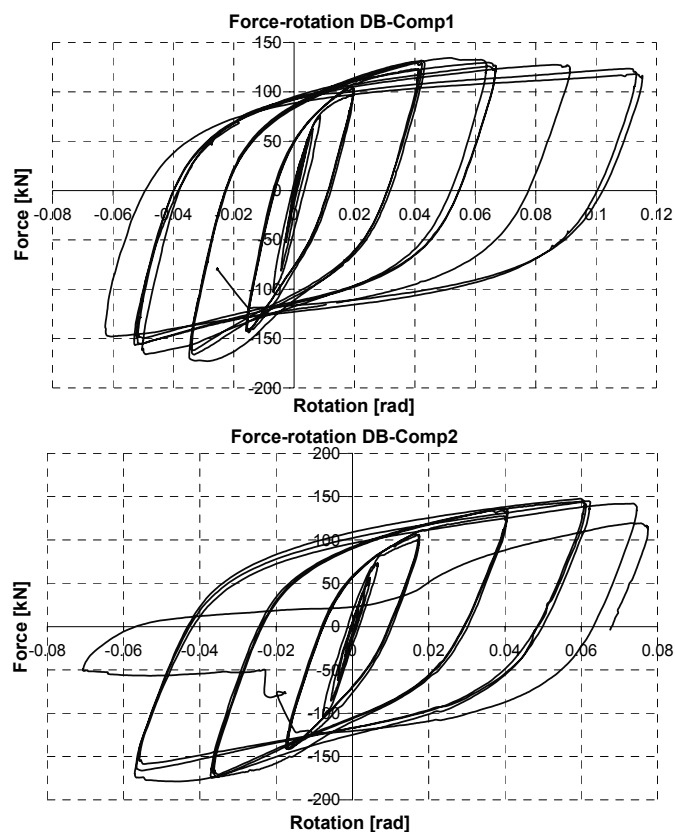
**Force-rotation DB-Comp1**



**Force-rotation DB-Comp2**



Figure 12. DB-C specimen: total rotation (left) and welding failure (right).

**RBS rotation**
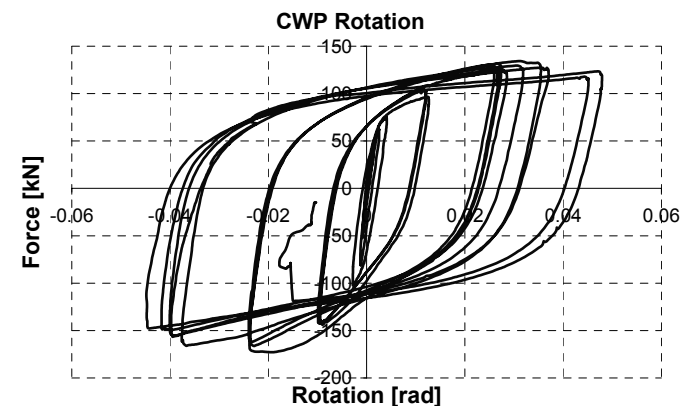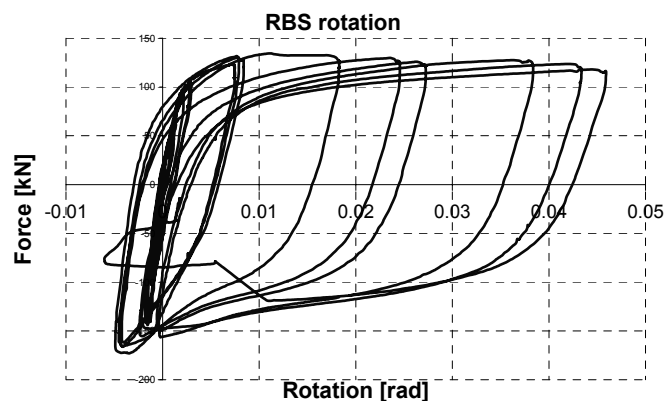


**CWP Rotation**



Figure 13. DB-Comp1 specimen: RBS zone and column web panel rotations.

However, two problems were found in plastic domain:

- the deficient penetration of the weld leaded in this case too to premature connection failure, similar to the case of DB-C specimen, The failure occurred in both cases at the inferior beam flange weld to column;

- the high values of the plastic rotations recorded are due only partially to the RBS zone. Due to the higher steel class of the beam material the column web panel contributed significantly to the total joint rotation, as it is shown in Figure 13. The asymmetry of the global curve is due to RBS zone which developed plastic rotation only for positive bending (concrete in tension) while the plasticization in negative bending is prevented by the resistance of composite section. Contrary to this, the column web panel rotation is symmetrical.

The Figure 14 shows as comparison the moment-rotation envelopes for DB cyclic tested specimens. The global behaviour of composite specimens is very similar and presents a higher resistance and a stiffer response, as compared to bare steel specimen. Practically both DB-comp specimens took advantage of the composite aspect and in consequence there are small differences in their behaviour although in case of DB-comp1 specimen no connectors were placed above the RBS zone. In comparison with the steel specimen, the composite ones show higher stiffness, especially on positive behaviour (42.95 kNm/mrad for DB-Comp1 and 36.72 kNm/mrad for Db-Comp2 in regard to 25.38 kNm/mrad for DB-M). The maximum resistance is also significantly higher for composite specimens:

- 321.98 kNm for composite and 268.69 kNm for steel specimens in positive bending;

- 392.90 kNm for composite and 321.67 kNm for steel specimens in negative bending.

Considering the fact that the main purpose of the study on the RBS composite specimens by dissipation only in the RBS zone was not achieved, the test series was completed by two new specimens: DB-C_RLD (steel specimen) and DB-Comp_RLD (composite specimen). Both specimens were tested cyclically. The column was replaced in both cases with a higher profile HEB 300 on S460 steel.
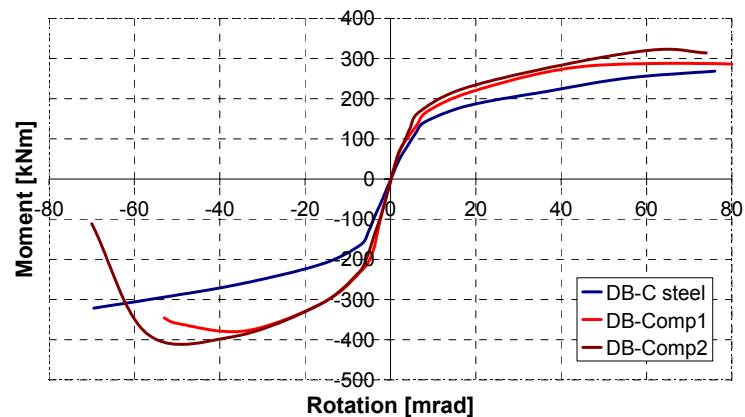
Figure 14. Comparison of moment-rotation envelope curves for DB cyclic specimens

For this new test series the difference between steel and composite aspect are more visible. Figure 15 show the cyclic force-rotation curves of both specimens as well as the comparison of monotonic curves.
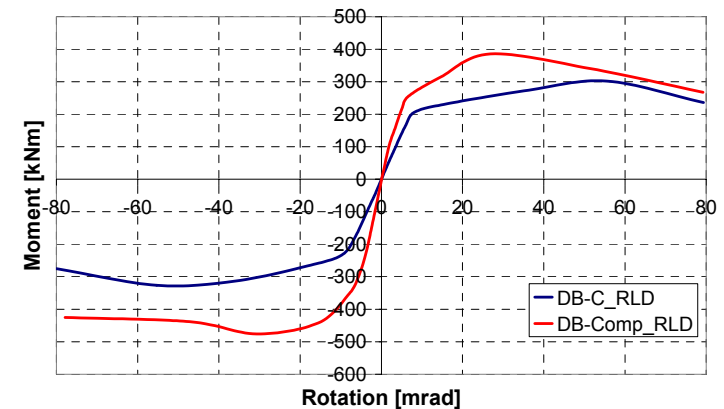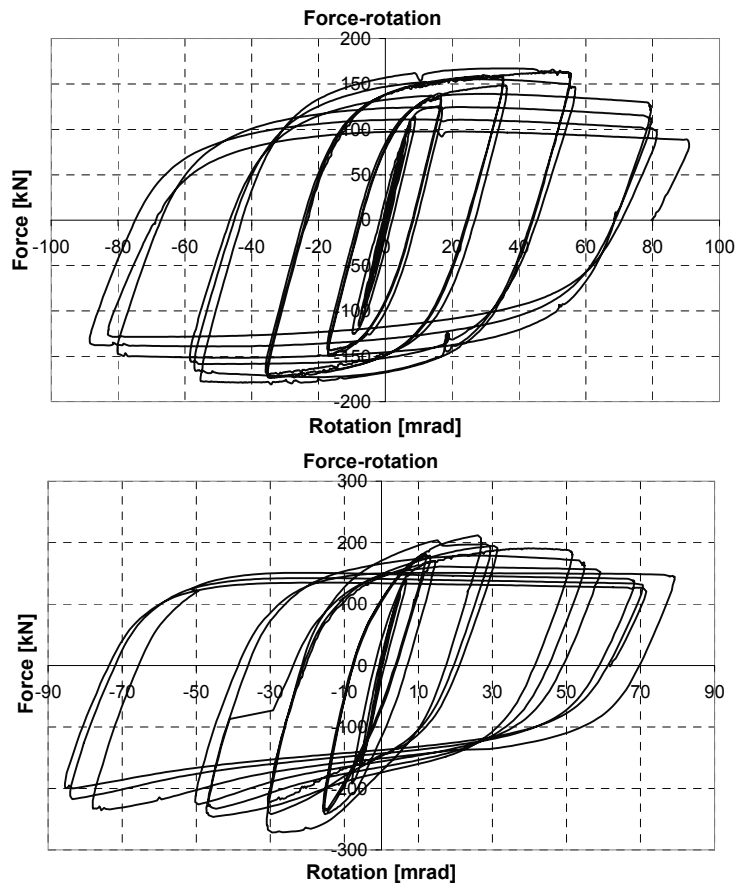






Figure 15. Cyclic force-displacement curves for the DB-C_RLD specimen (left), DB-Comp_RLD (centre) and moment-rotation envelope curves (right).

The results of the DB specimens confirmed the preliminary conclusions drawn as a result of the first joint test series. Comparing the envelopes of force-rotation curves recorded for the two additional specimens, it could be noticed similar rotation capacities (up to 70 mrad) and important gains in resistance and rigidity for the composite specimen especially in negative bending (slab under compression) as compared to steel bare connection.

The beam-to-column welds behaved this time in a satisfactory manner and both joints reached their maximum capable rotations by RBS plastic hinges. The failure type was similar for both cases, through ductile buckling of beam flange in the RBS and gradual reduction of joint resistance. In case of the composite specimen, the upper flange was restrained to buckle due to the presence of the concrete slab. However, its resistance gradually degraded during the plastic cycles by concrete cracks parallel to column flange when slab was in tension and respectively in compression, by crushing along the cracks already formed in tension (see Figure 16).

For the new joints, the total rotation (greater than 70 mrads) is due almost exclusively to RBS plasticization. In these cases, no real deformation was recorded in the column web panel. However, large amount of degradation was recorded in the column zone in case of composite specimen, around which the concrete was crushed and has fallen off massively.

Figure 16. RBS plastic hinges in case of the DB-C_RLD (left) and DB-Comp_RLD (right) specimens.

## 5. CONCLUSIONS OF THE STUDY

The main objective of the experimental analysis regarded the influence of the steel-to-concrete interaction on the cyclic response of dissipative zones formed in moment resisting and eccentrically braced frames. The concerned zones are the beam ends in case of MRFs and respectively the links in case of EBFs. The following main conclusions could be drawn from the study:

- The simple disconnection of the steel beam from the concrete slab over the dissipative zone is not sufficient to assure a pure steel-like behaviour. The resulted behaviour is practically very close to that of a full-composite specimen;
- In both situations the composite aspect improves the global resistance and stiffness characteristics of the dissipative zones while maintaining the ductile character of the solution. However, the composite behaviour should be considered in the design of the structure;
- A very careful detailing and execution should be applied to beam-to-column joints and links in order to reach the desired levels of ductility and resistance. On the contrary, the steel grade mismatch could change the plasticization order, while the defective execution of welds may lead to brittle failure of the element;
- The reduced beam section solution remains effective in the composite configuration, but the presence of the concrete slab changes the failure mode: the top flange is restrained in buckling, while the concrete slab is degraded by cyclic tension-compression alternating forces.

A complementary numerical study that integrates the behaviour of the real composite behaviour (throughout numerical calibration) of dissipative zones in frame analysis was also performed on several frames with 5, 6, 7, 9 and 13 storeys by means of incremental dynamic analysis on Romanian earthquake records.

The results show very clearly the fact that structures where the interaction between steel and concrete was modelled have had a different behaviour from the bare steel ones. The low-rise steel structures (5 and 6 storeys) have shown higher drift and rotation requirements than the similar frames modelled with composite beams. For the high-rise structures, with a higher vibration period, the increase in strength and rigidity induced by the composite effect leads also to smaller rotations in links and RBS.

Also, the values of the behaviour factor q, obtained for the analyzed steel structures, are close to the prescribed design values (e.g. q=6 for DUAL frames), confirming the good dissipation capacity of these systems. On contrary, in case of frames with composite beams it resulted smaller values of the behaviour factors (e.g. between 4 and 5, with respect to 6).

### REFERENCES

[1] Danku, G., 2011, *Study of the Development of Plastic Hinges in Composite Steel-Concrete Structural Members Subjected to Shear and/or Bending*, PhD Thesis, Politehnica University of Timisoara.

[2] EN 1993-1-1-2004. European Committee for Standardization – CEN. Eurocode 3: Design of Steel Structures. Part 1.1: General Rules and Rules for Buildings, Brussels.

[3] EN 1994-1-1-2004. European Committee for Standardization – CEN. Eurocode 4: Design of Composite Steel and Concrete Structures. Part 1.1: General Rules and Rules for Buildings, Brussels.

[4] EN 1998-1: 2004: European Committee for Standardization – CEN. Eurocode 8 Design of structures for earthquake resistance - Part 1: General rules, seismic actions and rules for buildings

[5] European Convention for Constructional Steelwork, Technical Committee 1, TWG 1.3 – Seismic Design, No.45, 1986, *Recommended Testing Procedures for Assessing the Behaviour of Structural Elements under Cyclic Loads*.

[6] P100-1-2006: Cod românesc de proiectare antiseismică; Oficiul Roman de Standardizare, 2006;

[7] Plumier, A. and Doneux, C., "European developments of seismic design guidelines for composite steel concrete structures", *Proceedings of ICSCS'01 Conference*, Pusan, Korea, 2001.

[8] Stratan, A., 2003, „Studiul Comportării Clădirilor Multietajate cu Cadre Metalice Duale Amplasate în Zone Seismice", *PhD thesis, UPT*, 2003.

# LOW CYCLE PERFORMANCE OF T-STUB COMPONENTS OF BOLTED MOMENT BEAM-TO-COLUMN CONNECTIONS

Ana-Maria Pop[1]; Daniel Grecea[1,2]; Adrian Ciutina[1]
[1] *Department of Steel Structures and Structural Mechanics,*
*Politehnica University of Timisoara, Romania*
[2] *Romanian Academy, Timisoara Branch, Romania*
anamaria.pop@ct.upt.ro ; daniel.grecea@ct.upt.ro ; adrian.ciutina@ct.upt.ro

## ABSTRACT

The paper presents a numerical investigation used to characterize the behaviour of bolted steel beam-to-column joints. The study is based on existing experimental investigation on T-stub components performed at the Politehnica University of Timisoara, using mild and high strength steel. First a calibration of numerical results is performed based on the monotonic experimental response. The FEM numerical investigation is represented by the calibration of cyclic curves, using adequate techniques for modelling the bolts and welds behaviour. The second step of the analysis represents a parametric investigation on response, by changing the geometrical disposition of bolts on the T-stub end-plate.

## 1. INTRODUCTION

In the seismic design of steel structures, the Moment Resisting Frames (MRF) are recognized as highly dissipative structures. In consequence, the seismic input energy is dissipated through plastic deformations concentrated in specific locations, whose behaviour has to be predicted by proper design.

According to the Eurocode 8 rules, the dissipative zones could be located either in elements or in beam-to-column joints. As shown by previous studies, the end-plate connections could prove adequate rotation capacity if special measures are taken, e.g. use of relatively thin end-plates, avoiding brittle failure of welds and bolts etc. From this point of view, the T-stub element (see Figure 1) represents the key-macro-component of the connection behaviour.

Globally the T-stub macro-component can lead to 3 types of failure modes, depending of the connection component characteristics (see Figure 1). Mode 1 represents generally a very ductile behaviour and is characteristic to thin end-plates, but cannot be considered a real solution to strength demands in case of seismic resistant structures. On contrary, the Mode 3 leads usually to a good T-stub resistance, while the failure mode is fragile in nature by bolt rupture. In consequence, the Mode 2 could answer well to both strength and ductility demands.

From this point of view, the Dual Steel (DS) concept can be extended to connections, based on the same philosophy used in structures: using High Strength

Steel (HSS) in non-ductile components that should poses over-strength and Mild Carbon Steel in ductile components in order to achieve both ductility and robustness criteria.
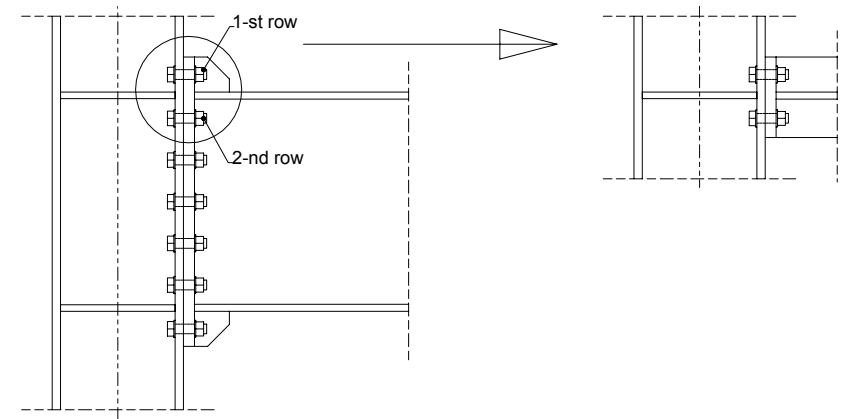


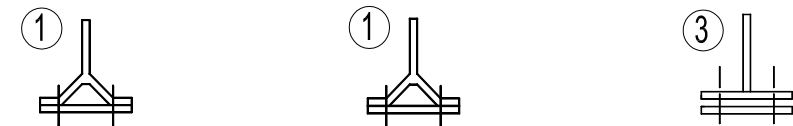Figure 1. End-plate connection: T-stub element



Figure 2. Types of T-stub failure modes

Based on this principle, a large experimental research program was carried out at the CEMSIG Research Centre of the "Politehnica" University of Timisoara, in order to study the performance of dual-steel configuration for beam-to-column joints under monotonic and cyclic loading. The experimental study was considering full joint specimens, T- stub and weld detail specimens (Dubina *et al.,* 2008 a, b, c). The present research is concentrated on the numerical investigation (by FEM) of the T-stub elements, through parametric studies and low-cycle fatigue interpretations of the results, focused on second mode of failure of elements.

## 2. RESULTS OF EXPERIMENTAL INVESTIGATION
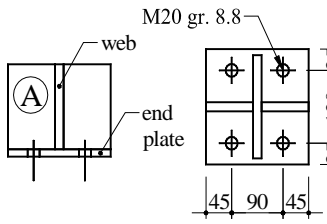
### 2.1. Summary of testing program

The main objective of the experimental program was to study the performance of welded and bolted end-plate beam to column joints realized from two different steel grades. For this purpose, the experimental program integrated experimental investigation on materials, welded components, T-stub components, and beam to column joints. In this way the main sources of ductility were investigated, in local (material and components) and global (joint tests) manner. Although the entire research is much larger, this paragraph describes only the investigations performed on T-stub components, chosen for numerical study. Previous papers by the same authors already summarized the results on materials, welded components, weld details and beam-to-column joints (Dubina *et al.,*. 2008 a, b, c).

Both monotonic and alternating cyclic tests were performed on T-stub specimens obtained by welding S235 web plates to S235, S460 and S690 end-plates, using K

bevel full-penetration welds. MAG welding was used, with G3Si1 (EN 440) electrodes for S235 to S235 welds, and ER 100S-G/AWS A5.28 (LNM Moniva) for S235 to S460 and S690 welds. T-stubs were connected using M20 gr. 8.8 bolts. The EN 1993-1.8 was used to obtain the design strength of T-stubs and failure modes. For the numerical analysis, the subset type A (see Table 1) leading to failure mode 2 was considered.

Table 1. T-stub characteristics

| T-stub type | Label | Web | End-plate | Design failure mode |
|---|---|---|---|---|
|  | TST-12A-S235 | S235 t=15mm | S235 t = 12 mm | 2 |
| | TST-20A-S235 | | S235 t = 20 mm | 2 → 3 |
| | TST-10A-S460 | | S460 t = 10 mm | 2 |
| | TST-16A-S460 | | S460 t = 16 mm | 2 → 3 |
| | TST-8A-S690 | | S690 t = 8 mm | 2 |
| | TST-12A-S690 | | S690 t = 12 mm | 2 → 3 |

## 2.2. T-stub performance on monotonic and cyclic loading

Table 2 shows the measured average values of yield stress $f_y$, tensile strength $f_u$ and elongation at rupture A. Bolts were tested in tension as well, showing an average ultimate strength of 862.6 N/mm$^2$.

Table 2. Material properties

| Nominal steel grade | $f_y$, N/mm$^2$ | $f_u$, N/mm$^2$ | A, % | Actual steel grade |
|---|---|---|---|---|
| S235 | 266 | 414 | 38 | S235 |
| S460 | 458 | 545 | 25 | S460 |
| S690 | 831 | 859 | 13 | S690 |

Loading was applied in displacement control under tension and force control under compression. In case of cyclic loading, the value of the compressive force was limited to prevent the specimen buckling. In general a good ductility was observed for all specimens. However, thick end-plate specimens, even for S235 steel grade show a smaller ductility. The conclusions of the experimental study proves the fact that the choice of thickness associated with steel grade is important in the conception of a proper connection, for obtaining a good balance between strength, stiffness and ductility of components.

Figure 3 shows as example the experimental results under the form of force-deformation relationships of T-stub specimens for monotonic and cyclic loading, while the photos in the same figure show for all the cases the failure mode 2. No significant differences in force values between failure modes of monotonic and cyclic specimens were recorded and the yielding resistance has similar values with the analytical predictions computed according to EN 1993-1.8 (Dubina *et al.,* 2010).
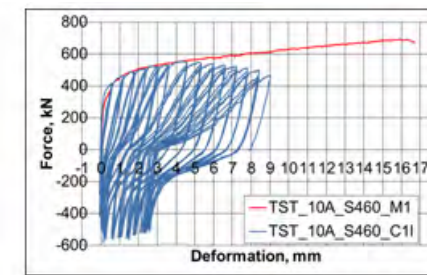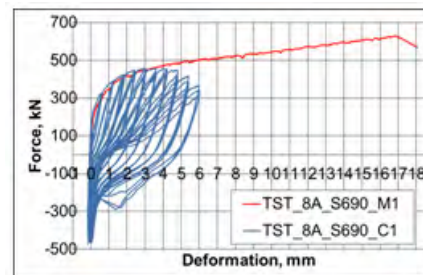


TST-8A-S690                    TST-10A-S460
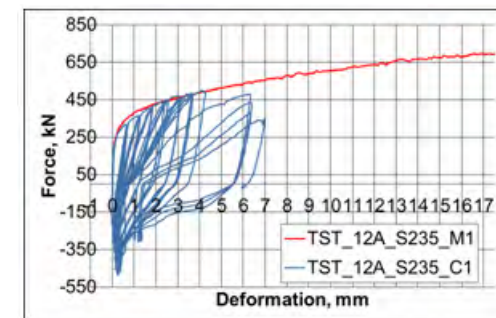


TST-12A-S235

*Figure 3. Examples of failure modes of T-stub specimens*

However, cyclic loading reduced the maximum resistance of the T-stub specimens, though the reduction was not significant. The ductility of the T-stub specimens was quantified through the ultimate displacement $D_u$. Under monotonic loading, ultimate displacement was smaller for specimens with thicker end-plates that failed in modes 2 and 3 involving bolt failure. Cyclic loading reduced significantly ultimate displacement of specimens with thinner end-plates that failed in mode 1. This behaviour is attributed to low-cycle fatigue that generated cracks in the HAZ near the welds, along yield lines. On the other hand, the cyclic loading did not affect much the ultimate displacements for specimens with thicker end-plates that failed in modes 2 and 3, governed by bolt response. It is to be emphasized that specimens realized from high-strength end plates (S460 and S690, with lower elongation at rupture), had a ductility comparable with the one of specimens realized from mild carbon steel (S235). The parameters governing the ductility of T-stubs were the type of loading (monotonic / cyclic) and failure mode (end-plate or bolts) (Muntean *et al.*, 2010).

## 3. NUMERICAL ANALYSIS

### 3.1. Calibration of T-stub FEM response

On the basis of experimental response of T-stub specimens, a parametric numerical analysis was made, for finding the best bolt geometrical disposition on end-plate. The first step was the validation of the numerical model through comparison with experimental evidence.

In general a FE mesh must be sufficiently refined to produce accurate results while keeping the number of elements and nodes as small as possible in order to limit the processing time of the analysis. Based on this idea, the following characteristics of the finite elements were used in the ABAQUS computer program:

- for T-stub plate members linear 8-nodes solid elements reduced integration (brick C3D8R element) were used;
- for meshing the assembly the chosen element shape was HEX and the technique used for meshing was structured with 16 elements per circle;
- for material uni-axial response a true stress-strain constitutive law ($\sigma_{true} - \varepsilon_{true}$) was used, based on $\sigma - \varepsilon$ engineering law through the following relationship:

$$\sigma_{true} = \sigma (1+\varepsilon) \text{ and } \varepsilon_{true} = ln (1+\varepsilon) \qquad .(1)$$

- the general contact type was used between elements: the tangential behaviour is defined by frictionless formulation while the normal behaviour is defined by a "hard" contact pressure-overclosure.

As concluded by the calibration process the overall response of the T-stub is influenced significantly by the bolt behaviour and the geometry of welding. In consequence, the modelling of these components is crucial.

The bolt model was simulating the real geometrical and mechanical characteristics: the shank diameter was corresponding to the threaded part, while the pre-tensioning effect was introduced through an elongation under an axial force corresponding to 50% pre-tensioning force.

In order to find close results with experimental characteristic curves, a special shape of welding geometry was considered in the model, based also on observations on failures of the double bevel welding (see Figure 4) during various experimental tests performed in the CEMSIG Laboratory in Timisoara. Practically it was noticed

that in most of the cases the welds do not fully penetrate on the full bevelled plate thickness (Figure 4b), although the theoretic shape presents it as full penetration (Figure 4a). Table 3 offers the geometrical values used for the calibration of experimental results through numerical models.



a) weld requirement          b) FEM weld dimensions



c) FEM disposition of welds
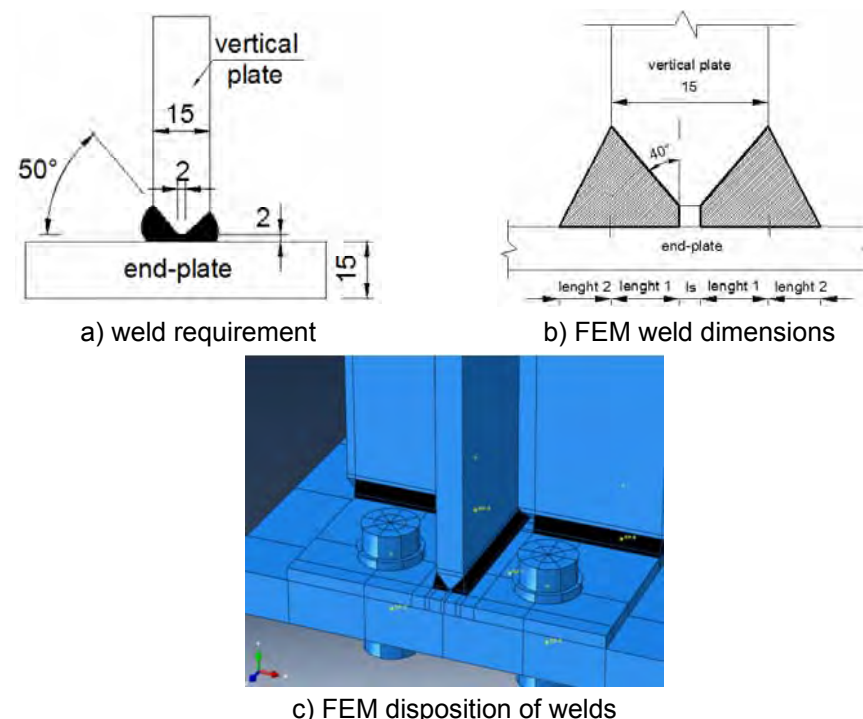
*Figure 4. Double bevel welding of elements*

Table 3. The welding geometry

| Label | Length 1 | Length 2 |
|---|---|---|
| TST-8A-S690 | 6.5 mm | 2.5 mm |
| TST-10A-S460 | 6.5 mm | 5 mm |
| TST-12A-S235 | 4.5 mm | 2.5 mm |

Figure 5 presents the comparison between numerical and experimental results under the form of axial force – end-plate deformation, as well as the deformation of the T-stub elements at maximum deformation. It could be concluded that the FE response follows with high accuracy the monotonic curves of experimental specimens. Moreover, the failure modes obtained were identical to the ones obtained experimentally, namely failure mode 2.

Table 4 gives as comparison the values of elastic limit ($F_y$) for resistance and elastic stiffness ($S_{j,ini}$) derived using the ECCS procedure and the analytical values resulted according to Eurocode 3-1.8 specifications, computed by using the real yielding strength of plate materials. Generally good agreement is found for $F_y$ values, while for initial elastic stiffness higher values are resulting for experimental results. However, the comparison of characteristics confirms the accuracy of FEM results.

Table 4. Characteristic values for T-stub elements

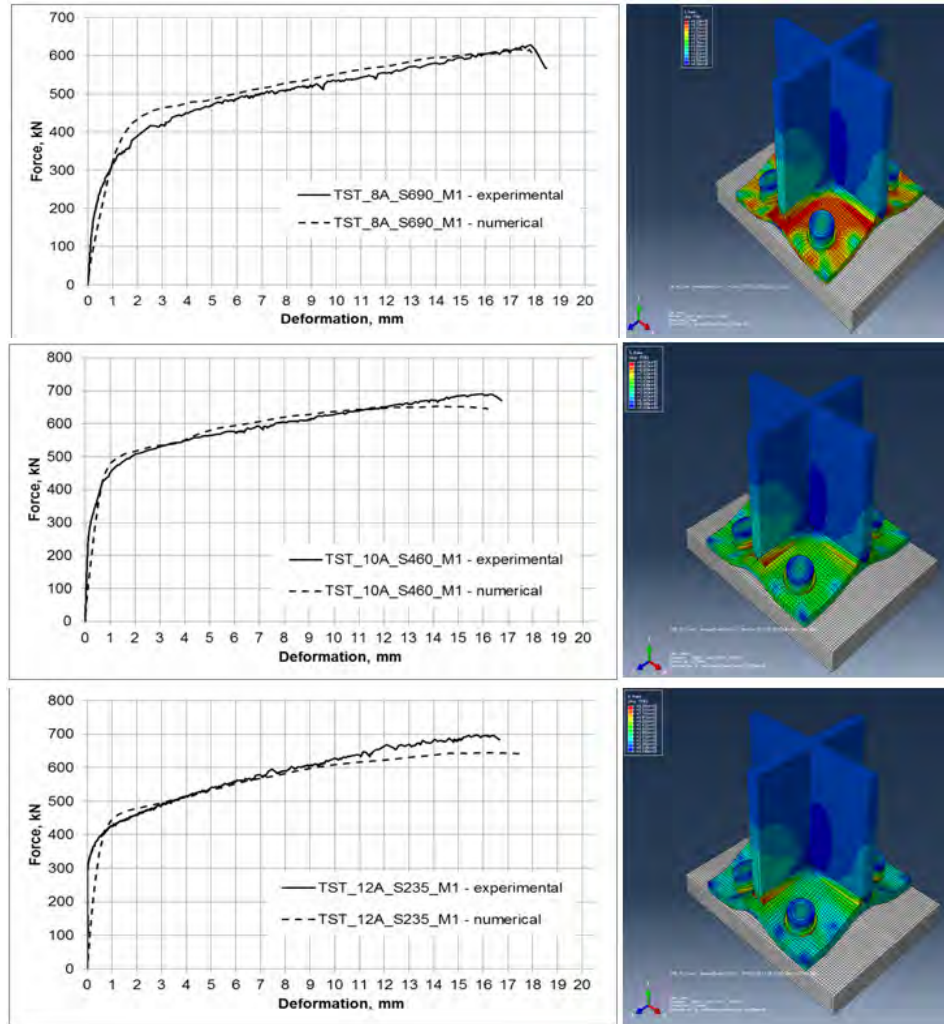| Label | Analysis | $F_y$ (kN) | $S_{j,ini}$ (kN/mm) |
|---|---|---|---|
| TST_8A_S690 | experimental | 429 | 685 |
| | numerical | 444 | 411 |
| | analytical | 405 | 402 |
| TST_10A_S460 | experimental | 515 | 1150 |
| | numerical | 519 | 879 |
| | analytical | 407 | 720 |
| TST_12A_S235 | experimental | 494 | 5812 |
| | numerical | 499 | 945 |
| | analytical | 402 | 1025 |



Figure 5. Graphical results and failure modes for numerical FE T-stub models

## 3.2. Optimisation of T-stub response through FE analyses

In order to optimise the behaviour of T-stub elements a parametric study was developed using different distance between bolt rows. The *e* and *p* distances defined in Eurocode 3 part 1-8 represent the distance between bolt axes and respectively the distance from the bolt axis to the end-plate edge. They are used in the evaluation of connection resistance, more precisely in the computation of its resistance. Figure 6 shows the values chosen for the numerical parameterisation, in which two new cases were considered.
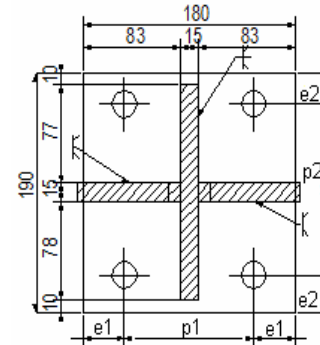


| | Initial case | Case 1 | Case 2 |
|---|---|---|---|
| e1 | 35 | 40 | 30 |
| p1 | 120 | 110 | 130 |
| e2 | 45 | 50 | 35 |
| p2 | 90 | 80 | 110 |

Figure 6. Values for e and p used for parametric study

Figure 7 shows the numerical responses under the form of characteristic force-deformation curves for the new analysis cases, in comparison with the initial case. Table 5 offers synthetically the values for resulted yield limit resistances ($F_y$) and elastic stiffness ($S_{j,ini}$) in comparison with the values obtained by analytical computation.

Both numerical and analytical results show very clearly that the change in the distance between bolts influences in great extent the resistance, initial stiffness and also the element ductility. If considering the *case 1* of geometrical disposition (increased distance between bolts), an increase in the resistance (up to 20%) and stiffness is obtained. However, this also conducts to an earlier plastification of weakest components – the end plate in this case, leading to and the presence of the discharging branch and consequently to a smaller rotation capacity. On contrary, the use of larger distances between bolts (*case 2* in this study), the resistance and elastic stiffness is reduced drastically. The second mode of failure of end-plate in bending remains unchanged in all cases.

Table 5. Elastic resistance and elastic stiffness for different distances between bolts

| Label | | Initial case | | Case 1 | | Case 2 | |
|---|---|---|---|---|---|---|---|
| | | $F_y$ | $S_{j,ini}$ | $F_y$ | $S_{j,ini}$ | $F_y$ | $S_{j,ini}$ |
| TST_8A S690 | numerical | 444 | 411 | 511 | 445 | 337 | 208 |
| | analytical | 405 | 402 | 426 | 524 | 354 | 311 |
| TST_10A S460 | numerical | 519 | 879 | 597 | 946 | 388 | 507 |
| | analytical | 407 | 720 | 442 | 909 | 370 | 570 |
| TST_12A S235 | numerical | 499 | 945 | 572 | 1022 | 380 | 538 |
| | analytical | 402 | 1025 | 437 | 1244 | 365 | 840 |

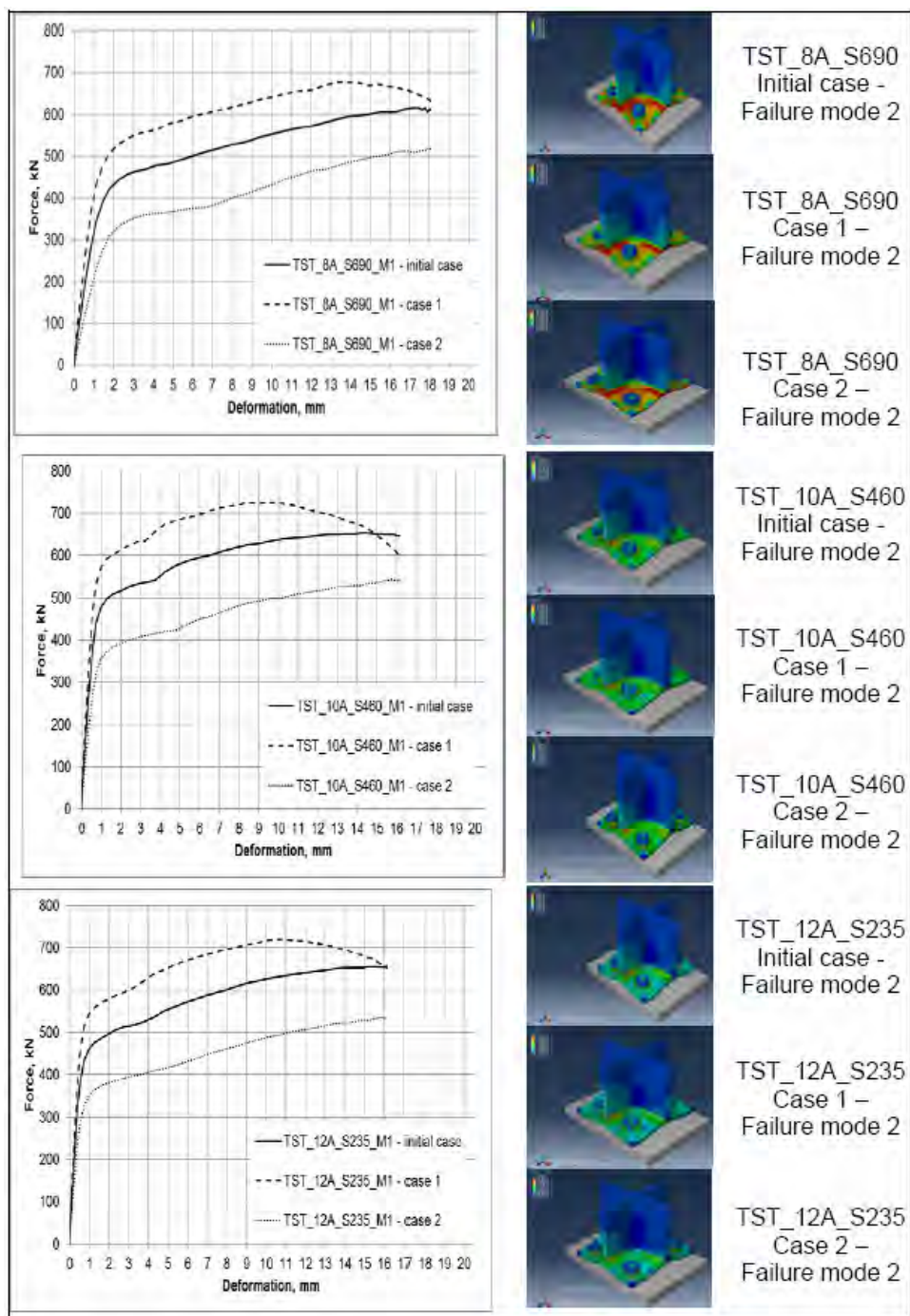* Forces $F_y$ are given in kN while the elastic stiffness is in kN/mm

*Figure 7. Characteristic Force-Deformation curves and failure conditions for different distances between bolts*

# 4. CONCLUSIONS

The strength and ductility of the bolted end-plate beam-to-column joint is highly influenced by the T-stub behaviour. By changing the end-plate thickness and steel grades, we can obtain the same failure modes and resistance values with minor differences in stiffness characteristics.

The FE model of some previously tested T-stubs show good agreement response under the form of force-deformation curves and following the experimental mode of failure. The parametric study performed on the distance between bolts show the fact that the best resistance of T-stub elements is obtained when they are closer to webs. However, the global T-stub element ductility might be affected, due to early plastification of end-plate.

The main conclusion of the study shows that in a bolted end-plate connections, the required levels of resistance and ductility can be controlled by a correct design of macrocomponents (such as the T-stubs), by choosing the proper geometrical and material characteristics of its components.

## ACKNOWLEDGMENTS

## REFERENCES

[1] EN 1993-1.8. 2003. Design of steel structures. Part 1-8: Design of joints, European standard.
[2] Dubina, D, Stratan, A, Muntean, N, Grecea, D, "Dual-steel T-stub behaviour under monotonic and cyclic loading", ECCS/AISC Workshop: Connections in Steel Structures VI, Chicago, Illinois, USA, 23-55, 2008a.
[3] Dubina, D, Stratan, A, Muntean, N, Dinu, F, "Experimental program for evaluation of Moment Beam-to-Column Joints of High Strength Steel Components", ECCS/ AISC Work-shop: Connections in Steel Structures VI, Chicago, Illinois, USA, June 23-55, 2008b.
[4] Dubina, D, Muntean, N, Stratan, A, Grecea, D, Zaharia, R, "Testing program to evaluate behaviour of dual steel con-nections under monotonic and cyclic loading", Proc. of 5th European Conference on Steel and Composite Structures - Eurosteel 2008, 3-5 September, Graz, Austria, 609-614, 2008c.
[5] Dubina, D, Grecea, D, Stratan, A, Muntean, A., " Performance of dual-steel connections of high strength components under monotonic and cyclic loading", STESSA 2009, Behaviour of Steel Structures in Seismic Areas, Taylor & Francis Group, London, 16-20 Aug. 2009, Philadelphia, USA, 437-442, 2009.
[6] ABAQUS Inc. "ABAQUS analysis user manual", version 6.10, 2010.
[7] Dubina, D, "Dual-steel frames for multistory buildings in seismic areas", Keynote lecture, Proceedings of SDSS'Rio 2010 International Colloquium Stability and Ductility of Steel Structures, 8-10 September, Rio de Janeiro, Brazil, 59-80, 2010.
[8] Muntean, N, Grecea, D, Dogariu, A, Dubina, D, "Strength and ductility of bolted T-Stub macro-components under mono-tonic and cyclic loading", Proceedings of SDSS'Rio 2010 International Colloquium Stability and Ductility of Steel Structures, 8-10 Sept, Rio de Janeiro, Brazil, 223-230, 2010.

# A DESIGN PROCEDURE FOR BOLTED TOP-AND-SEAT ANGLE CONNECTIONS FOR USE IN SEISMIC APPLICATIONS

Jared D. Schippers, Daniel J. Ruffley, Dr. Gian A. Rassati, and Dr. James A. Swanson
*School of Advanced Structures, University of Cincinnati, Cincinnati, OH*
*Jared.schippers@gmail.com; djruffley@gmail.com; gian.rassati@uc.edu;*
*swansojs@ucmail.uc.edu*

## ABSTRACT

Since the 1994 Northridge and 1995 Kobe earthquakes, bolted moment connections have garnered considerable interest for their application in Seismic Lateral Resisting Systems (SLRS). However, the considerable amount of research conducted over the last two decades has not produced many design procedures that would allow the applications of bolted connections either as fully-restrained or partially-restrained. This paper outlines a step-by-step design procedure for the design of bolted top-and-seat angle moment connections for seismic applications. The proposed procedure is used to design three practical examples of top-and-seat angle connections: two full-strength and one partial-strength. The connections are then are modeled in ABAQUS following a validated modeling approach that has been verified against multiple experimental tests, both quantitatively and mechanistically. The analysis results of these models are subsequently compared to the expected outcomes from the design procedure, as a proof-of-concept. The results of this comparison are presented and commented, and it is concluded that the proposed procedure is suitable for the design of top-and-seat angle connections for seismic applications.

## 1. INTRODUCTION

In the wake of the 1994 Northridge and 1995 Kobe earthquakes, numerous moment connections were investigated and studied. The earthquakes demonstrated that welded moment connections were far more brittle than previously thought, and as a result there arose an increased interest in bolted moment connections.

Moment connections can be classified in terms of strength, stiffness, and ductility. For strength, a connection is considered full-strength (FS) if the connection has enough capacity so the beam can develop a full plastic hinge. If the capacity of the connection is not enough for this to occur, it is considered to be partial-strength (PS). Concerning stiffness, a connection is considered fully-restrained (FR), partially-restrained (PR), or simple, depending on the relative rotational stiffness of the connection with respect to the connected beam. When the initial stiffness is greater

than 20EI/L, the connection is FR. If the initial stiffness is less than 2EI/L, the connection is simple. Anything between these two limits classifies the connection as PR. Finally, a connection is considered ductile if it has at least 80% of its nominal strength at a plastic rotation of 0.03 radians. Figure 1 shows a full-strength, partially-restrained, ductile connection (Swanson, 1999).

Currently, only full-strength, fully-restrained moment connections are allowed for use in seismic lateral resisting systems per ANSI/AISC 341-10 (2010) in intermediate moment frames (IMF) and special moment frames (SMF), and all other connections must be considered simple gravity connections. Previous research has shown that accounting for the moment contribution of these gravity connections in moment frames adds a considerable amount of lateral resistance during a seismic event (Barber, 2011, and Zhang, 2012).
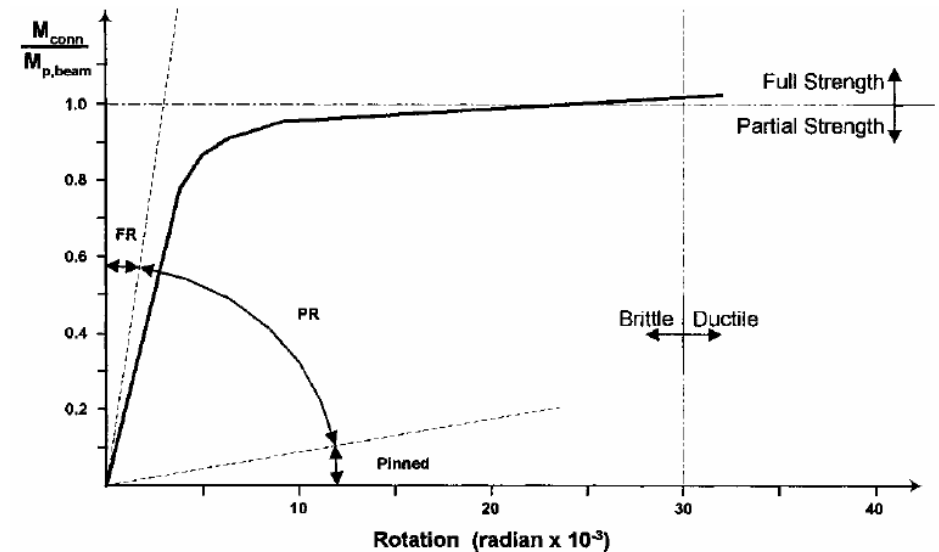


Figure 1. Moment-Rotation Curve
(Swanson and Leon, 2000)

With more and more research going into PR connections and frames consisting of PR connections, it is anticipated that the contribution of lateral resistance from PS, PR connections will eventually be allowed to be incorporated in seismic design per ANSI/AISC 341.

Additionally, it is envisioned in the future that the primary lateral resisting system in SMFs and IMFs will be permitted to also consist of FS, PR connections. Given these assumptions, this paper presents a general design procedure for bolted top-and-seat angle connections for use in seismic design. The design procedure has been verified through finite element modeling, both quantitatively and mechanistically, using the software ABAQUS. Three example connections, two FS and one PS, have been designed using the proposed procedure and modeled in ABAQUS. The results are then presented and commented.

## 2. BACKGROUND

In 1995, after the Northridge and Kobe earthquakes, the SAC Joint Venture and FEMA entered into an agreement to further research in seismic design pertaining to steel moment frames and connections (FEMA, 2000). SAC Subtask 7.03 was performed at the Georgia Institute of Technology and was concerned with bolted T-stub and TSA connections. As part of this research, 8 full-scale T-stub connections, 2 full-scale TSA connections, 48 bolted T-stub components, and 10 bolted clip angle components were experimentally tested (Smallidge, 1999; Swanson, 1999; and Schrauben, 2000). All full-scale tests were performed cyclically and the component tests led directly to Swanson (1999) developing the Modified Kulak Model for predicting prying forces in T-stub connections. Swanson and Gao (2000) later developed a similar prying model for predicting prying forces in heavy clip angle components, using previously compiled data from SAC subtask 7.03.

Schrader (2010) compiled the documentation to prequalify bolted T-stub connections as FR connections for use in IMFs and SMFs per the provisions of ANSI/AISC 358-10 (2010). He used the moment-rotation and other experimental data gathered from SAC Subtask 7.03. In addition to using existing data to meet the criterion for prequalifying a connection, a design procedure was created. This design procedure implemented the Modified Kulak Model and is currently being reviewed by the AISC Connection Prequalification Review Panel (CPRP). The design procedure outlined in this paper is molded after the design procedure in Schrader (2010).

## 3. TOP-AND-SEAT ANGLE DESIGN PROCEDURE

### 3.1. Methodology for Design Procedure

In order for AISC-CPRP to prequalify a connection, the connection must be qualified as FR to be considered for use in SMFs and IMFs. Previous TSA experiments have shown insufficient stiffness to be classified as FR, so this paper outlines a design procedure under the assumption that future provisions will allow the use of PR connections in seismic design. Under this assumption, this procedure is based on mechanistic principles and mostly follows provisions in ANSI/AISC 341-10 (2010) and ANSI/AISC 358-10 (2010). The portion of the procedure considering prying uses the Modified Kulak Model developed by Swanson and Gao (2000) and Gao (2001).

### 3.2. General

Top and seat angle (TSA) connections use a top angle and seat angle to provide the moment resistance in the connection. The angles are connected to the column and beam flanges by high-strength bolts as shown in Figure 2. The top and seat angles must be identical so the connection has equal resistance for a negative or positive moment. The shear connector is designed to carry all the shear resistance in the connection. The shear connector shown in Figures 2 and 3 is a shear plate bolted to the beam flange and welded to the column flange.

Due to the length limitations for this paper, a detailed list of all system limitations, provisions, and requirements could not be included. Most of these items strictly

follow current standards in ANSI/AISC 358-10 (2010), ANSI/AISC 360-10 (2010), and ANSI/AISC 341-10 (2010). For a detailed design procedure listing all these items, see Schippers (2012).
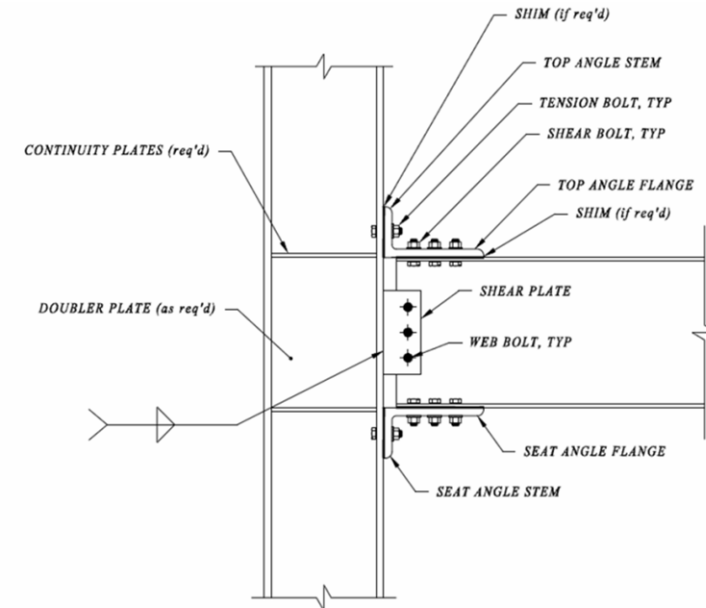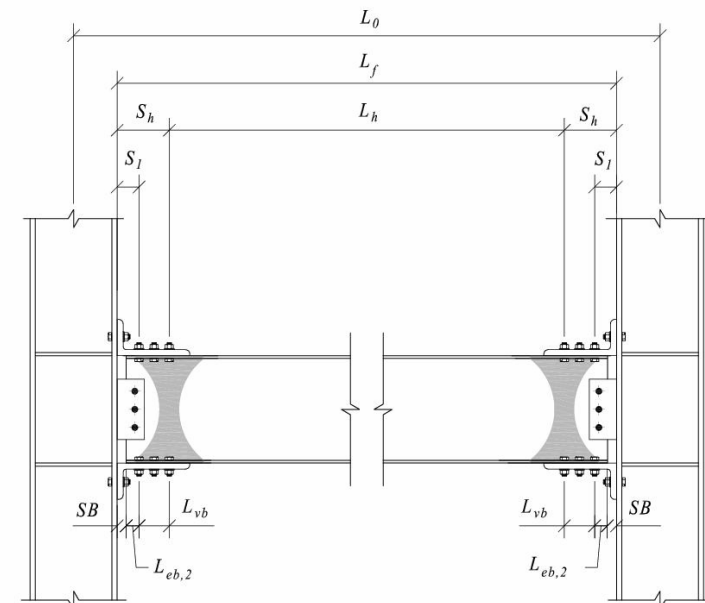


Figure 2. Typical TSA Connection



Figure 3. System Detail showing plastic hinge location
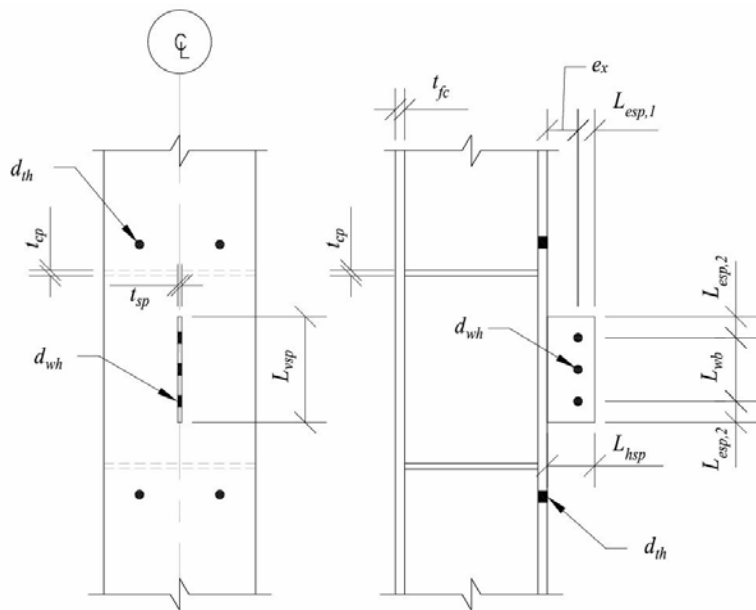
www.steelconstruct.com

Figure 4. Column and Shear Tab Details
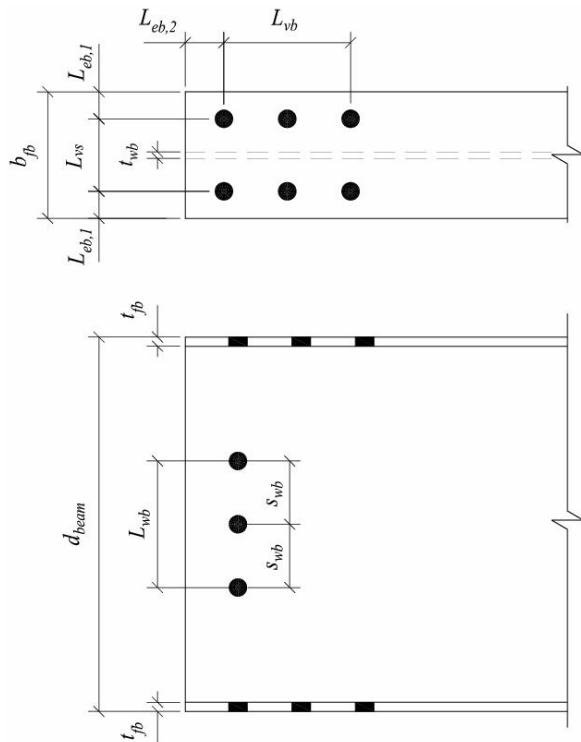


Figure 5. Beam Details
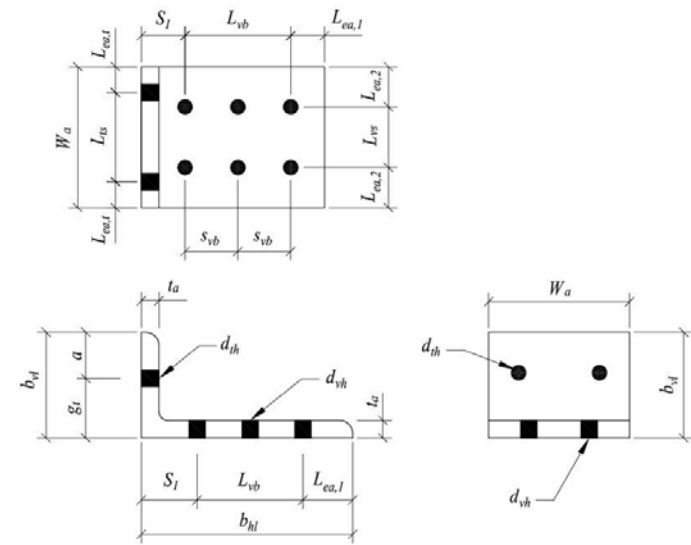


Figure 6. Angle Details

### 3.3. Design Procedure

For commentary on design procedure, see Schippers (2012).

Step 1: Compute the maximum expected moment (occurs at the beam hinge)

$$M_{pr} = PS_\% C_{pr} R_y F_{yb} Z_x \quad (1) \qquad where, \quad C_{pr} = \frac{F_{yb} + F_{ub}}{2 F_{yb}} \quad (2)$$

For a FS design, $PS_\%$ equals 100%, or 1. $R_y = R_t = 1.1$ per ANSI/AISC 358-10 (2010).

Step 2: Compute the maximum shear bolt diameter

To ensure a ductile failure in the beam, the following must be met:

$$R_t F_{ub} Z_{net} \geq R_y F_{yb} Z_x \tag{3}$$

$$y_{PNA} = \frac{1}{2 t_{wb}} \left[ \left[ b_{fb} - 2\left( d_{vh} + \frac{1}{16}" \right) \right] t_{fb} + t_{wb} d_{beam} - b_{fb} t_{fb} \right] \tag{4}$$

$$Z_{net} = Z_1 + Z_2 \tag{5}$$

$$Z_1 = \frac{(y_{PNA} - t_{fb})^2 t_{wb}}{2} + b_{fb} t_{fb} \left( y_{PNA} - \frac{t_{fb}}{2} \right) \tag{6}$$

$$Z_2 = \frac{(d_{beam} - y_{PNA} - t_{fb})^2 t_{wb}}{2} + \left[ b_{fb} - 2\left( d_{vh} + \frac{1}{16}" \right) \right] t_{fb} \left( d_{beam} - y_{PNA} - \frac{t_{fb}}{2} \right) \tag{7}$$

Step 3: Determine the preliminary shear strength per bolt

$$\phi r_{nv} = min \begin{cases} \phi_n \frac{\pi}{4} (d_{vb})^2 F_{nv} & \text{(Bolt Shear)} \\ \phi_d \, 2.4 d_{vb} t_{fb} F_{ub} & \text{(Beam Bearing)} \\ \phi_d \, 2.4 d_{vb} t_a F_{ua} & \text{(Angle Bearing)} \end{cases} \tag{8}$$

Step 4: Estimate the number of shear bolts needed for each beam flange

$$n_{vb} \geq \frac{1.25 M_{pr}}{d_{beam} \phi_n r_{nv}} \tag{9}$$

Step 5: Estimate the location of the plastic hinge in the beam

$$S_1 = SB + L_{eb,2} \tag{11}$$

$$S_h = S_1 + L_{vb} + \frac{1}{2} d_{beam} \tag{10}$$

$$L_{vb} = s_{vb} \left( \frac{n_{vb}}{2} - 1 \right) \tag{12}$$

Step 6: Calculate the shear force at the plastic hinge in the beam.

$$V_h = \frac{2 M_{pr}}{L_h} + \frac{w_u L_h}{2} \tag{13}$$

$$L_h = L_0 - d_{column} - 2 S_h \tag{14}$$

Step 7: Find the expected moment and corresponding force at the column face

$$M_f = M_{pr} + V_h S_h \tag{15}$$

$$F_{pr} \approx \frac{M_f}{1.05 d_{beam}} \tag{16}$$

Step 8: Approximate the thickness of the angles and size of the tension bolts

$$t_a \approx max \begin{cases} \dfrac{2 F_{pr}}{\phi_d F_{ya} W_a} & (Yielding) \tag{17} \\[3mm] \dfrac{2 F_{pr}}{\phi_n F_{ua}\left[ W_a - 2\left( d_{vh} + \frac{1}{16}^n \right) \right]} & (Fracture) \tag{18} \end{cases}$$

$$d_{tb} \approx \sqrt{\frac{5 F_{pr}}{n_{tb} \phi_n \pi F_{nt}}} \tag{19}$$

Step 9: Determine a preliminary configuration for the angles

$$p = \frac{W_a}{n_{tb}} \tag{20}$$

$$a = b_{vl} - g_t \leq 1.25 b \tag{21}$$

$$b = g_t - t_{s,eff} \tag{22}$$

$$a' = a + \frac{d_{tb}}{2} \tag{23}$$

$$b' = b - \frac{d_{tb}}{2} \tag{24}$$

$$If\ SB \leq 0.40 t_a, \quad t_{s,eff} = \frac{4 k_a + t_a}{5} \tag{25a}$$

$$\delta = 1 - \frac{d_{th}}{p} \tag{26}$$

$$If\ SB > 0.40 t_a, \quad t_{s,eff} = \frac{t_a}{2} \tag{25b}$$

Step 10: Find the required thickness of the angle when considering prying

$$r_{nt} = A_{tb} F_{nt} \tag{27}$$

$$T_{reqd} = \frac{F_{pr}}{n_{tb}} \tag{28}$$

Three limit states can control the tensile capacity of the connection. For more information on these limit states, see Swanson (1999).

$$\phi T_1 = \frac{(1 + \delta)}{4 b'} p \phi_d F_{ya} t_a^2 \tag{29}$$

$$t_a \geq 2 \sqrt{\frac{T_{reqd} b'}{p \phi_d F_{ya}(1 + \delta)}} \tag{30}$$

$$\phi T_2 = \frac{\phi_n r_{nt} a'}{a' + b'} + \frac{p \phi_d F_{ya} t_a^2}{4(a' + b')} \tag{31}$$

$$t_a \geq \sqrt{\frac{2.5 \phi_n r_{nt} b'}{p \phi_d F_{ya}}} \tag{32}$$

$$\phi T_3 = \phi_n A_{tb} F_{nt} \tag{33}$$

Step 11: Compute the actual force in the horizontal angle leg.

$$F_f = \frac{M_f}{d_{beam} + t_a} \tag{34}$$

Step 12: Confirm that the shear bolts provide adequate resistance

$$\phi r_{nv} n_{vb} \geq F_f \tag{35}$$

Step 13: Back-check the capacity of the horizontal angle leg

Check that $\phi R_n \geq F_f$ (in the order shown): gross section yielding, net section fracture, and compressive yielding or buckling.

$$\phi R_n = \phi_d F_{ya} W_a t_a \tag{36}$$

$$\phi R_n = \phi_n F_{ua}\left[ W_a - 2\left( d_{vh} + \frac{1}{16} \right) \right] t_a \tag{37}$$

$$\frac{KL}{r} = \frac{(0.75)(L_{eb,2} + SB - t_a)}{\sqrt{\dfrac{W_a t_a^3}{12 W_a t_a}}} = 2.5981 \frac{L_{eb,2} + SB - t_a}{t_a} \tag{38}$$

If $KL/r \leq 25$, compressive yielding governs, $\phi R_n$ is the exact same as in gross section yielding. If $KL/r > 25$, flexural buckling governs and the provisions of Section E3 of the ANSI/AISC 360-10 (2010) apply.

Step 14: Back-check all three limit states for tensile failure defined in step 10 ($\phi T_{1,2,3}$)

Step 15: Finalize Design

Lastly, bearing and tear-out and block shear in the beam flange and horizontal angle leg should be checked in accordance with Sections J3.10 and J4.3 in the ANSI/ AISC 360-10 (2010). Also, the shear connection needs to be detailed accounting for eccentricity. All applicable shear limit states should be checked per Chapter J in ANSI/ AISC 360-10 (2010). Panel zone strength shall be in accordance with Section 2.4.4 and 6 in ANSI/AISC 358-10 (2010). Finally, lateral bracing requirements shall meet the lesser length found in either ANSI/AISC 360/10 (2010) or ANSI/ AISC 341-10 (2010).

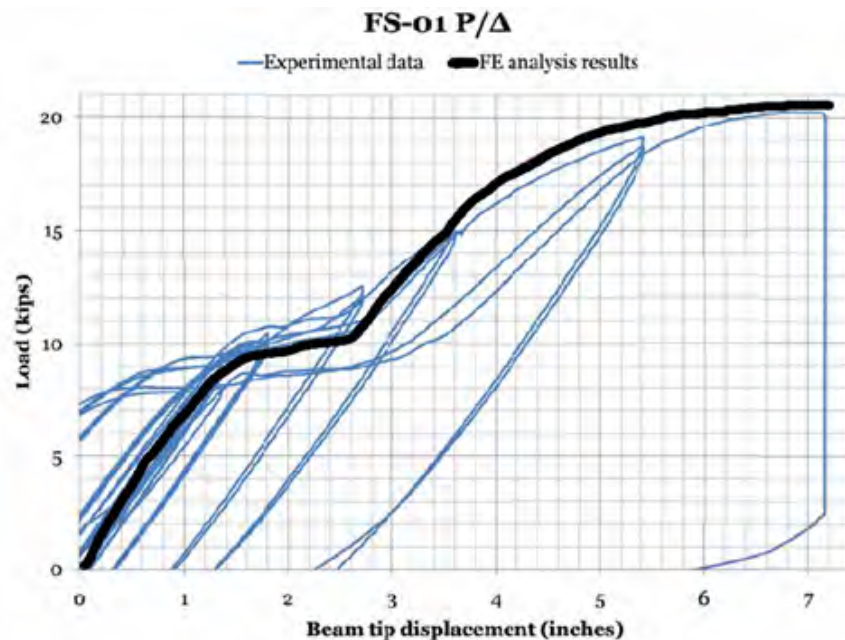www.steelconstruct.com

## 4. FINITE ELEMENT MODELING (FEM)
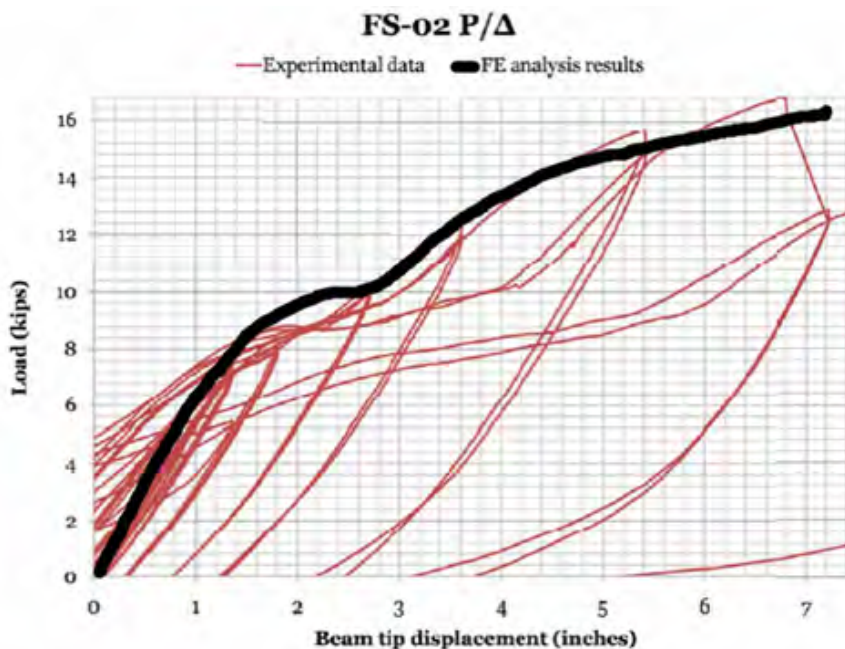


Figure 8. FS-01 Comparative Plots



Figure 9. FS-02 Comparative Plots

### 4.1. Modeling Existing Experimental Data

As previously mentioned, Schrauben (2000) tested two full-scale TSA connections and both of these experiments have been modeled in ABAQUS. For a detailed summary of the modeling procedure, see Ruffley (2011). Figures 8 and 9 show both force-displacement results of Schrauben's (2000) experimental data and the curve obtained by modeling the same connections in ABAQUS. It can be observed that the modeling procedure produced highly accurate results. Ruffley (2011) also modeled component tests that Swanson (1999) tested, in order to verify the procedure's capability of predicting various failure modes, obtaining very satisfactory results.

### 4.2. Modeling New Connections

In an attempt to verify the accuracy of the design procedure, three new connections have been modeled using the procedure outlined in Ruffley (2011). Two were FS, and one was PS (60%). Table 1 shows the summary of calculations of the three connections designed using the proposed procedure. Table 2 shows comparative results between the predicted forces computed in the design procedure and actual forces from analyzing the models. It should be noted that the analyses of all three models showed no signs of block shear in the beam flange or horizontal angle leg, which verifies the expected over-conservative nature of the block shear resistance calculation for this connection. Schrader (2010) had similar conclusions when analyzing T-stub connections concerning block shear. For this reason the design procedures allows a 10% reduction in $F_f$ when designing block shear. Prying forces were calculated by taking each element stress multiplied by its corresponding area, and then summing the forces for all elements in a cross section of a tension bolt.

The plastic mechanism in the angle, block shear, gross section yielding, and net section fracture were all analyzed by visually inspecting the equivalent plastic strain contours. Shear bolt forces were analyzed calculating the actual force transmitted by the horizontal leg of the angle. This force was calculated by summing the stress in each element of the horizontal leg of the angle and multiplying it by the element's cross-sectional area. It was assumed for the sake of simplicity that all shear bolts carried an equal load. All values in Table 2 correspond to the instant in which the beam in the model develops $M_{pr}$ as calculated in step 1 at the expected hinge location calculated in Step 5 of the design procedure.

### 4.3. Modeling Results

The FS W16x31 and PS W24x62 connections were both anticipated to be controlled by tension bolt capacity, which is precisely what the models verified. The quantitative errors in these two models were 11% and 9%, respectively. For the FS W18x35 model, the limiting state was expected to be formation of a plastic hinge in the top angle, and the model showed correspondingly signs of widespread inelastic deformation. The fact that the angle had yielded indicates that the capacity is being approached, although model is not capable of quantifying it explicitly. From a visual inspection, it is concluded that the prediction of plastic hinges forming in the angles is accurate, so the model is deemed to reproduce the predicted outcome. It should also be noted that the analyzed prying forces in the tension bolts were within 12% of the expected forces from the design procedure, once again validating its accuracy.

Table 1. *Design Procedure Results*

| DESIGN PROCEDURE RESULTS | | | |
|---|---|---|---|
| **Beam Size** | **W16x31** | **W18x35** | **W24x62** |
| Column Size | W14x211 | W14x211 | W14x211 |
| FS or PS Design | FS | FS | PS (60%) |
| Shear Bolt Size, $d_{vb}$ (in) | 3/4 | 7/8 | 7/8 |
| Shear Bolt Grade | A490X | A490X | A490X |
| No. Shear Bolts, $n_{vb}$ | 8 | 8 | 8 |
| Tension Bolt Size, $d_{tb}$ (in) | 1 1/4 | 1 1/2 | 1 1/2 |
| Tension Bolt Grade | A490X | A490X | A490X |
| No. Tension Bolts, $n_{tb}$ | 2 | 2 | 2 |
| Tension Bolt Gauge, $g_t$ (in) | 2 7/8 | 3 1/4 | 3 1/4 |
| Angle Width, $W_a$ (in) | 10 | 12 | 12 |
| Angle thickness, $t_a$ (in) | 1 | 1 | 1 1/8 |
| Set-back, $SB$ (in) | 3/8 | 3/8 | 3/8 |
| $M_{pr}$ (k-in) | 3416 | 4206 | 5806 |
| $M_f$ (k-in) | 4061 | 5050 | 7065 |
| $F_f$ **(kips)** | **240** | **270** | **285** |
| $\varphi T_1$ resistance (kips) | $290 \geq 240$ | $290 \geq 270$ | $339 \geq 285$ |
| $\varphi T_2$ resistance (kips) | $245 \geq 240$ | $305 \geq 270$ | $310 \geq 285$ |
| $\varphi T_3$ resistance (kips) | $269 \geq 240$ | $388 \geq 270$ | $388 \geq 285$ |
| Prying effect, $\varphi T_3 / \varphi T_2$ (%) | 10.2% | 27.2% | 25.2% |
| Bearing resistance (kips) | $367 \geq 240$ | $416 \geq 270$ | $578 \geq 285$ |
| Block shear resistance (kips) | $242 \geq 216$ | $262 \geq 243$ | $313 \geq 256$ |
| Angle GSY resistance (kips) | $500 \geq 240$ | $600 \geq 270$ | $675 \geq 285$ |
| Angle NSF resistance (kips) | $483 \geq 240$ | $585 \geq 270$ | $658 \geq 285$ |
| Shear bolt resistance (kips) | $267 \geq 240$ | $364 \geq 270$ | $364 \geq 285$ |

Table 2. Table 2: *Analysis Results*

| DESIGN PROCEDURE AND FEM COMPARITIVE RESULTS | |
|---|---|
| **W16x31 FS Connection** | |
| Expected prying force in tension bolts | 1.102(240) = 265 kips |
| Actual bolt tensile force at $M_{pr}$ | 293 kips |
| Percent error | 11% |
| Plastic Hinge Devolpment ($\varphi T_1$) at $M_{pr}$ | Minimal Hinge Development |
| Actual force in shear bolts at $M_{pr}$ | 194 kips |
| Block Shear | No inelastic deformation (I.E.) |
| GSY, NSF | No I.E., No I.E. |
| **W18x35 FS Connection** | |
| Expected Limiting State, $\varphi T_1$ | Analysis shows hinge development in angle; limit state has not been reached but is being approached |
| Expected pyring forces in bolts, $\varphi T_2$ | 1.272(270) = 343 kips |
| Bolt Tensile Force at $M_{pr}$ in F.E.M. | 384 kips |
| Percent error | 11.9% |
| Actual force in shear bolts at $M_{pr}$ | 246 kips |
| Block Shear | No inelastic deformation (I.E.) |
| GSY, NSF | No I.E., No I.E. |
| **W24x62 PS (60%) Connection** | |
| Expected prying force in tension bolts | 1.252(285) = 357 kips |
| Actual bolt tensile force at $M_{pr}$ | 389 kips |
| Percent error | 9.0% |
| Plastic Hinge in Angles ( $\varphi T_1$) | minimal |
| Actual force in shear bolts at $M_{pr}$ | 226 kips |
| Block Shear | No inelastic deformation (I.E.) |
| GSY, NSF | No I.E., No I.E. |

# 5. CONCLUSIONS

A design procedure has been presented for full-strength and partial-strength bolted top-and-seat angle beam-to-column connections for use in seismic design. It has been discussed that the moment contribution of these connections currently cannot be incorporated in IMFs and SMFs, but it is envisioned that this could change in the future. With this assumption, the design procedure closely follows the connection prequalification standards in ANSI/AISC 358-10 (2010). The accuracy of the procedure has been demonstrated through finite element modeling in ABAQUS by a modeling procedure that had been verified through actual experimental data. Using this modeling procedure, two full-strength and one partial-strength connections were designed using the proposed procedure and modeled in ABAQUS. The results clearly show the quantitative accuracy of the design procedure, especially concerning prying forces in the tension bolts. In addition, all three models show that the predicted limit state was the likely cause of failure, verifying the mechanistic accuracy of the design procedure. Future research should include physical experiments of the three connections discussed in this paper, which would provide the ultimate verification of the design procedure's accuracy.

## REFERENCES

[1] ANSI/AISC 360-10 (2010). *Specification for Structural Steel Buildings,* American Institute of Steel Construction, Chicago, IL.

[2] ANSI/AISC 358-10 (2010). *Prequalified Connections for Special and Intermediate Steel Moment Frames for Seismic Applications,* American Institute of Steel Construction), Chicago, IL.

[3] ANSI/AISC 341-10 (2010). *Seismic Provisions for Structural Steel Buildings,* American Institute of Steel Construction, Chicago, IL.

[4] Barber, (2011). *Contribution of Shear Connections to the Lateral Stiffness and Strength of Steel Frames,* MS Thesis, School of Advanced Structures, University of Cincinnati, Cincinnati, OH.

[5] FEMA-350 (2000). *Recommended Seismic Design Criteria for New Steel Moment-Frame Buildings,* Federal Emergency Management Agency*,* Washington D.C.

[6] Gao, X. (2001). "Strength Determination of Heavy Clip-Angle Connection Components." MS thesis, Dept. of Civil and Environmental Engineering, University of Cincinnati, Cincinnati, Ohio.

[7] Ruffley, D.J. (2010). *A Finite Element Approach for Modeling Bolted Top-and-Seat Angle Components and Moment Connections.* MS Thesis, School of Advanced Structures, University of Cincinnati, Cincinnati, Ohio.

[8] Schippers, J.D. (2012). *A Design Procedure for Bolted Top-and-seat Angle Connections for Use in Seismic Applications.* MS Thesis, School of Advanced Structures, University of Cincinnati, Cincinnati, Ohio.

[9] Schrader, C.A. (2010). *Prequalification and Design of Rolled Bolted T-stub Connections in Moment Resisting Frames.* MS Thesis, School of Advanced Structures, University of Cincinnati, Cincinnati, Ohio.

[10] Schrauben, C.S. (1999). *Behavior of full-scale bolted beam-to-column T-stub and clip angle connections under cyclic loading.* MS Thesis, School of Civil and Environmental Engineering. Georgia Institute of Technology, Atlanta, Georgia.

[11] Smallidge, J.M. (1999). *Behavior of Bolted Beam-to-Column T-stub Connections under Cyclic Loading.* MS Thesis, School of Civil and Env. Engrg, Georgia Institute of Technology, Atlanta, Georgia.

[12] Swanson, J.A. (2000). *Characterization of the strength, stiffness, and ductility behavior of Tstub connections.* PhD Dissertation, School of Civil and Env. Engrg. Georgia Institute of Technology, Atlanta, Georgia.

[13] Swanson, J.A. and Gao, X. (2000). "Strength Determination of Heavy Clip-Angle Connection Components", in *Connection in Steel Structures IV: Steel Connections in the New Millennium*, Roanoke, VA. Oct, 2000.

[14] Swanson, J.A., and Leon, R.T. (2000). "Bolted Steel Connections: Tests on T-stub Components." *Journal of Structural Engineering*, 126(1):50-56.

[15] Zhang, W. (2012). *Study of the Influence of Gravity Connections on the Lateral Response of Steel-Concrete Composite Moment Frames,* MS Thesis, School of Advanced Structures, University of Cincinnati, Cincinnati, OH.

# USING FINITE ELEMENT MODELING TO CREATE MOMENT-ROTATION CURVES FOR SHEAR TAB CONNECTIONS

John M. Schroeder
*Graduate Student, School of Advanced Structures, University of Cincinnati, OH*
*schroeder.mac@gmail.com*

Mindy A. Barber
*Design Engineer, THP Limited, Cincinnati, OH*
*MBarber@thpltd.com*

Gian A. Rassati
*Associate Professor, School of Advanced Structures, University of Cincinnati, OH*
*gian.rassati@uc.edu*

James A. Swanson
*Associate Professor, School of Advanced Structures, University of Cincinnati, OH*
*james.swanson@uc.edu*

## ABSTRACT

This paper investigates differences between fully restrained, partially restrained, and simple shear connections in steel, as well as previous experimental test setups and results. Using ETABS, PR hinge properties for three experimental gravity connections were explicitly defined, allowing development of extrapolation equations based on beam properties. Additional finite element modeling techniques including elastic-hinge and pushover analyses using both default and user-defined hinge parameters are compared. Three experimental setups were modeled and analyzed in ABAQUS to reproduce the experimental results and validate that the finite element modeling (FEM) techniques were able to recreate the experimental moment-rotation curves prior to using FEM for the creation of new moment-rotation curves based on anaylitical results of theoretical simple connections.

## 1. INTRODUCTION

Spurred by the abundance of welded moment connection failures observed in the 1994 Northridge earthquake, research efforts involving the capacity of simple gravity connections have since increased significantly. Typically, a building includes more gravity connections than moment connections, yet the moment resisting contributions of the gravity connections are neglected in design. If one begins to look at gravity connections as partially restrained instead of perfectly pinned, their lateral stiffness can be added to that of the lateral load resisting system to improve overall system response. To understand the effect of including gravity connection stiffness and strength, equations representing moment-rotation (MR) curves have been incorporated into prototype buildings to investigate the shear tab connection's overall lateral strength and stiffness contributions.

Additionally, if one were to account for the rotational stiffness of shear tab connections in the design of buildings, a way to predict the MR behavior of various connections must be developed due to the lack of experimental MR data for shear tab connections. Unfortunately there is not much recent test data for MR curves of simple shear tab connections. So due to the expense required to perform experimental connection tests, a finite element analysis program was used to model theoretical shear tab connections with practical beam and columns sizes so that MR curves can be created for the connections.

## 2. PREVIOUS SHEAR TAB RESEARCH AND EXPERIMENTS

### 2.1. Larson (1996)

Larson's focus was the experimental testing of several top and bottom flange T-stub connections. The objective of Larson's research was to be able to obtain data on the performance of T-stub connections under cyclic loading. After the Northridge earthquake of the early 1990s, many fully welded connections had experienced brittle failure of the welds and there was a need for further understanding of how non-welded connections perform under such loadings.

Of the five connections that Larson tested, four were T-stub connections. The fifth was a shear tab connection that was tested to "determine the moment-rotation characteristics of the web alone" (Larson, 1996). The shear tab connected a W14x426 column to a W36x150 beam with eight 1 in. diameter A325 bolts. Unlike the T-stub specimens, the shear tab connection specimen was loaded for only one cycle and was not tested to failure.

### 2.2. Liu and Astaneh-Asl (2000)

Liu and Astaneh-Asl's research attempted to gain an understanding of the lateral resistance of simple connections after events like the Northridge earthquake suggested that these connections added to the lateral stability of buildings even though they were not designed for these loadings. They performed eight tests on shear tab beam-column connections. The connections were configured with two beams connected to one column as is shown in Figures 1 and 2.

A W14x90 column made of A572 Gr. 50 steel was used in all tests. The majority of specimens included a concrete floor slab supported by the beams in the connection. This slab was cast on top of a 20 gauge metal deck with 3 in. ribs and with welded wire fabric as primary reinforcing. Two specimens were constructed without a floor slab as a control. All beams were also made of A572 Gr. 50 steel while the plates were made of A36 steel.

The lateral load was applied via the application of a drift angle measured as the lateral displacement at the top of the column divided by the distance between the top and bottom of the supporting column. To simulate the gravity load seen in the theoretical building, actuators located 5 ft. 6 in. away from the centerline of the column, were added to the system to provide additional vertical loading on the connections. The resulting moments in the connections from the applied gravity loads were 20-25% of the maximum moment the connections experienced during testing (Liu and Astaneh-Asl, 2000). The gravity loadings were not present during the two control tests.
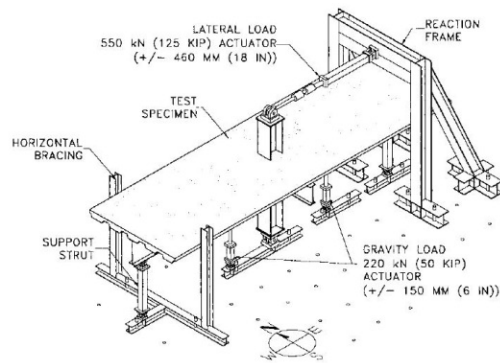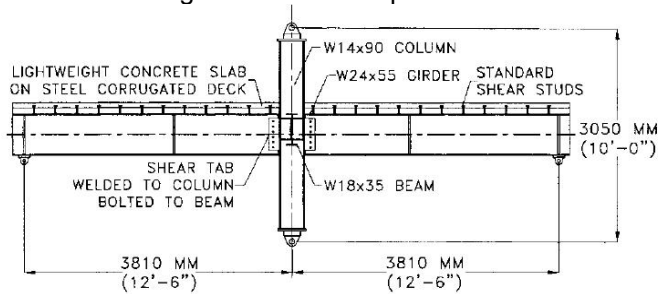
Figure 1. Test Set-up



Isometric

Figure 2. Test Set-up Elevation

Testing of the control specimens 1A and 2A showed that the connections sustained 15 to 20% of the beams moment capacity before failure (Liu and Astaneh-Asl, 2000). Failure of both specimens was similar, with shear tab yielding, beam and column flange contact, and fracture of the shear tab. The addition of the floor slab almost doubled the maximum moment capacities of the simple connections while not lowering the rotational capacities of the connections. This was due to loss of composite action with the concrete above rotations of 0.04 radians. The connections failed at approximately 30% and 60% of the W18x35 and W24x55 beam moment capacities respectively (Liu and Astaneh-Asl, 2000). After loss of composite action, the connections performed very similarly to the simple connections without the floor slabs present.

## 2.3. Crocker and Chambers (2004)

In their paper, Crocker and Chambers summarize the results of shear tab connection experiments they performed in the early 2000s. They tested three shear tab connections with varying plate depths and number of shear bolts. Their test set-up involved a column with fixed end supports connected through the shear tab to a beam supported by an actuator at the far end. During the testing of Specimen III, the top and bottom bolts experienced shear failure at a beam rotation of 0.04 radians followed by the next top bolt experiencing shear failure at a rotation of 0.05 radians (Crocker and Chambers, 2004). In Specimens I and II there was no shear failure observed in any of the bolts.

Analysis of the moment rotation curves created from the experiments led Crocker and Chambers to the conclusion that the number of bolts in the connection determines the connections stiffness (2004). From examining Specimen III they observed that after the first two bolts failed, Specimen III had the same stiffness as Specimen II. In addition, when the third bolt failed, the stiffness of Specimen III became the same as Specimen I.

## 3. SHEAR TAB CONNECTION LATERAL STIFFNESS CONTRIBUTION

### 3.1. Moment-Rotation Curve Equations

In the current effort, FE analyses performed on three different experimental connections were conducted in an attempted to quantify the lateral stiffness contribution of shear tab connections. The structural analysis program ETABS was used to create FE models of the shear tab connections tested by Liu and Astaneh-Asl (Specimens 1A and 2A) and Larson (Specimen 1). ETABS' default definitions for moment-rotation curves of connections, based on FEMA hinge properties, were then altered so that the resulting moment-rotation curves matched the data seen in the original experiments. Figure 3 illustrates how the ETABS hinge parameters relate moment and rotation for the connection.



A = Origin
B = Yield point
C = Ultimate pushover capacity
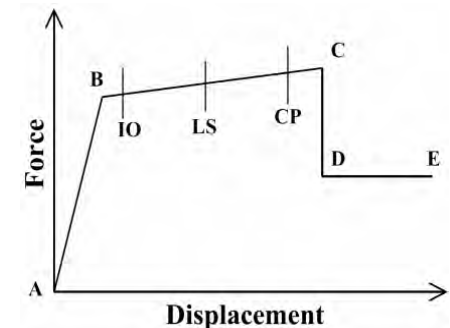D = Residual pushover strength
E = Total failure

Figure 3. ETABS Hinge Parameters (Computers and Structures, Inc)

From these altered hinge parameters, equations were created to calculate moment and hinge parameters for other beam and column connections, as is shown in Equations 1-5 below. The equations were specifically created to use only properties of the beam. With the MR parameters of the connection defined, the connection would then be classified as a partially restrained (PR) connection rather than the original classification of simple connection, which implies perfectly pinned behavior.

| Point | Moment Parameter | Rotation Parameter | |
|-------|-----------------|-------------------|----|
| A | $0$ | $0$ | (1) |
| B | $\dfrac{M_p L^2}{\left(\dfrac{h}{t_w}\right)^2} \le 0.06 M_p$ | $0$ | (2) |
| C | $\dfrac{M_p A^2 r_x t_w \left(\dfrac{2L t_w}{b_f}\right)^2}{S_x I_x} \le 0.17 M_p$ | $\dfrac{t_w}{t_f L r_x \left(\dfrac{d}{2}\right)^d}$ | (3) |

   www.steelconstruct.com

| Point | Moment Parameter | Rotation Parameter | |
|-------|------------------|--------------------|---|
| D | $\dfrac{M_p Z_x d b_f}{2 t_f d^{\left(a+\frac{t_f}{t_w}\right)}} \leq 0.14 M_p$ | $t_w \left(\dfrac{d}{2}\right)\left(\dfrac{r_x}{Z_x}\right)\left(\dfrac{r_x t_w b_f}{2 S_x h t_f}\right)^2$ | (4) |
| E | $\dfrac{M_p d}{2 d^d \left(\frac{S_x}{I_x}\right)^{\left(1+\frac{t_f}{I_x}\right)}} \leq 0.26 M_p$ | $\dfrac{b_f^2 r_x t_w^2}{\left(2 t_f^2 S_x h^2\right)\left(\frac{d}{r_x}\right)^{\left(\frac{I_x}{Z_x}\right)}}$ $\leq 1.75\ Rotation_{Point\ C}$ | (5) |

## 3.2. Structural Response: Simple vs. PR

Three hypothetical buildings were considered in an effort to determine the rotational stiffness contributions of including the PR behavior of simple connections. The three buildings examined varied in the number of stories, from three to eight, but the buildings mostly used moment frame lateral resisting systems. The ratio of non-rigid-to-rigid connections in the buildings also varied between one and four. Several models of each building were analyzed in ETABS. As a control, one model of each building with traditional simple connections was analysed under gravity and lateral loads. Further models were analysed under lateral loads with the new PR simple connection parameters while performing displacement and force-based pushover analyses. These models showed that by accounting for the PR rotational stiffness of the shear connections, the buildings, as a whole, could experience a 24% increase to the base shear while decreasing the average story drift by at least 22%, indicating an increase in stiffness. Additionally, the maximum moment experienced by the lateral load resisting beams and gravity beams decreased by 22% and 6% respectively.

## 4. FINITE ELEMENT MODELING OF SHEAR TAB CONNECTIONS

### 4.1. Experimental Models

Since the PR shear connection analyses indicated that shear tab connections could contribute to the lateral stiffness of buildings, additional modelling was undertaken to prove the validity of using analytical models to predict the MR behavior of the connections. Therefore, FE models of Liu and Astaneh-Asl's specimens 1A and 2A as well as Larson's specimen 1 were created in the computer program ABAQUS.

#### 4.1.1. Model Parts

The sizes of the components used in the FE analysis were based on the original member sizes listed in Liu and Astaneh-Asl (2000) and Larson (1996), which are summarized in Table 1. The material properties, specifically yield strength of the material in the experiments, were also taken from the original papers where possible and from AISC if they were not present in the original papers. Nominal yield strengths were then increased by the ratio of expected to minimum specified yield stress to obtain the expected yield stress (AISC, 2005b).

Table 1. Model Member Sizes

| Specimen | Column | Beam | Shear Tab | Bolts | Connection Orientation |
|----------|--------|------|-----------|-------|------------------------|
| 1A | W14x90 | W18x35 | 12x11.5x3/8 | 4 - 7/8" dia. | Weak Axis |
| 2A | W14x90 | W24x55 | 18x4.5x3/8 | 6 - 7/8" dia. | Strong Axis |
| 1 | W14x426 | W36x150 | 25x5x5/8 | 8 - 1" dia. | Strong Axis |

The creation of the bolts used in the testing presented an additional challenge due to the threads present in the bolt shank. According to AISC, the strength of structural bolts is dependent on the net area of this reduced bolt area (2005a). A good approximation of the net area can be obtained by using equation (1). By combining the value of $A_{net}$ with equation (2) the threaded portion of the shank can be modelled as a hollow tube. See Figure 4 for a cross-section of the bolt, washer, and nut assembly that illustrates the void created in the shank to account for the missing area due to the threads while maintaining the appropriate outer diameter for bearing considerations.

$$A_{net} = 0.7854 \times \left(d_b - \frac{0.9743}{n}\right)^2 \quad (1)$$

$$A_{Hollow\ Tube} = \frac{\pi}{4}(d_{outer}^2 - d_{inner}^2) \quad (2)$$



Figure 4. Bolt Cross-Section

#### 4.1.2. Model Assembly

While assembling the models, care was taken to accurately reproduce the boundary conditions in the original experiments. In all of the models, the beam and column ends were coupled to a reference point at the centerline of the member. Then the necessary boundary conditions were applied to this reference point to mimic the pin connections in the experiments.

Additionally, to pretension the bolts properly, a temperature differential was applied to the shank of the bolts. Using Hooke's law for one dimensional strain and the equation for strain due to temperature differential, an equation was derived to estimate the temperature change needed to reach the required pretension level. Several runs

of each model were still required to reach the proper pretension due to deformations in the shear tab and beam web that were not accounted for in the original equations.

### 4.1.3. Model Adjustments

For all of the models, several versions of each model were run to find the most accurate FE reproduction of the experimental results. The first modification included changing the test type from cyclic, like in the experiments, to monotonic to improve computation speed and accuracy. Afterward, the most common adjustment required between versions was changing the friction coefficient between surfaces. Previous research suggested that a reasonable estimate for the friction coefficient was 0.2 (Ruffley, 2011).

Additional changes were required in the modelling of Larson's specimen 1. To gain sufficient information on the dimensions of Larson's shear tab connection, research was performed on Larson's advisor's previous work. Larson's advisor had worked on welded column connections using the same column and beam sizes as Larson (Englehardt, 1994). Therefore it was hypothesized that the shear tabs used in those experiments were the same size as the shear tabs used in Larson's experiments.

### 4.1.4. Results

The results from the first set of analytical models were close in matching the overall response of the experimental connections. Several iterations of each model were completed to account for the adjustments mentioned above. Early iterations used multiple simplifications to obtain the general response of the analytical models with subsequent versions removing the simplifications to match the actual conditions of the experiments. The MR curves for Liu and Astaneh-Asl's specimen 1A and 2A can be seen in Figures 5 and 6 while the force-tip displacement curve for Larson's specimen can be seen in Figure 7. Larson reported his results in this manner and the model results are presented similarly for consistency.

In the review of the FE models, von Mises stresses were examined in the shear tabs, beam web, and bolts. Materials were modelled as elastic perfectly plastic, so it was not possible to determine when or if members failed or fractured. Therefore engineering judgement was used to determine if a specific component failed in the modelling.

In the descriptions provided by Liu and Astaneh-Asl, both specimens 1A and 2A experienced "fracture of the tab after much slip and yielding" (2000). From the FE models large amounts of yielding began to occur in the shear tabs at rotations of approximately 67 and 58 milliradians (mrad), respectively. The amount of yielding present around the lower bolts in the connection at maximum rotations strongly indicated that material fracture would likely have occurred. Additionally, while not specifically stated by Liu and Astaneh-Asl, the FE modelling reproduced the bearing of the beam end on the column face at larger rotations in specimen 2A. This bearing between the members is the cause of the sharp stiffness increase in both the analytical and experimental results at 60 and 65 mrad respectively.

Larson did not mention any bolt or shear tab fractures during his testing. The FEM confirmed this with little to no yielding present in the shear tab or bolts even at maximum rotation.

Review of the initial stiffness of each model showed close agreement between two of the models and their experimental counterparts. Liu and Astaneh-Asl's specimen 1A and 2A were within 1.6% and 8.7% respectively. For Larson's specimen 1, the model predicted an initial stiffness 44% greater than the initial stiffness measured during the experiment. The large difference is ascribed to the uncertainty in the material and geometric parameters of that connection.
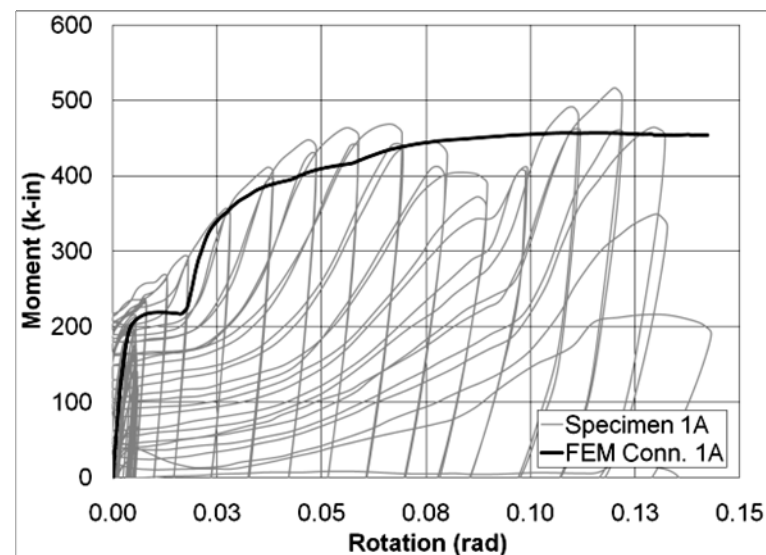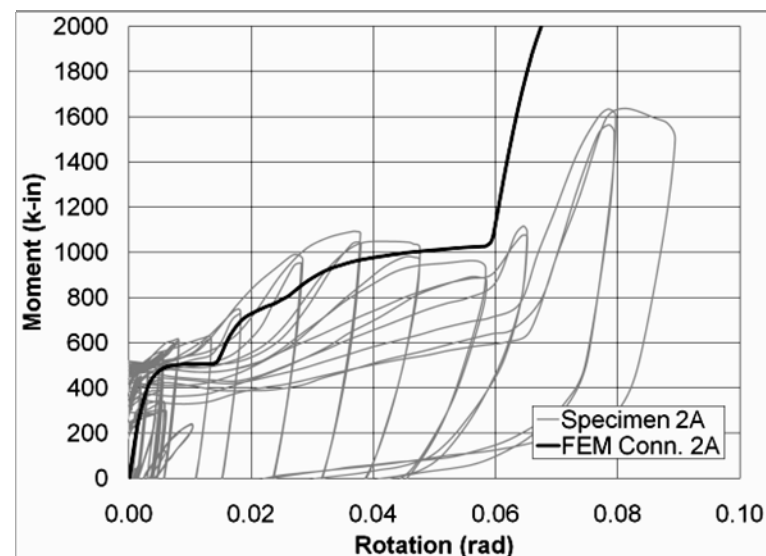


Figure 5. FEM Results: Liu Specimen 1A



Figure 6. FEM Results: Liu Specimen 2A
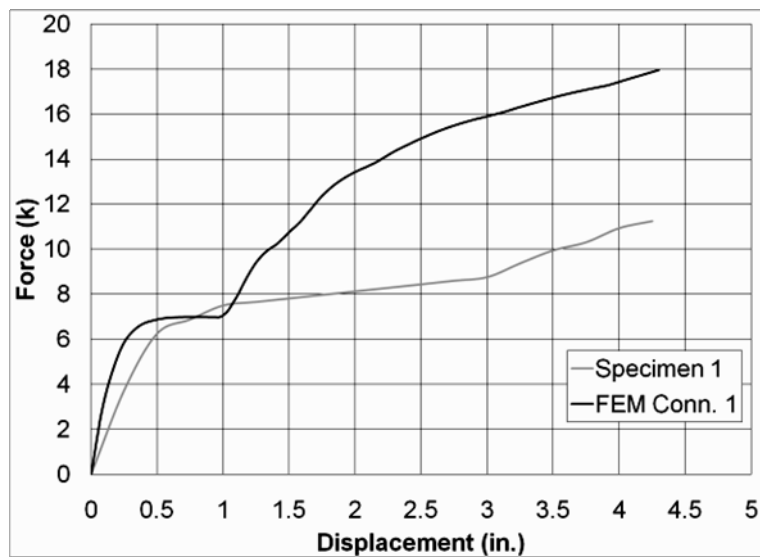
www.steelconstruct.com

Figure 7. FEM Results: Larson Specimen 1

The FEM of these connections revealed that this modelling technique can be very accurate at reproducing the results of experimental connections, provided that adequate information on materials and geometry are available. Once the physical properties of the experiment, such as member sizes, material properties, and physical constraints, are reproduced, the biggest factors affecting the results are the coefficient of friction and the amount of prestressing in the connection bolts.

## 4.2. Theoretical Models

Based on the information gained from the FEM of the experimental connections, theoretical connections were designed and modelled. These theoretical connections were intended to mimic the types of connections that would be present in current buildings.

### 4.2.1. Connection Design

The connections designed are part of a theoretical mid-rise building. The building is a five story office building with storage space on the lower floors, with one connection occurring in the office space and the other in the storage space. The floor loadings came from ASCE 7-10. The design of the beam and column members was based on the AISC Specification (2005b). The connections were also designed in accordance with AISC's conventional shear tab configuration, with checks for the following failure modes: bolt shear, block shear rupture, bolt bearing, shear tab yielding, shear tab rupture, and weld failure.

Table 2 summarizes the connections and their member sizes. Connection 1 supports the floor in the office space while connection 2 occurs in the storage space.

Table 2. Theoretical Connection Summary

| Conn. No. | Column | Beam | Shear Tab | Bolt | Connection Orientation |
|---|---|---|---|---|---|
| 1 | W10x45 | W24x76 | 12x4x1/2 | 3-7/8" dia. | Strong Axis |
| 2 | W12x79 | W27x94 | 12x4x1/2 | 4-7/8" dia. | Strong Axis |

### 4.2.2. Results

Using the information gained from the FEM of the experimental connections, several runs were performed on the designed theoretical connections. The friction coefficient used in these models was 0.275 and matched the average friction coefficient from the experimental models. The target rotation of the connections was 100 mrad.

The results of the FEM can be seen in Figure 8. The models predict bolt slippage occurring at rotations of 2.5-5 mrad. This matches the rotation amounts in both of the models based on Liu and Astaneh-Asl's connections. After the initial bolt slippage, the connections continue to resist loading until approximately 56 mrad. At this point a large increase in stiffness is observed, due to the beam flanges bearing on the column flange, cause large stresses in the connection.
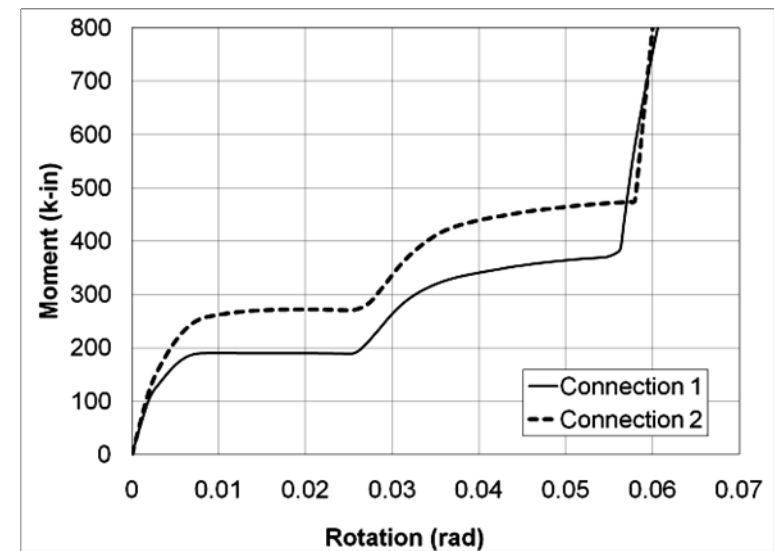


Figure 8. FEM Results: Theoretical Connections

During design, both theoretical connections were to be strong axis connections. In addition they were designed with a half inch of spacing between the beam end and the column flanges as recommended by AISC (2005a). This half inch of spacing is not sufficient to allow for the target rotation of the connection and the large stiffness increase is caused by the beam bearing on the column. The bearing of the beam on the column moves the neutral axis of the connection towards the bearing surface and places increased stresses on the bolts and shear tab at the other end of the

connection (Crocker, 2004). Analysis of the stresses in the shear tab at the full target rotation reveal that in a real experiment, the shear tab would likely have fractured, similar to the fractures seen in both of Liu and Astaneh-Asl's tests

## 5. CONCLUSIONS

The ETABS analyses of Liu, Astaneh-Asl, and Larson's connections have shown that the lateral stiffness of the simple connections can greatly add to the lateral stiffness of the resisting system. The addition of these PR shear connections to the building analysis can reduce inter-story drift by almost 22% when compared to the results of an analysis with assumptions of perfectly pinned simple connections, while reducing the moment experienced by the beams in the lateral resisting system.

The creation of ABAQUS FE models representing Liu, Astaneh-Asl, and Larson's experimental connections has also shown that FE modelling is able to accurately reproduce the results of experimental testing. All models were able to predict the onset of bolt slippage in addition to connection specific events. These events included the bearing of the beam on the column in Liu and Astaneh-Asl's specimen 2A, as well as the lack of shear tab yielding or fracture in Liu's specimen 1. The FE models were also able to very closely match the initial stiffness of both Liu and Astaneh-Asl's connections.

The accuracy with which the FEM was able to reproduce the experimental connections shows that it can be a valid technique for finding the response of other theoretical connections, provided that sufficient information on materials and geometry are known. Connection characteristics such as bolt slippage, initial stiffness, and bearing between connected elements can all be predicted by FEM. This allows for the possibility for future researchers to explore their theories before pursuing expensive and time-intensive full scale experimentation.

## REFERENCES

[1] American Institute of Steel Construction (AISC) (2005a). *ANSI/AISC 360-05: Specification for Structural Steel Buildings*, 13th Ed., American Institute of Steel Construction

[2] American Institute of Steel Construction (AISC) (2005b). *ANSI/AISC 341-05: Seismic Provisions for Structural Steel Buildings*, American Institute of Steel Construction

[3] American Society of Civil Engineers (AISC) (2010). *ASCE/SEI 7-10 Minimum Design Loads for Buildings and Other Structures*, American Society of Civil Engineers

[4] Computers &Structures, Inc.. "CSI Analysis Reference Manual for SAP2000, ETABS, and SAFE." <http://www.comp-engineering.com/downloads/manual/SAFE/SafeManuals/CSI%20Analysis%20Reference.pdf> (December 17, 2010)

[5] Crocker, J.P. and Chambers, J.J. (2004). "Single Plate Shear Connections Response To Rotation Demands Imposed by Frames Undergoing Cyclic Later Displacements," *Journal Of Structural Engineering*, vol. 130(6), (pp. 934-941)

[6] Englehardt, M.D., et al., (1994) "Northridge update I" American Institute of Steel Construction, Chicago, IL

[7] Jones, S.W., Kirby, P.A., and Nethercot, D.A. (1983). "The Analysis of Frames with Semi-Rigid Connections a State-of-the-Art Report," *Journal of Constructional Steel Research*, vol. 3(2), (pp. 2-13)

[8] Larson, P.C. (1996) "The Design and Behavior of Bolted Beam-to-Column Frame Connections Under Cyclical Loading," M.S. thesis, Univ. of Texas, Austin, TX

[9] Liu, J., and Astaneh-Asl, A., (2000). "Cyclic Testing of Simple Connections Including Effects of Slab," *Journal of Structural Engineering*, vol. 129(1), (pp. 32-39)

[10] Ruffley, D.J. (2011) "A Finite-Element Approach for Modeling Top-and-Seat Angle Components and Moment Connections," M.S. thesis, Univ. of Cincinnati, Cincinnati, OH

[11] Structural Stability Research Council (SSRC) Task Group 6 (1998). "Technical Memorandum No. 8: Standard Methods And Definitions For Tests For Static Yield Stress," John Wiley & Sons, Inc, 5th Edition

# INNOVATIVE BOLTED BEAM-TO-COLUMN JOINTS FOR SEISMIC RESISTANT BUILDING FRAMES

Ludivine Comeliau; Jean-François Demonceau; Jean-Pierre Jaspart
*ArGEnCo Department, University of Liège, Belgium*
*Ludivine.comeliau @ulg.ac.be; jfdemonceau@ulg.ac.be*;
*jean-pierre.jaspart@ulg.ac.be*

## ABSTRACT

In the present paper, innovative joint configurations leading to more economical solutions for full-strength beam-to-column joints for seismic building frames are detailed. The specificities of these joints are due to the fact that (i) the column is made of high strength steel while the beam are made of mild carbon steel and (ii) the design of some components allows partially neglecting the overstrength factor. Also, methods for the characterisation of specific joint components not directly covered by the Eurocode recommendations are proposed.

## 1. INTRODUCTION

According to Eurocode 8, earthquake resistant steel building frames shall be designed following either the "low dissipative structural behaviour concept" or the "dissipative structural behaviour concept". In the second concept, the ability of parts of the structure to resist earthquake actions through inelastic behaviour is taken into account: energy is dissipated in plastic mechanisms. In such a design, it has to be ensured that the dissipative zones form where they are intended to and that they yield before other zones leave the elastic range. In particular, moment resisting frames are designed in such a way that plastic hinges develop at the extremities of the beams. These dissipative zones can be located either in the beams or in the beam-to-column joints. In this paper, non-dissipative bolted beam-to-column connections are considered. They must be sufficiently resistant to remain in elastic range while cyclic yielding develops in the dissipative zones located in the beams. Besides, the possibility that the actual yield strength of the beam is higher than the nominal value has to be taken into account by a material overstrength factor. Such an approach generally leads to very strong and thus expensive joints.

In the present paper, a design strategy leading to more economical solutions for full-strength beam-to-column joints is detailed. This study is conducted within the framework of an RFCS project called HSS-SERF (High Strength Steel in Seismic Resistant Building Frames). The considered moment-resisting joints are part of seismic-resistant building frames made of high strength steel composite columns and mild carbon steel beams. The columns are either partially-encased wide-flange columns (H columns) or concrete-filled rectangular hollow-section columns (RHS columns).

The proposed joint configuration uses hammer-heads extracted from the beam profile. To fulfil the resistance requirement taking account of the possible overstrength of the beam, the resistant moment of the joint is decomposed in the contributions of the different components involved. Then, no overstrength factor needs to be considered for the components related to the beam itself and to the hammer-heads. This approach is in full accordance with the basic principles of Eurocode 8 and can decrease much the required resistance of the joints provided some conditions are fulfilled, meaning lower costs.

Also, the chosen joint configurations involved joint components not directly covered by the Eurocode recommendations. Methods for the characterisation of these components are proposed and discussed within the present paper.

## 2. PROPOSED JOINT CONFIGURATIONS

### 2.1. Wide-flange column

In the present approach, the joints are designed to be non-dissipative, which means they have to be full-strength in such a way that the plastic hinge at a beam extremity will form in the beam itself while the joint remains elastic. Besides, the possible overstrength of the beam material has to be taken into account. This approach thus leads to very strong joints.

The proposed joint configuration when partially-encased H columns are used is represented in Figure 1. Hammer-heads and lateral plates welded from one flange to the other both sides of the column at the joint level are required to ensure a sufficient joint resistant moment. The hammer-heads have the effect of increasing the lever arm between the compression and tension forces within the joint and of reinforcing the end-plate submitted to bending. The lateral plates act as reinforcement for the following components: the column web panel in shear, the column flange in bending, the column web in tension and the column web in compression.
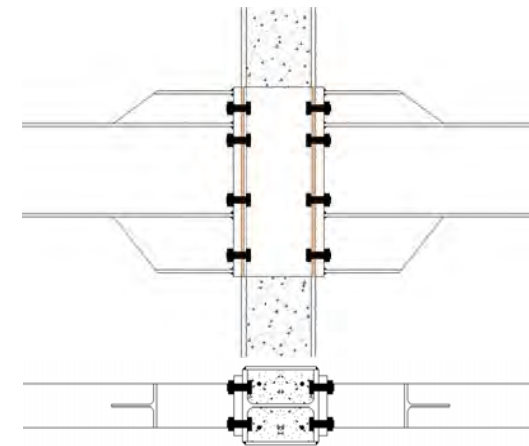


Figure 1. Joint configuration for a H column

In order to design as economical as possible full-strength joints fulfilling the resistance requirements of Eurocode 8 for non-dissipative connections, the hammer-heads have to be extracted from the same profile as the beam. The reason why this is important is explained in section 3.

The selection of this joint configuration results from a long process in which several other designs were investigated and appeared to be unsuitable, as explained in [4]. Two particular joints designed for the project HSS-SERF using the chosen configuration are also detailed in that document.

## 2.2. Rectangular hollow-section column

For concrete-filled RHS columns, the following joint configuration is proposed (Figure 2), in which the beam is fixed to the column via a U-shaped piece welded to the RHS column side walls. The bolted connection between the beam end-plate and the U front face is similar to the one proposed in 2.1 for H columns, and hammer-heads extracted from the beam profile are used.

This joint configuration as well as two particular joints designed for the project HSS-SERF are described in [5].
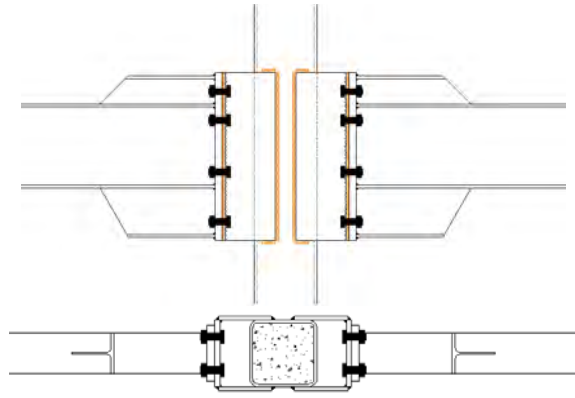


Figure 2. Joint configuration for a RHS column

## 3. DESIGN STRATEGY

In case of a seismic design in which it has to be ensured that the plastic hinges appear in the beams and not in the joints, the latter have to be over-resistant compared to the beams, taking account of the possible overstrength of the beams. Indeed, the actual resistance of the beam material may be higher than its nominal value. Accordingly, the following check has to be fulfilled (EN 1998-1 6.5.5 (3)):

$$M_{\text{Rd,joint}} > 1,1 \cdot \gamma_{ov} \cdot M_{pl,beam} \qquad (1)$$

Eurocode 8 suggests that the overstrength factor $\gamma_{ov}$ be considered equal to 1,25.

Actually, this inequality is only valid provided the plastic hinge forms just next to the column flange so that the joint is subjected to approximately $M_{pl,beam}$. But it will not be the case for the joint configurations that are under consideration here due to the hammer-heads reinforcing the beam in the vicinity of the joint. Consequently, it has to be taken into account that the moment in the joint is greater than the one acting in the beam cross section after the hammer-heads, where the plastic hinge is meant to appear (see Figure 3).

So, when the plastic hinge forms in the beam, the moment the joint is subjected to is greater than $M_{pl,beam}$. Then, in Eq.(1), "$M_{pl,beam}$" should be replaced by the moment $M_{\text{j - pl hinge in beam}}$ acting in the joint when the plastic hinge has formed in the beam section after the hammer-heads:

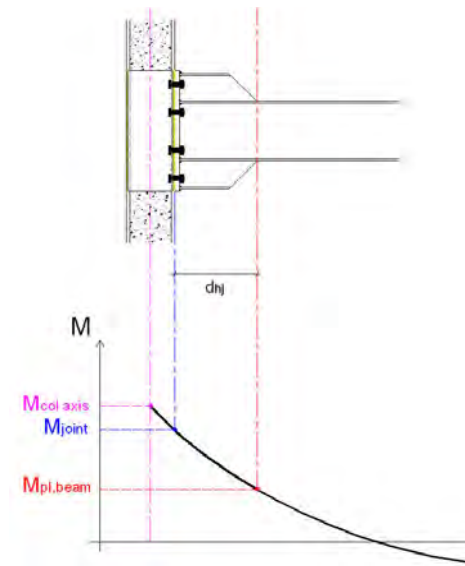$$M_{\text{Rd,joint}} > 1,1 \cdot \gamma_{ov} \cdot M_{\text{j - pl hinge in beam}} \qquad (2)$$



Figure 3. Moment in the joint and at the column axis when the plastic hinge appears in the beam section after the hammer heads

$M_{\text{j - pl hinge in beam}}$ is computed as follows as far as seismic circumstances are concerned (see Figure 4):

- maximum hogging moment in the joint:

$$M_{\text{j - pl hinge in beam,HOG}} = M_{pl,beam} + V_1 \cdot d_{hj} + p_{\max} \cdot \frac{d_{hj}^2}{2} \text{ , with}$$

$$V_1 = \frac{2 \cdot M_{pl,beam}}{l} + \frac{p_{\max} \cdot l}{2} \qquad (3)$$

- maximum sagging moment in the joint:

$$M_{\text{j - pl hinge in beam,SAG}} = M_{pl,beam} + V_2 \cdot d_{hj} - p_{\min} \cdot \frac{d_{hj}^2}{2} \text{ , with}$$

$$V_2 = \frac{2 \cdot M_{pl,beam}}{l} - \frac{p_{\min} \cdot l}{2} \qquad (4)$$

where:

- $M_{pl,beam}$ is the plastic moment of the beam cross section (based on the nominal value of the yield stress)
- $V_1$ is the shear force in the beam cross section after the hammer-heads when the plastic hinge appears, next to the joint subjected to hogging moment
- $V_2$ is the shear force in the beam cross section after the hammer-heads when the plastic hinge appears, next to the joint subjected to sagging moment
- $d_{hj}$ is the distance between the plastic hinge and the joint connection
- $l$ is the distance between the two plastic hinges developing at the extremities of the beam
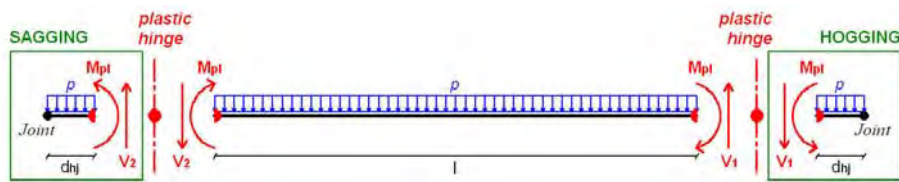
Figure 4. Internal forces at the beam extremities once plastic hinges have formed under seismic actions

Actually, the inequality of Eq. (2) is not totally right because, as shown in Eqs. (3) and (4); $M_{\text{j - pl hinge in beam}}$ does not only depend on the mechanical characteristics of the beam, but also on the external loads and there is no reason why the overstrength factor should multiply these loads. Consequently, using Eqs. (3) and (4) in Eq. (2)) and applying the overstrength factor only to the terms which are related to the beam material strength, the resistance requirements for the joint become:

$$M_{\text{Rd,joint,HOG}} > M_{pl,beam} \cdot 1,1 \cdot \gamma_{ov} +$$

$$+ \left( \frac{2 \cdot M_{pl,beam} \cdot 1,1 \cdot \gamma_{ov}}{l} + \frac{p_{\max} \cdot l}{2} \right) \cdot d_{hj} + p_{\max} \cdot \frac{d_{hj}^2}{2} \quad (5)$$

$$M_{\text{Rd,joint,SAG}} > M_{pl,beam} \cdot 1,1 \cdot \gamma_{ov} +$$

$$+ \left( \frac{2 \cdot M_{pl,beam} \cdot 1,1 \cdot \gamma_{ov}}{l} - \frac{p_{\min} \cdot l}{2} \right) \cdot d_{hj} - p_{\min} \cdot \frac{d_{hj}^2}{2} \quad (6)$$

The bending resistance of the joint is calculated using the component method in accordance with EN 1993-1-8. The resistant moment of the joint depends on the resistance of the different components involved. Amongst them, the component "beam web in tension" is part of the beam itself and so, obviously, no overstrength factor has to be taken into account to determine the required resistance of this component. If the hammer-heads are made from the same profile as the beam, then the same remark applies for the corresponding components ("hammer-head flange and web in compression", "hammer-head web in tension" and "hammer-head web in shear"). Indeed, if the yield stress of the beam material is higher than its nominal value considered in the computation of $M_{pl,beam}$, then the resistance of these four components will automatically increase in the same way.

To be able to take this beneficial effect into account, the resistant moment of the joint has to be decomposed into the contributions of the different components in Eqs. (5) and (6). The resistant moment of the joint is:

$$M_{\text{Rd,joint}} = \sum_{\text{rows} \, r} F_{Rd,r} \cdot h_r \quad (7)$$

where:

- $F_{Rd,r} = \min_{\text{components} \, k} \{ F_{Rd,r,k} \}$ is the resistance of row "r"

- $F_{Rd,r,k}$ is the resistance of component "k" in row "r"

- $h_r$ is the vertical distance from row "r" to the compression centre

Consequently, defining a "reduced" resistant moment as:

$$M_{\text{Rd,j,REDUCED}} = \frac{M_{Rd,\text{joint}}}{1,1 \cdot \gamma_{ov}} \quad (8)$$

It comes:

$$M_{\text{Rd,j,REDUCED}} = \sum_{\text{rows} \, r} \frac{F_{Rd,r}}{\gamma_{ov}} \cdot \frac{h_r}{1,1} \quad (9)$$

with:

$$\frac{F_{Rd,r}}{\gamma_{ov}} = \min_{k} \left\{ \frac{F_{Rd,r,k}}{\gamma_{ov,k}} \right\} \quad (10)$$

where the overstrength factor associated to component "$k$", $\gamma_{ov,k}$ , depends on the considered component (i.e. it is equal to 1,0 for the components related to the beam or to the hammer-heads if they are made from the same profile as the beam, and to 1,25 for the other components). Then a reduced resistance can be computed for each component using the proper value of the overstrength factor; and the reduced resistant moment of the connection is deduced from the reduced resistances of the different components involved.

Finally, the inequalities to fulfil are the following ones, for hogging and sagging moment respectively:

$$M_{\text{Rd,j,REDUCED,HOG}} > M_{pl,beam} + \left( \frac{2 \cdot M_{pl,beam}}{l} + \frac{p_{\max} \cdot l}{2 \cdot 1,1 \cdot \gamma_{ov}} \right) \cdot d_{hj} + \frac{p_{\max} \cdot d_{hj}^2}{2 \cdot 1,1 \cdot \gamma_{ov}} \quad (11)$$

where $\gamma_{ov}$ is taken equal to 1,0 (safe side); and

$$M_{\text{Rd,j,REDUCED,SAG}} > M_{pl,beam} + \left( \frac{2 \cdot M_{pl,beam}}{l} - \frac{p_{\min} \cdot l}{2 \cdot 1,1 \cdot \gamma_{ov}} \right) \cdot d_{hj} - \frac{p_{\min} \cdot d_{hj}^2}{2 \cdot 1,1 \cdot \gamma_{ov}} \quad (12)$$

in which $\gamma_{ov}$ is taken equal to 1,25 (safe side).

It is also important to note that, as far as the resistance check of the component "column panel in shear" is concerned, the possible overstrength of the beam has not to be taken into account according to Eurocode 8. Consequently, the inequality to fulfil is simply:

$$V_{\text{wp,Rd}} \geq V_{\text{wp,Ed}} \quad (13)$$

where:

- the resistance of the column panel in shear $V_{wp,Rd}$ is computed according to EN 1993-1-8 6.2.6.1 and EN 1994-1-1 8.4.4.1, taking also account of the prescriptions of Eurocode 8 regarding the resistance of the column panel in shear in composite columns (EN 1998-1 7.5.4 (3));

- the shear force the column panel is subjected to is $V_{wp,Ed} = \beta \cdot M_{col \, \text{axis,Ed}} / z$ (EN 1993-1-8 5.3), where $M_{col \, \text{axis,Ed}}$ is the moment applied to the considered joint, computed at the intersection of the beam and the column centrelines (Figure 3), and $z$ is the forces lever arm.

www.steelconstruct.com

# 4. COMPUTATION OF THE COMPONENT RESISTANCES

Both joint configurations introduced in Section 2 have the same "beam-part" which includes the beam itself, the hammer-heads and the end-plate. The corresponding components are exactly the same in both cases: end-plate in bending (see 4.1), hammer-head flange and web in compression (4.2), beam-web in tension (4.3), hammer-head web in tension (4.4), bolts in tension (4.5) and hammer-head in shear (4.6). The other components are specific to the column which is used. For the wide-flange column: column panel in shear (4.7), column in transverse compression (4.8), column flange in bending (4.9), column web in tension (4.10). And for the rectangular hollow-section column: column panel in shear (4.11), lateral faces of the U in transverse compression (4.12), front face of the U in transverse bending (4.13), lateral faces of the U in transverse tension (4.14).

Amongst all these components, some are directly covered by the Eurocode [2] or very similar to components directly covered in such a way the corresponding formulae can be extended. On the other hand, some components are not covered by [2] and need particular attention. All the components are listed below and explanations on how their resistances can be evaluated are given.

## 4.1. End-plate in bending

The case of bolt rows 2 and 3 (between the beam flanges) is covered by EN 1993-1-8, §6.2.6.5. The case of the first bolt row is particular because it is between the beam flange and the hammer-head flange. This situation is similar to the case where there is an intermediate stiffener between bolt rows. This problem is addressed in [7], section 3.2.1.3.

## 4.2. Hammer-head flange and web in compression

The resistance of this component is computed on the basis of EN 1993-1-8, §6.2.6.7. It is given by:

$$F_{Rd,6} = \frac{M_{c,Rd}}{h_b + h_1 + h_2 - t_{fh}}$$

where $M_{c,Rd}$ is the design moment resistance of the cross-section including the beam and the hammer-heads, neglecting the beam flanges; $h_b$ is the beam height; $h_1$ and $h_2$ are the heights of the upper and lower hammer-heads respectively.

## 4.3. Beam-web in tension

This component is covered by EN 1993-1-8, §6.2.6.8.

## 4.4. Hammer-head web in tension

This component is computed exactly the same way as the beam web in tension as recommended in EN 1993-1-8.

## 4.5. Bolts in tension

This component is covered by the Eurocode.

## 4.6. Hammer-head in shear

The compression force acting in the hammer-head flange and web has to be transferred to the beam, essentially by shear. However, when the shear resistance of the hammer-head web is reached, the system can still resist, until the flexural

mechanism represented at Figure 5 below is formed. The component named here "hammer-head in shear" actually involves both the hammer-head web in shear and the end-plate and the hammer-head flange in bending. Its resistance is evaluated by:

$$F_{Rd} = P_{pl} + F_{shear}$$

where $F_{shear}$ is the plastic shear resistance of the hammer-head web, and $P_{pl}$ is the force corresponding to the formation of the two plastic hinges (once the hammer-head web is already yielded).
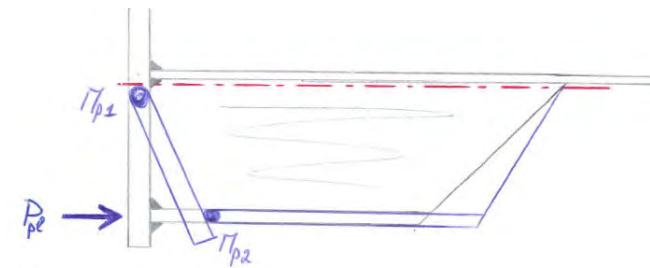


Figure 5. Plastic flexural mechanism including the end-plate and the hammer-head flange

## 4.7. Column panel in shear (for wide-flange column)

The resistance of the column panel in shear is computed considering the contributions of the steel profile web, the encasing concrete and the lateral plates, taking also account of the prescriptions of Eurocode 8 regarding the resistance of the column panel in shear in composite columns (EN 1998-1, §7.5.4 (3)).

The contribution of the steel profile web is covered by EN1993-1-8, §6.2.6.1 while the contribution of the encasing concrete is dealt with in EN1994-1-1, §8.4.4.1. The contribution of the lateral plates is evaluated the same way as the profile web (the formula given in EN1993-1-8 6.2.6.1 can easily be extended).

## 4.8. Column in transverse compression (for wide-flange column)

The resistance of the column in transverse compression includes the contribution of the steel profile web (covered by EN1993-1-8 6.2.6.2) and the contribution of the encased concrete (EN1994-1-1 8.4.4.2). No contribution of the lateral plates is considered (safe side).

## 4.9. Column flange in bending (for wide-flange column)

The column cross section made up of the H-profile and the lateral plates is equivalent to two hollow sections next to each other. Then, the formulae related to a face of a rectangular hollow cross section in transverse tension are used. These formulae are detailed in [8]. They correspond to those developed in [7], section 3.3, for minor axis beam-to-column joints.

## 4.10. Column web in tension (for wide-flange column)

Both the steel profile web and the lateral plates contribute to the resistance of this component. The resistance of the profile web is given in EN1993-1-8, §6.2.6.3. The formula can easily be extended to evaluate the resistance of the lateral plates in a similar way.

## 4.11. Column panel in shear (for RHS column)

The resistance of the column panel in shear is computed considering the contributions of the steel column webs and the U lateral faces (the contribution of the encased concrete is neglected, which is on the safe side). The resistance of the column webs and the U side faces is computed extending the formula given in EN1993-1-8, §6.2.6.1 for the web of a wide-flange column.

## 4.12. Lateral faces of the U in transverse compression (for RHS column)

The resistance of the U lateral faces in transverse compression can be evaluated based on EN1993-1-8, §6.2.6.2 which gives the resistance of a wide-flange column web in transverse compression. Indeed, the formula can be easily adapted.

## 4.13. Front face of the U in transverse bending (for RHS column)

The formulae related to a face of a rectangular hollow cross section in transverse tension are used to compute the resistance of the U front face in bending. These formulae are detailed in [8]. They correspond to those developed in [7], section 3.3, for minor axis beam-to-column joints. Three possible local failure modes are considered: flexural mechanism, punching shear mechanism and combined flexural and punching shear mechanism.

As the length of the U above or below the tension or compression zone is quite short, the possibility of an "edge" flexural mechanism (Figure 6) has to be taken into account for the compression zone as well as for the tension zone if row 1 is involved. No formula exists for a combined flexural and punching shear "edge" mechanism; so this effect couldn't be taken into account.
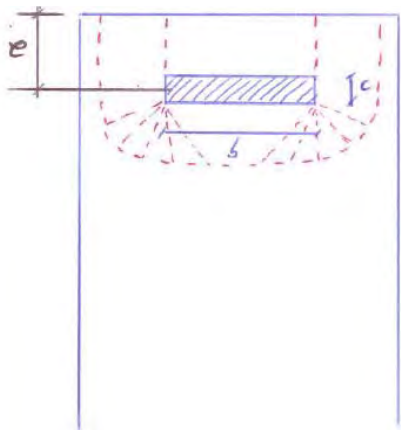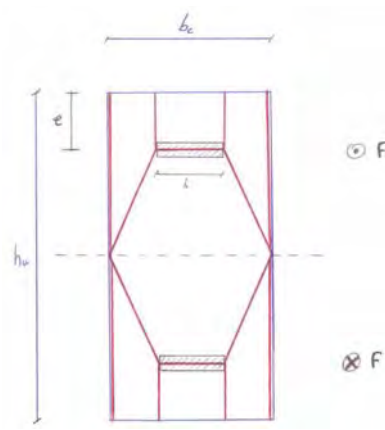


Figure 6. *Edge mechanism*



Figure 7. *Global mechanism*

Besides, the possibility of a global failure mechanism involving both the tension and the compression zones has also to be considered (Figure 7).

## 4.14. Lateral faces of the U in transverse tension (for RHS column)

The formula given in EN1993-1-8, §6.2.6.3 for the resistance of a wide-flange profile web in transverse tension can easily be extended to evaluate the resistance of the U lateral faces in a similar way.

## 5. CONCLUSIONS AND GENERAL RECOMMENDATIONS

Moment resisting frames designed according to the "dissipative structural behaviour concept" of Eurocode 8 have to dissipate seismic energy through cyclic yielding of plastic hinges located at the extremities of the beams. These dissipative zones can be either part of the beams or the beam-to-column joints. If the connections are meant to be non-dissipative and thus to remain in elastic range while plastic hinges develop in the beams next to the joints, they have to be full-strength, taking account of the possible overstrength of the beam material. This requirement customarily leads to very strong and expensive joints.

In this paper, particular joint configurations were proposed for such non-dissipative bolted joints, associated with a design strategy which can reduce the joint costs while in full accordance with both Eurocode 8 and the component method. The proposed design procedure is based on the principle that no overstrength factor needs to be taken into account for components that are part of the beam itself or of an element which is extracted from the same profile (e.g. the hammer-heads in the considered joint configuration). This method permits the use of a particular value of the overstrength factor for each component, through the concept of reduced resistance. Extending the fundamental principles of Eurocode 8, the proposed design procedure leads to less severe resistance requirements. Consequently, less strong and thus less expensive joints can be used provided they are designed in such a way that the weakest component, causing the failure of the connection (in terms of full resistance), is part of the beam itself or of an element extracted from the beam profile (for which the overstrength factor can be taken equal to 1,0).

### REFERENCES

[1] EN 1998-1:2004. *Eurocode 8: Design of structures for earthquake resistance – Part 1: General rules, seismic actions and rules for buildings*, European Standard, CEN, Brussels.
[2] EN 1993-1-8:2005. *Eurocode 3: Design of steel structures – Part 1-8: Design of joints*, European Standard, CEN, Brussels.
[3] EN 1994-1-1:2004. *Eurocode 4: Design of composite steel and concrete structures – Part 1-1: General rules and rules for buildings*, European Standard, CEN, Brussels.
[4] Comeliau L., Demonceau J.-F. and Jaspart J.-P., "hss-tn-0001-wp1-ulg-v3_Joint design - H column", internal report for the RFCS project HSS-SERF, Liège, 2010.
[5] Comeliau L., Demonceau J.-F. and Jaspart J.-P., "hss-tn-0007-wp1-ulg-v2_Joint design - RHS column with U", internal report for the RFCS project HSS-SERF, Liège, 2010.
[6] Comeliau L., Demonceau J.-F. and Jaspart J.-P., "hss-tn-0003-wp1-ulg-v1_Joint design - computation note Joint A - H case 1", internal report for the RFCS project HSS-SERF, Liège, 2010.
[7] Jaspart J.-P., "Recent advances in the field of steel joints – Column bases and further configurations for beam-to-column joints and beam splices", 1997.
[8] CIDECT Research Project 5BP, Draft final report – Volume 1, 2005.

# DESIGN AND BEHAVIOR OF POST-TENSIONED COLUMN BASES FOR SELF-CENTERING MOMENT RESISTING FRAMES

Hoseok Chi
*School of Civil Engineering, Purdue University, West Lafayette, IN, USA*
*hchi@purdue.edu*

Judy Liu
*School of Civil Engineering, Purdue University, West Lafayette, IN, USA*
*jliu@purdue.edu*

## ABSTRACT

A column base connection was developed for use in steel self-centering moment resisting frames (SC-MRFs). SC-MRFs exhibit negligible residual drift after a seismic event, and damage is limited to replaceable fuse elements. Self-centering behavior is achieved in the column base connection through the use of post-tensioned (PT) bars. The PT bars provide the restoring force in a connection for which the softening behavior is provided by gap opening rather than plastic hinging. The fuse elements in the column base are buckling-restrained steel (BRS) plates, which dissipate energy through yielding.

Large-scale tests on PT column base specimens have demonstrated the ability of the column to self-center with damage limited to the yielding BRS plates. Test parameters included initial post-tension force, initial axial force in the column and column size. Design equations for the PT column base were validated by and further refined based on the test results.

## 1. INTRODUCTION

Steel self-centering moment resisting frames (SC-MRFs) using post-tensioned (PT) beam-column connections have been developed to eliminate structural damage after earthquakes (Ricles et al. (2001, 2002), Christopoulos et al. (2002), Garlock et al. (2005, 2007)). The SC-MRF has the potential to return to its original position, or self-center, after earthquakes. However, the column bases in SC-MRFs may suffer structural damage due to inelastic deformations after earthquakes; this damage, in turn, may affect the self-centering capability of the frame. In order to overcome these issues, a post-tensioned connection was introduced at column bases for use in SC-MRFs (Chi, 2009). The schematic view of an SC-MRF with PT column base connections is shown in Figure 1. The PT connection consists of high strength PT bars (Dywidag bars), buckling restrained steel (BRS) plates, reinforcing plates, shim plates and Keeper plates. The PT column base is similar to the PT beam-column

connection in that the softening behavior is achieved through gap-opening at the column-grade beam interface rather than yielding in the column. The PT bars provide clamping force to connect columns and beams, and restoring force to close the gaps occurring at the interface of the column and grade beam.

As shown in Figure 1, the PT bars are anchored at mid-height of the first story column and near the bottom of the basement column. Anchorage locations were chosen to avoid congestion with connection details at PT beam-column joints in stories above. Furthermore, the design required sufficient PT bar length to avoid reaching yield and fracture strains even for the gap opening deformations in a Maximum Considered Earthquake (MCE). Location of the PT bar anchorage within the first story was also deliberately chosen so that axial demands from the bars would not compound flexural demands at the top of the first story and lead to plastic hinging.

Figure 2 shows the PT bars and other column base components. Dog-bone shaped BRS plates provide energy dissipation by yielding of a reduced section in tension and compression. Damage in the PT column base connection occurs only in the replaceable BRS plates. Bolted, T-shaped cover plates are used to prevent buckling (i.e., strong axis and weak axis inelastic buckling) of the BRS plates.

The BRS plate and Keeper plate are joined by complete joint penetration (CJP) welding to form one unit. The BRS-Keeper plate unit is bolted to the columns and grade beams. Keeper plates provide additional shear resistance through the slip-critical bolted connection. Meanwhile, the Keeper plates are bevelled at the connection with the BRS plate to allow rotation of the column.

Reinforcing plates provide additional contact area during gap opening. Therefore, bearing stresses in the column flanges can be reduced for strong and weak axis bending. Shim plates are used to fill any gaps between BRS plates and column flanges providing more restraint when the BRS plates are in compression. Shim plates are also used between columns and grade beams to prevent contact with the column web. Meanwhile, large slotted holes in the grade beam flanges are designed to permit lateral movement of the PT bars with gap opening without binding, or 'kinking', of the bars.
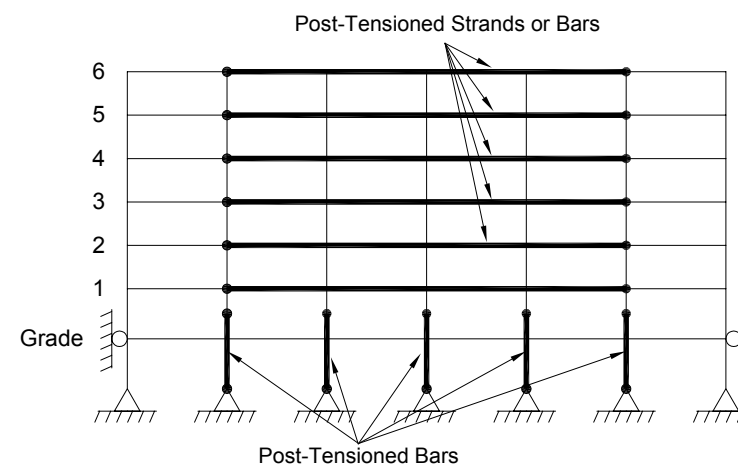


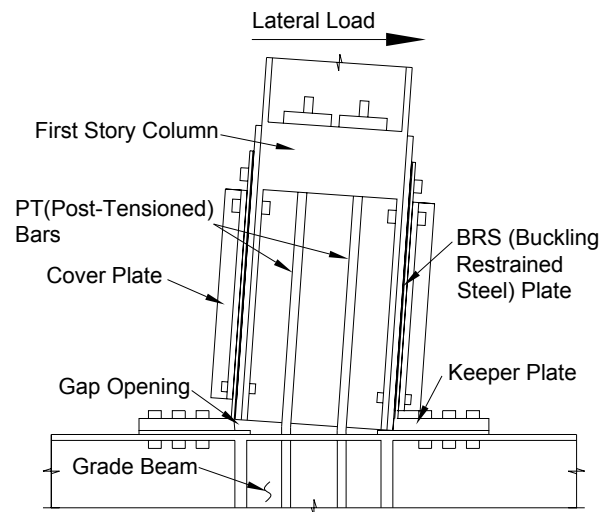Figure 1. Schematic view of SC-MRF with PT Column Bases

Figure 2. Configuration of PT column base connection

## 2. DESIGN AND BEHAVIOR OF PT COLUMN BASE CONNECTION

### 2.1. Moment-Rotation Relationship

The moment-rotation response of the PT column base connection has the characteristic 'flag-shaped' hysteresis of PT connections which have gap opening behavior and energy dissipating elements. When the column moment at the column base overcomes the moment resistance provided by initial PT force and axial force in columns, the connection decompresses, or a gap opening at column-grade beam interface begins to occur. After decompression, the column rotates about the contact surface in column flanges creating relative rotation at column-grade beam interface. As the gap opening increases due to applied moment, the PT bars and BRS plates begin to deform. The PT bars elongate, whereas one of the BRS plates elongates and the other plate shortens. After the decompression occurs, additional axial force from the PT bars as well as BRS plates is developed in the PT column base connection, providing additional moment resistance. As the gap opening increases further, the BRS plates yield. The stiffness of the PT column base connection after decompression is associated with the axial stiffness of the PT bars as well as the axial stiffness of the BRS plates. After the BRS plates form a plastic yielding zone, the stiffness of the connection depends mostly on the axial stiffness of the PT bars. When unloaded, the elastic PT bars provide a restoring force and the gap opening closes, or self-centers, without residual relative rotation.

The design basis earthquake (DBE) connection moment ($M_{DBE\_col(in)}$) is equal to the sum of the moment from the initial PT force ($\Delta M_{PTforce}$), moment from the initial axial force in column ($\Delta M_{axial}$), moment contribution from the tension BRS plate ($\Delta M_{BRS}$) and moment from the PT force due to PT bar elongation ($\Delta M_{PT}$) at the relative rotation of $\theta_{r\_col(DBE)}$. The center of rotation (COR) is at the column

flange in compression. The connection moment ($M_{DBE\_col(in)}$) at the relative rotation of $\theta_{r\_col(DBE)}$ is expressed as

$$M_{DBE\_col(in)} = \Delta M_{PTforce} + \Delta M_{axial} + \Delta M_{BRS} + \Delta M_{PT} \tag{1}$$

The moment contribution of the initial PT force in column ($\Delta M_{PTforce}$) at the relative rotation of $\theta_{r\_col(DBE)}$ is estimated as

$$\Delta M_{PTforce} = T_i(d_{2\_col} - h_{anchor}\sin(\theta_{r\_col(DBE)})) \tag{2}$$

where, $T_i$ = initial PT force after jacking loss

$d_{2\_col}$ = distance between COR and centroid of the column before decompression

$h_{anchor}$ = distance between the column-grade beam interface and top anchorage of PT bar

The moment contribution of the initial axial force in column ($\Delta M_{axial}$) at the relative rotation of $\theta_{r\_col(DBE)}$ is estimated as

$$\Delta M_{axial} = P_i(d_{2\_col} - h_{col}\sin(\theta_{r\_col(DBE)})) \tag{3}$$

where,

$P_i$ = initial axial force in column

$h_{col}$ = clear length of first story column

The total moment contribution of the tension BRS plate ($\Delta M_{BRS}$) at the relative rotation of $\theta_{r\_col(DBE)}$ is estimated as

$$\Delta M_{BRS} = F_{BRS\_y}d_{3\_col} + K_{BRS\_p}(\theta_{r\_col(DBE)}d_{3\_col} - \frac{F_{BRS\_y}}{K_{BRS\_i}})d_{3\_col} \tag{3}$$

where,

$K_{BRS\_i}$ = elastic stiffness of the BRS plate

$K_{BRS\_p}$ = post-yield stiffness of the BRS plate

$F_{BRS\_y}$ = yield force of the BRS plate

$d_{3\_col}$ = distance between the center of rotation and the centerline of BRS plate

The moment contribution of the additional axial force due to PT bar elongation ($\Delta M_{PT}$) at the relative rotation of $\theta_{r\_col(DBE)}$ is estimated as

$$\Delta M_{PT} = (K_{PT})(d_{2\_col} - h_{anchor}\sin(\theta_{r\_col(DBE)}))^2\theta_{r\_col(DBE)} \tag{4}$$

where,

$K_{PT}$ = axial stiffness of the PT bars

## 2.2. Shear resistance

The main contributor to shear capacity of the connection ($V_{col}$) is the friction force resulting from the axial force of the column at the column-grade beam interface ($V_f$). The friction force on the contact surface (i.e., column-grade beam interface) is associated with the axial force developed in the first story column as well as the static friction coefficient of steel. Additional shear resistance ($V_k$) is provided by the Keeper plates. The Keeper plates are bolted (i.e., slip critical connection) to the grade beam flanges, and friction resistance is also developed between Keeper plates and grade beam flanges. Therefore, when the shear demand exceeds $V_f$, the column flange bears against the Keeper plate, and the shear demand is transferred to the grade beam flange by friction.

The total axial force in a column ($P_{col}$) is determined by (1) initial PT force ($T_i$), (2) additional PT force due to elongation of the PT bars ($\Delta T_{PT}$) and (3) initial axial force in the column ($P_i$). For an exterior column, the axial force developed by overturning moment of the SC-MRF should also be considered.

The total axial force in a column ($P_{col}$) is

$$P_{col} = T_i + (K_{PT})(d_{2\_col} - h_{anchor}\sin(\theta_{r\_col}))\theta_{r\_col} + P_i \tag{5}$$

The shear resistance provided by friction at the column-grade beam interface ($V_f$) is

$$V_f = \mu P_{col} \tag{6}$$

$$V_f = \mu(T_i + K_{PT}(d_{2\_col} - h_{anchor}\sin(\theta_{r\_col}))\theta_{r\_col} + P_i) \tag{7}$$

where, $\mu = 0.35$ (AISC, 2005 a)

There are pretension losses in the bolts in first line, or row closest to the BRS plate. Therefore, the shear resistance provided by the Keeper plate ($V_k$) is calculated (AISC, 2005 a) as

$$V_k = \phi N_{bolt}(\mu D_u h_{sc} T_b N_s) \tag{8}$$

where,

$D_u$ = 1.13; a multiplier that reflects the ratio of the mean installed bolt pretension to the specified minimum bolt pretension

$h_{sc}$ = hole factor, 1.0 for standard size holes

$N_{bolt}$ = number of bolts excluding the bolts of first line in keeper plate

$N_s$ = number of slip planes, 1

$T_b$ = specified minimun fastener tension

$\phi = 0.85$

Therefore, the total shear resistance at a PT column base connection ($V_{col}$) is

$$V_{col} = V_f + V_k \tag{9}$$

$$V_{col} = \mu(T_i + K_{PT}(d_{2\_col} - h_{anchor}\sin(\theta_{r\_col}))\theta_{r\_col} + P_i) + \phi N_{bolt}(\mu D_u h_{sc} T_b N_s) \tag{10}$$

## 2.3. Experimental Evaluation

The test program explored PT column base parameters such as the initial PT force, initial axial force applied to the column, column size and loading history. The PT bars that did not yield and BRS plates that did not fracture were reused in the next test. The columns and beams were also used repeatedly since they remained elastic without structural damage (i.e., plastic hinging or local buckling) during the tests. The PTC-1 and PTC-1D tests and results are described herein. The PTC-1 test specimen was the base configuration, or baseline test. The PTC-1D specimen used the same connection configuration, but a higher PT force.

Figure 3 (a) shows the test-setup of PT column base connection subassembly, which represents two-thirds scale PT column base subassemblies based on design of the prototype 6-story 4-bay SC-MRF. One horizontal actuator and two vertical hydraulic actuators were used to impose horizontal cyclic displacement and axial load in the columns. Cyclic lateral displacements based on the AISC loading protocol (AISC, 2005 b) were applied with column axial loads. The distance between the horizontal actuator and grade beam was1.83m and the distance between the grade beam supports was 5.8m. In order to restrain the horizontal movement of the grade beam, one end of the beam was post-tensioned to the strong wall and the other end was simply supported by a column.

W18x86 columns and grade beams were used for the column base subassembly specimens as shown in Figure 3 (b). A992 Grade 50 steels were used for test specimens. Four 31.8mm diameter post-tensioned Dywidag bars were anchored between half-height of the column to close to the bottom of the below-grade column. The PT bars had nominal ultimate strengths of 1030MPa. The PT bar length was 3.75m, and the distance between the PT bars was 178 mm. Two A572 Grade 50 reinforcing plates (19.0 mm thick, 318 mm wide, 940 mm) were welded to column flanges with a 12.7mm fillet welds. A572 Grade 50 BRS plates (reduced section: 9.53 mm thick, 63.5mm inch wide, 63.8 mm long) were bolted to column flanges with 25.4 mm diameter A490 bolts. Cover plates were used to prevent the buckling of the buckling restrained plates. Shim plates are also used between columns and grade beams to prevent contact with and local bearing failure of the column web.

In the PTC-1 test, the initial PT forces before and after applying column axial load were 836.3 kN and 765.1 kN, respectively. The initial axial force in the column was 587.2 kN, based on loads for the prototype building. Once the axial force was applied to the column top, the total initial tension force of the PT bars decreased 8.5% due to shortening of the column. The total initial PT force after the axial loading was 765.1 kN. The lateral loading was applied according to the AISC loading protocol. The maximum applied drift in the PTC-1 test was 0.04 radians. The normalized moment vs. relative rotation response of PTC-1 is shown in Figure 4. The maximum moment achieved in the test was 70% of nominal plastic moment of the column. The maximum force in the PT bar was about 587.2 kN, which corresponded to 87.5% of the yield force of the bar. Figure 5 shows the deformed configuration of PT column base connection at the level of 4% drift. No significant damage (i.e., plastic hinges or local buckling) was observed in the column or grade beam during test.

In the PTC-1D test, a relatively high PT force was applied at the connection to have the PT bars yield at relatively low drift level. The purpose of the PTC-1D

test was to investigate the effect of PT bar yielding at an early stage on the behavior of the PT column base connection. The initial PT forces before and after applying column axial load were 1356.7 kN and 1285.5 kN, respectively. The initial axial force in the column was 587.2 kN. The lateral loading was applied according to the AISC loading protocol. The maximum applied drift in PTC-1D test was 0.04 radians. Each PT bar had an average tension force of 339.2 kN, which was about 51% of the yield force of the bar. The normalized moment vs. relative rotation response of PTC-1D is shown in Figure 6. The maximum moment achieved in this test was 77% of nominal plastic moment of the column. No significant yielding was observed in the column and beam during the test except for localized yielding in the panel zone and yielding of the column web. At about 3.4% drift, the PT bars began to yield near the ends of the bars. The loss of the total PT force was about 395.9 kN, which corresponded to 31% of the total initial PT force. However, no significant degradation occurred during 4% drift cycles. Even as the PT bars yielded, the column did self-center upon unloading.



(a)                                        (b)

Figure 5. Deformed configuration of PT column base connection (PTC-1)



(a)                                        (b)

Figure 3. Test-setup and specimen
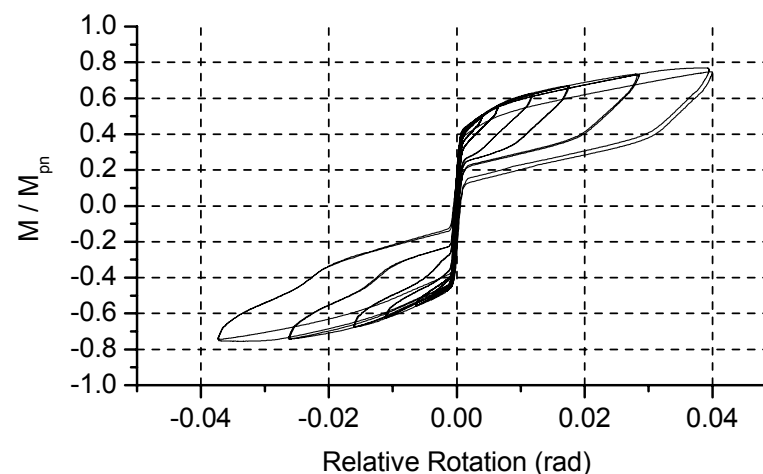


Figure 6. Normalized moment vs. relative rotation response of PTC-1D

### 2.4. Verification of design equations

The connection moments predicted by the equations presented earlier compare well with the connection moments from the post-tensioned column base connection subassembly tests. These comparisons are shown for PTC-1 (Figure 7) and PTC-1D (Figure 8). It is noted that the decompression moment corresponds to event (a) in Figure 7 and Figure 8, the connection moment at initiation of BRS plate yielding corresponds to event (b), the connection moment at relative rotation of 0.02 radians corresponds to event (c) and the connection moment at relative rotation of 0.04 radians corresponds to event (d), respectively. Equation (1) is used for events (b) – (d); the column rotation for BRS plate yielding is predicted based on geometry of the PT column base and the BRS plate yield strain. Event (a) is based on Equation (2) and (3), with corresponds to an assumed zero rotation.



Figure 4. Normalized moment vs. relative rotation response of PTC-1

Figure 7. Comparison of moment vs. relative rotation of PTC-1



Figure 8. Comparison of moment vs. relative rotation of PTC-1D

### 3. SUMMARY AND CONCLUSIONS

This paper presented a post-tensioned column base connection for use in steel self-centering moment resisting frames. The PT column base connection consists of PT bars, BRS plates, reinforcing plates, Keeper plates and shim plates. The PT bars provide clamping force and restoring force for the connection, and the BRS plates dissipate energy by yielding. Keeper plates provide additional shear resistance for the PT column bases. The moment-rotation behavior of the PT column base connection is characterized by gap opening and closing at the column-beam interface and yielding of the BRS energy dissipating elements. Results for a pair of PT column base tests demonstrated effects of a higher initial PT force. Design equations were verified with the moment-rotation test results of post-tensioned (PT) column base connection subassemblies subjected to cyclic lateral displacement and axial loading and showed good agreement with the experimental data.

### REFERENCES

[1] AISC (2005 a), Specification for structural steel buildings: ANSI/AISC360-05, Chicago, Illinois.

[2] AISC (2005 b), Seismic Provisions for Structural Steel Buildings: ANSI/AISC 341-05, Chicago, Illinois.

[3] Chi, H. (2009), "Development of post-tensioned column base connection for self-centering seismic resistant steel frame" Ph.D. Dissertation: School of Civil Engineering, Purdue University, West Lafayette, IN, USA

[4] Christopoulos, C., Filiatrault, A., Uang, C.-M., Folz, B. (2002), "Posttensioned energy dissipation connections for moment-resisting steel frames", *Journal of Structural Engineering,* Vol. 128, No. 9 (pp. 1111-1120).

[5] Garlock, M., Ricles, J., and Sause, R. (2005), "Experimental studies on full-scale post-tensioned steel connections", *Journal of Structural Engineering*, Vol. 131, No. 3 (pp. 438-448).

[6] Garlock, M., Sause, R., and Ricles, J. (2007), "Behavior and design of posttensioned steel frame system". *Journal of Structural Engineering*, Vol. 133, No. 3 (pp. 389-399).

[7] Ricles, J., Sause, R., Garlock, M, and Zhao, C. (2001), "Posttensioned seismic resistant connections for steel frames", *Journal of Structural Engineering*, Vol. 127(2) (pp. 113-121).

[8] Ricles, J., Sause, R., Peng, S.W., and Lu, L.W. (2002), "Experimental evaluation of earthquake resistant posttensioned steel connections", *Journal of Structural Engineering*, Vol. 128, No. 7, (pp. 850-859).
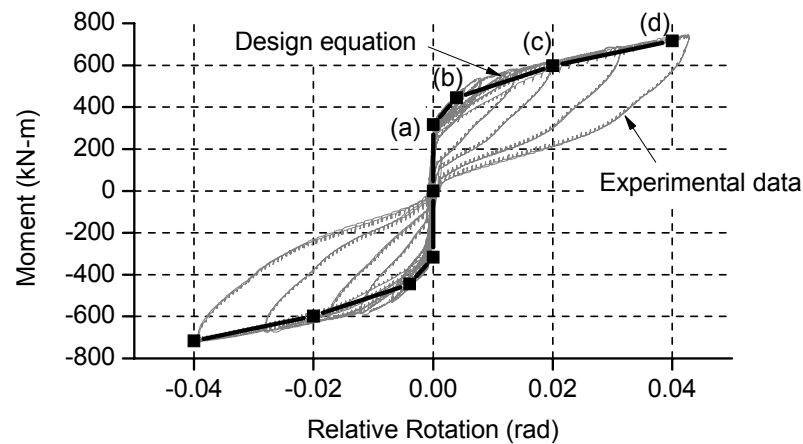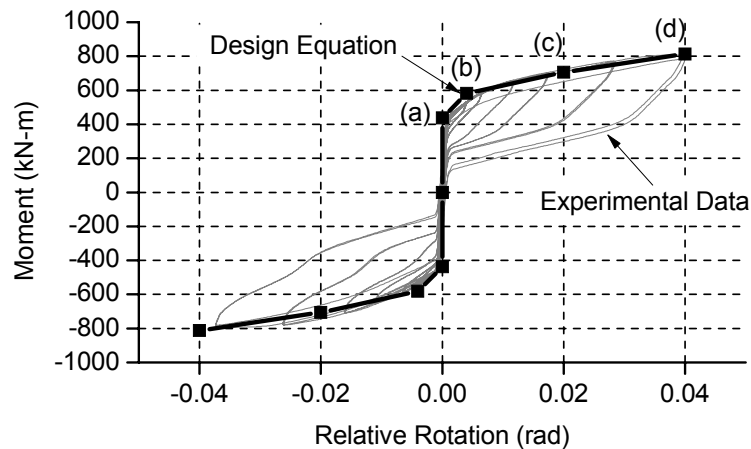
# STUDY ON THE DAMAGE BEHAVIOR AND CALCULATION MODEL OF WELDED CONNECTIONS IN STEEL FRAMES UNDER SEVERE EARTHQUAKES

*Yongjiu Shi; Meng Wang; Gang Shi; Jun Xiong; Yuanqing Wang*
*Department of Civil Engineering, Tsinghua University, China*
*shigang@tsinghua.edu.cn*

## ABSTRACT

In order to investigate the connection damage behaviours and influence factors, two series of tests focusing on welds and full-scale connections were separately conducted subjected to both monotonic and cyclic loading patterns. The influences of the material strength, geometry parameters and loading procedures on connection damage behaviours were studied. Then, the damage mechanism and finite element analysis were carried out, including crack mechanism of the connection welds, the damage evolution equation based on the plastic strain and damage developing models. A simplified model with the indicator "effective plastic rotation" was proposed for welded connections considering damage effect. The backbone and hysteretic curves of proposed model were derived and verified with experimental data. The comparison between the calculation results and test data revealed that the damage model proposed was favorable for predicting the damage behaviors of welded connections under cyclic loads and had a great value for engineering analysis and design application. Finally, based on the UMAT of ABAQUS, a method for the non-linear dynamic analyses of steel frames using the foregoing damage model was explored and verified. The analysis results showed that beam element model without damage overrated the structure deformation capacity, which caused unsafety, which should be paid more attention to.

## 1. INTRODUCTION

A number of welded connections in steel frames were found cracking at welds in Northridge and Kobe earthquake, resulting in the frame damage or failure. A majority of the researches on steel welded connections focused on the materials and construction details rather than the damage theory and calculation method, so the influence of the connection damage is hardly taken into account in the aseismic design of steel frames. In order to introduce the connection damage into numerical calculation, an accurate damage model should be proposed.

Researches paid little attention to damage evolution equation and simplified connection plastic hinge model with damage, especially the complete curves of the hysteretic model. The purpose of the work discussed in this paper was to establish damage evolution equation and damage model of steel frame welded connections, which can be applied in time history analysis of steel frames. To achieve this goal, experiments, finite element analysis and theoretical method were carried out. Two series of tests focusing on welds and full-scale connections separately were conducted. The damage mechanism and finite element analysis methodology were studied. Then a simplified calculation model was proposed for the damage process of the welded connections. The results of calculation and test data were also compared to reveal the predicting accuracy. Finally, the model was applied in the time history analysis of steel frames.

## 2. EXPERIMENTAL AND THEORETICAL STUDY ON DAMAGE BEHAVIOR OF LOCAL REGION OF WELDED BEAM-TO-COLUMN CONNECTIONS

### 2.1. Test specimens description

Learned from the Northridge earthquake and Kobe earthquake, it was clear that beam-to-column connections were susceptible to fracture at the bottom beam flange to column flange welds. To investigate the fracture performance of the welded connection, 20 specimens of local connections (shown in Figure 1(a)) were tested under monotonic tensile and cyclic loading patterns in this study. Figure 1(b) showed the details of specimens, which were fabricated from Q345 steel. Three cyclic loading patterns for SP-1B ~SP-9B were shown in Figure 2.
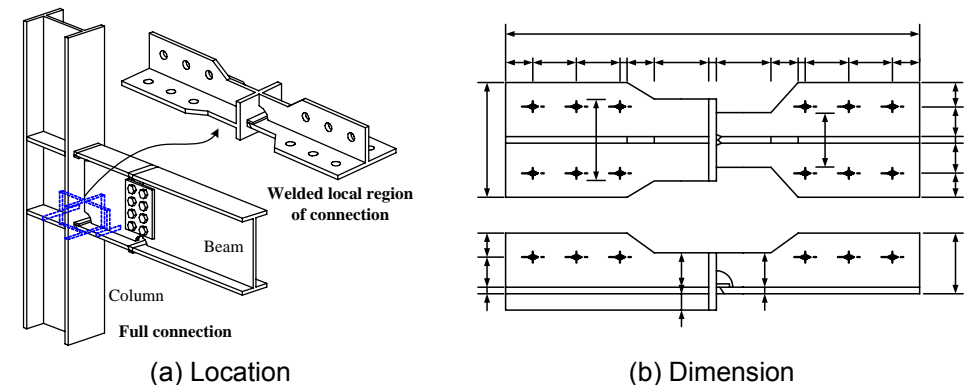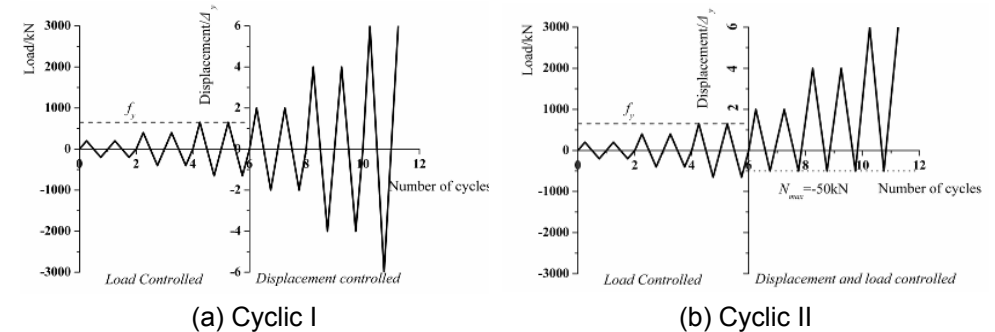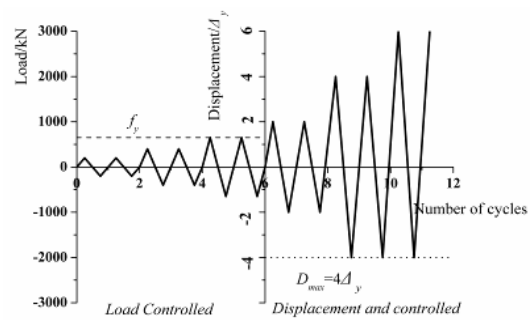


(a) Location　　　　　　　　(b) Dimension

Figure 1. Specimen dimension (mm)



(a) Cyclic I　　　　　　　　(b) Cyclic II

(c) Cyclic III
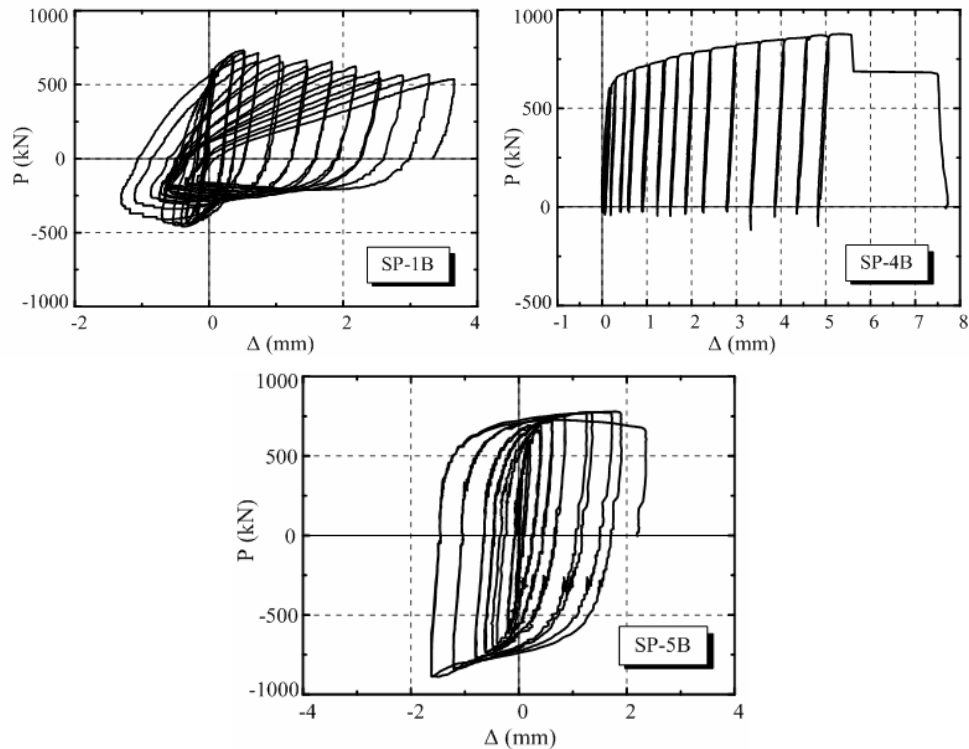Figure 2. Loading procedure



Figure 3. Hysteretic loops

## 2.2. Results and discussion

The typical cyclic curves of specimens subjected to cyclic loads were shown in Figure 3. All the cyclic specimens failed at the weld except two buckled (SP-6B and SP-8B). The experimental phenomena revealed that the cyclic load was an unfavorable factor for the weld. Furthermore compared to the monotonic loads, the cyclic loads weakened the specimens with a 4%~ 33% ultimate strength reduction and a 25%~90% ultimate deformation reduction. The specimens subjected to Cyclic II

and Cyclic III loads had better ductility than the ones subjected to Cyclic I load. Increasing the stress range could accelerate the material damage.

## 2.3. Comparison of damage models

In order to exactly and conveniently describe the damage behavior, some authors proposed the damage model based on experimental researches and damage mechanics. In the damage models, the damage level was described by the damage index $\omega$ ($\omega$=0 indicates no damage and $\omega \geq 1$ means collapse or failure).

The typical damage curve was illustrated in Figure 4（Displacement model of Cosenza and Manfredi, 1992; Combined model of Park and Ang, 1985; Engery model of Kumar, 1994. The comparison results of the commonly used damage evolution equations showed that the fitting data by the model with an indicator of plastic deformation had relatively small scatter with low sensitivity to geometry size and broader scope of application. But if the damage process of the welded connections needed be more accurately calculated, a more sophisticated model of evolution equation should be proposed.
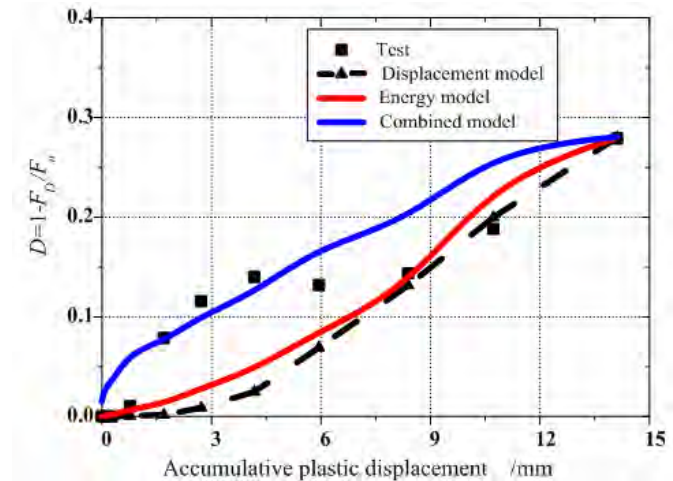


Figure 4. Comparison of the three damage models

## 2.4. Weld fracture analysis and simulation

The damage process of weld zone under axial cyclic loading was analyzed based on the damage mechanics theory. The displacement damage model was introduced into the finite element program. The damage process was simulated by using the ductility damage criteria (the Ductile Criterion) in ABAQUS. The feasibility of this method was verified by experiments. The shell element S4R was used for establishing models. The material properties of weld metal used the test results of Liao et al. (2010).

The calculated curves in Figure 5 showed that the finite element method based on the ductile damage mechanics could simulate the crack performance and degradation process of weld zoen under axial tension and compression,

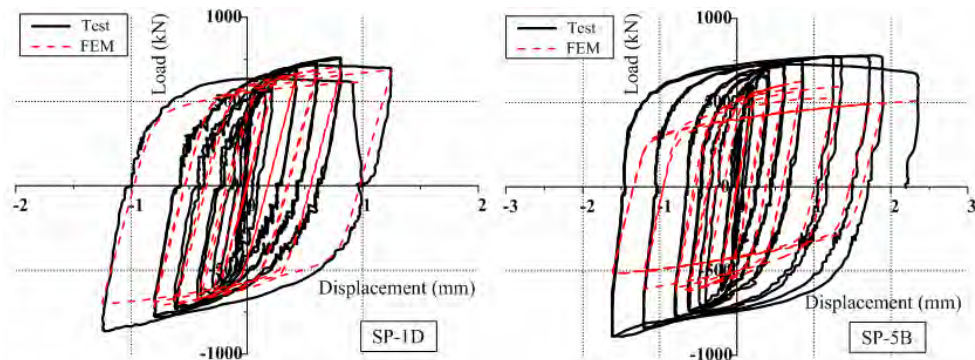which provided a more practical method for the analysis of connection damage mechanisms.



Figure 5. The comparative results

## 3. EXPERIMENTAL STUDY ON DAMAGE MECHANISM OF WELDED BEAM-TO-COLUMN CONNECTIONS IN STEEL FRAMES

### 3.1. Test specimens description

In order to further study the effect of loading history and amplitude on damage and degradation, 9 connection specimens were tested subjected to various cyclic loading patterns. The detail dimensions of beam and column as well as connecting method were shown in Figure 6, in which, $L_B$ of the beam was 1500mm for this series. The specimens described in this paper were fabricated from Q345B steel. A series of loading patterns were programmed as summarized in Figure 6, which simulated the various seismic actions in real situation.

### 3.2. Results and discussion

From the observations, part of connections finally fractured at the heat affected zone of top beam flange and the other specimens experienced local buckling. Typical hysteretic curves ($P$-$\Delta$) of specimens were shown in Figure 7. The loading amplitude had no significant effect on bearing capacity and ultimate deformation capacity. Damage was related to the loading history. The loading patterns with sudden peak were more unfavorable for connection performance than the one with a gradually increasing loading. The larger damage of bearing capacity caused by strong peak would be reflected in the later period. The cyclic amplitude had great effect on the damage development by comparing the damage curves of four specimens with constant amplitude loading. Based on the phenomenon from the damage process of each specimen, the following characteristics of connection damage could be observed:

1) the characteristics of the accelerative and exponential damage could be found.
2) the damage development was closely related with different cyclic loading patterns, based on the comparison of cyclic damage curves under four constant amplitude loading.
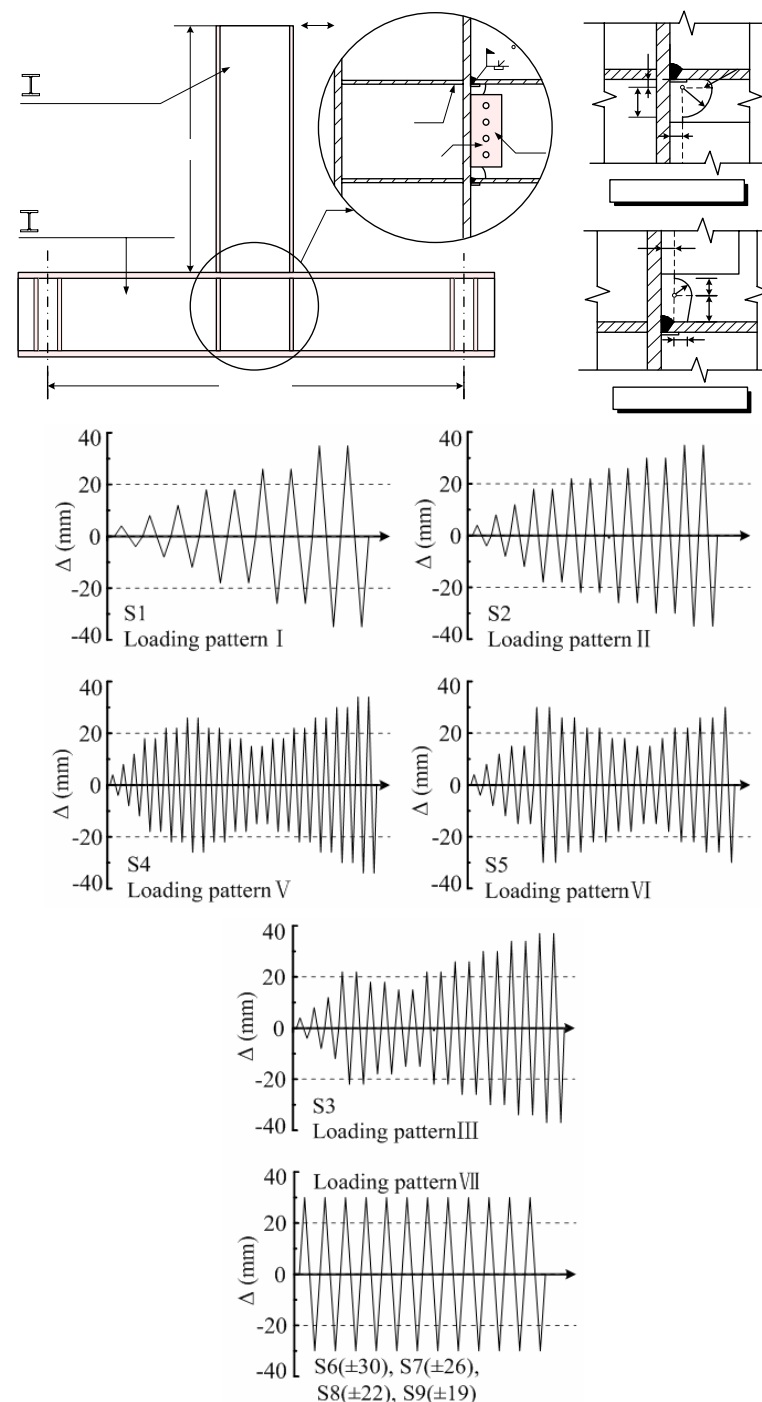


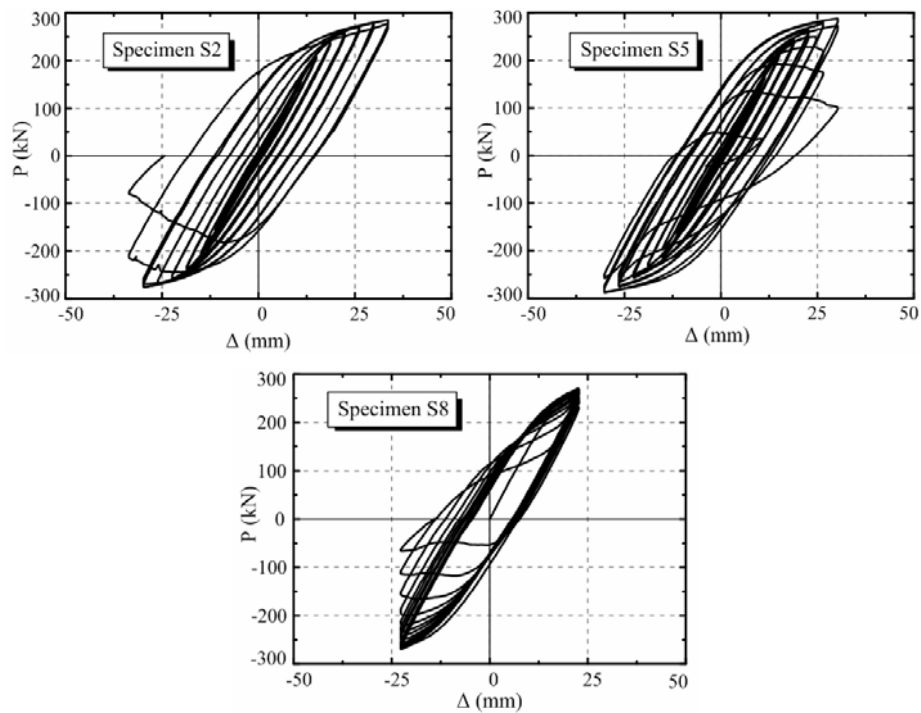Figure 6. Specimen details and loading patterns (mm)

Figure 7. Hysteretic loops



Figure 8. Comparison between damage functions and experiments

## 3.3. Damage developing curves

The linear cumulative damage model had large errors in simulating connection damage. Therefore, a power function or an exponential function should be adopted for the damage developing model.

The damage index could be simplified as a linear combination of the exponential functions, such as the Eq. (1).

$$D = \sum_{i=1}^{N} \left( \frac{\varphi_{pi}}{\varphi_u - \varphi_y} \right)^c \qquad (1)$$

Park-Ang model was improved based on exponential function, such as Eq. (2).

$$D = \left( \frac{\varphi_{max} - \varphi_y}{\varphi_u - \varphi_y} \right)^c + \beta \sum_{i=1}^{N} \left( \frac{\varphi_{pi}}{\varphi_u - \varphi_y} \right)^c \qquad (2)$$

Where the parameter $\beta$ is 0.23 and the index c was fitted by the test results.

The typical damage curves calculated by equations (1) and (2) were compared in Figure 8. The damage curves calculated by two equations were close and they were accurate for simulating the damage curves of the connections subjected to the variational amplitude loading patterns. For constant amplitude loading patterns, results of simulation were poor using the linearized and simplified model.
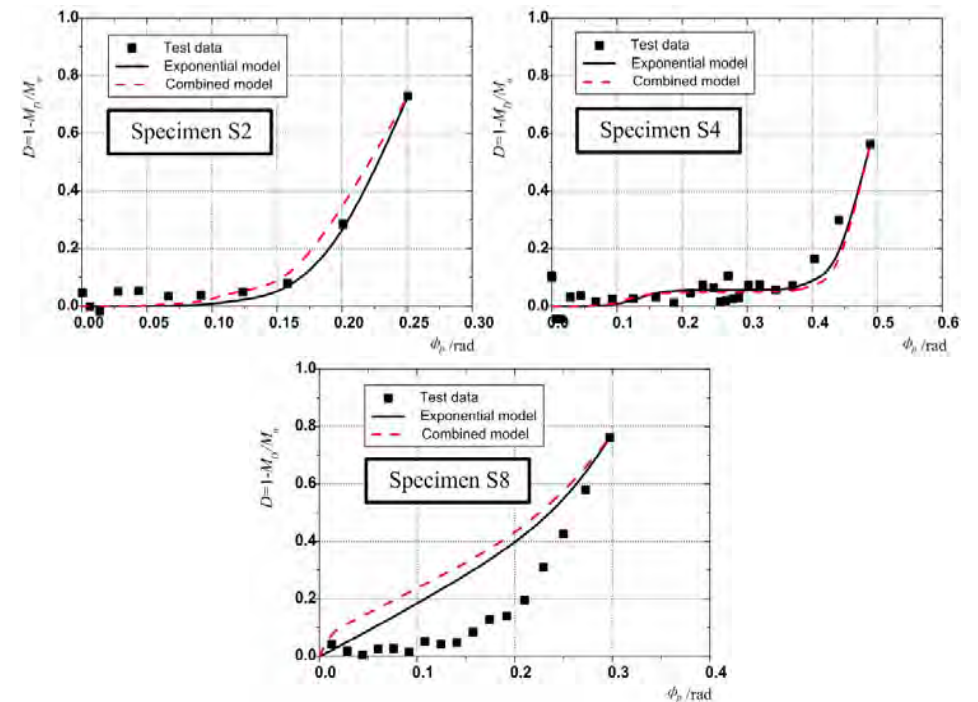
## 4. DAMAGE THEORY AND NUMERICAL ANALYSIS OF WELDED BEAM-TO-COLUMN CONNECTIONS IN STEEL FRAMES

### 4.1. Damage evolution equation and model

The damage process was defined with the variable of effective plastic strain. The damage evolution equation for the damage developing process subjected to the extremely low cyclic loading was derived based on the fatigue crack growth formula.

According to Manson- Coffin relationship (Manson, 1953; Coffin, 1954) and Paris formula (Paris, 1963) of fatigue crack growth curve, Solomon (1972) and Krawinkler (1983) proposed the relationship between crack length of the connection welds and the number of cycles under constant amplitude loading in tests.

$$\frac{da}{dN} = \alpha a (\Delta \varepsilon_p)^\beta \qquad (3)$$

Crack growth equation was defined as:

$$a_{i+1} = a_i e^{\alpha e^{1.5T} R^\beta (\Delta \varepsilon_{EPS})^\beta} \qquad (4)$$

Damage evolution equation of connection for ductile cracking was defined as:

$$D_i = \int_0^b \frac{a(x,i)}{bt} dx \qquad (4)$$

## 4.2. Damage parameters calibration

S6~S9 specimens under constant amplitude loadings were used for calibrating the value of $\beta$. According to the fitting results, the value of $\beta$ was classified by two stages based on cyclic amplitudes, as shown in Eq. (6).

$$\beta = \begin{cases} 1.15 & \Delta\varphi_p \geq 1.25\Delta\varphi_y \\ 1.45 & \Delta\varphi_p < 1.25\Delta\varphi_y \end{cases} \quad (6)$$

In which, $\Delta\varphi_p$ referred to the cyclic tensile or compressive amplitude of connection plastic rotation.

Various amplitude loadings were used to verify the parameters of damage model, as shown in Figure 9, which indicated the parameter was suitable.
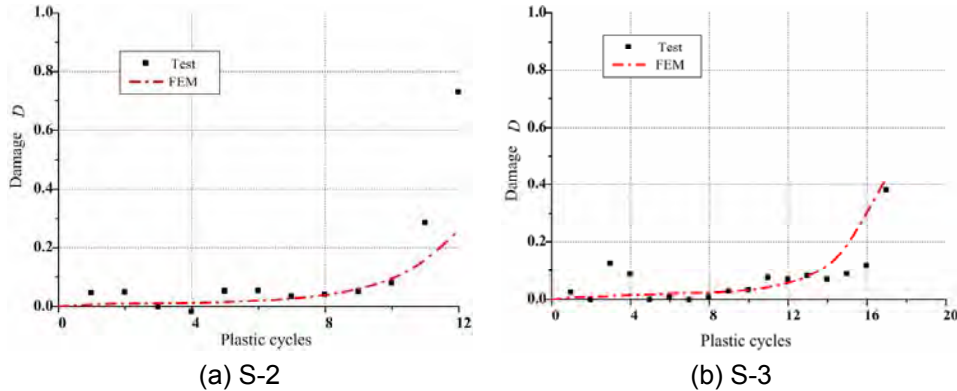


(a) S-2                                        (b) S-3

Figure 9. Damage curve of connections under various amplitude loads

## 4.3. Verification and application

Based on the above results of theoretical studies, the crack evolution equations were introduced into the finite element model. Complete decoupling could be used to compute the connection cracking. According to equation (5), the accumulative damage of connection was calculated by calculating the crack of each unit in each cycle (Dassault, 2010). The ABAQUS subroutine was written in Fortran Language. The crack developing process and damage development of connection were introduced into finite element analysis process. The finite element models of the connections tested in this article were established. The value of material parameter $\alpha_{TR = 1/3}$ was 13.7 in subroutine and $\beta$ values were determined by the fitting results.
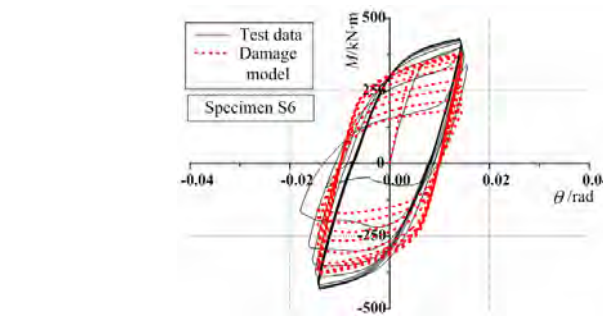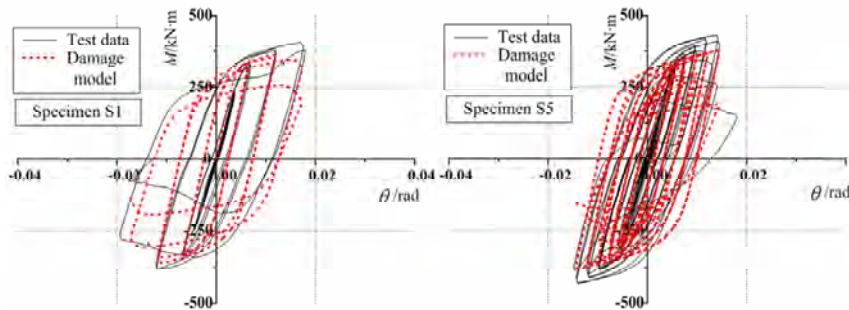




Figure 10. Comparison between FEA taking account of damage and experimental curves

The typical hysteresis curves of connections with damage were obtained as shown in Figure 10 by introducing the damage model into hysteresis curves calculated by the finite element analysis. Proposed model and test results were in good agreement and the accuracy of the model was ensured.

## 5. ANALYSIS AND APPLICATION OF DAMAGE MODEL OF WELDED BEAM-TO-COLUMN CONNECTIONS

### 5.1. Damage evolution equation of bilinear model

The relationship of plastic rotation and plastic strain of the beam end was:

$$\varphi_p = \frac{2L_p}{h}\varepsilon_p \quad (7)$$

In order to establish macro-level quantitative indicators of connection damage, the effective plastic rotation was introduced into the connection crack fatigue formula based on ductility cracking.

$$\frac{da}{dN} = a\alpha(\frac{h}{2L_p})^\beta (\Delta\varphi_{EPR})^\beta \quad (8)$$

The damage evolution equation described by effective plastic rotation was:

$$D_{i+1} = D_i \exp[(\frac{h}{2L_p})^\beta \alpha_{TR}(\Delta\varphi_{EPR,i})^\beta] \quad (9)$$

The method to obtain the damage index $\beta$ was the same as section 4 that constant amplitude loading curves were used for damage curves fitting. The fitting results were taken according to Eq. (10):

$$\beta = \begin{cases} 1 & \Delta\varphi_{EPR,i} \geq 1.25\Delta\varphi_y \\ 1.3 & \Delta\varphi_{EPR,i} < 1.25\Delta\varphi_y \end{cases} \quad (10)$$

### 5.2. Complete hysteretic curve of connections with damage

The connection moment - rotation curve considering damage was obtained by introducing connection damage evolution equation into the original moment - rotation

curve. The $D_i$ was calculated by Eq. (9) with cyclic accumulation. The connection moment - rotation curves considering damage subjected to constant amplitude loading and variable amplitude loading were respectively shown in Figure 11.
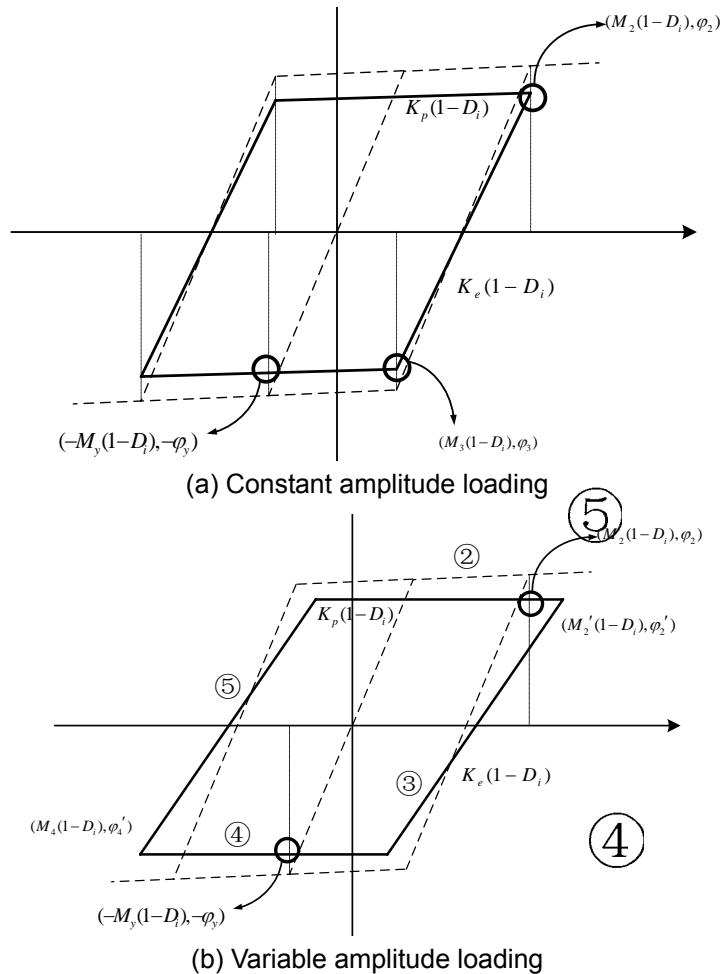


(a) Constant amplitude loading



(b) Variable amplitude loading

Figure 11. The hysteretic model of connection damage

## 5.3. Verification of the damage model for connections

In order to validate the proposed connection moment - rotation curve considering damage, the tests resutls were compared with the model results (Figure 12). The calculated damage curve accurately described the phenomenon of connection progressive damage with the loading process.

The cyclic loading tests of connection carried out by Goel and Stojadinovic (1997) and Ricles (2000) in Lehigh University were also selected to validate the proposed simplified calculation model. The numerical simulation using damage model compared well with the test results, as shown in Figures 13 and 14, which could accurately describe the cumulative damage and degradation behaviors of structures.
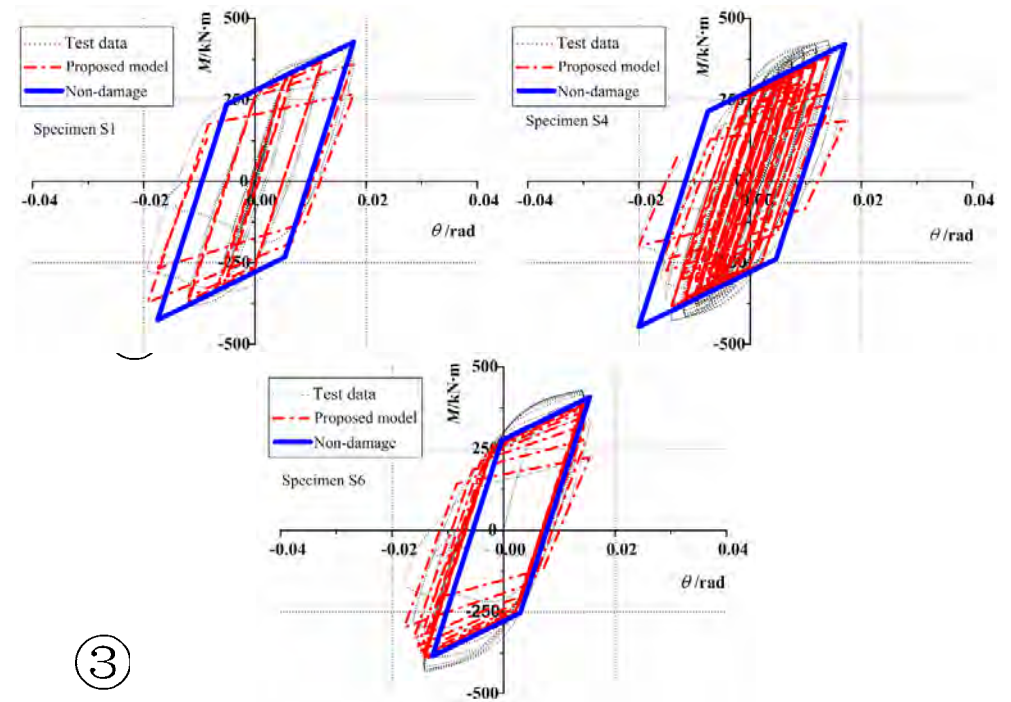


Figure 12. The comparison results of the tests in this paper

## 5.4. Application of the damage model in steel frames

The simplified plastic hinge model with damage was applied for dynamic time history analysis of steel frames. A five-storey steel frame model with one span was established. El Centro and Koyna earthquake waves were adopted. In order to study the behaviours of the structure under a severe earthquake, the seismic peak acceleration PGA was adjusted to 0.62g. The frame model was established by B21 beam element. The plastic hinge model with damage was used to consider the effect of connection damage on the steel structure.
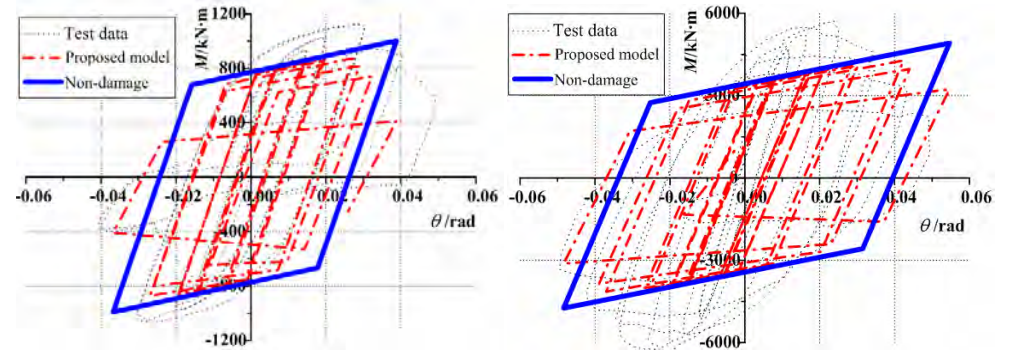


Figure 13. The comparison of Goel connection result



Figure 14. The comparison of Ricles connection result

From Figure 15，before the occurrence of damage and degradation, seismic indexes calculated by two models were in accordance. However, once damage and degradation occurred, the results of the two models were remarkably different. Beam element model without damage overrated the structure deformation capacity, which caused unsafety.
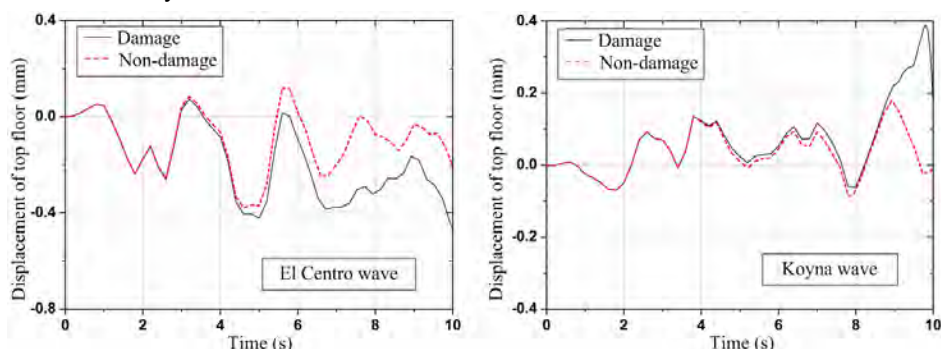


Figure 15. Time history curves of top floor displacement

## 6. CONCLUSIONS AND GENERAL RECOMMENDATIONS

Based on all the analyses above, some conclusions could be derived from the test and analyses.

1. Tests of 20 local specimens of connection welded regions subjected to monotonic tensile and cyclic loadings were carried out. The effect of material strength, loading patterns and geometric parameters on welded fracture and damage were studied and the fitting analysis of the test results using common damage evolution were carried out. The test results showed that the stress amplitude index of cyclic loading played a decisive role in the weld damage.

2. The experiments of 9 full-scale beam-column connections under cyclic loading were carried out. The damage mechanism of welded connections and the effect of loading amplitude, peak position on connection damage were further studied. The influence of loading history was closely related to the peak displacement position and number of cycles. The sudden strong peak caused the most terrible damage on the connections.

3. The "effective plastic strain" was introduced as the damage development index of metal materials according to the metal ductile fracture theory. By using this index, a damage evolution equation was proposed based on the effective plastic strain. The ABAQUS subroutine to calculate the whole process of connection damage was developed by the damage evolution equation. The model was validated by experimental results.

4. The definition of "effective plastic rotation" of the connection was creatively put forward. The damage evolution equation with the indicator of effective plastic rotation was established. The simplified calculation equation of bilinear model considering the damage for the whole hysteretic curve was derived. The welded connection test results of this article and other researchers were used to prove the accuracy. Finally, the model was applied into the nonlinear dynamic time history analysis of steel frames, which indicated the method had a great value for engineering analysis and design application.

## REFERENCES

[1] Bannantine, J.A., Comer, J. J. and Handrock, J.L.(1990), "Fundamentals of metal fatigue analysis", Prentice-Hall, Englewood Cliffs, N. J.

[2] Coffin, L. F. (1954), "A study of the effects of cyclic thermal stresses on a ductile metal", *Trans.* ASME, Vol. 76, (pp. 931–950).

[3] Cosenza, E. and Manfredi, G. (1992), "Seismic Analysis of Degrading Models by means of Damage Functions Concept", *Nonlinear Seismic Analysis and Design of Reinforced Concrete Buildings.*

[4] Dassault Systèmes. (2010), "Abaqus Analysis User's Manual", *Dassault Systèmes Simulia Corporation*, Providence, RI, U.S.A,.

[5] Kato, B. and Akiyama, H. (1975), "Aseismic Limit Design of Steel Rigid Frames", *Proceeding of Architectural Institute of Japan*, No.237.

[6] Kravinkler, H. and Zhorei, M. (1983), "Cumulative Damge in Steel Structures Subjected to Earthquake Ground Motions". *Computers and Structures*, Vol. 16(1-4).

[7] Kumar, S. and Usami, T. (1994), "A note on evaluation of damage in steel structures under cyclic loading", *Journal of Structure Engineering*, JSCE, Vol. 40A, (pp. 177-178).

[8] Liao, F.F., Wang, W. (2010), "Parameter calibrations of micromechanics-based fracture models of Q345 steel". *Science paper Online*, <http://www.paper.edu.cn/index.php/default/releasepaper/content/201007-457>.

[9] Manson, S.S. (1953), "Behavior of materials under conditions of thermal stress", *Proc., Heat Transfer Symp.*, University of Michigan Engineering Research Institute, Ann Arbor, Mich., (pp. 9–75).

[10] Park, A.J. and Ang, H.S. (1985), "Mechanistic Seismic Damage Model for Reinforced Concrete". *Journal of Structure Engineering*, Proc. ASCE, Vol.111(4).

[11] Paris, P. C. and Erdogan, F. (1963), "A critical analysis of crack propagation laws", *Journal of Basic Engineering*, Vol. 85, (pp. 528-534).

[12] Powell, G.H. and Allchabadi, R. (1988), "Seismic damage prediction by deterministic methods: Concept and procedures", *Earthquake Engineering and Structural Dynamics*, Vol. 16, (pp. 719-734).

[13] SAC. (1997), "Protocol for Fabrication, Inspection, Testing, and Documentation of Beam-Column Connection Tests and Other Experimental Specimens", Report No. SAC/BD-97/02, Michigan.

[14] SAC. (2000), "Protocol for Fabrication, Inspection, Testing, and Documentation of Beam-Column Connection Tests and Other Experimental Specimens", Report No. SAC/BD-97/02, Lehigh University.

[15] Solomon, H.D. (1972), "Low cycle fatigue crack propagation in 1018 steel", *J. Mater.,* Vol. 7(3), (pp. 299–306).

[16] Kumar S. and Usami T., A Note on Evaluation of Damage in Steel Structures under Cyclic Loading, J. Struct. Eng. JSCE, 1994, 40A: 177-178.

# EXPERIMENTAL BEHAVIOUR OF FRICTION T-STUB BEAM-TO-COLUMN JOINTS UNDER CYCLIC LOADS

Massimo Latour; Vincenzo Piluso; Gianvittorio Rizzano
*DICIV - Department of Civil Engineering, University of Salerno, Italy*
*mlatour@unisa.it; v.piluso@unisa.it; g.rizzano@unisa.it*

## ABSTRACT

Eurocode 8 has introduced the possibility of adopting partial strength joints in case of seismic-resistant MR-Frames, provided that connections are demonstrated to perform adequately under cyclic loads. An experimental program devoted to the investigation of the cyclic behaviour of traditional joint details has been recently carried out by the Authors. Within this experimental program, the analysis of the obtained results has evidenced that, even though connections designed to dissipate the seismic energy in bolted components can provide significant advantages because easy to repair after a destructive seismic event, they possess reduced dissipation capacity when compared to RBS connections and traditional full-strength connections. In this work, an advanced approach aimed to enhance the hysteretic behaviour of double split tee (DST) joints and to the ambitious goal of joint damage prevention is presented. The proposed system is based on the idea of using friction dampers within the components of beam-to-column joints. A preliminary set of prototypes has been experimentally tested and the joints performances under cyclic loading conditions have been compared to those of classical joint details. The experimental work has been carried out at the Materials and Structures Laboratory of Salerno University.

## 1. INTRODUCTION

According to the most recent seismic codes (CEN, 2005a; ANSI/AISC 341-10) moment resisting steel frames can be designed either according to the full-strength criterion and the partial-strength criterion. The first one is based on the dissipation of the seismic input energy at the beam ends, the second one concentrates damage in the connecting elements and/or the panel zone. In the former case, aiming to promote the yielding of the beam ends, the beam-to-column joint is designed to possess an adequate overstrength with respect to the connected beam to account for strain-hardening and random material variability effects which affect the flexural resistance actually developed by the beam end. In the latter case, the beam yielding is prevented as the joints are designed to develop a bending resistance less than the beam plastic moment, so that dissipation occurs in the connecting elements. In addition, as a consequence, regarding the column design, the hierarchy criterion has to be applied by making reference to the maximum moment that connections are able to transmit. This design philosophy, as demonstrated by Faella et al. (1998), is particularly cost/effective in cases where the beam size is mainly governed by vertical loads rather than lateral loads, i.e. low-rise/long span MRFs.

The traditional design of MRFs (Mazzolani & Piluso, 1996), based on the use of full-strength beam-to-column joints, requires only the prediction of the monotonic response of connections (CEN, 2005b; CEN, 2005c). In particular, in order to characterize the behaviour of such joints, only the prediction of the initial stiffness and of the plastic resistance is needed, whereas the cyclic behaviour is governed by the width-to-thickness ratios of the plate elements of the connected beam. Conversely, as the energy dissipation supply of semi-continuous MRFs relies on the ability of connections to withstand a number of excursions in plastic range without losing their capacity to sustain vertical loads, it is evident that, in order to successfully apply partial-strength joints, it is necessary to properly characterize and predict the response of connections under cyclic loading conditions (Astaneh-Asl, 1987; Bernuzzi et al., 1996; Faella et al., 1999; Piluso & Rizzano, 2008; Latour et al., 2011a). For this reason, the use of partial-strength joints is allowed, both in AISC and Eurocode 8 provided that a "conformance demonstration" of the cyclic behaviour of connections adopted in the seismic load resisting system is shown by the designer. As a result, joints have to be pre-qualified accordingly with the ductility class of MRFs. For this reason a set of pre-qualified connections with the corresponding design criteria is suggested (ANSI/AISC 358-10), whose cyclic behaviour has been experimentally investigated demonstrating the development of plastic rotation supplies compatible with the corresponding ductility class.

Unfortunately, pre-qualified connections are not suggested in Eurocode 8, therefore, aiming to provide engineers with the tools needed to predict the cyclic behaviour of joints, new efforts for the developments of analytical approaches are needed, unless specific experimental tests are carried out.

To this scope, in last two decades a number of experimental programs dealing with the characterization of the cyclic behaviour of beam-to-column connections has been carried out. In a recent work of the Authors research group (Iannone et al., 2011), the behaviour of bolted joints designed to possess the same strength, but detailed to involve in plastic range different components, has been experimentally investigated pointing out the hysteretic behaviour. In particular, it has been pointed out that the energy dissipation provided by the whole joint can be obtained as the sum of the energy dissipations due to the single joint components, provided that the joint components are properly identified and their cyclic response is properly measured. This result is very important, because it testifies the applicability of the component approach also to the prediction of the joint behaviour under cyclic loads (Latour et al., 2011a). Within the above research program, due to the significant advantages which are able to provide under the reparability point of view, Double Split Tee (DST) connections have been recognized as an interesting solution to be applied in dissipative semi-continuous MRFs. In fact, DST connections can be easily repaired after destructive seismic events and allow to govern the joint rotational behaviour (i.e. the rotational stiffness, strength and plastic rotation supply) by properly fixing the bolt diameter and by simply calibrating three geometrical parameters: the width and the thickness of the T-stub flange plate and the distance between the bolts and the plastic hinge arising at the stem-to-flange connection (Piluso et al., 2001a; 2001b). On the other hand, joints involving bolted components in plastic range provide also several disadvantages. First of all, even though experimental studies demonstrate that bolted components are able to dissipate significant amounts of energy, it has to be recognized that their hysteretic behaviour is less dissipative compared to other joint typologies or to the cyclic response of steel H-shaped sections. This is mainly due

to contact and pinching phenomena which usually lead to the quick degradation of strength and stiffness of the tee elements.

For this reason, on one hand, the use of hourglass shaped T-stub flanges has been recently proposed (Latour & Rizzano, 2012) where, in other words, the dissipative capacity of classical tee elements has been improved by applying to the T-stub flanges the same concepts usually developed to design hysteretic metallic dampers, such as ADAS devices (Aiken et al., 1993a; Whittaker et al., 1989; Christopoulos & Filiatrault, 2000; Soong & Spencer Jr, 2002). On the other hand, an innovative approach aimed to enhance the dissipation capacity of classical rectangular T-stubs by using friction pads has also been proposed (Latour et al., 2011b) with the primary aim of joint damage prevention.

This last approach, which can be considered an innovative application of the seismic protection strategy based on supplementary energy dissipation, is herein presented. The main scope of the work is to investigate the possibility of governing the dissipative capacities of DST connections by exploiting the cyclic behaviour of friction materials by contemporaneously preventing the joint damage. In particular, as shown in the following, two innovative DST joints are detailed aiming to dissipate the seismic input energy by means of the slippage of the stems of the tees on a friction pad, which is interposed between the tee stems and the beam flanges. In this way, under seismic loading conditions, structural elements do not undergo to any damage provided that rigorous design procedures for failure mode control are applied (Mazzolani & Piluso, 1997; Longo et al., 2012), but energy dissipation is provided by the alternate movement of the tee stems on the friction pads, which are preloaded by means of high strength bolts. Therefore, in the present paper a new type of dissipative beam-to-column joints, namely dissipative DST connections with friction pads, to be adopted in the seismic design of semi-continuous MRFs is proposed and its behaviour is investigated by means of experimental tests under displacement control in cyclic loading conditions.

## 2. EXPERIMENTAL TESTS ON FRICTION MATERIALS

Preliminarily, in order to investigate the frictional properties of different interfaces to be used in Double Split Tee friction joints, a sub-assemblage constituted by two layers of friction material or metal located between three steel plates made of S275JR steel has been realised at Materials and Structures Laboratory of Salerno University (Fig.1). In order to allow the relative movement of the steel plates on the interposed friction material, one of the inner plates has been realised with slotted holes.

Conversely, the other inner plate and the two outer plates have been realized with circular holes. The clamping force has been applied by means of 16 preloaded bolts M20 10.9 class, and the holes have been drilled with a 21 mm drill bit. Aiming to evaluate the magnitude of the friction coefficient, several different layouts of the sub-assemblage have been considered varying three parameters: the interface, the tightening torque, the number of tightened bolts and the type of bolt washers. The frictional properties of the following five different interfaces have been evaluated (Fig. 2):

- Steel on steel;
- Brass on steel;
- Friction material M0 on steel;
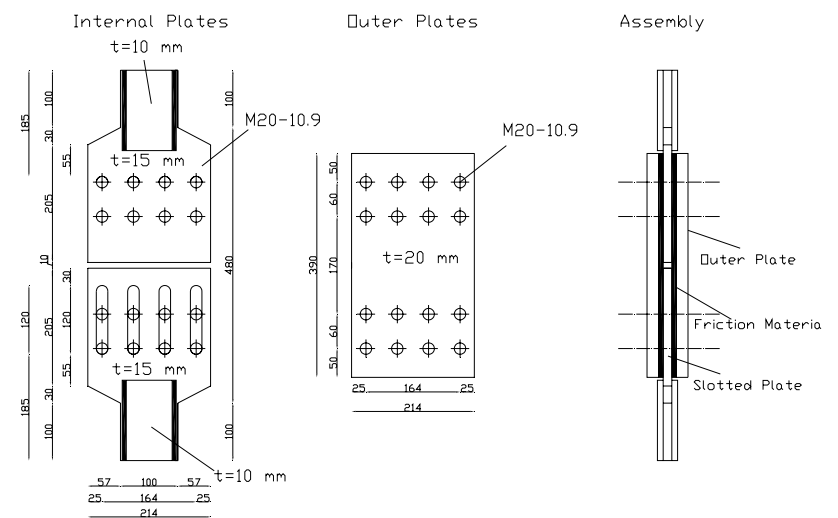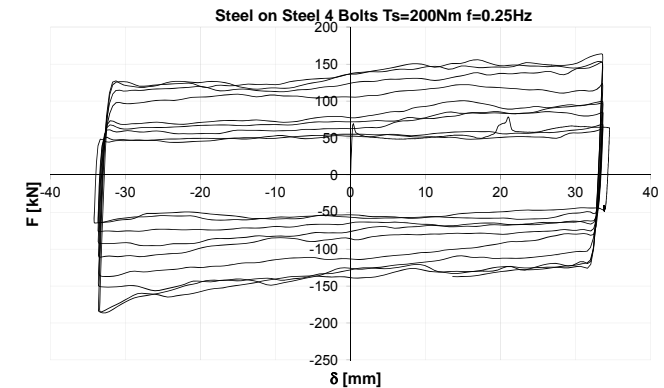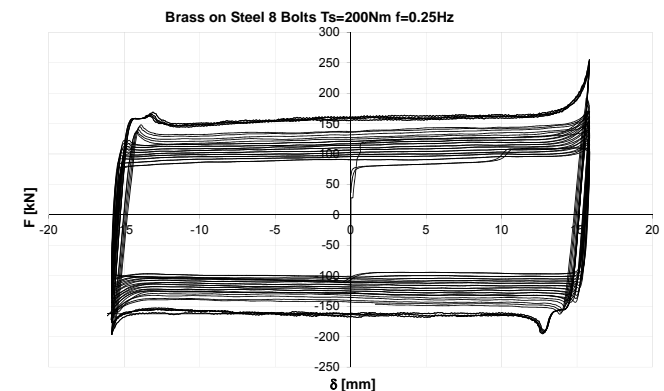- Friction material M1 on steel;
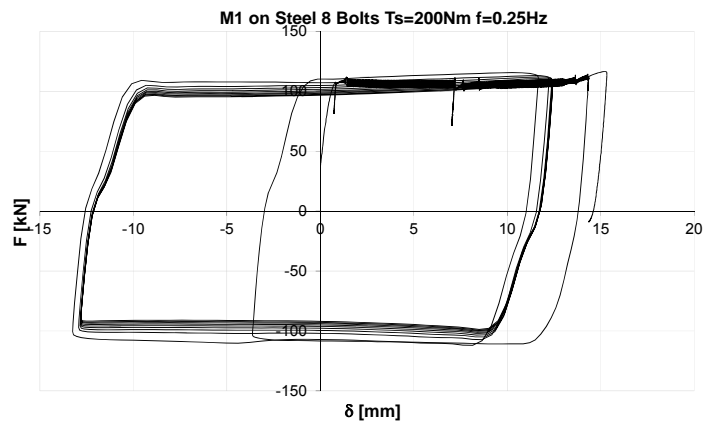- Friction material M2 on steel.



Figure 1. Scheme of the tested sub-assemblage



Steel on Steel Cycles 1-10 (Ts=200 Nm)



Brass on Steel Cycles 1-60 (Ts=200 Nm)

**M0 on Steel 4 Bolts Ts=200Nm f=0.25Hz**

M0 on Steel Cycles 1-20 (Ts=200 Nm)

**M1 on Steel 8 Bolts Ts=200Nm f=0.25Hz**

M1 on Steel Cycles 1-10 (Ts=200 Nm)

**M2 on Steel 8 Bolts Ts=200Nm f=0.25Hz**
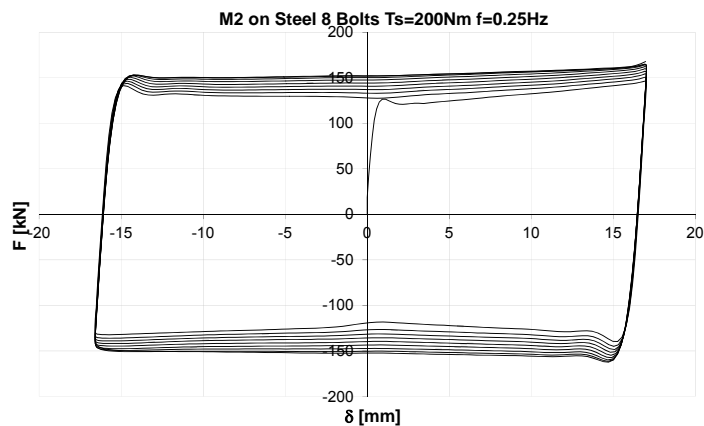
M2 on Steel Cycles 1-10 (Ts=200 Nm)

Figure 2. Force-Displacement Curves of interfaces

In particular, two different types of washers have been employed. In the first part of the experimental program, circular flat steel washers have been used, while in the second part of the campaign a packet of steel disc springs has been interposed between the bolt head and the steel plate (Fig. 3). In addition, the experimental analysis has been carried out by varying the bolt tightening level in the range between 200 Nm and 500 Nm, obtaining different values of the clamping force acting on the sliding surfaces. The main goal of the experimental program is to obtain the friction coefficients of the investigated materials, both static and kinetic, for values of the normal force varying in a range leading to sliding forces suitable for structural applications and for values of the velocity compatible with seismic engineering applications. In addition, the experimental analysis is also devoted to evaluate the variation of the sliding force as far as the number of cycles of the applied loading history increase. In fact, as already demonstrated by Pall & Marsh (1981), the response of an interface subjected to cyclic loading conditions can substantially be of two types. The first type of response provides a monotonically softening behaviour. In this case, the maximum sliding load is reached during the first cycle whereas in all the subsequent cycles only degradation behaviour is expected. The second type of response is characterized by three phases: first a hardening response, then a steady state phase and finally a load degradation phase.

The tests have been carried out by means of a universal testing machine Schenck Hydropuls S56. The testing apparatus is constituted by an hydraulic piston with loading capacity equal to +/- 630 kN, maximum stroke equal to +/- 125 mm and a self-balanced steel frame used to counteract the axial loadings. In order to measure the axial displacements the testing device is equipped with an LVDT, while the tension/compression loads are measured by means of a load cell. The cyclic tests have been carried out under displacement control for different displacement amplitudes at a frequency equal to 0.25 Hz (Figs. 2-3).

For all the tests the average values of the static and kinetic coefficient of friction have been determined considering the following expression:

$$\mu = \frac{F}{m\, n\, N_b}$$

(1)

where $m$ is the number of surfaces in contact, $n$ is the number of bolts, $N_b$ is the bolt preloading force and $F$ is the sliding force. The obtained values are delivered in Table 1.

Table 1. Values of the friction coefficient

| Interface | $\mu_{static}$ | $\mu_{dynamic}$ |
|---|---|---|
| Steel on Steel | 0.173 | 0.351 |
| Brass on Steel | 0.097 | 0.200 |
| M0 on Steel | 0.254 | 0.254 |
| M1 on Steel | 0.201 | 0.201 |
| M2 on Steel | 0.158 | 0.180 |

Concerning the behaviour exhibited by the five materials under cyclic loads, the main results of the experimental program can be summarized as follows:

- Steel on steel interface exhibited an high coefficient of friction, but with an unstable behaviour which is initially characterized by a significantly hardening behaviour and successively by a quickly softening behaviour;
- Brass on steel interface showed a significant hardening behaviour with a low static friction coefficient;
- Material M0, which is a rubber based material developed for automotive applications exhibited a very stable behaviour and high energy dissipation capacity also under high values of the preloading level;
- Material M1, which is a rubber based material developed for electrical machines, exhibited a cyclic behaviour with some pinching and with low friction coefficient and a quickly degrading behaviour;
- Material M2, which is an hard rubber based material developed for applications where low wearing is needed, developed a quite low value of the friction coefficient, but a very stable behaviour and high dissipation capacity.
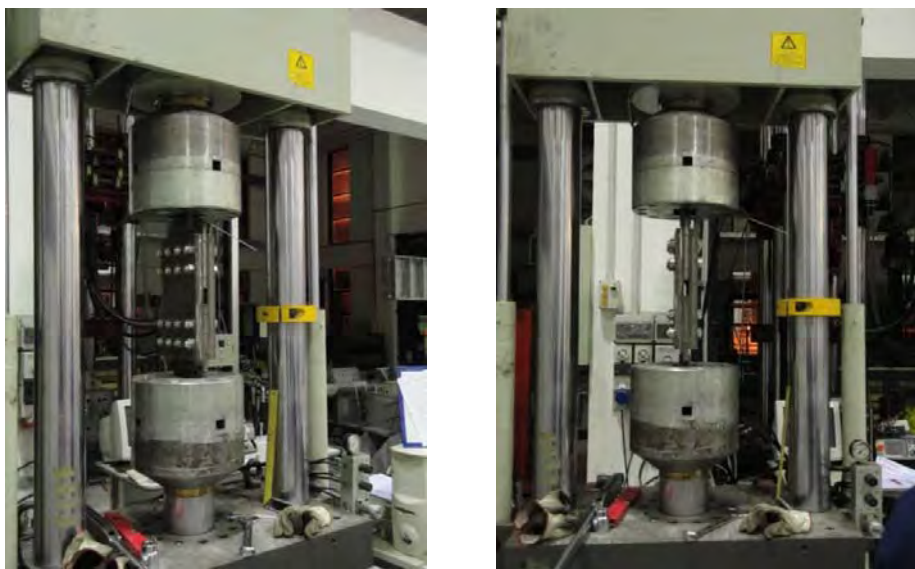


Fig. 3. Tested Specimen

### 3. EXPERIMENTAL TESTS ON DST JOINTS WITH FRICTION PADS

Starting from the component behaviour, i.e. the testing results of the sub-assemblage with friction pads presented in the previous section, the design of dissipative DST connections with friction pads, i.e. with interposed layers of friction material between the beam flanges and the stems of the tee elements, has been performed. The cyclic behaviour of the proposed innovative DST connections with friction pads can also be compared with the energy dissipation capacity of a traditional

double split tee connection tested in a previous work (Iannone et al., 2011), namely TS-CYC 04. Experimental tests have been carried out at Materials and Structures Laboratory of Salerno University. The testing equipment is that already adopted to test traditional beam-to-column connections (Iannone et al., 2011).

Two steel hinges, designed to resist shear actions up to 2000 kN and bolted to the base sleigh have been used to connect the specimens to the reacting system. The specimen is assembled with the column (HEB 200) in the horizontal position, connected to the hinges, and the beam (IPE 270) in the vertical position (Fig.4). The loads have been applied by means of two different hydraulic actuators. The first one is a MTS 243.60 actuator with a load capacity equal to 1000 kN in compression and 650 kN in tension with a piston stroke equal to +/- 125 mm which has been used to apply, under force control, the axial load in the column equal to 630 kN. The second actuator is a MTS 243.35 with a load capacity equal to 250 kN both in tension and in compression and a piston stroke equal to +/- 500 mm which has been used to apply, under displacement control, the desired displacement history at the beam end. The loading history has been defined according to ANSI-AISC 341-10. During the tests many parameters have been monitored and acquired, in order to get the test machine history imposed by the top actuator and the displacements of the different joint components.
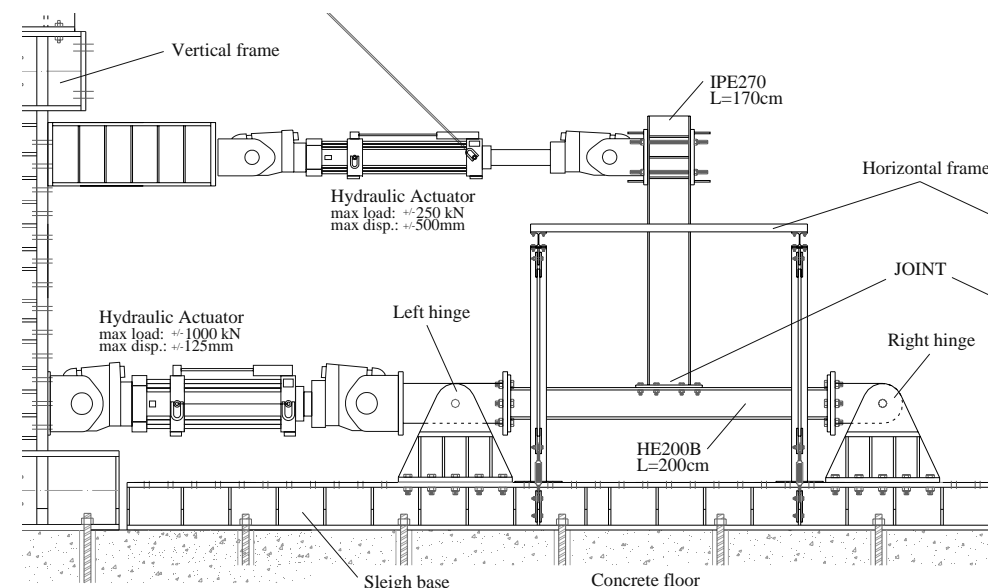


Fig. 4. Experimental testing equipment

Aiming at the evaluation of the beam end displacements due to the beam-to-column joint rotation only, the displacements measured by means of the LVDT equipping MTS 243.35 actuator have been corrected by subtracting the elastic contribution due to the beam and column flexural deformability according to the following relationship (Iannone et al., 2011):

$$\delta_j = \delta_{T3} - \frac{FL_b^3}{3EI_b} - \frac{FL_c L_b^2}{12EI_c}\left[\left(\frac{L_c}{L_c+2a}\right)^2 + \frac{6a}{L_c+2a}\right] \qquad (2)$$

where $I_b$ and $I_c$ are the beam and column inertia moments, $L_c$ is the column length, $L_b$ is the beam length and $a$ is the length of the rigid parts due to the steel hinges. The experimental tests carried out up to now concern four specimens (Fig. 5):

- TSJ-M1-460-CYC08, TSJ-M2-460-CYC09 and TSJ-B-460-CYC11, which are three double split tee connections. The first two are equipped with layers of friction material, namely M1 and M2, and the third one with a brass plate interposed between the Tee stems and the beam flanges. The slipping interfaces have been clamped by means of eight M20 class 10.9 bolts tightened with a torque equal to 460 Nm. In order to allow the relative movement between the stems of the T-stubs and beam flanges, two slotted holes have been realized on the tee stems. The slots have been designed in order to allow a maximum rotation of 70 mrad. The flanges of the T-stubs are fastened to the column flanges by means of eight M27 class 10.9 bolts located into holes drilled with a 30 mm drill bit.;
- TSJ-M2-DS-460-CYC010, which is a double split tee connection with the same characteristics of the other tested joints, but with a couple of disc springs interposed between the bolt nut and the beam flange.



t=30 mm
Bolts M27 class 10.9
t=10 mm
IPE 270
Friction Material
Slotted plate (t=15 mm)
Bolts M20 class 10.9
HEB 200

171
45 — 81 — 45
45
116
173
132
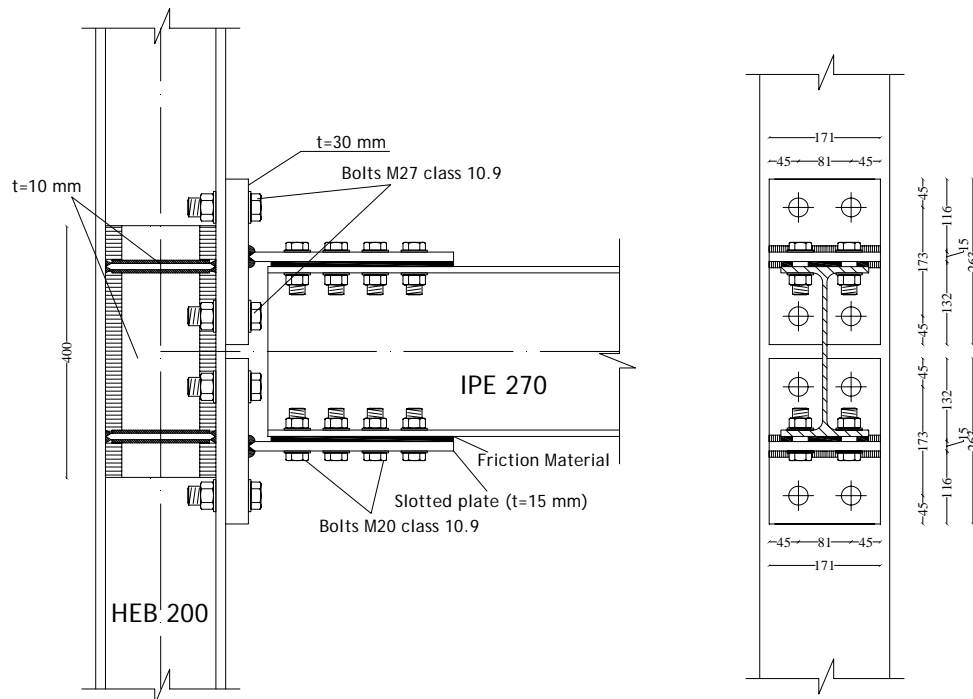15
263
45
132
173
15
263
45
116
45 — 81 — 45
171

Fig. 5. Geometrical detail and picture of tested joints

The identity tag of the tested specimens uniquely identifies the connection detail. In particular, the meaning of the letters is: 1 - Joint typology, i.e. Tee Stub Joint (TSJ); 2 – Friction interface, i.e. friction material M1 (M1), friction material M2 and Brass (B); 3 – Washer typology if different from the classical flat washer, i.e. Disc Spring (DS); 4 – Bolt tightening level; 5 -Test number, i.e. CYCnumber.

## 4. CYCLIC BEHAVIOUR OF SPECIMENS

As aforementioned, the main goal of the work herein presented is to provide an innovative approach to prevent structural damage in dissipative zones of MRFs where the main source of energy dissipation is due to the beam end damage in case of full-strength connections and to the damage of connecting plate elements in case of partial-strength connections. To this scope, the proposed beam-to-column joint typology is detailed in order to dissipate the seismic input energy through the slippage of the friction material interposed between the T-stub stem and the beam flange. In particular, hierarchy criteria at the level of joint components can be established to assure the desired connection behaviour. Therefore, starting from the design bending moment, equal to 100 kNm, established with the aim of developing the same degree of flexural strength of the traditional joints already tested in a previous research work (Iannone et al., 2011), all the remaining joint components (i.e. the T-stub flanges, the bolts and the column panel zone) have been designed to assure an adequate overstrength with respect to the friction resistance. In particular, the friction interface has been designed according to Eq. (1) considering that the force to be transmitted is simply obtained as the ratio between the design bending moment and the lever arm. Therefore, the desired friction resistance at the sliding interface has been obtained by properly fixing the number of bolts and the tightening force of the bolts fastening the tee stems to the beam flanges.

In perfect agreement with the adopted design criteria, all the experimental tests have not shown any damage of the joint components, pointing out only the involvement of the friction pads. Therefore, the most important result of the experimental program is that the proposed connection typology can be subjected to repeated cyclic rotation histories, i.e. to repeated earthquakes, by only substituting the friction pads and by tightening again the bolts to reach the desired preloading level. In addition, the rotation capacity can be easily calibrated by simply governing the length of the slots where the bolts are located. The results of the experimental program on DST connections with friction pads are in line with the results found by testing the friction component outlining that, as expected, the cyclic the behaviour of the joint is mainly governed by the cyclic behaviour of the weakest joint component (i.e. the friction component in the examined cases).

In fact, as verified during the test TSJ-M1-460-CYC08, where material M1 was adopted, the response of the joint has been very similar to that evidenced during the uniaxial tests investigating the friction interface behaviour. A significant pinching and strength degradation behaviour was exhibited, after that the design resistance of 100 kNm was reached (Fig.6). This was also due to the premature fracture of the friction pad, which was not observed in component testing. For this

reason, this material will be excluded from the forthcoming developments of this research activity.
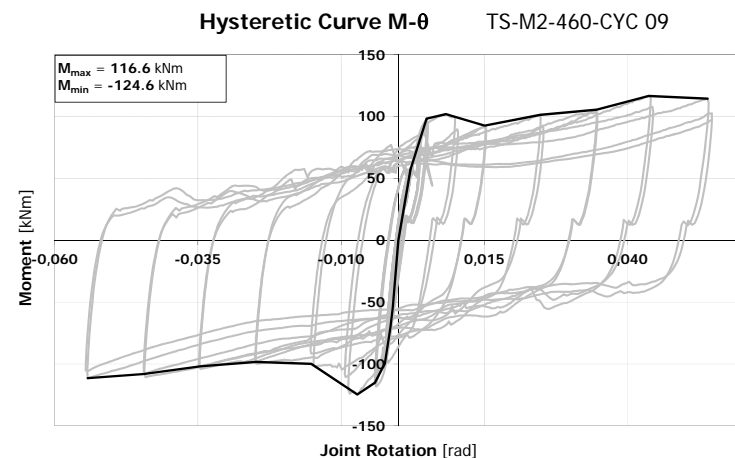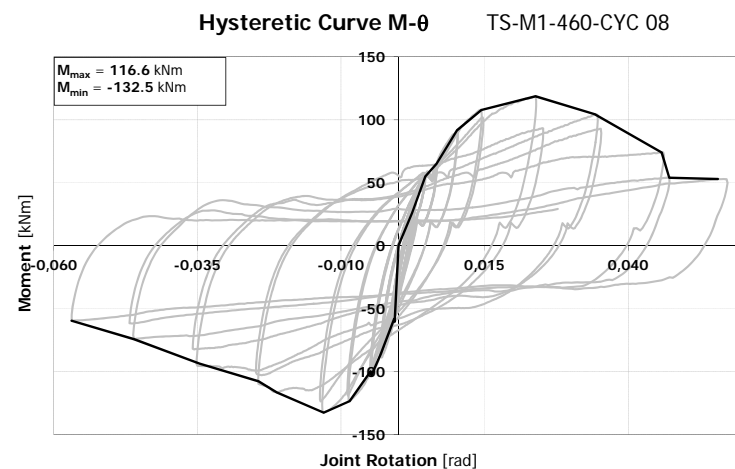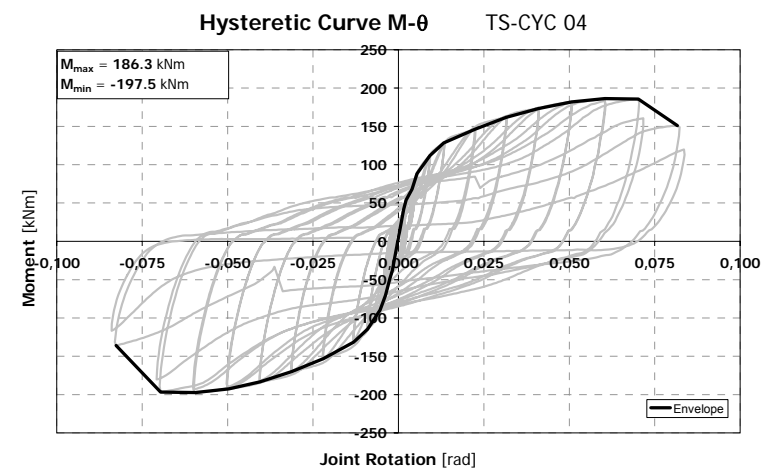
In case of friction material M2 (TSJ-M2-460-CYC09), a stable cyclic response with a hardening behaviour due to the increase of local stresses caused by the beam rotation and by the rotational stiffness due to the bending of the tee stems has been pointed out (Fig.6). In addition, the results show that a slight strength and stiffness degradation begins at high rotation amplitudes probably due to the consumption of the friction pads during the sliding motion.

The test on brass friction pads, TSJ-B-460-CYC11, also exhibited a good behaviour in terms of shape of the cyclic response. In fact, the obtained cycles are very stable also at high values of the plastic rotation. Nevertheless a value of the bending moment lower than the design value of 100 kNm was obtained, because of poor friction resistance. This result can be justified on the base of the results obtained by component testing. In fact, in case of brass on steel interface (Table 1) the value of the static friction coefficient is much lower than the dynamic one and, as a consequence, a bending moment lower than the expected one has been obtained (Fig.6). For this reason and considering the high cost of this material, the use of brass for friction pads will be excluded in the forthcoming research developments.

Finally, in order to reduce the problems related to the consumption of the friction material observed during the test TSJ-M2-460-CYC09, another test, namely TSJ-M2-DS-460-CYC10, with the same layout but adopting disc springs interposed between the bolt head and the tee web plate has been carried out. Such a type of washer is a high resistance cone shaped annular steel disc spring which flattens when compressed and returns to its original shape if compression loading is released. In this way, the wearing of the friction material, which would lead to the partial loss of bolt preload, is compensated by the action of the disc spring which restores the force by maintaining the bolt shaft in tension. In fact, the results of test TSJ-M2-460-CYC10 have demonstrated the effectiveness of the adopted disc springs. Therefore, higher dissipation capacity and lower strength and stiffness degradation was obtained (Fig.6).

In addition, in order to compare the cyclic behaviour of DST connections with friction pads with that of a traditional DST partial strength joint dissipating in the bolted components and characterized by same resistance, reference has been made to the test TS-CYC04 (Fig. 6) (Iannone et al., 2011). In particular, the envelopes of the cyclic moment-rotation curves are reported in Fig. 7 for all the tested specimens, both innovative and traditional.

It can be observed that the bending moment corresponding to the knee of the curves, corresponding to the design value of the joint resistance, is similar for all the tests adopting friction materials, but the obtained post-elastic behaviours are quite different with respect to traditional DST connections. In fact, compared to the case of joint TS-CYC04, friction DST joints do not exhibit significant hardening behaviour whose magnitude is limited to the effects coming from the bending of the T-stub stems.
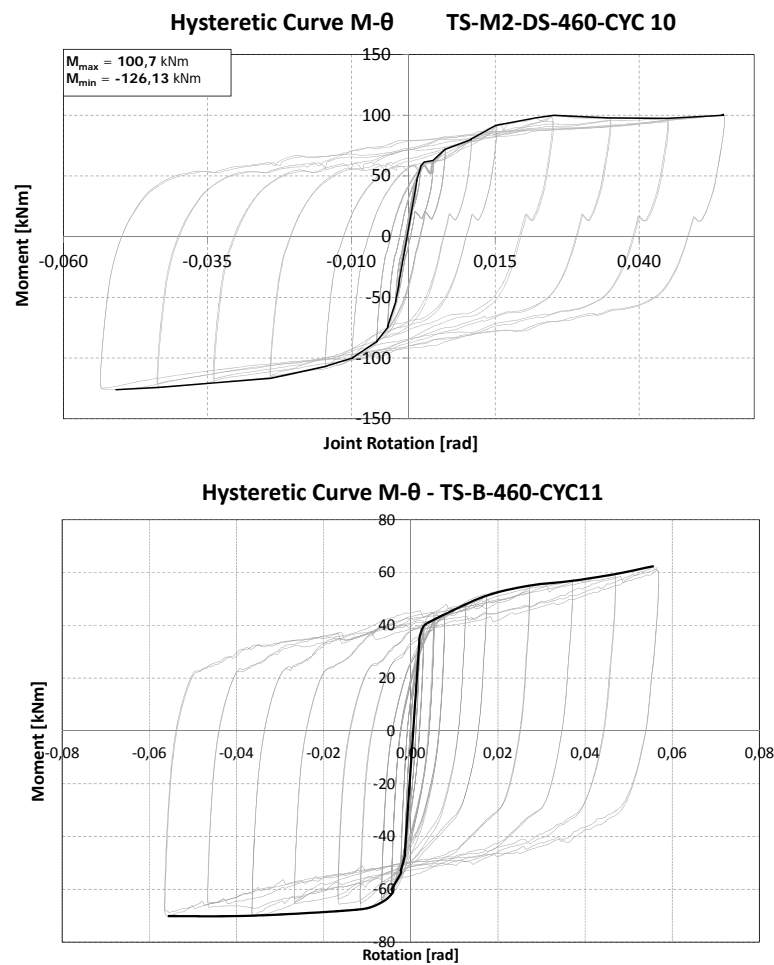


Hysteretic Curve M-θ        TS-CYC 04

$M_{max}$ = **186.3** kNm
$M_{min}$ = **-197.5** kNm



Hysteretic Curve M-θ        TS-M1-460-CYC 08

$M_{max}$ = **116.6** kNm
$M_{min}$ = **-132.5** kNm



Hysteretic Curve M-θ        TS-M2-460-CYC 09

$M_{max}$ = **116.6** kNm
$M_{min}$ = **-124.6** kNm

**Hysteretic Curve M-θ      TS-M2-DS-460-CYC 10**



**Hysteretic Curve M-θ - TS-B-460-CYC11**



Fig. 6**.** Hysteretic curves of tested joints

With reference to TS-M2-460-CYC09 and TS-M2-DS-460-CYC10 tests, it is worth to note that the hysteresis cycles are wide and stable with no pinching. This is the reason why the joints, in spite of the less hardening behaviour, are able to dissipate more energy than connection TS-CYC04 (Fig. 7).

## 5. CONCLUSIONS

In this paper the possibility to enhance the cyclic behaviour of traditional DST joints dissipating the seismic input energy in bolted components has been analysed. In particular, the cyclic rotational response of four Double Split Friction Tee Stub beam-to-column joints adopting different friction materials has been investigated. The response in terms of energy dissipation and shape of the hysteresis loops of the proposed connection structural details has been compared to that of a traditional

DST joint tested in a recent experimental program. The presented results are very encouraging confirming the goodness of the proposed approach.

**Hysteretic Curve M-θ**
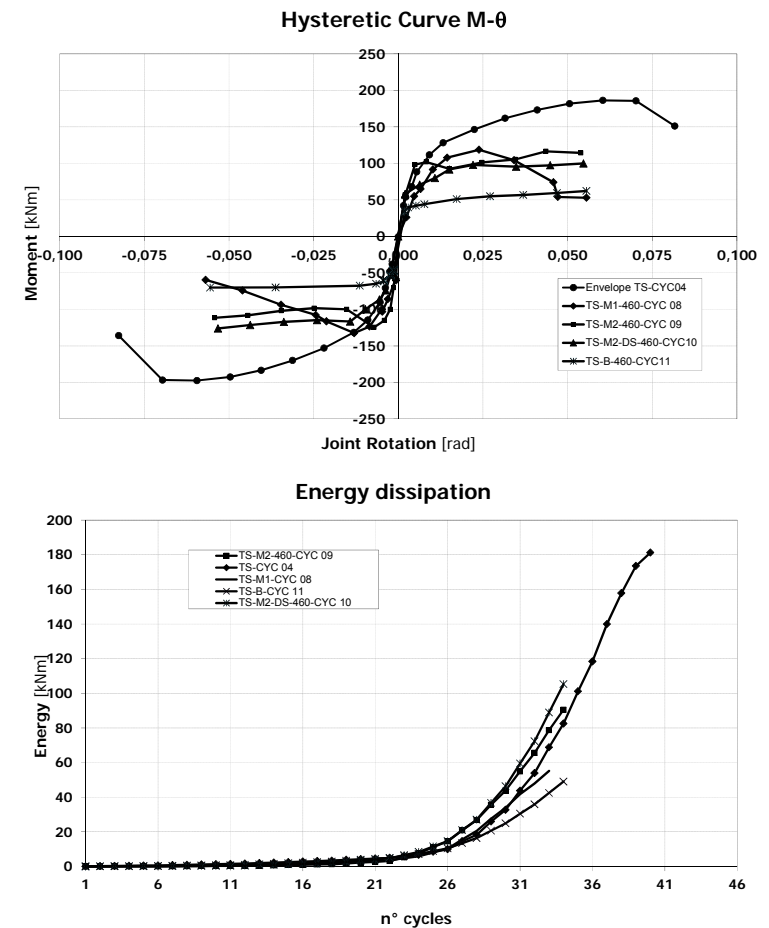


**Energy dissipation**



Figure 7. Cyclic envelopes and energy dissipation of tested DST connections

In particular, all the experimental tests have confirmed that the strategy of adopting friction pads within the components of bolted connections can be effective for the ambitious goal of damage prevention, because the proposed DST connection is able to withstand repeated cyclic rotation histories, i.e. repeated earthquakes, by simply substituting the friction pads and by restoring the tightening of the connecting bolts.

## ACKNOWLEDGEMENTS

www.steelconstruct.com

# REFERENCES

[1] Aiken, I., Nims, D., Whittaker, A. & Kelly, J., 1993a. Testing of Passive Energy Dissipation Systems. Earthquake Spectra, 9(3).

[2] ANSI/AISC 341-10. American National Standard: Seismic Provisions for Structural Steel Buildings. June 22, 2010. American Institute of Steel Construction, Chicago, Illinois, USA.

[3] ANSI/AISC 358-10. American National Standard: Prequalified Connections for Special and Intermediate Steel Moment Frames for Seismic Applications. Including Supplement No. 1: ANSI/AISC 358s1-11. American Institute of Steel Construction, Chicago, Illinois, USA.

[4] Astaneh-Asl, A., 1987. Experimental Investigation of Tee Framing Connection. AISC.

[5] Bernuzzi, C., Zandonini, R. & Zanon, P., 1996. Experimental analysis and modelling of semi-rigid steel joints under cyclic reversal loading. Journal of Constructional Steel Research, 2, pp.95-123.

[6] CEN, 2005a. Eurocode 8: Design of structures for earthquake resistance - Part 1: General rules, seismic actions and rules for buildings.

[7] CEN, 2005b. Eurocode 3: Design of steel structures - Part 1-1: General rules and rules for buildings.

[8] CEN, 2005c. Eurocode 3: Design of steel structures - Part 1-8: Design of joints.

[9] Christopoulos, C. & Filiatrault A., 2000. Principles of Passive Supplemental Damping and Seismic Isolation. IUSS PRESS. Pavia. Italy

[10] Faella, C., Montuori , R., Piluso, V. & Rizzano, G., 1998. Failure mode control: economy of semi-rigid frames. In Proceedings of the XI European Conference on Earthquake Engineering. Paris, 1998.

[11] Faella, C., Piluso, V. & Rizzano, G, 1999. Structural Steel Semirigid Connections, CRC Press, Boca Raton, Ann Arbor, London, Tokyo, 1999. ISBN 0-8493-7433-2.

[12] Iannone, F., Latour, M., Piluso, V. & Rizzano, G., 2011. Experimental Analysis of Bolted Steel Beam-to-Column Connections: Component Identification. Journal of Earthquake Engineering, Volume 15, Number 2, February 2011, pp. 214-244(31).

[13] Latour, M., Piluso, V. & Rizzano , G., 2011a. Cyclic Modeling of Bolted Beam-to-Column Connections: Component Approach. Journal of Earthquake Engineering, 15(4), pp.537-63.

[14] Latour, M., Piluso, V. & Rizzano, G., 2011b. Experimental Analysis of Innovative Dissipative Bolted Double Split Tee Beam-to-column Connections, DOI: 10.1002/stco.201110009, Steel Construction, Volume 4, Issue 2, pages 53–64, June, 2011.

[15] Latour, M. & Rizzano, G., 2012. Experimental Behaviour and Mechanical Modeling of Dissipative T-Stub Connections. Journal of Structural Engineering, 138(2), pp.170-82.

[16] Longo, A., Montuori, R. & Piluso, V., 2012. Theory of Plastic Mechanism Control of Dissipative Truss Moment Frames. Engineering Structures. 37 (2012) pp. 63-75.

[17] Mazzolani, F.M. & Piluso, V., 1996. Theory and Design of Seismic Resistant Steel Frames, E & FN Spon, An imprint of Chapman & Hall, First Edition, 1996. ISBN 0-419-18760-X.

[18] Mazzolani, F.M. & Piluso, V., 1997. Plastic Design of Seismic Resistant Steel Frames, Earthquake Engineering and Structural Dynamics, Volume 26, Issue 2 (1997), pp. 167-191.

[19] Pall, A. & Marsh, C., 1981. Response of Friction Damped Braced Frames. Journal of the Structural Division, 108(6), pp.1313-23.

[20] Piluso, V., Faella , C. & Rizzano, G., 2001a. Ultimate behavior of bolted T-stubs. Part I: Theoretical model. Journal of Structural Engineering ASCE, 127(6), pp.686-93.

[21] Piluso, V., Faella , C. & Rizzano, G., 2001b. Ultimate Behaviour of Bolted T-stubs – II. Experimental Analysis, Journal of Structural Engineering, ASCE, Volume 127, Issue 6, pp. 694-704, 2001.

[22] Piluso, V. & Rizzano, G., 2008. Experimental Analysis and modelling of bolted T-stubs under cyclic loads. Journal of Constructional Steel Research, 64, pp.655-69.

[23] Soong, T. & Spencer Jr, B., 2002. Supplemental Energy Dissipation: State-of-the-Art and State-of-the-Practice. Engineering Structures, 24, pp.243-59.

[24] Whittaker, A., Bertero, V., Alonso , J. & Thompson, C., 1989. UCB/EERC-89/02 Earthquake Simulator Testing of Steel Plate Added Damping and Stiffness Elements. Berkeley: College of Engineerign University of California.

# NON LINEAR BEHAVIOR OF SHEAR LUGS AND STEEL BUILDINGS RESPONSE

Aguirre Carlos

*Department of Civil Engineering, Universidad Santa María, Chile.*
*carlos.aguirre @usm.cl*

## ABSTRACT

Shear Lugs are frequently used in seismic areas where large lateral forces have to be transferred to the foundations. It is normally assumed that there are two controlling limits states for a shear lug: the bearing strength of concrete and the flexural yielding strength of the steel. Tests results performed during the last three years at Santa Maria University's Laboratory show that the steel failure normally occur in shear yielding and this failure mode is more ductile than concrete bearing failure. In this paper, some typical steel building subjected to selected ground motion records was studied. It was found that ductile shear lugs have a slight isolation effect but it has no influence in the global performance of the buildings.

## 1. INTRODUCTION

Shear lugs are frequently used when large lateral forces occur, especially in structures built in seismic areas. Several types of steel shapes can be used as shear lugs; Fig. 1 illustrates a Cross type shear lug, it has to provide strength in any direction of the horizontal loads. Present codes design is based on methodologies coming from the engineering experience and some basic theoretical principles. There are only a few studies related to shear lugs design. This research work is a continuation of a research program developed at Santa Maria University. The first part of this program included the experimental testing of different type of shear lugs cross sections (Aguirre C and Palma I, 2009). The geometry of tested specimens is shown in Table 1, some of them were selected to produce failure in the steel and some others to produce the concrete failure. Fig.1 shows a detail of the cross type shear lug.
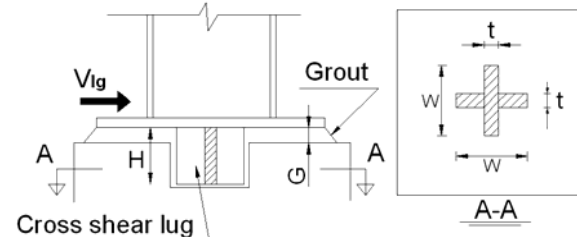


Figure 1. Cross Type Shear Lug

The first group of specimens (N° 1 up to N° 12) are cross steel shapes, the second group (N°13 up to N°20) are W steel shapes with the load applied on the strong axis, the third group (N°21 up to N°26) are W shapes too but the load is applied on the weak axis and finally Specimens N°10, 11 and 12 were extra samples, made with higher grout thicknesses, to evaluate the influence of the grout thicknesses on the results. The failure of a shear lug can happen either in the steel lug or in the surrounding concrete. Tests results demonstrate that the steel failure is shear yielding type and concrete failure is bearing type, Fig. 2 shows one of the samples tested. In a difference with the current design practice based on AISC N° 1 Design Guide (2010), the testing program demonstrated that the steel failure is normally a shear yielding type. The flexural yielding steel failure never occurs



Figure 2. Cross type shear lug

Table 1. Specimens Geometry

| 1.- Cross type shear lug | | | | |
|---|---|---|---|---|
| Test N° | W (mm) | H (mm) | t (mm) | G (mm) | |
| 1 | 100 | 100 | 5 | 8 | |
| 2 | 100 | 75 | 5 | 8 | |
| 3 | 100 | 50 | 5 | 8 | |
| 4 | 100 | 100 | 8 | 11 | |
| 5 | 100 | 75 | 8 | 11 | |
| 6 | 100 | 100 | 12 | 15 | |
| 7 | 100 | 75 | 12 | 15 | |
| 8 | 100 | 50 | 12 | 15 | |
| 9 | 100 | 100 | 19 | 20 | |
| 10 | 140 | 140 | 5 | 40 | |
| 11 | 140 | 140 | 8 | 40 | |
| 12 | 140 | 140 | 12 | 40 | |

| 2.- W type shear lug-Strong Axis | | | | | |
|---|---|---|---|---|---|
| Test Nº | W (mm) | H (mm) | S (mm) | t (mm) | G (mm) |
| 13 | 100 | 100 | 90 | 5 | 15 |
| 14 | 100 | 50 | 90 | 5 | 15 |
| 15 | 100 | 75 | 225 | 3 | 15 |
| 16 | 100 | 75 | 75 | 3 | 15 |
| 17 | 100 | 75 | 75 | 19 | 15 |
| 18 | 100 | 75 | 225 | 19 | 15 |
| 19 | 150 | 130 | 130 | 3 | 15 |
| 20 | 150 | 130 | 130 | 6 | 15 |
| 21 | 100 | 100 | 90 | 5 | 15 |
| 22 | 100 | 50 | 90 | 5 | 15 |
| 23 | 100 | 75 | 75 | 3 | 15 |
| 24 | 100 | 75 | 150 | 19 | 15 |

| 3.- W type shear lug-Weak Axis | | | | | |
|---|---|---|---|---|---|
| Test Nº | W (mm) | H (mm) | S (mm) | t (mm) | G (mm) |
| 25 | 100 | 75 | 75 | 19 | 15 |
| 26 | 100 | 100 | 90 | 19 | 15 |

| 4.- O type shear lug | | | | |
|---|---|---|---|---|
| Test Nº | D (mm) | H (mm) | t (mm) | G (mm) |
| 29 | 114.3 | 100 | 6.02 | 15 |
| 30 | 114.3 | 75 | 6.02 | 15 |

The dotted red line on the picture emphasizes the shape of a typical shear deflection, which normally happens in short members. It suggests that shear lug strength can be obtained by using the shear capacity of the steel shape, expressed by equation (1).

$$V_{steel} = 0.6\, F_y \cdot A_{shear} \tag{1}$$

## 2. DESIGN APPROACH

Shear Lug Design use to be done by applying either AISC N° 1 Design Guide (2010) or ACI 349-01 Code (2001), both of them assume two possible controlling limit states:

- Bearing of Concrete
- Flexural Yielding of the Steel

AISC Steel Design Guide N°1, accepts both ASD and LRFD design methods. When ASD design method is used, it is assumed for the bearing stress of concrete a safe value of $0.35 \cdot f'c$ (unconfined concrete). For LRFD design method a $0.85 \cdot \varphi_c \cdot f'c$ is assumed as a nominal bearing stress. The dimensions of shear lugs must provide enough bearing area between the shear lug and concrete to fulfil the concrete limit state (without considering the grout), as it is shown on Table 1. The shear lug is assumed a steel plate behaving as a cantilever beam. The design is based on the maximum moment ($M_{lg}$) at the base. The shear lug thickness is obtained considering the steel plate moment strength, according to Table 2 and figure 2.

Table 1. Required bearing area

| DESIGN METHOD | |
|---|---|
| ASD | LRFD |
| $t_{lg} = \sqrt{\dfrac{6 \cdot M_{lg}}{0.75 \cdot F_y}}$ | $t_{lg} = \sqrt{\dfrac{4 \cdot M_{lgu}}{0.90 \cdot F_y}}$ |

Table 2. Shear lug thickness.

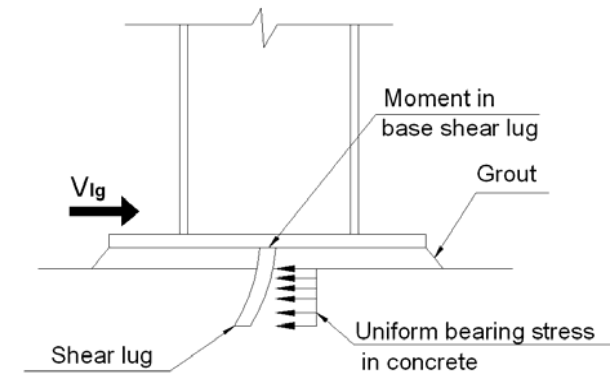| DESIGN METHOD | |
|---|---|
| ASD | LRFD |
| $A_{lg} = \dfrac{V_{lg}}{0.35 \cdot f'_c}$ | $A_{lg} = \dfrac{V_{lgu}}{0.85 \cdot \varphi_c \cdot f'_c}$ |



Figure 2 - Load and deflection of the Shear lug

ACI 349-01 Code states that design compression stress, either for concrete or grout, shall not exceed $1.3 \cdot \phi \cdot f'_c$ (LRFD method), and $\phi$ reduction is 0.70. A comparison of ACI and AISC nominal stress is shown in Table 3. It can be seen that ACI nominal stress is 78% larger than AISC nominal stress, that means ACI proposal for the concrete bearing pressure is less conservative than AISC-Guide N°1. In spite of this approach ACI produces safe designs of the lugs. It seems that there is no reason for a more conservative approach.

www.steelconstruct.com

Table 3. ACI-349 and AISC-Guide N°1 comparison

| Nominal stress (LRFD) ACI 349-01 | Nominal stress (LRFD) Guide N°1, AISC |
|---|---|
| $\sigma_{nom} = 1.3 \cdot \phi \cdot f'_c = 0.91 \cdot f'_c$ | $\sigma_{nom} = 0.85 \cdot \varphi_c \cdot f'_c = 0.51 \cdot f'_c$ |

Both approaches are based on Rotz and Reifschneider (1989) research work, who studied the behavior of the plates under a combination of shear and axial load, in tension and compression. The results of their tests presented a prime and first failure type denominated "bearing mode", related to concrete compression bearing capacity. The "bearing mode" is associated to the formation of shallow fracture plane on the top surface of the specimen, a fast increase of horizontal and vertical displacement, and a fast reduction of the shear load strength. From this study, expression (2) for the shear capacity was proposed.

$$V_{concrete} = K_b \ f'_c \ A_{lg} + K_c \ (P_y - P_a) \qquad (2)$$

The first term of the equation is the typical compression strength of concrete; the second term is the concrete confinement effect on the base plate produced by the anchor bolts, it increases the strength capacity. $K_b$ and $K_c$ are parameters empirically obtained.
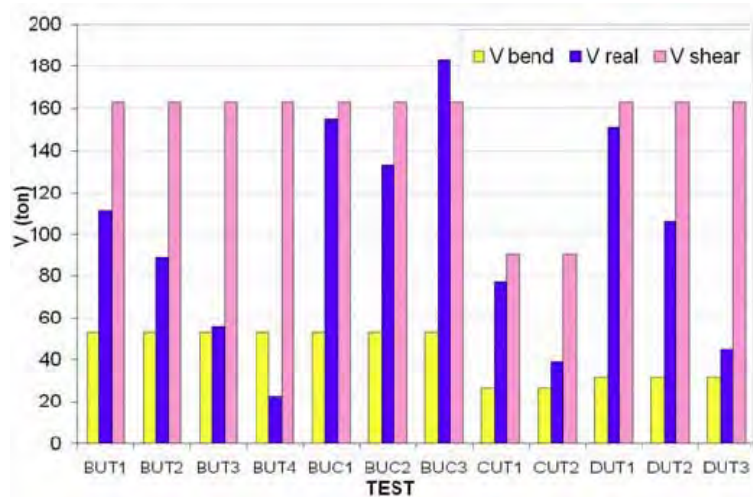


Figure 3. Rotz tests results

In order to understand the predominant failure mode of the steel, the chart on Figure 3 was prepared. It is a comparison of Rotz tests results and the calculated strengths of the shear lug. $V_{real}$ is the test result, $V_{bend}$ was determined assuming the lug behaves as a cantilever beam clamped at the base plate, who yield in bending. $V_{shear}$ was obtained assuming a shear yielding failure (Equation 1). It can be seen that the steel flexural yielding was the smallest strength in most of the cases (92%),

which means that the shear lugs should have been failed into this first mode. But the failure mode reported by the authors is the bearing of concrete, which according to Fig. 3 exhibit a larger strength than the flexural yielding mode in almost all of the tests. In other words concrete bearing was the typical failure mode in spite of its strength is larger than the flexural steel yielding strength. On the other hand, the shear steel yielding mode has the highest strength; such a result agrees well with Rotz's tests failures in concrete bearing.

Fig. 4 is a comparison of concrete and steel failure modes obtained from tests results. It can be seen the higher ductility level of shear yielding of the steel compare to the concrete bearing failure mode. From the standpoint of the earthquake engineering larger ductilities are advantageous, but the difficulty to replace a shear lug after a severe earthquake, have to be considered in any design approach.
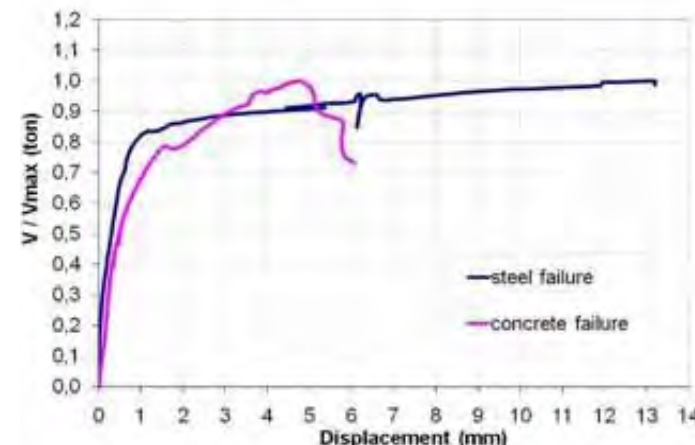


Fig. 4. Comparison of typical steel shear yielding failure and concrete bearing failure for cross section

## 3. NON LINEAR BUILDING ANALYSIS

In order to study the influence of the shear lug ductility in the seismic behaviour of buildings, a set of steel frame buildings was chosen and analyzed under the action of some selected ground motion records occurred during the last 30 years. The goal was to determine whether the shear lug ductility reduces or increases the structural damage of the buildings and to explore the possibility of using the lug properties to get safer and more economic structures.

Figure 5 shows a sketch of a typical building, the number of stories selected was 4, 8, 12 and 16; the plan is the same for all of them. The ground motions records selected are presented in Table 4. The building analyses were performed under two assumptions: (1) the columns are fixed to the base and (2) the columns are connected to the base through a non linear shear lug. The non linear properties were obtained from the experimental tests results (Palma, I., 2008).

www.steelconstruct.com
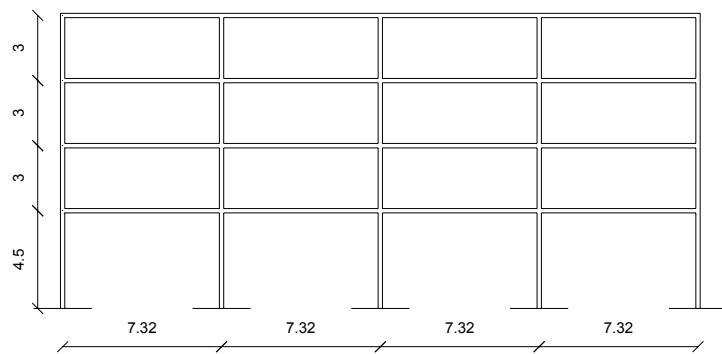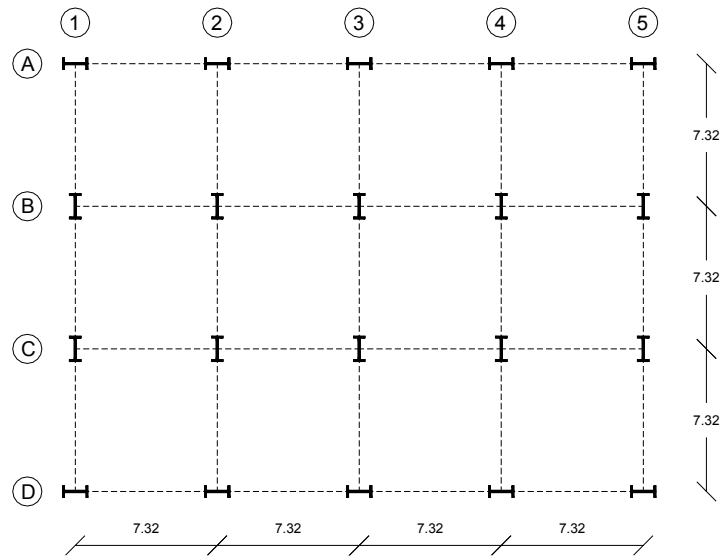
(a) Elevation



(b) Plan

Figure 5. Plan and Elevation of the selected buildings

Shear lug design was performed according two approaches: (1) AISC Design Guide N° 1 (AISC, 2010) assuming that the limit state that for the lug design is the yielding in flexure and (2) according to Palma, I (2008) proposal, assuming that the limit state is shear yielding. In order to avoid the concrete bearing failure, a larger concrete strength was provided. Table 5 shows the Design Base Shear for all the buildings and the geometric properties of the shear lugs according to both design approaches. It can be seen that the first approach produces stronger shear lugs.

Time history analyses of the buildings were performed by using the elasto-plastic hysteresis model included in Ruaumoko program. Shear lugs were modelled by considering elasto-plastic shear elements at the base of the columns, the properties were obtained from the experimental results Palma, I (2008). Fig. 6 shows some characteristic curves of cross type shear lugs.

Table 4. Ground Motion Records

| Earthquake | Record | Duration (s) | Richter Magnitude | Amax (g) |
|---|---|---|---|---|
| Chile [03-03-1985] | Viña | 60 | 7,8 | 0,36 |
| Chile [03-03-1985] | Llolleo | 60 | 7,8 | 0,71 |
| México [19-09-1985] | SCT | 60 | 8,1 | 0,17 |
| U.S.A [17-01-1994] | Northridge | 60 | 6,8 | 0,84 |
| Japan [17-01-1995] | Kobe | 60 | 6,9 | 0,84 |
| Chile [27-02-2010] | Concepcion | 60 | 8,8 | 0,48 |

Table 5. Design Parameters

| Building Height Stories | Base Shear Q [kN] | Flexural Yielding W [cm] | H [cm] | t [cm] | Shear Yielding W [cm] | H [cm] | t [cm] |
|---|---|---|---|---|---|---|---|
| 4 | 1804 | 15 | 9 | 2 | 20 | 17 | 0,5 |
| 8 | 1557 | 15 | 8 | 2 | 18 | 16 | 0,5 |
| 12 | 2199 | 15 | 10 | 2 | 24 | 20 | 0,5 |
| 16 | 2950 | 15 | 12 | 2 | 22 | 21 | 0,8 |

## 4. RESULTS

In order to understand the influence of the shear lug ductility in the building behavior, the amount of plastic hinges formed under both kind of the column base conditions was selected as a measure of the building damage. The comparison is shown on Table 6, it can be seen some reduction of the number of hinges when ductile shear lugs are used, with the exception of Kobe and Mexico earthquakes. Table 7 shows the maximum demanded member ductility in every building. In some cases can be observed a slight isolating effect and sometimes a sort of a slight increase in the member ductility demands, but this is a minor effect and in some cases there is no effect.
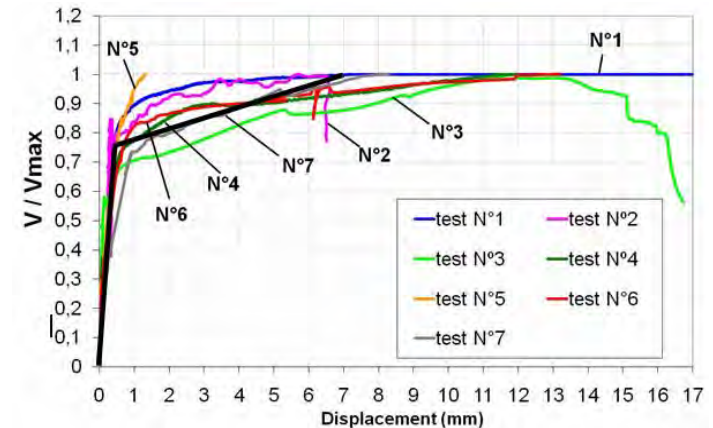


Figure 6. Shear Lug Curves

Table 6. Amount of Plastic hinges formed depending on the base type

| Stories | Base Support | Kobe 1995 | Llolleo 1985 | México 1985 | North. 1994 | Viña 1985 | Conc. 2010 |
|---------|--------------|-----------|--------------|-------------|-------------|-----------|------------|
| 4 | Fixed | 37 | 29 | 0 | 37 | 23 | 27 |
| 4 | Ductile | 37 | 21 | 0 | 31 | 5 | 6 |
| 8 | Fixed | 69 | 53 | 0 | 69 | 48 | 61 |
| 8 | Ductile | 69 | 37 | 0 | 69 | 34 | 59 |
| 12 | Fixed | 93 | 84 | 60 | 77 | 46 | 69 |
| 12 | Ductile | 93 | 73 | 52 | 77 | 41 | 68 |
| 16 | Fixed | 123 | 105 | 106 | 113 | 15 | 87 |
| 16 | Ductile | 123 | 105 | 106 | 113 | 14 | 86 |

Table 7. Ductility demand at the most demanded member in each building

| Stories | Base Support | Kobe 1995 | Llolleo 1985 | México 1985 | North. 1994 | Viña 1985 | Conc. 2010 |
|---------|--------------|-----------|--------------|-------------|-------------|-----------|------------|
| 4 | Fixed | 10 | 3,6 | 1 | 5 | 3,1 | 3 |
| 4 | Ductile | 9,4 | 2,6 | 1 | 4,6 | 2,4 | 2,4 |
| 8 | Fixed | 5,4 | 1,7 | 1 | 7 | 1,5 | 3,7 |
| 8 | Ductile | 4,5 | 1,7 | 1 | 7 | 1,4 | 3,4 |
| 12 | Fixed | 4,3 | 2,8 | 4,2 | 7,7 | 1,7 | 2 |
| 12 | Ductile | 4,7 | 2,8 | 4,8 | 8,2 | 1,6 | 2,6 |
| 16 | Fixed | 6,5 | 3,3 | 9,7 | 9,5 | 1,2 | 2,7 |
| 16 | Ductile | 7,6 | 3,8 | 9,6 | 9,4 | 1,2 | 3,2 |

Table 8 shows the ductility demands to the shear lugs. When the shear lug remains in the elastic zone the demanded ductility is 1 and when the ductility demand exceeds 14 it was considered a shear lug failure.

Table 8. Demanded ductilities at shear lugs

| Stories | Kobe 1995 | Llolleo 1985 | México 1985 | North. 1994 | Viña 1985 | Conc. 2010 |
|---------|-----------|--------------|-------------|-------------|-----------|------------|
| 4 | Failure | Failure | 1 | Failure | Failure | Failure |
| 8 | Failure | Failure | Failure | Failure | Failure | Failure |
| 12 | Failure | Failure | Failure | Failure | 9,6 | Failure |
| 16 | Failure | 9,8 | Failure | Failure | 3,8 | 8,5 |

It can be seen that ductile shear lugs often fail and even though it does not mean a building collapse it's necessary to replace the shear lug, which is expensive and difficult. The shear lug designed according to AISC Design Guide N° 1 does not require ductility capacity, however those shear lugs has no strength capacity considerations in their design and they could fail in a brittle fashion.

# 5. CONCLUDING REMARKS

1. Shear lugs should be designed to fail after the failure of the structure in order to avoid the necessity to be replaced because the replacing is difficult and expensive.
2. In the event of a shear lug failure, it is better to have the steel failure first than the concrete failure, which is normally a brittle failure mode.
3. In order to guarantee a ductile steel failure, shear lug design should include capacity considerations to avoid a premature steel failure. In that sense the provided concrete strength should be larger than steel strength.
4. The steel failure mode is a typical shear yielding failure. Tests show that flexural yielding mode did not happen. As a consequence, shear steel yielding should be the controlling limit state for the steel lug design.
5. The more flexible the shear lug the higher is the isolation effect, however flexible shear lugs fails and the replacement is difficult and expensive.
6. The influence of shear lug ductility in the building behavior depends of the ground motion characteristics, the building and shear lugs structural properties. It produces a reduction of the earthquake forces but, in practice, it does not change substantially the damage of the structure.

## REFERENCES

[1] ACI Committee 349 (2001): "Code Requirements for Nuclear Safety Related Concrete Structures", American Concrete Institute, USA.
[2] Aguirre C, Palma I. (2009): "Shear Lugs for Column Bases", Steel Structures in Seismic Areas (STESSA), Philadelphia, USA.
[3] AISC-a (2010): "Specification for Structural Steel Buildings, American Institute of Steel Construction, Chicago, IL, USA.
[4] AISC-b (2010): "Seismic Provisions for Structural Steel Buildings, American Institute of Steel Construction, Chicago, IL, USA.
[5] AISC-c (2010): "Design Guide 1: Base Plate and Anchor Rod Design", 2nd Edition, American Institute of Steel Construction, Chicago, IL, USA.
[6] Carr, A. (2004): "Ruaumoko: Theory and User Guide to Associate Programs". University of Canterbury, New Zealand, 2004.
[7] Grauvilardell, J.E., Lee D., Hajjar, J.F., Dexter, R.J. (2005): "Synthesis of Design, Testing and Analysis Research on Steel Column Base Plate Connections in High Seismic Zones, Structural Engineering Report N° ST-04-02, Department of Civil Engineering, University of Minnesota, Minneapolis, Minnesota.
[8] INN 2002. NCh2369-2002 - Diseño Sísmico de Estructuras e Instalaciones Industriales, Instituto Nacional de Normalización Santiago, Chile.
[9] Palma, I. (2008): "Estudio experimental de llaves de corte en cruz". Tesis para obtener el grado de Magíster en Ciencias de la Ingeniería Civil. Valparaíso. UTFSM, Departamento de Obras Civiles, 2008.
[10] Rotz, J.V. & Reifschneider, M. (1989): "Combined Axial and Shear Capacity of Embedments in Concrete", 10th International Conference: Structural Mechanics in Reactor Technology, Anaheim, CA.
[11] Rotz, J.V. & Reifschneider, M. (1991): "Combined Axial and Shear Load Capacity of Steel Embedments in Concrete", Report by Bechtel Power Corporation.

# EXPERIMENTAL AND NUMERICAL EVALUATION OF A RBS COUPLING BEAM FOR MOMENT STEEL FRAMES IN SEISMIC AREAS

Florea Dinu[1,2]; Dan Dubina[1,2]; Calin Neagu[1]; Cristian Vulcu[1]; Ioan Both[1];Sorin Herban[1]

[1] The "Politehnica" University of Timisoara, Department of Steel Structures and Structural Mechanics, Romania
[2] Romanian Academy, Timisoara Branch, Romania
florea.dinu@ct.upt.ro

Dragos Marcu
Popp & Asociatii, Bucharest, Romania
dragos.marcu@popp-si-asociatii.ro

## ABSTRACT

Beams with span-to-depth ratio shorter than four are not very common in the design of moment resisting frames. For such beams, the shear stresses may become a controlling factor in the design, as the moment capacity is influenced by the presence of the shear. This is an important matter when such a beam is part of the seismic lateral force resisting system that is designed according to the dissipative concept. In this case, the contribution from the shear force affects the dissipation capacity and plastic mechanism. The paper presents the test-based evaluation of moment frames with short beams and reduced beam section connections, with the purpose to check availability of application the plastic hinge model. Full scale specimens, extracted from an 18 story building, have been tested. Test results and their interpretation are summarised hereafter.

## 1. INTRODUCTION

Moment resisting frames are often used as part of the seismic force resisting systems, due to their inherent ductility. Inelastic behaviour is intended to be accommodated through plastic hinges in beams near the beam-to-column connections, and also at column bases. Even considered deemed-to-comply connections, welded beam-to-column connections experienced serious damage and even failures during strong seismic events. These failures included fractures of the beam flange-to-column flange groove welds, cracks in beam flanges, and cracks through the column section (AISC 341-05, 2005). To reduce the risk of brittle failure of such connections, either connection strengthening (Figure 1.a) or beam weakening (Figure 1.b) can be applied. First approach consists in providing sufficient overstrength to connection, for instance by means of haunches or cover plates. The second approach can take benefit from the "Reduced Beam Section" (RBS) or "dog-bone" concept, initially proposed by Plumier (1990) and then developed and patented by ARBED, Luxembourg (ARBED waived in 1995 all patent and claim rights associated with the RBS for the benefit of the structural design community).

Proper detailing of the reduced beam section, including flange cutouts and beam to column welding is needed to ensure the formation of plastic hinges in the reduced zones.

It is economical to keep the width of bays in some limits, because long bays make the structure flexible and therefore increase the drift, which may control the design. On the other hand, short bays can cause a reduction of the dissipation capacity due to the presence of large shear forces. As a result, the connection qualification specifies minimum span-to-depth ratio to be used for moment frame connections. When prequalified connections are utilized outside the parametric limitations, project specific qualification must be performed to permit the prediction of behaviour and acceptance criteria (AISC 341-05, 2005).

This paper presents part of a research project that was performed to check the validity of the moment frame connections of a 18-story structure. The paper describes the calibration of numerical models for two types of reduced beam connections using the general-purpose finite element analysis program ABAQUS (2007). The finite element models were calibrated using experimental tests performed on four full-scale specimens at the Laboratory of Steel Structure, "Politehnica" University of Timisoara, Romania. The particularity of the project consists of very short bay widths coupled with the use of reduced beam section connections for the moment frame connections. In addition, the project incorporates flush-end plate bolted connections for beam splices and therefore the study addresses concerns regarding the potential for brittle failure of the bolts.

## 2. EXPERIMENTAL PROGRAM

### 2.1. Specimens and testing set-up

The study is connected with the design of a 18-story office building, located in Bucharest, Romania. The building height is 94 m, and the plan dimensions are 43,3m x 31,3m, see Figure 2. The building site is located in a high seismic area, which is characterized by a design peak ground acceleration 0.24g for a returning period of 100 years, and soft soil conditions, with TC=1.6 s. It is noteworthy the long corner period of the soil, which in this case may affect flexible structures. For serviceability check, the returning period is 30 years, while for collapse prevention it is 475 years.

Lateral force-resisting system consists of exterior steel framing with closely spaced columns and short beams. The central core is also made of steel framing with closely spaced columns and short beams. The ratio of beam length-to-beam height, L/h, varies from 3.2 to 7.4, which results in seven different types of beams. Some beams are below the general accepted inferior limit (L/h=4). The moment frame connections employee reduced beam section connections that are generally used for beams loaded mainly in bending (Figure 3). Circular radius cuts in both top and bottom flanges of the beam were used to reduce the flange area. The detailing followed the recommendations from AISC 341-05. Welds of beam flanges and web to column flange are complete joint penetration groove welds. Two types of beams, which have the shortest L/h ratio, have been selected for the experimental program. Table 1 shows the characteristics of the beams tested experimentally. The first beam,

denoted as RBS-S, has a clear length of 1450 mm, and the lowest span over height ratio, L/h=3.2. The second type, denoted as RBS-L, has a clear length of 2210 mm, and a corresponding span over height ratio L/h of 4.9 (Figure 3). The thickness of the web and flanges for both beam types is 20 mm and 14 mm, respectively. The initial designed solution adopted for the splice beam connection was a bolted flush end-plate slip resistant connection. After the first series of tests, it was decided to change this solution with a classical shear slip resistant splice connection (Table 1). The column has a cruciform cross-section made from two hot-rolled profiles of HEA800 and HEA400 section.

Table 1. Characteristics of beams tested experimentally

| Type | h [mm] | b [mm] | L [mm] | $f_y$ [N/mm²] | $M_p$ [KNm] | $V_p$ [KN] | $M_p/V_p$ | L/h | Splice connection |
|---|---|---|---|---|---|---|---|---|---|
| RBS-S1, 2 | 450 | 250 | 1450 | 355 | 641 | 1845 | 0.35 | 3.2 | Flush end-plate |
| RBS-L1, 2 | 450 | 250 | 2210 | 355 | 641 | 1845 | 0.35 | 4.9 | Flush end-plate |
| RBS-S3 | 450 | 250 | 1450 | 355 | 641 | 1845 | 0.35 | 3.2 | Gusset-plate connection |
| RBS-L3 | 450 | 250 | 2210 | 355 | 641 | 1845 | 0.35 | 4.9 | Gusset-plate connection |



Figure 1. Plan layout and elevation of the building
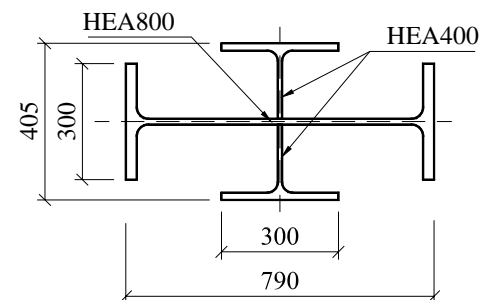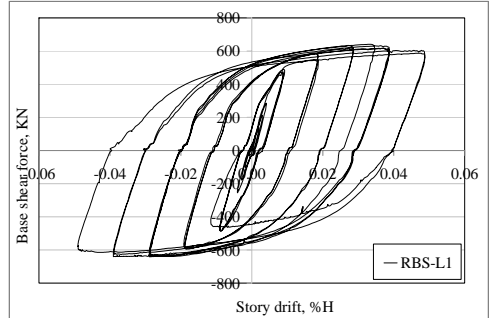


Figure 3. Cruciform cross-section of the columns

Both beams and columns are made from S355 grade steel. The base material characteristics have been determined experimentally. The measured yield strength and tensile stress of the plates and profiles were larger than the nominal values. The highest increase has been recorded for the hot rolled sections, being lower for plates. One notices the ratio between nominal and actual yield stress is limited to 1.25 by seismic design code EN1998-1 (2004).

Table 2. Material properties of rolled profiles

| Section | Steel grade | Element | $f_y$ [N/mm²] | $f_u$ [N/mm²] | $A_u$ [%] |
|---|---|---|---|---|---|
| HEA800 | S355 | Flange | 410.5 | 618.5 | 15.0 |
| | | Web | 479.0 | 671.2 | 13.0 |
| HEA400 | S355 | Flange | 428.0 | 592.0 | 15.1 |
| | | Web | 461.0 | 614.0 | 12.8 |

Table 3. Material properties of flat steel.

| Section | Steel grade | Element | $f_y$ [N/mm²] | $f_u$ [N/mm²] | $A_u$ [%] |
|---|---|---|---|---|---|
| 14 mm | S355 | Beam flange | 373.0 | 643 | 17.0 |
| 20 mm | S355 | Beam web | 403.0 | 599 | 16.5 |



a)



b)

Figure 2. Moment frame with short beam: a) bolted flush end-plate connection; b) shear slip resistant connection

Figure 5 displays the test setup. Specimens were tested under cyclic loading. The cyclic loading sequence was taken from the ECCS Recommendations (ECCS, 1986). Thus, according to the ECCS procedure, the yielding displacement Dy and

www.steelconstruct.com

the corresponding yielding force Fy are obtained from the monotonic force vs. displacement curve (Figure 5.a). In order to reduce the number of tests, the monotonic test was replaced by the push-over curve obtained numerically using the general-purpose finite element analysis program ABAQUS. The yielding displacement is then used for establishing the cyclic loading. It consists in generating 4 successive cycles for the ranges of displacement ±0.25Dy, ±0.5Dy, ±0.75Dy, ±1.0Dy followed up to failure by series of 3 cycles each with a range ± 2n×Dy where n is =1, 2, 3…etc (Figure 5.b).
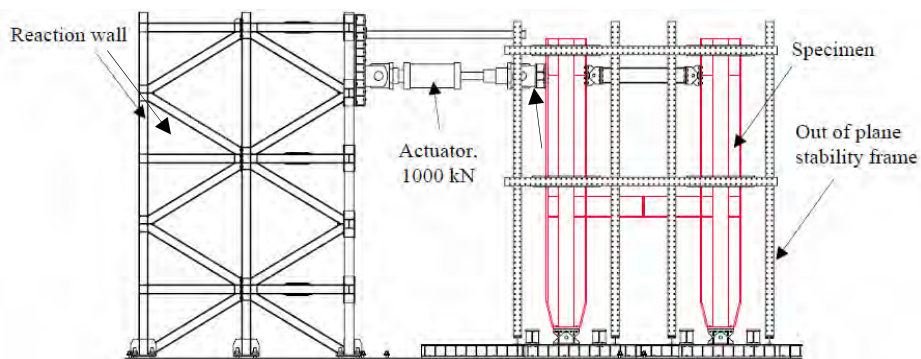
Figure 4. Cruciform cross-section of the columns
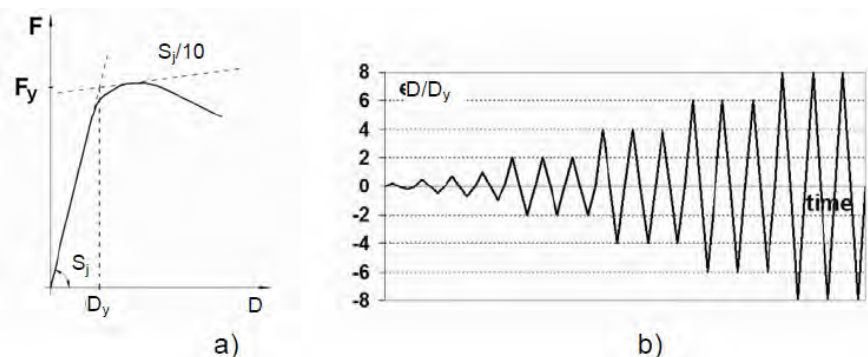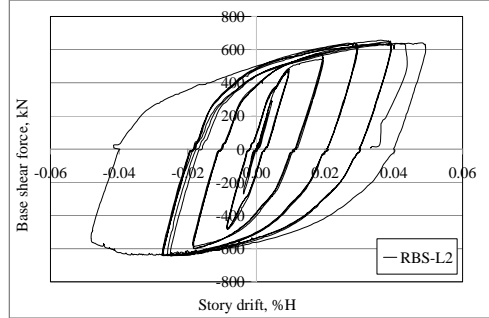
Figure 5. Loading protocol: a) determination of yielding displacement; c) cyclic loading protocol

## 2.2. Results

Table 4 summarizes the experimental results, with observations regarding the behaviour and failure mode of each specimen.

Specimens with longer beams, RBS-L1 and RBS-L2, remained elastic until a drift of 30 mm, or 0.6% of the story height. Two failure modes were recorded. First mode involved the fracture of the top beam flange to column flange welding, that after propagated in the beam web. The second failure mode involved the fracture of the bottom flange, due to the large tensile forces at ultimate loading stage. Both failures occurred at interstory drifts larger than 5% of the story height. The plastic behaviour was dominated by the buckling of the flange in compression and out of plane buckling of the web.

Table 4. Results of experimental tests

| Specimen | Failure mode | Details: failure mode and force-displacement curve | Observations |
|---|---|---|---|
| RBS-L1 | - cracks initiated in top flange to column welding, fracture propagated in web | | - failure at interstory drift of 5% <br> - no slip at splice connection <br> - large dissipation capacity, reduce cyclic degradation |
| RBS-L2 | - failure due to fracture of the flange in the reduced area, then propagation in the web | | - failure at interstory drift of 5% <br> - no slip at splice connection <br> - large dissipation capacity, reduce cyclic degradation |

| RBS-L3 | - cracks initiated in bottom flange to column welding, fracture propagated in web |  | - failure at interstory drift of 4.5%<br>- no slip in the splice connection<br>- large dissipation capacity, reduce cyclic degradation |
| RBS-S1 | - failure due to fracture of the flange in the reduced area, then propagation in the web |  | - failure at interstory drift of 5%<br>- moderate slip at splice connection<br>- large dissipation capacity, reduced cyclic degradation |

| RBS-S2 | - failure due to fracture of the bolts at beam splice connection |  | - failure at large interstory drift<br>- large slip at splice connection<br>- large dissipation capacity, reduced cyclic degradation |
| RBS-S3 | - failure due to fracture of the flange in the reduced area, then propagation in the web |  | - failure at interstory drift of 5%<br>- no slip in the splice connection<br>- large dissipation capacity, reduced cyclic degradation |

Specimens with shorter beams, RBS-S1 and RBS-S2, have remained elastic until a drift of 25 mm, or 0.5% of the story height. The visible buckling of the flange in compression was first observed, followed by out-of-plane buckling of the web. Failure of the first short specimen, RBS-S1, involved fracture of the bottom flange due to the large tensile forces at ultimate stage, then followed by the fracture of the beam web. The failure of the second specimen, RBS-S2, involved the fracture of the bolts at the splice connection. The plastic behaviour was dominated by the buckling of the flange in compression and shear buckling of the web.

Figure 6 and Figure 7 show the evolution of web out of plane plastic deformations in the zone adjacent to the column. Under the increasing lateral force, the plastic mechanism in the web involves both bending moment and shear force. The contribution from the shear force to the overall deformation is more important for the short specimens, RBS-S, and it can be observed following the inclination of the shear buckling waves of the web (Figure 6, Figure 7, Figure 8).



Figure 8. VIC measurements with the scale on the right, RBS-L3

Figure 9 shows the recorded moment-rotation curve for all specimens. The total rotation of the joint has two major components: rotation of the beam (reduced beam section) and distortion of the web panel in the reduced region. Due to the large stiffness of the columns, the contribution of the column web panel can be neglected. The specimens exhibited good rotation capacity and stable hysteretic behaviour up to 5% interstory drift. This capacity supports the design of the structure which is based on a 2.5% interstory drift limitation at the Ultimate Limit State. The specimens showed a reduced degradation of both strength and stiffness. The bolts slip during testing of short specimens, and this is clearly indicated by the shape of the hysteretic curves.
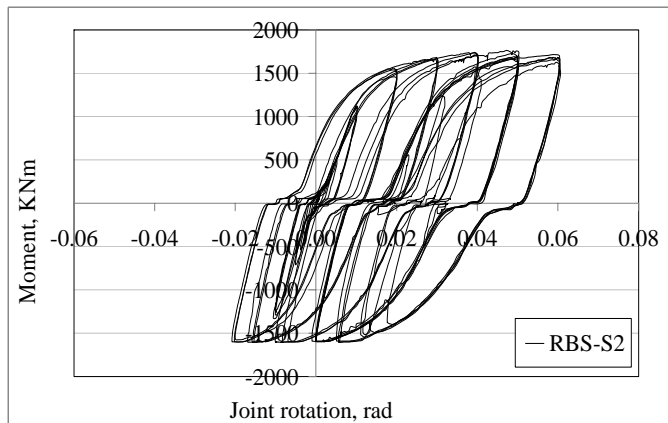


Figure 6. Shear web deformation history, specimen RBS-L1
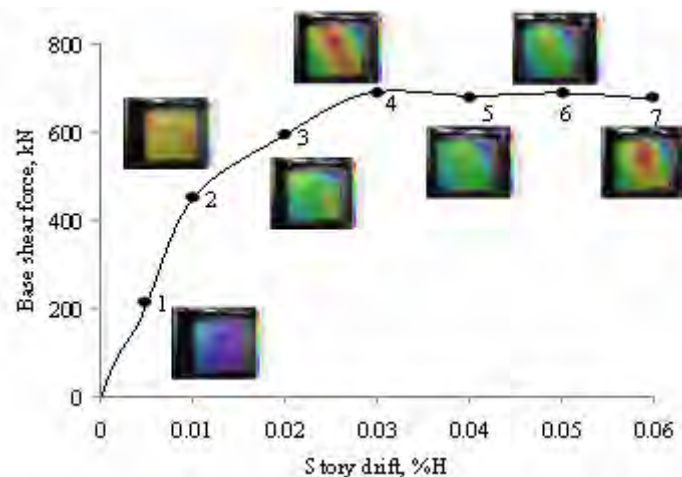


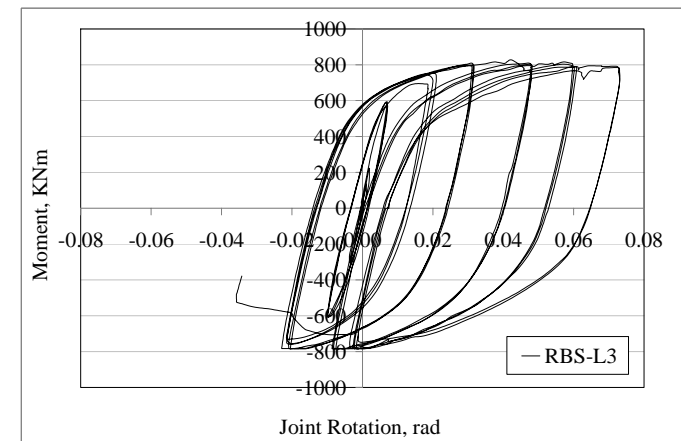Figure 7. Shear web deformation history, specimen RBS-S2
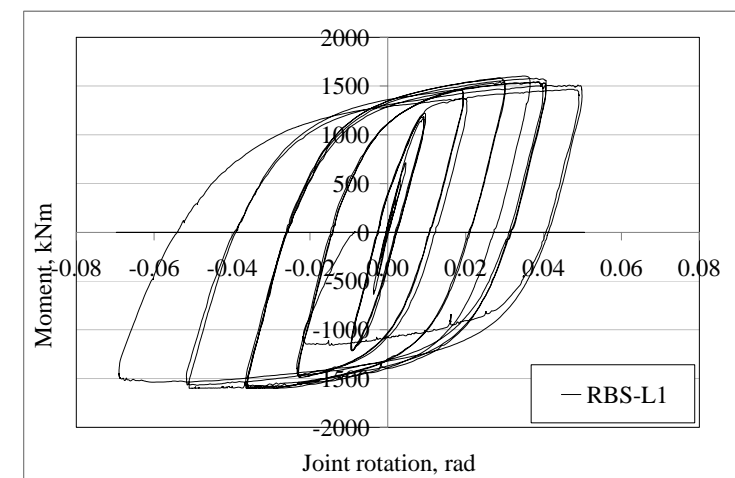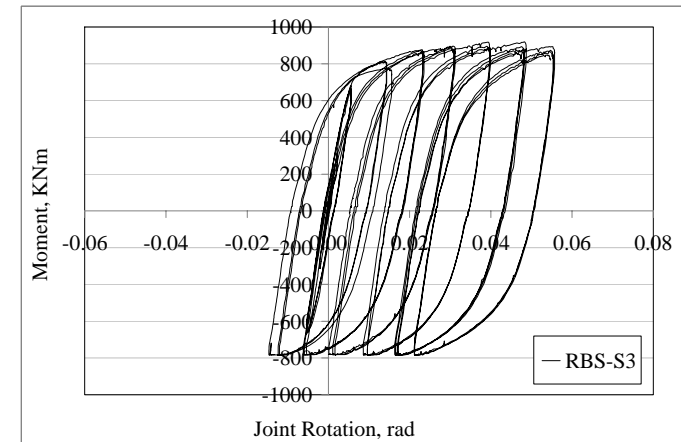


RBS-L1
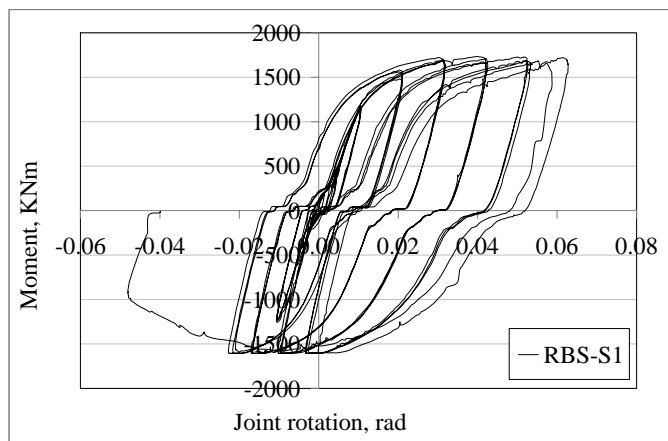
RBS-S1
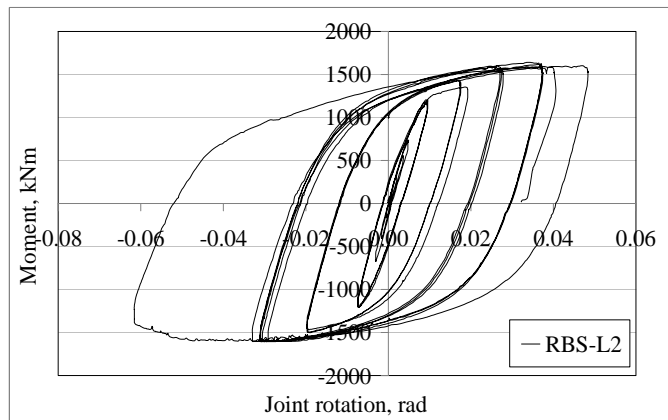


RBS-L2



RBS-S2



RBS-L3



RBS-S3

Figure 9. Moment-rotation relationship for cyclic loaded joints

## 3. NUMERICAL INVESTIGATION

### 3.1. Description of the numerical model

Due to the high concentration of stresses near welds, in the heat affected zone (HAZ), which caused unexpected fracture of the beam flange of RBS-L3 specimen, a numerical simulation investigation was carried out, in order to better understand the cause of the failure. On this purpose, a numerical model, able to simulate the post-elastic large strain cyclic deformation was calibrated for specimens RBS-S3 and RBS-L3. All the components were modelled using solid elements. In order to have a uniform and structured mesh, some components with a complex geometry were partitioned into simple shapes. The engineering stress-strain curves of the steel grades obtained from tensile tests were computed into true stress-true plastic strain and used further in the numerical model. The modulus of elasticity was considered equal to

www.steelconstruct.com

210000 N/mm$^2$ and the Poisson coefficient equal to 0.3. For the cyclic analysis, a combined isotropic/kinematic hardening model was used for the material, containing the cyclic hardening parameters from Dutta *et al.* (2010). A dynamic explicit type of analysis was used. The load was applied through displacement control at the top of the columns.

### 3.2. Results

Numerical simulation was first used to evaluate the solution with shear slip resistant splice connection, after the problems revealed after tests of bolted flush-end plate splice connection specimens. The second goal of numerical simulation was to optimise the shape of the cut-out in the beam flanges in the reduced zone. Figure 10. shows the hysteretic curves of tested specimens RBS-S3 and RBS-L3, having a splice type connection. As expected, this type of connection prevented the bolt slippage and therefore a continuous beam was taken into account within the numerical simulations. It can be observed that the behaviour anticipated by the numerical simulation is confirmed by the tests.
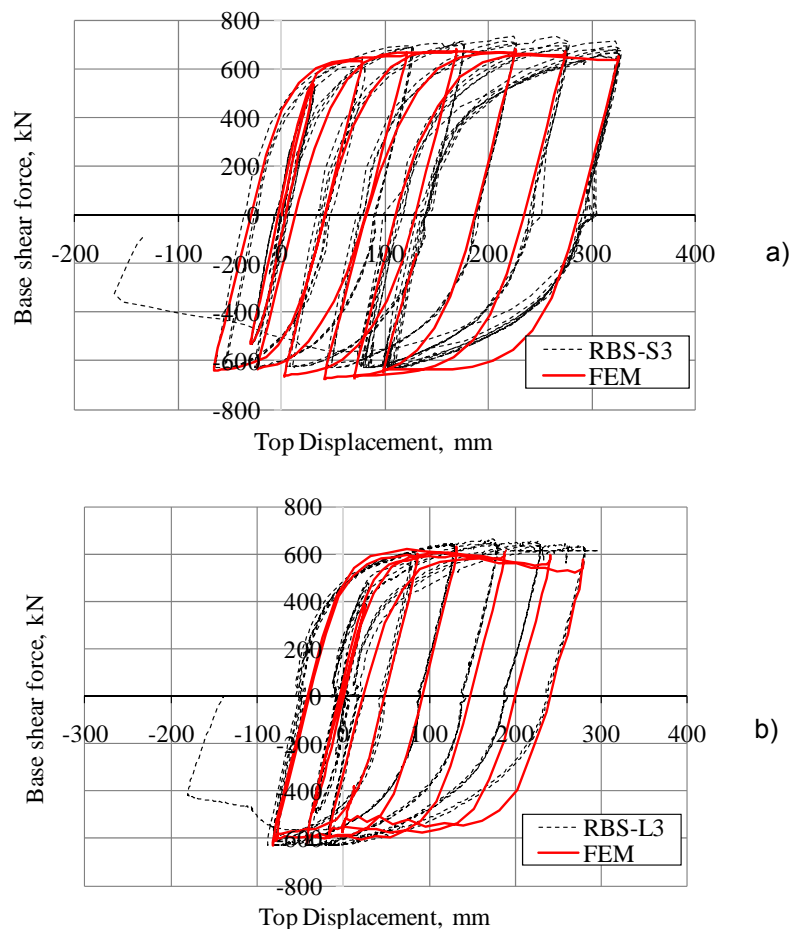


Figure 10. Hysteresis curves: a) RBS-S3; b) RBS-L3

Based on the observed results it was proposed a reconfiguration of the reduced beam section where the length of the RBS was reduced from 450mm to 300 mm (as for short beams) (Figure 11.b, c). This new solution did not affect the stiffness but decreased the amount of shear force (Figure 11a).
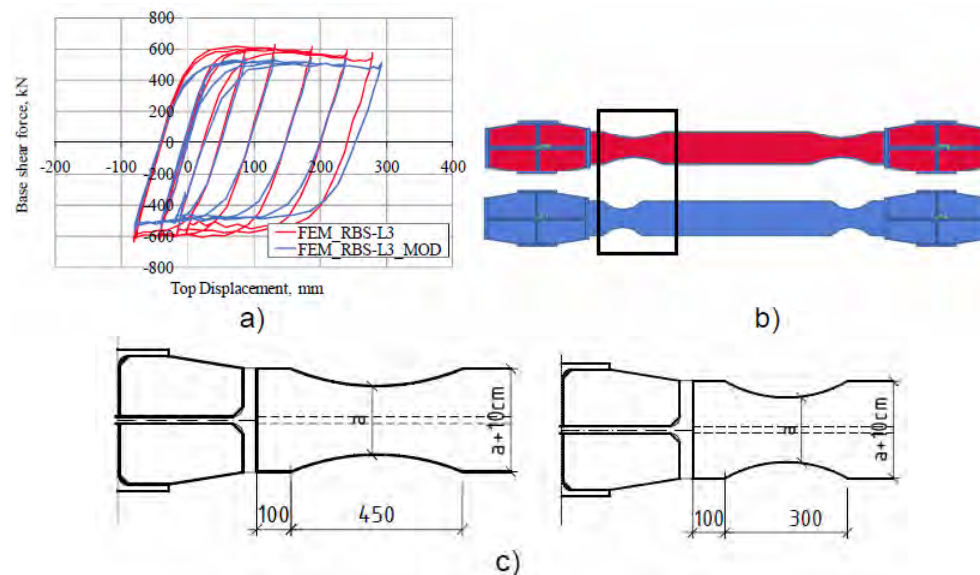


Figure 11. Comparison between RBS-L3 and RBS-L3_MOD (FEM):
a) cyclic behaviour; b) beam configuration; c) dimensions of the flange cut-out

As it can be seen in Figure 12b, the plastic deformation are developed only in the reduced beam section, in comparison with the initial configuration (RBS-L3) shown in Figure 12a. The von Misses stress distribution for the two cases is presented in Figure 13.
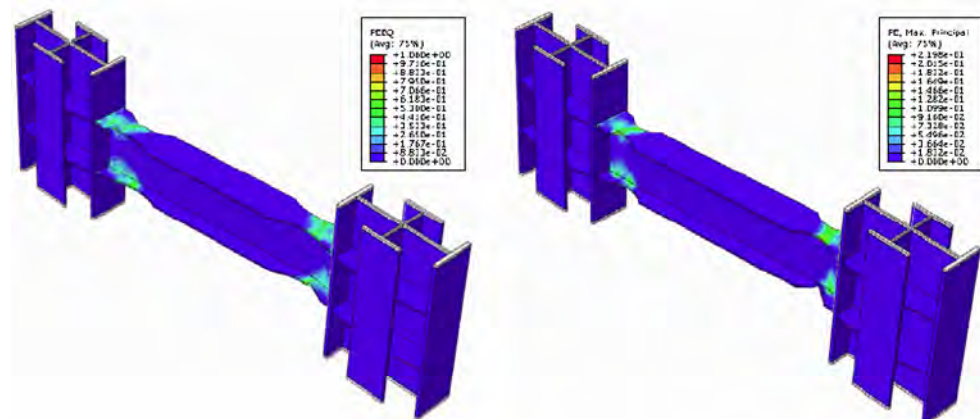


Figure 12. Equivalent plastic strain: (a) RBS-L3; (b) RBS-L3_MOD.
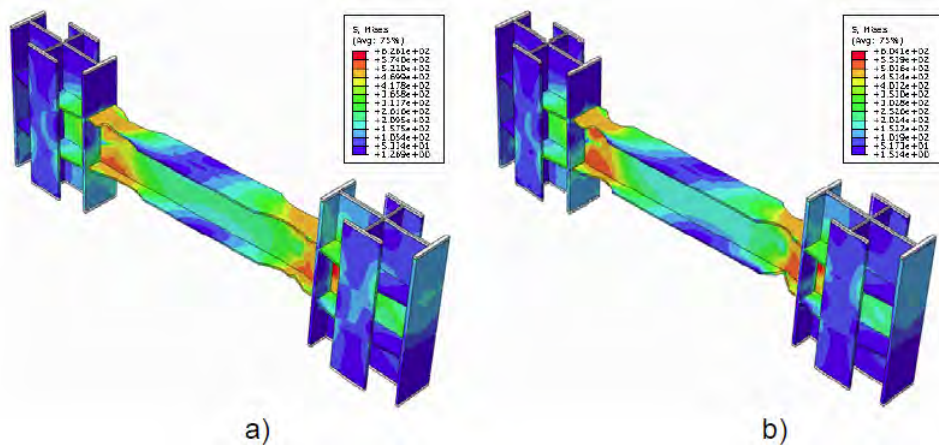
Figure 13. Von-Misses equivalent stress: (a) RBS-L3; (b) RBS-L3_MOD.

## 5. CONCLUSIONS AND GENERAL RECOMMENDATIONS

Main conclusions on the experimental tests and numerical analysis on reduced beam sections connections of short coupling beams can be summarizes as follows:

i)  Experimental test on two types of short beams of RBS connections confirmed the design procedure. The specimens exhibited excellent ductility and rotation capacity up to 60 mrad before failure. However, the flush end plate connection exhibited significant slippages which lead to reduction of the stiffness. Based on these observations, the splice connection was redesigned using a detail that is more appropriate for the predominant shear stress state at the mid-length of the beams. This new connection detail consists of gusset plates on web and flanges and preloaded high strength bolts. This new configuration can prevent the bolt slippage, and therefore both the stiffness and axial straightness of the assembly will not be altered.

ii) For very short beams, the interaction between the shear and normal stresses causes an inclination of the buckled shape in the web. The plastic rotation capacity has two major components, i.e. rotation of the beam (reduced beam section) and distortion of the web panel in the reduced region. Due to the large stiffness of the columns, the contribution of the column web panel can be neglected.

iii) Numerical simulation allowed to calibrate a modified RBS configuration in order to eliminate the stress concentration near the beam to column welding. The results showed the concentration of stresses takes place in the reduced beam section.

## ACKNOWLEDGMENTS

## REFERENCES

[1] AISC 341-05 (2005). Seismic provisions for structural steel buildings. American Institute for Steel Construction.

[2] B. Johansson, R. Maquoi, G. Sedlacek, C. Müller, D. Beg (2007). Commentary and worked examples to EN 1993-1-5, JRC – ECCS cooperation agreement for the evolution of Eurocode 3, European Commision.

[3] Dutta A., Dhar S., Acharyya S. K. (2010), Material characterization of SS 316 in low-cycle fatigue loading, Journal of Materials Science, Vol. 45, Issue 7, pp. 1782-1789.

[4] ECCS 1986. European Convention for Constructional Steelwork, Technical Committee 1, Structural Safety and Loadings; Working Group 1.3, Seismic Design. Recommended Testing Procedure for Assessing the Behavior of Structural Steel Elements under Cyclic Loads, First Edition.

[5] EN 1993-1-1 (2005). Eurocode 3. Design of steel structures. General rules and rules for buildings, CEN, EN 1993-1-1.

[6] EN 1993-1-5 (2006). Eurocode 3. Design of steel structures. Part 1-5: General rules - Plated structural elements, CEN, EN 1993-1-5.

[7] EN 1998-1-2004. European Committee for Standardization – CEN. Eurocode 8: Design provisions for earthquake resistance of structures. Part 1.1: General rules. Seismic actions and general requirements for structures, Brussels.

[8] Hibbit. D., Karlson, B. and Sorenso, P (2007), ABAQUS User's Manual, Version 6.9.

[9] Plumier, A. (1990), "New Idea for Safe Structures in seismic Zones", *IABSE Symposium,* Mixed structures including new materials, Brussels 1990 (pp.431- 436).

# SEISMIC RESISTANT WELDED CONNECTIONS FOR MRF OF CFT COLUMNS AND I BEAMS

Cristian Vulcu[1]; Aurel Stratan[1]; Dan Dubina[1,2]

[1] Department of Steel Structures and Structural Mechanics, "Politehnica" University of Timisoara, Romania

[2] Romanian Academy, Timisoara Branch, Romania
cristian.vulcu@ct.upt.ro; aurel.stratan@ct.upt.ro; dan.dubina@ct.upt.ro

## ABSTRACT

The paper displays the experimental program aiming to characterize the behaviour of two types of moment resisting joints in multi-storey frames of concrete filled high strength RHS columns and steel beams. Moment resisting joints are of welded connection in two different typologies: with reduced beam section (RBS) and with cover plates (CP). The paper describes the design procedure of the joints and displays the specific detailing for these two solutions. Numerical simulations were realised prior to the testing in order to anticipate the behaviour of the joints and to find answers to problems for which decisions were taken in the design process. The material model used in the numerical simulations was calibrated based on the results from tensile tests. Finally, the results from the numerical analysis are presented.

## 1. INTRODUCTION

The design philosophy of a structure to seismic action allows for plastic deformations in dissipative members, the global stability of the structure being provided by the non-dissipative members. With the aim to investigate the seismic performance of dual frames (Vulcu *et al.* 2012), in the current research project, the beams are made of mild carbon steel (MCS) and the columns of high strength steel (HSS) (Figure 1). The investigated frames are considered to be Moment Resisting Frames (MRF), Dual Concentrically Braced Frames (D-CBF) and Dual Eccentrically Braced Fames (D-EBF).
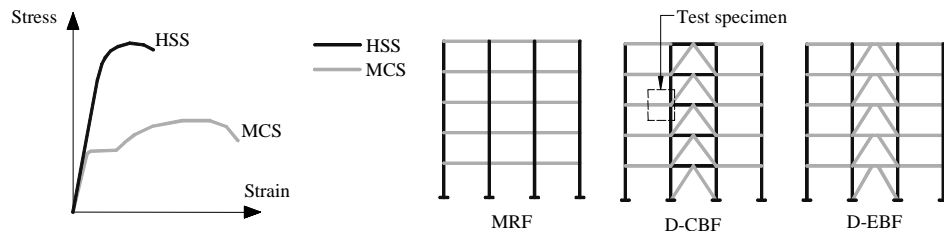


Figure 1. Frames (MRF, D-CBF, D-EBF) realized in the dual-steel concept

For the three frame typologies, the columns are realized as concrete filled high strength steel tubes. Cold formed rectangular hollow section tubes will be used for this purpose. In case of composite columns, several situations are practiced:

- The case in which the beam passes through the steel tube and transfers the load directly to the concrete core; in this case the tube has a secondary role;
- The case in which the concrete inside the tube is inactive (connectors are not positioned); it is counted on the concrete core just in case of fire;
- The case in which the concrete is active and the efforts are introduced using connectors.

In the current research program, the goal is to count on both materials (steel and concrete) and to have a composite action ensured by the use of shot fired nails. As basis for definition of the experimental program on beam-column joints, cross-sections from the D-CBF frame were used, considering two combinations of HSS/MCS:

- RHS 300x12,5 S460 column and IPE 400 S355 beam;
- RHS 250x10 S700 column and IPE 400 S355 beam.

The beams are welded to the columns considering two types of connections: with reduced beam section (RBS) (see Figure 2a), and with cover plates (CP) (see Figure 2b). Due to the flexibility of the tube walls under transverse forces, the flanges of the beam and the cover plates will not work on the entire width - which means that efforts will be transferred to the side walls of the tube by an effective width $b_{eff}$ (see Figure 2c and Figure 2d). This is not enough to ensure a higher resistance of the connection with regard to the strength of the beam.
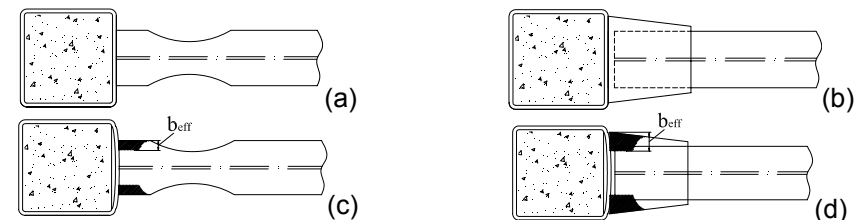


Figure 2. a) Joint with RBS, b) joint with CP, c) and d) the corresponding effective width

In the literature, different joint typologies have been studied for tubes of rectangular section as well as for tubes of circular section, see Figure 3.
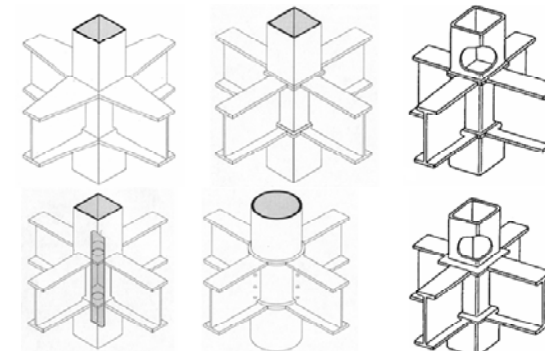


Figure 3. Existing connection solutions for welded beam-to-column joints

In order to transfer the loads uniformly to the cross section of the tube, interior diaphragms, through diaphragms as well as outer diaphragms have been used (Morino and Tsuda, 2003, and Park *et al.,* 2005). Design guidelines have been developed for these types of connections as well (Kurobane *et al.,* 2004).

## 2. DESIGN OF JONTS

The connection solution of the beams and columns within the current research is based on the use of stiffeners that are welded around the steel tube, and which form an outer diaphragm. From the design of the joint, the thickness of the stiffeners was higher than the thickness of the beam flanges and cover plates. Because of this, at the connection with the beam, it was proposed that a preparation of the stiffeners to be performed (see Figure 4 and Figure 5) so as to avoid the concentration of the efforts due to the variation of the thickness. This solution has the advantage that no preparations are necessary for the flanges of the beam, and respectively cover plates.
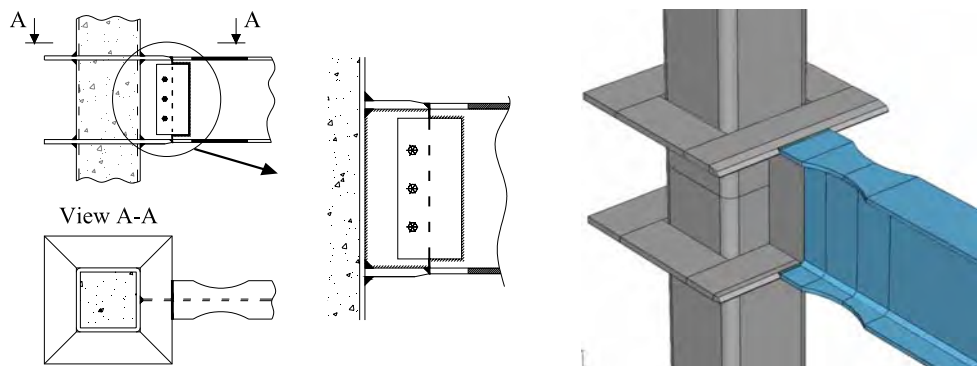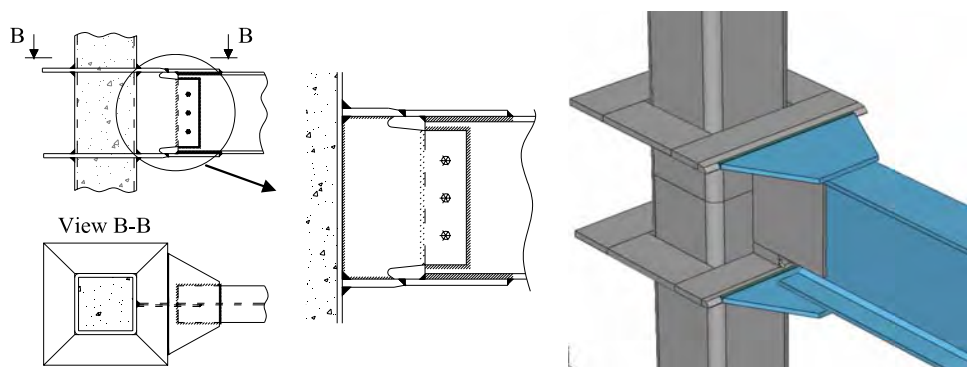


Figure 4. Joint with reduced beam section (RBS)



Figure 5 Joint with cover plates (CP)

Beam flanges and cover plates are welded to the column stiffeners using full-penetration butt welds. A shear tab bolted connection between the beam web and vertical column stiffener is used for erection. The final connection of the beam web

is realized as full-penetration weld for the RBS joint and as fillet welds for the CP joint. The main components covered within the joint design are illustrated in Figure 6.
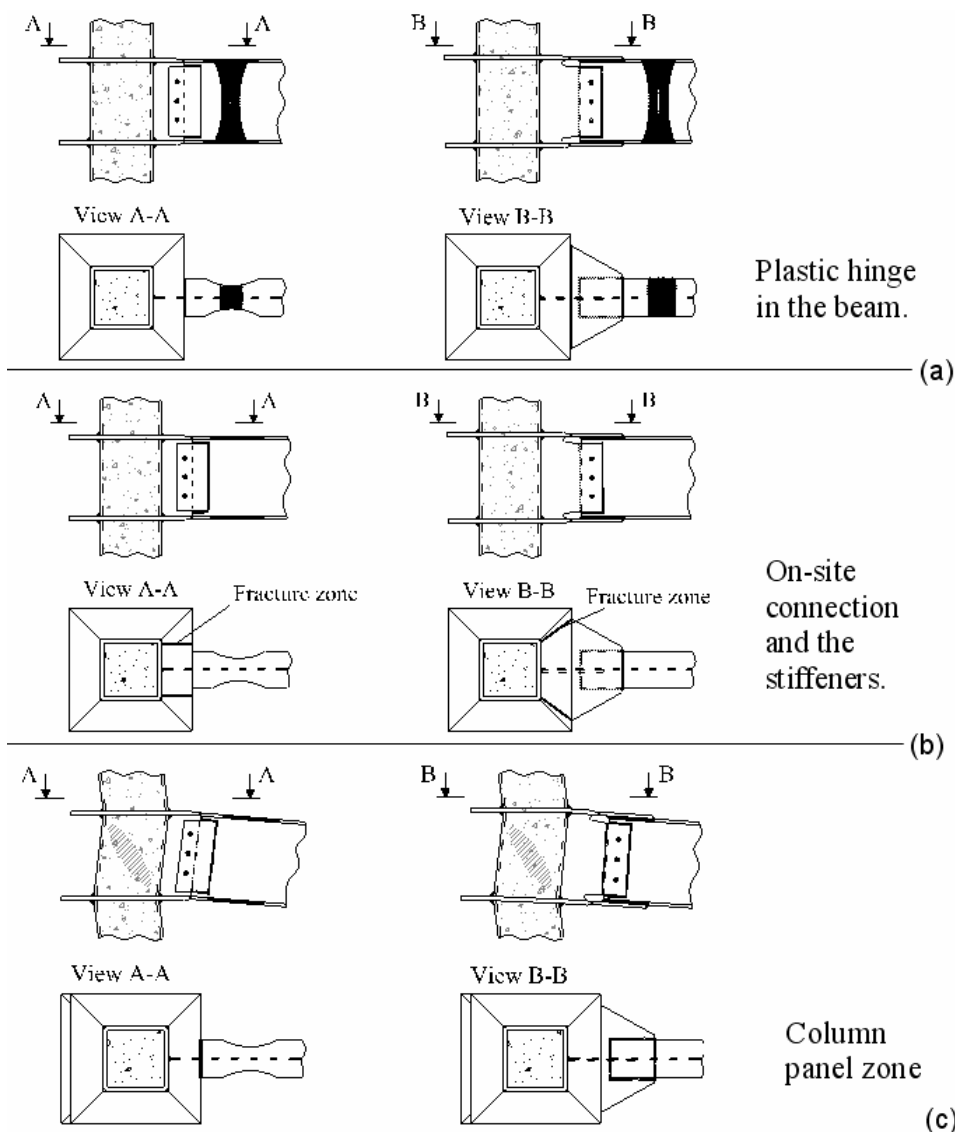


Figure 6. Main components taken into account in the design of the joints

The design of the joints was performed considering plastic hinge formation in the beams (Figure 6a). Further with bending moment and the shear force from the plastic hinge, the components of the connection were designed (welded on-site connection, stiffeners and column panel) so as to reach a higher resistance than the beam. The assumptions considered in the design of the joint components are presented further:

    www.steelconstruct.com

### 2.1. Plastic hinge position

The geometry of the reduced beam section was determined according to AISC 358-2005, and for the joint with cover plates it was assumed that the plastic hinge would develop at $h_{beam}/3$ from the cover plate ending based on PEER 2000/07 (Figure 6a).

### 2.2. Bending moment and shear force in the plastic hinge

The probable maximum moment ($M_{pl,hinge}$) and shear force ($V_{Ed,hinge}$) in the plastic hinge were determined by considering that a fully yielded and strain hardened plastic hinge develops in the beam.

$$M_{pl,hinge} = \frac{\gamma_{sh} \cdot \gamma_{ov} \cdot W_{pl} \cdot f_y}{\gamma_{M0}} \qquad (1)$$

$$V_{Ed,hinge} = \frac{M_{pl,hinge}}{L'} \qquad (2)$$

where $\gamma_{sh}$ represents the strain hardening ($\gamma_{sh}$ =1.10), $\gamma_{ov}$ is the overstrength factor ($\gamma_{ov}$=1.25), $f_y$ is the nominal yield strength of the beam, $\gamma_{M0}$ is the material safety factor, $W_{pl}$ is the plastic section modulus, and $L'$ the distance between the plastic hinge and the load application point;

### 2.3. Welded connection between beam and cover plates

The welded connection between beam and cover plates was checked assuming that the flanges carry the moment only, while the web carries the shear force.

### 2.4. On-site connection

The probable maximum moment ($M_{Ed,sc}$) and shear force ($V_{Ed,sc}$) at the on-site connection were determined by considering that a fully yielded and strain hardened plastic hinge develops in the beam. As no weld access holes are used for the RBS joint, the plastic modulus of the gross cross-section of the beam was considered. The cover plates were checked assuming that the flanges carry moment only, while the web carries the shear force. It was checked that the relation $V_{Ed,sc} \leq 0.5 \cdot V_{pl,Rd}$ is satisfied.

### 2.5. Strength of stiffeners

The probable maximum moment ($M_{Ed,cf}$) and shear force ($V_{Ed,cf}$) at the column face were determined by considering that a fully yielded and strain hardened plastic hinge forms in the beam. The force developed in the stiffeners at the connection with the beam flanges (respectively cover plates), was determined by considering that the bending moment is carried by stiffeners alone. Stiffeners were checked to fracture along the path shown in Figure 6b, neglecting the direct connection to the column wall.

### 2.6. Shear resistance of the column panel zone

The shear force in the column panel zone corresponds to fully-yielded plastic hinges in the beams framing into the joint. According to EN 1998-1-2004, no overstrength is required ($\gamma_{sh}$=1.0 and $\gamma_{ov}$=1.0). It was assumed that the bending moments in the beam corresponds to $\beta$=1,0. The resistance of the column panel zone in shear (Figure 6c) was checked based on the provisions within EN 1998-1-2004 and EN 1994-1-1-2004 design codes.

### 3. EXPERIMENTAL PROGRAM

The objective of the experimental tests will be to pre-qualify by tests welded connections in moment resisting frames and dual braced frames designed using the dual-steel concept. Experimental tests on large specimens (see Figure 7) will be performed in order to demonstrate that joint detailing (8 configurations) and welding technology perform adequately under seismic loading (reverse cyclic loading in the inelastic range). The main purpose is to obtain plasticization in the beam (8 specimens) and in the connection zone (8 specimens).



RHS 300x12,5 S460 - RBS

RHS 250x10 S700 - RBS

RHS 300x12,5 S460 - CP

RHS 250x10 S700 - CP

RHS 300x12,5 S460 - RBS

RHS 250x10 S700 - RBS

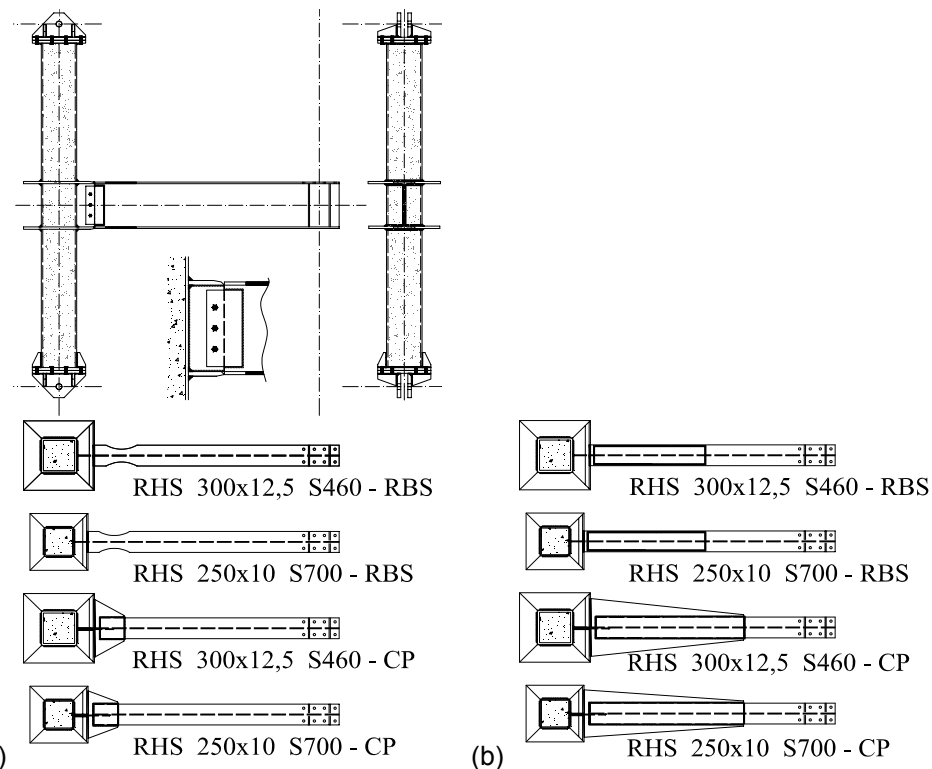RHS 300x12,5 S460 - CP

RHS 250x10 S700 - CP

(a)     (b)

Figure 7. a) Configuration of the designed joint specimens, and b) the reinforced joints

The experimental program to be performed on beam-to-column joints is summarized in Table 1. The variations in the configuration of the beam-to-column joints are given by two joint typologies (reduced beam section and cover-plate), two steel grades for the tubes (S460 and S700) and two failure modes (plasticization in the beam and in the connection zone).

Table 1. Test program on welded beam-to-column joints

| Parameter | Variable | No. of variations | No. of specimens |
|---|---|---|---|
| Loading procedure | Monotonic and cyclic | 2 | |
| Joint type | RBS and CP | 2 | 16 |
| HSS grade | S460 and S700 | 2 | |
| Failure mode | Weak beam / Weak connection | 2 | |

The member cross sections and the main components of the four designed joints (see Figure 7a) are summarised in Table 2.

Table 2. Components of the joint specimens displayed in Figure a

| Joint | Column | Stiffeners | Cover plates | Beam |
|---|---|---|---|---|
| RBS | RHS 300x12.5 - S460 | 150x20 - S460 | - | IPE 400 - S355 |
| RBS | RHS 250x10 - S700 | 120x20 - S690 | - | IPE 400 - S355 |
| CP | RHS 300x12.5 - S460 | 150x20 - S460 | 500x15 - S355 | IPE 400 - S355 |
| CP | RHS 250x10 - S700 | 120x20 - S690 | 500x15 - S355 | IPE 400 - S355 |

It is intended to extend the experimental program with joint configurations, of larger cross section members, that could not be tested. The cross section of beams and columns (Figure 8), were obtained from frame design performed by Silva *et al.* 2011.



Beam: HEB 360 - S355

Column: SHS 300x12 - S355

Beam: HEB 450 - S355

Column: SHS 400x20 - S460

Beam: HEB 500 - S355

Column: Box 500x20 - S690

Beam: HEB 550 - S355
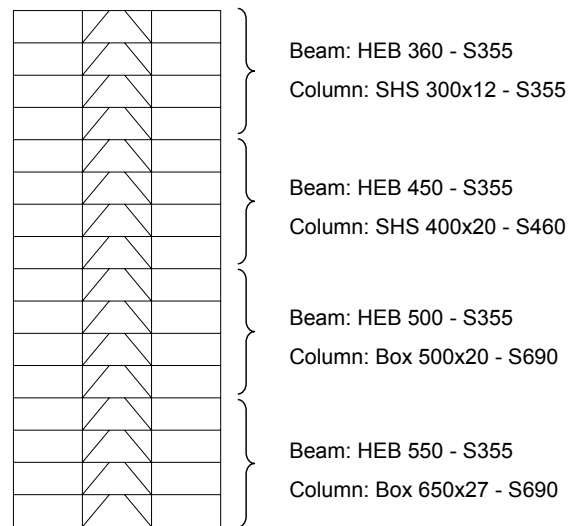
Column: Box 650x27 - S690

Figure 8. Member cross section of the 16 storey D-EBF designed for soft soil

A number of four additional joints were designed following the same design procedure. The components of the designed joints for the extension of the experimental program are summarised in Table 3.

Table 3. Components of the joints (extension of the experimental program)

| Joint | Column | Stiffeners | Cover plates | Beam |
|---|---|---|---|---|
| RBS | Box 500x20 - S690 | 200x25 - S690 | - | HEA 500 - S355 |
| CP | Box 500x20 - S690 | 200x30 - S690 | 700x25 - S355 | HEA 500 - S355 |
| RBS* | Box 650x27 - S690 | 200x30 - S690 | - | HEB 550 - S355 |
| CP* | Box 650x27 - S690 | 250x35 - S690 | 850x30 - S355 | HEB 550 - S355 |

Note: The cases marked with "*" are presented in Figure 9
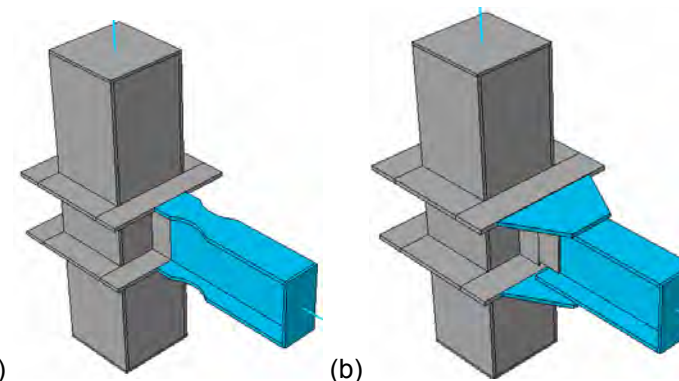


(a)          (b)

Figure 9. Extension of the experimental program: a) RBS joint, and b) CP joint

## 4. NUMERICAL INVESTIGATION

### 4.1. Numerical testing of the joint specimens

Due to the innovative joint configurations, it was needed to have an accurate prediction for the behaviour of the joints in order to avoid unacceptable failure during the experimental tests. Therefore, numerical simulations have been performed with the finite element modelling software Abaqus (2007). The following parts of the joint configurations were used in the numerical models: concrete filled tube (RHS 300x12.5 S460/RHS 250x10 S700 and concrete C30/37), column stiffeners (plates of S460 and S690 steel grade), beam (IPE 400 S355) and cover plates (S355). All the components of the beam-to-column joint were modelled using solid elements. In order to have in the end a uniform and structured mesh, some components with a complex geometry were partitioned into simple shapes. The engineering stress-strain curves of the steel grades were obtained from the steel producers. The material model was therefore calibrated based on results from tensile tests, converting the engineering stress-strain curves into true stress - true strain curves (Figure 10).

For the concrete core, the 'concrete damaged plasticity' model was used (Korotkov *et al.*, 2004). The different components were assembled together according to each joint configuration. Due to the large amount of contact surfaces between the concrete core and the steel tube, the dynamic explicit type of analysis was used.

   www.steelconstruct.com

For the interaction between the steel tube and the concrete core, a normal contact was defined that allows the two parts to separate. The weld between the different parts of the joint configurations was modelled using the tie contact. The load was applied through a displacement control of 250 mm at the tip of the beam and the column was considered as double pinned. The mesh of the elements was done using linear hexahedral elements of type C3D8R.





Figure 11. Joint with RBS: von Misses stresses and plastic deformation



Figure 12. Joint with CP: von Misses stresses and plastic deformation

Figure 13 shows the contribution of the components considered in the design (i.e. beam, column stiffeners and column panel zone) to the overall joint rotation. Low rotation can be observed within the column panel and stiffeners, the main deformations being developed in the beam.
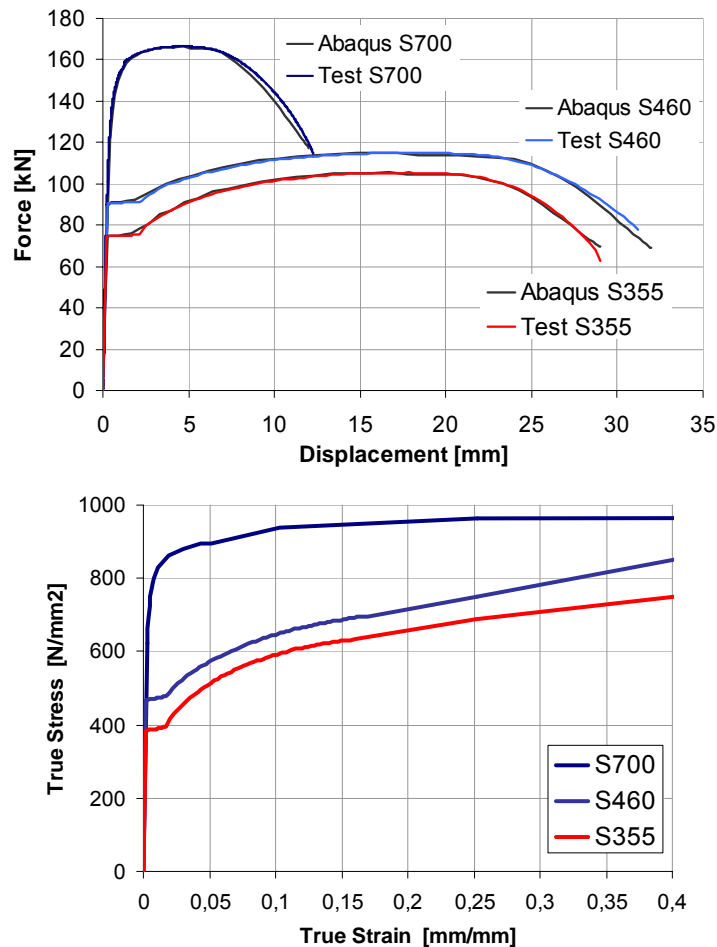
Figure 10. Calibration of the stress-strain curve for the steel grades, a) comparison between test and simulation, and b) the corresponding true stress-strain curves

From the simulations, for each joint configuration, the moment-rotation curve was obtained as well as the stress distribution and plastic strain in the connection and concrete core. According to this, for the RBS and CP joints, yielding was initiated in beam flanges (Figure 11 and Figure 12). Further loading showed an increase of the plastic strain in the upper flange and local buckling of the lower flange and web. For these configurations, the low deformations of the concrete core confirm that the encased concrete does not crush under the compression at the lower flange level.
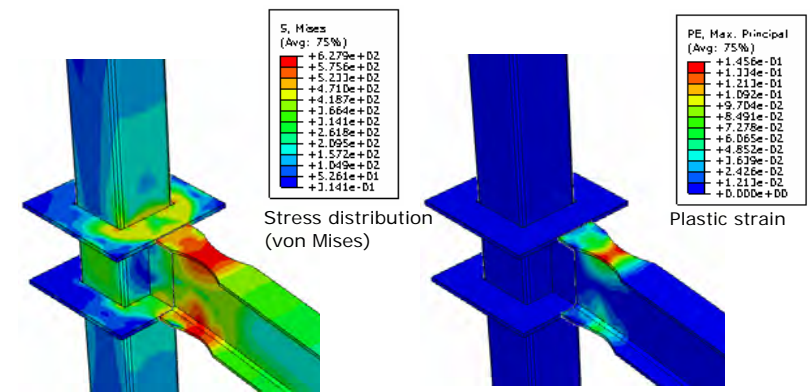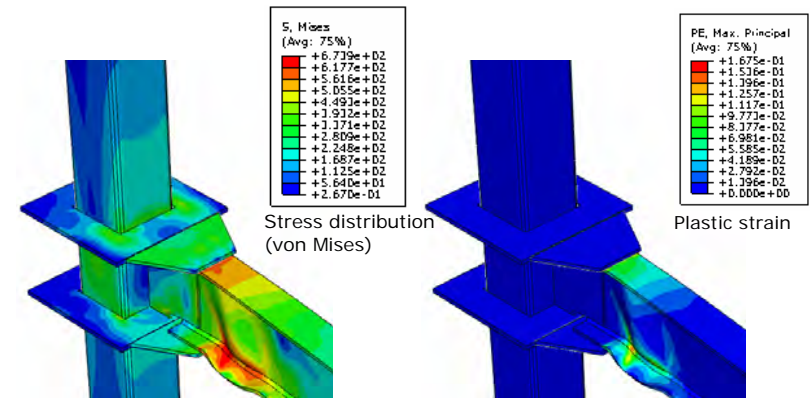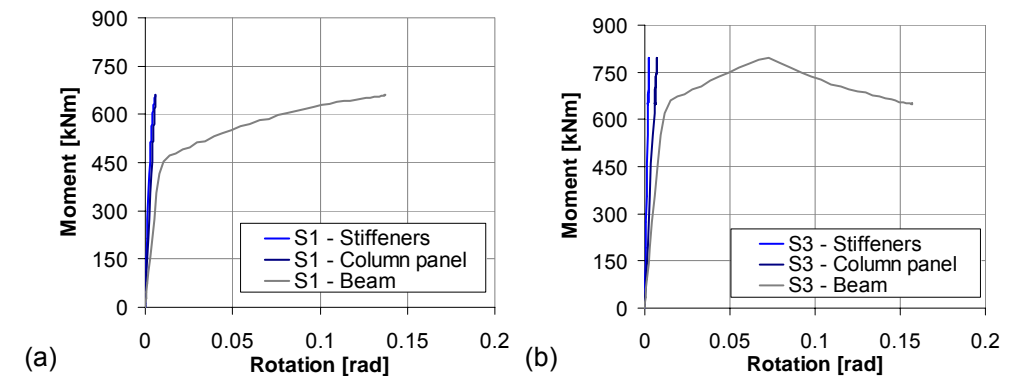


Figure 13. Contribution of components to joint rotation: a) RBS, b) CP

For the joints with strengthened beam, yielding was initiated in the adjacent area of the welded on-site connection (Figure 14), and respectively in the column panel zone (Figure 15). For these configurations, the failure mechanism is described by large plastic deformations in the upper flange connection for the strengthened RBS joint and steel tube and concrete core for the strengthened CP joint.
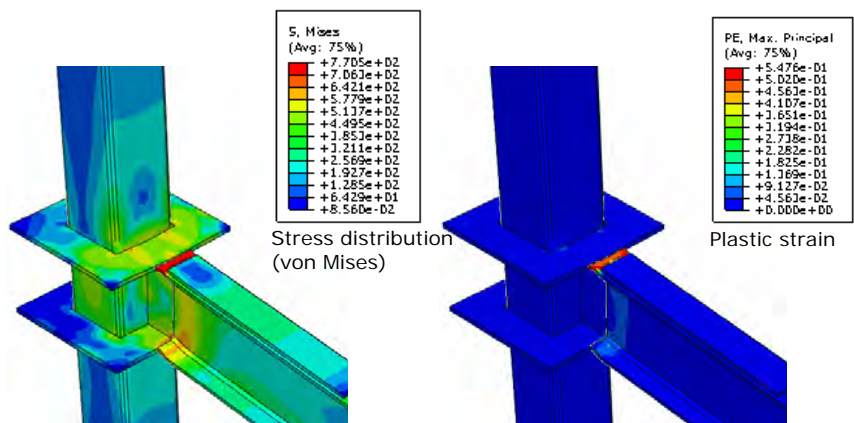


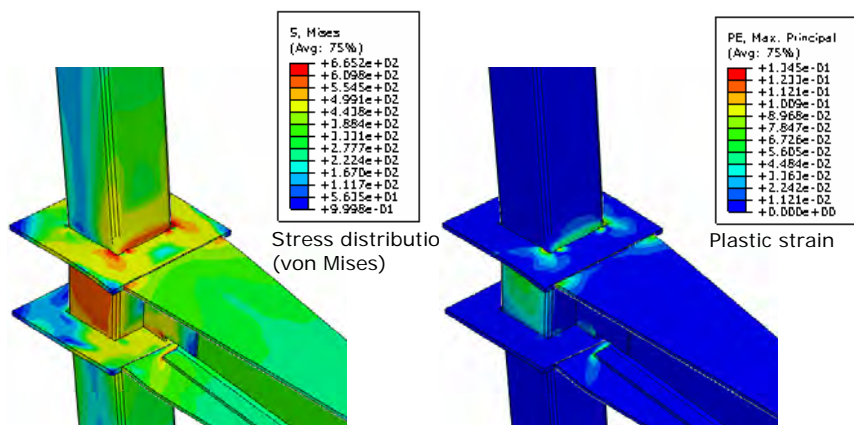Figure 14. Joint with strengthened flanges: von Misses stresses and plastic deformation



Figure 15. Joint with extended cover-plates: von Misses stresses, plastic deformation

Figure 16 shows the contribution of the components to the overall joint rotation for the joints with strengthened beam. In the first case, low rotations can be observed within the column panel, the main rotations being developed in the beam near the welded connection and in a lower amount in the stiffeners. In the second case, the rotations in the beam are extremely low, the main rotations being developed in the column panel zone and in a lower amount with the stiffeners.

Considering the overall displacement of 250 mm applied at the tip of the beam, the maximum plastic strain reached a value of 14% in the upper flange of the RBS joints, 16% in the upper flange of the CP joints, 54% in the upper flange of the

strengthened RBS joints, and 13% in the steel tube of the strengthened CP joints. Comparing these values with the material model described in Figure 10, it can be observed that in the case of the designed RBS and CP joints the plastic strain is lower than the ultimate tensile strain related to fracture. In contrast, for the case of the joints with strengthened beam, the values of the plastic strain are higher than the expected strain at fracture.
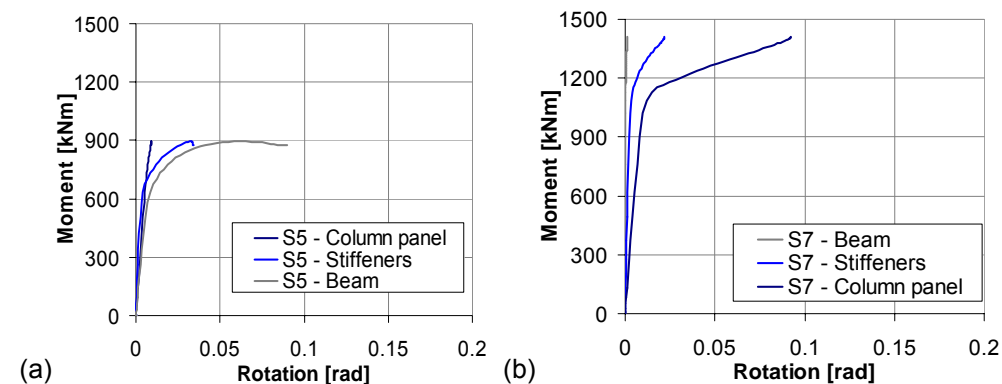


Figure 16. Contribution of components to joint rotation: a) strengthened RBS joint, b) joint with extended cover plates

Therefore, these preliminary numerical simulations predict the failure mechanism and confirm the assumptions used for the design of the joints (formation of the plastic hinge in the beam), and check the feasibility of the adopted solution for the testing set-up and instrumentation.

The moment-rotation curves corresponding to the joints with weak beam as failure mode (formation of the plastic hinge in the beam) are shown in Figure 17. It can be observed that the joints with cover plates (CP) have a higher resistance compared to the joints with reduced beam section (RBS). For the same joint typology, the stiffness is higher for the case with larger column cross section (RHS 300x12.5).
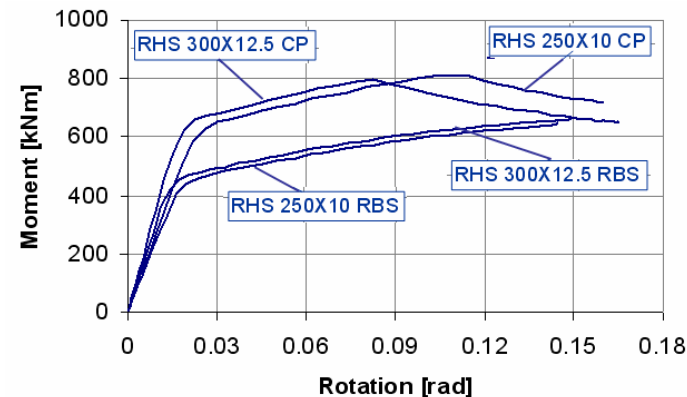


Figure 17. Moment-rotation curves for joints with weak beam as failure mode

## 4.2. Extension of the experimental program

Numerical simulations were performed also for the joints with larger cross section members. The contribution of the components considered in the design (i.e. beam, column stiffeners and column panel zone) to the joint rotation, are shown in Figure 18a for the RBS joint and in Figure 18b for the CP joint. As in the case of the joints designed for the experimental program, low rotations can be observed within the column panel zone and stiffeners, the main deformations being developed, for both cases, in the beam. In addition, the stress distribution and plastic strain, shown in Figure 19 and Figure 20, confirm the development of large plastic deformations in the beam.
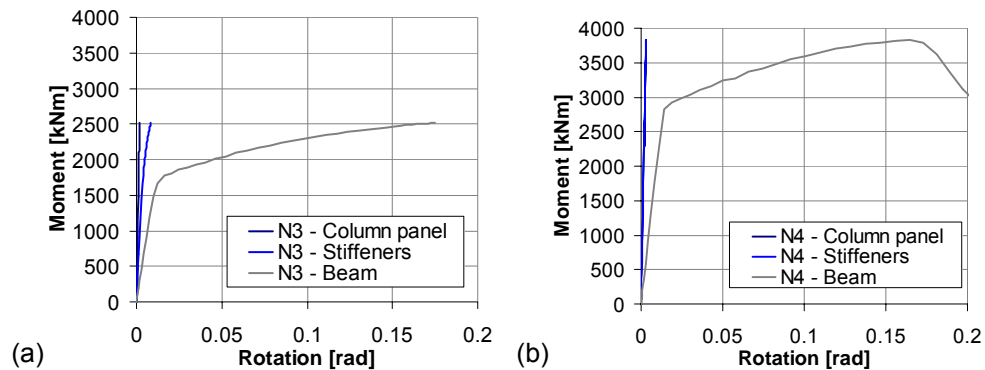


Figure 18. Contribution of components to joint rotation: (a) RBS joint, (b) CP joint
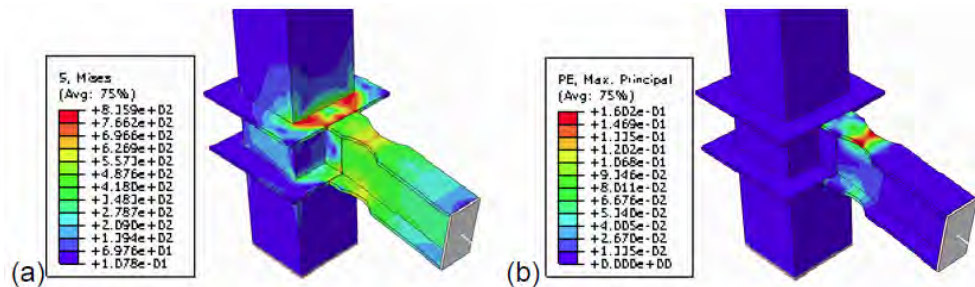


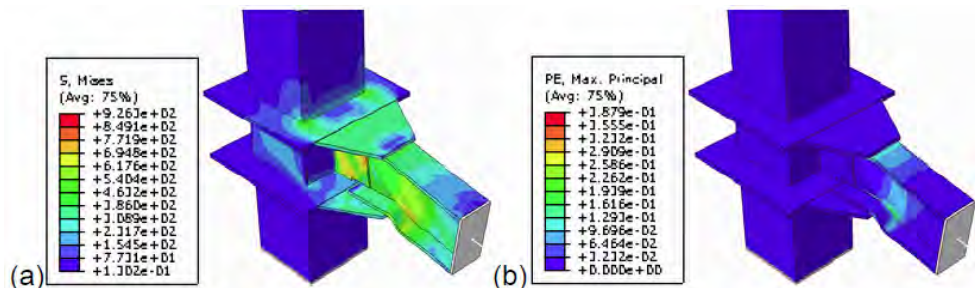Figure 19. RBS joint: von Misses stresses, plastic deformation



Figure 20. CP joint: von Misses stresses, plastic deformation

In addition, for the joint with cover plates (CP) designed for the experimental program, a numerical analysis was performed with the aim to investigate the influence of the axial force within the column on the behaviour of the joint. The level of axial force introduced in the column was $0.5 \cdot N_{pl,Rd}$. Figure 21 shows the moment-rotation curves corresponding to the joint without axial force in the column and to the compressed column. No significant difference can be observed between the two cases, with the remark that the axial force lead to a very low increase in resistance.
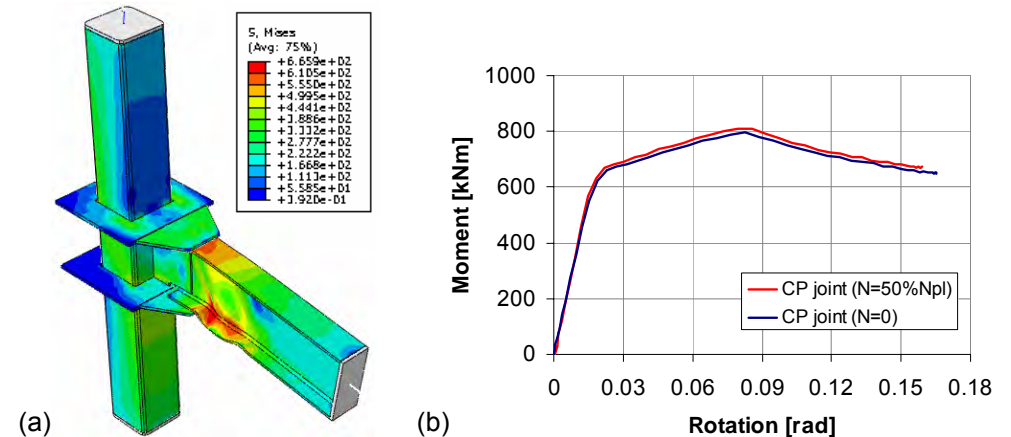


Figure 21. CP joint: a) von Misses stresses, b) moment-rotation curves

## 5. CONCLUSIONS

The paper makes a short description of the dual-steel concept that is to be investigated through experimental tests on beam-to-column joints. The purpose is to assess the joint characteristics in terms of resistance, stiffness and rotation capacity. Components of each joint connection were identified and designed according to current design codes. The question is if there are components that were not taken into account in the design process. Therefore the experimental tests on joint specimens will help investigate the main components of the joints. The joint typology and the connection details between beams and columns were presented together with the assumptions taken into account in the design process. Additionally, due to the innovative joint configuration, a set of numerical simulations has been performed for the joints designed for the experimental program, as well as for joints with larger cross section members. Based on the results obtained, the numerical simulations prove a good configuration and design of the joints. For the joints where the plastic hinge formed in the beam, the other components (welded on-site connection, stiffeners, column panel) fulfil their job. In contrast, for the joints with strengthened beams, the simulations evidence a weakness of the joint configurations in terms of welded on-site connection and column panel. The axial force in the column was observed to have a low influence on the joint behaviour.

Further research activities will be devoted to the calibration of the numerical models based on joint tests. The joint characteristics obtained experimentally and from the numerical simulations will be applied on the investigated structures with the purpose to assess the seismic performance and robustness of dual-steel frames.

## 6. ACKNOWLEDGEMENT

## REFERENCES

[1] Morino S., Tsuda K. Design and construction of concrete-filled steel tube column system in Japan, Earthquake Engineering and Engineering Seismology, Vol. 4, No. 1, 2003, pp. 51−73.

[2] Park J. W., Kang S.M., Yang S. C. Experimental studies of wide flange beam to square concrete-filled tube column joints with stiffening plates around the column, Journal of Structural Engineering © ASCE, Vol. 131, No. 12, 2005, pp. 1866−1876.

[3] Kurobane Y., Packer J. A., Wardenier J., Yeomans N. Design guide for structural hollow section column connections, TÜV Verlag, Köln, 2004.

[4] AISC 358 (2005), Prequalified Connections for Special and Intermediate Steel Moment Frames for Seismic Applications, AISC, American Institute of Steel Construction.

[5] PEER Report 2000/07 (2000), Cover-Plate and Flange-Plate Reinforced Steel Moment-Resisting Connections, Pacific Earthquake Engineering Research Center.

[6] EN1998-1-1 (2004), Eurocode 8, Design of structures for earthquake resistance - Part 1, General rules, seismic actions and rules for buildings, CEN, European Committee for Standardization.

[7] EN1994-1-1 (2004), Eurocode 4, Design of composite steel and concrete structures - Part 1, General rules and rules for buildings, European Committee for Standardization.

[8] Abaqus (2007) Analysis User's Manual I-V. Version 6.7. USA: ABAQUS, Inc., Dassault Systèmes.

[9] Korotkov V., Poprygin D., Ilin K., Ryzhov S. (2004), Determination of dynamic reaction in concrete floors of civil structures of nuclear power plant in accidental drops of heavy objects, ABAQUS Users' Conference, Boston, 25-27 May, 2004, pp. 399-408.

[10] Silva L.S., Rebelo C., Serra M., Tenchini A. (2011), "Selection of structural typologies and design of optimized dual-steel multi-storey frames", Mid Term Report HSS-SERF Project: "High Strength Steel in Seismic Resistant Building Frames", Grant N0 RFSR-CT-2009-00024.

[11] Vulcu C., Stratan A., Dubina D. (2012 – in print), Seismic Performance of EB Frames of Composite CFHS High Strength Steel Columns, *10th International Conference on Advances in Steel Concrete Composite and Hybrid Structures*, Singapore, 2–4 July 2012, (in print).

[12] Vulcu C., Stratan A., Dubina D. (2012 – in print), Seismic performance of dual frames with composite CF-RHS high strength steel columns, *15th World Conference on Earthquake Engineering, Lisbon*, 24–28 September 2012, (in print).

# DEVELOPMENT OF I-BEAM TO CHS COLUMN MOMENT CONNECTIONS WITH EXTERNAL DIAPHRAGMS FOR SEISMIC APPLICATIONS

Alireza Bagheri Sabbagh, Tak-Ming Chan

*School of Engineering, University of Warwick, Coventry, UK*
*a.bagheri-sabbagh@warwick.ac.uk; t.m.chan@warwick.ac.uk*

## ABSTRACT

In this paper monotonic FE analysis is used to develop I-beam to CHS column full strength moment connections for earthquake applications. The main components are external diaphragm plates bolted to the beam and welded to the whole circumference of the column to transfer the beam forces to both near and far sides of the column. In the FE models, connector elements are used in places of the bolts to incorporate the connection bolt slip in the analysis. The target performance is to produce large plastic deformation in the beam while the column remains elastic. The web panel zone and other connection components are allowed to partially contribute in the overall inelastic deformation of the connection. Excessive yielding and distortion in the web panel and large stress concentration in the diaphragms in front of the column walls should be avoided as these can lead to weld fracture between the diaphragm plates and the column. Various ring widths for the diaphragm plates were examined and the value designed for the full strength of the beam flanges found to limit the web panel yielding and distortion. In addition, different types of vertical stiffeners are used in the connection region to eliminate the stress concentration in the diaphragms. Two pairs of triangular vertical stiffeners with the length extended to the end of the diaphragm plates provide the required performance. Cyclic FE analysis was also performed and shown that a degree of cyclic deterioration occurs in the moment-rotation behaviour, but similar conclusions as in the monotonic FE analyses can be drawn for the developed connections.

## 1. INTRODUCTION

The integrity of the common I-beam to H- section column moment connections can be provided by using continuity plates inside the column in front of the beam flanges [1-3]. This well known detailing, however, cannot be easily employed for tubular columns which typically produce higher load resistance in both framing directions than H- section columns. Different configurations for I-beam to tubular column connections have been investigated including through diaphragm, external diaphragm and through plate connections [4-11]. Experimental work on various details of I-beam-to-CHS column connections was performed by Alostaz and Schneider to investigate their elastic and inelastic behaviour [5, 6]. They showed that a direct connection to the tubular column wall causes premature flange fracture and severe local distortion on the tube wall [5, 6]. External diaphragm plates (Fig. 1a) have been

used to transfer the beam forces around the column [4-9]. It is found that if appropriately designed the inelastic behaviour of the connections equipped with the diaphragm plates can be improved compared with the direct connection [4-9]. Stress concentration and out-of-plane failure deformation in the diaphragm plates as well as large web panel distortion have been reported [5-9] which led to fracture of the plates, welds and columns (Fig. 1b). Shifting the beam away from the face of column [5, 6] and designing the diaphragm ring width for the full strength of the beam flange [9] have been recommended to provide uniform stress flow around the column.
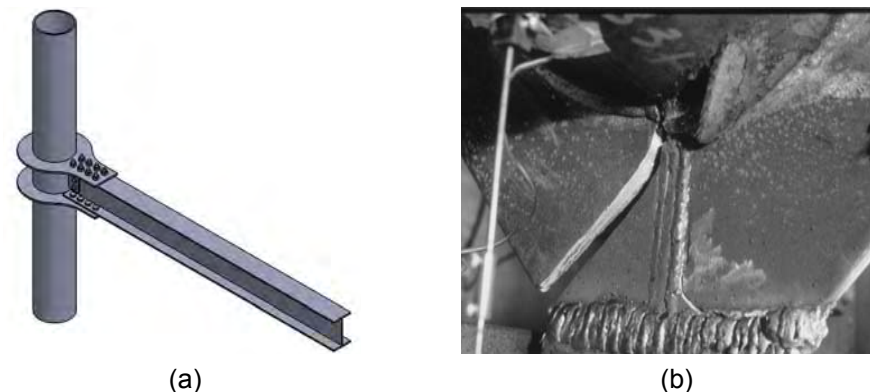


(a)                    (b)

Figure 1. (a) Schematic drawing of external diaphragm connections (b) Fractures in diaphragm plate, weld and column of an external diaphragm connection [6]

In this paper, an evolutionary process for I-beam to CHS column connections is presented by means of FE analysis leads to an optimum ring width for external diaphragm plates. The web panel excessive yielding and deformation need to be avoided. Furthermore, appropriate stiffeners are developed to eliminate stress concentration in the diaphragm plates in front of the column which potentially causes weld fracture between the diaphragm and the column.

In the FE analyses presented in this paper, connector elements are used in places of the bolts representing the slip-bearing action of the connections which found to be highly beneficial to achieve stable hysteretic cycles [12-14]. This method has already been used by Lim and Nethercot [15, 16] for monotonic FEA and by Bagheri Sabbagh et al. [17, 18] for both monotonic and cyclic FEA. A more complex method models the body of the bolts and accounts for contact interactions to simulate the slip-bearing action [19-20]. This method can be excessively time consuming especially for cyclic loading analysis and deals with more complicated converging issues compared with the modelling method using connector elements.

## 2. DESIGN CONSIDERATIONS OF THE I-BEAM-TO-CHS COLUMN CONNECTIONS

The connections were designed so as to accommodate plastic hinges in the beam at the location after the connection while the column and connection components remain elastic according to the well known strong-column-weak-beam concept. A degree of inelastic behaviour was allowed in the column web panel [21]. Overstrength and strain hardening factors of 1.25 and 1.1, respectively were used in the design of the connection according to Eurocode 8 [2]. The slip resistance ($R_n$) of the bolts using AISC Specification [22] was such that no slip occurs in the elastic region up to

the plastic moment of the beam. The connection slip, however, was allowed in the inelastic region which in the cyclic loading results in stable hysteresis behaviour [12, 13]. After a few cycles the slip resistances of the bolts degrade significantly mainly due to the reduction of the frictional coefficient and clamping forces of the bolts [12, 13& 18]. This was accounted for both in monotonic and cyclic FEA by assuming 50% reduction in the design slip resistance [13, 18].

A cantilever beam-to-column connection was used with 2m length column and beam (Fig. 2), representing distances between inflection points of an external frame with 4m span under lateral loading. The schematic view and dimensions of the designed connection using standard beam, UB 203×133×30, CHS column, 244×10 and the diaphragm plates are shown in Fig. 2. The diaphragm thickness is 15mm designed for the coupling forces projected to the connection from the overstrength plastic moment in the beam using nominal yield stress of 275MPa. The ring width of the diaphragm plates (*w*) varies to find out the optimum value as presented in Section 5. A complete ring welded to the column circumference was chosen because in a partial ring, stress concentration at the toes of the weld lines can causes initiation of crack. A web plate with 8mm thickness and 160mm height used to transfer the shear forces to the column.
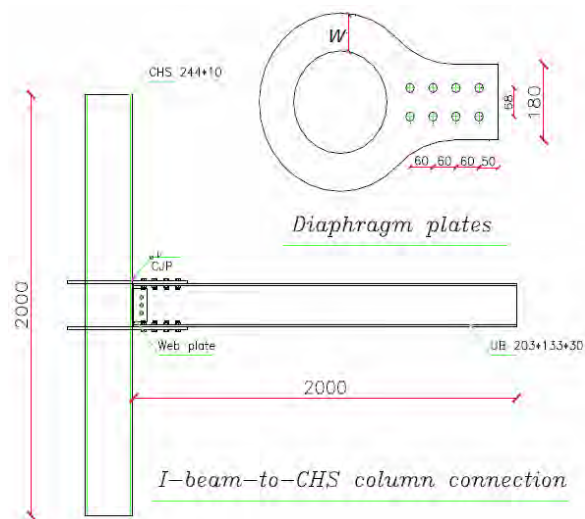


Figure 2. Dimensions and section sizes of the investigated I-beam-to-CHS column connections with external diaphragm plates

## 3. DETAILS OF THE FE MODELS

FE analysis employing *ABAQUS* [23] was used for the investigation on the I-beam to CHS column connections with external diaphragms. The boundary conditions, lateral restraints and loading points are shown in Fig. 3a and the connector elements in places of the bolts are shown in Fig. 3b. The lateral restraints were applied at both the top and bottom flanges at the plastic hinge region and loading end of the beams according to the AISC Seismic Provisions [3]. Tie constraints were used for the welded connections between the diaphragm and web plates and the column. Other parameters of the FE models are:

Element type: Shell elements with 8 nodes and reduced integration, S8R, Mesh sizes: 10×10mm for the beam and diaphragm and web plates and 20×20mm for the column, and Material: bi-linear stress-strain behaviour with yielding stress of 275MPa (S275) for the beams and the plates and yielding stress of 355MPa (S355) for the columns, E=210GPa (modulus of elasticity), Es=E/100 (Second modulus) and $\upsilon$=0.33 (Poisson`s ratio). Kinematic hardening rule was applied to the Von-Mises yielding surface for the cyclic analyses.
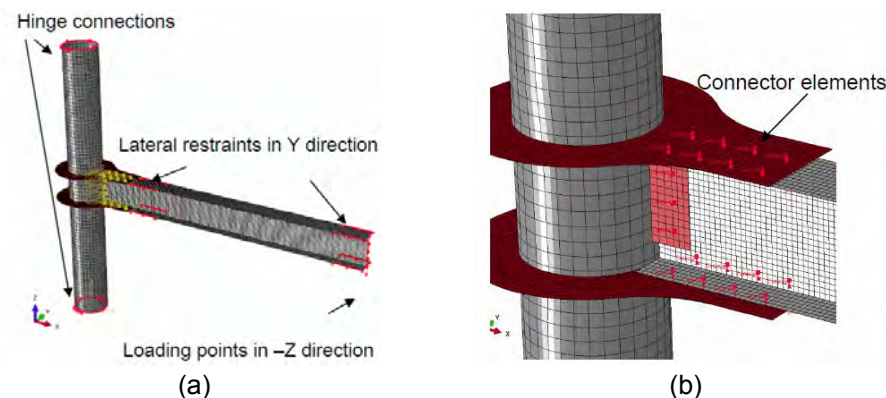


(a)           (b)

Figure 3. (a) Boundary conditions, lateral restraints and loading points
(b) Connector elements

The connector elements from *ABAQUS* library [23] were a parallel combination (Fig. 4) of *a CARTESIAN* element for elastic- plastic behaviour and a *STOP* element for limiting the movement range within the clearance of the bolt holes (±1mm by assuming the bolts at the centre of the holes). The behaviour of the connector elements (Fig. 4) was rigid up to the slip resistance ($R_n$) of the bolts, movement of the bolts within the tolerances of the bolt holes (±1mm) and rigid bearing hardening. These assumptions were made since the exact positions of the bolts in the holes and therefore contact behaviour are unknown in the actual connection assemblies. This slip-bearing action model has already been used by Shen and Astaneh-Asl [24] and Bagheri Sabbagh et al. [18].
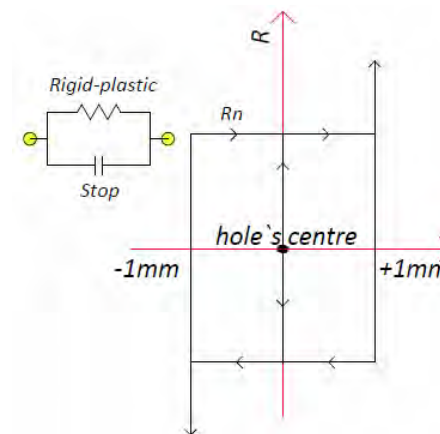


Figure 4. Slip-bearing action of the connector elements

## 4. FE RESULTS FOR DEVELOPMENT OF I-BEAM-TO-CHS COLUMN CONNECTIONS WITH DIFFERENT DIAPHRAGM RING WIDTHS

An evolutionary process was used for the development of the external diaphragms for the I-beam-to-CHS column connections. Stress distribution and failure deformations of the FE analyses are shown in Fig. 5 and normalised moment-rotation ($M/M_p$-$\theta$) curves calculated at the plastic hinge location are shown in Fig. 6. $M_p$ is the overstrength plastic moment of the beams (1.25 times the nominal plastic moment). The horizontal portion of the $M/M_p$-$\theta$ curves (Fig. 6) occurred at around $0.5M_p$ corresponds to the connection slip activated in the FE analyses as discussed previously in Section 2.

The FEA without the external diaphragm plates (direct connection) showed large yielding area and excessive distortion in the column web panel and no yielding in the beam (Figs. 5 and 6, $w$= 0). By using a diaphragm ring tied to the whole circumference of the column with the width of $w$= 30mm, a degree of yielding was mobilised in the beam, although the distortion and yielding in the column web panel still took over (Figs. 5 and 6, $w$= 30). By increasing the ring width from 30mm to 50mm, local buckling occurred in the beam after the connection region and the column web panel contributed less in the overall deformation (Fig. 5, $w$= 50) than the connection with $w$= 30mm. Local flange and web buckling in the beam led to strength degradation at around 0.08rad in the moment-rotation curve (Fig. 6, $w$= 50). The connection with $w$= 70mm showed even less yielding in the web panel (Fig. 5, $w$ = 70) and strength degradation (Fig. 6, $w$= 70) due to the beam local buckling initiated earlier (at around 0.07rad) than the connection with $w$= 50mm.

The failure deformations and moment rotation curves of the connections with $w$=90 and 110mm were close to those of the connection with $w$=70mm (Figs. 5 and 6). Increasing the diaphragm ring width, however, reduced the yielding region in the web panel (shown in Fig. 5, $w$=90 and 110mm) which in the connection with $w$= 110mm was nearly vanished. The diaphragm plate with $w$= 90mm showed a degree of yielding in the web panel which is acceptable according to the current design codes [1-3; 22] discussed by El-Tawil et al [21], therefore in this case assumed as the optimum diaphragm width. The diaphragm width of $w$= 90mm also meets the design criteria proposed by Wang et al. [9] to resist full strength of the beam flanges.

In all the FE analyses presented in this section for different diaphragm widths ($w$= 0, 30, 50, 70, 90 and 110mm), stress concentration occurred in the diaphragm plates in front of the column face. This potentially leads to weld fracture between the diaphragm and the column as well as local buckling in the diaphragm plates (reported by other researchers [5-9]). This stress concentration cannot be eliminated in the compressive diaphragm either by increasing the diaphragm thickness from 15mm to 20mm or the material yielding strength from 275MPa to 355MPa (Fig. 7). The reason can be second order effects in the compressive diaphragm which can be intensified by initiation of the beam local buckling and large deformations. This phenomenon is addressed in the next section.
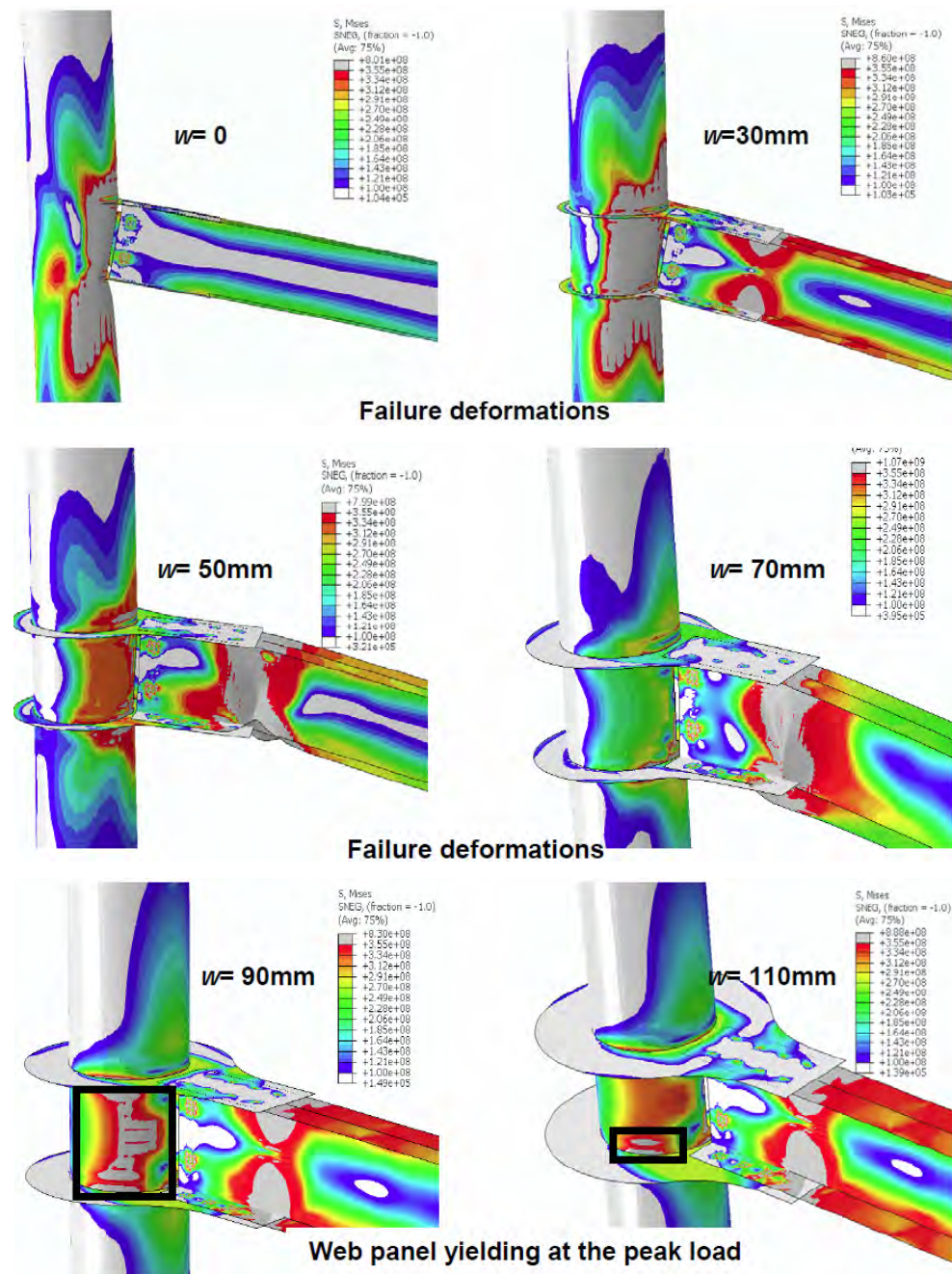


Figure 5. Failure deformations and Von-Mises stress contours of the I-beam-to-CHS column connections with different diaphragm ring widths ($w$=0, 30, 50, 70, 90 and 110mm)
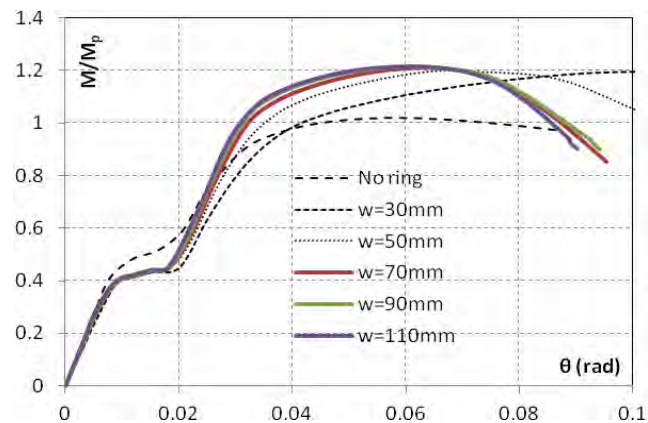
Figure 6 Moment-rotation curves of the I-beam-to-CHS column connections with different diaphragm ring widths (*w*=0, 30, 50, 70, 90 and 110mm)
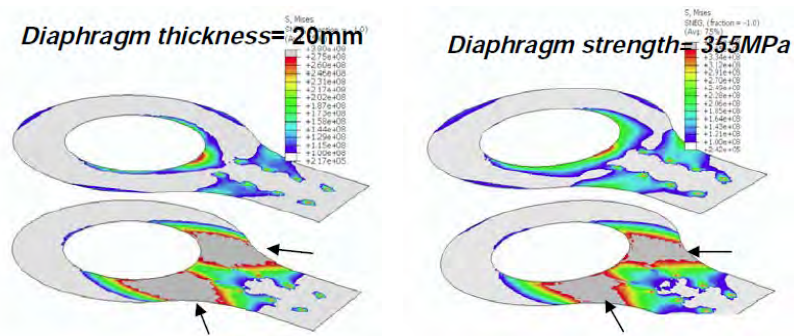


Figure 7. Stress concentration in the diaphragm plates with increased thickness from 15mm to 20mm and the material strength from 275MPa to 355MPa

## 5. FE RESULTS FOR DEVELOPMENT OF I-BEAM-TO-CHS COLUMN CONNECTIONS WITH DIFFERENT DIAPHRAGM STIFFENERS

Different configurations of vertical stiffeners tied to the external diaphragms (with *w*= 90mm) and the column were examined to minimise the stress concentration in the diaphragm plates (Fig. 8). Firstly, the stiffeners inside the connection were used between the diaphragm plates which have less architectural impact than the outside stiffeners on top of the diaphragm plates. In the model equipped with 100mm length vertical stiffeners (Fig. 8, St1), the stress concentration initiated at the tip of the stiffeners in the compressive diaphragm and propagated towards the face of the column at the larger load increments. By extending the vertical stiffeners further inside the connection (Fig. 8, St2), similar stress concentration was observed. The stress concentration also occurred in the compressive diaphragm plate in the connection with separated pairs of vertical stiffeners (with 50mm height) extended to the end of connection for each of the diaphragm plates (Fig. 8, St3). The stress concentration, however, is minimised by using the same vertical stiffeners as St3, but placed outside of the connection on top of the diaphragm plates (Fig. 8, St4). The reason is higher connection stiffness provided by using outside stiffeners and consequently less

second order effects in the diaphragm plates. By using a more effective triangular shape for the outside vertical stiffeners with 100mm height in front of the column (Fig. 8, St5), the stress concentration was completely removed in front of the column in the compressive diaphragm, although a degree of yielding appeared at the toe of the tension diaphragm. The reason is excessive transverse deformation of the diaphragm plates by increasing the stiffness of the connection. By trimming the stiffeners (Fig. 8, St6) the stress concentration again initiated at the tip of the stiffeners and propagated at the larger load increments similar to the behaviour of the connections with St1 and St2. Therefore, using the vertical stiffeners with the shorter length than the whole connection length should be avoided in this type of connections.
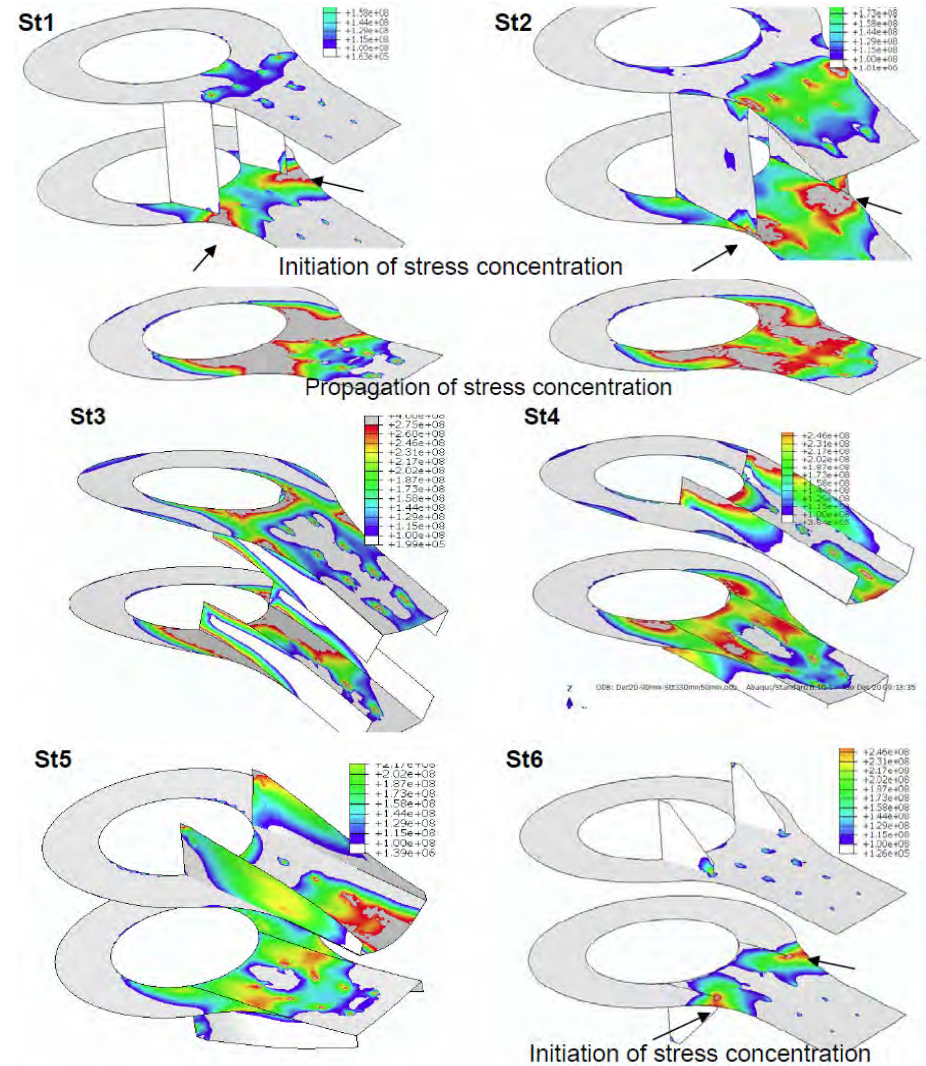


Figure 8. Stress concentration in the diaphragms of the connections with different vertical stiffeners connected to the diaphragm plates and the column

The moment-rotation curves of the connections with all the examined stiffeners (Fig. 9, St1-6) are similar to that of the connection without stiffener. The strength degradation starts at around 0.07rad due to local buckling in the beam after the connection region. The slip resistance load level was increased by increasing the connection stiffness (Fig. 9, St1-6). The moment-rotation curves of the connections using St5 and with w=70, 90 and 110mm (shown by dashed lines in Fig. 9) are very close to each other. The stress concentration in the connections with St5, w=70 and 110mm was also removed in the compressive diaphragms in front of the column similar to the connection with St5, w=90mm (Fig. 8, St5). The connection with triangular stiffeners (St5) can be assumed as optimum in this case.


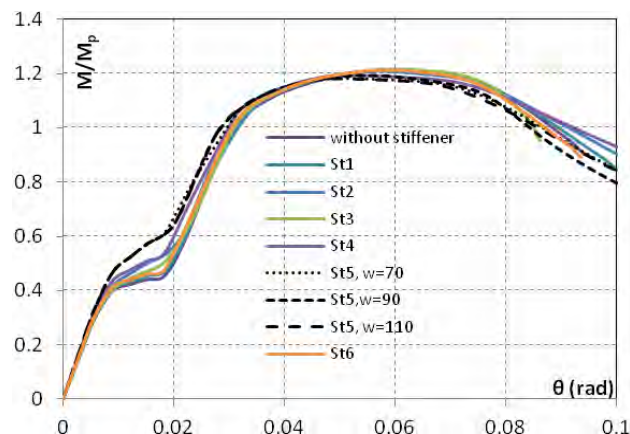
Figure 9. Moment-rotation curves of the I-beam-to-CHS column connections with different vertical stiffeners

## 6. CYCLIC FE RESULTS FOR THE DEVELOPED CONNECTION CONFIGURATIONS

Cyclic loading applied to the FE models using $w$= 70 and 90mm diaphragm plates with and without the optimum vertical stiffeners, St5, examined in the previous section. In the cyclic FEA, surface to surface contact was used between the diaphragm plates and the beam flanges to avoid their penetration during the buckling deformation. The cyclic moment-rotation curves as well as the monotonic curves are shown in Figs. 10a and b. It is evident that the strength degradation occurred earlier in the cyclic curves than the monotonic curves (Fig. 10) due to the cyclic deterioration effect. The deterioration is even sharper in the cyclic FEA with w= 70mm than that of the FEA with w=90mm (Fig. 10a). Similar to the results obtained in the monotonic FE analyses (presented in the previous sections) it can be concluded that: (i) web and flange buckling after the connection region (Fig. 11) is the main reason for the strength degradation, (ii) the connection using $w$= 90mm showed less web panel yielding than the connection with $w$= 70mm and (iii) the use of vertical stiffeners St5, eliminated the stress concentration in the diaphragms in front of the column face.
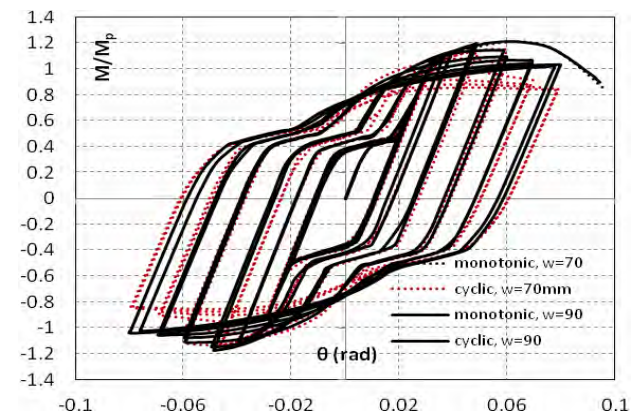


(a)  **Without vertical stiffeners**
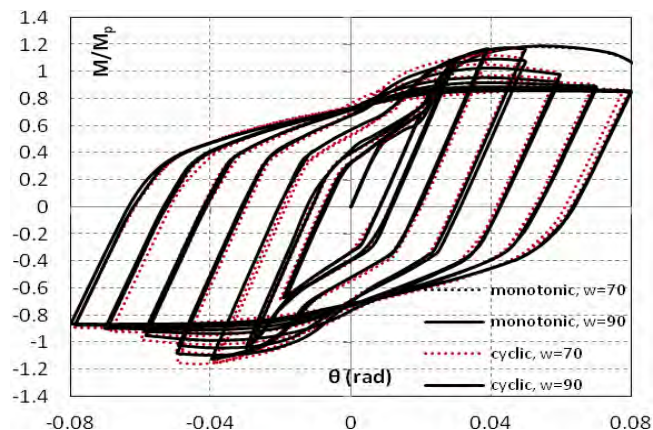


(b)  **With vertical stiffeners St5**

Fig. 10. Cyclic and monotonic moment-rotation curves of the connections using $w$= 70 and 90mm (a) without vertical stiffeners and (b) with St5



Fig. 11. Failure deformations and Von-Mises stress contours for the cyclic FE analyses of the connections using (a) $w$= 90mm and (b) $w$= 90mm with St5

# 7. CONCLUSIONS

Optimum configurations for I-beam-to-CHS column moment resisting connections with external diaphragm plates were developed using monotonic FE analysis. Two types of connection failure were eliminated: web panel distortion and stress concentration in the diaphragm plates.
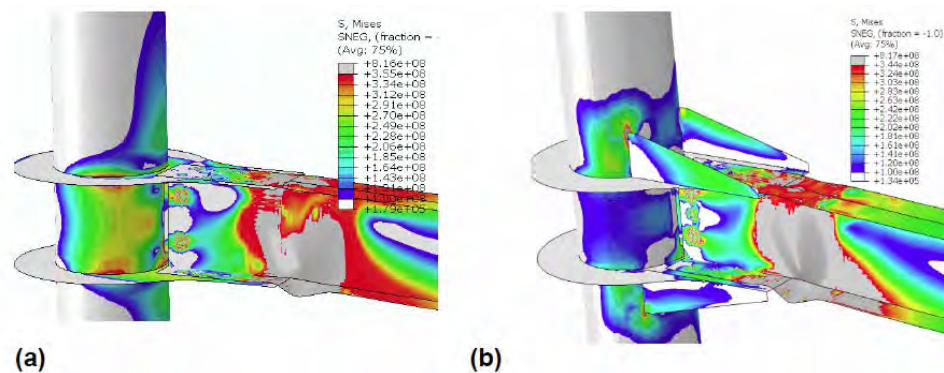
A full ring welded to the column as external diaphragm plates is needed to reduce excessive yielding and distortion in the web panel zone. By designing the total ring width for the full strength of the beam flanges ($w$= 90mm in this study) slight yielding occurred in the web panel zone which is acceptable according to the current design codes.

Two pairs of triangular vertical stiffeners found to eliminate the stress concentration in the diaphragm plates in front of the column face. These stiffeners were welded to the column face and to the top of the diaphragms outside the connection and extended to the end of the diaphragms (St5 in this study).

Cyclic FEA also performed and confirmed the results achieved in the monotonic FEA. Cyclic deterioration effect caused earlier strength degradation in the developed connections (using $w$= 70 and 90mm with or without St5).

# ACKNOWLEDGEMENTS

# REFERENCES

[1] Eurocode 3: Design of steel structures: Part 1.8: Design of joints, EN 1993-1-8: 2005

[2] Eurocode 8: Design of structures for earthquake resistance. Part 1, General rules, seismic actions and rules for buildings. BS EN 1998-1: 2004

[3] ANSI/AISC 341-05, 2005, Seismic Provisions for Structural Steel Buildings, American Institute of Steel Construction (AISC), Illinois

[4] Y. Kurobane, J. A. Packer, J. Wardenier, N. Yeomans, Design guide for structural hollow section column connections, CIDECT, 2004

[5] Yousef. M. Alostaz & Stephen P. Schneider, Analytical behavior of connections to concrete-filled steel tubes, Journal of Constructional Steel Research Vol. 40, No. 2 (1996), pp. 95-127

[6] Stephen P. Schneider & Yousef M. Alostaz, Experimental behavior of connections to Concrete-filled steel tubes, Journal of Constructional Steel Research Vol. 45, No. 3 (1998), pp. 321–352

[7] Lin-Hai Han, Wen-Da Wang, Xiao-Ling Zhao, Behaviour of steel beam to concrete-filled SHS column frames: Finite element model and verifications, Engineering Structures 30 (2008) 1647–1658

[8] Wen-Da Wang, Lin-Hai Han, Brian Uy, Experimental behaviour of steel reduced beam section to concrete-filled circular hollow section column connections, Journal of Constructional Steel Research 64 (2008) 493–504

[9] Wei Wang, Yiyi Chen, Wanqi Li and Roberto T. Leon, Bidirectional seismic performance of steel beam to circular tubular column connections with outer diaphragm, Earthquake Engng Struct. Dyn. 2011; 40:1063–1081

[10] Mirghaderi S.R., Torabian S., Keshavarzi F., I-beam to box column connection by a vertical plate passing through the column, Engineering Structures, 32 (2010) 2034-2048

[11] Shahabeddin Torabian, Seyed Rasoul Mirghaderi, Farhad Keshavarzi, Moment-connection between I-beam and built-up square column by a diagonal through plate, Journal of Constructional Steel Research 70 (2012) 385–401

[12] Kurt Michael McMullin, Abolhassan Astaneh-Asl, Steel Semirigid Column–Tree Moment Resisting Frame, Journal of Structural Engineering, Vol. 129, No. 9, 2003

[13] Bagheri Sabbagh A., Petkovski M., Pilakoutas K., Mirghaderi R., Experimental work on cold-formed steel elements for earthquake resilient moment frame buildings, Engineering Structures, under review

[14] Bagheri Sabbagh A., Cold-formed steel elements for earthquake resistant moment frame buildings, PhD thesis, University of Sheffield (2011)

[15] Lim J.B.P., Nethercot D.A., Finite element idealisation of a cold-formed steel portal frame, Journal of Structural Engineering, 10, 1061/ (ASCE) 0733-9445 (2004) 130:1 (78)

[16] Lim J.B.P., Nethercot D.A., Ultimate strength of bolted moment-connections between cold-formed steel members, Thin-Walled Structures 41 (2003) 1019–1039

[17] Bagheri Sabbagh A., Petkovski M., Pilakoutas K., Mirghaderi R., Development of cold-formed steel elements for earthquake resistant moment frame buildings, Thin-Walled Structures, 53 (2012) 99–108

[18] Bagheri Sabbagh A., Petkovski M., Pilakoutas K., Mirghaderi R., Cyclic behaviour of bolted cold-formed steel moment connections: FE modelling verification including slip, Journal of Constructional Steel Research, under review

[19] Swanson J.A., Kokan D.S., Leon R.T., Advanced finite element modeling of bolted T-stub connection components, Journal of Constructional Steel Research 58 (2002) 1015–1031

[20] Citipitioglu A.M., Haj-Ali R.M., White D.W., Refined 3D finite element modeling of partially restrained connections including slip, Journal of Constructional Steel Research 58 (2002) 995–1013

[21] Sherif El-Tawil, Egill Vidarsson, Tameka Mikesell, and Sashi K. Kunnath, Inelastic behavior and design of steel panel zones, Journal of Structural Engineering, Vol. 125, No. 2, February, 1999

[22] ANSI/AISC 360-05, Specification for Structural Steel Buildings, American Institute of Steel Construction, 2005, Illinois

[23] Abaqus/CAE User's Manual, 2007, version 6.7, USA

[24] Shen J., Astaneh-Asl A., Hysteresis model of bolted-angle connections, Journal of Constructional Steel Research 54 (2000) 317–343

# EXPERIMENTAL STUDY ON FLANGED JOINTS OF TUBULAR MEMBERS UNDER BIAXIAL BENDING

*Henri Perttola, Markku Heinisuo*
Tampere University of Technology
*Research Centre of Metal Structures,*
*Frami, Kampusranta 9 C, FI-60320 Seinäjoki, Finland*
henri.perttola@tut.fi, markku.heinisuo@tut.fi

## ABSTRACT

Six isolated joint tests on flanged joints of tubular members of cold formed rectangular hollow steel sections are described. These bolted end plate joints were loaded with biaxial bending or weak axis bending. The testing arrangements and selected results are reported. The tests are part of research on the suitability of the component method presented in EN1993-1-8 (2005) for three-dimensional (3D) analysis is studied. A mechanical model suited for 3D modelling is introduced and the test cases are analysed by it. The results are compared with the test results.

## 1. INTRODUCTION

There are no reports in literature on isolated joint tests on bolted end plate joints of steel structures mainly focused on biaxial bending. Instead, the main motive behind the tests has usually been to study joint behaviour under strong axis bending associated with in-plane response of a typical joint of a plane frame. If out-of-plane bending has been considered, the focus has usually been on weak axis bending. Murude Celikag and Patrick Kirby have reported on the results of out-of-plane tests (Celikag et al, 1989) for common joint types including flush end plate joints. In their tests, the members connected by the joints were British Universal Beams (UB) and Columns (UC), i.e., I- or H-profiles. Celikag and Kirby suggested that "two similar specimens should be loaded up to the failure in different directions to find out the load carrying capacity of a joint in each direction". To date, however, most of the joint tests have been arranged in order to study the strong axis bending (in-plane behaviour) of joints and little experimental knowledge is available on the 3D behaviour of joints. Some data on out-of-plane bending behaviour of bolted steel joints can be found in articles concerned with joints under earthquake loads (typically horizontal loads in any direction). For example, Lee et al have experimentally investigated the weak axis bending of column bases (Lee et al, 2008).

Six biaxial and weak axis bending tests on end plate joints of steel tubes are described in this paper (three of them in more detail). They belong to a larger series of tests reported in (Perttola et al, 2011). Two related tests were also carried out in fire conditions (Ronni et al, 2011). Nine earlier tests on corresponding end plate joints of steel tubes under strong axis bending (with flexible bolts) are reported in (Ronni et al, 2010). The test series "bending tests of bolted end plate joints in cold formed rectangular hollow sections" (Wheeler et al, 1997a) comprising only strong axis bending tests can be regarded as a forerunner to the present tests. In Wheeler's series, the focus was on the study of the behaviour of the end plate joint with bolts located outside the edge lines of the tube cross section in the end plate (i.e., with the bolts at the corners of the end plate). A design model suggested for this type of connections is presented in (Wheeler et al, 1997b).

The component method described in European standard EN1993-1-8 (2005) serves as a practical approach to predicting the behaviour of joints. The stiffness and resistance of a joint can be determined by the component model achieved by dividing the joint into its basic components. Although, the component method is primarily meant for the analysis of joints under in-plane (strong axis) bending, in theory it does not matter, if the individual components are analysed in an in-plane model or a 3D joint model. In this paper, the mechanical model called the rake model (rake) is used in the analysis of the tested joints under biaxial bending and the components of the component method are embedded in the model. The analysis with the rake was performed in accordance with the formulas given in EC3 as far as possible. The computational results are compared with the tests results.

## 2. TESTS

### 2.1. Tests and specimens

Three-point loading tests on rectangular tube splices are considered, as shown in Figures 1 and 2. In this paper, only six tests (Figure 1: TE1, TE2, TE3, TE7, TE8, TE11) from the series of 12 joint tests are described. The included tests were arranged with normally assembled bolts, whereas the other six excluded tests were carried out with long bolts accompanied by bush rings. A report on all tests can be found in (Perttola et al., 2011).

In tests TE1–TE3 and TE11 (4 tests), the rectangular tubes (CFRHS 250x150x10) and the joint were at an inclined angle, i.e., they were rotated 55º from their vertical position. Tests TE7 and TE8 were arranged under weak axis bending (joints in horizontal position). The nominal thicknesses ($t_{pn}$) of the end plates 290x390x$t_p$ mm$^3$ were 10 mm, 15 mm and 20 mm. The measured thicknesses ($t_p$) as well as the material properties of the end plates are shown in Table 1.

Table 1. Thicknesses and material properties of end plates 290x390x$t_p$.

| Tests | $t_{pn}$ [mm] | $t_p$ (measured) [mm] | $R_{eH}$ [MN/m$^2$] | $R_m$ [MN/m$^2$] | $R_{eH}$/ $R_m$ | A5 % |
|---|---|---|---|---|---|---|
| TE1, TE7, TE11 | 10 | 11.0 | 429 | 582 | 0.74 | 24 |
| TE2 | 15 | 15.0 | 407 | 555 | 0.73 | 28.4 |
| TE3, TE8 | 20 | 20.3 | 380 | 564 | 0.67 | 26 |

M20x70 grade 10.9 full-thread bolts were used. The grade of the nuts and washers (M20) was also 10.9. Three randomly selected bolts were pulled to failure. The average ultimate load was 277.7 kN corresponding the stress 1133 MN/m$^2$. The bolts situated on the tension side of the joint were tightened to 400 Nm, while the tightening moment of the bolts on the compression side was only 70 Nm. As an exception, the tightening moment of all bolts in test TE1 was 70 Nm.

The specimen was loaded as a simple beam (span *L*=1 m) with the load applied directly to the splice at mid span. The test set-up used is shown in Figure 2. The specimen was placed under the hydraulic jack so that the hinge and the ball joint together allowed movement of the specimen in the transverse but not in the longitudinal direction of the specimen. The transverse degree of freedom must be allowed because it inevitably occurs in addition to downward deflection in biaxial bending. Because of their simplicity, three-point tests were preferred to four-point tests, which could have been used 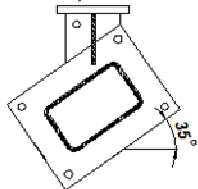to arrange the constant bending moment in the joint area. However, the four-point tests should have been arranged with two loading points, both accompanied by a transverse degree of freedom.
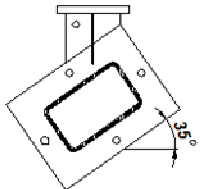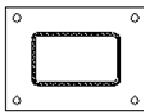


Figure 1. Tests on tube splices, detailed data is given in report (Perttola et al, 2011).

In the biaxial tests (TE1-TE3, TE11), the angle between the direction of the load and the weak axis of the tube section was $\alpha$ = 35° (Figure 1). A special shelf welded to the end plates was constructed for the biaxial tests, through which the force of the hydraulic jack was transferred to the specimen. This extra construction, assured the stability of the loading arrangement. The shelf was in the compression zone of the joint in the bending tests whereby its influence on the response of the specimen must have been quite insignificant. To avoid any influence of the rotational restraints on the test results at the supports, the lower edges of the support plates were chamfered to imitate freely supported end conditions (DET A in Figure 1). The supporting plate was lying on a disk pack of steel plates with roller bearings underneath at both supports. The longitudinal degree of freedom was restrained by the hydraulic jack at mid span. Force needed to prevent the corresponding movement (by friction between the jack and the shelf) was not significant.

## 2.2. Testing procedure and measurements

The load was applied on the specimen using the force control of the hydraulic jack. Two loading cycles were arranged, one in elastic range and another one in which the load was increased (at rate 0.1 kN/s) up to failure. The first cycle was conducted in order to avoid unwanted early stage movements (caused mainly by gaps) in the second cycle. The force and axial elongation of the jack were measured by the instrumentation built in the hydraulic jack. These quantities allow determining the moment rotation dependence of the joint, as explained in section 3. Separate displacement transducers and strain gauges were used in the measurement, too, but the results they yielded are not included in this paper. A more detailed description of the measurement is given in research report (Perttola et al, 2011).



Figure 2. Testing arrangement in the room temperature tests.

## 3. TEST RESULTS

The tests were arranged with the force control of the hydraulic jack whereby (rotational) resistances and initial stiffnesses were the main results. The bending of the joint governed the behaviour of the specimen in each conducted test. In practi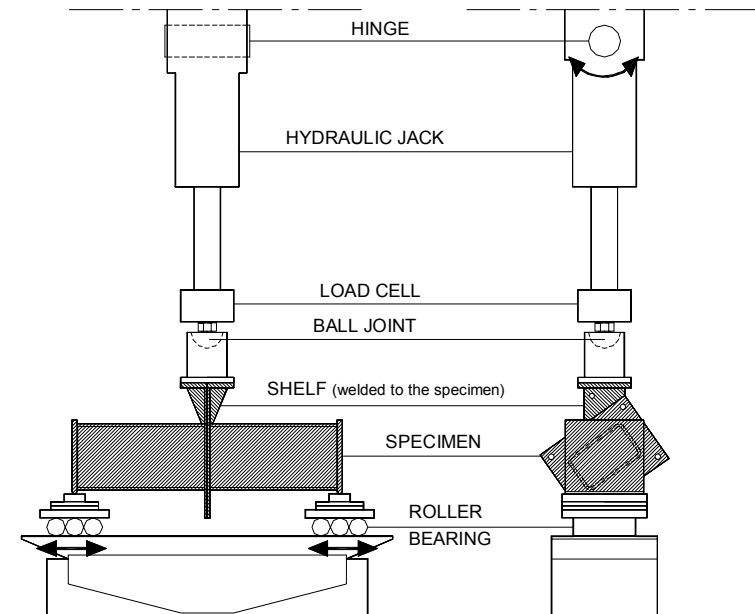ce, all permanent deformations were concentrated on the joint. Thus, by investigating the relationship between the bending moment and the corresponding rotation of the joint, the main characteristics of the behaviour of the specimen can be revealed. To determine these quantities from the measured data, the formulas presented below are needed. The resultant bending moment $M_R$ in the joint caused by jack force $P$ is

$$M_R = PL/4. \tag{1}$$

Displacement $v$ in the direction of force $P$ at mid span includes the elastic part $v_{b,el}$ accumulated across the entire length of the beam by the deformations caused by bending and shear. Thus, the rotation of a joint can be determined by the formula

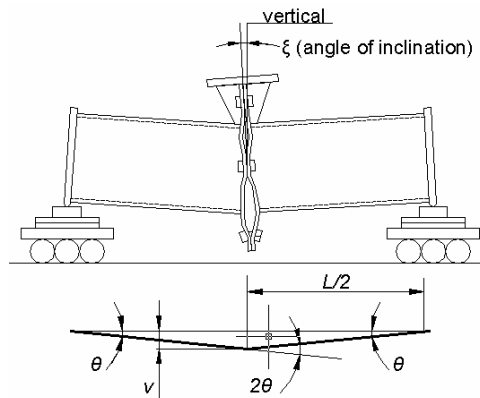$$\theta = 2(v - v_{b,el})/L = \theta_g - \theta_{eb} \tag{2}$$



Figure 3. Definition of rotation $\theta$

In the case of the dimensions of the specimens the reduction term $\theta_{eb} = 2v_{b,el}/L$ is quite small in comparison with the value of "the gross rotation" $\theta_g = 2v/L$. Formulas (1) and (2) define the conversion needed when $M$-$\theta$ curves based on the measured quantities are determined. It should be noted that rotation $\theta$ is defined here as half of the total rotation of the splice in a way as illustrated by Figure 3. The inclination (angle $\xi$) from the vertical could possibly occur in the tests, but it was omitted in their analysis. Then rotation $\theta$ represents the average deformation of one end plate and half length of the connector (bolt+nut+washers).

The moment-rotation curves of the joints based on tests TE1–TE3,TE7,TE8 and TE11 are shown in Figure 4. They describe the relationship between the resultant moment $M_R$ (marked as $M$) and the corresponding rotation $\theta_R$ (marked as $\theta$) obtained by Formulas (1) and (2). It can be seen from the $M$–$\theta$ curves that rotations over 50 mrad were achieved in every test. Thus, the rotation in failure was significant even in the tests with the thickest end plate ($t_{pn}$=20 mm). The maximum value of rotations MAX $[\theta_g - \theta_{b,el}]$ obtained was about 154 mrad in test TE7 with $t_{pn}$=10 mm. The deformability of the joints was mainly due to the large deformations

associated with yielding in the end plates. In accordance with this, deformation capacity if defined as rotation corresponding the maximum moment (given in Tables 2 and 3) is dependent on plate thickness. The thinner the plate is, the larger rotation is expected at failure.
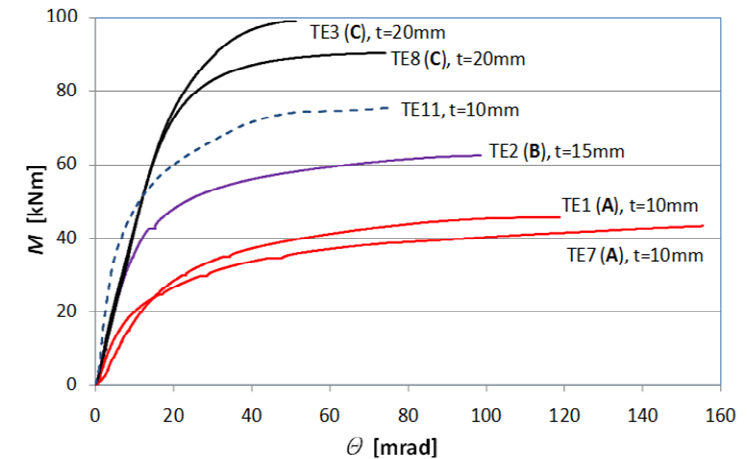


Figure 4. Moment-rotation curves for tests TE1–TE3, TE7, TE8 and TE11.

It is notable that the $M$-$\theta$ curve of test TE11 (dashed line) with a 10 mm plate and the bolts in the middle of the sides of the end plates indicates larger initial stiffness and resistance than those obtained in tests TE1 and TE7 with an end plate of the same thickness but a different layout of the corner bolts. Furthermore, test TE2 with the 15 mm end plates and corner bolts gave, in general, a softer response than test TE11. Even the initial stiffness observed in tests TE3 and TE8 with the thicker 20 mm end plates and the corner bolts was clearly smaller than the stiffness in test TE11 with a 15 mm end plate and bolts in the middle of the edges of the end plate.

Tests TE1 (biaxial test) and TE7 (weak axis test) were associated with the same joint (**A**) as the only difference between them is the rotated position (different angles $\alpha$, see Figures 1 and 11) of the joint and the tubes. Correspondingly, tests TE3 and TE8 were associated with the same joint (**C**) under biaxial and weak axis bending, respectively. Test TE2 is associated with the joint marked by bold letter **B**. Joints **A**–**C** (under arbitrarily inclined bending) are selected as examples when the results obtained with the rake are demonstrated later in section 4.

### 3.1. Resistances, stiffnesses

The value of the maximum moment ($M_{R,MAX}$) achieved in a test represents an ultimate rotational resistance. Maximum moments $M_{R,MAX}$ as well as the corresponding rotations MAX$[\theta_g - \theta_{b,el}]$ and MAX$[\theta_g]$ with and without elastic reduction $\theta_{b,el}$, respectively, are tabulated in Tables 2 and 3. The values of maximum rotations MAX$[\theta_g]$ without elastic reduction were 1 to 6% larger compared to the corresponding values of MAX$[\theta_g - \theta_{b,el}]$ with elastic reduction in the biaxial bending tests. In the weak axis bending tests these differences were about 1 to 5%. For the biaxial bending test, components $M_S$ and $M_W$ of moment $M_{R,MAX}$ corresponding to strong and weak axis bending, respectively, are given in the last two columns of Table 2.

The maximum registered resistance of a joint was about 99 kNm in test TE3 with the thickest end plate ($t_{pn}$=20 mm). The minimum value of 43.2 kNm for maximum moment was measured in weak axis test TE7 with the thinnest end plate ($t_{pn}$ = 10 mm). A clear dependence of resistance on thickness of the end plate was observed, i.e. an increase in end plate thickness resulted in increased strength of the joint. However, the moment resistance in test TE11 with the 10 mm end plate was greater than the resistances obtained in test TE2 (Figure 4, Table 2) with the thicker end plate ($t_{pn}$=15 mm). Obviously, the placement of the bolts in the middle of the sides of end plates makes the joint more effective than having the bolts at the corners if higher resistance (and stiffness) is sought.

Table 2. Maximum moments obtained in biaxial bending tests.

|  | $M_{R,MAX}$ [kNm] | MAX[$\theta_g$] [mrad] | MAX[$\theta_g - \theta_{b,el}$] [mrad] | $M_W$ [kNm] | $M_S$ [kNm] |
|---|---|---|---|---|---|
| TE1, corner bolts, $t_{pn}$ = 10 mm | 45.7 | 119.9 | 118.3 | 38.2 | 25.2 |
| TE2, corner bolts, $t_{pn}$ = 15 mm | 62.5 | 100.2 | 98.2 | 52.4 | 34.1 |
| TE3, corner bolts, $t_{pn}$ = 20 mm | 99.0 | 53.8 | 50.6 | 81.9 | 55.8 |
| TE11, bolts in the middle, $t_{pn}$ = 10 mm | 75.4 | 76.1 | 73.7 | 62.5 | 42.2 |

Table 3. Maximum moments obtained in weak axis bending tests.

|  | $M_{R,MAX}$ [kNm] | MAX[$\theta_g$] [mrad] | MAX[$\theta_g - \theta_{b,el}$] [mrad] |
|---|---|---|---|
| TE7, corner bolts, $t_{pn}$ = 10 mm | 43.2 | 153.7 | 152.0 |
| TE8, corner bolts, $t_{pn}$ = 20 mm | 90.2 | 70.1 | 66.6 |

The Initial stiffness was defined as

$$S_{ini} = (M_2 - M_1)/(\theta_2 - \theta_1) \qquad (3)$$

where moments $M_1$ and $M_2$ (>$M_1$) belong to the straight portion of the $M$-$\theta$ curve. Symbols $\theta_1$ and $\theta_2$ represent the corresponding rotations. Tables 4 and 5 give the initial stiffnesses of the joints of all tests. The lower and higher values of the moment used to determine stiffnesses by Formula (3) are also given. They must be selected in such a way at the beginning of the second loading cycle that the disturbances at the beginning of the tests are excluded and any permanent deformations have not yet taken place. In practice, the $M$-$\theta$ curves were plotted as large-scale and the starting point of the straight portion (elastic part) of the curve was identified at the beginning of the second cycle.

Based on the comparisons between tests TE1, TE2 and TE3 ($t_{pn}$=10, 15 or 20 mm), it is clear that an increase in end plate thickness resulted in an increase in the strength of the joint. The same holds for initial stiffnesses only when tests TE1 ($t_{pn}$ = 10 mm) and TE2 ($t_{pn}$=15 mm) are compared with each other. However, the initial stiffness determined in test TE2 with a nominal thickness of 15 mm was a little higher than the stiffness determined in tests TE3 with a thicker end plate with ($t_{pn}$=20 mm). The reason for this may be the absence of the prying action at the beginning of the loading in test TE3. In other words, with the thinner end plate ($t_{pn}$=15 mm), the contact associated with the prying action plays a more significant

role in the response of the joint at the beginning of the loading, resulting in enhanced stiffness. The nonlinearity related to contact problems makes the situation at hand complicated. Actually, confirmation of these speculations will require more testing or a detailed numerical study not included in this article.

The highest value of initial stiffness $S_{ini}$ of the joint was found in test TE11 with a nominal end plate thickness of 10 mm and the bolts (normal assembly) placed in the middle of the sides of the end plates. Clearly, a layout with bolts at the corners is associated with more flexible behaviour.

Table 4. Intial stiffnesses $S_{in}$ in biaxial bending tests.

|  | $M_{R1} \to M_{R2}$ [kNm] | $S_{ini}$ [kNm/mrad] |
|---|---|---|
| TE1[1], corner bolts, $t_{pn}$ = 10 mm | 5 → 10 | 2.2 |
| TE2, corner bolts, $t_{pn}$ = 15 mm | 1.5 → 5 | 4.7 |
| TE3, corner bolts, $t_{pn}$ = 20 mm | 1.5 → 5 | 4.2 |
| TE11, bolts in the middle, $t_{pn}$ = 10 mm | 5 → 10 | 12.0 |

1 = second cycle started with zero load

Table 5. Initial Stiffnesses $S_{in}$ in weak axis bending tests.

|  | $M_{R1} \to M_{R2}$ [kNm] | $S_{ini}$ [kNm/mrad] |
|---|---|---|
| TE7, corner bolts, $t_{pn}$ = 10 mm | 3.5 → 5 | 3.0 |
| TE8, corner bolts, $t_{pn}$ = 20 mm | 15 → 20 | 4.7 |

### 3.2. Description of tests TE1, TE2 and TE3

Three biaxial joint tests TE1–TE3 are presented here more comprehensively than the others. The failure modes observed in these tests are described. Tests TE1–TE3 are associated with joints **A**–**C** analysed by the rake (section 4).

Test TE1 ($t_{pn}$=10 mm) was interrupted when the specimen collapsed onto the underlying table. At the time the load of the jack was 183 kN ($M$=45.7 kNm). The yielding of the end plates was the primary reason for the softening response of the specimen. The substantially deformed shapes of the end plates after the failure are shown in Figure 5. Cracks in the strongly bent end plates near the lowest corners of the tubes at the edges of the welds were observed. They formed in a very late stage of the test and, therefore, crack formation can be considered only as a secondary reason for the softening. No visible necking was observed in the shank of the lowest bolt after test TE1. The appearance of the prying action was obvious, as can be deduced from the strongly deformed shapes of the end plates, i.e., the end plates were forced into contact at the corners by the bolts in spite of the largely increased opening between the end plates. Failure mode was clearly mode I (plate yielding).

In test TE2 ($t_{pn}$=15 mm), the specimen collapsed when the load of the jack was 250 kN ($M$= 62.5 kNm). Deformation (yielding) of the end plates was strong but not quite as advanced as in test TE1 (Figures 5 and 6), and no cracks were observed. The lowest bolt was bent and a slight necking had occurred (difficult to measure because of threads). Anyway, failure mode I (flange yielding) with prying action

prevailed because of the clear plastic deformations of the end plates (it is easy to imagine the yield mechanism in Figure 6). Therefore, the deformation of the lowest bolt must have played a secondary role in the failure. In tests TE2, end plate thickness was approximately the same as the heights of the bolt head and nut. Thus, the end plate can wrench the bolt head and the nut more efficiently than, for example, in test TE1 with a thinner endplate. Furthermore, the influence of the size of the distribution area of loading (i.e., area under the washer) is, obviously, not as important as in the case of a more flexible end plate in relation to the bolt.

Test TE3 ($t_{pn}$= 20 mm) was aborted by the testers when the slope of the force-displacement curve became almost horizontal. At that moment, the load of the jack was 396 kN ($M$ = 99.0 kNm). The softening of the response was partly due to the propagation of yielding of the end plates and partly caused by the deformations of the bolts under combined tension and bending (Figure 7). The necking of the shank of the lowest bolt was obvious. Comparison of the photographs in Figures 5 to 7 shows that the deformations of the end plates in tests TE1 and TE2 with thinner plates were clearly larger than in test TE3 with the 20 mm thick end plate. The contact area was clearly concentrated near the corners of the end plates which pried the bolts quite efficiently. The yield lines appearing near the bolts in mode I failure, cannot be detected in the end plates of test TE3 (where the only formed yield lines pass through near the tube corner). Here we are, obviously, dealing with failure mode II, i.e., the plate and bolt yield at the same time as the prying effect occurs.



Figure 5. Strongly deformed end plates after test TE1 ($t_{pn}$=10 mm).



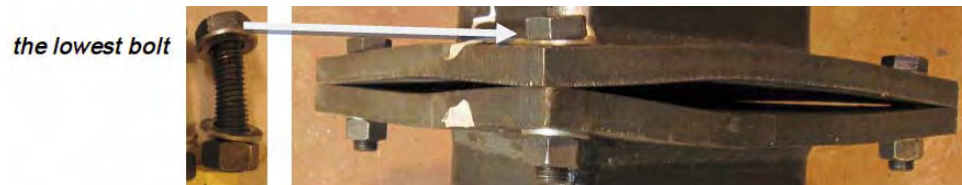Figure 6. Deformations after test TE2 ($t_{pn}$=15 mm), slight necking of the bolt.



Figure 7. Deformations after test TE3 ($t_{pn}$=20 mm), clear necking of the bolt.

The observations made during the tests on end plate joints under biaxial bending were quite similar to those that can be made in the case of in-plane (strong axis) bending tests. The analogy between these cases is clear.

## 4. RAKE

The component method, as introduced in European Standard EN1993-1-8, is the starting point of the model used next in the analysis of the end plate joints under biaxial bending. Outside the application area of the standard are 1) the bending in inclined direction and 2) the lack of a proper equivalent T-stub needed with the bolts at the corners of the end plate. The enlargement due to the out-of-plane bending is achieved by replacing the joint with the 3D mechanical model called the rake model or simply the rake (Heinisuo et al, 2009). First, the general nature of the rake is described. Figure 8 illustrates a simple model with a rigid plane supported by four springs. Individual spring in the rake can only transfer compression or tension to the foundation. Besides axial force (N), the system can also carry biaxial bending (Mx, My) as a whole. An equivalent model can be built up by connecting the springs with rigid links, as shown in figure 8 on the right. Then the model is like a rake with springs at the ends of the dents. As part of the structural model, the centre of the dents can be assumed to be the point shared by the joint and the connected member. The lengths of the springs in the model are immaterial, i.e., the stiffness and resistance of the springs can be defined without dimensions. The rake model can be, for example, interpreted as 0-dimensional when integrated into a system with one-dimensional elements (space frame with beams), which are connected at the intersection points of their system lines (e.g. the lines associated with centres of torsion). The rake is a 3D discrete model in its character. To be stable, the rake (or rather the plane of the rigid links) must have at least three support points, which are not aligned on a same straight line. The influence of this on the resistance values estimated by the rake is conservative.
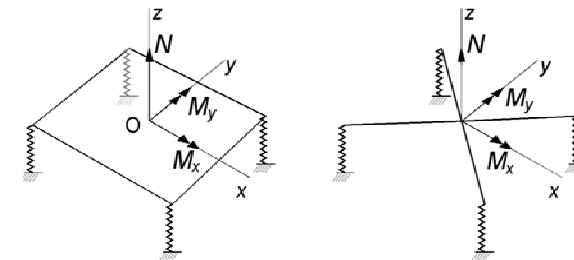


Figure 8. Rake model.

A 3D joint model can be generated by embedding the components of the component method presented in EN1993-1-8 in the rake. In principle, the rake model should be built up in such a way that the solution achieved by it under strong axis bending coincides with the solution offered by the standard. In the following, this process is outlined in the case of joints **A**–**C** associated with the tests.

### 4.1. Tension and compression components, assembly

The tension component associated with "*the end plate in bending accompanied with the corner bolt*" is considered. The corner bolt and the end plate in bending work together as a series-connected system. Their positions are the same as the locations of the bolts (Figure 10). The weaker link in the series determines the resistance of the whole component. The stiffness and resistance of the bolts themselves are the same as presented in EN1993-1-8. By contrast, the properties of the other

www.steelconstruct.com

part in series (plate in bending) are not defined by the standard. An appropriate yield mechanism can be used in determining its resistance. The exploited yield patterns and a systematic way to derive the associated resistances (upper limit load) are presented in (Heinisuo et al, 2012). Corner mechanisms 8 to 10 associated with prying forces are presented in Figure 9. In those, each yield line going through the bolt hole to the edge of the end plate is always parallel to the corresponding yield line going through the tube corner to the edge of the end plate. In theory, these mechanisms give upper limits for the resistances of the components with corner bolts. The possible occurrence of a prying force can be concluded based on the instructions of Standard EN1993-1-8. Methods based on yield mechanisms are not usable when the stiffness of a (corner) plate is analysed. The stiffness approximation used for the tension components will be discussed below in Section 4.

The compression components are associated with the contact areas between the end plates on the compressed side of the joint under bending. The potential compression components are positioned according to the tube profile, i.e., their positions follow the centreline of the profile, as shown in Figure 10. This presumption holds the better, the more flexible (thinner) the end plates are. Three components are used for both the short and long sides of the rectangular tube. This is a practical choice based on the aim to keep the model as simple as possible. The justification for this division of the compression components is studied as a part of ongoing research but is not discussed in this paper. The resistance of the (compressed) tube (wall) may, in principle, restrict the resistance on the joint. This is not the case with joints **A**–**C**. The stiffness of the compression components will be discussed bellow in Section 4.
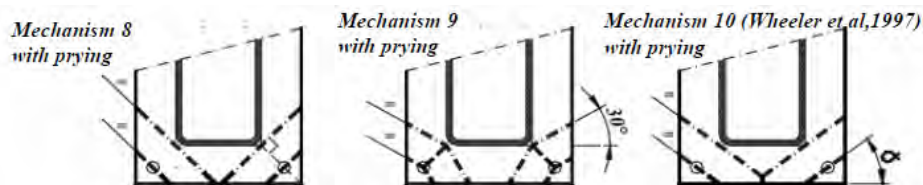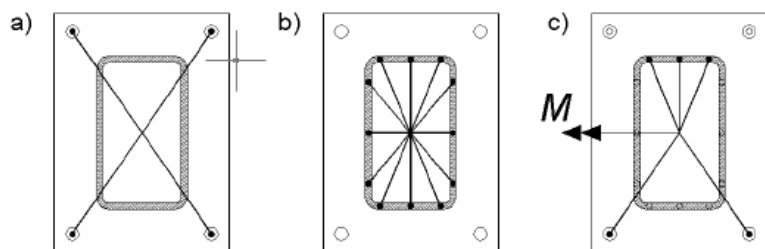


Figure 9. Corner mechanisms (Heinisuo et al, 2011).



Figure 10. Potential a) tension and b) compression components. c) Active components with the rigid links of a joint under strong axis bending.

The rake can be assembled when the potential compression and tension components have been identified, i.e., after their positions and properties have been determined. The centre of the rake is set to the centre of symmetry of the joint (i.e., on the extended axis of the torsional centres of the rectangular tubes). Then the (potential) components are connected by rigid links. When the model is strained by bending in an arbitrary direction, the active components balance the imposed

moment. The tension components are active only in tension and, correspondingly, compressive components are active only if compressed. The stiffness and resistance of a whole joint can be estimated by the rake on condition that the properties of the components are properly selected. For example, if the aim is to determine the resistance of the rake, the resistances of the predominant components must, in principle, have finite values. The properties of the rake are dependent on the number and position of the components, too.

### 4.2. Moment-moment interaction of joints A-C

End plate joints **A**–**C** with corner bolts and three different end plate thicknesses ($t_{pn}$ = 10, 15 and 20 mm) under arbitrarily inclined bending are analysed by the rake. These three joints are associated with a total of five conducted tests as explained in section 3.1 (**A**: TE1, TE7, **B**: TE2, **C**: TE3, TE8). The rotational resistances were estimated using the actual geometrical dimensions and material properties of the joints (section 2).

The initially vertical point load **P** (|**P**| = P) is supposed to act at mid span of the splice beam in such a way that its line of action goes through the centre of symmetry of the joint (and tubes) as shown in Figure 11. The angle between the weak axis direction and the line of action of load **P** is denoted by α. Then the direction of the resultant moment vector **M**$_R$ is indicated by the same angle α with respect to the strong axis direction. The absolute value of the resultant moment $M_R$ can be expressed by the components $M_y$ and $M_x$ associated with weak and strong axis bending, respectively, as

$$|\boldsymbol{M}_R| = M_R = M_x^2 + M_y^2 . \qquad (4)$$
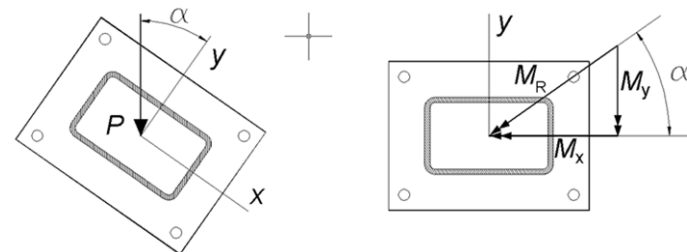


Figure 11. Load **P** and associated bending moment **M**$_R$ in the joint.

The tension component is the predominant component for joint response in all the cases considered here. Corner mechanism 8 with prying (Figure 9) gives the minimum resistances amongst all yield mechanisms in question. Otherwise the resistances were determined as far as possible in accordance with Table 6.2 of EN1993-1-8. The resistance values of equivalent T-stubs (defined here per bolt) are given in Table 6. For joints **A** and **B** ($t_{pn}$=10 or 15 mm), mode I (=complete yielding of the flange) gives the lowest resistance values, whereas the lowest resistance value for joint **C** with the thickest end plate ($t_{pn}$=20 mm) is given by mode II (= bolt failure with yield of the flange). According to the standard, "the possible modes of failure of the flange of an equivalent T-stub may be assumed to be similar to those expected to occur in the basic component that it represents". These modes are compatible with the observations made during tests TE1–TE3 (Figures 5 to 8). However, for joint **B**, the minimum resistance values given by mode I (method 2) and by mode II are quite close (dashed box in Table 6). If the plate thickness were

15.1 mm, these modes could give equal minimum resistances. In general, the resistance formula used with method 2 is more relevant with the thinner end plates. Based on partly intuitional reasoning, method 1 should be used with joint **B** whose associated failure mode is near the borderline between mode I (method 2) and mode II. This is compatible with the observations made during test TE2 whose failure mode was clearly consistent with mode I (flange yields completely under prying). The resistance values exploited in the rake in bold in Table 6.

Table 6. Resistances of tension components.

| Joint and its orientation | | Resistances $F_{tRd}$ [kN] | | |
|---|---|---|---|---|
| | | A (TE1,TE7) $t_{pn}$ = 10 mm | B (TE2) $t_{pn}$ = 15 mm | C (TE3,TE8) $t_{pn}$ = 20 mm |
| mode I | method 1 | 61.8 | **109** | 186 |
| | method 2 | **77.5** | 137 | 233 |
| mode II | | 125 | 138 | **160** |
| mode III | | 250 | 250 | 250 |

After the assembly of the rake, the rotational resistances of the considered joints could be determined for arbitrarily inclined bending moment. The results are presented in Figure 12 as moment-moment interaction curves ($M_x$–$M_y$) for joints **A**–**C**. Calculations were done only for selected values of angle $\alpha$ belonging to the first quarter of the coordinate system ($\alpha$=0°, 10°, 20°,...,´90°). Based on the double symmetry of the joint, the interaction curves were extended to other quarters.

In the moment-moment interaction curve, the distance from origin (4) gives the resistance value ($M_{Rd,\alpha}$) of resultant bending moment in the arbitrary direction. The shapes of the interaction curves are elongated. Ratio $M_S/M_W$ between resistances in strong axis bending ($\alpha$ = 90°) and in weak axis bending ($\alpha$ = 0°) is about 1.5 for all joints **A**–**C**. For comparison, the $M_x$-$M_y$ curves determined by method 1 for joint **A** and by method 2 for joint **B** are also drawn in Figure 12 as dashed lines. The test points are indicated by red circles. Calculated resistance values of $M_{Rd,\alpha}$ are given in Table 7 (decisive resultant value in bold). Ratio $M_{Rd,\alpha}/M_{test}$ is given in the lowest row of the table. They indicate that resistances can be evaluated quite well. In every case, ratio $M_{Rd,\alpha}/M_{test}$ is, roughly appropriate (=on the same level) compared to typical approximations achieved by the component method in strong axis bending cases. However, the selection of method 1 or 2 associated with the mode I is not a foregone conclusion. This can be investigated, for example, by parametric study based on FE simulations.

Table 7. Resistances estimated by the rake (decisive values in bold)

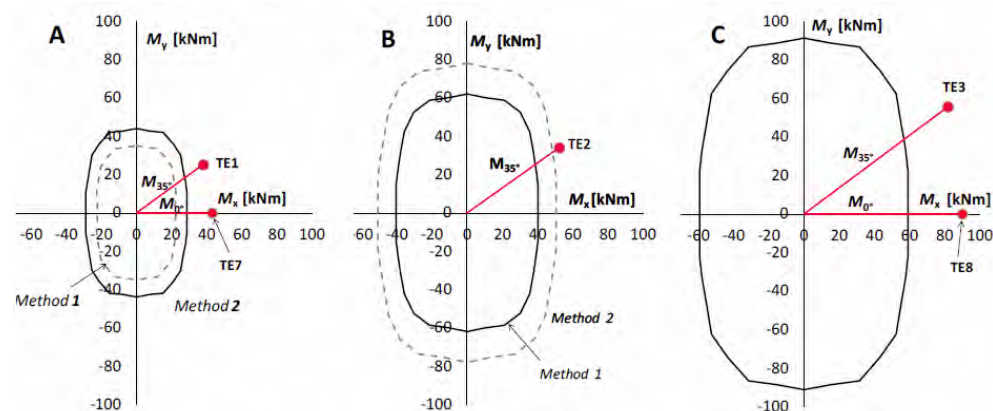| Joint and its orientation | | Resistances $M_{Rd,\alpha}$ [kNm] | | | | |
|---|---|---|---|---|---|---|
| | | A: $t_{pn}$ = 10 mm | | B: $t_{pn}$ = 15 mm | C: $t_{pn}$ = 20 mm | |
| | | 0° (TE7) | 35° (TE1) | 35° (TE2) | 0° (TE8) | 35° (TE3) |
| mode I | method 1 | 22.9 | 26.7 | **47.0** | — | — |
| | method 2 | **28.8** | **33.5** | 59.1 | — | — |
| mode II | | — | — | — | **59.3** | **69.3** |
| $M_{Rd,\alpha}/M_{test}$ = | | 0.73 | 0.67 | 0.75 | 0.66 | 0.70 |



Figure 12. $M_x$-$M_y$ interaction curves of joints **A**–**C**.

In addition to resistance, also (initial) stiffness can be estimated by a rake. The active components determine the rotational stiffness of a joint. The compression components of joints **A**–**C** are very stiff compared to their tension components. The selected stiffness of the compression component was $10^3$ times the stiffness of the tension component. Larger multipliers (from $10^4$ to $10^{6)}$ were tried out, too, but their influence on the solution was negligible and, moreover, caused some numerical problems. There are no formulas to evaluate the stiffness (or the resistance) of the tension components associated with corner bolts in EN1993-1-8. As a first approximation, the formulas given for normally positioned bolts in the standard were exploited (Table 6.11 of EN1993-1-8) with the difference that the equivalent length $l_{eff}$ at issue was replaced by the value determined for the corner mechanism. This procedure, however, produces clearly too high calculated rotational stiffness values for all joints. This can be seen from Table 8 in the case of tests TE1–TE3, TE7 and TE8. The low accuracy of the estimates stands out especially with the thicker end plates when ratio $S_{ini,\alpha}/S_{ini,test}$ has far too high values.

Table 8. Rotational stiffnesses of joints.

| Joint and its orientation | Stiffnesses $S_{ini,\alpha}$ [kNm/mrad] | | | | |
|---|---|---|---|---|---|
| | A: $t_{pn}$ = 10 mm | | B: $t_{pn}$ = 15 mm | C: $t_{pn}$ = 20 mm | |
| | 0°(TE7) | 35°(TE1) | 35°(TE2) | 0°(TE8) | 35°(TE3) |
| mode I | 11.7 | 14.9 | 32 | — | — |
| mode II | — | — | — | 43.1 | 55.9 |
| $S_{ini,\alpha}/S_{ini,test}$ = | 4.0 | 5.5 | 7.0 | 9.6 | 13.6 |

## 5. CONCLUSIONS

The rotational resistances and stiffnesses of the three joints **A**–**C** were analysed by a 3D mechanical model called the rake model. The method represents an enlargement of the component method presented in standard EN1993-1-8. The motive for conducting the tests described in this article (and the larger series of tests they

belong) was to develop the 3D model. The research is still going on (2012) and only preliminary results were presented.

Based on these few examples it appears that the component method integrated with the principles of plasticity theory (limit state analysis based on plastic mechanisms) for bolted end plate joints could be applied easily to the 3D analysis of end plate joints. On the other hand, the poor quality of the estimates of initial stiffness is obvious. The main reason for this is that an end plate in bending accompanied by a corner bolt is much more flexible than an end plate in bending with normally positioned bolts, (test TE11 compared to the others, section 3.3). The used stiffness formulas found from the standard are based on the analogy between flange behaviour and one-dimensional beam analysis (i.e. their applicabilty is limited only to "normally positioned" bolts). The stiffness estimates for flanges with corner bolts definitely need to be derived separately. Because of the (unavoidable!) two-dimensional character of the flange bending problem with the corner bolts, more appropriate analytical formulas are, however, cumbersome to formulate. Perhaps, a more attractive approach is to determine proper multipliers for "associated one dimensional formulas" by the aid of numerical analysis (FEA) supported by tests.

Numerical analysis plays an important role in addition to the experimental study in the ongoing research of 3D modelling of end plate joints. Numerical analysis makes it possible to investigate issues difficult to reach by tests only. Parametric considerations are especially valuable there. Numerical analysis methods usually offer a more economical way to study complicated structural problems than experimental ones.

## 6. CLOSING REMARKS

There is an obvious lack of experimental research on bolted (end plate) joints under 3D loading conditions, including joints under biaxial bending. Many more tests will be needed before the enough comprehensive verification data for the validation process of the 3D component method is available. Besides the joint types considered in this paper, many other types under different loading conditions will also need a similar experimental basis for their own validation processes. The presence of an axial normal force in addition to (biaxial) bending would, for example, give important information on the behaviour of joints for the practical design. In addition to Except 3D joint tests at room temperature, tests in fire conditions are also needed.

## REFERENCES

[1] Celikag, M., Kirby, P.A. (1998), Out-of-plane moment rotation response for common joints. International Colloquium, Bolted and special structural connectors, USSR, Moscow, May 15-20, 1998, pp. 136-142.

[2] EN 1993-1-8 (2005). Eurocode 3: Design of steel structures, Part 1-8: Design of joints, CEN, Brussels.

[3] Heinisuo, M., Laine, V., Lehtimäki, E. (2009), Enlargement of the component method into 3D, Proceedings: Nordic Steel Constructional Conference 2009, Malmö, Sweden, September 2-4, 2009, pp. 430-437.

[4] Heinisuo M., Ronni H., Perttola H., Aalto A., Tiainen T. (2012), End plate and base plate joints with corner bolts for rectangular tubular member, Journal of Constructional Steel Research, Vol. 75, pp. 85-92.

[5] Lee, D-Y., Goel, S., Stojadinovich, B. (2008), Exposed Column-Base Plate Connections Bending About Weak Axis: II. Experimental Study, Steel Structures, Vol. 8, pp. 29-42.

[6] Perttola H., Heinisuo, M. (2011), Test Report, End Plate Joints of Steel Tubes, Biaxial and Weak Axis Bending Tests, Research Report 155, Tampere University of Technology, Department of Civil Engineering, Structural Engineering.

[7] Ronni, H., Heinisuo, M. 2011, Test Report, End Plate Joints of Steel Tubes, Biaxial Bending Tests in Fire, Research Report 156, Tampere University of Technology, Department of Civil Engineering, Structural Engineering.

[8] Ronni, H., Heinisuo, M. (2010). Test Report, End Plate Joints of Steel Tubes, Strong Axis Bending, Research Report 149, Tampere University of Technology, Department of Civil Engineering, Structural Engineering.

[9] Wheeler, A, Clarke, M, Hancock, G, (1997a), Bending Tests of Bolted End Plate Connections in Cold Formed Rectangular Hollow Sections, Research Report No. R736, University of Sydney, Department of Civil Engineering, Centre of Advanced Structural Engineering.

[10] Wheeler, A, Clarke, M, Hancock, G, Murray T M (1997b), Design Model for Bolted Moment End Plate Connection using Rectangular Hollow Sections, Research Report No. R745, University of Sydney, Department of Civil Engineering, Centre of Advanced Structural Engineering.

# WELD DESIGN AND FABRICATION
# FOR RHS CONNECTIONS

**Matthew R. McFadden and Min Sun**
Research Assistants, Department of Civil Engineering,
University of Toronto, Canada
matthew.mcfadden@mail.utoronto.ca and min.sun@utoronto.ca

**Jeffrey A. Packer**
Bahen/ Tanenbaum Professor of Civil Engineering, University of Toronto, Canada
jeffrey.packer@utoronto.ca

## ABSTRACT

The 2010 AISC *Specification for Structural Steel Buildings* has expanded the scope in Chapter K: *Design of HSS and Box Member Connections* to include a Section K4: *Welds of Plates and Branches to Rectangular HSS*. This paper discusses the historical development of the effective weld properties and analyses the structural reliability of the provisions contained therein. Additionally there is a discussion on recent changes in the U.S. and Canadian specifications/codes with regard to the limit states for fillet weld design and the acceptance/ rejection of the (1.00 + 0.50 $\sin^{1.5}\theta$) term. Finally, the details of an experimental research programme being performed at the University of Toronto, in collaboration with AISC to determine the weld effective length in RHS T-connections under branch in-plane bending moments, are discussed. In conclusion, it is found that the inclusion of the (1.00 + 0.50 $\sin^{1.5}\theta$) term for RHS gapped K- connections and T- and X- connections, based on the limit state of shear failure along the effective throat of the weld, may be unsafe for fillet weld design when used in conjunction with the current weld effective length rules.

## 1. INTRODUCTION

With welded connections between rectangular hollow sections (RHS) there are currently two design methods that can be used for weld design (Packer et al., 2010):

(i) The welds may be proportioned to develop the yield strength of the connected branch wall at all locations around the branch. This approach may be appropriate if there is low confidence in the design forces, uncertainty regarding method (ii) or if plastic stress-redistribution is required in the connection. This method will produce an upper limit on the required weld size and may be excessively conservative in some situations.

(ii) The welds may be designed as "fit-for-purpose", and proportioned to resist the applied forces in the branch. The non-uniform loading around the weld perimeter due to the relative flexibility of the connecting RHS face requires the use of effective weld lengths. This approach may be appropriate when there is high confidence

in the design forces or if the branch forces are particularly low relative to the branch member capacity. When applicable, this approach may result in smaller weld sizes providing a more economical design with increased aesthetic value.

The primary focus of this paper is method (ii), but it is interesting to compare the results of method (i) for the design of fillet welds in various steel specifications/ codes (see Table 1). Clearly there is quite a disparity.

Table 1. Comparison of fillet weld effective throats to develop the yield resistance of the connected branch member wall in Figure 1(a)

| Specification or Code | $t_w$ |
|---|---|
| ANSI/AISC 360-10 Table J2.5 | $1.43t_b$ |
| AWS D1.1/D1.1M: 2010 Clause 2.25.1.3 and Fig. 3.2 | $1.07t_b$ |
| CSA S16-09 Clause 13.13.2.2 | $0.95t_b$ |
| CAN/CSA S16-01 Clause 13.13.2.2 | $1.14t_b$ |
| CEN (2005) or IIW (2012) | $1.10t_b$ |

Fillet welds, being the least expensive and easiest weld type, are the preferred and most common weld type for hollow section connections. The design of fillet welds in structural steel buildings in the U.S. is governed by Table J2.5 of the AISC *Specification* and is based on the limit state of shear failure along the effective throat using a matching (or under-matching) filler metal. For a simple 90° RHS T-connection under branch axial tension (see Figure 1(a)) the LRFD strength of a single weld is given by:

$$\emptyset R_n = \emptyset F_{nw} A_{we} = (0.75)(0.60 F_{EXX})(D/\sqrt{2})(l_w)$$

The design of fillet welds in Canada is governed by CSA S16-09 Clause 13.13.2.2 and, although different coefficients are used, an identical resistance is obtained. The prior edition, CAN/CSA S16-01, included an additional check for shearing of the base metal at the edge of a fillet weld along the fusion face (see Figure 1(b)), which frequently governed and thus resulted in generally larger weld sizes. However, the current fillet weld design requirements for both AISC 360-10 and CSA S16-09 are based solely on the limit state of shear failure along the effective throat.
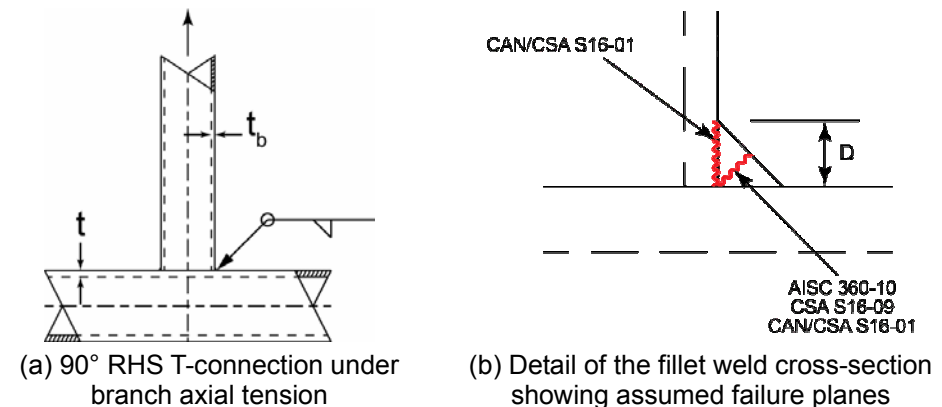


(a) 90° RHS T-connection under branch axial tension

(b) Detail of the fillet weld cross-section showing assumed failure planes

Figure 1. Comparison of fillet weld limit state design checks

## 2. HISTORICAL TREATMENT OF WELD DESIGN FOR RHS CONNECTIONS

In 1981 Subcommission XV-E of the International Institute of Welding (IIW) produced their first design recommendations for statically-loaded RHS connections, which were updated and revised with a second edition later that decade (IIW, 1989). These recommendations are still the basis for nearly all current design rules around the world dealing with statically-loaded connections in onshore RHS structures, including those in Europe (CEN, 2005), Canada (Packer and Henderson, 1997) and the U.S. (AISC, 2010).

Research at the University of Toronto (Frater and Packer, 1992a, 1992b) on fillet-welded RHS branches in large-scale Warren trusses with gapped K-connections showed that fillet welds in that context can be proportioned on the basis of the loads in the branches, thus resulting in relatively smaller weld sizes compared to IIW (1989). It was concluded simplistically that the welds along all four sides of the RHS branch could be taken as fully effective when the chord-to-branch angle is 50° or less, but that the weld along the heel should be considered as completely ineffective when the angle is 60° or more. A linear interpolation was recommended when the chord-to-branch angle is between 50° and 60°. Based on this research, the formulae for the effective length of branch member welds in planar, gapped, RHS K- and N-connections, subject to predominantly static axial load, were taken in Packer and Henderson (1992) as:

When θ ≤ 50°: 
$$L_e = \frac{2H_b}{\sin\theta} + 2B_b \qquad (1a)$$

When θ ≥ 60°: 
$$L_e = \frac{2H_b}{\sin\theta} + B_b \qquad (1b)$$

In a further study by Packer and Cassidy (1995), by means of 16 large-scale connection tests which were designed to be weld-critical, new weld effective length formulae for T-, Y- and Cross- (or X-) connections were developed. It was found that more of the weld perimeter was effective for lower branch member inclination angles for T-, Y- and Cross (or X-) connections. Thus, the formulae for the effective length of branch member welds in planar T-, Y- and Cross- (or X-) RHS connections, subjected to predominantly static axial load, were revised in Packer and Henderson (1997) to:

When θ ≤ 50°: 
$$L_e = \frac{2H_b}{\sin\theta} + B_b \qquad (2a)$$

When θ ≥ 60°: 
$$L_e = \frac{2H_b}{\sin\theta} \qquad (2b)$$

A linear interpolation was recommended between 50° and 60°.

The latest (third) edition of the IIW recommendations (2012) requires that the design resistance of hollow section connections be based on failure modes that do not include weld failure, with the latter being avoided by satisfying either of the following criteria:

(i) Welds are to be proportioned to be "fit for purpose" and to resist forces in the connected members, taking account of connection deformation/rotation capacity and considering weld effective lengths, or

(ii) Welds are to be proportioned to achieve the capacity of the connected member walls.

This IIW (2012) document thus specifically acknowledges the effective length concept for weld design.

## 3. 2010 AISC SPECIFICATION, SECTION K4 WELD DESIGN PROCEDURES

In Section K4 of the AISC *Specification* (AISC, 2010) a detailed design method considering effective weld properties for various RHS connection types is given.

- **For T-, Y- and Cross- (or X-) connections under branch axial load or bending**

Effective weld properties are given by:

$$L_e = \frac{2H_b}{\sin\theta} + 2b_{eoi} \qquad (3)$$

$$S_{ip} = \frac{t_w}{3}\left(\frac{H_b}{\sin\theta}\right)^2 + t_w b_{eoi}\left(\frac{H_b}{\sin\theta}\right) \qquad (4)$$

$$S_{op} = t_w\left(\frac{H_b}{\sin\theta}\right)B_b + \frac{t_w}{3}\left(B_b^2\right) - \frac{t_w/3\left(B_b - b_{eoi}\right)^3}{B_b} \qquad (5)$$

$$b_{eoi} = \frac{10}{B/t}\left(\frac{F_y t}{F_{yb} t_b}\right)B_b \leq B_b \qquad (6)$$

When β > 0.85 or θ > 50°, $b_{eoi}$/2 shall not exceed 2$t$. This limitation represents additional engineering judgement.

In contrast to Equations 2a and 2b, the weld effective length in Equation 3 was – for consistency – made equivalent to the branch wall effective lengths used in Section K2.3 of the AISC *Specification* for the limit state of local yielding of the branch(es) due to uneven load distribution, which in turn is based on IIW (1989). The effective width of the weld transverse to the chord, $b_{eoi}$, is illustrated in Figure 2(b). This term, $b_{eoi}$, was empirically derived on the basis of laboratory tests in the 1970s and 1980s (Davies and Packer, 1982). The effective elastic section modulus of welds for in-plane bending and out-of-plane bending, $S_{ip}$ and $S_{op}$ respectively (Equations 4 and 5), apply in the presence of the bending moments, $M_{ip}$ and $M_{op}$ as shown in Figure 2(b).

While being based on informed knowledge of general RHS connection behaviour, Equations 4 and 5 have not been substantiated by tests, and therefore are purely speculative.
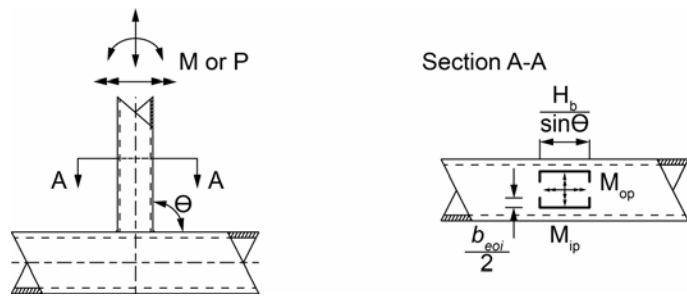
(a) Various load cases      (b) Weld effective length dimensions

Figure 2. Weld effective length terminology for T-, Y- and Cross- (or X-) connections under branch axial load or bending

- **For Gapped K- and N-Connections under Branch Axial Load**

    Effective weld lengths are given by:

    When $\theta \leq 50°$:  $L_e = \dfrac{2(H_b - 1.2t_b)}{\sin\theta} + 2(B_b - 1.2t_b)$  (7a)

    When $\theta \geq 60°$:  $L_e = \dfrac{2(H_b - 1.2t_b)}{\sin\theta} + (B_b - 1.2t_b)$  (7b)

When $50° < \theta < 60°$ a linear interpolation is to be used to determine $L_e$.

    Equations 7a and 7b are similar to Equations 1a and 1b but the former incorporate a reduction to allow for a typical RHS corner radius. The simplified nature of these effective length formulae (Equations 7a and 7b) was preferred, for gapped K- and N-connections, to the more complex ones that would result if the branch effective widths of the RHS walls in the AISC *Specification* Section K2.3 were adopted. Weld effective length provisions for overlapped RHS K- and N-connections were also provided in the AISC *Specification* Section K4 (AISC, 2010), based on branch effective widths of the RHS walls in Section K2.3, however in this case no research data on weld-critical overlapped RHS K- and N-connections was available.

    The available strength of branch welds is determined, allowing for non-uniformity of load transfer along the line of weld, as follows by AISC (2010):

$$R_n \text{ or } P_n = F_{nw} t_w L_e \quad (8)$$

$$M_{n-ip} = F_{nw} S_{ip} \quad (9)$$

$$M_{n-op} = F_{nw} S_{op} \quad (10)$$

where,

$$F_{nw} = 0.60 F_{EXX} \quad (11)$$

## 4. EVALUATION OF AISC 2010 SPECIFICATION WITH EXPERIMENTS ON RHS WELDS UNDER PREDOMINANTLY AXIAL LOADS

    Two large-scale, 39.4-ft (12.0-m) and 40.0-ft (12.2-m) span, simply supported, fillet-welded, RHS Warren trusses, comprised of 60° gapped and overlapped K-connections,

were tested by Frater and Packer (1992a, 1992b). Quasi-static loading was performed in a carefully controlled manner to produce sequential failure of the tension-loaded, fillet-welded connections (rather than connection failures). In addition, a series of weld-critical tests have been performed by Packer and Cassidy (1995) on four T-connections and 12 X-connections, with the branches loaded in quasi-static, axial tension. The effective leg sizes of the welds, measured along the branch member and chord member respectively, plus the throat sizes, were recorded. Measured geometric and mechanical properties of these trusses and welds and the failure loads of all welded connections are subsequently used herein to evaluate nominal weld strengths and predicted weld design strengths according to the AISC *Specification* with weld failure as the only limit state.
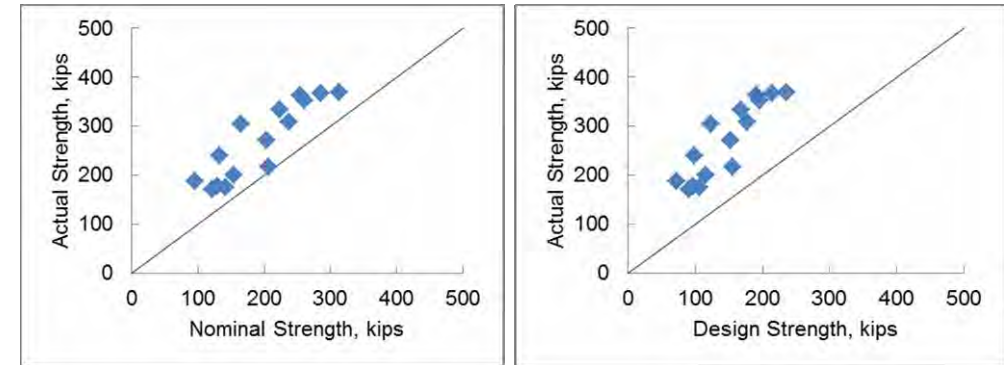


(a) Actual strength vs. Predicted nominal strength ($R_n$)    (b) Actual strength vs. Predicted LRFD strength ($0.75R_n$)

Figure 3. Correlation with test results for gapped K-connections without the inclusion of the $(1.00 + 0.50 \sin^{1.5}\theta)$ term
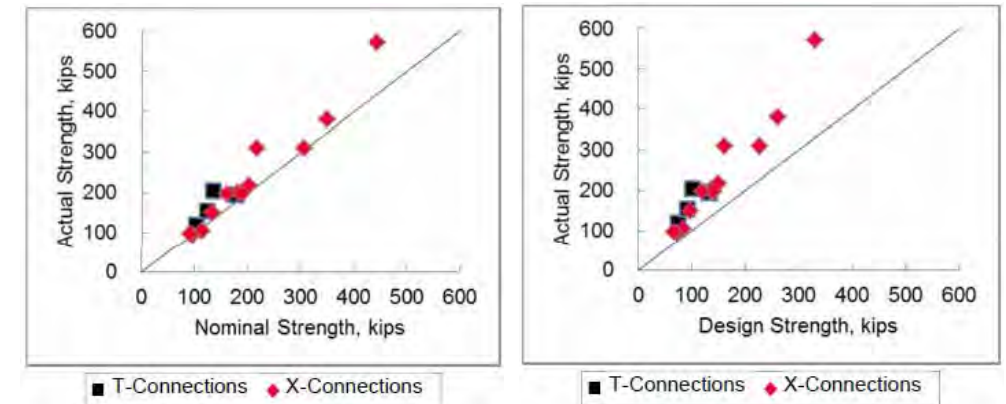


(a) Actual strength vs. Predicted nominal strength ($R_n$)    (b) Actual strength vs. Predicted LRFD strength ($0.75R_n$)

Figure 4. Correlation with test results for T- and X-connections without inclusion of the $(1.00 + 0.5 \sin^{1.5}\theta)$ term

Table J2.5, Section J4 (AISC, 2010) and Equations 3, 6, 7 and 8 were used to calculate the nominal strengths (excluding the resistance factor) of the 31 welded connections tested by Frater and Packer (1992a, 1992b) and Packer and Cassidy (1995). The predicted strength of each welded connection, without a fillet weld directional strength increase of [1.00 + 0.50 sin$^{1.5}$θ] (discussed in the following section), was determined by the summation of the individual weld element strengths along the four walls around the branch footprint and is given as a predicted nominal strength, $R_n$.

In order to assess whether adequate, or excessive, safety margins are inherent in the correlations shown in Figures 3a and 4a, one can check to ensure that a minimum safety index of β+ = 4.0 (as currently adopted by AISC per Chapter B of the Specification Commentary) is achieved, using a simplified reliability analysis in which the resistance factor Φ is given by Equation 12 (Fisher et al., 1978); (Ravindra and Galambos, 1978).

$$\Phi = m_R \exp(-\alpha\beta^+ COV) \qquad (12)$$

where $m_R$ = mean of the ratio: (actual element strength)/(nominal element strength = $R_n$); COV = associated coefficient of variation of this ratio; and α = coefficient of separation taken to be 0.55 (Ravindra and Galambos, 1978). Equation 12 neglects variations in material properties, geometric parameters and fabrication effects, relying solely on the so-called "professional factor". In the absence of reliable statistical data related to welds this is believed to be a conservative approach. Application of Equation 12 produced Φ = 0.959 for welded connections in gapped K-connections and Φ = 0.855 for T- and X- (Cross-) connections. As both of these exceed Φ = 0.75 the effective weld length concepts advocated in Section K4 of the AISC *Specification* can, on the basis of the available experimental evidence, be deemed adequately conservative.

## 5. INTRODUCTION OF THE (1.00 + 0.50 sin$^{1.5}$θ) TERM

A debate about the application of an enhancement factor to the nominal strength of the weld metal (of 1.00 + 0.50 sin$^{1.5}$θ) for fillet welds loaded at an angle of θ degrees to the weld longitudinal axis in hollow section connections has recently emerged. In the U.S., the AISC does not permit the fillet weld directional strength increase whereas in Canada, the CSA and CISC do not explicitly disallow it, so designers use it. Adopting this enhancement factor leads to a greater calculated resistance for a fillet weld group in a RHS connection and hence much smaller weld sizes (as demonstrated in Table 1).

The correlation plots in Figures 3 and 4 have been recomputed with weld metal failure as the only limit state and the inclusion of the (1.00 + 0.5 sin$^{1.5}$θ) in Figures 5 and 6. If the (1.00 + 0.5 sin$^{1.5}$θ) term is taken into consideration in the analysis of the data presented in this paper, the statistical outcomes change to:

- For gapped K-connections: $m_R$ = 0.999, COV = 0.180 and Φ = 0.673 (using Equation 12 with β$^+$ = 4.0)
- For T- and X- (Cross-) connections: $m_R$ = 0.819, COV = 0.164 and Φ = 0.571 (using Equation 12 with β$^+$ = 4.0).

As both of these Φ-factors are below 0.75, the effective length formulae, with the (1.00 + 0.50sin1.5θ) term included, may be unsafe to use for fillet weld design.
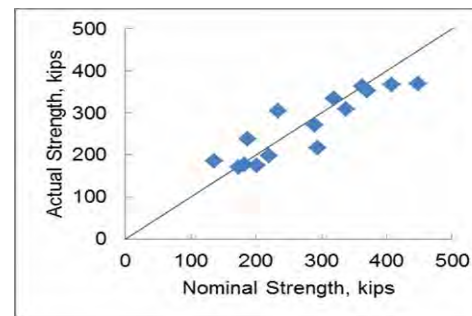


(a) Actual strength vs. Predicted nominal strength ($R_n$)
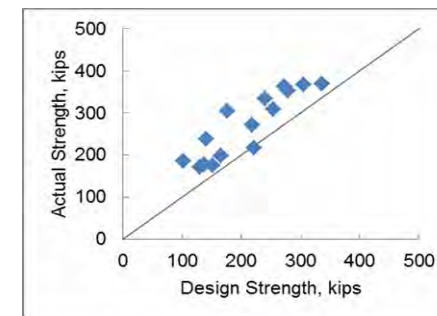
(b) Actual strength vs. Predicted LRFD design strength (0.75$R_n$)

Figure 5. Correlation with test results for gapped K-connections with inclusion of the (1.00 + 0.5 sin$^{1.5}$θ) term
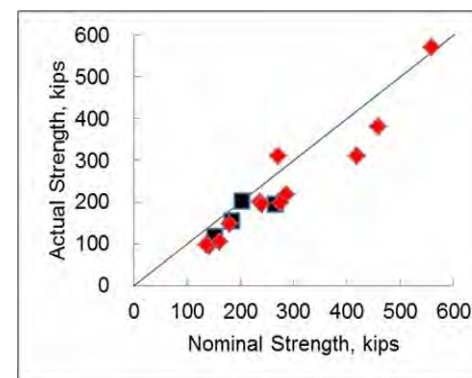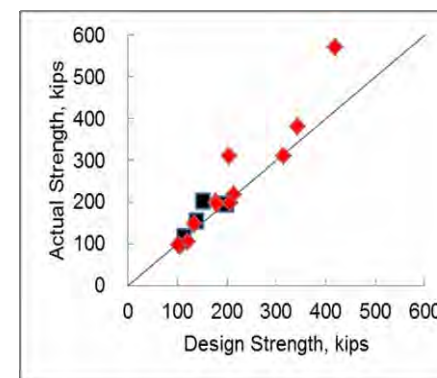


■ T-Connections ◆ X-Connections     ■ T-Connections ◆ X-Connections

(a) Actual strength vs. Predicted nominal strength ($R_n$)

(b) Actual strength vs. Predicted LRFD design strength (0.75$R_n$)

Figure 6. Correlation with test results for T- and X-connections with inclusion of the (1.00 + 0.5 sin$^{1.5}$θ) term

## 6. CURRENT RESEARCH ON RHS MOMENT CONNECTIONS

A further experimental study to determine the weld effective length in RHS T-connections subject to branch in-plane bending moments is being carried out at the University of Toronto. The test specimens have been designed such that they are weld-critical under the application of branch in-plane bending moments (weld failure to precede connection failure). The bending moment at the connection is induced by the application of a lateral point load to the end of the branch in a quasi-static manner until weld failure. Key parameters such as branch-to-chord width ratios (β-ratios) of 0.25, 0.50, 0.75 and 1.00 with chord wall slenderness values of 17, 23 and 34 are being investigated. In order to determine the effectiveness of the weld in

resisting the applied forces, the nonuniform distribution of normal strain and stress in the branch near the connection will be measured using strain gauges oriented along the longitudinal axis of the branch at numerous locations around the footprint. This will give a representative strain and stress distribution around the adjacent weld and hence the effectiveness of the weld can be determined. Based on the results of the experimental programme, the values postulated in Table K4.1 of the 2010 AISC *Specification* (AISC, 2010) will be verified or adjusted.

Fabrication of the specimens was performed at Lincoln Electric Co.'s Automation Division in Cleveland, Ohio. An experienced robotic welding technologist controlled a Fanuc Robot Arc-Mate 120iC 10L, adapted to perform the gas metal arc welding process with spray metal transfer (GMAW-P), to weld the connections. For the experimental programme, robotic welding offers several advantages: improved weld quality, excellent weld/base-metal fusion and root penetration, continuous electrodes, consistent travel speeds and the capability of welding in all positions.
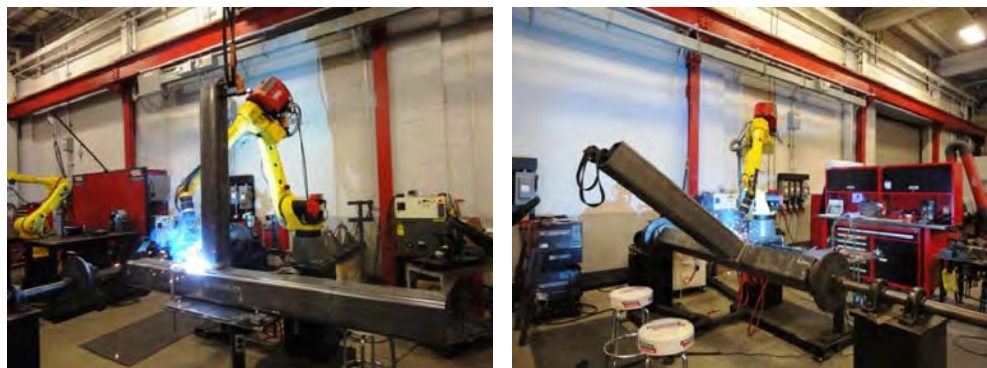


(a) Stepped box connections welded in the horizontal position

(b) Matched box connections welded in the flat position using coordinated motion

Figure 7. Automated welding of specimens at Lincoln Electric Co.

The welding process parameters used were as follows: 0.035" diameter AWS ER70S-6 MIG wire, 23 Volts, 375 ipm wire feed speed, 90% Ar - 10% $CO_2$ shielding gas mixture at 30 to 50 CFH, ¼" to ½" contact tube to work distance and varying travel speeds depending on the weld type and size. Stepped connections (β ≤ 0.85) were clamped to a level table and welded in the horizontal position as shown in Figure 7a. The matched connections (β > 0.85) were mounted to rotating chucks and welded in the flat position using coordinated motion, shown in Figure 7b, with fillet welds along the transverse branch walls and PJP flare-bevel-groove welds along the longitudinal branch walls.

The test specimens are at the University of Toronto Structural Testing Facilities undergoing full-scale testing. The test setup assembly, shown in Figure 8a, consists of pin and roller supports for the chord with a 77kip-capacity MTS Actuator mounted to a rigid steel frame and attached to a point load application device on the branch member. Figure 8b shows the typical observed failure mode of weld rupture due to shear failure along the weld effective throat



(a) Elevation view of the test setup assembly

(b) Shear failure along the weld effective throat

Figure 8. Full-scale testing at the University of Toronto

## 7. CONCLUSIONS

Design guides or specifications/codes requiring the welds to develop the yield capacity of the branch members produce an upper limit on the required weld size and may be excessively conservative in some situations. While this is considered to be a simplified design method for fillet welds, it is shown that there is quite a disparity for the required effective throat size to develop the branch wall yield capacity. Additionally, the current fillet weld design requirements for both AISC 360-10 and CSA S16-09 are based solely on the limit state of weld metal shear failure along the effective throat whereas previous versions (CSA S16-01) included an additional check for shearing of the base metal at the edge of a fillet weld along the fusion face, which frequently govered and resulted in generally larger weld sizes.

Alternate design methods that consider weld effective lengths have the potential to provide a relatively smaller weld size, thus achieving a more economical design with increased aesthetic value. By comparing the actual strengths of fillet-welded joints in weld-critical T-, X- (Cross-) and gapped K- connection specimens to their predicted nominal strengths and design strengths, it has been shown that the relevant effective length design formulae in the AISC *Specification* Section K4 (AISC, 2010) – without use of the $(1.00 + 0.50 \sin^{1.5}\theta)$ term for fillet welds – result in an appropriate weld design with an adequate safety level. Conversely, it is shown that the inclusion of the $(1.00 + 0.50 \sin^{1.5}\theta)$ term for such connections based solely on the limit state of weld failure along the effective throat of a fillet weld may be unsafe for design as it results in an inadequate reliability index.

A limitation of this study is that all test specimens were under predominantly axial loads in the branches. However, the weld effective length formulae for T-, Y- and X- (Cross-) connections in the AISC *Specification* Table K4.1 (AISC, 2010) also address branch bending. The available test data does not provide an opportunity to evaluate the accuracy of formulae applicable to branch bending loads and therefore the equations postulated are purely speculative. The objective of the research being performed at present at the University of Toronto is to verify or adjust these equations.

## ACKNOWLEDGEMENTS

## NOTATION

$A_{we}$ – effective (throat) area of the weld

$B$ – overall width of RHS chord member, measured 90 degrees to the plane of the connection

$B_b$ – overall width of RHS branch member, measured 90° to the plane of the connection

$D$ – weld leg size

$F_{EXX}$ – filler metal classification strength

$F_{nw}$ – nominal stress of the weld metal

$F_y$ – yield strength of the hollow section chord member material

$F_{yb}$ – yield strength of the hollow section branch member material

$H_b$ – overall height of RHS branch member, measured in the plane of the connection

$L_e$ – effective length of groove and fillet welds to RHS for weld strength calculations

$M_{ip}$ – in-plane bending moment

$M_{op}$ – out-of-plane bending moment

$M_{n\text{-}ip}$ – nominal weld resistance of in-plane bending moment

$M_{n\text{-}op}$ – nominal weld resistance of out-of-plane bending moment

$P_n$ – nominal strength of the welded joint

$R_n$ – nominal strength of the welded joint

$S_{ip}$ – weld effective elastic section modulus for in-plane bending

$S_{op}$ – weld effective elastic section modulus for out-of-plane bending

$b_{eoi}$ – effective width of the transverse branch face welded to the chord

$l_w$ – weld length

$m_R$ – mean of ratio: (actual element strength)/(nominal element strength) = professional factor

$t$ – design wall thickness of hollow section chord member

$t_b$ – design wall thickness of hollow section branch member

$t_w$ – effective weld throat thickness

$\alpha$ – separation factor = 0.55

$\beta$ – width ratio = the ratio of overall branch width to chord width for RHS connection

$\beta^+$ – safety (reliability) index for LRFD and Limit States Design

$\theta$ – acute angle between the branch and chord (degrees); angle of loading measured from a weld longitudinal axis for fillet weld strength calculation (degrees)

## REFERENCES

[1] ANSI/AISC 360-10:2010. Specification for structural steel buildings. American Institute of Steel Construction, Chicago, USA.

[2] AWS D1.1/D1.1M:2010. Structural welding code – steel, 22nd edition, American Welding Society, Miami, USA.

[3] CAN/CSA-S16-01:2001. Limit states design of steel structures, Canadian Standards Association, Toronto, Canada.

[4] CSA-S16-09:2009. Design of steel structures, Canadian Standards Association, Toronto, Canada.

[5] Davies, G., Packer, J.A. (1982), "Predicting the strength of branch plate–RHS connections for punching shear". *Canadian Journal of Civil Engineering* 9 (3), (pp. 458 – 467).

[6] EN 1993-1-1:2005(E). Eurocode 3: Design of steel structures, Part 1-1: General rules and rules for buildings, European Committee for Standardization, Brussels, Belgium.

[7] Fisher, J.W., Galambos, T.V., Kulak, G.L. and Ravindra, M.K. (1978), "Load and resistance factor design criteria for connectors". *Journal of the Structural Division* 104 (9), (pp. 1427 – 1441).

[8] Frater, G.S., Packer, J.A. (1992a), "Weldment design for RHS truss connections, I: Applications". *Journal of Structural Engineering* 118 (10) (pp. 2784 – 2803).

[9] Frater, G.S., Packer, J.A. (1992b), "Weldment design for RHS truss connections, II: Experimentation". *Journal of Structural Engineering* 118 (10) (pp. 2804 – 2820).

[10] IIW Doc. XV-701-89:1989. Design recommendations for hollow section joints – predominantly statically loaded, 2nd. edition, International Institute of Welding, Paris, France.

[11] IIW Doc. XV-1402-12:2012. Static design procedure for welded hollow section joints – recommendations, 3rd. edition, International Institute of Welding, Paris, France.

[12] Packer, J.A., Cassidy, C.E. (1995), "Effective weld length for HSS T, Y, and X connections". *Journal of Structural Engineering* 121 (10) (pp. 1402 – 1408).

[13] Packer, J.A., Henderson, J.E. (1992), Design guide for hollow structural section connections, 1st. edition. Canadian Institute of Steel Construction, Toronto, Canada.

[14] Packer, J.A., Henderson, J.E. (1997). Hollow structural section connections and trusses – a design guide, 2nd. edition. Canadian Institute of Steel Construction. Toronto, Canada.

[15] Packer, J.A., Sherman, D.R. and Lecce, M. (2010). Hollow structural section connections, AISC steel design guide no. 24. American Institute of Steel Construction. Chicago, USA.

[16] Ravindra, M.K., Galambos, T.V. (1978). "Load and resistance factor design for steel", *Journal of the Structural Division* 104 (9) (pp. 1337 – 1353).

# OVERVIEW OF TUBULAR JOINTS – EC3 X NEW CIDECT FORMULATIONS

Raphael Santos da Silva
*PGECIV – Post Graduate Program in Civil Engineering, UERJ, Brazil*
*raphaelsantos_rj@yahoo.com.br*

Luciano Rodrigues Ornelas de Lima, Pedro Colmar Gonçalves da Silva Vellasco,
José Guilherme Santos da Silva
*Structural Engineering Department, UERJ, Brazil*
*luciano@eng.uerj.br, vellasco@eng.uerj.br, jgss@eng.uerj.br*

Arlene Maria Sarmanho Freitas, Gabriel Vieira Nunes
*Civil Engineering Department, School of Mines, UFOP, Brazil*
*arlene@em.ufop.br, gvnunes@gmail.com*

## ABSTRACT

The intensive worldwide use of tubular structural elements, mainly due to its associated aesthetical and structural advantages, led designers to be focused on technologic and design issues. Consequently, their design methods accuracy plays a fundamental role when economical and safety points of view are considered. Additionally, recent tubular joint studies indicate further research needs, especially for some geometries. This is even more significant for particular failure modes where the collapse load predictions lead to unsafe or uneconomical solutions. In this paper a numerical study (i.e. non-linear finite element simulations) based on a parametric analysis is presented for tubular T joints with CHS and RHS chords and tubular K joints with CHS chords. The braces were made of CHS profiles for all studied joints.

## 1. INTRODUCTION

The intensive worldwide use of tubular structural elements mainly due to its associated aesthetical and structural advantages, led designers to be focused on their technological and design issues (Rondal *et al*, 1992 and Wardenier, 2000). Currently in Brazil there is still no code specifically devoted to the tubular joint design, fact that induces designers to use other international tubular joint design codes. Additionally, recent tubular joint studies indicate that further research is needed, especially for some particular geometries. This is even more significant for some failure modes where the collapse load predictions lead to unsafe or uneconomical solutions.

One of the first comprehensive investigation published in this area was made by Korol and Mirza (1982) focusing on a numerical FE model with shell elements,

and indicated a proportional increase of the joint resistance with the variable $\beta$ and/or the variable $\gamma$. The authors also referred to the need for establishing a deformation limit criteria for those connections. Packer et al. (1989) also observed that the connection resistance is proportional to the increase of $\beta$ and/or $\gamma$. The authors also developed a failure path theory to estimate the connection plastic load capacity.

Other authors like Zhao and Hancock (1993), Zhao (2000), Lu and Wardenier (1998), Cao *et al.*(1998a, 1998b), Kosteski and Packer (2000, 2003) and Kosteski *et al.*(2003) also observed that both the connection resistance and the initial stiffness are proportional to the increase of $\beta$ and/or $\gamma$.

Lu et al. (1994a, 1994b) (cited in Kosteski *et al.*2003), and validated by Zhao (1993), established an approximate $3\%d_0$ deformation limit criteria presented in Figure 1. This $3\%d_0$ limit ($N_u$) is widely accepted and is the value adopted by the International Institute of Welding (IIW, 1989) for the maximum acceptable displacement associated to the ultimate limit state, while a $1\%d_0$ limit ($N_s$) is adopted for the serviceability limit state. If the ratio of $N_u/N_s$ is greater than 1.5, the joint strength should be based on the serviceability limit state, and if $N_u/N_s< 1.5$, the ultimate limit state controls the design. In the case of CHS joints, $N_u/N_s< 1.5$ and the appropriate deformation limit to be used to determine the ultimate joint strength should be equal to $0.03d_0$.
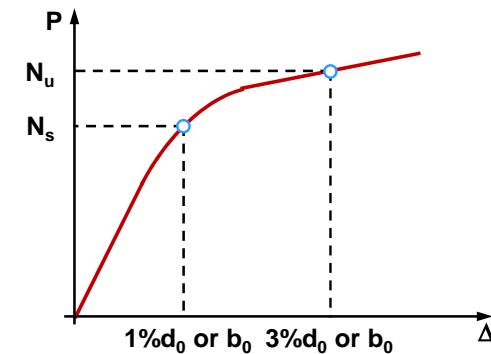


Figure 1. Deformation limit criteria (Lu *et al*., 1994a, 1994b).

In this paper a numerical study (i.e. based on non-linear FEM simulations) supported by a parametric study is presented, for the analysis of the following joints presented in the Figure 1:

- K joint with CHS chord and braces;
- T joint with CHS chord and brace;
- T joint with RHS chord and CHS braces.

The proposed models were calibrated against experiments and analytical results suggested by the Eurocode 3 (1995), by the new CIDECT guides (Packer *et al*. 2008 and Packer *et al*. 2009) and to literature classic deformation limits (Lu *et al*., 1994a, 1994b). The main variables of the present study were the brace diameter to chord diameter ratio and the thickness to chord face diameter ratio. These parameters were chosen based on recent studies results that indicated some Eurocode 3 (1995) recommendations discrepancies to the actual failure loads.

## 2. EUROCODE 3 AND CIDECT DESIGN CODES PROVISIONS

Based on extensive investigations combined with additional finite elements models, Wardenier *et al.* (2008) and Packer *et al.* (2008) proposed a new design formulation for CHS and RHS joints presented in the new CIDECT Guides. The parameters influence was determined through a numerical model retro analysis. After some simplifications, the equations were applied to Makino *et al.*(1996) experimental results and to Qian *et al.*(2008) numerical models.

The Eurocode 3 (2005) geometrical requirements should also be verified, but, in some particular cases, the validity range of the parameter $\gamma$ could be enlarged. The IIW (1989) limited the ratio to $2\gamma \le 50$ and for ratios beyond this limit, states that the joint design is governed by deformation limits. This is due to the fact that in those cases the joint deformation capacity will not be sufficient to redistribute the secondary moments. In the joint design equations, the chord bending effects due to brace loads are included in function of the chord stress $Q_f$, enabling a better evaluation of the joint capacity. The previous formulation for the chord plastification failure was based on experimental results. These results were influenced by the chord bending due the experimental tests layout.

As cited before, according to Eurocode 3 (2005) and CIDECT (Wardenier *et al.*, 2008 and Packer *et al.*, 2008) some geometrical limits need to be verified prior to the evaluation of the joint resistance – Table 1. The formulation for the design of a in plane joint type T, X and K is based on design equations proposed by Kurobane *et al.*(1986) and, after some simplifications and design rules evaluation performed by Wardenier (1982), were incorporated in the IIW Recommendations (1989).
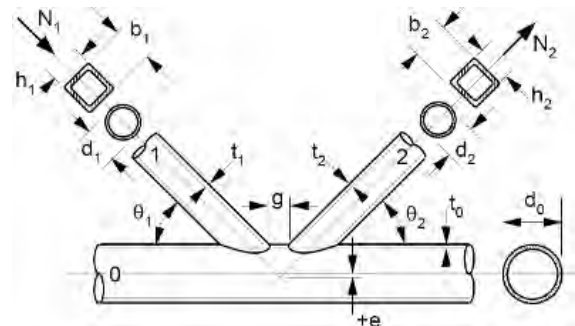


a) CHS K joint
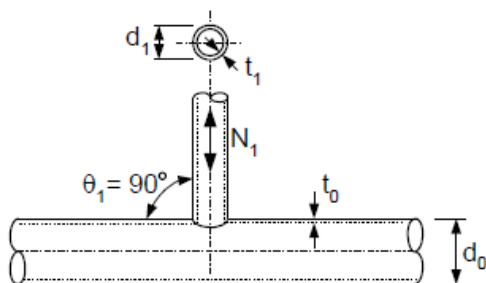


b) CHS T joint
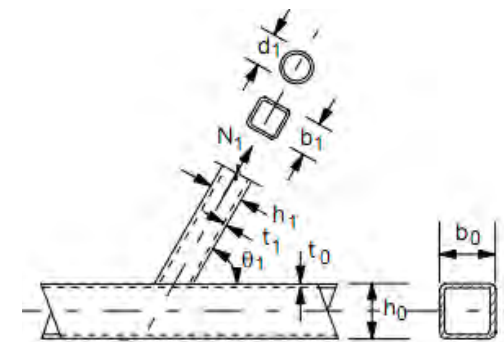


c) RHS with CHS T joint

Figure 2. Geometrical properties of the K and T joints (Packer *et al.* 2008, 2009).

For the CHS to CHS and CHS to RHS joints considered in this work, the Eurocode 3 (2005) and new CIDECT guides (Wardenier *et al.*, 2008 and Packer *et al.*, 2008) establishes that the chord plastification failure is the controlling ultimate limit state since the joint geometrical parameters observe the geometrical limits considered in Table 1. The joint resistances for the chord plastification failure are obtained from Tables 2 and 3.

Table 1.Validity scope of welded joints.

| CHS brace members and CHS chords | | CHS brace members and RHS chords | |
|---|---|---|---|
| T joints | K joints | T joints | |
| Eurocode | New CIDECT | Eurocode | New CIDECT |
| $30^o \le \theta \le 90^o$ | $30^o \le \theta \le 90^o$ | $30^o \le \theta \le 90^o$ | $30^o \le \theta \le 90^o$ |
| $0.2 \le \beta = \dfrac{d_1}{d_0} \le 1.0$ | $0.2 \le \beta = \dfrac{d_1}{d_0} \le 1.0$ | $0.4 \le d_1 / b_0 \le 0.8$ | $0.25 \le d_1 / b_0 \le 0.8$<br>$d_1 / b_0 \le 0.1 + 0.01 b_0 / t_0$ |
| tension<br>$\mu_i = d_i / t_i \le 50$<br>Compression<br>class 1 or 2 | tension<br>$\mu_i = d_i / t_i \le 50$<br>Compression<br>class 1 or 2 | tension<br>$d_i / t_i \le 50$<br>Compression<br>class 1 | tension<br>$d_i / t_i \le 50$<br>Compression<br>class 1 or 2<br>$d_i / t_i \le 50$ |
| tension<br>$d_0 / t_0 \le 50$<br>Compression<br>class 1 or 2 | tension<br>$d_0 / t_0 \le 50$<br>Compression<br>class 1 or 2 | $b_0 / t_0 \le 35$<br>$h_0 / t_0 \le 35$<br>Class 1 or 2 | tension<br>$b_0 / t_0 \le 40$<br>$h_0 / t_0 \le 40$<br>Compression -<br>class 1 or 2<br>$b_0 / t_0 \le 40$<br>$h_0 / t_0 \le 40$ |
| $t_1 \le t_0$ | $t_1 \le t_0$ | | |
| | $g \ge t_1 + t_2$ | | |

Table 2. CHS to CHS K and T Joints Design Formulae.

| Eurocode 3 | | | New CIDECT | | |
|---|---|---|---|---|---|
| Chord plastification failure | Type | | Chord plastification failure | Type | |
| $N_{1,Rd} = \dfrac{k_p k_g f_{y0} t_0^2}{\sin\theta_1} \cdot (1.8 + 10.2\beta)/\gamma_{M5}$ | (K) | (1) | $N_i^* = Q_u Q_f \dfrac{f_{y0} t_0^2}{\sin\theta_1}$ | (K,T) | (6) |
| $N_{1,Rd} = \dfrac{\gamma^{0.2} k_p f_{y0} t_0^2}{\sin\theta_1} \cdot (2.8 + 14.2\beta^2)/\gamma_{M5}$ | (T) | (2) | $Q_u = 1.65\left(1 + 8\beta^{1.6}\right)\gamma^{0.3} \cdot \left[1 + \dfrac{1}{1.2 + (g/t_0)^{0.8}}\right]$ | (K) | (7) |
| $k_p = 1 + 0.3 n_p - 0.3 n_p^2$ if $n_p < 0$ and $k_p = 1$ $(n_p \geq 0)$ | | (3) | $Q_f = \left(1 - |n|\right)^{C_1}$ $C_1 = 0.25$ $(n<0)$ $C_1 = 0.20$ $(n \geq 0)$ | (K) | (8) |
| $k_g = \gamma^{0.2}\left[1 + \dfrac{0.024\gamma^{1.2}}{1 + \exp(0.5g/t_0 - 1)}\right]$ | | (4) | $Q_u = 2.6\left(1 + 6.8\beta^2\right)\gamma^{0.2}$ $C_1 = 0.45 - 0.25$ $(n<0)$ $C_1 = 0.20$ $(n \geq 0)$ | (T) | (9) |
| Extra information | | | Extra information | | |
| $n_p = \dfrac{\sigma_{0,Ed}}{f_{y0}}$ $\sigma_{0,Ed} = \dfrac{N_{0,Ed}}{A_0} + \dfrac{M_{0,Ed}}{W_{el,0}}$ | (K,T) | (5) | $n_p = \dfrac{N_0}{N_{pl,0}} + \dfrac{M_0}{M_{pl,0}}$ | (K,T) | (10) |

where $N_{1,Rd}$ is the chord plastification failure or punching shear failure load according to Eurocode 3 (2005); $N_i^*$ is the chord plastification load according CIDECT guides (Wardenier *et al.*, 2008 and Packer *et al.*, 2008).

## 3. NUMERICAL MODEL CALIBRATION

The numerical models were developed in the Ansys 12.0 (2010) FEM package using shell elements - SHELL181 – with six degrees of freedom per node, i.e., translations and rotations about X, Y and Z axis. These models are presented in Figure 3, where it can be noticed that the mesh was more refined near the welds and more regular and coarse in the remaining parts to avoid numerical convergence problems. The same element was used for the welds according to the Figure 3 as well such as proposed by Lee (1999). The applied load was based on an equivalent displacement control. The physical nonlinearity was considered through the von Mises yield criteria and the geometrical nonlinearity used an Updated Lagrangian Formulation. All the considered numerical models were calibrated with experimental results, Table 4. The comparison between experimental and numerical results for these three models are presented in Figure 4 and Figure 5 in terms of load *versus*

displacement or peak load for the G2B test. As can be observed in these curves, a good agreement was obtained in all calibrations models.

Table 3. CHS to RHS T Joints Design Formulae.

| Eurocode 3 | | New CIDECT | |
|---|---|---|---|
| Chord plastification failure | | | |
| $N_{1,Rd} = \left(\dfrac{\pi\, k_n f_{y0} t_0^2}{4(1-\beta)\sin\theta_1}\left(\dfrac{2\eta}{\sin\theta_1} + 4\sqrt{1-\beta}\right)/\gamma_{M5}\right)$ | (11) | $N_i^* = Q_u Q_f \dfrac{f_{y0} t_0^2}{\sin\theta_i}$ | (14) |
| $k_n = 1.3 - 0.4 n/\beta$ if $n<0$ and $k_n = 1$ $(n \geq 0)$ | (12) | $Q_u = \dfrac{2\eta}{(1-\beta)\sin\theta_1} + \dfrac{4}{\sqrt{1-\beta}}$ | (15) |
| | | $Q_f = \left(1 - |n|\right)^{C_1}$ $C_1 = 0.6 - 0.5\,\geq 0.1\,(n<0)$ and $C_1 = 0.10$ $(n \geq 0)$ | (16) |
| Extra information | | Extra information | |
| $n = \dfrac{\sigma_{0,Ed}}{f_{y0}}$ $\sigma_{0,Ed} = \dfrac{N_{0,Ed}}{A_0} + \dfrac{M_{0,Ed}}{W_{el,0}}$ | (13) | $n = \dfrac{N_0}{N_{pl,0}} + \dfrac{M_0}{M_{pl,0}}$ | (17) |

where $N_{1,Rd}$ is the chord plastification failure according to Eurocode 3 (2005); $N_i^*$ is the chord plastification load according CIDECT guides (Wardenier *et al.*, 2008 and Packer *et al.*, 2008).
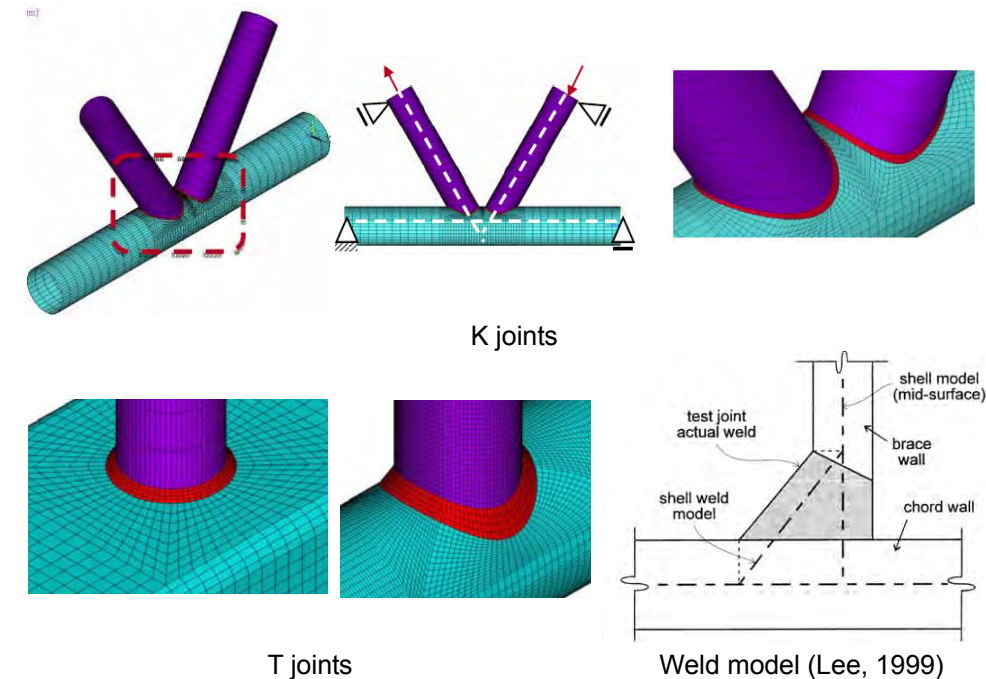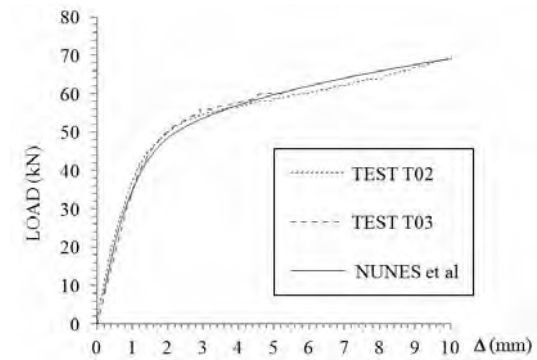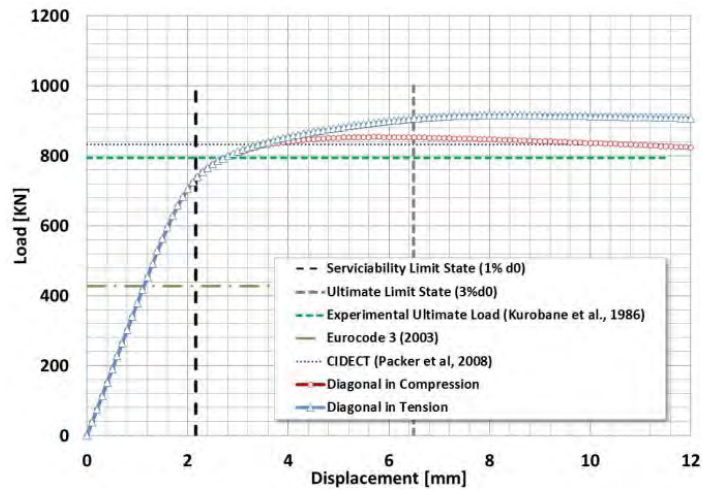


K joints



T joints      Weld model (Lee, 1999)

Figure 3. Finite element models.

Table 4. Numerical models geometrical and mechanical properties

| | CHS to CHS K G2B | CHS to CHS T EX-02 | CHS to RHS T T01, T02 |
|---|---|---|---|
| $d_0$ or $h_0 \times b_0$ [mm] | 216.3 | 409.5 | 110x60 |
| $d_1$ and $d_2$ [mm] | 165.0 | 221.9 | 38.1 |
| $t_0$ [mm] | 7.82 | 8.1 | 4.8 |
| $t_i$ [mm] | 4.32 | 6.8 | 3.2 |
| $L_0$ [mm] | 1560 | 2840 | 1000 |
| $L_i$ [mm] | 800 | 1100 | 714 |
| $f_{y,chord}$ [MPa] | 460 | 285 | 456 |
| $f_{y,brace}$ [MPa] | 409 | 300 | 250 |
| [°] | 60 | 90 | 90 |
| Load on braces | T and C | T | C |
| Reference | Kurobane *et al*., 1986 | Choo *et al*., 2005 | Mendes, 2012 |



a) G02-B (Kurobane et al., 1986)



b) EX-02 (Choo et al., 2005)



c) EX-02 (Mendes, 2012)

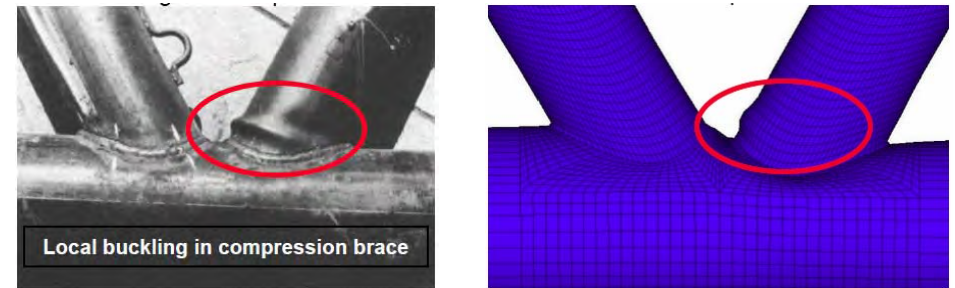Figure 4. Experimental *versus* numerical results comparison.
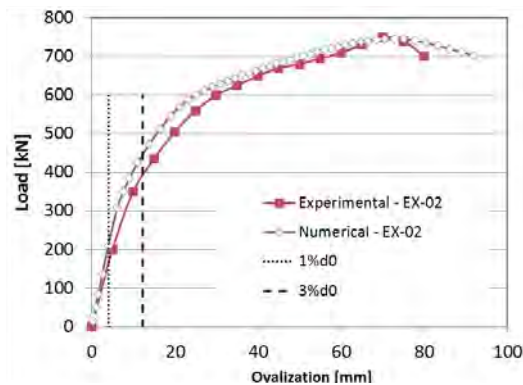


Figure 5. Deformed shape CHS K joint - experimental (Kurobane *et al*., 1986) and developed numerical model.

According to Equation (1), for the CHS K joint, the maximum load to be applied in the braces that not cause failure in the chord is $N_{1,Rd}$ = 427.67 kN corresponding to the Eurocode 3 design (2005). On the other hand, by the new CIDECT formulation (Wardenier *et al*., 2008), a value of $N_1^*$ = 832.50 kN is obtained. The experimental value obtained by Kurobane et al. (1986) was equal to 794.00 kN corresponding to the chord plastification failure followed by the local buckling in the compression brace. The deformed shapes obtained in the experimental and numerical evaluations, presented in Figure 6, indicated a good agreement. Since the ratio $N_u/N_s$ is less than 1.5, $N_u$ controls the joint design and the maximum load to be applied on the braces is $N_u$ = 852.70 kN. These facts indicate that the Eurocode 3 proposal lead to overdesigned joints when compared to new CIDECT and deformation limit criteria values and to the experiments. It could also be observed that the values obtained with the new CIDECT design rules led to safe design values when compared to the deformation limits but to unsafe predictions when compared to the experiments. At this point it is important to emphasize that the new CIDECT formulation led to a better match with the deformation limits and experiments.

On the other hand, according to Equation (2), for the CHS T joint, the maximum load to be applied in the brace that not cause failure in the chord was $N_{1,Rd}$ = 248.64 kN corresponding to the Eurocode 3 design (2005). Alternatively, with the new CIDECT formulation (Wardenier *et al*., 2008), a value of $N_1^*$ = 277.96 kN was obtained. The maximum experimental value obtained by Choo et al. (2005) was equal to 750.00

kN. Since the ratio $N_u/N_s$ (450/200=2.25) is greater than 1.5, $N_s$ controls the joint design and the maximum load to be applied on the braces was $N_s$ = 200 kN. Comparing the design codes values, a safe design is reached. It is interesting to observe that part of the joint capacity is not considered due to the large difference between these values. To tackle this case, Choo *et al.* (2005) suggested the use a 6%$d_0$ (24.57mm) deformation limit criteria for this joint type that induces a resistance of 595 kN. Despite this issue, and to keep the same criteria for all joints, the deformation limit criteria purposed by Lu et al. (1994a, 1994b) will be considered.

## 4. NUMERICAL MODEL RESULTS

This section presents the results of the developed parametrical analysis. As previously mentioned, four different joint configurations were considered and the numerical models were calibrated with experiments. Table 5 presents the results for CHS to RHS T joints considering that Eurocode 3 (2005) and new CIDECT formulations produce the same joint resistance magnitudes. The results for CHS to CHS K joints are presented in Table 6. For this joint configuration, the adopted mechanical properties were the same from the previous calibration model G2B, Table 4. Finally, Table 7 depicts the results for the CHS to CHS T joints.

Analysing the results presented in Table 5, it can be concluded that when the parameter    increase, the joint resistance also increases. For some joints, the load magnitudes obtained with the numerical analysis were less than the ones evaluated with the adopted design codes. Another interesting conclusion is that when the new CIDECT guide formulation was used for K joints, a better match was reached with the numerical and analytical results.

## 5. CONCLUSIONS AND GENERAL RECOMMENDATIONS

This paper presented a Finite Element numerical study using the Ansys 12.0 (2010) program of CHS to RHS T joints, CHS K and T joints, calibrated against experiments performed by Mendes (2012), Choo *et al.* (2005) and Kurobane *et al.* (1986). The results were compared to analytical results obtained from the Eurocode 3 (2005) and New CIDECT formulations (Wardenier et al., 2008 and Packer et al., 2008) and to deformation limit criteria proposed by Zhao (2000) and Lu *et al.* (1998).

Table 5.CHS to RHS T joints geometrical parameters and individual resistances

| ID | $h_0$ (mm) | $b_0$ (mm) | $t_0$ (mm) | $d_1$ (mm) | $t_1$ (mm) | $\beta$ | $2\gamma$ | $N_{1,Rd}$ (kN) | $\dfrac{N_u}{N_s}$ | $N_u$ (kN) | $\dfrac{N_{1,Rd}}{N_u}$ |
|---|---|---|---|---|---|---|---|---|---|---|---|
| 01 | 200 | 150 | 13 | 80 | 5 | 0.40 | 15.38 | 393.26 | 1.30 | 432.0 | 0.91 |
| 02 | 110 | 60 | 4.8 | 48.3 | 3.7 | 0.44 | 22.92 | 56.99 | 1.33 | 64.0 | 0.89 |
| 03 | 110 | 60 | 4.8 | 60.3 | 3.6 | 0.55 | 22.92 | 69.13 | 1.38 | 88.0 | 0.79 |
| 04 | 110 | 60 | 4.8 | 70 | 4 | 0.64 | 22.92 | 83.62 | 1.25 | 110.0 | 0.76 |
| 05 | 110 | 60 | 4.8 | 77 | 4 | 0.70 | 22.92 | 98.77 | 1.00 | 110.0 | 0.90 |
| 06 | 200 | 150 | 7.5 | 80 | 5 | 0.40 | 26.67 | 130.89 | 1.61 | 123.0 | 1.06 |
| 07 | 200 | 150 | 7.5 | 90 | 5 | 0.45 | 26.67 | 141.62 | 1.57 | 138.0 | 1.03 |
| 08 | 200 | 150 | 7.5 | 100 | 5 | 0.50 | 26.67 | 154.25 | 1.50 | 162.0 | 0.95 |
| 09 | 200 | 150 | 7.5 | 110 | 5 | 0.55 | 26.67 | 169.37 | 1.41 | 190.0 | 0.89 |
| 10 | 200 | 150 | 7.5 | 120 | 5 | 0.60 | 26.67 | 187.85 | 1.38 | 220.0 | 0.85 |

Table 6.CHS to CHS K joints geometrical parameters and individual resistances

| ID | $d_0$ (mm) | $t_0$ (mm) | $d_1=d_2$ (mm) | $t_1=t_2$ (mm) | $\beta$ | $2\gamma$ | $N_{1,Rd}$ | $N_1^*$ | $N_u$ (Ansys) | $N_s$ | $\dfrac{N_u}{N_s}$ | $\dfrac{N_{1,Rd}}{N_u}$ | $\dfrac{N_i^*}{N_u}$ |
|---|---|---|---|---|---|---|---|---|---|---|---|---|---|
| 1 | 168.3 | 5.0 | 88.9 | 5.0 | 0.53 | 16.83 | 130 | 171 | 240 | 250 | 0.96 | 0.54 | 0.71 |
| 2 | 168.3 | 5.0 | 101.6 | 5.0 | 0.60 | 16.83 | 141 | 187 | 282 | 272 | 1.04 | 0.5 | 0.66 |
| 3 | 168.3 | 5.0 | 114.3 | 5.0 | 0.68 | 16.83 | 155 | 285 | 316 | 306 | 1.03 | 0.49 | 0.9 |
| 4 | 168.3 | 5.0 | 127.0 | 5.0 | 0.75 | 16.83 | 172 | 327 | 354 | 345 | 1.03 | 0.49 | 0.92 |
| 5 | 219.1 | 8.0 | 114.3 | 8.0 | 0.52 | 13.69 | 324 | 410 | 592 | 601 | 0.99 | 0.55 | 0.69 |
| 6 | 219.1 | 8.0 | 127.0 | 8.0 | 0.58 | 13.69 | 348 | 582 | 648 | 658 | 0.98 | 0.54 | 0.9 |
| 7 | 219.1 | 8.0 | 139.7 | 8.0 | 0.64 | 13.69 | 377 | 656 | 703 | 719 | 0.98 | 0.54 | 0.93 |
| 8 | 219.1 | 8.0 | 159.0 | 8.0 | 0.73 | 13.69 | 439 | 776 | 799 | 818 | 0.98 | 0.55 | 0.97 |
| 9 | 298.5 | 8.0 | 152.4 | 8.0 | 0.51 | 18.66 | 364 | 475 | 682 | 673 | 1.01 | 0.53 | 0.7 |
| 10 | 298.5 | 8.0 | 168.3 | 8.0 | 0.56 | 18.66 | 384 | 516 | 747 | 736 | 1.02 | 0.51 | 0.69 |
| 11 | 298.5 | 8.0 | 193.7 | 8.0 | 0.65 | 18.66 | 416 | 571 | 862 | 845 | 1.02 | 0.48 | 0.66 |
| 12 | 298.5 | 8.0 | 219.1 | 8.0 | 0.73 | 18.66 | 455 | 865 | 988 | 966 | 1.02 | 0.46 | 0.88 |

Table 7.CHS to CHS T joints geometrical parameters and individual resistances

| ID | $d_0$ (mm) | $t_0$ (mm) | $\beta$ | $d_1$ (mm) | $t_1$ (mm) | $2\gamma$ | $N_{1,Rd}$ | $N_1^*$ | $N_u$ (Ansys) | $N_s$ | $\dfrac{N_u}{N_s}$ | $\dfrac{N_{1,Rd}}{N_s}$ | $\dfrac{N_i^*}{N_s}$ |
|---|---|---|---|---|---|---|---|---|---|---|---|---|---|
| 1 | 88.9 | 8 | 5.56 | 33.7 | 6.3 | 0.38 | 154.9 | 164.5 | 279.8 | 224.4 | 1.25 | 0.44 | 0.47 |
| 2 | 88.9 | 8 | 5.56 | 42.4 | 6.3 | 0.48 | 193.0 | 212.0 | 314.9 | 264.3 | 1.19 | 0.49 | 0.54 |
| 3 | 88.9 | 8 | 5.56 | 48.3 | 6.3 | 0.54 | 223.8 | 250.3 | 345.8 | 278.2 | 1.24 | 0.52 | 0.58 |
| 4 | 88.9 | 8 | 5.56 | 51.0 | 6.3 | 0.57 | 239.2 | 269.5 | 362.2 | 289.0 | 1.25 | 0.53 | 0.60 |
| 5 | 88.9 | 8 | 5.56 | 60.3 | 6.3 | 0.68 | 298.8 | 343.6 | 378.3 | 326.1 | 1.16 | 0.63 | 0.73 |
| 6 | 298.5 | 25 | 5.97 | 114.3 | 16.0 | 0.38 | 1548.4 | 1646.8 | 2328.1 | 1773.0 | 1.31 | 0.53 | 0.57 |
| 7 | 298.5 | 25 | 5.97 | 139.7 | 16.0 | 0.47 | 1874.6 | 2052.9 | 2529.5 | 1988.9 | 1.27 | 0.59 | 0.65 |
| 8 | 298.5 | 25 | 5.97 | 159.0 | 16.0 | 0.53 | 2166.0 | 2415.7 | 2691.7 | 2221.5 | 1.21 | 0.65 | 0.72 |
| 9 | 298.5 | 25 | 5.97 | 168.3 | 16.0 | 0.56 | 2319.8 | 2607.3 | 2739.9 | 2361.5 | 1.16 | 0.68 | 0.76 |
| 10 | 298.5 | 25 | 5.97 | 193.7 | 16.0 | 0.65 | 2784.6 | 3185.9 | 2922.5 | 2552.1 | 1.15 | 0.76 | 0.88 |
| 11 | 660.0 | 60 | 5.50 | 244.5 | 40.0 | 0.37 | 8534.6 | 9033.4 | 10862.9 | 9084.9 | 1.20 | 0.63 | 0.67 |
| 12 | 660.0 | 60 | 5.50 | 323.9 | 40.0 | 0.49 | 11178.7 | 12325.5 | 11810.5 | 10229.7 | 1.15 | 0.76 | 0.84 |
| 13 | 660.0 | 60 | 5.50 | 355.6 | 40.0 | 0.54 | 12440.6 | 13896.8 | 12303.4 | 10664.6 | 1.15 | 0.81 | 0.91 |
| 14 | 660.0 | 60 | 5.50 | 368.0 | 40.0 | 0.56 | 12966.3 | 14551.3 | 12409.5 | 10734.3 | 1.16 | 0.84 | 0.94 |
| 15 | 660.0 | 60 | 5.50 | 457.0 | 40.0 | 0.69 | 17268.1 | 19907.3 | 13957.2 | 11483.3 | 1.22 | 0.99 | 1.15 |

The results indicated that the new CIDECT formulation presented a better performance when compared to the numerical results than the Eurocode 3 (2005) design results. This situation was more evidenced for CHS to CHS K and T joints. The results for RHS to CHS T joint configuration indicated that a good match was obtained when the deformation limit criteria was used to evaluate the joint numerical resistance and compared to the design codes formulae.

## ACKNOWLEDGMENTS

## REFERENCES

[1] Ansys 12.0 ®, ANSYS - Inc. Theory Reference, 2010.

[2] Cao, J.J., Packer, J.A., Kosteski, N., "Determination of connection strength between longitudinal plates and RHS columns", Journal of Constructional Steel Research, vol. 46: 1-3, paper nº134, 1998.

[3] Cao, J.J., Packer, J.A., Yang, G.J., "Yield line analysis of RHS connections with axial loads", Journal of Constructional Steel Research, vol. 48, nº1, pp 1-25, 1998.

[4] Choo, Y.S.; van derVegte, G.J.; Zettlemoyer, N.; Li, B.H; and Liew, J.Y.R., Static Strength of T-Joints Reinforced with Doubler or CollarPlates. I: Experimental Investigations, Journal of Structural Engineering, ASCE, 131(1): 119-128.

[5] EN 1993-1-8-2005. European Committee for Standardization – CEN. Eurocode 3: Design of steel structures. Part 1.8: Design of joints, Brussels.

[6] International Institute of Welding (IIW). (1989). Design recommendation for hollow section joints—Predominantly statically loaded, 2nd Ed., IIW Document XV-701-89, Cambridge, U.K.

[7] Korol, R., Mirza, F., 1982.Finite Element Analysis of RHS T-Joints, Journal of the Structural Division, ASCE, vol.108, No. ST9, pp 2081-2098.

[8] Kosteski, N., Packer, J.A., "Bracing connections to rectangular HSS columns", Connections in Steel Structures IV - Behaviour Strength and Design, Proceedings Fourth International Workshop Oct 2000, Roanoke, Virginia, USA, AISC/ECCS, 2002, pp 788-797, 2000.

[9] Kosteski, N., Packer, J.A., "Welded Tee-to-HSS connections", Journal of Structural Engineering, vol. 129, nº2, pp 151-159, 2003.

[10] Kosteski, N., Packer, J.A., Puthli, R.S., "A finite element method based yield load determination procedure for hollow structural section connections", Journal of Constructional Steel Research, vol. 59, pp 453-471, 2003.

[11] Lee, M.M.K., "Strength, stress and fracture analyses of offshore tubular joints using finite elements", Journal of Constructional Steel Research, vol. 51, pp 265-286, 1999.

[12] Lu, L.H., Wardenier, J., "The ultimate mean strength of I-beam to RHS column connections", Journal of Constructional Steel Research, vol. 46: 1-3, paper nº 139, 1998.

[13] Lu LH, Puthli RS, Wardenier J. In: Ultimate deformation criteria for uniplanar connections between I-beams and RHS columns under in-plane bending. Proceedings of the 4th International Offshore and Polar Engineering Conference, ISOPE-94, Osaka (Japan), 1994.

[14] Lu, L.H., de Winkel, G.D., Yu, Y., Wardenier, J., Deformation limit for the ultimate strength of hollow section joints, 6th International Symposium on Tubular Structures, Melbourne, pp 341-347, 1994.

[15] Makino, Y., Kurobane, Y., Ochi, K., Vegte, G.J. van der, and Wilmshurst, S.R., 1996: Database of test and numerical analysis results for unstiffened tubular joints. IIW Doc. XV-E-96-220.

[16] Mendes, F. C., Freitas, M.S.R., Freitas, A. M. S. Estudo Teórico Experimental de Ligações "T" e "KT, REM, 2012 (in portuguese) (in press).

[17] Packer, J., Morris, G., Davies, G., "A limit states design method for welded tension connections to I-section webs", Journal of Constructional Steel Research, vol.12, pp 33-53, 1989.

[18] Packer, J. A., Wardenier, J., Kurobane, Y., Dutta, D., and Yeomans, N, (2008). Design guide for retangular hollow section (RHS) joints under predominantly static loading, CIDECT 3, Second Edition.

[19] Packer, J.A., Wardenier, J., Zhao, X.-L., G.J. van der Vegte and Y. Kurobane, Design Guide - For Rectangular Hollow Section (RHS) Joints Under Predominantly Static Loading - 2nd Edition, CIDECT, 2009.

[20] Qian, X.D., Choo, Y.S., Vegte, G.J. van der, and Wardenier, J., 2008: Evaluation of the new IIW CHS strength formulae for thick-walled joints. Proceedings 12th International Symposium on Tubular Structures, Shanghai, China, Tubular Structures XII, Taylor & Francis Group, London, UK, pp. 271-279.

[21] Rondal, J., Wurker, K.G., Wardenier, J., Dutta, D., and Yeomans, N, (1992). Structural Stability of Hollow Sections, CIDECT.

[22] Wardenier, J., (2000).Hollow Sections in Structural Applications, CIDECT.

[23] Wardenier, J, Kurobane, Y, Packer, JA, van der Vegte, GJ and Zhao XL, Design Guide - For Circular Hollow Section (CHS) Joints Under Predominantly Static Loading – 2nd Edition, CIDECT, 2008.

[24] Zhao, X., Hancock, G., "Plastic Mechanism analysis of T-joints in RHS subject to combined bending and concentrated force", Proceedings of the Fifth International Symposium on Tubular Connections held at Nottingham, UK, 1993, E & FN Spon, London, pp 345-352, 1993.

[25] Zhao, X., "Deformation limit and ultimate strength of welded T-joints in cold-formed RHS sections", Journal of Constructional Steel Research, vol. 53, pp 149-165, 2000.

# TO BASE PLATES OF HOLLOW SECTIONS COLUMNS

Kamila Horová, Jan Tomšů, František Wald

*Department of Steel and Civil Structures, Czech Technical University in Prague*
*kamila.horova@fsv.cvut.cz; jan.tomsu@fsv.cvut.cz; wald@fsv.cvut.cz*

## ABSTRACT

This work describes the analytical prediction model of CHS and RHS column bases consisting of a base plate and anchor bolts under axial force and bending moment. An analytical model, which is based on the component method applied in EN 1993-1-8: 2005, allows determining axial force and bending moment resistance and the rotational stiffness. The analytical model consists of two components, base plate in bending and anchor bolts in tension, which is suitable for evaluation of hollow section base plates. The effective length of T-stub in tension was derived analytically using the yield line theory and checked by finite element simulation. The model is compared to the published experimental results in order to verify the resistance and the stiffness predictions. The comparison shows a good accuracy of the prediction of the moment-rotation curve.

## 1. INTRODUCTION

Column bases are one of the least studied structural elements in the frame of European research. Contrarily to beam to column connections, the number of available tests is limited to about 200 with various complexity of data description. Classical approaches to design of base plates, see (Melchers, 1992), use an elastic analysis, based on the assumption that the section, consisting of anchor bolts and a base plate, remains plane in compression. By solving equilibrium equations, the maximum stress in the concrete can be determined, assuming a triangular stress distribution along the dimension of the stress block and tension in the holding down assemblies. Although this procedure proved to be satisfactory in service over many years, such approach ignores flexibility of the base plate in bending and behaviour of the holding down assemblies and of the concrete. The traditional elastic models for column base design give a safe, conservative solution with relatively thick base plates and expensive anchoring systems.

The column base stiffness has an important effect on the calculated frame behaviour, particularly on frame sway. Traditionally, column bases are modelled as either pinned or as fixed, whilst the reality lies somewhere between these two extremes. In the European codes of practice (EN 1993-1-8, 2005) the elastic design models were replaced by inelastic, and the model of foundation for crushing of the concrete under the flexible base plate was refined, see (Wald et al, 2008). The guidance for modelling the base by component method including stiffness prediction is available. In portal frames, the base stiffness has a major influence on the collapse mode in extreme situations caused by exceptional loading, such as fire, see (Song et al, 2009). The design of base plates is also crucial for seismic design, where the deformation capacity, see (Hsu and Liu, 2006) and detailing play important role and the base plate connections are tested during each earthquake loading, see (Di Sarno, 2007). Traditional design of base plates for hollow section columns is described in (Wardenier et al, 1995). The elastic design was exchanged for an inelastic proposal, see (Liu, 2006), which focused on base plate uplift (Wikinson et al, 2009) and design or sign and lightening structures (Ansley et al, 2000). The anchor bolts, an important part of the column base, are evaluated as products according to ETAG (2002) or by developed prediction models, see (Eligehausen, 2006).

Further research in the area of base plates is focused on innovative connections and on hollow sections. Between years 2007 and 2011, the development of design models of steel to concrete joints for the European standards and design rules were the objective of a project RFSR-CT-2007-00051 InFaSo, led by Prof. Ulrike Kuhlman from the Institute of Structural Design at the University of Stuttgart, see (Kuhlmann, et al 2011). Within this project, connections of steel beam to concrete wall and a base plate with embedded plate using long headed studs were developed. A design method for both connections including the increase if resistance by stirrups were published, see (Henriques et al, 2011).
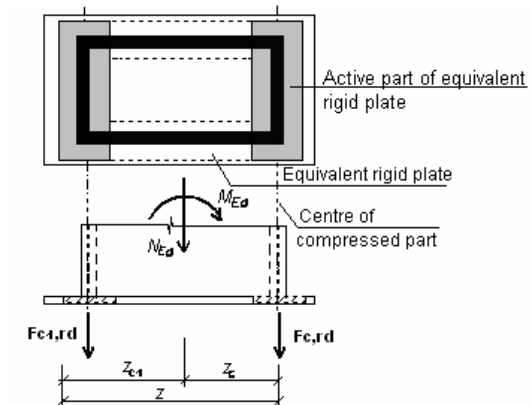


Figure1. Force equilibrium for RHS column base with simplified effective area, both parts in compression.

## 2. COMPONENT METHOD

Joints as well as the base plates are modelled using component method. This method is based on evaluation of resistance and stiffness, which are derived from the resistance and stiffness of each part of the joint. The first step of the component method is identification of individual connection parts - components. The base plate connection is disintegrated into two parts: base plate in bending plus concrete in compression, and base plate in bending plus anchor bolts in tension. There are also components of column web and flange in shear and compression, and bolts in shear, which should be checked during the design.

The calculation of the column base bending resistance, based on the force equilibrium on the base plate, is given in (Wald et al, 2008). The connection is loaded by axial force $N_{Ed}$ and bending moment $M_{Ed}$, as shown in Figures 1 and 2. The position of the neutral axis is calculated according to resistance of the tension part $F_{T,Rd}$. The bending resistance $M_{Rd}$ is determined assuming plastic distribution of internal forces as it is shown in Figure 2. The effective area $A_{eff}$ under the base plate

represents the equivalent rigid plate and is calculated from an equivalent T-stub, with an effective width *c*. The compression force is assumed to act at the centre of the compressed part and the tensile force is located at the anchor bolts or in the middle when there are more rows or bolts.

The calculation of stiffness of the base plate is compatible with beam to column stiffness calculation. The difference between these two procedures lies in the fact, that by the base plate connection the normal force has to be introduced.

The detailed design procedure for based plates under columns of rectangular hollow section was described in (Wald et al, 2005) and of circular hollow section in (Horová et al, 2011). The failure mode derived by the yield line theory was evaluated by FEM simulation.
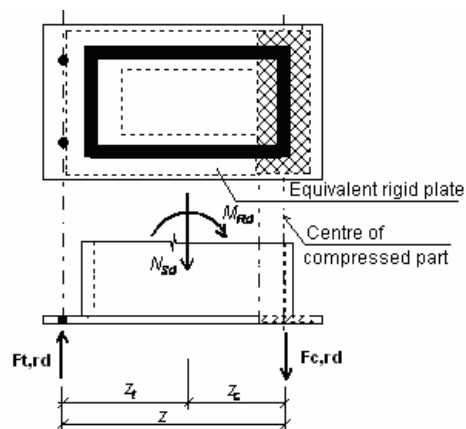


Figure 2. The stiffness model of the base plate connection of RHS column.

## 3. EVALUATION ON EXPERIMENTS

### 3.1. Nakashima experiments

Study performed by Shigetoshi Nakashima in Japan (Nakashima 1992) examined the mechanical characteristics of a column base, subjected to bending and shear forces, such as initial rigidity, hysteresis characteristics, ultimate strength and strain of main components. A life size steel column with a square base and a concrete block, as it is shown in Figure 3, was used as a specimen. Diameter and arrangement of the anchor bolts, thickness of the base plate, and cross-sectional dimensions of the column and concrete footing were the tested variables.

The diameter of bolt hole in the base plate was 55 mm. As it is shown in Table 1, at anchoring of the base plate, the clearance at the bottom surface of the plate was 30 mm. Non-shrinking mortar was injected into the space under the base plate and into the clearance between anchor bolts and holes in the base plate. There was no initial tightening force in anchor bolts. Table 1 shows for tested specimens the characteristics of the column, the base plate, anchor bolts and the concrete foundation. In this paper, test results of fourteen specimens are described. For evaluation, only five set ups without stiffeners are chosen.

Table 2 presents mechanical characteristics of the steel. The strength of the concrete used for manufacturing of specimens was 28,5 N/mm$^2$ and of grout 45,2 N/mm$^2$. The concrete block was reinforced with steel bars.
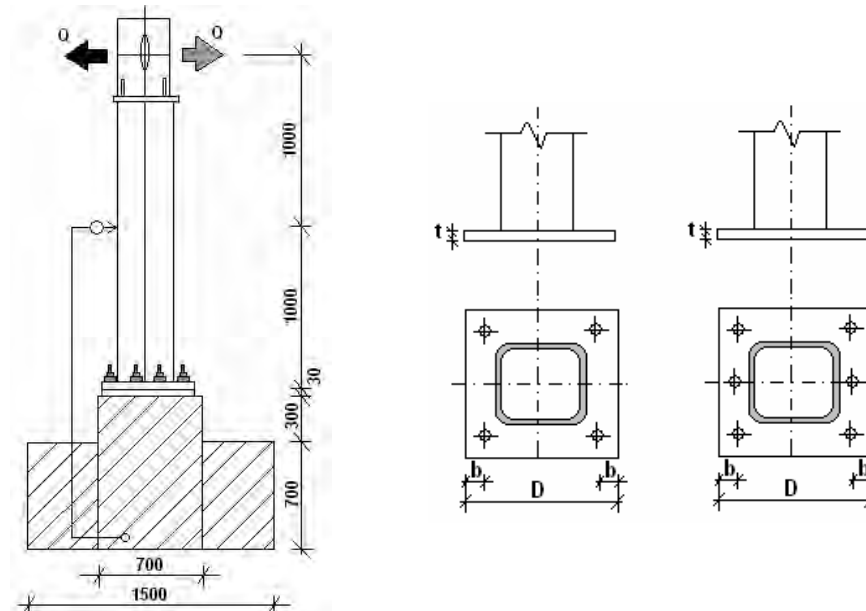


Figure 3. The test set up of base plates with four bolts and six bolts.

Table 1. Selected specimens geometry.

| Specimens | Steel column | Base plates | | | Anchor bolts | | | Foundation |
|---|---|---|---|---|---|---|---|---|
| Symbols | A x B x t (mm) | D (mm) | b (mm) | t (mm) | Quantity | Thread | Shank | b x D (mm) |
| I-20-09 | 200x200x9 | 415 | 73 | 32 | 4 | M36 | D38 | 535x535 |
| I-20-12 | 200x200x12 | 420 | 65 | 32 | 4 | M36 | D38 | 550x550 |
| II-25-09 | 250x250x9 | 460 | 60 | 32 | 6 | M33 | D35 | 580x580 |
| II-25-12 | 250x250x12 | 480 | 65 | 36 | 6 | M36 | D38 | 600x600 |
| II-25-16 | 250x250x16 | 480 | 65 | 40 | 6 | M36 | D38 | 600x600 |

Table 2. Mechanical properties of steel.

| Steel | | $\sigma_y$ (N/mm$^2$) | $\sigma_t$ (N/mm$^2$) | El (%) |
|---|---|---|---|---|
| Steel columns | 200x200x9 | 400 | 480 | 19 |
| | 200x200x12 | 390 | 470 | 22 |
| | 250x250x9 | 430 | 510 | 19 |
| | 250x250x12 | 380 | 450 | 20 |
| | 250x250x16 | 390 | 460 | 18 |
| Base plates | t = 32 mm | 370 | 640 | 45 |
| | t = 36 mm | 380 | 570 | 37 |
| | t = 40 mm | 340 | 520 | 37 |
| | t = 50 mm | 370 | 580 | 40 |
| Anchor bolts | D35 | 390 | 660 | 28 |
| | D38 | 400 | 620 | 37 |

Behaviour of the column base from Nakashima´s test is represented by moment-rotation curve. This curve describes the stiffness as well as bending resistance of the joint. In Figure 4, there is a comparison of the two curves, the first obtained from the experiment and the second from the calculations worked out in (Horova, 2010).
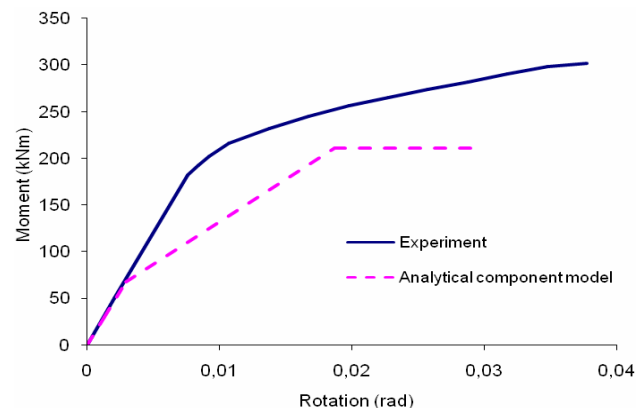


Figure 4. The comparison of presented model to test II-25-09.

Comparing the initial stiffness, the experimental and analytical results are close to each other with difference of about 4 % (0,24 kNmrad$^{-1}$ from the test and 0,23 kNmrad$^{-1}$ from the analytical model). The difference between resistances reflects the design model, which is focused on yielding of steel; there is also a good agreement between experimental and analytical results. The border of plasticizing of the first component as well as the maximum resistance of the column base is lower when using analytical component model. This is due to the use of nominal values of material properties in the analytical model, whereas the experiment results reflect the real behaviour of material.

Summing up, it can be stated that the calculated values and measured values of the initial stiffness correlate well. The analytical component model can be used for design and prediction of the base plate resistance and stiffness.

## 3.2. Takamatsu and Tamai experiments

After the earthquake in Hyogoken-nanbu, Japan, in 1995, during which many steel column bases were damaged, Takao Takmatsu and Hiroyuki Tamai from Hiroshima Institute of Technology performed their experimental study on RHS exposed-type column base, see (Takamatsu and Tamai, 2005). This study described force characteristics of an exposed-type column base with anchor bolts and thick base plate as well as a of a new exposed-type column base, improved by driving a wedge into the gap between the nut of the anchor bolt and the base plate, causing plastic elongation of the anchor bolt.

Experiment was carried out on fixed column base using rolled threaded anchor bolts. The tested specimen is shown in Figures 5 and 6. The mechanical properties of the steel material and the dimensions of its parts are summarized in Table 4. A cold-formed square hollow section was used for the column and anchor bolts standardized by the Japanese Society of Steel Construction were used. In Figure 7 there is a comparison of the analytical component model to the experimental result.
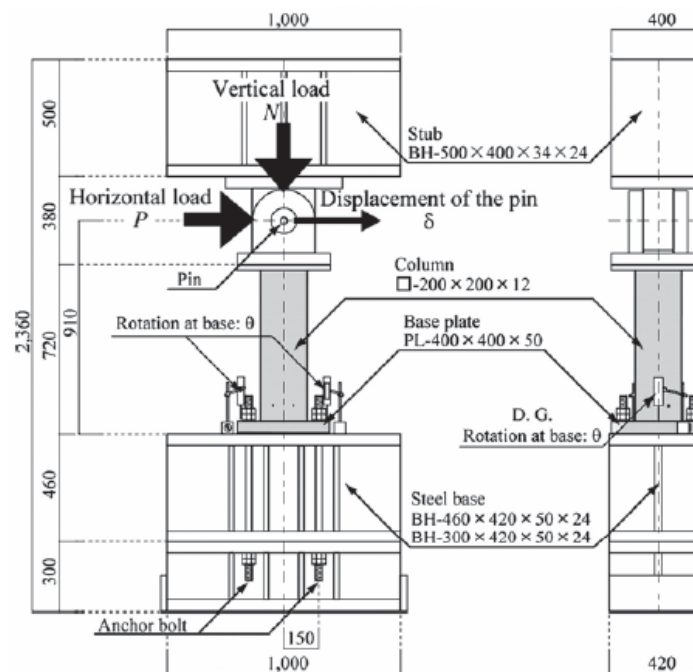


Figure 5. Measuring and loading system of tested specimen.

Table 3. Geometry and material properties of tested specimen.

| Column (mm) | Base plate (mm) | Anchor bolt | | |
|---|---|---|---|---|
| | | Ø (mm) | A (mm$^2$) | $l_{eff}$ (mm) |
| 200x200x12 | 400x400x50 | 27,52 | 595 | 560 |

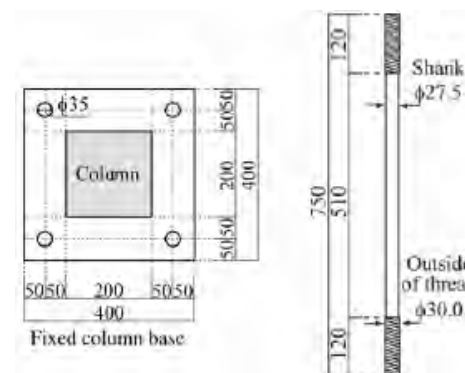| Material | E (N/mm$^2$) | $\sigma_y$ (N/mm$^2$) | $\sigma_u$ (N/mm$^2$) | $\sigma_y/\sigma_u$(%) | $\varepsilon_u$ (%) |
|---|---|---|---|---|---|
| Anchor bolt | 205000 | 289 | 428 | 68 | 43 |
| Base plate | 205000 | 261 | 414 | 63 | 37 |
| Column | 205000 | 374 | 439 | 85 | 35 |



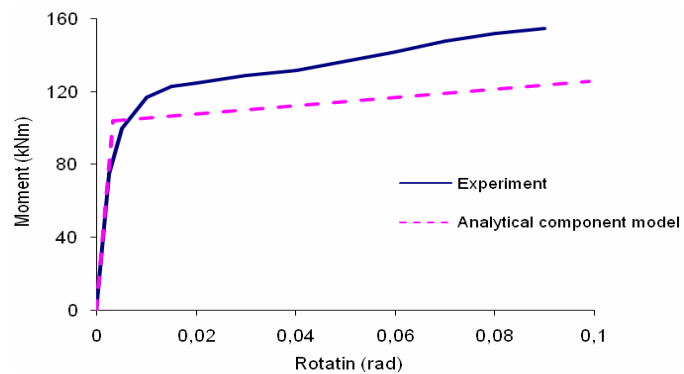Figure 6. Base plate and anchor bolt of tested specimen.

Figure 7. Comparison of moment-rotation curves of prediction to tests results for zero axial force.

Regarding the initial stiffness, the difference between the experimental and analytical value is about 12%, which is more than in case of comparison of the analytical model and Nakashima's experiment. However, discrepancy is limited and thus results obtained from analytical component model can be considered satisfactory. In the experimental study, the resistance was based on yielding of anchor bolts. The border of plasticizing of the first component in experimental moment-rotation diagram is represented by plasticizing of anchor bolt (125,40 kNm). On the other hand, based on the analytical component calculation, the base plate resistance (104,24 kNm) was proved as the lowest, thus failure of the column base is supposed to govern collapse. Nevertheless, values of the yield strength of anchor bolts in tension and of the base plate in bending are close to each other, so both the base plate and the anchor bolts can be the critical components. The fact that in performed calculation the base plate is the critical component is caused by calculation of the effective length of T-stub, which slightly differ in the analytical model from the real one.

Despite these slight differences, the values calculated accordingly to the analytical component model and measured values obtained from this experimental study - especially the initial stiffness - correlate well. Also according to this comparison, it can be stated, that the analytical model, introduced in (Horova, 2010) can be used for design and prediction of the base plate resistance and stiffness.

## 5. CONCLUSIONS

This paper is focused on comparison of predictions obtained using the analytical model of base plates of hollow sections columns with the real test results. Both in case of Nakashima's and Takamatsu's experiments, the values predicted by the analytical model show a good agreement with the test results, especially regarding the initial stiffness. In conclusion, the analytical model based on the component method allows a satisfactorily accurate prediction of resistance and stiffness for engineering purposes and thus can be used for design.

## ACKNOWLEDGMENTS

## REFERENCES

[1] Ansley M.H., Cooc R.A. and Tia M., *Use of grout pads for sign and lightening structures*, Structural research report No. BB-512, University of Florida, 2000.
[2] Di Sarno L., Pecce M.R. and Fabbrocino G., Inelastic response of composite steel and concrete base column connections, *Journal of Constructional Steel Research*, 63, 2007, pp. 819–832.
[3] Mallée R. and Silva J. F., *Anchorage in Concrete Construction*, Ernst and Sohn Verlag, Darmstadt, 2006, ISBN 978-433-01143-0.
[4] EN 1993-1-8, European Committee for Standardization – CEN. Eurocode 3: Design of steel structures. Part 1.8: *Design of joints*, Brussels 2005.
[5] ETAG 001, *Guideline for European technical approval of metal anchors for use in concrete*, Parts1 to 5, Brussels, 2002.
[6] Henriques J., Ožbolt A., Kuhlmann U. et al, Behaviour of Steel-To-Concrete Joints - Moment Resisting Joint of a Composite Beam to Reinforced Concrete Wall, *Steel Construction,* 2011, vol. 4, no. 3, pp. 161-165. ISSN 1867-0520.
[7] Horova K., *Base plates of hollow sections*, Diploma thesis, Czech Technical University in Prague, 73 p., Prague, 2010.
[8] Horová K., Wald F. and Sokol Z., *Design of Circular Hollow Section Base Plates*, Eurosteel 2011, 6th European Conference on Steel and Composite Structures, Budapest, 2011, vol. 1, pp. 249-254. ISBN 978-92-9147-103-4.
[9] Hsu H.L. and Lin H.W., Improving seismic performance of concrete-filled tube to base connections, *Journal of Constructional Steel Research*, 62, 2006, pp. 1333–1340.
[10] Kuhlmann et al, INFASO, Final report, RFSR-CT-2007-00051, 2011.
[11] Liu D., Design of circular base plates, ASCE, *Practice Periodical on Structural Design and Construction*, 11, 2006, pp. 1-13.
[12] Melchers R. E., Column-base response under applied moment, *J. Construct. Steel Research*, 23, 1992, pp. 127-143.
[13] Nakashima S., *Experimental Behavior of Encased Steel Square Tubular Column-Base Connections*, in Proceedings of the First Word Conference on Constructional Steel Design, Elsevier Applied Science, 1992, pp. 240-249.
[14] Song Y., Huang, Z. Burgess, I.W, Plank, R.J., The behaviour of single-storey industrial steel frames in fire, *Advanced Steel Construction,* 5 (3), 2009, pp.289-302.
[15] Takamatsu T., Tamai H., Non-slip-type restoring force characteristics of an exposed-type column base, *Journal of Constructional Steel Research*, 61, 2005, pp. 942–961.
[16] Wald F., Bouguin V., Sokol Z. Muzeau J. P: Component Method for Base Plate of RHS, Proceedings of the Conference Connections in Steel Structures IV: Steel Connections in the New Millenium, October 22-25, Roanoke 2000, pp. IV/8- IV/816.
[17] Wald F., Sokol Z., Steenhouis M. and Jaspart, J.P., Component Method for Steel Column Bases, *Heron*, 2008, vol. 53, no. 1/2, pp. 3-20, ISSN 0046-7316.
[18] Wardenier J., Dutta D., Yeomans N., Packer J.A. and Bucak O., *Design guide for structural hollow section in mechanical applications*, CIDECT, Construction with hollow section steel sections, Verlag TUV Rheinland Gmbh, Köln, 1995.
[19] Wilkinson T., Ranzi G., Williams P. and Edwards M., *Bolt prying in hollow section base plate connections*, Sixth International Conference on Advances in Steel Structures and Progress in Structural Stability and Dynamics, Hong Kong 2009, ISBN 978-988-99140-5-9.

# BEHAVIOUR OF BOLTED CIRCULAR FLANGE JOINTS SUBJECTED TO A BENDING MOMENT AND AN AXIAL FORCE

Maël Couchaux
*CTICM, France*
*mcouchaux@cticm.com*

Mohammed Hjiaj
*INSA of Rennes, France*
*mohammed.hjiaj@insa-rennes.fr*

Ivor Ryan
*Consultant, France*
*ivorryan@gmail.com*

## ABSTRACT

Bolted circular flange connections are used for tubular members in buildings as well as in structures such as chimneys and pylons for lighting, communication, wind turbines and ski-lift installations. In this paper, a model is proposed for the determination of the global behaviour (elastic and elasto-plastic) of bolted circular flange connections subjected to a bending moment combined with an axial tensile or compressive force. Particularly, a model, based on the component method and quite similar to that of Eurocode 3 part 1-8, is proposed to determine the rotational stiffness. A parametric study was performed based on a 3D finite element model considering elasto-plastic material behaviour and using contact elements. The results obtained from the proposed analytical model are in good agreement with those obtained from the finite element model.

## 1. INTRODUCTION

Most of the existing models permit to determine the tensile capacity of bolted circular flange joint connections (Igarashi et al, 1985, Couchaux et al, 2010). Stamatopoulos & Ermopoulos (2008) proposed to evaluate the plastic bending resistance of these joints using an incremental procedure. The possible occurrence of a non ductile failure mode or the development of an elasto-plastic regime has been considered by Couchaux et al (2011). The strength of a joint plays an important in design. However, its stiffness can have an important impact on the global behaviour of the structure. A model has been proposed by Kozlowski & Wojnar (2008) to determine the rotational stiffness of these joints but the calculation method involves an iterative procedure and is not easy to directly apply. The objective of this paper is to propose a model which allows a full characterization of the complete behaviour of this type of joints, and particularly the moment rotation curve. As suggested in EN 1993-1-8, the moment rotation curve is evaluated via two essential characteristics of the joint; the bending resistance and the initial rotational stiffness. The bending resistance of joint is evaluated considering the possibility of the development of a fully plastic mechanism or an elasto-plastic regime (Couchaux et al, 2011). The initial rotational stiffness is determined considering the component method. The results obtained via this analytical model are compared with those of numerical analyses.

## 2. ANALYTICAL MODEL: MOMENT-ROTATION CURVE

### 2.1. Initial rotation stiffness of the joint

#### 2.1.1. General hypothesis

The cross-section located at the junction between the tube-wall and the flange is supposed to remain plane after loading (see Figure 1). This cross-section is subjected to a rotation $\theta_j$. The interaction between the flange and the tube-wall is modeled considering springs positioned along the circumference of the tube. Their stiffness is different in compression and in tension. The distribution of the forces applied by the tube-wall to the flange is linear in both compression and tension.
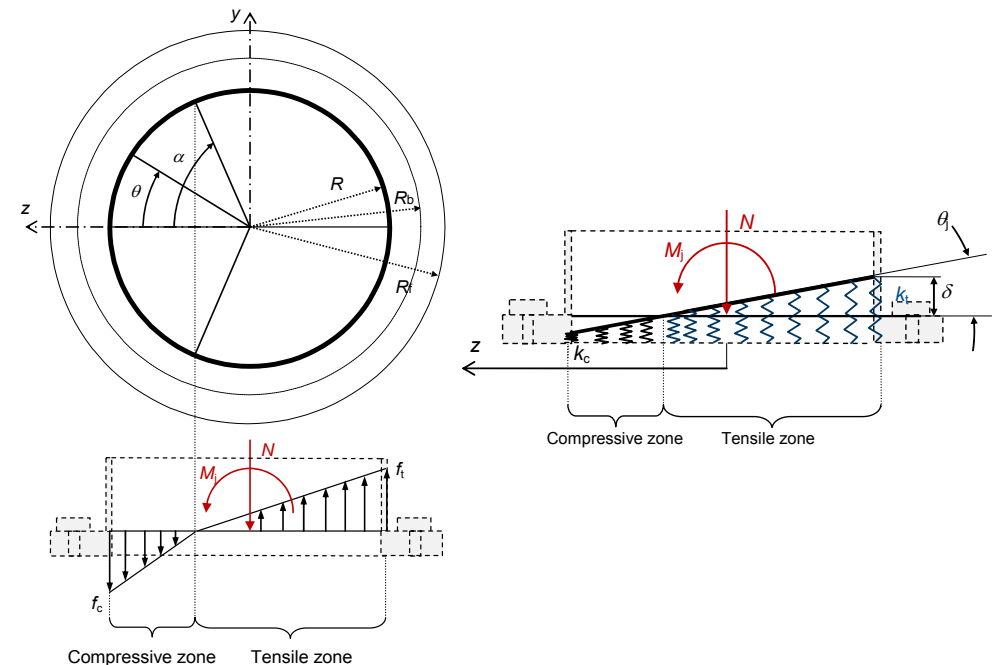


Figure 1. Deformation of the joint with a dominant bending moment

Considering the plane cross-section assumption, the displacement of the flange at the junction with the tube-wall (see Figure 1) can be expressed as follows:

$$\delta(\theta) = \begin{cases} -\delta_c \dfrac{\cos\theta - \cos\alpha}{1 - \cos\alpha} & \text{when} \quad 0 \le \theta \le \alpha \\[2mm] \delta_t \dfrac{\cos\alpha - \cos\theta}{\cos\alpha + 1} & \text{when} \quad \alpha \le \theta \le \pi \end{cases} \tag{1}$$

where $\delta_c$ is the maximum displacement in the compressive zone ($\theta = 0$), $\alpha$ the angle defining the position of the neutral axis and $\delta_t$ the maximum displacement in the tensile zone ($\theta = \pi$).

The displacement $\delta_t$ and $\delta_c$ can be expressed as function of the rotation $\theta_j$ of the joint:

$$\delta_t = R \,(1 + \cos\alpha)\theta_j \tag{2}$$

$$\delta_c = R(1 - \cos\alpha)\theta_j \tag{3}$$

The relation between the force per unit length and the displacement is:

$$f(\theta) = k\delta(\theta) \tag{4}$$

where $k$ is stiffness coefficient per unit length; equal to $k_t$ in the tensile zone and $k_c$ in the compressive zone, respectively.

Therefore, the force applied by the tube-wall to the flange is given by:

$$f(\theta) = \begin{cases} f_c \dfrac{\cos\theta - \cos\alpha}{1 - \cos\alpha} & \text{when} \quad 0 \le \theta \le \alpha \\[2ex] f_t \dfrac{\cos\alpha - \cos\theta}{\cos\alpha + 1} & \text{when} \quad \alpha \le \theta \le \pi \end{cases} \tag{5}$$

Finally, two of behavior modes are possible for the joint:

- The bending moment is dominant and both a compressive and tensile zone develops at the junction between the tube-wall and the flange. It is therefore necessary to determine the position of the neutral axis, which depends on the loading and the relative rigidity of the tensile and compressive parts of the joint,
- The axial force is dominant and the joint is completely in compression or in tension.

The initial rotational stiffness, $S_{j,ini}$, is defined as the ratio of the bending moment divided by the rotation:

$$S_{j,ini} = \frac{M_j}{\theta_j} \tag{6}$$

This stiffness will be determined respectively in paragraph 2.1.3 and 2.1.4 for both cases described above.

### 2.1.2. Position of the neutral axis for a dominant bending moment

If the bending moment is dominant, the stress distribution comprises a compressive zone and a tensile zone as indicated in Figure 1. Considering relation (5), the axial forces generated by the compressive and the tensile stresses are given by:

$$F_{t,tot} = 2Rf_t \frac{\sin\alpha + (\pi - \alpha)\cos\alpha}{1 + \cos\alpha} \tag{7}$$

$$F_{c,tot} = 2Rf_c \frac{\sin\alpha - \alpha\cos\alpha}{1 - \cos\alpha} \tag{8}$$

The equilibrium along the tube axis gives:

$$F_{c,tot} = N + F_{t,tot} \tag{9}$$

The bending moments generated by the compressive and tensile stresses, respectively, are given by:

$$M_{j,c} = \frac{2R^2 f_c}{1 - \cos\alpha}\left[\frac{\alpha - \cos\alpha\sin\alpha}{2}\right] - R\cos\alpha F_{c,tot} \tag{10}$$

$$M_{j,t} = \frac{2R^2 f_t}{1 + \cos\alpha}\left[\frac{\pi - \alpha + \cos\alpha\sin\alpha}{2}\right] + R\cos\alpha F_{t,tot} \tag{11}$$

The total bending moment $M_j$ reads:

$$M_j = M_{j,t} + M_{j,c} + NR\cos\alpha \tag{12}$$

Finally, the bending moment has the following expression:

$$M_j = -\frac{R\cos\alpha N}{2} + R^2\left[f_c(1 + \cos\alpha)\alpha + f_t(1 - \cos\alpha)(\pi - \alpha)\right] \tag{13}$$

The previous expression depends on the angle $\alpha$ which can be determined (Couchaux, 2010) via the following equation:

$$\frac{1}{\mu} = -\cos\alpha + \frac{\sin\alpha^2\left[\alpha + m_k(\pi - \alpha)\right]}{\sin\alpha - \alpha\cos\alpha - m_k\left(\sin\alpha + (\pi - \alpha)\cos\alpha\right)} \tag{14}$$

where

$$\mu = \frac{NR}{2M_j}, \quad m_k = \frac{k_t}{k_c}.$$

Due to the fact that $\alpha$ is comprised between 0 and $\pi$, the relation (13) is valid when the absolute value of $\mu$ is less than 1. For other value of $\mu$, the flange is completely in tension ($\mu \le -1$), or completely in compression ($\mu \ge 1$).

### 2.1.3. Initial Rotational stiffness: dominant bending moment

When the bending moment is dominant, combining (2), (3), (4) and (5) yields to:

$$f_t = k_t \, R \,(1 + \cos\alpha)\theta_j \tag{15}$$

$$f_c = k_c \, R \,(1 - \cos\alpha)\theta_j \tag{16}$$

Considering relations (13), (15) and (16), the bending moment applied by the tube to the flange is:

$$M_j = \theta_j R^3\left\{(k_t - k_c)\left(\frac{\sin 2\alpha}{2} - \alpha\right) + k_t\pi\right\} \tag{17}$$

Thus the initial rotational rigidity of the joint is:

$$S_{j,ini} = R^3\left\{(k_t - k_c)\left(\frac{\sin 2\alpha}{2} - \alpha\right) + k_t\pi\right\} \tag{18}$$

This formulation depends on the angle $\alpha$, which is obtained from equation (14) and is comprised between 0 and $\pi$. Outside this range, the axial force is dominant and the joint is completely in tension or completely in compression.

## 2.1.4. Initial Rotational stiffness: dominant axial force

When the axial force is dominant, the stiffness is the same along the circumference of the joint and is equal to $k_t$ or $k_c$. The rotation is directly related to the displacement of the flange due to the bending moment.

Considering the plane cross-section assumption, the displacement $\delta$ is given by (see Figure 2):

$$\delta(\theta) = \theta_j d(\theta) = \theta_j R |\cos\theta| \qquad (19)$$

Thus, the bending moment can be obtained via relations (4) and (19):

$$M_j = 4 \int_0^{\pi/2} f(\theta) d(\theta) R d\theta = k R^3 \pi \theta_j \qquad (20)$$

The initial rotational stiffness is:

$$S_{j,ini} = k R^3 \pi \qquad (21)$$
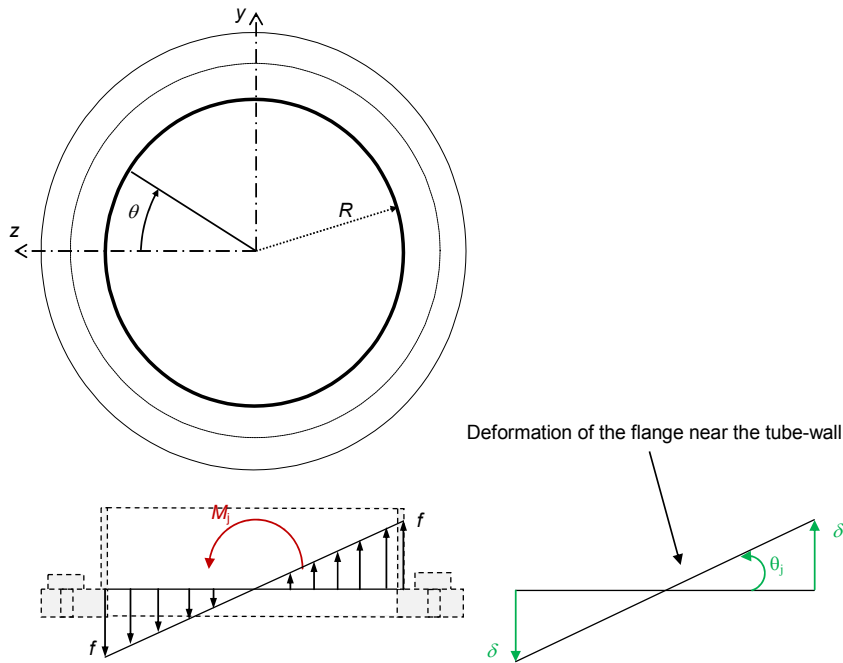


Figure 2. Deformation of the flange due to the bending moment

## 2.2. Rigidity of the compressive part

The stiffness of the compressive component corresponds to the ratio of the force applied by the tube-wall to the flange, $f_c$, and the displacement of the flange $\delta_c$. Kozlowski & Wojnar (2006) proposed a formulation based on a parametrical study for three type of welds. A theoretical solution is proposed here for full penetration butt welds (see Figure 3.a).
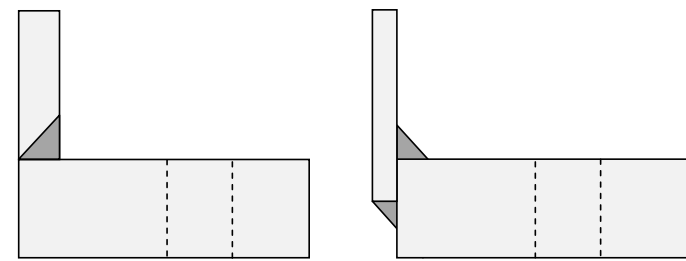


(a) Full penetration butt weld     (b) Fillet welds

Figure 3. Welds configurations

The opposite flanges in contact are modeled via the beam model proposed by Couchaux et al (2009). Stamatopoulos & Ermopoulos (2008) studied a flange subjected to a compression when the yield strength is reached at the tube-wall and proposed a form of the contact pressure base on numerical analysis:

$$p(x) = p_1 \text{ when } -t_t/2 \le x \le t_t/2$$

$$p(x) = p_1 \frac{\xi_c + t_t/2 - x}{\xi_c} \text{ when } t_t/2 \le x \le \xi_c + t_t/2$$

These expressions of the contact pressure will be considered to simplify the analytical expressions and $\xi_c$ ($\approx 0.98 \times t_f$) will be considered equal to $t_f$.
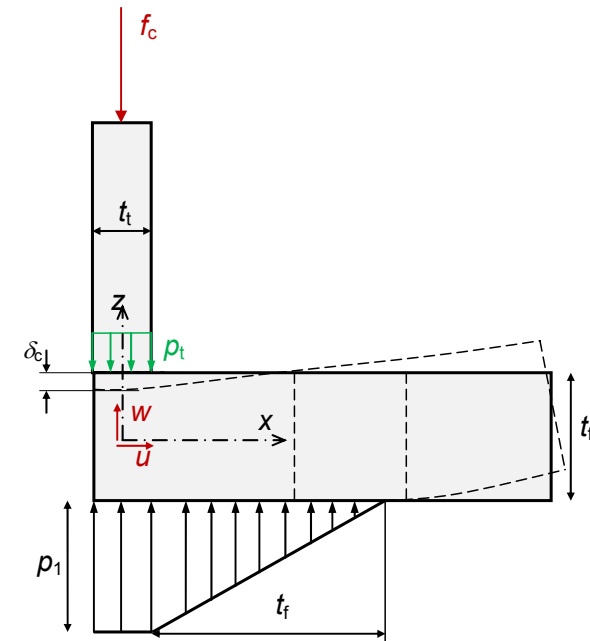


Figure 4. L-stub in compression

Hence, if the flange in contact with a rigid support is modeled via the mechanical model of Couchaux et al (2009), its transversal displacement, $w$, is:

$$w(x,z) = \frac{1}{4}\left[2z - 3\frac{z^2}{t_f} + 2\frac{z^4}{t_f^3}\right]\frac{(p_t - p_1)}{E} - \frac{p_t z}{E} - \frac{6\nu M(x)z^2}{E t_f^3} + w_0(x)$$

where $M(x)$ is the bending moment per unit length in the flange, $w_0(x)$ the transversal displacement at $z = 0$ and:

$$w_0(x) = -\frac{t_f}{32E}[13p_1 + 3p_t] + \frac{3\nu}{2E t_f}M(x)$$

Hence the stiffness is:

$$k_c = \frac{f_c}{\delta_c} = \frac{f_c}{w(0, t_f/2)} = E\frac{\lambda_t(2\lambda_t + 1)}{2\lambda_t + 1/2} \qquad (22)$$

where $\lambda_t = \frac{t_t}{t_f}$.

The application of the present model to fillet welds (see Figure 3.b) is not possible because the compression is transmitted by the two fillet welds. A formulation based on the numerical results of Kozlowski & Wojnar (2006) is proposed:

$$k_c = 100[\ln\lambda_t + 6] \qquad (23)$$

## 2.3. Stiffness of the tensile part

The stiffness of the tensile component corresponds to the ratio of the force applied by the tube-wall to the flange, $f_t$, and the displacement of the flange $\delta_t$. Two type of component can be considered depending on the flanges:

- Half a T-stub model for one bolt in presence of blank flange, the formulation of EN 1993-1-8 can be used,
- An L-stub model in presence of a ring flange. The flange is modelled via beam and is either in contact with the adjacent flange over a certain distance, $e_2$-$\xi$ or simply in contact at the free edge (see Figure 5).



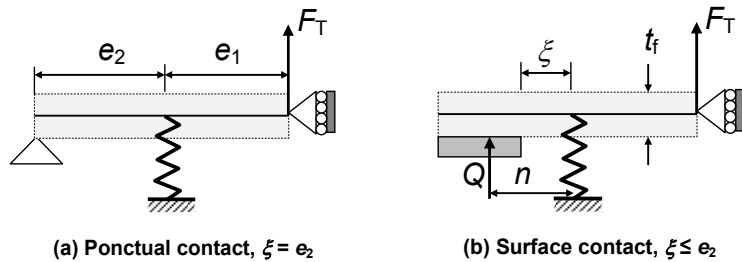**(a) Ponctual contact, $\xi = e_2$**      **(b) Surface contact, $\xi \le e_2$**

Figure 5. Contact configurations for L-stub

It has been proposed by Couchaux et al (2010) to directly determine this separation length:

$$\xi = e_2\sqrt{\frac{\alpha_{R,0}}{\alpha_R}} \le e_2 \qquad (24)$$

where $L_b$ is the tensile bolt length, calculated via EN 1993-1-8, $n_b$ the number of bolts, $A_s$ the cross section area of one bolt.

$$\alpha_R = 4\left(\frac{e_1}{t_f}\right)^3\frac{A_s}{L_b p_b}, \; p_b = \frac{2\pi R}{n_b}, \; \alpha_{R,0} = \frac{e_2/e_1 + 1}{(e_2/e_1)^3}.$$

When $\xi$ obtained via relation (24) is less than $e_2$, the flange is clamped at the end of the contact zone and the stiffness per unit length is:

$$k_t = \frac{1}{l_{eff}}\frac{1}{\dfrac{(\xi + e_1)^3}{3EI_f} - \eta\dfrac{\xi^2(2\xi + 3e_1)}{6EI_f}} \qquad (25)$$

where $l_{eff}$ is the effective length calculated via EN 1993-1-8.

$$\eta = \frac{n + e_1}{n}, \; I_f = \frac{l_{eff}t_f^3}{12}.$$

On the contrary, when the length $\xi$ is equal to $e_2$ the flange is simply in contact with his free edge and the stiffness is thus:

$$k_t = \frac{1}{l_{eff}}\frac{1}{\dfrac{L_b}{2EA_s}\left(1 + \dfrac{e_1}{e_2}\right)^2 + \dfrac{e_1^2(e_1 + e_2)}{3EI_f}} \qquad (26)$$

## 2.4. Moment rotation curve

The moment-rotation curve is defined as proposed in EN 1993-1-8 via the bending resistance and the initial rotational stiffness. The initial rotational stiffness is determined via expressions (18) and (21) given in paragraph 2.1. The bending resistance is determined via the model of Couchaux et al (2011) which consider two failure modes, ductile and non-ductile.

The constitutive law of the moment-rotation curve is:

$$M_j = \begin{cases} S_{j,ini}\theta_j & \text{when} \quad 0 \le M_j \le 2M_{j,pl}/3 \\[2mm] \left[S_{j,ini}\theta_j(2M_{j,pl}/3)\right]^{\frac{1}{\psi+1}} & \text{when} \quad 2M_{j,pl}/3 \le M_j \le M_{j,pl} \end{cases} \qquad (27)$$

In EN 1993-1-8, the value of $\Psi$ is equal to 2,7 for bolted flange joints. The bolted circular flange joints can be classified in this category. However this formulations lead to an overestimation of the rotation capacity when the failure mode is non ductile (buckling just after the elastic range). Thus a value of $\Psi$ equal to 1 is considered for non ductile failure modes.
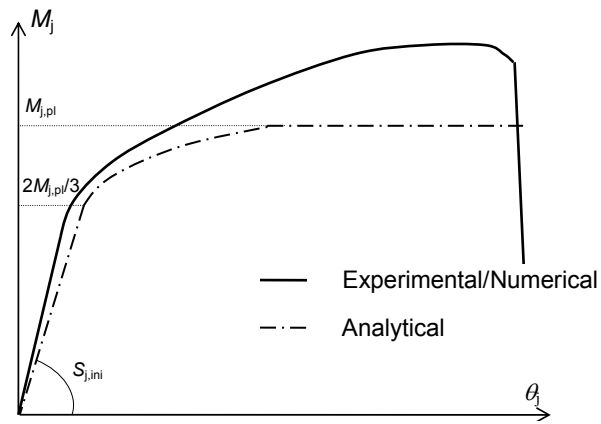
Figure 6. Analytical and experimental curve

## 3. CONFRONTATION TO EXPERIMENTAL AND NUMERICAL RESULTS

### 3.1. Numerical model

A numerical model has been developed (Couchaux et al 2011) to carry out a parametric study and to complete the available experimental results (Yamaguchi 1996, and Jakubowski, 2003). The numerical model was built using the Finite element code ANSYS V11.0 with contact and brick elements. Due to symmetry, just an half of the connection is studied. A symmetry plane cut the joint and a rotation is applied.
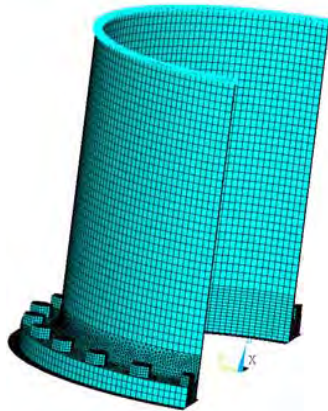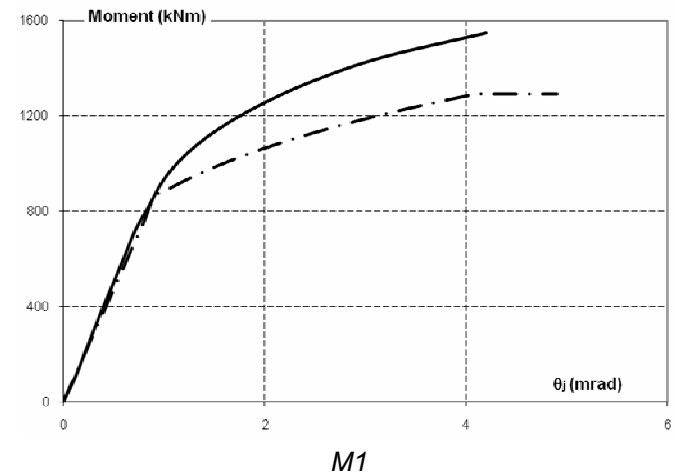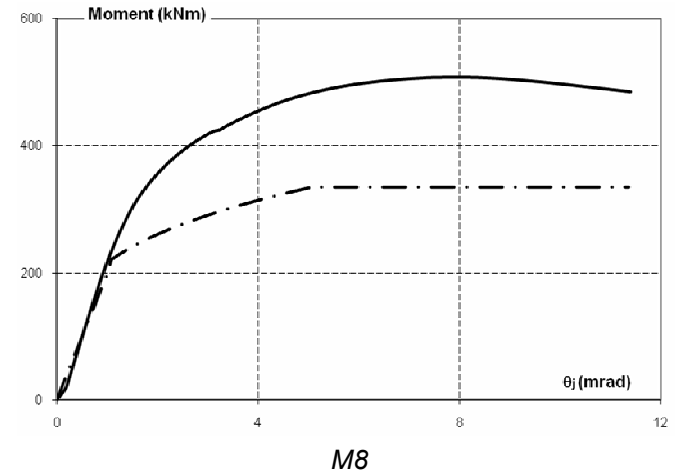


Figure 7. Finite element model

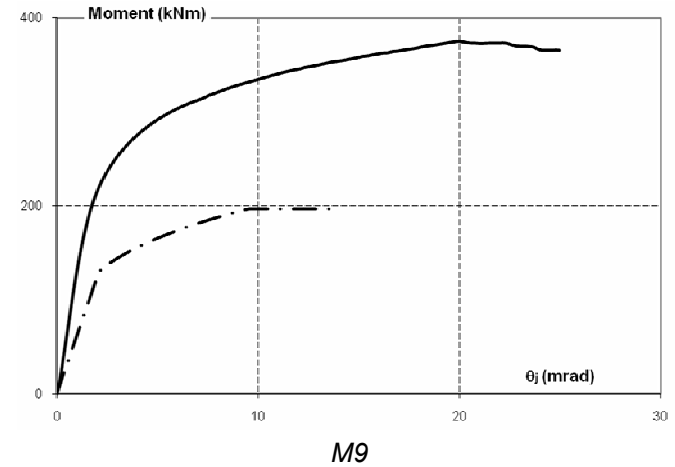### 3.2. Comparison of analytical and numerical results

The curve calculated by the analytical model for joint M1, M8, M9 and INSA (joint tested in INSA of Rennes) are compared against those obtained by numerical or experimental tests. The initial rotational stiffness is well approach by the analytical model.



*M1*



*M8*
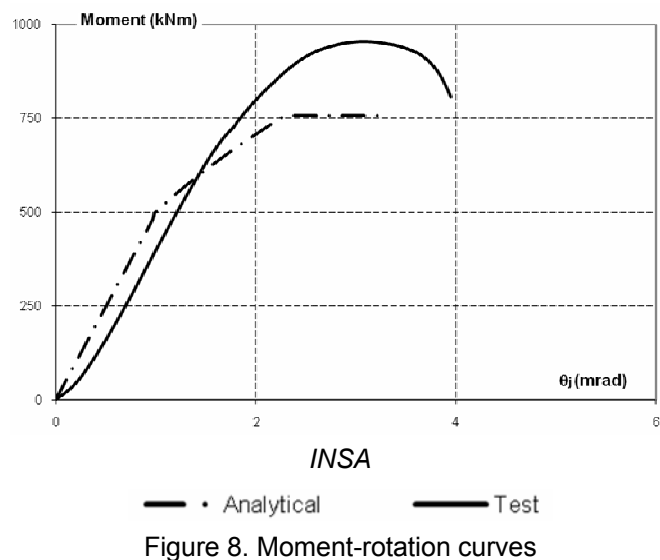


*M9*

*INSA*

— · Analytical     —— Test

Figure 8. Moment-rotation curves

For joint M9, the initial rotational stiffness is clearly underestimated. The thickness of the flange is thin and equal to 10 mm in this case. The stiffness of the tensile area, $k_t$, is evaluated without the consideration of the influence of the tube-wall which have a certain influence for thinner flanges. Furthermore, the hypothesis of planar motion of the flange is not so adequate when the flange is thin.

## 4. CONCLUSION

An analytical model has been proposed in the present paper to derive the moment-rotation curve of a bolted circular flange joint which can be calculated via the initial rotational stiffness and the bending resistance (Couchaux et al, 2011). A model, based on the component method, is proposed to determine the initial rotational stiffness. A coefficient of rigidity is evaluated for the compression area which could be used for different joint configurations. The results are compared with those of the numerical and experimental tests and quite good agreements are obtain. The rotational stiffness is underestimated in presence of thin flange. Finally, the present model could be applied to determine the initial rotation stiffness of circular base plate joint.

## REFERENCES

[1] Bourrier, M., Lefeuvre, M., (1976), anchorage of chimney, *Revue Construction Métallique*, Vol. 13 (3), (pp. 66-70), (in french).

[2] Couchaux, M., Hjiaj, M., Ryan, I., Bureau, A., (2009), Effect of contact on the elastic behaviour of bolted flange connections, *11th Nordic Steel Construction Conference*, Malmö, Sweden.

[3] Couchaux, M., (2010),Behaviour of bolted circular flange joints, PhD Thesis, INSA of Rennes, (in French).

[4] Couchaux, M., Hjiaj, M., Ryan, I., (2010) Static Resistance of bolted circular flange joints under tensile force, *Proc. 13st International Symposium on tubular structures*, Hong-Kong, Vol. 1, (pp. 27-35).

[5] Couchaux, M., Hjiaj, M., Ryan, I., Bureau, A., (2011) Resistance of bolted circular flange joint subjected to bending moment and axial force, *Eurosteel 2011, 6th conference on steel and composite structures*, Budapest, Hungary, (pp. 219-224).

[6] EN 1993-1-8-2005. European Committee for Standardization – CEN. Eurocode 3: Design of steel structures. Part 1.8: Design of joints, Brussels.

[7] Igarashi, S., Wakiyama, K., Inoue, K., Matsumoto, T., Murase, Y. (1985), Limit design of high strength bolted tube flange joints: Part 1. Joint without rib-plates and ring-stiffeners, *Journal of structural and construction engineering, Transactions of AIJ*, Vol. 354, (pp. 52-66), (in Japanese).

[8] Jakubowski, A., Schmidt, H., (2003), Experimentelle Untersuchungen an vorgespannten Ringflanschstössen mit Imperfektionen, *Stahlbau*, Vol. 72 (3), (pp. 188-197), (in German).

[9] Kozlowski, A., Wojnar, A. (2006), Mechanical model for assessment of the stiffness of bolted flange joint, *Proceedings of the XIth International Conference on metal Structures*, Rzeszow, Poland.

[10] Kozlowski, A., Wojnar, A., (2008), Initial stiffness of flange bolted joints and their influence on the behaviour of steel chimneys, *Eurosteel 2008, 5th conference on steel and composite structures*, Graz, Austria, (pp. 663-668).

[11] Stamatopoulos, G., Ermopoulos, J., (2008), Interaction curve for non-preloaded bolted connections in tubular members, *Eurosteel 2008, 5th conference on steel and composite structures*, Graz, Austria, (pp. 657-662).

[12] Yamaguchi, T., (1996), Fundamental study on high strength bolted tensile joints, Dissertation of the Faculty of Engineering of Kyoto University.

# FRICTION STIR WELDING OF STEEL CONNECTIONS

Andrea E. Surovek

*Department of Civil and Environmental Engineering, SDSM&T, Rapid City, SD USA*
*surovek@sdsmt.edu*

Bharat K. Jasthi, Christian A. Widener

Arbegast Materials Processing and Joining Lab, SDSM&T, Rapid City, SD USA
*Bharat.Jasthi@sdsmt.edu, Christian.Widener@sdsmt.edu*

## ABSTRACT

Friction Stir Welding (FSW) is a relatively recent addition to joining technology, having been developed in the early 1990's by The Welding Institute (TWI) in the UK. FSW is a solid state process that has been shown to have many benefits over traditional arc welding, particularly in the areas of joint quality and environmental impacts. While the technology readiness level of FSW of aluminum has reached a stage where it has been employed by multiple industries, most notably in shipbuilding, transportation, and aerospace industries, FSW of steel has not achieved the same level of industrial readiness. FSW remains relatively unknown in the area of civil engineering structures.

This paper will provide an overview of the FSW process with a particular emphasis on current advancements in the area of steel FSW. Examples of joint configurations, materials welded, and resulting microstructures and properties will be provided from the literature and ongoing investigations at the Arbegast Materials Processing and Joining Laboratory, a member of the Center for Friction Stir Processing (CFSP), an NSF Industry/University Cooperative Research Center (I/UCRC), founded by the South Dakota School of Mines and Technology. In addition, the paper will provide potential applications for FSW in the civil engineering / structural arena.

## 1. INTRODUCTION

Structural steel connections are traditionally comprised of a combination of bolted and/or welded elements. The mild steels used in structural applications are considered to be reasonably easy to weld, whether in the shop or in the field. However, for steel to remain competitive among rapid advances in other materials, including composites, advances in other joining technologies can be examined to establish when special processes may offer an advantage over traditional arc welding.

A workshop on innovations in steel design was held on March 28, 2012 to develop a list of potential innovations and research needs to advance steel design in the new millennium (Surovek and Liu 2012). Example questions that were asked of the participants included:

- What do you see as the most important near future advances in steel design?
- What basic knowledge do we need to advance steel design to the next level of innovation?
- What technologies would help improve steel design?

From the workshop emerged six overarching themes, one of which was the development of novel and/or improved joining methods. Included in the ideas generated on joining methods were new welding methods and reduced requirements for weld inspection. Because weld inspection compromises a large time and labour requirement in construction a method that produces defect free welds could provide significant cost and time saving in construction.

One potential avenue for such advances in steel fabrication and joining technology is friction stir welding (FSW), a solid state welding process originally developed by the Welding Institute for welding aluminum (Thomas et. al. 1991). Early research in FSW focused on metals with low to moderate melting temperatures with an emphasis on aluminum welding. Based on this research and applications of FSW in industry, FSW has been shown to have a number of advantages over traditional arc welding (Arbegast 2006). Friction stir welding is revolutionizing the welding of aluminum in industry (Thomas et. al. 2002), due to allowing welding of alloys that could previously only be joined by mechanical means such as rivets (Dracup and Arbegast 1999).

Research on FSW of steel has primarily been centered on industry driven applications with an emphasis on specialized steel alloys and stainless steels. As the technology becomes more commercially viable, knowledge of its application to traditional structural steels has the potential for application in steel construction; for example, FSW of steel could broaden the potential grades and combinations of steels used in structural applications, because FSW is particularly suitable to join highly dissimilar materials. By expanding options for fabrication of steel members with the potential for increased fatigue strength and a reduction in residual stresses, FSW could provide new avenues for steel construction.

It is also worth noting that one of the four identified discussion areas at the innovations workshop was sustainability. Sustainability and green construction continue to gain ground as being considered necessary advancements in steel construction, so knowledge on construction techniques such as FSW that have reduced environmental impact will be beneficial to the industry as a whole.

## 2. FRICTION STIR WELDING

The South Dakota School of Mines and Technology (SDSM&T) is home to the Arbegast Materials Processing and Joining Laboratory, a world leader for research and development in the emerging FSW and friction stir processing (FSP) technologies. As one of the founding members of the National Science Foundation (NSF) sponsored Industry/ University Collaborative Research Center (I/UCRC) on FSP, SDSM&T is focused on developing large scale structural applications for FSW as well as design guidelines for structural members fabricated using FSW. The focus of the center to date has been on FSW of both ferrous and non-ferrous alloys and built-up shapes based on industry driven desires and potential military applications. SDSM&T is home to one of the most versatile and capable friction stir weld systems in any academic institution (see Figure 1).
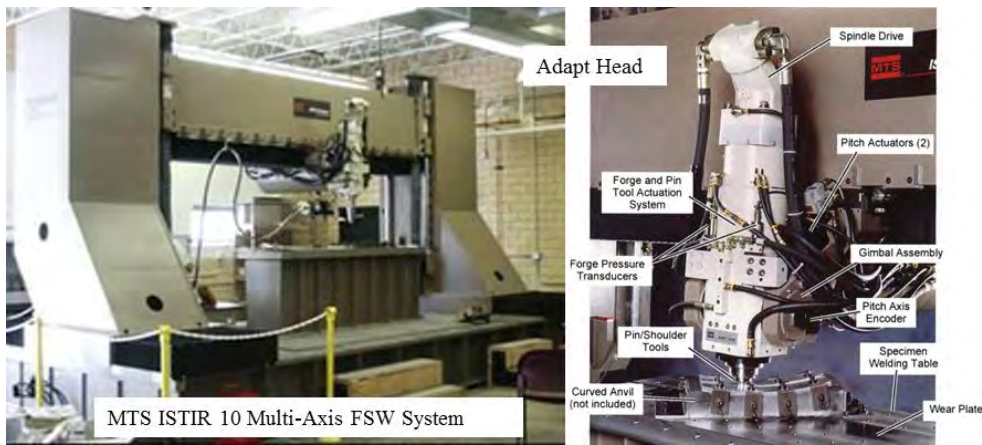
Figure 1. SDSM&T Friction Stir Welding Tool



Figure 2. Typical butt joint being created by friction stir welding.

FSW is a solid state joining process that has been described as one of the most significant advances in joining technology in last fifty years (OSTP 1995). This process uses a rotating tool with a combination of a pin which penetrates the material and a shoulder that travels over the surface as the "pin tool" traverses along a weld joint or simply through the material using modified milling equipment, firm fixturing tooling, and backside supports (weld anvil). The material around the pin tool is frictionally heated, plasticized and extruded/forged to the back of the pin tool where it consolidates and cools under hydrostatic pressure conditions. Since it is a solid-state process, there is no liquid to solid phase change, and all of the defects that are associated with the melting and re-solidification of conventional welding (e.g. hot cracking and porosity) are not present. Creation of a typical butt joint using the friction stir process is shown in Figure 2. A longitudinal diagram of the FSW process showing the metal working steps that the material experiences as tool advances was developed by Arbegast in 2003, and is shown in Figure 3. The figure shows that, rather being a true welding process, FSW is really a localized extrusion and forging process; however, the resulting weld zone, like fusion welding, does typically form a heat-affected-zone, or HAZ, as shown in Figure 4. Unlike fusion welding, though, there is also a thermo-mechanically affected zone, which is a partially deformed transition zone between fully reworked and recrystallized material within the weld nugget and heat affected material surrounding the weld zone.

At a prototype level, FSW has been used to manufacture butt welds, overlap welds, T-sections, fillet, and corner welds in aluminum (see Fig. 5). The FSW process can also cope with circumferential, annular, non-linear, and three-dimensional welds. Since gravity has no influence on the solid-phase welding process, it has been successfully demonstrated for use in all positions including horizontal, vertical, overhead and orbital. The potential to develop complex structural shapes can be seen in Figure 6, in which the stiffened shape has been fabricated with friction stir welds on three sides and in multiple orientations. FSW is even possible under water, or in the presence of liquid contaminants, because the high forging pressures in the weld zone expel any liquids as the tool advances, preventing entrapment of contaminants in the weld zone.
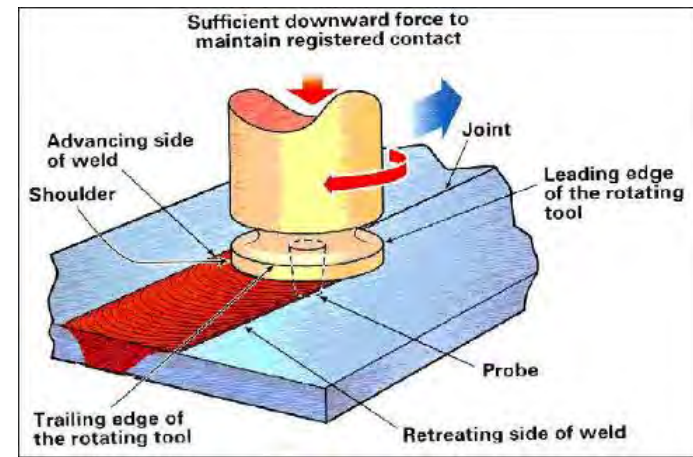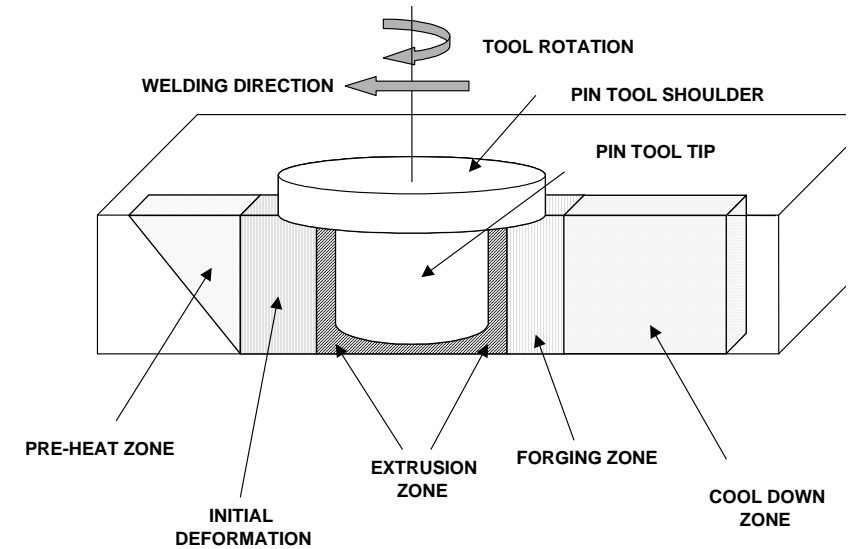


Figure 3. Longitudinal diagram of the FSW process showing the five principle steps in the process (Arbegast 2003).
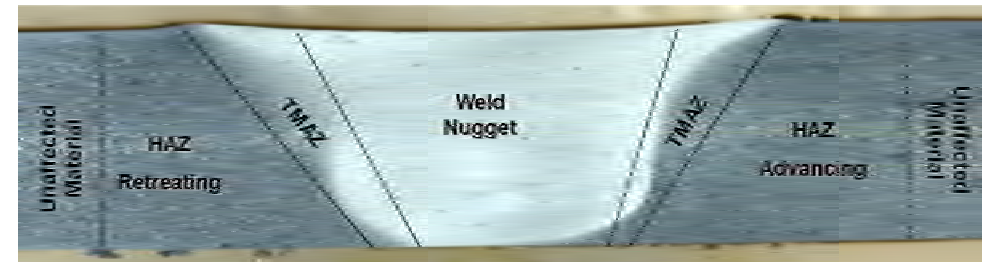


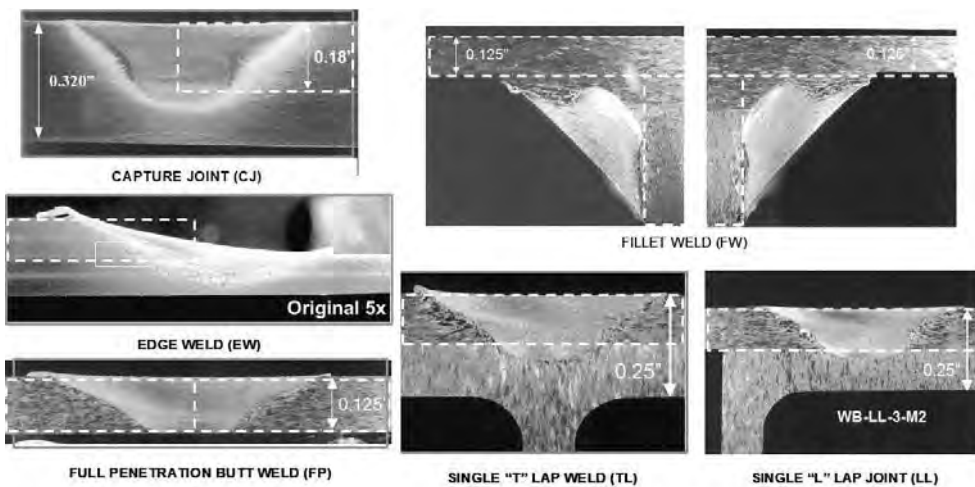Figure 4. Typical friction stir weld nugget indicating weld zones (shown in aluminum).

Figure 5. Typical Friction Stir Weld Joints in Aluminum



Figure 6. Front, side and rear views of a fabricated shape using multiple orientations of friction stir lap welds (location of welds indicated by arrows).

FSW has shown simpler processing, higher strength, higher toughness, fewer weld defects, more predictable microstructure, lower residual stresses, and less distortion as compared to the traditional methods (Arbegast and Hartley 1998). The primary reasons for the improvement in properties is that FSW produces wrought microstructure, rather than cast (no re-solidified liquid weld pool), with very fine grain size (typically between 1 – 5 um), significantly less heat input, and no liquid to solid phase changes. It has become an accepted replacement technology for fusion welding (VPPA, GTAW, GMAW) of aluminum alloys because the process allows the welding of previously un-weldable aluminum alloys, like 2XXX and 7XXX series alloys, and even dissimilar alloy welding. Traditionally, these alloys have found use only in mechanically joined structures (Dracup and Arbegast 1999). Friction stir welding is considered to be revolutionizing the welding of aluminum in industry (Thomas et. al 2002). FSW can weld aluminum alloys, as well as welding combinations of wrought, extruded and cast alloys that have not previously been possible.

The impact of FSW on the aluminum industry presents a strong argument for greater development of FSW of steel. Basic research and applications research has reached the point in Aluminum FSW that it is being actively used in industrial applications. Examples of industries currently using FSW of aluminum include aerospace, civil aviation, shipbuilding, railroad, bridges, automotive, and architectural.

## 3. FRICTION STIR WELDING RESEARCH ON MILD STEELS

The earliest research in FSW was focused on low to medium softening temperature metals, such as aluminium, lead, magnesium and zinc. Thomas (1999) first demonstrated the feasibility of friction stir welding of steels, a high softening temperature material, and much of the research since the initial feasibility studies has focused on development of appropriate pin tools and the effect of FSW on steel microstructure (e.g. Jashti et. al 2005 Ramasubramanian et. al 2005, Leinert et al 2003 and Steel et al 2005.)

In Thomas' original study, defect free welds of equal strength to the base material were made on 12mm thick sheets of low carbon, 12% chromium alloy steel using a two pass approach. Failure of the joint occurred in the parent metal and not in the heat affected zone of the weld. The primary difficulty encountered is that the pin tools, an essential part of the FSW process, had to be replaced after approximately four metres of weld length. Ozekcin et. al (2004) performed a microstructural examination of welds made in X80 and L80 API-grade steels, which have significantly different chemical make-up, and found that both could be successful friction stir welded with no defects. They also determined that properties of the weld such as hardness could be modified based on the process parameters used when welding the materials. Studies on welding of T-joints in ASTM A36 steel (Steel et al 2005) produced fully consolidated welds, but NDT detected a defect in the form of a ligament on the interfaces of the vertical and horizontal members. With changes in the weld parameters, including rotational speed of the tool, defects were reduced in the weld. The researchers anticipated that the defects could be eliminated with additional work on optimizing process parameters and joint configuration.

Of particular importance in the development of FSW of steel has been the research on tool materials and process improvements. Important tool material qualities include elevated temperature strength and stability, wear resistance, tool reactivity, fracture toughness and thermal expansion. Tungsten and tungsten-rhenium tools were initially studied, but durability of the pin tool proved to be a problem. Subsequent research into tool materials for high melting temperature alloys has developed polycrystalline cubic boron (PCBN) tools, and Tungsten and Molybdenum based metal matrix composite alloys for pin tools. Current development of these tools has allowed for welds up to 12mm thick and for weld lengths that are sufficient for commercial development (Fuller 2007).

## 5. POTENTIAL APPLICATIONS AND IMPACT

Perhaps the most promising application of FSW in steel lies in the potential for joining high strength steels, since high strength steels are being used more and more frequently in civil engineering applications. Significant cost savings have been achieved using higher strength steels, such as ASTM A913 Gr 65, in numerous building

www.steelconstruct.com

and bridge projects in the US (Axmann 2003), and ultra high strength steels, such as H-SA 70 ($F_y$ = 700 MPa) are be used in seismic and high-rise construction in Japan. Other common applications include off-shore oil platforms and long-span building structures. While mild carbon steels (e.g. ASTM A36 and A992) are considered easy to weld using conventional arc welding techniques, difficulties in high strength steel welding have been reported. For example, Lawlor (2000) discussed the difficulties and careful consideration required in joining high strength steel (EN10210, Fy = 460 MPa) as well as joining 460MPa to 350 MPa steel. Special attention to preheating and heat input during the process was required. In that project, high strength steels were necessary for a long span retractable roof to lower the weight of the support structure and to facilitate retraction of the roof. The offshore industry is making significant use of high strength steels, and it has been estimated that over 50% of the expense of building a platform lies in the cost of forming and welding (Billingham et al 2003). Another potential advantage of FSW over arc welding, even in mild carbon steels, is a reduction in weld distortion as compared to traditional fusion welds. For longer welds and especially in thinner material, where residual stress is more likely to manifest as significant distortion, this can be particularly advantageous.

Currently, FSW is impacting the steel pipe industry (Defalco and Steel 2009). Portable FSW equipment developed specifically to produce orbital welds can now be used for field welding of steel pipe. The reported savings in energy for using FSW is over 80%. Defalco and Steel enumerate a number of advantages for FSW in steel pipe welding including (but not limited to) time savings due to the use of single-pass full-penetration welds with no root pass required, significantly lower costs, elimination of the need for skilled welders, low distortion, adaptability to external environmental conditions, and reduction in defects. With reported challenges in welding of hollow steel sections (HSS) (Packer and McFadden 2012) FSW could be considered for welding HSS given its ability to produce low distortion, single pass welds of up to and beyond 13mm (½ inch) in thickness.

A compelling argument for greater development and application of FSW of steels lies in the potential economic and environmental impacts. Arbegast (2007) reports two sets of data that provide a compelling argument for the increased development of FSW. First, the US industry could see a benefit of nearly $5 billion dollars due to the improved weld properties, reliability and environmental benefits of FSW. Second, FSW could provide a reduction of 500 million pounds per year of greenhouse gas emissions over traditional joining methods if FSW were used for only 10% of the US market. In the original study on feasibility of FSW in steel, Thomas (1999) performed a cost analysis that included both cost of labor and consumables and determined a savings of a factor of 3 or greater could be achieved with FSW over traditional fusion welding. However, problems with tool wear have slowed more rapid implementation of FSW in steel. Currently there are two primary weld tool materials choices for steel, ceramic tools like polycrystalline cubic boron nitride (PCBN), and refractory tool materials like tungsten-25% rhenium alloy tools. PCBN tools are known to have excellent wear resistance but at a high cost with poor fracture resistance. Refractory tool materials on the other hand, have higher fracture resistance, but with less wear resistance; however, where PCBN tools must be scrapped when

they break, refractory tools can be re-machined. As reported in Rai et. al (2011), the cost of tools like PCBN may prove to limit the cost effectiveness of FSW of steels until the tool cost can be reduced. As with any developing technology, it is anticipated that the cost of the tools will reduce as the research advances and the technology matures.

In addition to the previously mentioned positive environmental impact of replacing arc welding with FSW, another advantage is the reduction of hazardous fumes currently produced by arc welding. Sorensen and Nelson (2007) report on a study at Rockwell that did a side-by-side comparison of arc welding and FSW to determine the hazardous fumes produced by each process. This is significant considering anticipated changes in OSHA regulations regarding hexavalent chromium emissions. The FSW process produced both hexavalent chromium and manganese well below detectable levels and in the case of manganese, 3 orders of magnitude below the arc welding process.

## 6. CONCLUSIONS AND GENERAL RECOMMENDATIONS

FSW represents a significant advancement in joining technology and has the potential to replace traditional arc welding for many applications. It has been shown to produce welds of higher quality with no defects, reduced cost and lower environmental impact when compared to traditional fusion welding of steels. Current applications in pipe and offshore industries and studies on high strength steels provide evidence of potential for civil engineering applications. While additional advances are required in processes and pin tools to ensure economic viability in industrial applications, FSW could prove to fulfil one of the predicted needs for innovation in steel design and construction.

## REFERENCES

[1] Arbegast, William and Hartley, Paula (1998), "Friction Stir Weld Technology Development at Lockheed Martin Michoud Space Systems – An Overview," *Proceedings of the 5th International Conference on Trends in Welding Research*, Pine Mountain, GA., June.

[2] Arbegast, W.J. (2003), "Modeling Friction Stir Joining as a Metalworking Process," Hot Deformation of Aluminum Alloys III, TMS Annual Meeting, San Diego, CA, 2-6 March, 2203, pp. 313-327.

[3] Arbegast, William (2006), "Friction Stir Welding – After a Decade of Development", *Welding Journal*, Vol. 85, No. 3, p 28-35.

[4] Arbegast, William (2007), "Chapter 6: Application of Friction Stir Welding and Related Technologies," in Mishra and Mahoney (eds.), *Friction Stir Welding and Processing*, ASM International, Materials Park, OH 272-308.

[5] Axmann, Georges (2003), "Steel Going Strong," *Modern Steel Construction*, AISC, January.

[6] Billingham, J., Sharp. J.V., Spurrier, J., Kilgallon, (2003), "Chapter 5. Fabrication and Welding" in *Review of the Performance Of High Strength Steel Used Offshore*, Research Report 105, Health and Safety Executive, HSE Books, Suffolk UK, 117 pp.

[7] Block, F., Burgess, I. Davison, B. and Plank, R.J. (2007), "The development of a component-based connection element for end-plate connections in fire". *Fire Safety Journal*, vol. 42(6-7) (pp. 498-506).

[8] Defalco, Jeffrey and Steel, Russell (2009), "Friction Stir Process Now Welds Steel Pipe," Welding Journal, American Welding Society, Vol. 88, No. 5, 44-48.

[9] Dracup, B.J. and Arbegast, W.J. (1999), Friction stir welding as a rivet replacement technology, *Society of Automotive Engineers Annual Conference*, paper 1999-01-3432, Oct. 1999, Nashville TN.

[10] Fuller, Christian (2007), "Chapter 2. Friction Stir Tooling: Tool Materials and Design," in Mishra, R. and Mahoney, M. (eds.), *Friction Stir Welding and Processing*, ASM International, Materials Park, OH, p 7-36.

[11] Jashti, B., Howard, S., Arbegast, W., Grant, G., Koduri, S. and Herling, D. (2005), "Friction Stir Welding of MA 957 Oxide Dispersion Strengthened Ferritic Steel, Proceedings of the TMS Annual Meeting, San Francisco, CA, February.

[12] Konkol, P.J., Mathers, J.A., Johnson, R. and Pickens, J.R. (2003), "Friction Stir Welding of HSLA-65 Steel for Shipbuilding," Journal of Ship Production, Vol. 19, No. 3, August, pp. 159-164.

[13] Lienert, T.J., Stellwag, W. L., Grimmett, B. B., and Warke, R. W., "Friction Stir Welding Studies on Mild Steel," *Welding Research: Supplement to the Welding Journal*, January, pp 1-S to 9-S.

[14] Lienert, T.J., Stellwag, W.L., Grimmett, B.B., and Warke, R.W. (2003), "Friction Stir Welding Studies on Mild Steel," Welding Research: Supplement to the Welding Journal, January, pp 1-S to 9-S.

[15] Office of Science and Technology Policy (OSTP). (1995), *National Critical Technologies Report*. Washington, DC: National Critical Technologies Panel, Chapter 6, p 5.

[16] Ozekcin, A., Jin, H.W., Koo, J.Y., Bangaru, N.V., Ayer, R., Vaughn, G., Steel, R. and Packer, S. (2004), "A Microstructural Study of Friction Stir Welded Joints of Carbon Steels" International Journal of Offshore and Polar Engineering, Vol. 14, No. 4.

[17] Packer, J.A. and McFadden, M. R. (2012), "Welding of Hollow Steel Sections," *Modern Steel Construction*, AISC, April.

[18] Ramasubramanian, U., Tweedy, B. and Arbegast, W. (2005), "Friction Stir Processing of Ferrous Alloys Using Induction Preheating," Proceedings of the TMS Annual Meeting, San Francisco, CA, February.

[19] Steel, Russell J., Nelson, Tracy W., Sorensen, Carl D. and Packer, Scott, M. (2005), "Friction Stir Welding of Steel T-joint Configurations," Proceedings of the Fifteenth International Offshore and Polar Engineering Conference, Seoul, Korea, June.

[20] Sorensen, Carl and Nelson, Tracy W, (2007), "Chapter 6: Friction Stir Welding of Ferrous and Nickel Alloys," in Mishra, R. and Mahoney, M. (eds.), *Friction Stir Welding and Processing*, ASM International, Materials Park, OH, p 111 – 122.

[21] Surovek, Andrea and Liu, Judy, (2012), "Innovation in Design of Steel Structures: Research Needs for Global Competitiveness," *Modern Steel Construction*, AISC, April.

[22] Thomas, W. M., (1999) "Friction Stir Welding of Ferrous Materials; A Feasibility Study," *Science and Technology of Welding and Joining*, Vol. 4, No. 1, P 1-11.

[23] Thomas, WM; Nicholas, ED; Needham, JC; Murch, MG;Temple-Smith, P;Dawes, CJ. (1991), *Friction-stir Butt Welding*, GB Patent No. 9125978.8, International patent application No. PCT/GB92/02203, (1991)

[24] Thomas, W.M., Nicholas, E.D., Watts, E.R. and Staines, D.G. (2002). "Friction based welding technology for aluminum.", *The $8^{th}$ International Conference on Aluminium Alloys,* Cambridge, UK.

# EXPERIMENTAL BEHAVIOUR OF HEATED COMPOSITE STEEL-CONCRETE JOINTS SUBJECT TO VARIABLE BENDING MOMENTS AND AXIAL FORCES

Cécile Haremza, Aldina Santiago, Luís Simões da Silva
*ISISE - Department of Civil Engineering, University of Coimbra, Portugal*
*haremza@dec.uc.pt; aldina@dec.uc.pt; luisss@dec.uc.pt*

## ABSTRACT

Seven experimental tests performed at the University of Coimbra on a two dimensional composite steel-concrete beam-to-column sub-frame are presented in this paper. These experimental tests were part of a global study of the robustness of composite steel-concrete open car park buildings subject to fire. The tested sub-frame was extracted from a real composite open car park building, keeping the cross-section dimensions of the beams (IPE 550) and the columns (HEB 300), and using bolts M30 grade 10.9 in the composite connection; this sub-frame was subject to mechanical (bending and axial forces) and thermal loadings (constant temperature equal to 20ºC, 500ºC or 700ºC; or linear increase up to 800ºC). The interaction between the bending moment and axial loads in the heated internal joint after the loss of the column is the objective of the tests. In order to reach this goal, the effect of the axial restraint to beam was simulated: three tests were performed without any restraint to the beam, two tests with total axial restraint to the beam and two tests with a realistic axial restraint to the beam (spring restraint). The behaviour of the internal beam-to-column joint is investigated and discussed in detail.

## 1. INTRODUCTION

Since the partial collapse of the Ronan Point apartment in London in 1968, and the recent collapse of the WTC towers in 2001, the robustness of steel and composite steel-concrete structures has been much investigated. Progressive collapse of buildings were addressed in the design codes (UK Building Regulations, Eurocodes, US codes, …); Eurocode 1 part 1.7 (EN1991-1-7: 2002) describes principles and application rules for the assessment of accidental actions on buildings and bridges (impact forces, actions due to internal explosions, actions due to local failure from an unspecified cause). In this code, the robustness is defined as the ability of a structure to withstand events like fire, explosions, impact or the consequences of human error, without being damaged to an extent disproportionate to the original cause. Annex A from Eurocode 1 part 1.7 provides rules and methods for designing buildings with an acceptable level of robustness to sustain localised failure (due to an accidental event) without a disproportionate level of collapse. However, in most of the cases, only a very few practical guidelines on how to achieve this goal are provided, and even basic requirements to fulfil are not clearly expressed (Jaspart *et al.*, 2007).

The European RFCS ROBUSTFIRE project (Demonceau *et al.*, 2012) focused on the study of the robustness applied to steel and composite open car park structures under fire. The research significance of this study was justified by the growing number of cars in Europe during the last decades, as well as the number of large shopping centres, airports and railway stations that considerably increased the number of car park buildings (Le Pense, 2002). Nowadays, part of these car parks are built above the ground ("open" car parks) because of a lower price per parking place, lower energy consumption, use of natural light, and natural ventilation. Consequently, an easy and low cost way for the construction of open car park buildings is to use a composite steel-concrete structure. However, the increase of the market share for steel and composite car parks in Europe is somewhat limited by the lack of information on how these structures behave under exceptional localised fire (the large natural ventilation in this kind of buildings keeps the fire localised to the ignition zone). A philosophy aiming at the economical design of car parks exhibiting a sufficient robustness under localised fire was developed in the present project, and practical design guidelines for the application of this design philosophy throughout Europe were derived (Demonceau *et al.*, 2012). In order to reach this goal, experimental, numerical and analytical works were developed. The work presented in this paper is focused on experimental work package of this research project.

## 2. EXPERIMENTAL TESTS

### 2.1. The experimental programme

The interaction between the bending moment and axial loads in the heated internal joint after the loss of the column is the objective of the tests. The effect of the localised fire (that led to the column loss) was simulated by the application of elevated temperatures in the composite joint zone. The temperatures considered in these tests were based on previous observations: in the past, real tests performed in composite steel-concrete open car park buildings subject to burning cars showed that the beam bottom flanges temperature was lower than 500ºC (Jaspart *et al.*, 2008); however temperatures of 700ºC were measured in recent tests performed in France (Joyeux *et al.*, 2002), probably due to the manufacture evolution of cars, with more combustible plastic materials as well as higher petrol tank capacity. Seven beam-to-column sub-frames were tested in the University of Coimbra: one reference test at ambient temperature; five tests at 500ºC or 700ºC; and a demonstration test, for which the sub-frame was subject to an increase of the temperature up to the failure of the column. The effect of the axial restraint to beam coming from the unaffected part of the building was also studied: three tests without beam axial restraint; two tests with total beam axial restraint; and two tests with realistic beam axial restraint (Figure 1).
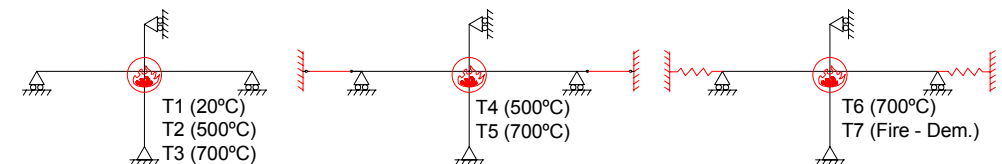


Figure 1. Seven experimental tests

## 2.2. Sub-frame and testing arrangement

A typical open car park structure was specially designed for the European ROBUSTFIRE project (Demonceau *et al.,* 2012). This building was defined as the most common as possible in order to obtain, at the end of the project, general design rules for such structures, ensuring sufficient robustness under fire conditions. The selected structure was a braced open car park building with eight floors of 3 m height, composite slabs, composite beams and steel columns. The tested sub-frame was selected from the fifth floor of this real car park building; however, because of the laboratory dimensions, the beam length was reduced from 10 m in the real building to 3 m in the tested sub-frame. The sub-frame was defined by two unprotected composite beams IPE 550 steel cross-sections, grade S355, and one unprotected HEB 300 cross-section steel column, grade S460 (Figure 2). A reaction frame, perpendicular to the plane of the sub-frame, was used to fix the hydraulic jack, which was linked by a pin to the top of the column. The column base was hinged and fixed to a reinforced concrete footing. The hydraulic cylinder located at the column base (except for the last test 7) simulated the progressive loss of the column (by decreasing the oil pressure). A smaller steel profile HEB 140 cross-section was used at the bottom column in order to allow: i) the concreting of the specimens (the composite sub-frames were located at the floor level), ii) the simulation of the column loss under fire in test 7 (buckling failure). The column was restrained at the top of the joint and at the bottom column (column restraint in Figure 2). This restraints system avoided any horizontal displacement or rotation in the plane or out of the plane of the sub-frame.
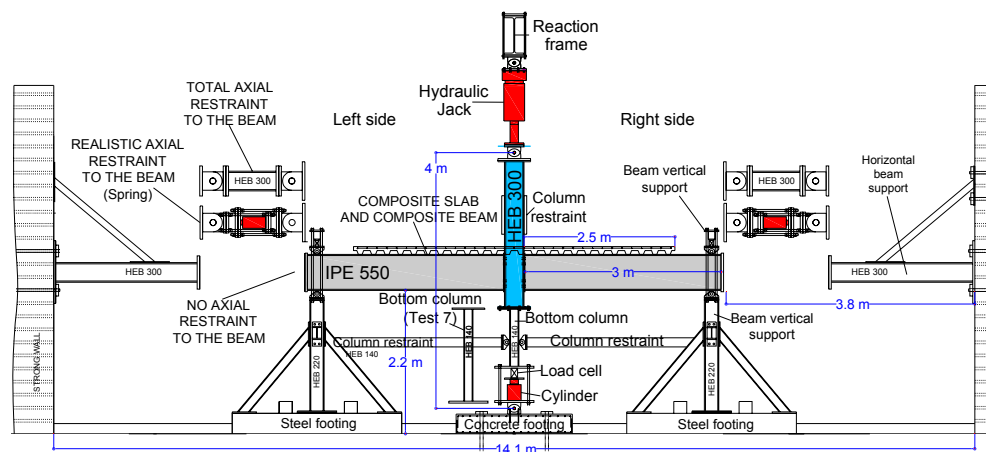


Figure 2. General layout, longitudinal view

The steel beam was fully connected to the 130 mm thickness composite slab by 22 shear studs (diameter = 19 mm; height = 100 mm). The composite joint, with the bolts M30 grade 10.9 is shown in Figure 3. In order to ensure the composite behaviour of the beam-to-column connections, ten steel rebars of diameter 12 mm were placed in the composite slab (five at each side of the column).
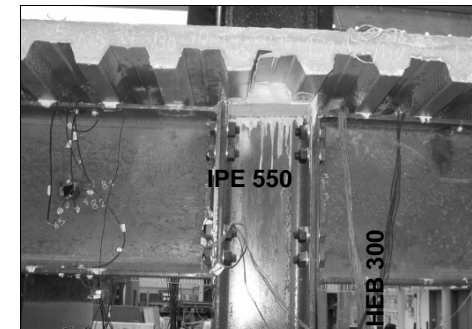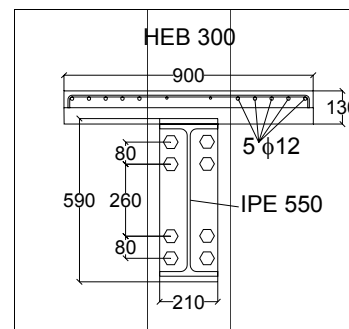


Figure 3. Tested joint

## 2.3. Description of the loading sequence

The tests 1 to 6 were performed under constant temperature and they were divided into 3 main steps: *step 1* - application of an initial hogging bending moment in the joint as in the real car park (-450 kNm in test 1 at ambient temperature, and -236 kNm in tests 2 to 6, as defined in Demonceau *et al.* (2012); *step 2* - heating of the joint zone with a linear rate of 300ºC/hour (up to reach 500ºC or 700ºC in beams bottom flanges); and *step 3* - simulation of the progressive loss of the column and increase of the joint sagging bending moment (by increasing the vertical load at the column top) up to the failure of the joint under constant temperature.

The test 7 (demonstration test) simulated the loss of the column due to the increase of temperatures under constant loading. This test was divided into 4 steps: *step 1* - application of an initial hogging bending moment in the joint (-236 kNm); *step 2* - application of a constant compression load at the column top (+250 kN). Due to the capacities of the loading and measuring equipment, the steel section of the bottom column was reduced from HEB 300 to HEB 140 in order to reach the column buckling failure under 800ºC or less when it is subject to the 250 kN at the column top; *step 3* - heating of the joint zone and the bottom column, respectively up to 400ºC (measured in the beam bottom flanges) and 800ºC (the column should failed under lower temperatures), under faster heating rate in the bottom column. The joint temperature was limited to 400ºC in order to avoid the joint failure before the collapse of the column; this value was defined taking into account the constant temperature tests: at 500ºC, the load at the column top reached maximum 400 kN in test 2, and under 700ºC, it reached 200 kN; moreover, additional compression load due to thermal expansion effects should be considered; *step 4* - heating of the joint zone up to the failure of the sub-frame (the load at the column top (+250 kN) and the temperature in the bottom column (800ºC) were kept constant).

## 2.4. Mechanical and thermal loadings

Steel temperatures in tests 2 to 7 were increased using Flexible Ceramic Pad heating elements (concrete was not heated). In tests 2 to 6, the heated zone was defined by a length of 0.6 m of the beam to each side of the joint, the bolts and 1 m of column. In test 7 (demonstration test), the bottom column (HEB 140) was heated, and the joint zone was reduced to a beam length of 0.4 m. Servosis hydraulic jack ($F_{max.}$ = 1000 kN; $\Delta_{max.}$ = 280 mm) was used to apply the mechanical loading at the column top. Three different restraints stiffness's from the unaffected part of the building

were considered: tests 1, 2 and 3 - no beam axial restraint; tests 4 and 5 - total beam axial restraint; and tests 6 and 7 - realistic beam axial restraint (spring restraint). When no restraint was applied, the beams were free to the axial movement. For the total beam axial restraint, a steel beam HEB 300 cross-section, linked from the end of each tested beam to strong walls, was used to totally restrain the beam in the axial direction, allowing the rotation. The spring restraints were simulated using hydraulic cylinders, each one being independently and manually controlled in order to adjust the spring stiffness (50 kN/mm).

### 3. CONTROL TESTS

Control tests were performed in order to determine material properties of the steel joint components and concrete slab for future calibration of numerical and analytical models against the test results. Compression tests on 24 concrete blocks were performed and the concrete properties C25/30 were confirmed. Mechanical properties of the steel from the beam, the column, the end-plate and the bolts were defined by 53 tensile coupon tests under ambient and elevated temperatures, and results are described in Demonceau *et al.* (2012). Steady-state tests were considered: the coupon was heated up to a specific temperature and then it was tested in tension (constant displacement speed). Figure 4 presents the stress/strain curves of the tensile coupons tests of bolts M30, grade 10.9, at each temperature (20ºC, 200ºC, 400ºC, 500ºC, 600ºC, 700ºC and 800ºC). Tests show that yield and ultimate stresses increase at 200ºC before decreasing at higher temperature. Such behaviour could be attributed to the dynamic strain aging (DSA), austenite to martensite transformation, and high temperature softening in addition to tempering of bainite (Akbarpour and Ekrami, 2008). The Young's modulus decreased with temperature, and the ductility was significantly increased after 500ºC.
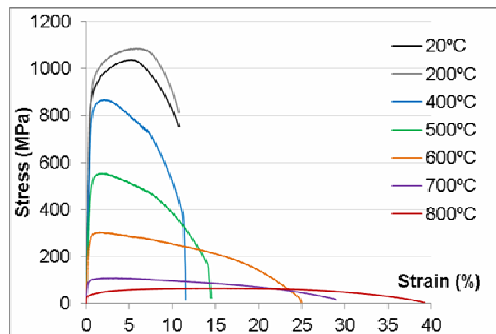


Figure 4. Stress-strain curves of coupons from bolts M30 10.9, at ambient and elevated temperatures

### 4. EXPERIMENTAL TESTS RESULTS

In order to simplify the presentation of tests results as well as the comparisons between them, the results of only one connection from each tested internal joint are presented: left connections for tests 1, 2, 3, 5 and 7, and right connection for tests 4 and 6.

#### 4.1. Temperature results

Tests 2 to 6 were performed under constant temperatures, controlled in the beams bottom flanges (at 250 mm from each end-plate). Figure 5a depicts the temperatures

evolution during test 3 (700ºC) in the left side of the frame: in the beam, at 200 mm from the connection (in the bottom flange, web and top flange), in the column flange and web, in bolt from row 4, and in the concrete rib in contact with the steel beam near the joint. The reduced web thickness allowed a faster temperature increase; because top flanges were shielding by the concrete slab and heated only by heat transfer, steel temperatures were much lower than the one measured in the lower flanges and webs. In all the tests, concrete temperatures did not rise above 300ºC. More information about the temperature results for each test can be found in Demonceau *et al.* (2012).
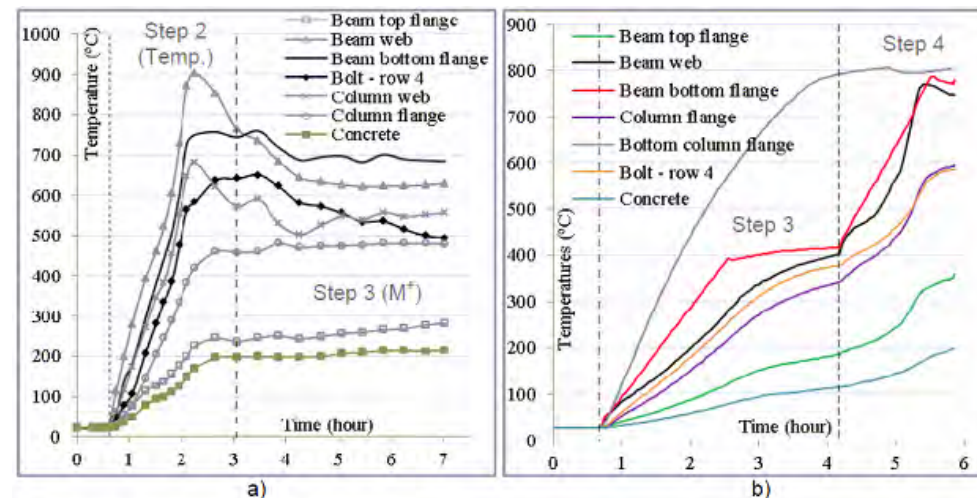


Figure 5. Evolution of the temperatures during a) test 3 at 700ºC, b) test 7 (demonstration test)

Figure5b presents the temperatures evolution during the entire test 7. In step 3 (1st increase of temperatures), the beams bottom flanges were heated up to 400ºC (rate of 200ºC/hour), whereas webs, joint components and column HEB 300 reached slight lower temperatures (between 300ºC and 400ºC). The bottom column (HEB 140) reached its maximum resistance capacity and failed under the average temperature of 658ºC (686ºC measured in flange at the centre of the column). In step 4 (2nd increase of the temperatures), the temperatures in the beams bottom flanges attained 800ºC (rate of 300ºC/hour), and finally, the entire sub-frame collapsed. The maximum temperature measured in the shear studs in the composite slab, near the joint, was 179ºC, and temperature of 200ºC was measured in the concrete slab.

#### 4.2. Mechanical results and failure modes of tests 1 to 6

Figure 6 depicts, for each test, the evolution of the bending moment versus the rotation of each connection. The joint rotation was estimated using the vertical displacements measured at: i) 1500 mm from the end-plate, and ii) at the column top. The bending moment was calculated using the reaction loads at the beams supports and ends. In step 1, the applied hogging bending moment reached: -501 kNm for the reference test 1, and around -236 kNm in tests 2 to 6. At the beginning of the heating phase (step 2), the reaction loads increased under thermal expansion effects and they reached a minimum value: the minimum hogging bending moments attained around -500 kNm in tests 3, 5 and 6 (under 700ºC), and around -357 kNm

in tests 2 and 4 (under 500°C). Finally, these reaction loads decreased because of the degradation of steel properties at elevated temperatures.

Under sagging bending moment (step 3), concrete crushing in compression was the first failure mode, due to the joint rotation and the resulting high compressive strain at the upper concrete surface: first the concrete crushed against the column flanges, then the entire slab width failed at the upper concrete surface, and finally over the entire thickness. Bolts failures happened in tests 1, 2 and 6 (respectively under 48 mrad, 74 mrad and 83 mrad of connection rotation for the first bolt failure); the other tests were ended because the maximum vertical displacement of the hydraulic jack at the column top was reached. The failed bolts were identified in the bottom bolt rows, because of higher tensile forces under sagging bending moment.
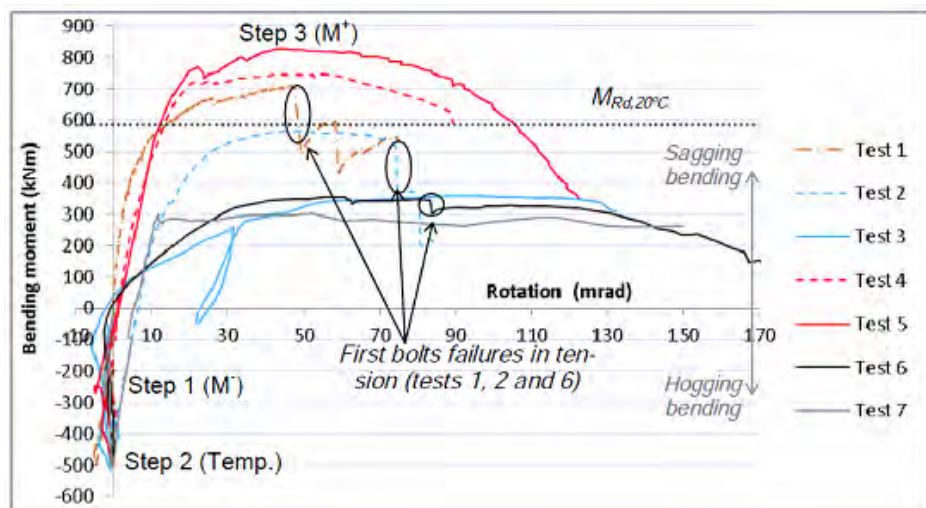


Figure 6. Joint bending moment versus rotation at the connection

The evolution of the bending moment at the joint versus the axial restraint load is presented in Figure 7. The restraints were connected to the beams since the beginning of the test. During step 1, the reaction loads and displacements due to the mechanical loadings were not sufficient to develop axial forces in the beams axial restraints. During the heating phase (step 2), due to the thermal expansions of beams, the beams ends moved in the outward direction, and compression loads were applied by the restraints. After the column loss (step 3), the axial restraints increased the compression loads because beams ends continued moving in the outward direction. Two reasons are highlighted: i) when the column began to go downward, the joint was subject to sagging bending moment: the concrete slab was in compression against the column flange whereas the joint bottom part was in tension. While the concrete was resisting, it prevented any inward horizontal displacement of the composite section. It was only after the concrete crushing in compression (or after large vertical column displacement) that the composite beam began to displace inward; ii) the horizontal displacement of the beam end was measured at the centroid of the steel beam but not at the centroid of the composite section, so, when the beam rotated, the measured displacements at the centroid of the steel beams ends continued to show an outward movement even after inward movement of the centroid of the composite beams.

In tests 4 and 5 (total axial restraint), the concrete crushed under smaller joint rotations (around 25 mrad) in comparison to test 6 (35 mrad) due to the much higher axial restraint loads developed when the beams ends tried to displace outward while they were restrained. Finally, tensile loads were observed at the end of the test 6.
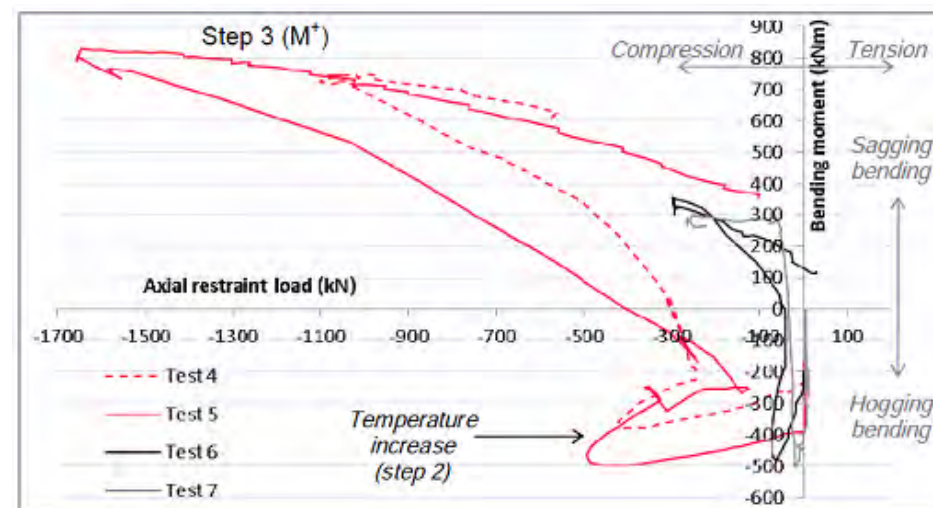


Figure 7. Joint bending moment *versus* axial load restraint

Figure 8 shows the final deformations of test 1 (20°C) and test 3 (700°C). The steel end-plates deformed in the bottom and centre parts and showed a high ductility of this joint. The deformation at the centre of the end-plate happened because of the joint configuration: i) 4 bolt rows and a high distance between the rows 2 and 3 (260 mm), ii) the end-plate (15 mm) was thinner than the column flange (19 mm), and iii) an initial gap was noticed just after the bolts pre-loading (0.6 mm was measured for the reference test). Moreover, it seems that the beam web was pulling the end-plate due to the sagging bending moment (tensile loads at the bottom part). Due to high stresses/deformations, a crack at the base steel end-plate, just above the weld, was observed at the end of the test 1 at ambient temperature (Figure 8a).
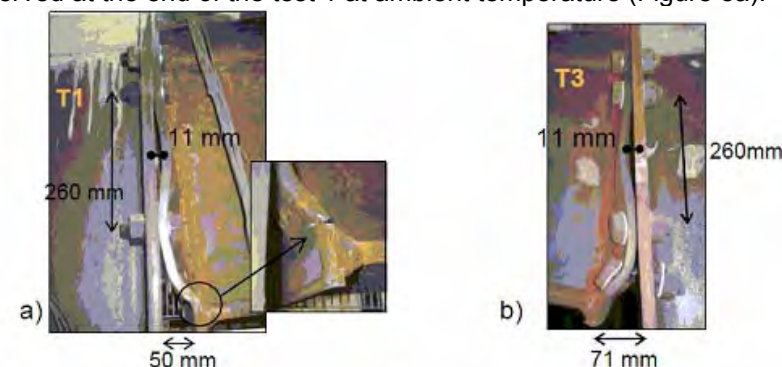


Figure 8: Deformations of the connections in: a) test 1 (ambient temperature), and b) test 3 (700°C)

www.steelconstruct.com

Table 1 summarizes the failure modes and the local deformations of each test.

Table 1. Failure modes and local deformations of each test

| Test | Temp (ºC) | Restraint (kN/mm) | |
|------|-----------|-------------------|---|
| T1 | 20 | 0 | Concrete crushing in compression; failure of 2 bolts in tension (left side); crack at the end-plate (bottom – left). Local deformations at the end-plates (bottom and centre). |
| T2 | 500 | 0 | Concrete crushing in compression; failure of 3 bolts in tension (left side) Local deformations at the end-plates (bottom and centre). |
| T3 | 700 | 0 | Concrete crushing in compression; failure of 2 bolts in tension (left side) during the cooling phase. Local deformations at: the end-plates (bottom and centre); column web (bottom part); beam bottom flange (left). |
| T4 | 500 | Total | Concrete crushing in compression; failure of 2 bolts in tension (right side) during the cooling phase. Local deformations at: the end-plates (bottom and centre); column web (top part); beams webs; column flange (left). |
| T5 | 700 | Total | Concrete crushing in compression. Local deformations at: the end-plates (bottom and centre); column web (bottom part); beam bottom and top flanges (right). |
| T6 | 700 | 50 | Concrete crushing in compression; failure of 3 bolts in tension (2 on the right - 1 on the left). Local deformations at: the end-plates (bottom and centre); beams bottom flanges. |
| T7* | 400; 800 | 50 | Bottom column failure; concrete crushing in compression; failure of 3 bolts in tension (left side); crack at the end-plate (bottom - left). Local deformations at the end-plates (bottom and centre) |

* Test 7 (demonstration test) is presented in §3.3.

From the results of tests 1 to 5, the effect of the temperatures and the effect of the axial restraint to the beam on the joint behaviour can be discussed. Table 2 summarises the values of the maximum sagging bending moment reached for each test, as well as the corresponding axial load and connection rotation.

Table 2. Comparisons of the results related to maximum sagging bending moment $M^+_{max}$ (tests 1 to 6)

| | T1 | T2 | T3 | T4 | T5 | T6 |
|---|----|----|----|----|----|----|
| Temperature | 20ºC | 500ºC | 700ºC | 500ºC | 700ºC | 700ºC |
| Beam axial restraint | 0 | 0 | 0 | total | total | 50 kN/mm |
| $M^+_{max}$ (kNm) | 710.1 | 565.0 | 357.1 | 746.4 | 828.0 | 355.5 |
| Rotation $\theta_{M+max}$ (mrad) | 46.9 | 49.5 | 92.3 | 54.9 | 43.0 | 55.1 |
| Axial load (kN) | 0 | 0 | 0 | -990.7 | -1646.7 | -297.3 |

### 4.2.1. Effects of the temperature

The three first tests, performed without beam axial restraint, showed that the increase of temperature:
- Decreases the maximum sagging bending moment of the joint (by 20% between test 1 (20ºC) and test 2 (500ºC) and by 50% between test 1 and test 3 (700ºC);
- Increases the capacity of rotation and the ductility of the joint, by i) increasing the connection rotation corresponding to the maximum sagging moment (by 97% from test 1 to test 3, and by 87% from test 2 to test 3); ii) increasing the maximum joint rotation at the first bolt failure (in tests 1 and 2, the first bolt failed for respectively 49 mrad and 74 mrad of rotation (increase of 55%), and no bolts were failed at 132 mrad of rotation in test 3);
- Decreases the initial stiffness, by 36% and 49% between test 1 (20ºC) and respectively test 2 (500ºC) and test 3 (700ºC).

In test 1, the maximum sagging bending moment was equal to 710 kNm, which is 21% higher than the theoretical value (588 kNm) calculated in Demonceau *et al.* (2012).

### 4.2.2. Effect of the axial restraints to the beams

Tests 2 and 4 were both performed under 500ºC, respectively with none and total beam axial restraints, and tests 3, 5 and 6 were performed under 700ºC, respectively with none, total and spring beam axial restraints. It was observed that the beam axial restraint, and consequently, the compression axial load in the joint:
- Increases the maximum sagging bending moment, by 32% between test 2 and test 4, under 74 mrad of joint rotation (corresponding to the first bolt failure in test 2), due to the axial compression load equal to 773 kN in test 4. Note that between tests 3 and 6, the maximum bending moment was not affected by the axial restraint to the beam (difference of 0.5%); however, the corresponding rotation was 40% lower in test 6;
- Increases the joint rotation capacity and, consequently, the joint ductility: the compression load from the axial restraint combined with sagging bending moment, moved the neutral axis of the connection downward, allowing the development of additional compression loads in the concrete slab, and the reduction of the tensile loads in the bottom bolt rows. Once the concrete crushed against the column slab and along the entire slab width, tests 4 and 5 were still able to continue to deform without failure: between the maximum sagging bending moment and the end of the test, the rotation increased by 113% in test 4 and by 184% in test 5;
- Increases the initial stiffness of the bending moment/rotation curves, by 83% at 500ºC (from test 2 to test 4) and by 54% at 700ºC (from test 3 to test 5).

### 4.3. Mechanical results and failure modes of test 7 (demonstration test)

The bending moment/rotation and bending moment/axial load curves were depicted in Figure 6 and Figure 7. The hogging bending moment was initially reached during step 1 (-281 kNm). During step 2, the hydraulic jack increased the load at the column top up to reach +250 kN. The axial force in the bottom column was then equal to 341 kN (due to the additional reaction loads created by the initial hogging bending moment applied in the joint). In step 3, the reaction loads first increased

under thermal expansion effects, and the axial force in the bottom column reached 604 kN (hogging bending moment equal to -505 kNm); the bottom column reached its maximum resistance capacity under 658ºC and failed. The failure of the column was progressive, and was defined as the moment at which the vertical reaction load came back to its initial value at the beginning of the step 3 (341 kN). As in tests 4, 5 and 6, compression axial restraint loads were developed during step 3, and continued to increase in step 4. During this step 4, the temperature in the joint increased under the constant load (+250 kN) applied at the top of the column and reached 770ºC in the beam bottom flanges (see Figure 5b). At this moment, the concrete slab was crushed in compression against the column flanges, and the vertical displacement increased faster. Once the concrete slab was crushed along the entire slab width, the sub-frame rapidly collapsed (beam bottom flanges temperature reached 800ºC). For security reasons, the test was stopped at a vertical displacement equal to 280 mm and left connection reached 150 mrad of rotation. The day after the test showed the failure of three bolts in the bottom bolt rows of the left connection. However, bolts failures were not observed on bending moment/rotation curve because failures were very smooth due to the increase of ductility of the bolt after 500ºC (see Figure 4). The steel end-plates also deformed in the bottom and centre part and due to high stresses/deformations, a crack at the base steel end-plate, just above the weld, was also observed (Demonceau *et al.*, 2012).

## 5. CONCLUSIONS

The main objective of the experimental tests was to observe the combined bending moment and axial loads in the heated composite steel-concrete joint after the loss of the column. The effect of the localised fire (that led to the column failure) was simulated by the application of elevated temperatures in the composite joint zone. Seven beam-to-column sub-frames were tested: one reference test at ambient temperature; five tests at 500ºC or 700ºC; and a demonstration test, for which the sub-frame was subject to an increase of the temperature up to the failure of the column. The effect of the axial restraint to beam coming from the unaffected part of the building was studied.

In the six first tests, a hogging bending moment was initially applied in the joint, followed by a variation of this moment during the increase of temperatures. Then the column loss was simulated under constant temperature, and the sagging bending moment was increased. The first failure observed in all the tests was the concrete crushing in compression; some bolts from the bottom bolt rows failed later in tension under higher joint rotations in tests 1, 2 and 6; similar local deformations at the centre and bottom part of the end-plate were observed in all the tests. From tests performed without axial beam restraint, it was observed that the joint rotation capacity, as well as the ductility, was increased with the temperature, whereas the maximum sagging bending moment was lower. The advantage of the compression axial loads coming from the beams restraints was the increase of: i) the joint rotation capacity and its ductility, and ii) the capacity of the joint to sustain a higher sagging bending moment without bolt failure: the compression load from the axial restraint combined with sagging bending moment, moved downward the neutral axis of the connection, allowing the development of additional compression loads in the concrete slab, and reducing tensile loads in the bottom bolt rows.

The objective of the demonstration test was to show the real behaviour of the sub-frame when subject to a localised fire which leads to the loss of the column. A constant gravity load was applied to the frame in order to approximate to the real behaviour of the structure, and then beams, joint and column were heated in order to reproduce a localised fire (the temperature in the bottom column has raised faster than the temperature in the beam and joint). The bottom column failed under 658ºC; after that, it was observed that once the beams reached 700ºC, the vertical displacement of the joint under sagging bending moment began to increase faster, then composite slab crushed, and finally the sub-frame collapsed. In this demonstration test, the sub-frame shown sufficient robustness provision; the loss of the column did not led directly to fragile failure of the joint, because of the ductility and capacity of the joint to deform and continue transferring loads. Besides, the composite slab considerably increased the joint resistance under the localised fire.

## ACKNOWLEDGMENTS

## REFERENCES

[1] Abaqus (2010), Theory Manual & Users Manuals, Version 6.10, Hibbitt, Karlsson and Sorensen, Inc. USA.

[2] Akbarpour, M.R. and Ekrami, A. (2008). "Effect of temperature on flow and work hardening behavior of high bainite dual phase (HBDP) steels", *Materials Science and Engineering*, 475(1-2), pp. 293–298, 2008.

[3] Demonceau J.F., Huvelle C., Comeliau L., Hoang L. V., Jaspart J.P., Fang C., *et al.* (2012) "Robustness of car parks against localised fire", European Commission, Grant Agreement Number RFSR-CT-2008-00036, Final report.

[4] EN 1991-1-7: 2002, "Eurocode 1 - Actions on structures - Part 1-7: General actions - Accidental actions", European committee for standardization, July 2006.

[5] Jaspart, J.-P.and Demonceau, J.-F. (2007). "Contribution to the derivation of robustness requirements for steel and composite structures", 5th International Conference on Advances in Steel Structures, Editors: J.Y. Richard Liew & Y.S. Choo, Singapore, 5-7 December.

[6] Jaspart J.-P., Demonceau J.-F., Fang C., Izzuddin B., Elghazouli A., Nethercot D., *et al.* (2008) "Deliverable I: Definition of the problem and selection of the appropriate investigation ways", Robustness of car parks against localised fire, Grant Agreement Number RFSR-CT-2008-00036.

[7] Joyeux, D., Kruppa J., Cajot L.G., Schleich J.B., van de Leur P. and Twilt L. (2002). "Demonstration of real fire tests in car parks and high buildings". European Commission, Contract no 7215-PP/025, CTICM, Final Report, EUR 20466EN.

[8] Le Pense, "Les parkings aériens en structure acier: développements récents / Multi-storey car parks in steel structure: last developments", La Revue de Métallurgie - CIT, p867-874, Octobre 2002.

# DESIGN MODEL FOR COMPOSITE BEAM TO REINFORCED CONCRETE WALL JOINTS

José Henriques; Luís Simões da Silva
*ISISE - Department of Civil Engineering, University of Coimbra, Portugal*
*jagh@dec.uc.pt; luisss@dec.uc.pt*

Isabel Valente
*ISISE - Department of Civil Engineering, Engineering School, University of Minho, Portugal*
*isabelv@civil.uminho.pt*

## ABSTRACT

In this paper, a design model for composite beam to reinforced concrete wall joints is presented and discussed. The proposed model is an extension of the component method to this type of joints. The characterization of the active components is therefore performed in terms of force-deformation curves. In this type of joints, special attention is paid to the steel-concrete connection where "new" components, not covered in EN1993-1-8, are activated. The application of the model allows obtaining the joint properties in terms of moment-rotation curve. The accuracy of the proposed model is verified by comparison against available experimental and numerical results. The latter were developed in the FE program ABAQUS and previously validated against experimental results.

## 1. INTRODUCTION

In many office and car park type of buildings there is the need to combine reinforced concrete structural walls with steel and/or composite members. In such structural systems the design of the joints is a challenge due to the absence of a global approach. Designers are faced with a problem that requires knowledge in reinforced concrete, anchorage in concrete and steel/composite behaviour. Because of the different design philosophies, especially in what regards the joints, no unified approach is currently available in the Eurocodes.

The component method is a consensual approach for the design of steel and composite joints with proven efficiency. Therefore, in this paper, a design model extending the scope of the component method to steel-to-concrete beam-to-wall joints is proposed. To address the problem, a composite beam to reinforced concrete wall joint, experimentally tested within the RFCS research project "InFaSo" [1], was chosen. The joint configuration under analysis was developed to provide a semi-continuous solution, allowing transfer of bending moment between the supported and supporting members. The joint depicted in Figure 1 may be divided in two zones: i) upper zone, connection between the reinforced concrete slab and the wall; ii) bottom

zone, connection between the steel beam and the reinforced concrete wall. In the upper zone, the connection is achieved by extending and anchoring the longitudinal reinforcement bars of the slab (*a*) into the wall. Slab and wall are expected to be concreted in separate stages and therefore, the connection between these members is only provided by the longitudinal reinforcement bars. In the bottom zone, fastening technology is used to connect the steel beam to the reinforced concrete wall. Thus, a steel plate (*b*) is anchored to the reinforced concrete wall using headed anchors (*c*), pre-installation system. The plate is embedded in the concrete wall with aligned external surfaces. Then, on the external face of the plate, a steel bracket (*d*) is welded. A second plate (*e*) is also welded to this steel bracket however, not aligned in order to create a "nose". The steel beam with an extended end plate (*f*) sits on the steel bracket, and the extended part of the end plate and steel bracket "nose" achieve an interlocked connection avoiding the slippage of the steel beam out of the steel bracket. A contact plate (*g*) is placed between the beam end plate and the anchor plate, at the level of the beam bottom flange.



a – Longitudinal reinforcement bars
b – Anchor plate
c – Headed anchors
d – Steel bracket
e – Steel plate welded to steel bracket
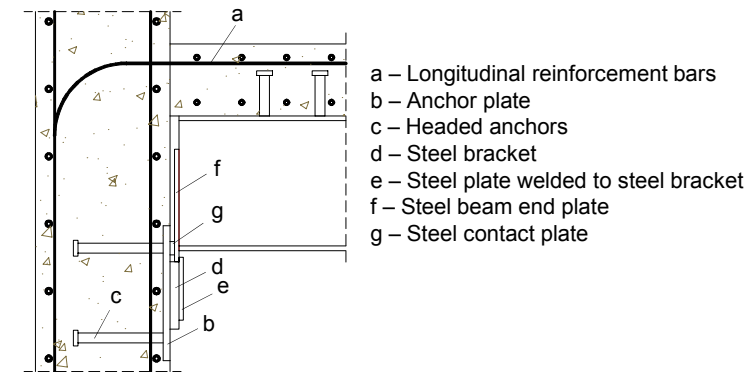f – Steel beam end plate
g – Steel contact plate

Figure 1. Composite beam to reinforced concrete wall joint configuration studied in [1]

According to the structural demands, the joint configuration can cover a wide range of combination of design loads (M-V-N) without modifying significantly the connection between the steel and the concrete parts. The versatility of the joint is illustrated in Figure 2. Three working situations are possible: i) semi-continuous with medium/high capacity to hogging bending moment, shear and axial compression; ii) pinned for high shear and axial compression; iii) pinned for high shear and axial tension. According to the detailing of Figure 2, because of the weakness of the "nose" system, the sagging bending moment capacity is very limited and strongly dependent of the "nose" resistance. For the same reason, the resistance to tensile loading is also reduced. Therefore, the application to cyclic loading, such as seismic action, is restricted. Pinned behaviour of the joint is very easily obtained by removing the connection between the slab and the wall. Consequently, in terms of erection, this is a very efficient solution; however, for the above reasons, the joint should not be subject to axial tension. Whenever this is a requirement, adding a fin plate as shown in Figure 2 (iii) provides a straightforward solution. In this case, the tension capacity is improved and due to the symmetry of the joint, cyclic loading may be applied. In the present paper only the semi-continuous joint solution subject to hogging bending moment is analysed.
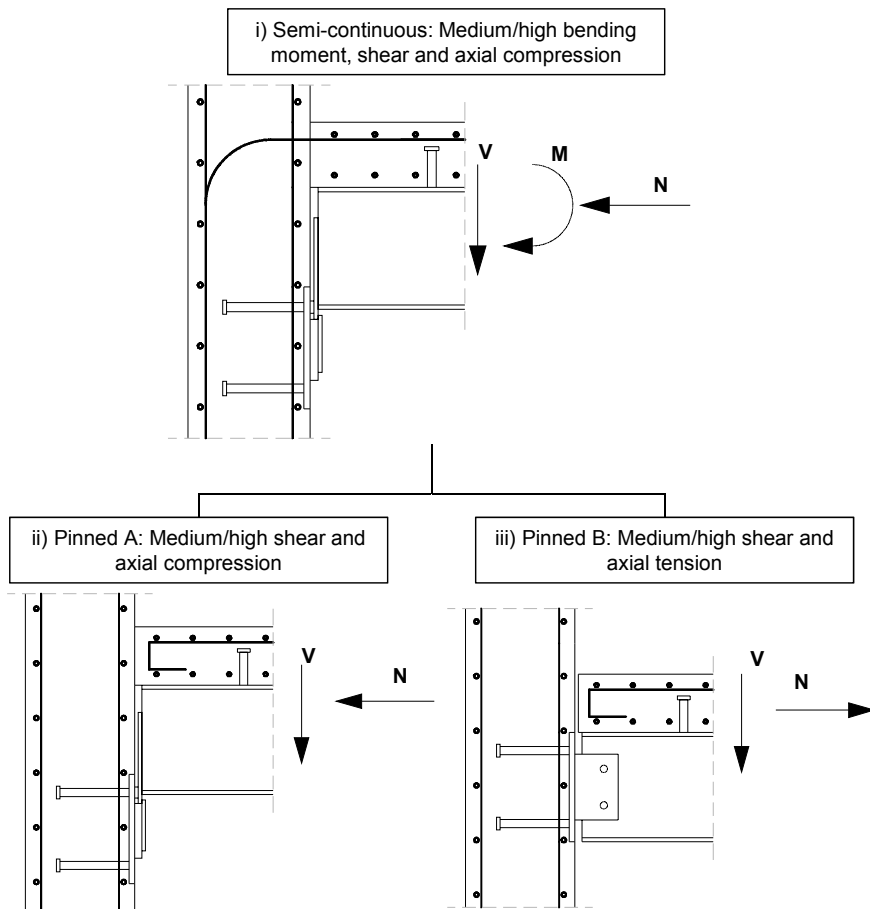
Figure 2. Versatility of the steel-to-concrete joint for different loading conditions

## 2. SOURCES OF JOINT DEFORMABILITY AND JOINT MODEL

To understand the behaviour of the joint under bending moment and shear force the mechanics of the joint is identified. The assumed stress flows are schematically represented in Figure 3. Accordingly, in the upper zone, only tension is transferred through the longitudinal reinforcement. Also, in this region, there is no shear and no tension is assumed to be transferred through the concrete, from the slab to the wall, as the small bond developed is neglected. In the bottom zone, the shear load is transferred from the steel beam to the reinforced concrete wall according to the following path: a) from the beam end-plate to the steel bracket through contact pressure; b) from the anchor plate to the reinforced concrete wall through friction, between the plate and the concrete and between the shaft of the headed anchors and the concrete through bearing. Also in the bottom zone, compression is transferred to the reinforced concrete wall through the contact plate between the beam end-plate and the anchor plate. Then, in the reinforced concrete wall the high tension and compression loads introduced by the joint flow to supports.
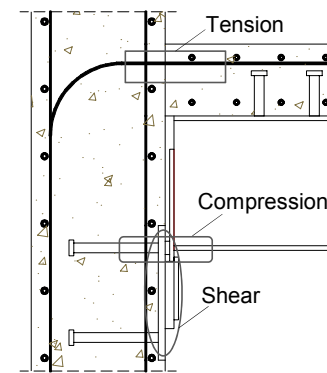


Figure 3. Stress flow on the semi-continuous joint under bending moment and shear loading

According to the described stress flows, corresponding to hogging bending moment, the active components are identified and listed in Table 1 and their location is shown in Figure 4-a). Note that the number attributed to the joint components is set for the present paper and disregards the usual numbering proposed in [2]. Components 7, 8, 9 and 10 should not control the behaviour of the joint as their activation only results from the out-of-plane deformation of the bottom and top edges of the anchor plate in compression at the level of the upper anchor row. Due to the presence of an anchor row at the bottom part, this should act similarly to a prying force and consequently, this anchor row is activated in tension. In what respects to component 11, denominated as "joint link", it represents the equilibrium of stresses in the reinforced concrete wall zone adjacent to the joint.

Table 1. List of active components in the composite beam to reinforced concrete wall joint subject to hogging bending moment

| Component ID | Basic joint component | Type/Zone |
|---|---|---|
| 1 | Longitudinal steel reinforcement in slab | Tension |
| 2 | Slip of composite beam | Tension |
| 3 | Beam web and flange | Compression |
| 4 | Steel contact plate | Compression |
| 5 | Anchor plate in bending under compression | Bending/Compression |
| 6 | Concrete | Compression |
| 7 | Headed anchor in tension | Tension |
| 8 | Concrete cone | Tension |
| 9 | Pull-out of anchor | Tension |
| 10 | Anchor plate in bending under tension | Bending/Tension |
| 11 | Joint link | Tension and Compression |

According to the identified components, a representative spring and rigid link model is illustrated in Figure 4-b). Three groups of springs are separated by two vertical rigid bars. The rigid bars avoid the interplay between tension and compression components, simplifying the joint assembly. Another simplification is introduced by considering a single spring to represent the joint link. In what concerns the tension springs, it is assumed that slip and the longitudinal reinforcement are at the same level

www.steelconstruct.com

although slip is observed at the steel beam – concrete slab interface. In this model, at the bottom part of the joint, rotational springs (5) are considered in the anchor plate to represent the bending of this plate. In a simplified model, the behaviour of these rotational springs, as well as the effect of the bottom anchor row, should be incorporated into an equivalent translational spring representing the contribution of the anchor plate to the joint response. Each group of components is discussed in the next chapter.



a) Location of the joint components identified

b) Joint component model
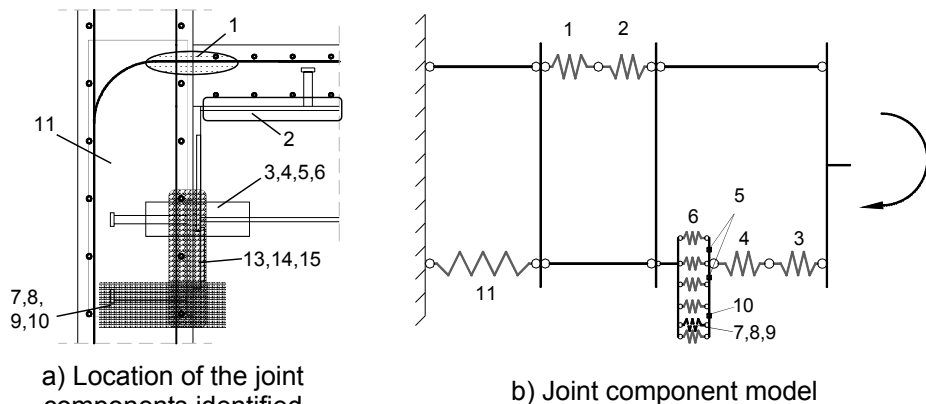
Figure 4. Application of the component method to a composite beam to reinforced concrete wall joint subject to hogging bending moment

## 3. CHARACTERIZATION OF ACTIVATED JOINT COMPONENTS

### 3.1. Components in tension zone

In case full interaction is achieved between the slab and the steel beam, the longitudinal reinforcement in tension limits the resistance of the tension zone of the joint. This component is common in composite joints where the longitudinal reinforcement is continuous within the joint or its anchorage is assured. In EN 1994-1-1[3], each layer of longitudinal reinforcement is considered as an additional bolt row contributing to the resistance of the joint. The longitudinal reinforcement within the effective width of the concrete slab is assumed to be stressed up to its yield strength. In terms of deformation, a stiffness coefficient is provided by the code which takes into account: i) the configuration of the joint, double or single sided; ii) the depth of the column; iii) the area of longitudinal reinforcement within the effective width of the concrete flange; iv) the loading on the right and left side, balanced or unbalanced bending moment. No guidance is provided to estimate the deformation capacity. Sufficient deformation capacity to allow a plastic distribution of forces should be available if the ductility class of the reinforcement bars is B or C, according to EN 1992-1-1[4]. A more sophisticated model of this component can be found in [5] where the behaviour of the longitudinal reinforcement is modelled taking into account the embedment in concrete and the resistance goes up to the ultimate strength of steel. The component is modelled by means of a multi-linear force-displacement curve with hardening. This model allows to estimate the deformation at ultimate resistance. This deformation is then assumed as the deformation capacity of the component. Table 2 summarizes the analytical expressions for both models. Figure 5 illustrates the force-deformation curves characterizing the behaviour of the components according to these models.

In the ECCS [5] model, the initial range is very stiff as the concrete is uncracked. Then, as cracks form in the concrete a loss of stiffness is noticed until there is stabilization in cracking. At this stage, the response of the longitudinal reinforcement bar recovers the proportionality between stress and strain of the bare steel bar up to the yield strength. Finally, the ultimate resistance is achieved assuming that the bars may be stressed up to their ultimate strength. In the Eurocode model, linear elastic behaviour is considered up to the yielding of the longitudinal reinforcement bar.

Table 2. Analytical expressions for longitudinal reinforcement component

| Reference | | Expressions |
|---|---|---|
| EN 1994-1-1 [3] | Resistance | $F_{sy} = \sigma_y A_{sr}$ |
| | Stiffness coefficient | $k_{sr} = \dfrac{A_{sr}}{3,6h}$ |
| | Deformation capacity | Not given |
| ECCS Publication Nº109 [5] | Resistance | $F_s = \sigma_{sr,i} A_{sr}$ with $\sigma_{sr1} = \dfrac{f_{ctm} k_c}{\rho}\left[1 + \rho \dfrac{E_s}{E_c}\right]$ $\sigma_{srn} = 1,3\sigma_{sr1}$ |
| | Deformation | $\Delta \leq \Delta_{sry}: \quad \Delta = \varepsilon(h + L_t)$ $\varepsilon_{sr1} = \dfrac{\sigma_{sr1}}{E_s} - \Delta\varepsilon_{sr}$ $\Delta\varepsilon_{sr} = \dfrac{f_{ctm} k_c}{E_s \rho}$ $\rho < 0,8\%: \quad \Delta_{sru} = 2L_t \varepsilon_{srmu}$ $\rho \geq 0,8\%$ and $a < L_t: \quad \Delta_{sru} = (h + L_t)\varepsilon_{srmu}$ $\rho \geq 0,8\%$ and $a > L_t: \quad \Delta_{sru} = (h + L_t)\varepsilon_{srmu} + (a - L_t)\varepsilon_{srmy}$ |

In this joint, the composite beam is designed to have full interaction between the steel beam and the RC slab; therefore, no limitation to the joint resistance is expected from component 2: slip of composite beam. In what concerns the deformation of this component, as verified in [6], a small contribution to the joint rotation may be observed. According to [7], the slip at the connection depends on the nearest stud to the wall face. Under increasing load this stud provides resistance to slip until it becomes plastic. Additional load is then assumed to be resisted by the next stud deforming elastically until its plastic resistance is reached. Further load is then carried by the next stud and so forth. The deformation capacity of the component is then limited by the deformation capacity of the shear connection between the concrete slab and the steel beam. In EN 1994-1-1 [3], the contribution of the slip of the composite beam is taken into account by multiplying the stiffness coefficient of the longitudinal steel reinforcement in tension by a slip factor ($k_{slip}$).

### 3.2. Components in the compression zone

In the compression zone, the beam web and flange in compression and the steel contact in compression are components already covered by EN1993-1-8 [2]
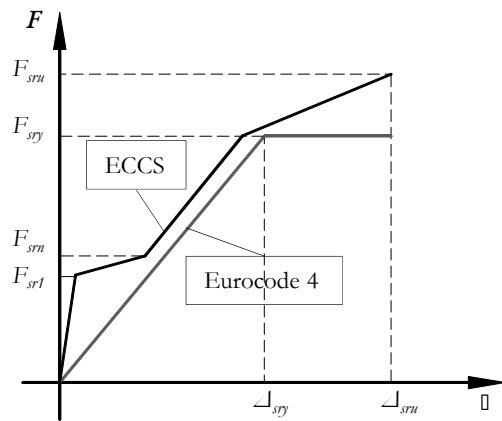
Figure 5. Behaviour of the component longitudinal steel reinforcement bar in tension



b) Reference numerical model

Figure 6. Anchor plate connection

and EN 1994-1-1 [3]. Furthermore, according to the scope of the experimental tests [1], their contribution to the joint response was limited to the elastic range. In this way, for the characterization of these components, reference is given to [2] and [3].

In what concerns the anchor plate in compression, this connection introduces into the problem the anchorage in concrete. Because the main loading is compression, the anchorage is not fully exploited. In order to reproduce its behaviour, a sophisticated model of the anchor plate in compression is under development. As illustrated in Figure 4, several components are activated carrying tension, compression and bending loading. Due to the similarities of the problem, the model under development is a adapted version of the Guisse *et al.* [8] for column bases. In the absence of specific tests on the anchor plate in compression, the model is based on numerical investigations. Figure 6 depicts the idealized mechanical model and the reference numerical model. The steel-concrete contact is reproduced by considering a series of extensional springs that can only be activated in compression. Because of the deformation of the anchor plate, the anchor row on the unloaded side is activated in tension and increases anchor plate in compression resistance and stiffness. For the anchor row on the unloaded side, a single extensional spring concentrates the response of three components: i) anchor shaft in tension; ii) concrete cone failure; iii) headed anchor pull-out failure. Then, three rotational springs are considered to reproduce the bending of the plate according to its deformation. The location of these springs is based on the numerical observations (see Figure 6-b). The properties of these components are given in Table 3. For the involved parameters please check the references given in the table.
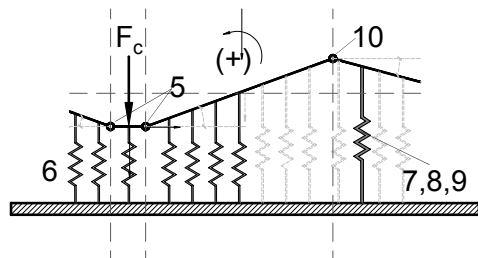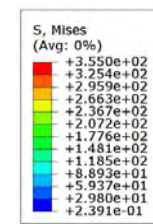
Table 3. Analytical characterization of the components relevant for the anchor plate in compression

| Component | | Reference | |
|---|---|---|---|
| 6 | Resistance | Guisse *et al.[8]* | $R_i = \left[ \frac{f_j - E_c \varepsilon_{c2}}{\varepsilon_{c1}^2} \left( \frac{\delta_i}{h_{c,eq}} \right)^2 + E_c \left( \frac{\delta_i}{h_{c,eq}} \right) \right] A_{c,i}$ |
| | Deformation | | $\delta_i = \varepsilon_i h_{c,eq}$ |
| 7 | Resistance | EN 1993-1-8[2] | $N_{st} = n \left( \frac{\pi d^2}{4} \right) f_y$ |
| | Deformation | | $\delta_{st,y} = \frac{N_{st}}{k_{st}}$ with $k_{st} = \frac{E_c \left( \frac{\pi d^2}{4} \right)}{h_{ef}}$ |
| 8 | Resistance | CEN-TS[9] | $N_c = \left( \frac{A_{c,N}}{A_{c,N}^0} \right) \psi_m N_c^0$ with $N_c^0 = 16.8 \sqrt{0.95 f_{ck,cube}} h_{ef}^{1.5}$ |
| | Deformation | - | rigid |
| 9 | Resistance | CEN-TS[9] | $N_{PO} = 11 f_{ck} \frac{\pi (d_h^2 - d^2)}{4}$ |
| | Deformation | Furche[10] | $\delta_{PO} = \alpha_p \frac{k_a k_A}{C_1} \left( \frac{N}{A_h 0.95 f_{ck,cube} n} \right)^2$ |
| 5 and 10 | Resistance | Conventional | $M_y = f_y \frac{b_{ap} t_{ap}^2}{6}$ $M_{pl} = f_y \frac{b_{ap} t_{ap}^2}{4}$ |
| | Deformation | | $\Phi_u = \frac{2 \times 0.15}{t_{ap}}$ |



a) Idealized mechanical model

www.steelconstruct.com

Figure 7 shows the comparison between the results of the numerical and the analytical model. These are given in terms of load applied on the anchor plate and deformation in the direction of the load at the point of application of the load. Despite the good accuracy of the analytical model, its full validity is yet to be established, as a parametric study has shown some deviations between the models. The final calibrated model should be presented in [11].
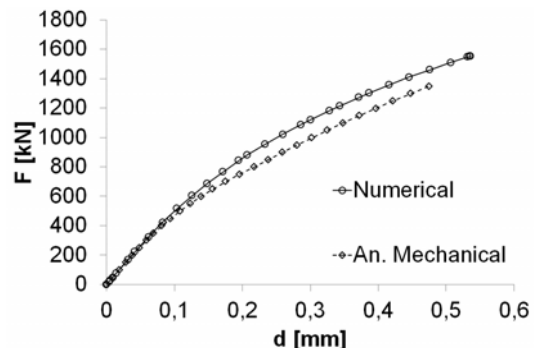


Figure 7. Comparison of results between analytical and numerical model

The above model aims to accurately reproduce the behaviour of the anchor plate in compression. However, it is perhaps too complex for design purposes. Thus, a simplified modelling of the anchor plate in compression is envisaged. Again because of the similarities of the problem, a modified version of the T-stub in compression [2] is foreseen as follows:

- For resistance and stiffness, the $\beta$ factor is set equal to 1, as the use of grout between plate and concrete is not expected.
- For stiffness, an exact value of the bearing width $c$ has been determined according to [12] instead of the approximation given in the EN 1993-1-8 [2]. Thus, $c$ is taken equal to $1,4t$ instead of $1,25t$.

Consequently, components 5 to 10 are replaced in the joint component model, shown in Figure 4, by a single equivalent spring representing the T-stub in compression. This is the model used later in section 4.

### 3.3. Joint Link

The joint link is a component to consider the resistance and deformation of the reinforced concrete wall in the zone adjacent to the joint. The loading on this member coming from the above part of the structure may affect this component. However, only the joint loading is considered in the present study. As for the anchor plate under compression, no specific experimental tests have been performed to analyse this part of the joint. Therefore, a simplified analysis has been performed numerically. Because of the nature of this part of the joint, reinforced concrete, the model is based on the strut-and-tie method commonly implemented in the analysis of reinforced concrete joints. The problem is 3D, increasing its complexity, as the tension load is introduced with a larger width than the compression, which may be assumed concentrated within an equivalent dimension of the anchor plate (equivalent rigid plate as considered in T-stub in compression). Thus, a numerical model considering only the reinforced concrete wall and an elastic response of the material has been

tested to identify the flow of principal stresses. These show that compression stresses flow from the hook of the longitudinal reinforcement bar to the anchor plate. In this way the strut-and-tie model (STM) depicted in Figure 8-a) is idealized. Subsequently, in order to contemplate the evaluation of the deformation of the joint, a diagonal spring is idealized to model the diagonal compression concrete strut, as illustrated in Figure 8-b). The ties correspond to the longitudinal steel reinforcement bars already considered in the joint model. The properties of this diagonal spring are determined as follows.

- Resistance is obtained based on the strut and nodes dimension and admissible stresses within these elements. The node at the anchor plate is within a tri-axial state of compression. Therefore, high stresses are attained (confinement effect). In what concerns the strut, a "bottle shape" is identified. Because of the 3D nature, stresses tend to spread between nodes. Giving the dimensions of the wall (infinite width), the strut dimensions should not be critical to the joint. As stated in [13], because nodes are bottlenecks of the stresses, it can be assumed that the concrete strut is safe if the nodes failure criterion is satisfied. Thus, the node at the hook of the bar is assumed to be the critical component of the joint link. The resistance of the spring is then obtained according to the dimensions of this node and to the admissible stresses in the node. The admissible stresses are defined according to EN 1992-1-1 [4].
- In what respects the deformation, the problem is more complex as the strain field within the diagonal strut is highly variable. Though, several numerical calculations [11], considering geometrical variations (wall thickness, beam height, bend radius), showed that the shape of force-deformation is independent of these variables. Thus, as simplification, a mathematical equation is proposed to approximate the horizontal component of the deformation (in $mm$) of the joint link in function of the horizontal load on the joint ($F_{j,h}$ in $kN$), as expressed in (1).
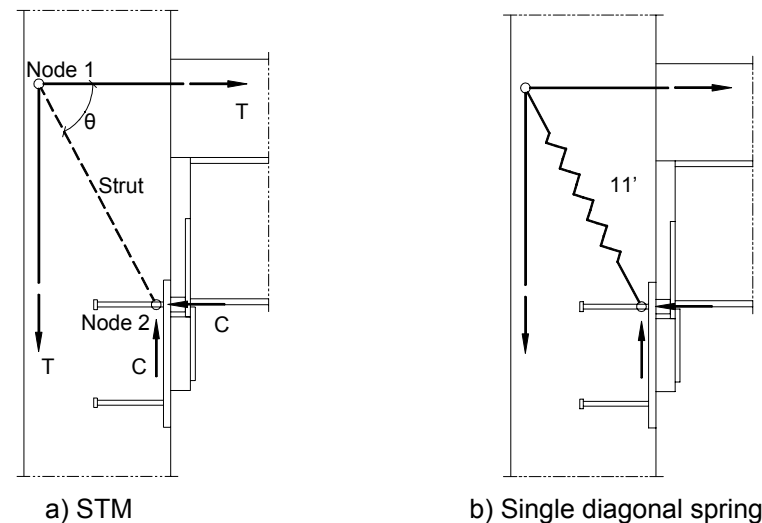


a) STM  　　　　　　　　b) Single diagonal spring

Figure 8. Joint link modelling

$$d_{j,h}=\left(6,48\mathrm{E}^{-8}\,F_{j,h}^{2}+7,47\mathrm{E}^{-6}\,F_{j,h}\right)\mathrm{Cos}\,\theta \qquad (1)$$

Table 4 gives the admissible stresses for nodes according to EN 1992-1-1 [4]. Node 1, illustrated in Figure 9, is characterized by the hook longitudinal reinforcement bar. The represented dimension is assumed as defined in the CEB Model Code [14]. In what concerns the width of the node, based on a numerical study [11], equation (2) was derived to determine an effective width "under" each reinforcement bar contributing to the node resistance.

Table 4. Admissible stresses in STM nodes according to EN 1992-1-1[4]

| Node | Admissible stresses |
|------|---------------------|
| 1 | $0,75vf_{cd}$ |
| 2 | $3vf_{cd}$ |
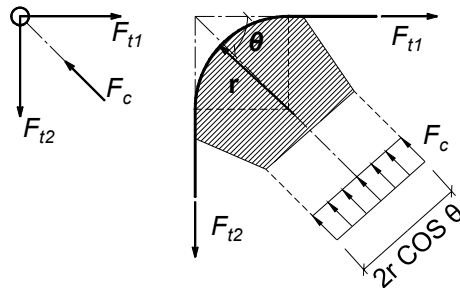


Figure 9. Definition of the dimension related to the hook of the longitudinal reinforcement bar in Node 1, according to the CEB Model Code [14]

$$\begin{cases} s_{rb} \geq 80\,mm. \quad b_{eff,rb} = 40,9 \left(\dfrac{d_{rb}}{12}\right)^{0,96} \left(\dfrac{\cos \theta}{\cos 45^\circ}\right)^{-1,05} \\[2ex] s_{rb} < 80\,mm. \quad b_{eff,rb} = 40,9 \left(\dfrac{d_{rb}}{12}\right)^{0,96} \left(\dfrac{\cos \theta}{\cos 45^\circ}\right)^{-1,05} \left(\dfrac{s_{rb}}{80}\right)^{0,61} \end{cases} \qquad (2)$$

where: $b_{eff,rb}$ is the effective width "under" each reinforcement bar; $s_{rb}$ is the reinforcement bars spacing; $d_{rb}$ is the diameter of the reinforcement bars; and $\theta$ is the angle of the diagonal strut assumed in the model.

Finally, to simplify the assembling of the joint model, the diagonal spring representing the joint link component is converted in a horizontal spring as represented in Figure 4. The properties of the horizontal spring are directly obtained from the diagonal spring determined as a function of the angle of the diagonal spring.

## 4. APPLICATION OF THE DESIGN MODEL TO A COMPOSITE BEAM TO REINFORCED CONCRETE WALL JOINT

In order to obtain the joint properties, the assembly of the model depicted in Figure 4 is performed, simplified by the use of a modified version of the T-stub in compression model, as described in section 3. The assembly procedure is then direct, no distribution of resistance is required amongst rows, as only one tension row is identified. In order to determine the joint bending moment and rotation, it is required to define the lever arm $h_r$ of the joint. According to the joint configuration, it

is assumed that the lever arm is the distance between the centroid of the longitudinal steel reinforcement and the mid thickness of bottom flange of the steel beam. Thus, the smallest resistance of the activated components governs the bending moment resistance and may be expressed as follows.

$$M_j = Min(F_i).h_i \qquad (3)$$

$F_i$ represents the resistance of all activated components within the joint under bending moment loading determined as described above.

In what respects the joint rotation, the contribution of all components should be considered. Again, as only one tension and one compression row is activated, the joint rotation can easily be obtained. The component governing the resistance controls the rotation capacity of the joint. The joint rotation capacity may be determined as follows.
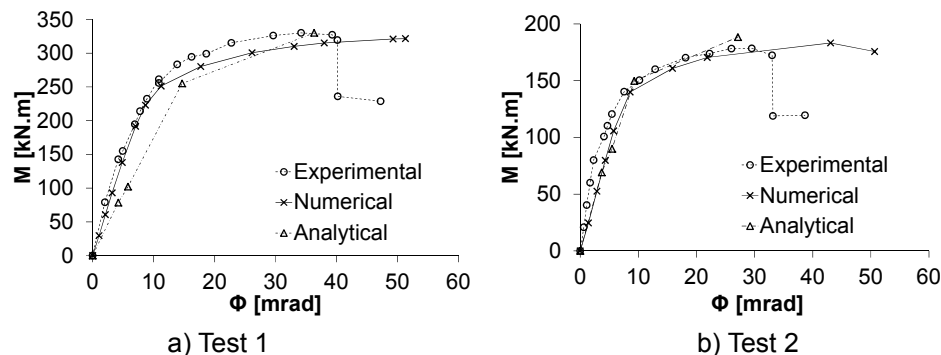
$$\Delta_u = \frac{\sum_1^n \Delta_i}{h_r} \qquad (4)$$

$\Sigma \Delta_i$ represents the sum of the deformation of the activated components for a load level equal to the resistance of the governing component. In the case of the governing component, all its deformation capacity should be considered.

The accuracy of the described model has been assessed using the experimental results performed at the University of Stuttgart within the RFCS research project InFaSo [1]. The tested specimens consisted of a cantilever composite beam supported by a reinforced concrete wall. The joint configuration depicted in Figure 1 was used to connect both members. A vertical load was applied at the free edge of the composite beam up to failure. The load induced in the joint a hogging bending moment. The geometrical and material properties, as well as detailed discussion of the tests, may be found in [15].

In Figure 10, the moment-rotation curves for two of the tested specimens are compared. The results of a numerical model are also included. The calibration and validation of this numerical model is presented in [16]. The parameter varied between the selected specimens is the diameter of the longitudinal reinforcement bars (percentage of reinforcement within the slab): Test 1 – 6xΦ16; Test 2 – 6xΦ12. In what concerns the analytical model, the ECCS [5] model for the longitudinal steel reinforcement was considered. For the slip of the composite beam, the approach proposed in [7] is used. The curves show a good approximation between analytical, numerical, and experimental results. The accuracy of the analytical and numerical approaches in relation to the experimental results are quantified in Table 5.

In terms of resistance the approximation is excellent. In terms of rotation at maximum bending moment, the results of the analytical approach are interesting taking into account that this parameter usually is not quantified. The resistance of each component according to the analytical model is given in Table 6. The percentage of resistance activated of each component is also included. It can be observed that as in the experimental tests, the longitudinal reinforcement bar in tension is the governing component. According to the analytical estimation, in Test 1, the beam web and column in compression is close to its full activation. On the other hand, in both tests, the steel contact plate and the anchor plate in compression are the components with lowest level of activation in comparison to their load capacity.

a) Test 1                    b) Test 2

Figure 10. Moment-rotation curves comparing experimental, numerical and analytical results

Table 5. Summary of the global results of the joint properties and quantification of the approximation to experimental results

| Approach | Test | $M_i/M_{j,test}$ | $\Phi_i/\Phi_{j,test}$ | $S_i/S_{j,test}$ |
|---|---|---|---|---|
| Analytical | 1 | 0,99 | 0,90 | 0,85 |
| | 2 | 1,05 | 0,92 | 0,87 |
| Numerical | 1 | 0,97 | 1,27 | 1,10 |
| | 2 | 1,02 | 1,46 | 0,88 |

Table 6. Resistance of the components according to analytical model and % of activation

| Components | Test 1 | | Test 2 | |
|---|---|---|---|---|
| | $F_{r,i}$ [kN] | % Active | $F_{r,i}$ [kN] | % Active |
| 1 | 811,9 | 100,0 | 460,9 | 100,0 |
| 2 | 1200,0 | 67,7 | 1200,0 | 38,4 |
| 3 | 824,9 | 98,4 | 824,9 | 55,9 |
| 4 | 2562,0 | 31,7 | 2562,0 | 18,0 |
| 5 to 10 | 2017,6 | 40,2 | 2017,6 | 22,8 |
| 11 | 1224,8 | 66,3 | 930,0 | 49,6 |
| *Governing* | *Component 1* | | *Component 1* | |

## 5. CONCLUSIONS AND GENERAL RECOMMENDATIONS

In this paper, a design model based on the component method for composite beam to reinforced concrete wall is proposed and compared with experimental and numerical results. Although some of the approaches of the individual components are incomplete, at the current stage, the model demonstrates to be accurate. Based on the presented results and considerations achieved during this research work, some design suggestions are proposed:

i) Designing the longitudinal reinforcement in the composite beam to be the governing component allows a better control of the joint response. The characterization of this component can be more accurate in an inelastic range in comparison with the other activated components. Furthermore, if the steel reinforcement bars are class C (according to [4]) a ductile response can be obtained.

ii) Due to the complexity of the problem, reducing the Joint Link component to a single spring is a simplification with practical interests. However, this approach is limited and therefore, the failure of the joint in this component should be avoided.

## REFERENCES

[1] Kuhlmann U, Eligehausen R, Wald F, Simões da Silva L, Hofmann J. New market chances for steel structures by innovative fastening solutions. Final report of the RFCS project INFASO, project Nº RFSPR-CT-2007-00051, Brussels, 2012.

[2] European Committee for Standardization – CEN. EN 1993-1-8. Eurocode 3: Design of steel structures. Part 1-8: Design of joints, Brussels, 2005.

[3] European Committee for Standardization – CEN. EN 1994-1-1. Eurocode 4: Design of composite steel and concrete structures. Part 1-1: General rules and rules for buildings, Brussels, 2004.

[4] European Committee for Standardization – CEN. EN 1992-1-1. Eurocode 2: Design of concrete structures. Part 1-1: General rules and rules for buildings, Brussels, 2004.

[5] European Convention for Constructional Steelwork – ECCS. Design of Composite Joints for Buildings. ECCS Publication nº109, Technical Committee 11, Composite Structures, First Edition, Belgium, 1999.

[6] Aribert, J M. "Influence of Slip on Joint Behaviour", Connections in Steel Structures III, Behaviour, Strength and Design, Third International Workshop, Trento, Italy, May 29-31, 1995.

[7] Anderson D, Najafi A A. "Performance of Composite Connections: Major Axis End Plate Joints", Journal of Constructional Steel Research, vol. 31, pp. 31-57, 1994.

[8] Guisse S, Vandegans D, Jaspart J-P. Application of the component method to column bases: Experimentation and development of a mechanical model for characterization. Research Centre of the Belgian Metalworking Industry, MT195, Liège, 1996.

[9] European Committee for Standardization – CEN. CEN/TS 1992-4: Design of fastenings for use in concrete, Final Draft, Brussels, 2009.

[10] Furche J. ZumTrag‐ und Verschiebungsverhalten von Kopfbolzenbeizentrischem

[11] Zug. PhD Thesis (in German), University of Stuttgart, 1994.

[12] Henriques J. Behaviour of joints: simple and efficient steel-to-concrete joints. PhD Thesis, University of Coimbra (To be published).

[13] Steenhuis M, Wald F, Sokol Z, Stark J. Concrete in compression and base plate in bending. Heron 2008; Vol. 53 No. 1/2; 51-68.

[14] Schlaich J, Schäfer K, Jennewein M. Toward a Consistent Design of Structural Concrete. PCI Journal, 32(3), pp. 74-150, 1987.

[15] Comité Euro-International du Béton - CEB. CEB-FIP Model Code 1990: Design Code. Lausanne, 1993.

[16] Henriques J, Ozbolt A, Žižka J, Kuhlmann U, Simões da Silva L, Wald F. Behaviour of steel-to-concrete joints II: Moment resisting joint of a composite beam to reinforced concrete wall. Steel Construction Design and Research (Ed. Ernst & Sohn), Volume 4 (Nº3), 161-165, 2011.

[17] Henriques J, Simões da Silva L, Valente I. Numerical modeling of composite beam to reinforced concrete wall joint. Part II: Global behavior. Engineering Structures, 2012 (Submitted).

# EXPERIMENTAL AND NUMERICAL INVESTIGATION ON UNSTIFFENED AND STIFFENED T-STUBS

Nadia Baldassino, Valerio Mancini, Riccardo Zandonini
*Department of Mechanical and Structural Engineering, University of Trento, Italy*
*nadia.baldassino@unitn.it, valerio.mancini@unitn.it, riccardo.zandonini@unitn.it*

## ABSTRACT

In the framework of a project on robustness recently carried out in Trento, an experimental study of unstiffened and stiffened T-stub elements associated with a flush end-plate beam-to-column connection was carried out. The work focused on the response of the column flange T-stub under pure tension and under combined axial and shear forces. In the tests, three positions of the stiffener with respect to the bolts' row were considered. Experimental results were then used to develop and validate reliable F.E. numerical models.

The paper presents and discusses the tests and the principal outcomes of their evaluation. Furthermore, some results of the numerical analyses are also introduced and briefly discussed.

## 1. INTRODUCTION

In the structural field, robustness refers to the design against accidental actions (i.e.; explosion, impact, fire, earthquake...). Despite studies and researches on this topic began in the '60 after the Ronan Point collapse in London [Griffiths *et al.*, 1968], the complexity of the various issues involved in the damage effects caused by accidental actions and the limited availability of suitable computational tools, prevented the definition of specific design criteria even for the more common structural typologies. The tragic consequences of terroristic attacks of 2000' stressed the importance of specific design strategies and of effective requirements for accidental design situations. Currently, strategies for robustness are well established and studies are in progress to transpose them into specific criteria and design rules. The peculiarities of the design accidental actions and of the structural system allow selecting two different design strategies. In case of identified actions the structural design should enable the structure to sustain the action, either adopting measures preventing or reducing the value of the action or designing the structure to have a minimum required level of robustness. When unidentified accidental actions are concerned, the design has to be performed limiting the extent of localised failure. The approach can focus on enhancing the redundancy, designing the key elements for notional accidental actions or adopting prescriptive rules. In case of framed steel structures, the 'tying' strategy is a simple viable solution to avoid the spreading of localized damages [Liu *et al.*, 2005]. In case of collapse of a column, beams have to be able to sustain and transfer to the undamaged part of the structure the loads applied to the column just above the lost one. The nearby beams and/or joints reach then their full plastic resistance

under combined internal forces, and their response evolves with the activation of large inelastic displacements, resulting in increasing tensile axial load and decreasing bending moment. At the end of the process internal forces in the beam and the joint are substantially different from the initial ones with a tension axial force prevailing.

If the joint is the weakest component, robustness implies that the joint should possess significant ductility to allow for large displacements, and adequate resistance under different combinations of axial force, shear force and bending moment allowing occurrence of the redistribution of the internal forces needed to reach the new equilibrium condition.

In a steel connection, the rotational capacity mainly depends on the deformation of its components, and in particular of its less ductile components. In flanged beam-to-column bolted connection a significant part of the plastic rotation is given by the deformation of the column flange and of the beam end-plate. The behaviour of these components can be analyzed through equivalent T-stub elements. The "T-stub approach" is the basis of the so-called "component method", a general model enabling analytical evaluation of the mechanical properties of the connection (strength and stiffness). Numerical and experimental studies carried out in recent years allowed the definition of relationships enabling approximation of the T-stub response when subject to pure tensile force. The performance of T-stubs under combined forces, i.e. under axial and shear forces, remains a rather unexplored field. Few studies are known to the Authors: Faella, Piluso and Rizzano [Faella *et al.*, 1999] applied a simplified theoretical approach to quantify the influence of the shear force on the ultimate load capacity of a T-stub when the collapse is associated with mode 1 or 2. They found that the influence of shear can be neglected but in the case of slender flanges. On the other hand, the numerical and experimental study on double clip angle connections carried out by Bursi and Gerstle [Bursi *et al.*, 1994] showed a noticeable influence of the loading conditions on both the ultimate load and on the failure modes. Clearly, these studies provide a general and very limited background to the problem. Within the framework of the component method, there is the need of developing a component model accounting for the interaction between the axial and shear forces. To this aim, tests were performed on T-stubs under different combinations of N and V. Experimental results were then used to develop and validate reliable F.E. numerical models.

The paper presents and discusses the tests and their main outcomes. The key features of the F.E. numerical models developed and calibrated against the experimental results are also illustrated. Some results of a study of stiffened T-stub under combined axial and shear forces conclude the paper.

## 2. TESTS ON T-STUBS

### 2.1. Specimens layout and tests' procedure

The experimental study considers the beam-to-column steel joint configuration presented in Figure 1. A series of tests on T-stubs elements of both the end-plate and the column flange were carried out [Kuhlmann *et al.*, 2001], aimed at investigating the response of the tensile zone of the joint. In this paper the attention focuses on the response of the column T-stub for which stiffened and unstiffened configurations were considered.

The specimens were designed, in accordance to the prescription of the EN1993-1-8, to collapse, under tension, by a flange mechanism mode, i.e. collapse

mode 1. Figure 2 illustrates the layout of the specimens. The values of the geometrical parameters indicated in Figure 2 are summarised in Table 1. In order to investigate the influence of possible stiffeners, three different stiffener's locations relative to bolts row (distance $d_i$, i=1,2,3 in Figure 2) were selected.

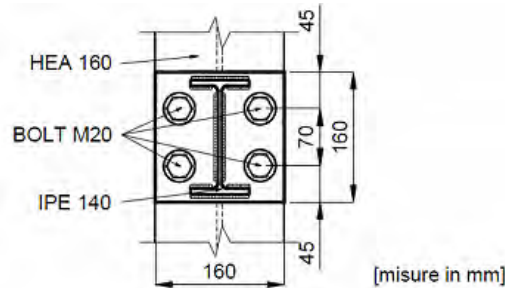The length of the stiffened T-stubs was maintained the same as for the unstiffened ones, i.e. 256mm.
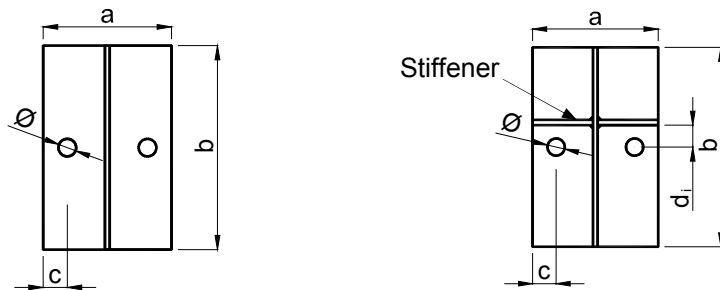


Figure 1. Considered beam-to-column steel joint.



Figure 2. Main geometrical parameters for the T-stubs' configurations.

Table 1. T-stubs' configuration.

| Spec. configuration | Test ID | a (mm) | b (mm) | c (mm) | $d_i$ (mm) | Φ (mm) | Thickness (mm) | | |
| --- | --- | --- | --- | --- | --- | --- | --- | --- | --- |
| | | | | | | | flange | web | stiffener |
| Unstiffened | 1CB | | | | ------ | | | | ------ |
| Stiffened 1 | 2CA | 160 | 256 | 30 | 32 | 20 | 9 | 6 | 8 |
| Stiffened 2 | 2CB | | | | 60 | | | | |
| Stiffened 3 | 2CC | | | | 88 | | | | |

The study comprises tests on:
- unstiffened T-stubs. A total of 21 tests were carried out: 5 tests under tension (Figure 3a) and 16 tests under combined axial and shear forces (Figure 4) were performed;
- stiffened T-stubs. 12 tensile tests (Figure 3b), i.e. four tests for each specimen's configuration (Figure 2 – Table 1), were performed.

In the tests under pure tension the T-stub specimens had the flange connected to a rigid support, and the load was applied concentrically to the bolts connecting the flange to the support (Figure 3). The tests under a combination of axial and shear forces required the design of an 'ad hoc' testing apparatus (Figure 4). The two 'rigid

parts' of the apparatus were joined by means of the T-stub specimen which was bolted to both of them. The apparatus was connected to a strong floor and to a hydraulic actuator, allowing application of a tensile force. The axis of application of the force passed through the bolt line at the interface between the T-stub flange and the upper part of the apparatus. By changing the location at which the testing apparatus was connected, it was possible to "rotate" the T-stub with respect to the load line. Such a 'rotation' allowed effective application of different combinations of axial and shear forces. In particular the values of angle α of 0°, 15°, 30°, 45°, 60° and 75° were explored (Figure 4a). The condition of α=0° corresponds to the case of pure shear.
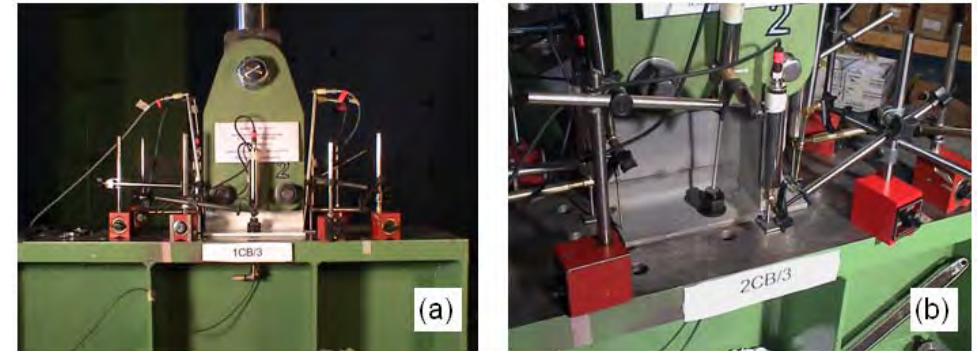


Figure 3. Tests' set-up for tensile tests: a) unstiffened T-stub, b) stiffened T-stub.
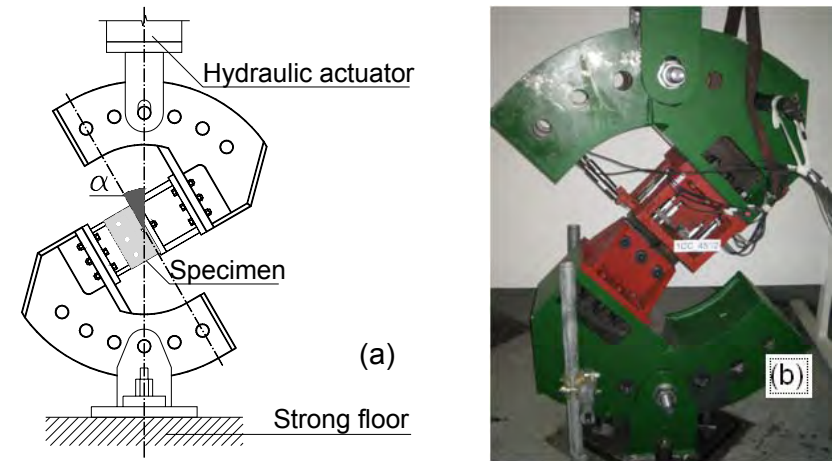


Figure 4. Test set-up for T-stub tests under axial and shear forces.

In all the tests the connection of the T-stub flange to the testing apparatus was realised by means of bolts M20 class 8.8 preloaded to a force of 125kN. At the connection of the specimens to the testing apparatus, the T-stub web was stiffened by means of additional steel plates in order to avoid its premature failure and to allow for the activation of a "flange mechanism". Before testing, the main geometrical dimensions of the specimens were measured, in order to point out possible dimensional deviations with respect to the nominal values. The measures indicate deviations consistent with the fabrication tolerances. Tensile coupon tests were also performed in order to determine

the mechanical properties of steel of the T-stub flange and of the bolts. The T-stub tests were carried out under displacement control. The loading process comprises of a preliminary cycle up to approximately 10% of the expected collapse load, aimed at eliminating the effect of lack of fit, and of a subsequent cycle up to collapse. During the tests the key components of the flange displacements were measured (Figure 5).



Figure 5. Typical transducers set-up.

### 2.2. Tests results

Tension tests showed that failure of both unstiffened and stiffened T-stubs was achieved after the development of a remarkable plastic deformation of the flange associated with significant bending of the bolts (Figure 6).

In all tests the collapse was due to the fracture of the bolts associated with bearing deformation of the holes increasing with the shear force component.



Figure 6. Residual displacements at collapse for tensile tests.

In case of tension-shear tests, different bolts and flange responses were observed for different value of the angle α. Figure 7 shows three typical deformed shapes of the bolts at collapse: on the left the pure tension test (α =90°), in the centre the test with α =45° (N = V), on the right the pure shear test (α =0°). The comparison between these deformed shapes points clearly out the variation of the effect of the shear force and flange bending. The latter increases with the importance of the tension force. As to the flange mechanism, it was activated with the development of non negligible inelastic deformations, but for the values of $\alpha$ lower than 30°. Higher the tensile force component higher the flange deformation.

A summary of the test results is reported in Tables 2 and 3, related to unstiffened and stiffened T-stubs, respectively. The tables summarise main details concerning the tests (e.g., the number of tests and angle of inclination of the applied load in case of tests under combined actions), average values of the collapse load ($F_{unstiff}$, $F_{stiff}$) and, as an appraisal of the scatter of the tests' results, the coefficient of variation. In case of tests under combined axial (N) and shear (V) forces (Table 2), the applied force's components in the parallel and in the perpendicular direction with respect to the flange are also reported. Furthermore, the last column of Table 3 reports the ratio between the average collapse loads of stiffened ($F_{stiff}$) and unstiffened T-stubs ($F_{unstiff}$, specimens 1CB in the last row of Table 2).



Figure 7. Deformation of the bolts at collapse in tests under axial and shear load.

Table 2. Test's results of unstiffened T-stubs.

| Test ID | Angle of tests | Number of tests | Collapse load ($F_{unstiff}$) | Coefficient of variation | Axial Component (N) | Shear component (V) |
|---|---|---|---|---|---|---|
| | | | (kN) | | (kN) | (kN) |
| 1CC_0° | 0° | 4 | 352,55 | 0,032 | ---- | 352,55 |
| 1CC_15° | 15° | 2 | 334,40 | 0,008 | 86,55 | 323,01 |
| 1CC_30° | 30° | 2 | 329,20 | 0,014 | 164,60 | 285,10 |
| 1CC_45° | 45° | 2 | 316,08 | 0,003 | 223,50 | 223,50 |
| 1CC_60° | 60° | 4 | 314,44 | 0,054 | 272,31 | 157,22 |
| 1CC_75° | 75° | 2 | 305,00 | 0,044 | 294,61 | 78,94 |
| 1CB | 90° | 5 | 285,73 | 0,020 | 285,73 | ---- |

Table 3. Test's results of stiffened T-stubs.

| Test ID | number of tests | Collapse load ($F_{stiff}$) | Coefficient of variation | $\dfrac{F_{stiff}}{F_{unstiff}}$ |
|---|---|---|---|---|
| | | (kN) | | |
| 2CA | 4 | 382,90 | 0,016 | 1,34 |
| 2CB | 4 | 347,77 | 0,027 | 1,22 |
| 2CC | 4 | 314,86 | 0,043 | 1,10 |

The results of Table 2 are plotted in Figure 8: Figure 8a describes the variation of the collapse load ($F_{unstiff}$) as a function of the angle $\alpha$ of the T-stub with respect to the vertical direction (Figure 4), while Figure 8b shows the related axial (N) - shear

forces (V) domain. In the figures the blue dots indicate the experimental results while the red curves represent the fitting curves obtained applying the least squares method.
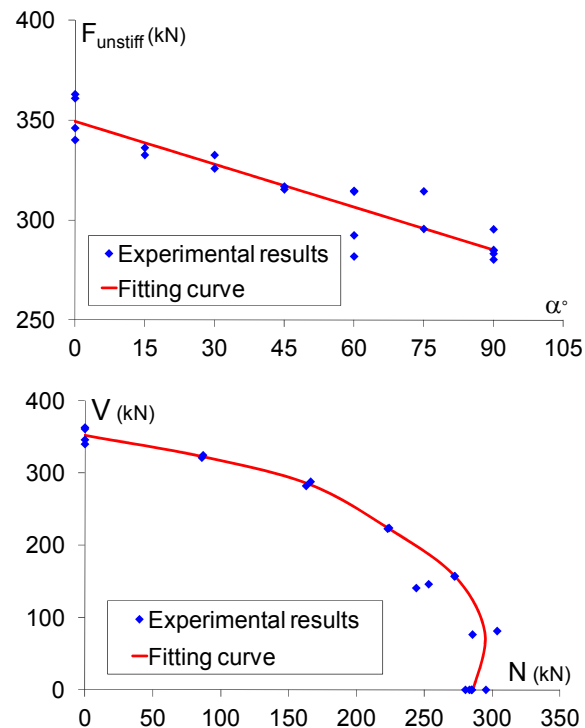


Figure 8. F- α° relationship and N-V domain for unstiffened T-stub.

Figure 8 point out:
- a linear relationship between the collapse load and the angle α;
- a not negligible interaction between axial (N) and shear forces (V). In the range 0≤α≤30° a linear relationship can be adopted while for α≥30° the V-N relationship appears remarkably non linear;
- the modest influence of V for values of α greater than 60°.

The analyses of the residual deformation of the T-stub flanges after collapse showed that flange mechanisms activated for angles α≥30°. When α becomes lower than 30° the shear force tends to progressively prevail: the activation of a flange mechanism is prevented, and the shear mechanism develops.

Results in Table 3 confirm the sensitivity of the T-stub response to the presence of stiffeners and in particular to the stiffeners' position. This is also apparent in Figure 9, where typical experimental responses of unstiffened and stiffened T-stubs are compared. Assuming as a 'benchmark' the unstiffened T-stub (curve in red in figure 9), the closer stiffener position results in an increase of 34% on average of the ultimate load and in a decrease of 41% of the maximum ultimate flange displacement. This effect tends to reduce when the stiffener 'moves' away from the bolts' position.

The increase of the collapse load appears nevertheless not negligible even for the farthest stiffener position.
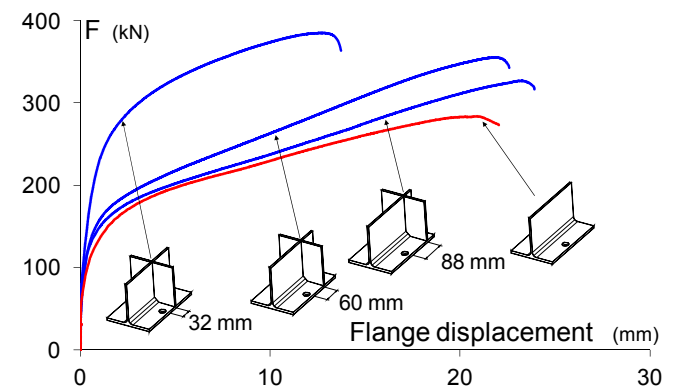


Figure 9. Typical load-displacement responses.

## 3. NUMERICAL SIMULATIONS

### 3.1. Numerical models

A better and more complete understanding of some key aspects of the T-stub response can be achieved by 3D numerical analyses. In particular, they provide useful information on the interaction of the axial and shear forces on the plastic deformation and resistance, as well as of the stiffener's effect. Numerical models were hence developed and calibrated against the experimental results (Mancini, 2012). At this aim, the commercial software Abaqus v.6.8 was adopted. Each model reproduces half of the specimen taking advantage of the symmetry and is characterized by five different parts: the T-stub (including the stiffener in stiffened T-stubs), the rigid support, the bolt (including head and nut), and the two washers. Eight nodes solid element type C3D8R was adopted to model all the parts. The formulation of this F.E. element allows for nonlinear analyses involving contact, plasticity, and large deformations. An 'optimal' mesh (Figure 10) was defined on the basis of preliminary analyses aiming to balance the complexity of the model and the solution's accuracy. The models were defined taking into account the average dimensions of the actual specimens, as determined by the geometrical measures.

The central role of the bolts in the T-stub response required particular attention in the modelling phase of these components. The bolt shank was hence modelled by considering also the section reduction in correspondence of the threaded part. This allowed for taking into account the variation of stiffness and strength between the threaded and unthreaded parts of the shank. Furthermore, in case of stiffened T-stub models, the welds between the stiffener and the T-stub were also modelled. The interactions between the parts of the models were reproduced by means of contact elements. The choice of the interaction contact formulation was made on the basis of the results of preliminary numerical analyses which allowed calibrating the parameters governing the contact formulation against the experimental results. Stress strain-relationships of the steel of both the T-stub flange and the bolts were modelled on the basis of the experimental results of the tensile coupon tests.

All the simulations were carried out in large displacements, taking into account mechanical and geometrical nonlinearities.
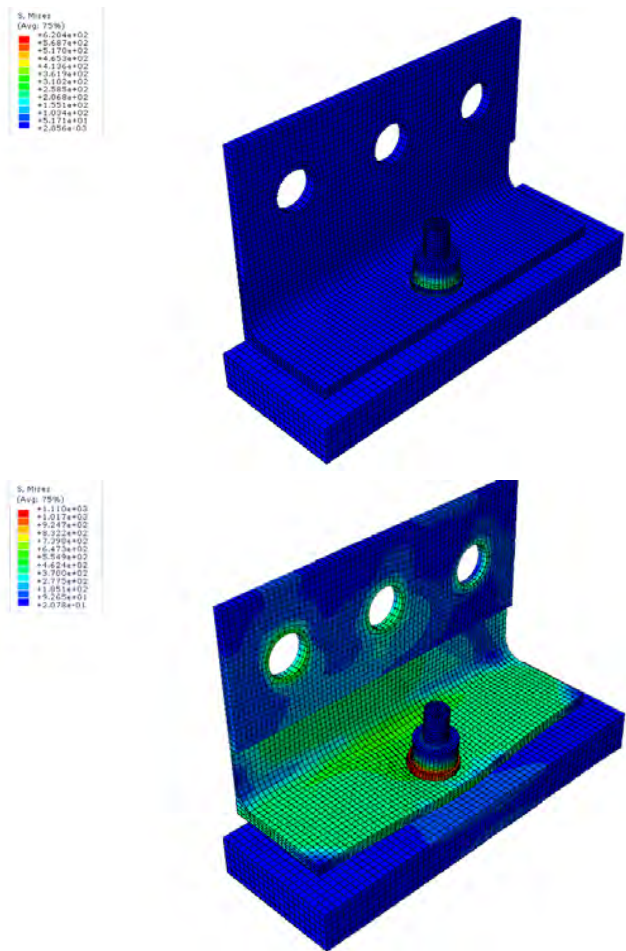
Figure 10. F.E. models for unstiffened T-stubs.

## 3.2. Numerical results

The F.E. models were validated against a wide range of experimental measurements. The attention was paid to the overall and local response. The former is described by the collapse load and the load-displacement curve, while the latter is characterized by the main load-displacements relationships obtained from the set of transducers used in the tests, and by the residual flange and bolt deformations after collapse. Some of the comparisons between experimental and numerical analyses are presented in Table 4 and in Figure 11. Table 4 summarises the results of the tensile tests on both unstiffened and stiffened T-stubs in terms of collapse load, and Figure 11 compares results of tests under combined actions in terms of axial (N) and shear (V) components of the applied load (F).

The agreement between numerical results and tests' outcomes is more than satisfactory, and suggested to extend to stiffened T-stubs the investigation of the

effect of combined axial and shear forces. At this aim, the stiffened T-stub configurations tested under pure tension (specimens 2CA, 2CB and 2CC of Table 1) were considered. As loading conditions, the N-V combinations characterized by α=0°, 15°, 30°, 45°, 60°, 75° (Figure 4) were assumed.

The results of the analyses allowed drawing the axial (N)-shear (V) forces domains showed in Figure 12. These domains:

- confirm the not negligible interaction between axial (N) and shear (V) forces, already observed for the unstiffened T-stub (Figure 8);
- appear remarkably non linear since for low value of the α angle, independently from the bolts-stiffener position;
- are not affected by the presence of a stiffener when shear predominates preventing the development of a flange mechanism (α <30°). As soon as a flange mechanism activates (α ≥30°) the presence of a stiffener leads to not negligible increases of the T-stub failure load. The closest the stiffener to the bolts' position the highest the 'beneficial' effect in terms of strength.

Table 4. Numerical and experimental results of tensile tests.

| Test ID | F$_{num}$ (kN) | F$_{exp}$ (kN) | $\dfrac{F_{num}}{F_{exp}}$ |
|---------|---------|---------|---------|
| 1CB | 300,00 | 285,73 | 1,05 |
| 2CA | 395,25 | 382,90 | 1,03 |
| 2CB | 347,85 | 347,77 | 1,00 |
| 2CC | 328,00 | 314,86 | 1,04 |
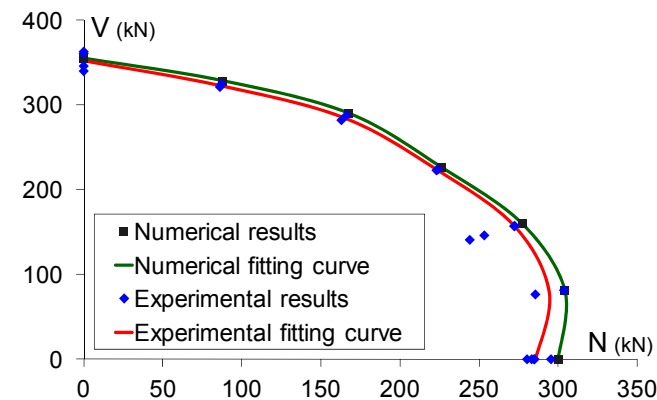


Figure 11. Comparison between numerical and experimental results of T-stubs under combined N and V.

Results of these analyses provide only preliminary information on the influence of shear on the T-stub response in tension. However, the results indicate that the presence of combined actions significantly affects the response and ultimate strength of T-stubs. This influence has to be considered if design aims to robust structures.

# 4. CONCLUSIONS

The paper presents and discusses the results of an experimental and numerical study of the response of the T-stub components of end-plate connections subject to combined forces. The research was carried out as part of a project on the robust response of composite frames. At this aim T-stubs tests associated to both the end-plate and the column flange were performed. This paper presents the study of the column's T-stubs. Unstiffened and stiffened T-stub configurations were tested in tension and under different combination of axial and shear forces. In case of stiffened T-stubs, three different bolt-to-stiffener distances were considered.

Tests enabled understanding of some key aspects of the T-stubs response and supplied useful information on the interaction of the shear and axial force on the plastic deformation capacity and ultimate resistance. 3D numerical models were then developed and calibrated against the experimental results. They enabled extension of the study on stiffened T-stubs to the case of combined N-V forces. Experimental and numerical results allowed the definition of N-V domains for both unstiffened and stiffened T-stubs which enabled a 'quantitative appraisal' of the influence of shear on the tensile strength of T-stubs.
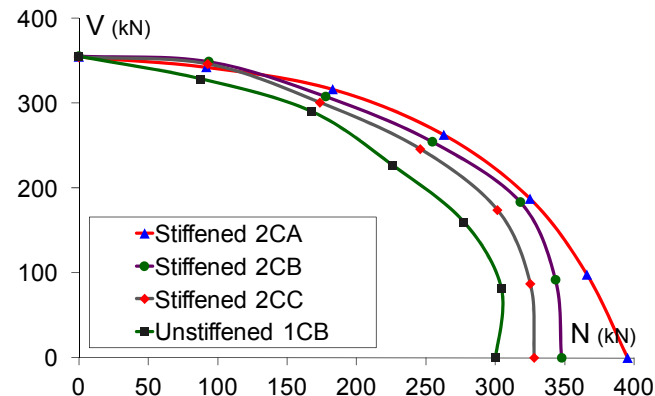


Figure 12. Numerical N-V domain for stiffened T-stubs.

## ACKNOWLEDGMENTS

## REFERENCES

[1] Griffiths, H., Pugsley, A. and Saunders, O. (1968), "Report of the inquiry into the collapse of flats at Ronan Point Canning Town", Her Majesty's Stationery Office, London.

[2] Liu, R., Davison, J.B., and Tyas, A. (2005), "Is catenary action sufficient to resist progressive collapse in a steel framed building", Proc. of 4th European Conference on Steel and Composite Structures, Maastricht, June, (pp 155-162).

[3] Faella, C., Piluso, V. and Rizzano, G. (1999), "Structural steel semirigid connections. Theory, design and software", CRC Press (pp. 505).

[4] Bursi, O.S. and Gerstle, K. (1994), "Analysis of flexibly connected braced steel frames", *Journal of constructional steel research*, vol. 30 (1) (pp. 61-83).

[5] Kuhlmann, U., Rölle, L., Jaspart, J.P., Demonceau, J.F., Vassart, O., Weynand, K., Ziller, C., Busse, E., Lendering, M., Zandonini, R. and Baldassino, N. (2009), "Robust structure by joint ductility", Research project final report (contract RFSR-CT-2004-00046, European Commission, Luxemburg (pp. 165).

[6] Mancini, V. (2012), "Response of flush end-plate joints under combined actions", Doctoral Thesis, Doctoral School in Engineering of Civil and Mechanical Structural Systems, Department of Mechanical and Structural Engineering, University of Trento (pp. 182).

# TENSION TESTS ON WELDED THREADED STUDS WITH A TENSILE STRENGTH OF 800 N/mm²

Dieter Ungermann and Stephan Schneider
Dortmund University of Technology, Institute of Steel Construction,
August – Schmidt – Straße 6, 44227 Dortmund, Germany
stahlbau@tu-dortmund.de

Rainer Trillmich
KÖCO Köster & Co GmbH
Spreeler Weg 32, 58256 Ennepetal, Germany
r.trillmich@koeco.net

## ABSTRACT

Welding studs have to consist of a weldable material because of the joining process. It is for this reason that currently only a few austenitic steels and carbon steels out of strength class 4.8 according to EN ISO 898-1, with a maximum carbon content of C = 0,20%, are accredited for welding studs. If higher ultimate tensile strengths are required, the manufacturer used in the past the cold headed steel 20MnB4, which achieves ultimate tensile strengths close to strength class 8.8 due to a thermally post – tempering. Welding of the 20MnB4 with a maximum carbon content of C = 0,23% is suitable only to a limited extent. By reason of additional costs for thermally post-tempering processes the 20MnB4 studs has not prevailed in the market. Another alternative material is the cold headed steel 8MnSi7 (1.5113), which was used for the first time from the manufacturer KÖCO to produce high strength studs. It has a maximum carbon content of C = 0,10% which suspects a good weldability. The ultimate tensile strength of 8MnSi7 wire rod is approximately between 520 to 620N/mm² and in addition by cold forging it reaches a level of 800N/mm², so that studs made of 8MnSi7 could be classified as strength class 8.8. To verify the weldability and the classification of the strength class 91 axial tension tests on threaded studs with a statically load were performed in the course of a German research project. The present paper gives an overview of the results of the research project.

## 1. INTRODUCTION

### 1.1. Cause and subject of the research project

Stud welding has its roots in ship building in the early 20th century and nowadays it is also being used in many other applications like composite constructions, mechanical and civil engineering. Stud welding is a highly sophisticated, very economic fastening technology but due to the joining process it is limited to weldable materials with a low carbon content respectively carbon equivalent.

The strengths for approved materials are generally below 450N/mm². Against the background of the increasing use of high strength material for steel and composite constructions the need for welded threaded studs out of high strength steel is obvious. 8MnSi7 is a weldable cold headed steel which reaches the strength of class 8.8 by cold forging. In this research project the weldability of studs type PD (threaded stud) and RD (threaded stud with reduced shank) made of 8MnSi7 were tested in 91 tension tests with static load. Furthermore the applicability of the design rules for the tension resistance of the threaded part and the shank based on EC3-1-8 was verified. In case of thin steel plates the ultimate load was limited by the shear strength of the steel plate material and did not achieve the tension resistance of the studs. To cover this failure mode, a design approach was suggested, founded on the results of the tests with shear failure in the steel plate material.

8MnSi7 was used for the first time from the manufacturer KÖCO to produce high strength studs. Due to this KÖCO supported the research project with the studs and the welding equipment. Since October 2010 KÖCO is worldwide the only manufacturer with a general technical approval (DIBt Z-14.4-585) using 8MnSi7 for studs with a strength comparable to strength class 8.8 and sell them under the brand name K800. Further trade mark rights on the European level are submitted.

### 1.2. Welding processes and stud types

Arc stud welding can be divided into two main welding processes: stud welding with tip ignition on the one hand and drawn arc stud welding on the other hand. Based on the welding time, the weld pool backup and the source of the welding energy EN ISO 4063 defines different subcategories of arc stud welding. The most common welding process for applications in civil engineering is "drawn arc stud welding with ceramic ferrule or shield gas" (reference number 783 according to EN ISO 4063). Figure 1.1 illustrates the basic principles of drawn arc stud welding. The stud is placed against the steel plate and then the stud is lifted while the current is flowing and these lights up the drawn arc which melts the surface of the steel plate and the tip of the stud. Afterwards the stud is plunged in the weld pool and a cross sectional joint is achieved.



**Legend:**
L lifting
P excess length
X time
Y current
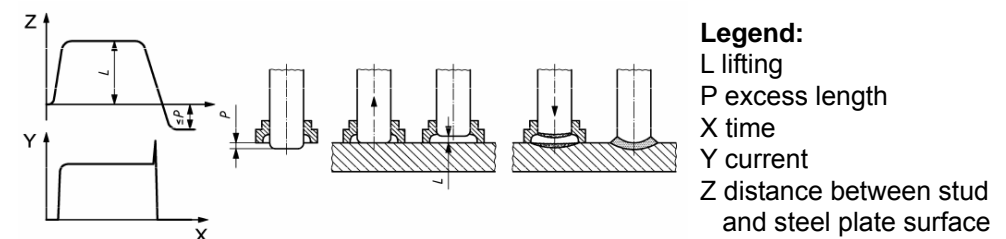Z distance between stud and steel plate surface

Figure 1.1. Procedure of drawn arc stud welding according to EN ISO 14555

The geometry of the studs is standardized in EN ISO 13918. Three exemplary selected threaded studs are shown in Figure 1.2. The associated welding process is given in the caption.

A cone shaped stud end is characteristic for the drawn arc stud welding. The point angle $\alpha$ indicates the welding time, the smaller the point angle the shorter is the welding

time. Studs for welding with tip ignition have a small tip – which lights up the drawn arc when lifted up from the steel plate – instead the cone shaped end. The welding time, the weld pool backup and the peak current determine the limitations of the welding processes. For drawn arc stud welding the limitations are summarized in Table 1.1.

Welding process: drawn arc stud welding
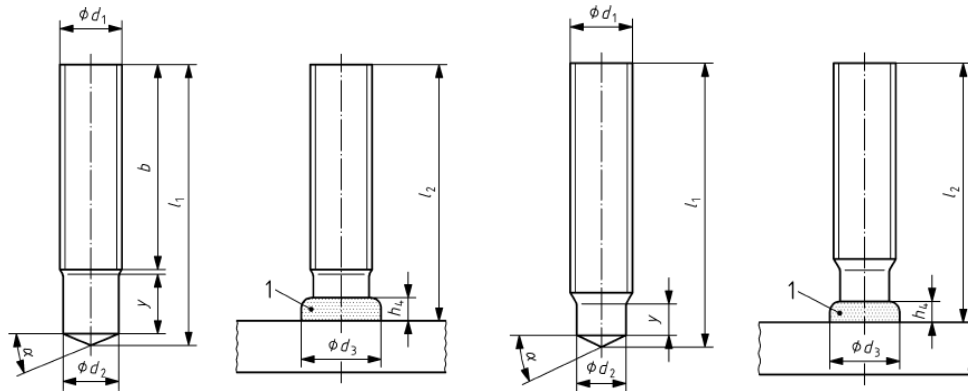


Stud welding with tip ignition
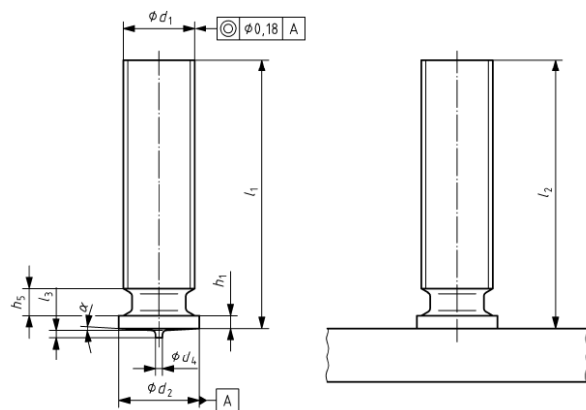


PD – Stud (M6 – M24)     RD – Stud (M6 – M24)     PT – Stud (M3 – M8)

Figure 1.2. Threaded studs according to EN ISO 13918

Table 1.1. Limitations for drawn arc stud welding according to EN ISO 14555

| | stud diameter d [mm] | peak current I [A] | welding time $t_W$ [ms] | weld pool backup | workpiece surface | workpiece thickness $t_{min}$ [mm] |
|---|---|---|---|---|---|---|
| **drawn arc stud welding** | 3 to 25 | 300 to 3.000 | > 100 | ceramic ferrule (CF) or shield gas (SG) | blank, rolling layer, initial rust | 1/4d (CF), 1/8d (SG), 1mm |

Further information for other welding processes can be found in Annex A of EN ISO 14555.

# 2. EXPERIMENTAL RESEARCH

## 2.1. Test program overview and material properties

The experimental program consisted of two test series with threaded studs type PD and RD with nominal diameter of M8 and M20, see Figure 1.2. Currently the 8MnSi7 wire rod is limited to a maximum diameter of 18,15mm and due to this studs with a nominal diameter above M20 are not available.

The studs were tested in tension tests according to EN ISO 14555. The test setup and detailed information of the test procedure are given in chapter 2.2 of this paper. To verify the weldability in the first test series (VS – series) a steel plate with a thickness of 40mm was used. The large thickness of the steel plate leads to a disadvantageous thermal gradient in the heat affected zone (HAZ) and with it the hardness increases. In the second test series (VT – series) the thickness of the steel plate depends on the nominal diameter of the studs according to the minimum requirements for the draw arc stud welding with ceramic ferrule, Table 1.1. In the VS – series the predicted failure mode was a tensile fracture in the threaded part of the PD – studs respectively in the reduced shank of the RD – studs. Due to the very small thickness of the steel plate in the VT – series a shear fracture of the steel plate should occur along the outer boundary of the welding bead, Table 2.1.

Table 2.1. Test series and predicted failure mode

| Test series | stud type | No. of tests | predicted failure mode | workpiece material | workpiece thickness | studs material | studs diameter |
|---|---|---|---|---|---|---|---|
| **VS - Series** | PD-stud | 20 | tensile fracture in the thread | S690QL | 40mm | 8MnSi7 | M8 - M20 |
| | RD-stud | 20 | tensile fracture in the reduced shank | | | | |
| **VT - Series** | PD / RD | 30 | shear failure in the workpiece | SZBS800 | 2mm | 8MnSi7 | M8 |
| | PD / RD | 21 | | S690QL | 5mm | | M20 |

All steel plates used for the investigations are made of high strength steels with nominal yield strength of approximately 690N/mm². In case of the 5 and 40mm steel plates it was a high strength quenched and tempered, fine grained steel according to EN 10025, part 6 and the 2mm steel plates are made of a thermo-mechanical rolled, microalloyed steel. The chemical composition of the steel plates and the studs are given in Table 2.2 and 2.3.

Table 2.2. Chemical compositions of the steel plates

| | C | Si | Mn | P | S | N | B | Cr | Cu |
|---|---|---|---|---|---|---|---|---|---|
| **No. 01 S690QL** t = 40mm | 0,17 | 0,29 | 1,17 | 0,0110 | 0,0042 | 0,0051 | 0,0048 | 0,331 | 0,035 |
| **No. 02 SZBS800** t = 2mm | 0,086 | 0,53 | 1,90 | 0,0100 | 0,0013 | 0,0076 | 0,0011 | 0,034 | 0,013 |
| **No. 03 S690QL** t = 5mm | 0,15 | 0,29 | 1,36 | 0,013 | 0,0040 | 0,0070 | 0,0021 | 0,042 | 0,034 |

| | Mo | Nb | V | Ti | Ni | Zr | As | Sn | Sb |
|---|---|---|---|---|---|---|---|---|---|
| **No. 01 S690QL** t = 40mm | 0,207 | 0,028 | 0,0025 | 0,0200 | 0,048 | 0,0031 | 0,0043 | 0,0100 | 0,0110 |
| **No. 02 SZBS800** t = 2mm | 0,0058 | 0,033 | 0,0050 | 0,157 | 0,338 | 0,0034 | 0,0150 | 0,0044 | 0,023 |
| | | Nb + V + Ti = 0,195 | | | | | | | |
| **No. 03 S690QL** t = 5mm | 0,110 | 0,027 | 0,0040 | 0,013 | 0,043 | 0,0031 | 0,017 | 0,0051 | 0,0082 |

www.steelconstruct.com

In general the weldability depends on the carbon content and should be less than C = 0,20%. As shown in Table 2.2 and 2.3 all material fulfills these requirements. The effect of other alloyed elements on the weldability can be reviewed by the carbon equivalent PCM, based on the work of *Ito* and *Bessyo*. A good weldability could be assumed, if the carbon equivalent is less than PCM = 0,45, calculated according to Equation (2.1).

$$PCM = C + \frac{Si}{30} + \frac{Mn + Cu + Cr}{20} + \frac{Ni}{60} + \frac{Mo}{15} + \frac{V}{10} + 5 \cdot B \qquad (2.1)$$

The carbon equivalent varied between PCM = 0,20 for the stud material and PCM = 0,29 for the 40mm thick steel plate made of S690QL, therefore a good weldability could be assumed.

Table 2.3. Chemical compositions of the studs

| material: 8MnSi7 | C | Si | Mn | P | S | V | Cr | Ni | W |
|---|---|---|---|---|---|---|---|---|---|
| No. 04 studs M8 (wire rod ⌀7,06mm) | 0,074 | 1,03 | 1,68 | 0,014 | 0,0052 | 0,018 | 0,028 | 0,017 | 0,034 |
| No. 05 studs M20 (wire rod ⌀18,15mm) | 0,081 | 1,03 | 1,70 | 0,015 | 0,0051 | 0,018 | 0,024 | 0,014 | 0,033 |

The mechanical properties of the wire rod and the studs where measured in coupon tests. The results are summarized in Table 2.4.

It is particularly noticeable, that the yield strength and ultimate tensile strength of the studs is lower than the strength of the corresponding wire rod and the M20 studs did not reach the minimum strength requirements of strength class 8.8 according to EN ISO 898-1. Further investigations on PD-studs M20 have shown that the yield and ultimate tensile strength did not depend on the diameter of the test specimen. For this reason an inhomogeneous distribution of the yield and ultimate tensile strength over the cross section could be excluded. The drop in strength can only be assumed in the manufacturing process of the studs, but no further investigations were made in the frame of this research project.

Table 2.4: Mechanical properties of the wire rod and the studs

| | measured values | | | | requirement acc. to EN ISO 898-1 | |
|---|---|---|---|---|---|---|
| | $R_{p0,2}$ [N/mm²] | $R_m$ [N/mm²] | $f_u / f_y$ [-] | E [N/mm²] | $R_{p0,2}$ [N/mm²] | $R_m$ [N/mm²] |
| wire rod (⌀7,06mm) | 852 | 884 | 1,04 | 184.000 | 640 | 800 |
| PD / RD stud M8 | 671 | 842 | 1,25 | 180.000 | | |
| wire rod (⌀18,15mm) | 770 | 824 | 1,07 | 175.000 | 660 | 830 |
| PD / RD stud M20 | 627 | 777 | 1,24 | 178.000 | | |

## 2.2. Welding parameters and tension test setup

Previously to the VS – and VT – series a small series of test studs were welded in the downhand position (Figure 2.1) using different welding times and peak currents. In order to obtain suitable welding parameters these studs were subjected to bending

test according to EN ISO 14555 and if the studs did not fail by a brittle fracture in the welding area, the used welding parameters are acceptable for the stud type. Due to the different diameter at the cone shaped end of PD and RD studs the welding parameters differ slightly. The average values for studs M8 are: $t_W$ = 300ms and $I_W$ = 600A and for studs M20: $t_W$ = 750ms and $I_W$ = 1.400A. It should be noted that all welding parameters are setting values at the stud welding system.
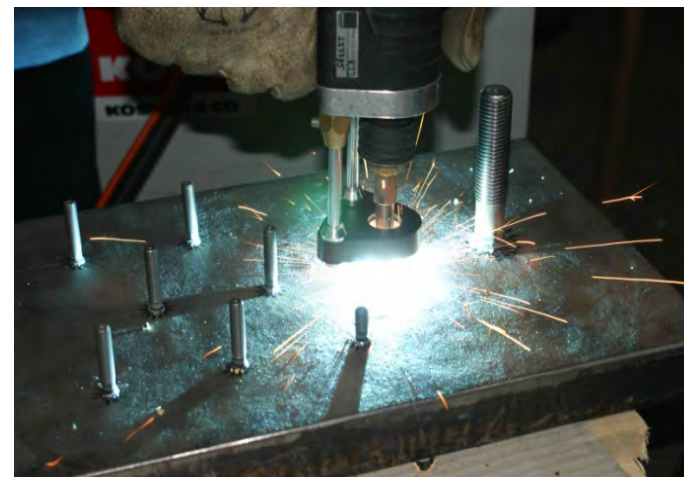


Figure 2.1. Sample picture from stud welding



Figure 2.2. Hydraulic jack

The tests of the VS – series were carried out with a hydraulic jack as shown in Figure 2.2. The elongations of the studs were measured by two displacement transducers, which were placed oppositely. The tension force was applied on the test studs by a threaded rod which was fixed at the top of the jack. To exclude effects

of load eccentricities, a hinge bearing was placed between the jack and the load cell. All test of the VT – series were performed in a 630kN hydraulic testing machine with a comparable measurement system.

In both tests series packing pieces were used with the aim to ensure a uniform ratio of drilling diameter $d_i$ and welding beat diameter $d_3$, Figure 2.3. To avoid a significant bending of the thin steel plates in test series VT a small drilling diameter was chosen ($d_3/d_i \approx 0,65$). Due to the bending resistance of the 40mm thick steel plate in the VS test series the drilling diameters of the packing piece does not need to be as small as in the VT series, therefore a ratio of $d_3/d_i \approx 0,30$ was used.
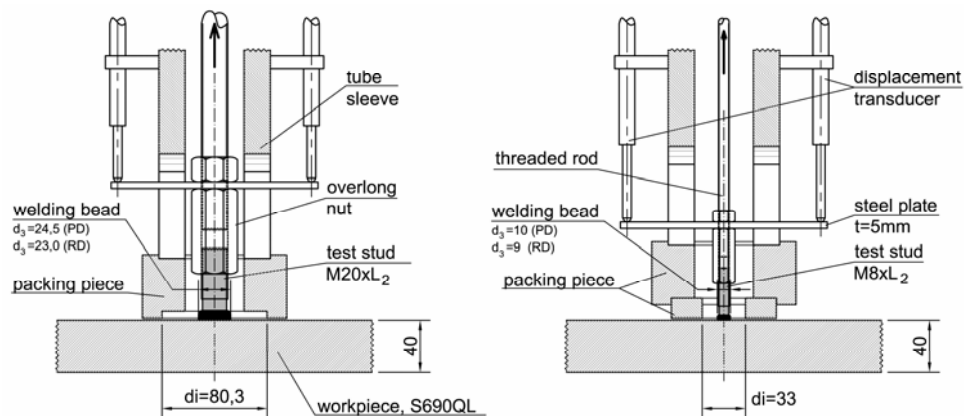


Figure 2.3. Detailed sketch of the test setup

During the test the measurements were recorded by a data acquisition system from HBM and stored in ASC II – files for further evaluations.

## 2.3. Results of VS test series

In the VS series 40 tests were performed with thread studs type PD and RD with different length of the studs. With exception of one test stud M20x35-RD (No. 63) – which failed by a brittle fracture in the welding area – all test studs shows the expected failure modes: tensile fracture in the threaded part (PD – studs, see Figure 2.4) respectively tensile fracture in the shank (RD – studs). The test results and the theoretical tension resistance are summarized in Table 2.5.

The theoretical tension resistance was computed based on EC3-1-8 by equation (2.2) and (2.3). The comparisons of the ultimate test loads (mean value of five tests) with the theoretical tension resistance indicate the applicability of both approaches.

$$F_{u,theo.} = k_2 \cdot A_{Sp} \cdot f_u \quad \text{fracture in the threaded part} \quad \text{where: } k_2 = 0,9 \quad (2.2)$$

$$F_{u,theo.} = A \cdot f_u \quad \text{fracture in the unthreaded shank} \quad (2.3)$$

In case of a failure in the threaded part the reduction factor $k_2 = 0,90$ is needed to cover the scatter in the tension resistance. If the failure occurs in the unthreaded shank of the stud, a reduction factor is negligible.

Table 2.5. Test results of VS test series – thickness of the steel plate $t = 40mm$

| stud type | \varnothing d_1 | l_2 | \varnothing d_2 | A | A_{sp} | A_{sp}/A | f_{yb} | f_{ub} | F_{u,theo.} acc. to equation (2.2)/(2.3) | mean value ultimate load F_{u,m} | standard deviation | F_{u,m}/F_{u,theo.} |
|---|---|---|---|---|---|---|---|---|---|---|---|---|
| | [-] | [mm] | [mm] | [mm²] | [mm²] | [-] | [N/mm²] | [N/mm²] | [kN] | F_{u,m} [kN] | SD [kN] | [-] |
| **PD** | | | | | | | | | | | | |
| M8 | 20 | 7,19 | 40,6 | 40,6 | 36,6 | 0,901 | 673 | 845 | 27,8 | **30,8** | 0,76 | 1,11 |
| | 40 | | | | | | | | | **28,4** | 0,88 | 1,02 |
| M20 | 60 | 18,38 | 265,3 | 265,3 | 245 | 0,923 | 634 | 774 | 170,7 | **200,0** | 1,48 | 1,17 |
| | 100 | | | | | | | | | **190,9** | 0,87 | 1,12 |
| **RD** | | | | | | | | | | | | |
| M8 | 20 | 6,2 | 30,2 | 30,2 | 36,6 | 1,212 | 669 | 838 | 25,3 | **28,8** | 0,78 | 1,14 |
| | 40 | | | | | | | | | **28,3** | 0,52 | 1,12 |
| M20 | 35 | 16,5 | 213,8 | 213,8 | 245 | 1,146 | 619 | 780 | 166,8 | **196,1** | 3,17 | 1,18 |
| | 100 | | | | | | | | | **192,6** | 1,70 | 1,15 |

Except the test stud No. 63, which failed by a brittle fracture caused by gas pore in the welding area, all test studs shows a ductile load bearing behavior, Figure 2.5. Possible explanations for the critical porosity in the welding area of stud No. 63 are an insufficient preparation of the steel plate surface or a not perfect fitted ceramic ferrule. This question could not be finally answered, but it was just one of more than 40 welded studs in the VS – series and therefore it should not be overrated. As mentioned in chapter 2.1, the large thickness of the steel plate in the VS – series was chosen in order to generate a disadvantageous thermal gradient in the heat affected zone. The fast heat dissipation in the welding zone increased the local hardness, which should be less than 380HV according to EN ISO 15614-1. To measure the Vickers hardness macrosections were made on selected test studs including stud No. 63, see Figure 2.6.





VS-series - PD / RD-Studs M8

Figure 2.4. Test stud M20x100-PD; failed in threaded part of the stud
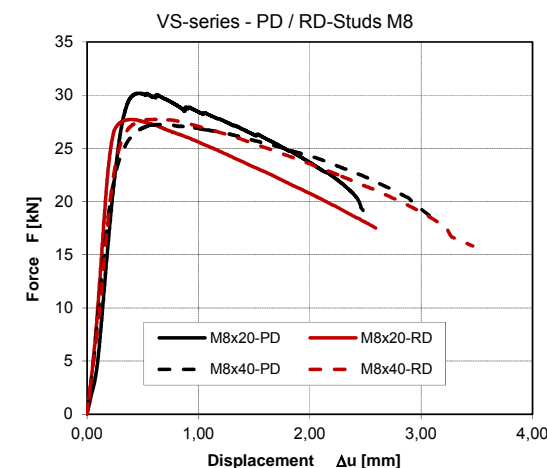
Figure 2.5. Load – displacement – curves from selected studs M8-PD and M8-RD
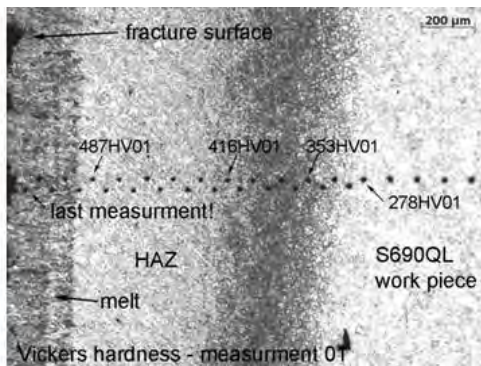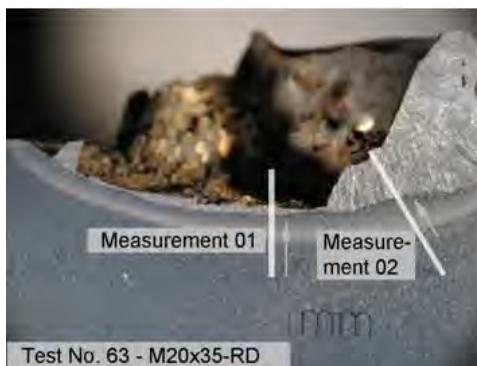
Figure 2.6. Macrosection of test No. 63, M20x35-RD (location of measurements



Figure 2.7. Measured hardness of test No. 63, M20x35-RD (Measurement 01)

The Vickers hardness varied in all three measurements between 280HV01 for the steel plate made of S690QL and maximum values of approximately 490HV01 in the HAZ, as shown in Figure 2.7. Because the exceeding of the hardness limit value given by EN ISO 15614-1 was detected in all measurements, it could be assumed, that a local hardness above the limit did not reduce the load bearing capacity and the ductility of the stud welding in case of studs made of 8MnSi7. This estimation should not be assigned to stud welding in general without further investigations.

## 2.3. Results of VT test series

To verify the weldability of studs made of 8MnSi7 on thin steel plates 51 tension tests were performed in the VT series. According to EN ISO 14555 the minimum requirement for drawn arc stud welding using ceramic ferrules as weld pool backup is $t_{min} = 1/4d$, therefore steel plates with a thickness 2mm (M8) respectively 5mm (M20) were used.

In each stud welding of the VT series the penetration was less than the steel plate thickness, see Figure 2.8. The required welding energy to achieve a cross sectional joint for studs made of 8MnSi7 is comparable to studs of strength class 4.8 and due to this the minimum thickness requirement of $t_{min} = 1/4d$ is applicable.
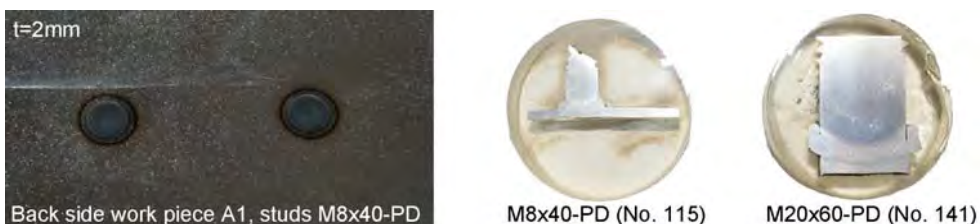


Figure 2.8. Back side of steel plate A1 and macrosections of studs from the VT series

In general the studs failed by a shear fracture in the steel plate. Only in one subset with studs M8x40-RD three tests failed in the welding area caused by gas pores, which are a result of a slight underestimation of the peak current and the welding time. Therefore ten additional studs M8x40-RD with modified welding parameters were tested and all failed by a shear fractures in the steel plate.

The test results of the VT – series, excluding the first subset of M8x40-RD studs, are summarized in Table 2.6. As a first approximation the shear resistance $F_{u,theo.}$ was computed by equation (2.4) using the diameter of the stud shank ($d_2$) to define the shear stressed area.

$$F_{u,theo.} = A_v \cdot f_u / \sqrt{3} \qquad \text{where: } A_v = \pi \cdot d_2 \cdot t \qquad (2.4)$$

A good accordance of the theoretical shear resistance and the test results was given only for studs M20-PD. Depending on the stud type and nominal diameter the theoretical approach leads to a significant underestimation (M8-PD, M8-RD) or overestimation (M20-RD) of the shear resistance. By close examination of the fracture pattern the reason for this is obvious, see Figure 2.9. For studs M8-PD the shear fracture occurs along the outer edge of the welding bead and if the shear resistance was calculated with $d_3$ instead of $d_2$ the deviation is less than 27% (computed with the nominal yield strength!). In all tests with RD – studs the fracture pattern scatter significantly. It is particularly noticeable in Figure 2.9, that the area of the shear fracture surface decrease with an increasing stud diameter. For this reason the theoretical approach leads to an overestimated shear resistance for studs M20-RD.

Table 2.6. Test results of VT test series – thickness of the steel plate $t = 1/4d_{1,nom}$

| stud type | geometry of the studs and the welding bead | | | | material and geometry properties of the work piece | | | | | | test results | | comparison |
| | | | | | material strength | | shear resistance | | | | mean value ultimate load | standard deviation | |
| | $\varnothing d_1$ | $l_2$ | $\varnothing d_2$ (shank) | $\varnothing d_{3,nom}$ (welding bead) | $f_y$ | $f_u$ | $t$ | $A_v = \pi \cdot d_2 \cdot t$ | $F_{u,theo.} = f_y \cdot A_v / \sqrt{3}$ | | $F_{u,m}$ [kN] | $SD$ [kN] | $F_{u,m}/F_{u,theo.}$ |
| | [−] | [mm] | [mm] | [mm] | [N/mm²] | [N/mm²] | [mm] | [mm²] | [kN] | | | | [-] |
| PD | M8 | 20 | 7,19 | 10,0 | 680 | 800 | 2 | 45,2 | 17,7 | | 31,4 | 0,69 | 1,77 |
| | | 40 (1) | | | | | | | | | 29,9 | 0,58 | 1,69 |
| | M20 | 60 | 18,38 | 24,5 | 776 | 834 | 5 | 288,7 | 129,4 | | 129,2 | 4,68 | 1,00 |
| | | 100 | | | | | | | | | 132,5 | 9,24 | 1,02 |
| RD | M8 | 20 | 6,2 | 9,0 | 680 | 800 | 2 | 39,0 | 15,3 | | 18,8 | 2,35 | 1,23 |
| | | 40 | | | | | | | | | 18,9 | 2,22 | 1,24 |
| | M20 | 35 | 16,5 | 23,0 | 776 | 834 | 5 | 259,2 | 116,1 | | 79,0 | 6,80 | 0,68 |
| | | 100 | | | | | | | | | 84,1 | 6,15 | 0,72 |

(1) 3 of 5 studs failed by a tensil fraction in the threaded part of the stud

The comparison of the measured ultimate loads of RD – studs with those of PD – studs with the same nominal diameter reveals a constant ratio of approximately 0,62. Therefore equation (2.4) could be enlarged by an additional coefficient $k$ that covers the reduced shear fracture surface of RD – studs:

$$F_{u,theo.} = k \cdot \pi \cdot d_2 \cdot f_u / \sqrt{3} \quad \text{where: } k = \begin{cases} 1,00 & \text{PD – studs} \\ 0,62 & \text{RD – studs} \end{cases} \qquad (2.5)$$

The modified approach given in equation (2.5) should be verified by additional tests using studs with a nominal diameter between M8 and M20 to ensure that the suggested linear interpolation did not overestimate the shear resistance.
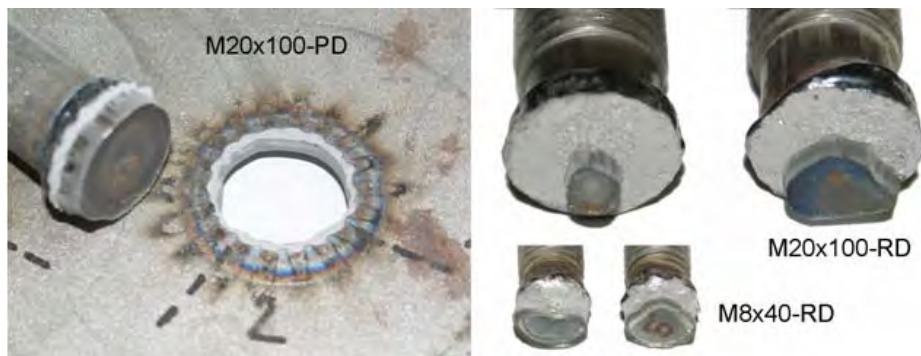
Figure 2.9. Detail photo from PD and RD studs tested in the VT series

## 3. CONCLUSIONS

In the course of the research project the weldability of high strength studs made of 8MnSi7 was verified. The basic principles for drawn arc stud welding according to EN ISO 14555 could be utilized for the high strength studs.

Further statistical evaluations – which are not part of the presented paper – have shown that the drop in strength from the studs with a nominal diameter of M20 did not affect the safety level, even if the nominal ultimate strength was used to determine the tensile resistance. Due to this, the high strength studs could be classified as strength class 8.8. To cover shear failure in case of thin a thin steel plate, a design approach was proposed, founded on the test results. By reason of the scattering of the fracture pattern and the supposed linear interpolation for stud diameters between M8 and M20 additional tests should be performed.

## ACKNOWLEDGEMENTS

## REFERENCES

[1] CEN (2010) EN 1993, *Design of steel structures – Part 1-8: Design of joints*; German version EN 1993-1-8:2010

[2] CEN (2002) EN 10263, *Steel rod, bars and wire for cold heading and cold extrusion - Part 2: Technical delivery conditions for steels not intended for heat treatment after cold working*; German version EN 10263-2:2001

[3] CEN (2009) EN ISO 898, *Mechanical properties of fasteners made of carbon steel and alloy steel - Part 1: Bolts, screws and studs with specified property classes - Coarse thread and fine pitch thread*, German version EN ISO 898-1:2009

[4] CEN (2000) EN ISO 4063, *Welding an allied processes – Nomenclature of processes and reference numbers*, German version EN ISO 4063:2000

[5] CEN (2008) EN ISO 13918, *Welding – Studs and ceramic ferrules for arc stud welding*, German version EN ISO 13918:2008

[6] CEN (2006) EN ISO 14555, *Welding – Arc stud welding of metallic materials*, German version EN ISO 14555:2006

[7] Trillmich, R., Welz, W.: *Bolzenschweißen Grundlagen und Anwendung*; Fachbuchreihe Schweißtechnik, Band 133; DVS – Verlag, Düsseldorf; 1997

[8] Ungermann, D., Schneider, S.: *Welded threaded studs with a tensile strength of 800N/mm²*, Schlussbericht FOSTA Forschungsvorhaben P787; published by FOSTA

# INJECTION BOLTS IN STEEL STRUCTURES WITH SHORT DURATION HIGH LOADS

Nol Gresnigt
*Delft University of Technology, The Netherlands*
*a.m.gresnigt@tudelft.nl*

Darko Beg
*University of Ljubljana, Faculty of Civil and Geodetic Engineering*
*darko.beg@fgg.uni-lj.si*

Frans Bijlaard
*Delft University of Technology, The Netherlands*
*f.s.k.bijlaard@tudelft.nl*

## ABSTRACT

The present recommended design bearing stress for injection bolts is based on long duration creep tests. The criterion is that the displacement will not be larger than 0.30 mm. This is the same criterion as for high strength friction grip bolts. Injection bolts have the advantage that in case of overloading no sudden large displacements occur as may happen in high strength friction grip bolts when they slip.

In the European Recommendations for Bolted Connections with Injection Bolts (ECCS, 1994) the design bearing stress as determined in long duration testing is used for the serviceability limit state verification. For the ultimate limit state a higher bearing stress is given (factor 1.2), motivated by the above mentioned advantage of injection bolts. It was expected that the chosen values would be sufficient to avoid that the ultimate limit state would govern the design.

In recent applications of injection bolts, such as a new glass roof in Amsterdam Central Railway Station, it appeared that the short duration loads in the glass supporting steel structures due to wind may be much more than anticipated when the ECCS recommendations were drafted. Short duration cyclic tests were carried out, some with more than double the recommended bearing stresses. These test results were additional to the results of cyclic short duration testing in the University of Ljubljana and were sufficient to allow much higher bearing stresses for the glass roof in Amsterdam.

In the paper the test results are given and a recommendation and motivation to modify the present rules in Eurocode 3 and EN1090-2.

## 1. INTRODUCTION

The present recommended design bearing stresses for injection bolts are based on long duration creep tests. The criterion is that the displacement is not larger than 0.3 mm. This is the same criterion as for high strength friction grip bolts.

Injection bolts however, have the advantage that in case of overloading no sudden large displacements occur as may happen in high strength friction grip bolts when they slip.

In the European Recommendations for Bolted Connections with Injection Bolts (ECCS, 1994) the design bearing stress as determined in long duration testing is used for the serviceability limit state verification. For the ultimate limit state a higher bearing stress is given (factor 1.2), motivated by the above mentioned advantage of injection bolts. The factor 1.2 was chosen by engineering judgement; virtually no test results were available. It was expected that the chosen values would be sufficient to avoid that the ultimate limit state would govern the design. The Eurocode 3 rules are formulated somewhat different, but are practically the same.

In recent applications of injection bolts, such as a new glass roof in Amsterdam Central Railway Station, it appeared that the short duration loads in the glass supporting steel structures due to wind may be much more than anticipated when the ECCS recommendations were drafted.

It was asked whether it would be possible to allow much higher bearing stresses for short duration loadings. To answer this question the results of research performed in the University of Ljubljana could gratefully be used. In addition to that short duration tests were performed in the Stevin Laboratory of Delft University of Technology. The test results together with test results from the research in Ljubljana were sufficient to allow much higher bearing stresses for the glass roof in Amsterdam.

In this publication the main results are summarized and a recommendation is given for a modification to the present design rules in the Eurocode 3.

## 2. INJECTION BOLTS

Injection bolts are bolts in which the cavity produced by the clearance between the bolt and the wall of the hole is completely filled up with a two component resin. Filling of the clearance of an injection bolt is carried out through a small hole in the head of the bolt. After injection and full curing of the resin, the connection is slip resistant. Shear load is transferred through bearing and shear of the bolt.
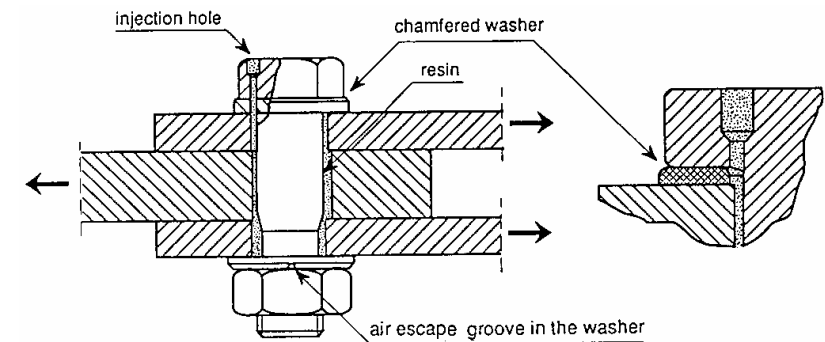


Figure 1. Injection bolt in a double lap joint.

Injection bolts can be manufactured from normal standard structural bolts. The bolts and washers are adapted to enable the injection of the resin. As compared to other mechanical fasteners, injection bolts have several advantages. A distinction is made between the application in existing structures and in new structures. In many

cases the advantages apply both for repair and strengthening of existing structures, as well as for new structures. Design rules are given in the ECCS Recommendations (1) and in Eurocode 3 Part 1-8 (4). Rules for testing the resin and execution can be found in EN 1090-2 (5).

Since resins are susceptible to creep deformation if the bearing stress is too high, the bearing stress needs to be kept within certain limits. In the Fourth International Workshop on Connections in Steel Structures (2), test results from long duration testing were presented on the two component epoxy resin Araldit SW 404 with HY 2404 hardener. At present it is owned by Huntsman and available as RenGel SW 404 + Ren HY 2404.

The main conclusions as presented in (2) are:
a. Injection bolts are an excellent alternative for replacing faulty rivets in (old) riveted structures.
b. Injection bolts can successfully be used for strengthening of corroded plates, especially where welding or HSFG bolting is difficult to apply.
c. Long duration creep tests were still going on at a bearing stress of 250 N/mm$^2$ without exceeding the allowable displacement.
d. A high temperature of 70 $^o$C as may occur in bridges has only a moderate influence on the deformations. The average creep for ambient temperature (20 °C) is 0,19 mm and for 70 °C 0,24 mm (at a bearing stress of 250 N/mm$^2$)
e. The allowable bearing stress may be raised from 130 N/mm$^2$ up to 175 or 200 N/mm$^2$.

## 3. TEST RESULTS UNIVERSITY OF LJUBLJANA

To promote the use of injection bolts in Slovenia and wider, a testing programme on standard bolted lap connections was conducted at the University of Ljubljana. Altogether 22 tests were performed on three different types of connections:
a. Slip resistant connections
b. Connections with injection bolts
c. Connections with preloaded injection bolts.

For comparison, one test was also performed on a standard connection with bolts in bearing.

Monotonic long- and short-duration tests were performed according to EN 1090-2 as well as additional four cyclic tests for a better insight into the behaviour of injection bolts.

### 3.1. Description of the test programme

#### ❑ Monotonic tests

For all three types of connections monotonous tension tests followed strictly the procedure given in Annexes G and K of EN 1090-2. With the results of these tests the slip factor $\mu$ and the bearing strength of the resin $f_{b.resin}$ are determined for slip resistant connections and connections with injection bolts, respectively. The same procedure was also used to determine the resistance of connections with preloaded injection bolts, although this is explicitly not allowed for in EN 1090-2.

The geometry of the standard test specimen with M20 bolts and instrumented test specimens at the beginning of the test are shown in Figure 2 and Figure 3, respectively. For each connection type four short-duration tests have to be done (10 min – 15 min) and the resistance is determined at 0.15 mm slip. The fifth test is long-duration creep test at constant load equal to 90% of the average resistances

from the first four tests. Because each specimen has two connections, there are actually eight results. The average slip in each of the four connections for the time period of 5 minutes – 3 hours after the full load is applied should not exceed 0.002 mm. If this is achieved, the specimen is tested to reach the slip of 0.15 mm and the characteristic resistance is determined based on the obtained results (mean - 2.05 x standard deviation). If the creep test shows slip that exceeds 0.002 mm, the long-duration test should be extended until safe extrapolation of slip at 50 years is obtained; this slip should be smaller than 0.3 mm to guarantee appropriate long-term behaviour of the connection.

It is worth mentioning that for connections with preloaded injection bolts EN 1993-1-8 allows summation of design slip resistance and design bearing resistance of the resin.
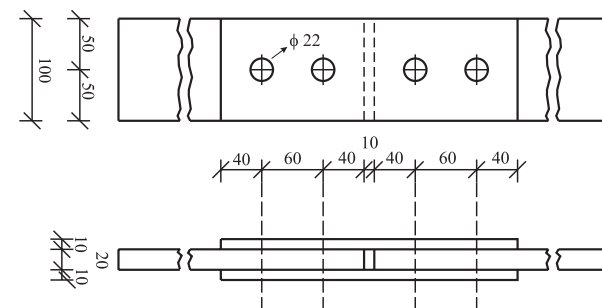


Figure 2. Geometry of standard test specimens.
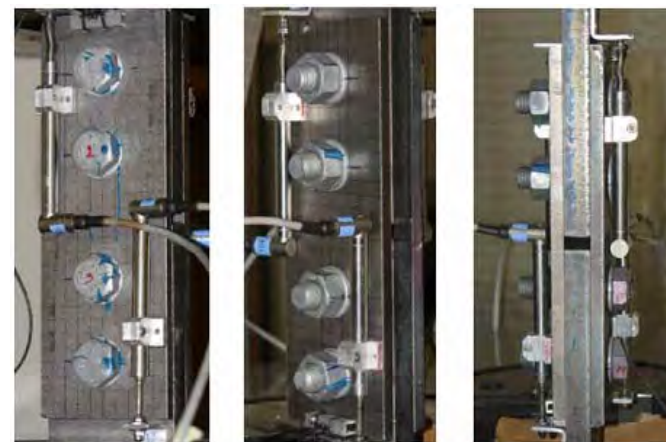


Figure 3. Instrumented test specimen.

#### ❑ Cyclic tests

For connections with injection bolts cyclic tests are not standardised. Two tests at constant displacement amplitude of 0.135 mm (90% of allowable slip) and two tests at increasing displacement amplitude were performed. The first of the constant amplitude tests was done at low frequency of 0.05 Hz for 120 cycles. The second test was performed at increasing frequency (0.5 Hz – 4 Hz) for 8000 cycles. The tests at increasing displacement amplitude were executed at low cyclic frequency 0.05 Hz.

## 3.2. Test results

### ❑ Monotonic tests

The results of the first four short-duration tests for all three types of connections are given in Figure 4 to Figure 7 in terms of the average force-displacement diagrams. Average values were determined for eight results (4 tests x 2 connections in each test specimen). For connections with injection bolts without preloading additional two "eccentric" tests were carried out (Figure 6), where the outer plates were shifted in relation to the inner plates as much as the hole clearance allowed. By this procedure the maximum thickness of the resin was 2 mm. This is the most unfavourable situation regarding the 0.15 mm slip criterion.

We can see that at 0.15 mm slip the maximum value of the slip resistance is reached (Figure 4). The diagrams for injection bolts (Figure 5 and Figure 6) show a practically linear force-displacement relation and after the limit slip at 0.15 mm is exceeded, the force still increases. The results for the most unfavourable eccentric test specimens give somewhat larger deformability that results in 14% smaller resistance, but from the diagram (Figure 6) it is evident that at slightly larger slip of 0.20 mm the same resistance as for "normal" test specimens can be obtained.
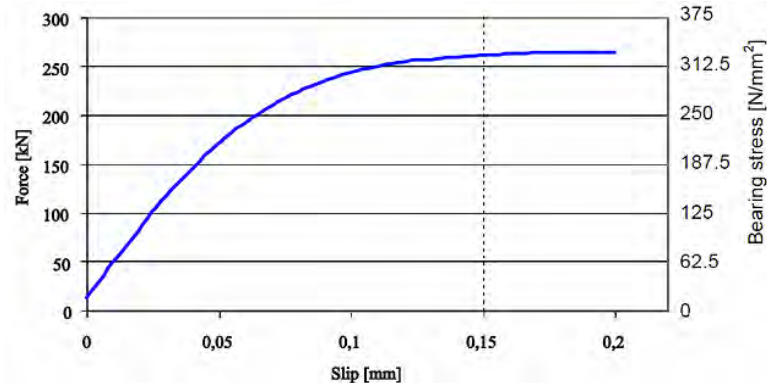


Figure 4. Slip resistant connection – force-slip diagram for average results from first four short-duration tests.
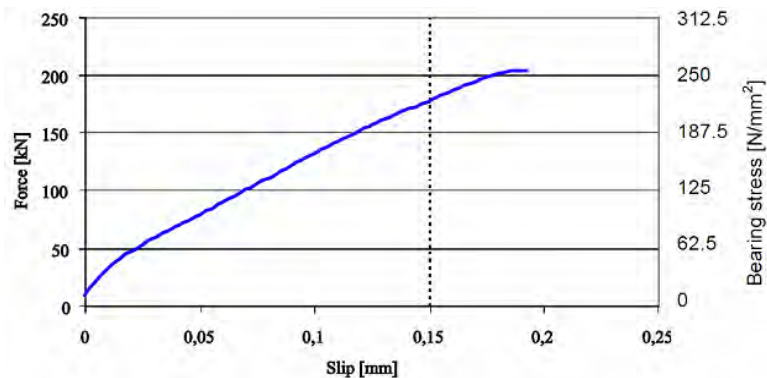


Figure 5. Connection with injection bolts – force-slip diagram for average results from first four short-duration tests.
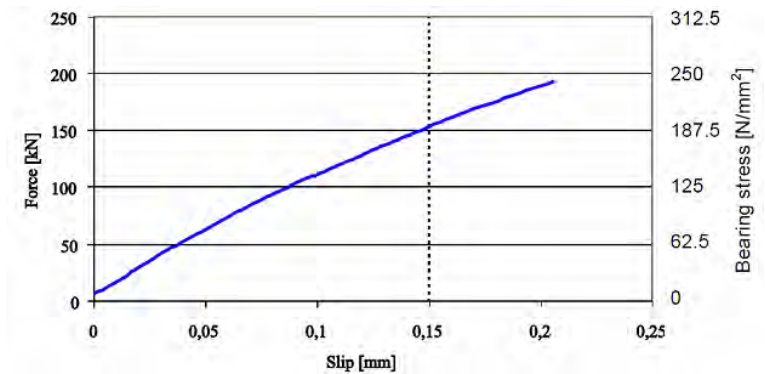


Figure 6. Eccentric connection with injection bolts – force-slip diagram for average results from first four short-duration tests
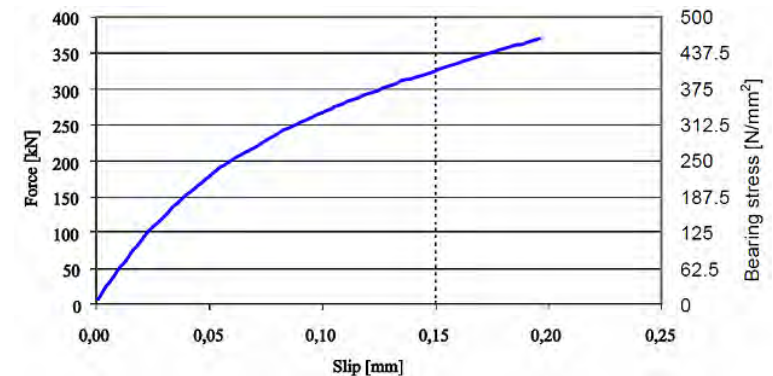


Figure 7. Connection with preloaded injection bolts – force-slip diagram for average results from first four short-duration tests

The results for preloaded injection bolts (Figure 7) show favourable summation of the contribution from the slip resistance and the bearing resistance without a force plateau at 0.15 mm slip.

In Figure 8 to Figure 11 the results for three hour long-duration creep test are shown. As required in EN 1090-2, the tests were performed at 90% of average resistance from previous short-duration tests. For slip resistant connection (Figure 8) and connection with preloaded injection bolts (Figure 9) the additional creep limit of 0.002 mm was not exceeded. For the connection with injection bolts this limit was exceeded (Figure 10), but from tangent extrapolation to 50 years creep (Figure 11) it is evident that this creep is less than 0.3 mm.

Because creep tests prove to be satisfactory, the creep test specimens were tested with short-duration tests and the final results are shown in Table 1 and Figure 12.

For the first two types of connections the characteristic values of the slip factor and of the bearing resistance of resin can be determined easily from the characteristic resistances given in Table 1 and taking account of the corresponding resistance formulas from EN 1993-1-8:

$$\mu_k = 0.33$$
$$f_{b,resin} = 200 \text{ MPa}$$

Unfavourable eccentric location of bolts can reduce this bearing resistance up to 15%, if the same standard deviation is assumed for eccentric specimens, as was obtained for normal specimens.

$$f_{b.resin} \, min \approx 170 \, MPa.$$
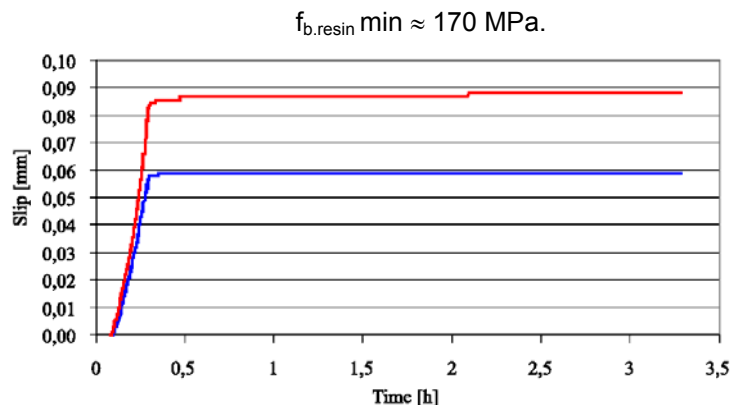


Figure 8. Slip resistant connection - slip-time diagram for the for the long-duration test
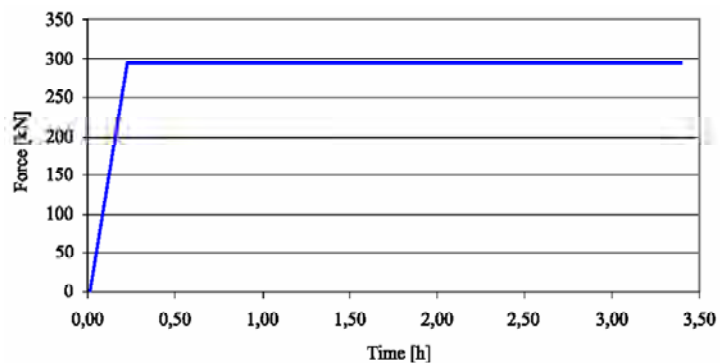


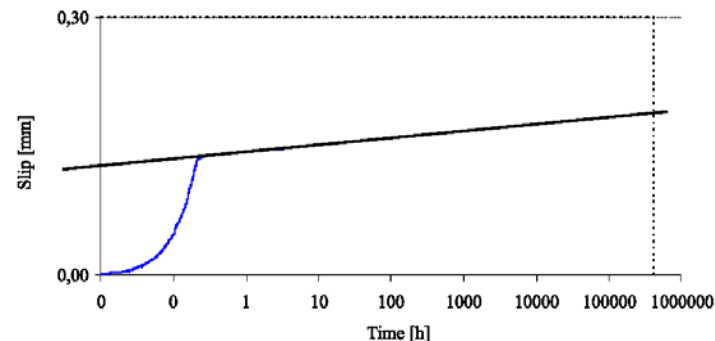Figure 9. Connection with preloaded injection bolts - slip-time diagram for the for the long-duration test
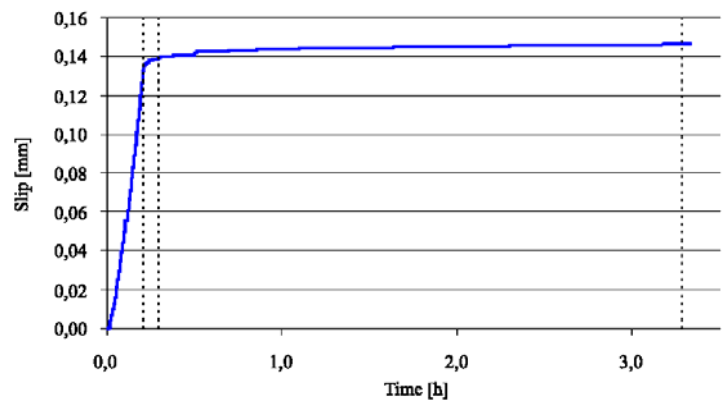


Figure 10. Connection with injection bolts - slip-time diagram for the for the long-duration test



Figure 11. Connection with injection bolts - long-duration test and extrapolation of slip at 50 years

Table 1. Test results of monotonous tests.

| | Slip resistant | Injection bolts | Preloaded injection bolts |
|---|---|---|---|
| | $F_{TEST}$ | $F_{TEST}$ | $F_{TEST}$ |
| Test 1 | 259.5 | 185.1 | 302.2 |
| | 251.2 | 166.3 | 320.2 |
| Test 2 | 264.3 | 186.9 | 324.8 |
| | 255.5 | 182.0 | 303.5 |
| Test 3 | 291.9 | 174.3 | 348.8 |
| | 286.1 | 188.5 | 337.9 |
| Test 4 | 237 | 171.2 | 323.4 |
| | 244.3 | 177.7 | 331.3 |
| Test 5 | 281.3 | 201.5 | 388.6 |
| | 285.8 | 197.4 | 407.9 |
| $F_{TEST, AVER.}$ | 261.2 | 183.1 | 338.8 |
| s | 19.2 | 11.2 | 15.9 |
| $F_{RK}$ | 221.8 | 160.1 | 306.2 |

In all test groups the spread of the results was small enough (s/mx100 ≤ 8%) that no additional tests (according to EN 1090-2) were necessary.

The final comparison of the results is shown in Figure 12 in terms of average force-displacement diagrams. Also characteristic resistances are added (circle marks). We can see that the pure bearing connection experiences free slip at small displacements and it gains resistance only at much higher displacements. Connections with injection bolts have smaller resistance than the slip resistance connection, but the linearly increasing force-displacement diagram is more favourable. Connections with preloaded injection bolts show good performance, but the obtained characteristic resistance $F_{RK}^{TEST}$ = 306.2 kN is smaller than the sum of characteristic resistance of the slip resistant connection and the connection with injection bolts ($F_{RK}^{SUM}$ = 381.7 kN). It means that in this case the resistance obtained from EN 1993-1-8 (based on $\mu_K$ and $f_{b.resin,K}$ from the tests) is more than 20% higher than the test resistance of the connections with preloaded injection bolts. As stated above, this test resistance was determined with the same test procedure as for the basic two types of connections, although EN 1090-2 does not explicitly include this type of connections. On the other

hand, from Figure 12 it is evident that the Eurocode resistance is easily reachable at a slip that is a bit larger than 0.15 mm (0.20 mm – 0.25 mm).
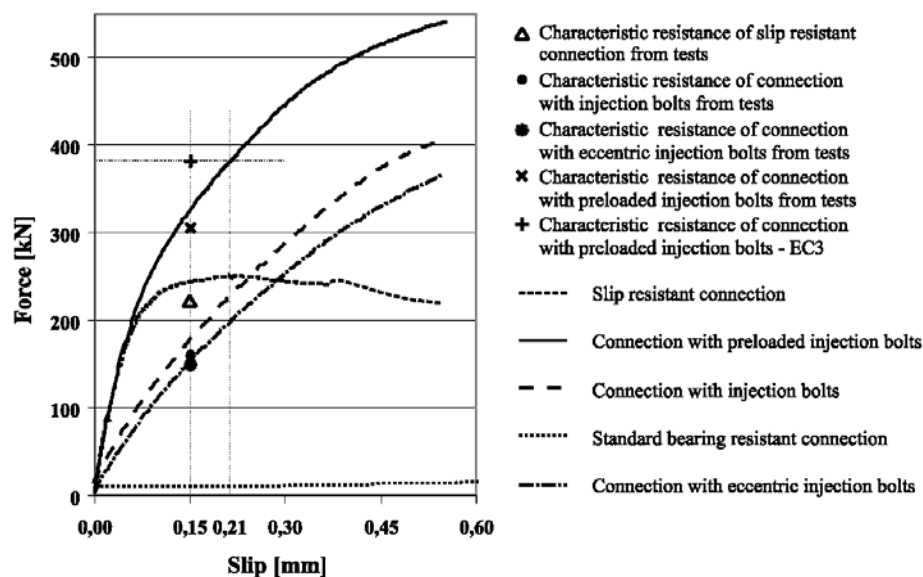


Figure 12. Comparison of results for all types of connections - force-slip diagrams for average test results

## ❑ Cyclic tests

Bridges under traffic loading and buildings under wind loading and in seismic events are subjected to cyclic loading. The basic idea is to examine the behaviour of connections with injection bolts at cyclic loading that does not lead to exceeding of the bearing resistance of the resin. Namely, for larger actions such connection behaves as normal bearing connections with bolts in shear. For this reason only results of two cyclic tests at constant displacement amplitude of 0.135 mm are presented. Force displacement diagrams for both tests are shown in Figure 13 and Figure 14.
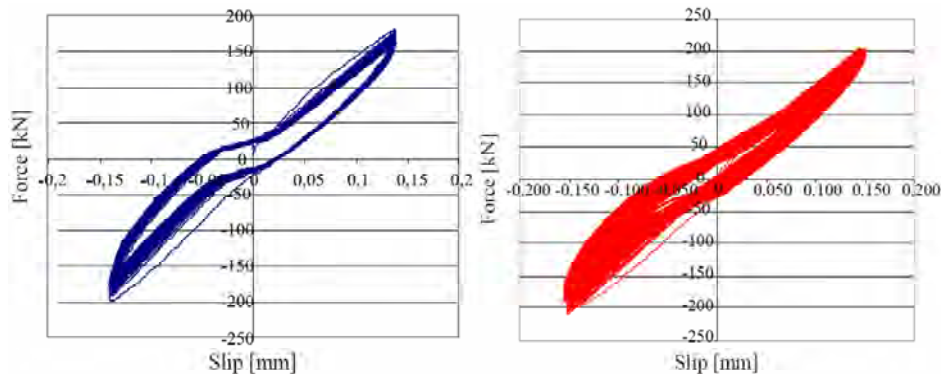


Figure 13. Force-slip diagrams for cyclic tests, a) test at 0.05 Hz, b) test at 0,5 Hz to 4 Hz
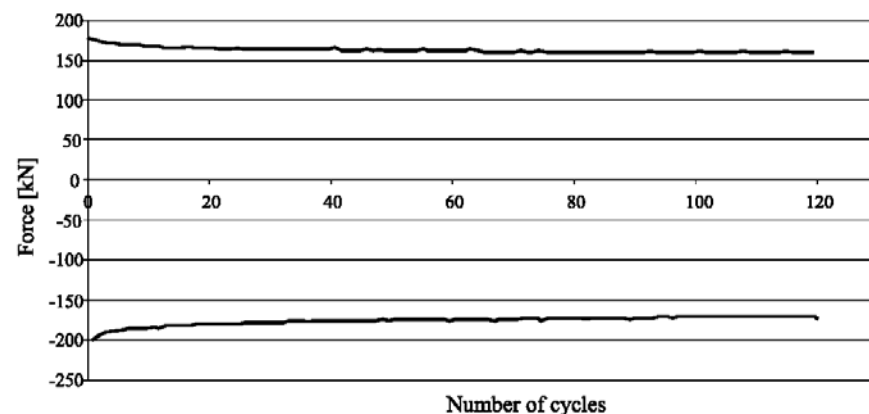


Figure 14. Force amplitudes for cyclic test at 0.05 Hz

In both cases almost elastic behaviour is observed with narrow hysteresis loops (Figure 13) and without visible influence on the loading frequency. In the first 10 or 20 cycles the force amplitude decreases by about 10%, but then it remains practically constant (Figure 14). This means that the behaviour of connections with injection bolts at displacement amplitudes of 90% of the allowable slip is very good.

## 4. TEST RESULTS DELFT UNIVERSITY OF TECHNOLOGY

In Amsterdam an extension to the railway station is under construction (2011-2012) with a large glass roof (Figure 15). High demands were put on the stiffness of the glass supporting steel structure. Displacements in bolted connections had to be reduced to very low values. The main reason for that was the safety requirement in case of fire (bus station beneath). To avoid too much uneven heating of the glass a narrow supporting width of the glass panels was required.



Figure 15. Artist impression of the extension Railway Station Amsterdam and the glass roof under construction
(April 2012, the project is called IJSEI, with Google many sites to view).

The application of high strength friction grip bolts was problematic because of the need to remove locally the corrosion protection (paint system) and the risk of corrosion traces later on. Then it was decided to investigate the application of injection bolts M27.

The main load on the roof is wind load, which is short duration. It was asked whether it would be safe to allow higher bearing stresses for this load case than the bearing stresses based on long duration creep testing. Injection bolts would be applied in normal size and oversized holes.

The design equation for the bearing strength (Eurocode 3) is

$$F_{b,Rd,re\sin} = \frac{k_t \cdot k_s \cdot d \cdot t_{b,re\sin} \cdot \beta \cdot f_{b,re\sin}}{\gamma_{M4}}$$

where

$F_{b,Rd,resin}$ = bearing resistance
$k_t$ = factor depending on the limit state: serviceability limit state $k_t$ = 1,0 and for the ultimate limit state $k_t$ = 1,2
$k_s$ = factor depending on the hole clearance
$d$ = diameter of the bolt
$t_{b,resin}$ = length of the bolt in bearing
$\beta$ = factor depending on thickness of plates
$f_{b,resin}$ = bearing resistance of the resin

The value $k_t$ = 1.2 for the ultimate limit state was chosen expecting that this would not cause problems for short duration loads (that it would not govern the design). That may be correct for e.g. bridges, but not for the glass roof.

To answer the question about the allowable short duration bearing stresses, the results of the tests in the University of Ljubljana were most helpful. The authorities however requested for extra testing focusing at the application in Amsterdam.

### 4.1. Test programme

In total six tests were performed on test specimens with M27 bolts as shown in Figure 16. The preparation of the test specimens was done by the contractor guided by the engineering office. The engineering office decided for at random position of bolts to simulate the situation in practice. This resulted in different distances of the main plates (position of bolts in the holes), giving different sizes of the gap ("spleet").
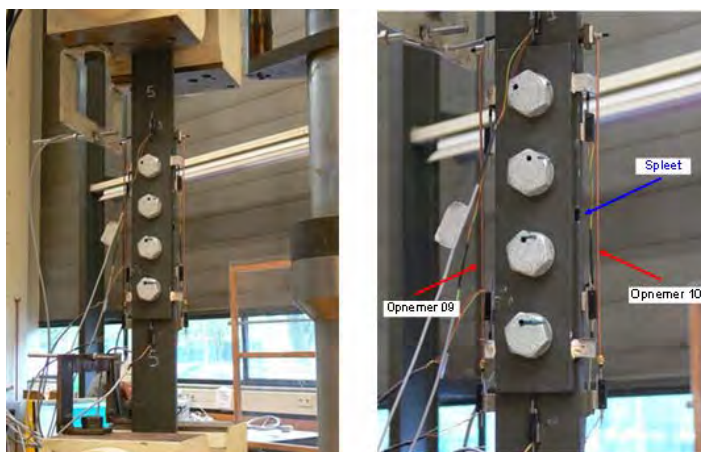


Figure 16. Test specimen with four "short" LVDT's and two "long" LVDT's (opnemer = LVDT, Dutch texts to be translated in final versions).

The design bearing stress would be based on the allowed maximum displacement of 0.95 mm = 0.30 mm per bolt + 0.35 mm because of the elongation of the steel. Per test specimen 10 cycles were performed, with a loading speed of 2 kN/sec = 2 minutes till maximum load. Then waiting time was 5 sec followed by quick unloading, waiting 10 sec and start new cycle.

### 4.2. Test results

Test main result of the first test is given in Figure 16. Other tests gave similar values.

The tests were displacement controlled. The maximum average displacement was 0.95 mm. The maximum bearing stress per cycle is given in Figure 18. The decline is the largest in the first cycles and then the average tends to stabilize at about 310 N/mm$^2$. It is noted that the last cycle had somewhat smaller displacement than 0.95 mm.

In test 5 and 6 the test was continued after the first 10 cycles with displacement 0.95 mm up to displacement 1.55 mm (Figure 19). Also at this larger displacement the decline in the bearing stress was very limited.
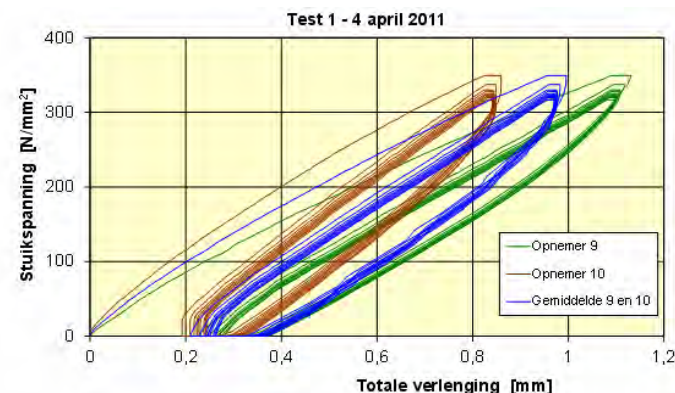


Figure 17. Main result of test 1: bearing stress – elongation. The green line is the recording from one of the long LVDT's (Opnemer 9) and the red line is the other long LVDT. The average is the blue line.
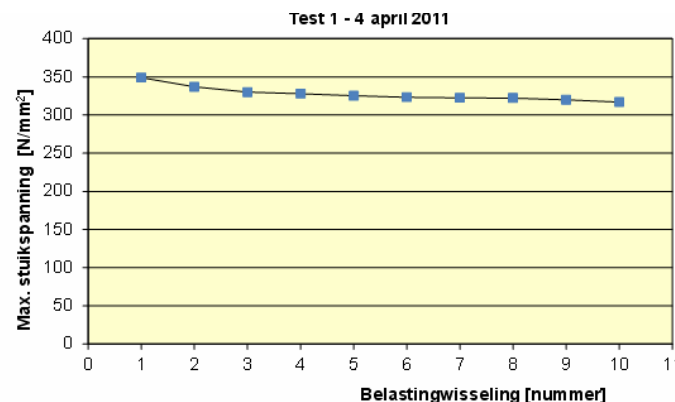


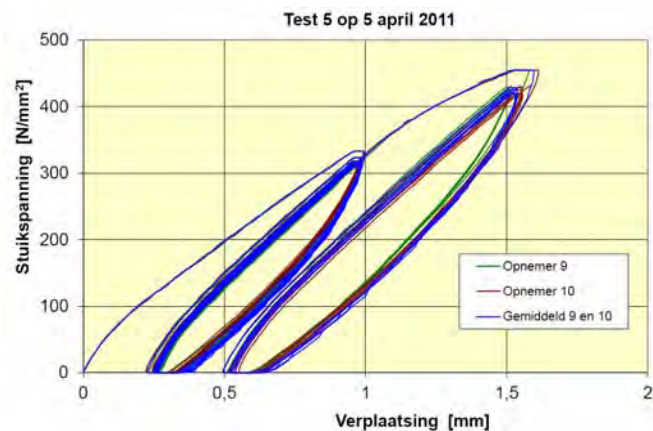Figure 18. Maximum bearing stress per cycle in test 1.

Figure 19. Main result of the fifth test: bearing stress – elongation. The green line is the recording from one of the long LVDT's (Opnemer 9) and the red line is the other long LVDT. The average is the blue line.

In Table 2 an overview of the main test results is given. Differences in the results probably must be mainly attributed to the differences in the position of the bolts in the holes as explained before.

Table 2. Overview of test main test results.

| Test | F after 10th load cycle (kN) | $f_{b,resin}$ (N/mm$^2$) |
|---|---|---|
| 1 | 257 | 317 |
| 2 | 233 | 287 |
| 3 | 242 | 298 |
| 4 | 262 | 323 |
| 5 | 250 | 309 |
| 6 | 242 | 299 |

If a 95% chance of exceeding the design value is accepted, it was calculated that the allowable design bearing stress would be 284 N/mm$^2$. It was decided to adopt for the injection bolts in the glass roof the following values.

$$f_{b,resin,long\ duration}=200\ N/mm^2,\ f_{b,resin,short\ duration} = 280\ N/mm^2.$$

When short duration and long duration loads are considered in relation to creep it is noted that in the Eurocode this is only applicable to structures where creep is relatively long duration (concrete, timber). In injection bolts the creep process is quicker. Wind load is very short duration and will not lead to significant creep, but e.g. snow load and temperature load could be longer duration. In view of this it was decided to consider the following load combinations for the glass roof for the "middle long term" loads

$$1,2G+1,0Q_{snow}+0,5Q_{temp}\ and\ \ \ \ \ \ \ 1,2G+1,0Q_{temp}$$

For the short term loads (wind) the standard load combinations were checked.

## 5. CONCLUDING REMARKS AND RECOMMENDATION

To fill the gap in knowledge on the bearing resistance of injection bolts, a programme of 22 tests was conducted at the University of Ljubljana. Three types of connections were tested: slip resistant connections, connections with injection bolts and connections with preloaded injection bolts. Short- and long-duration monotonic tests were carried out according to EN 1090-2. The resulting characteristic bearing resistance of the resin was 200 N/mm$^2$. Additional cyclic tests proved good performance of the injection bolts.

Additional testing was performed at Delft University of Technology in connection with a request for larger allowable bearing stresses for short duration loadings as may occur in roofs.

The main conclusions and recommendation from the research in the Universities of Ljubljana and Delft are:

a. The long duration bearing stress of the tested resin can be taken as 200 N/mm$^2$. It was proposed in the 2000 Roanoke paper (2) on bases of the tests reported in that paper and conformed in the present testing.

b. The short duration bearing stress can be taken considerably higher than the long duration bearing stress.

c. It is recommended to modify Eurocode 3 part 1-8 and EN 1090-2 accordingly and make a distinction between long duration and short duration load combinations.

### ACKNOWLEDGEMENT

### REFERENCES

[1] ECCS, (1994). European recommendations for bolted connections with injection bolts. ECCS publication No. 79, Brussels.

[2] Gresnigt, A.M., Sedlacek, G., Paschen, M. (2000). *Injection bolts to repair old bridges*. Fourth International Workshop on Connections in Steel Structures, held October 22-25, 2000 in Roanoke, VA, USA.

[3] EN 1993-1-1, (2005). Eurocode 3, Design of Steel structures. Part 1.1 - General Rules and Rules for Buildings. CEN, Brussels.

[4] EN 1993-1-8, (2005). Eurocode 3 Design of Steel Structures, Part 1-8: Design of joints. CEN, Brussels

[5] EN 1090-2, (2008). Execution of steel structures and aluminium structures, Part 2: Technical requirements for steel structures. CEN, Brussels.

[6] Gresnigt A.M., Stark J.W.B. *Design of Bolted Connections with Injection Bolts*. Connections in Steel Structures III, Behaviour, Strength & Design, Proceedings of the Third International Workshop, Trento, Italy, 29-31 May 1995, Pergamon, pp 77-87.

[7] Sedlacek G., Paschen M., Gresnigt A.M. (1997). Bericht zur Erstanwendung der Injektionsschrauben bei der Hauptträgerstegverstärkung an der Schlossbrücke Oranienburg, Berlin, Rheinisch-Westfälische Technische Hochschule, Lehrstuhl für Stahlbau, Aachen, Germany.

[8] Van Lint H.J., Van Wolfswinkel J.C., Gresnigt A.M., *Besparen op injectiebouten (Economic design with injection Bolts).* Bouwen met Staal 226, April 2012, pp 44-46 (in Dutch language; the April issue contains several papers on the design and construction of the new glass roof in Amsterdam).
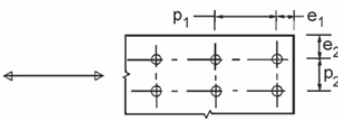
# BEARING STRENGTH OF BOLTS IN PLATES WITH NON-RECTANGULAR ENDINGS

P. de Vries, F.S.K. Bijlaard, A.M. Gresnigt
*Delft University of Technology, The Netherlands*
*p.devries@tudelft.nl; f.s.k.bijlaard@tudelft.nl; a.m.gresnigt@tudelft.nl*

## 1. INTRODUCTION

The bearing strength of an end bolt in a plate can be determined with the rules in Eurocode 3 Part 1-8 "Design of Joints" (see Table 1). The essential parameters are the material strength and the geometry in terms of the end and edge distance and the plate thickness. These rules are well statistically evaluated against test results for steel up to steel grade 460. However, the rules are only valid in cases where the plates in the lap joints have rectangular endings as shown in the figure in that table.

Table 1. Beam-to-column joint configuration.

| EC3 model |
|---|
| Bearing resistance $F_{b,Rd} = \dfrac{k_1 \cdot \alpha_b \cdot f_u \cdot d \cdot t}{\gamma_{M2}}$ <br>  |
| Perpendicular to the direction of the load transfer: <br><br> $k_1$    for edge bolts:    MIN( $2.8 \cdot \dfrac{e_2}{d_0} - 1.7$ , $2.5$ ) <br><br> $k_1$    for inner bolts:    MIN( $1.4 \cdot \dfrac{p_2}{d_0} - 1.7$ , $2.5$ ) |
| $\alpha_b$    MIN( $\alpha_d$ ; $\dfrac{f_{ub}}{f_u}$ ; $1.0$ ) <br><br> In the direction of the load transfer: <br><br> for end bolts:    $\alpha_d = \dfrac{e_1}{3d_0}$ <br><br> for inner bolts: $\alpha_d = \dfrac{p_1}{3d_0} - \dfrac{1}{4}$ |

There are cases where it is logic to use non-rectangular endings of the plates, e.g. in cases where the plates (strips) are used as diagonals and where there is

little space for rectangular endings and the use of non-rectangular endings may be a solution (see Fig. 1). In that case the question is whether the Eurocode 3 rules for bearing of bolts can be used and how the parameters are to be interpreted.
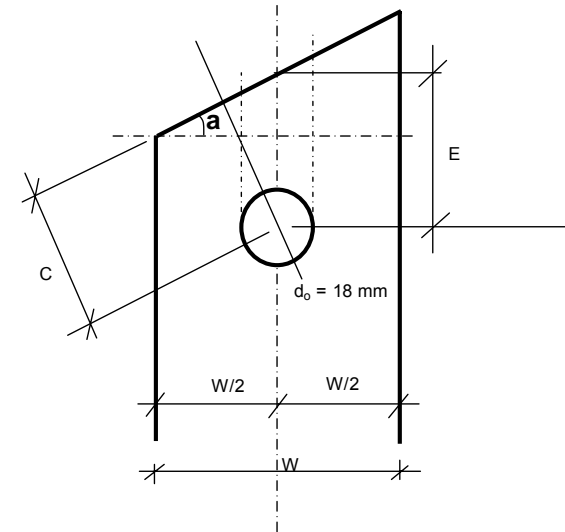


Figure 1. End bolt in a plate with a non-rectangular ending

To investigate whether the present EC3 rules can be used with a certain interpretation of the parameters, tests have been performed. In chapter 2 these tests are described.

## 2. DESCRIPTION OF THE TESTS

Two steel grades are used as mentioned in Table 2. In that table the actual plate thickness and the actual material properties are given.

Table 2. Actual material specifications

| Material specifications | | | |
|---|---|---|---|
| Steel grade | Plate thickness [mm] | $f_y$ [N/mm²] | $f_u$ [N/mm²] |
| S (S460) | 5.4 | 475 | 627 |
| H (S690) | 5.0 | 772 | 808 |

These actual material properties are determined with tensile tests. In Figure 2 and 3 the stress-strain curves are presented. The left hand graph shows the recording of the strain measured directly on the material test piece. The measuring range of that device is limited to 17% and beyond that the device falls off. The right hand graph shows the recording of the strain measured via the testing machine, which includes the possible slip in the clamps of that machine. So that is less accurate but by comparing the recordings for S460 (see Fig. 2) with those for S690 (see Fig. 3) these graphs give sufficient qualitative information. From the Figures 2 and 3 it can be seen that the strain at failure for S460 is about two times larger than that for S690.
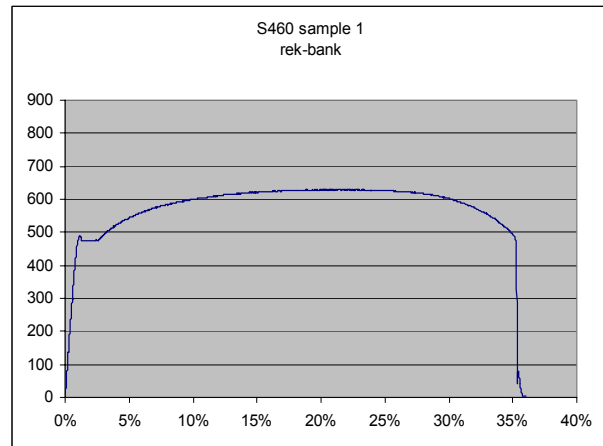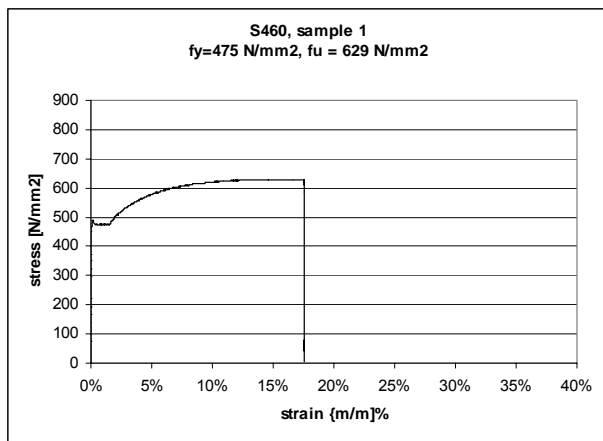
Figure 2. Actual stress-strain curve for the plate material used in the tests of steel grade S460
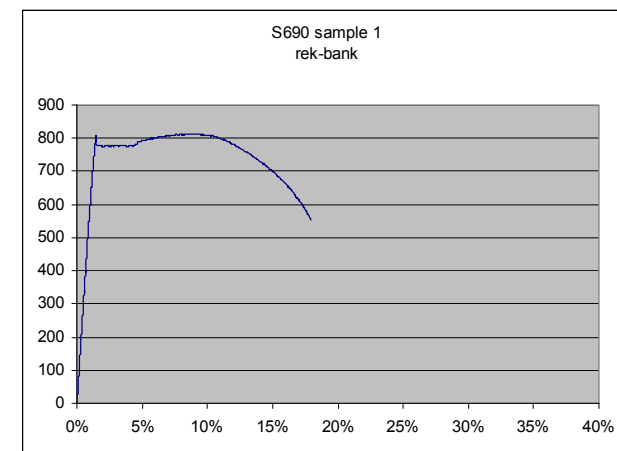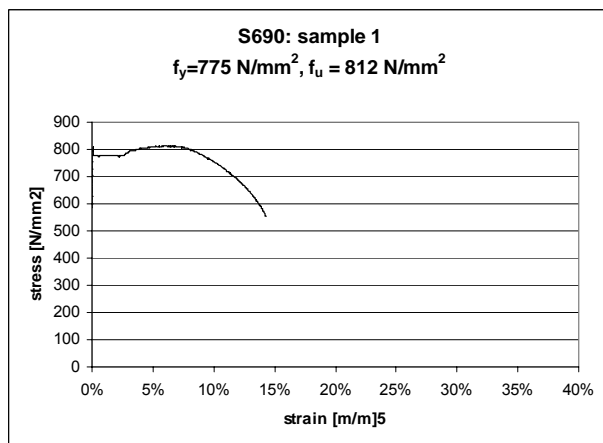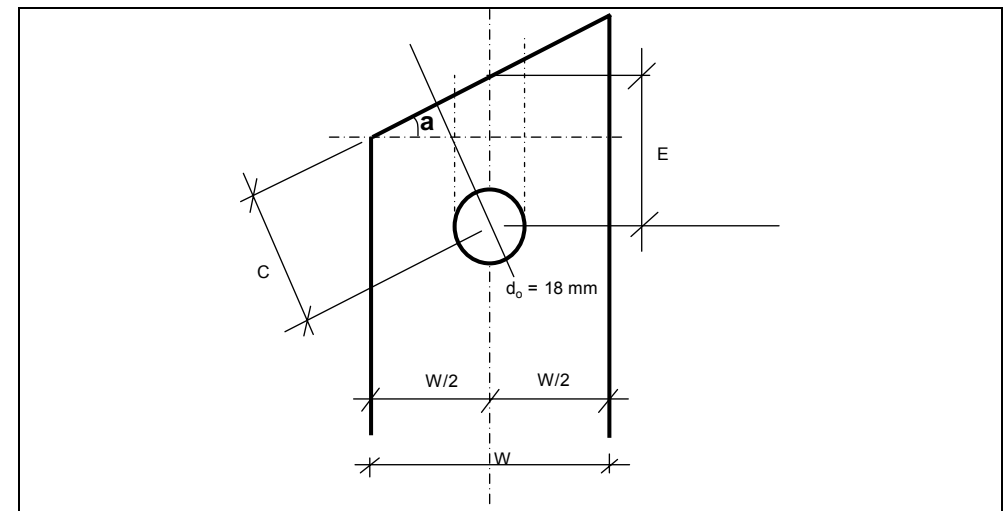


Figure 3. Actual stress-strain curve for the plate material used in the tests of steel grade S690

In Table 3 the geometry of the test pieces is presented.

Table 3. Geometry of the test pieces



**specimen ID: W-S-AA-CC**

key:

| width | W | N, W | narrow / wide | 54 , 72 mm |
|-------|---|------|---------------|------------|
| steel | S | S, H | standard / HSS | S460 , S690 |
| angle | AA | 15, 30, 45 | cutting angle | |
| end dist. | CC | ( 07, 09 ) 10, 12, 15, 18 | end distance C ( see figure below ): | C = CC/10 x $D_{hole}$ |

| specimen geometry | C [mm] | E [mm] | E [ /$D_{hole}$ ] |
|---|---|---|---|
| 15-10 | 18.0 | 18.6 | 1.0 |
| 15-12 | 21.6 | 22.4 | 1.2 |
| 15-15 | 27.0 | 28.0 | 1.6 |
| 15-18 | 32.4 | 33.5 | 1.9 |
| 30-10 | 18.0 | 20.8 | 1.2 |
| 30-12 | 21.6 | 24.9 | 1.4 |
| 30-15 | 27.0 | 31.2 | 1.7 |
| 30-18 | 32.4 | 37.4 | 2.1 |
| 45-10 | 18.0 | 25.5 | 1.4 |
| 45-12 | 21.6 | 30.5 | 1.7 |
| 45-15 | 27.0 | 38.2 | 2.1 |
| 45-18 | 32.4 | 45.8 | 2.5 |

## 3. TEST RESULTS

In Table 4 the test results are presented.

Table 4. Test results

| specimen-ID | test result TNS [kN] | Test results | specimen-ID | test result TWS [kN] | Test results |
|---|---|---|---|---|---|
| N-S-15-10 | 55.8 | **T NS** | W-S-15-10 | 59.9 | **T WS** |
| N-S-15-12 | 72.3 | | W-S-15-12 | 74.5 | |
| N-S-15-15 | 89.8 | **N**arrow specimen of steel grade **S** (S460) | W-S-15-15 | 93.7 | **W**ide specimen of steel grade **S** (S460) |
| N-S-15-18 | 114.0 | | W-S-15-18 | 108.3 | |
| N-S-30-10 | 55.1 | | W-S-30-10 | 62.8 | |
| N-S-30-12 | 72.8 | | W-S-30-12 | 74.2 | |
| N-S-30-15 | 92.3 | | W-S-30-15 | 92.6 | |
| N-S-30-18 | 114.7 | | W-S-30-18 | 112.2 | |
| N-S-45-10 | 59.5 | | W-S-45-10 | 68.1 | |
| N-S-45-12 | 78.5 | | W-S-45-12 | 77.1 | |
| N-S-45-15 | 97.1 | | W-S-45-15 | 98.2 | |
| N-S-45-18 | 115.6 | | W-S-45-18 | 123.3 | |
| N-S-45-10 | 60.1 | | W-S-45-10 | 64.6 | |
| N-S-45-12 | 77.4 | | W-S-45-12 | 78.8 | |

| specimen-ID | test result TNH [kN] | Test results | specimen-ID | test result TWH [kN] | Test results |
|---|---|---|---|---|---|
| N-H-15-10 | 63.5 | **T NH** | W-H-15-10 | 62.6 | **T WH** |
| N-H-15-12 | 79.0 | | W-H-15-12 | 81.3 | |
| N-H-15-15 | 97.3 | **N**arrow specimen of steel grade **H** (S690) | W-H-15-15 | 105.0 | **W**ide specimen of steel grade **H** (S690) |
| N-H-15-18 | 119.5 | | W-H-15-18 | 123.1 | |
| N-H-30-10 | 61.6 | | W-H-30-10 | 70.8 | |
| N-H-30-12 | 79.0 | | W-H-30-12 | 84.9 | |
| N-H-30-15 | 101.7 | | W-H-30-15 | 104.6 | |
| N-H-30-18 | 121.6 | | W-H-30-18 | 122.4 | |
| N-H-45-10 | 69.9 | | W-H-45-10 | 76.5 | |
| N-H-45-12 | 86.5 | | W-H-45-12 | 89.9 | |
| N-H-45-15 | 106.8 | | W-H-45-15 | 106.4 | |
| N-H-45-18 | 131.5 | | W-H-45-18 | 131.4 | |
| N-H-45-10 | 67.8 | | W-H-45-10 | 72.4 | |
| N-H-45-12 | 84.4 | | W-H-45-12 | 88.8 | |

In Figure 4 the test set-up is shown and in Figure 5 typical examples of failed test pieces are shown.
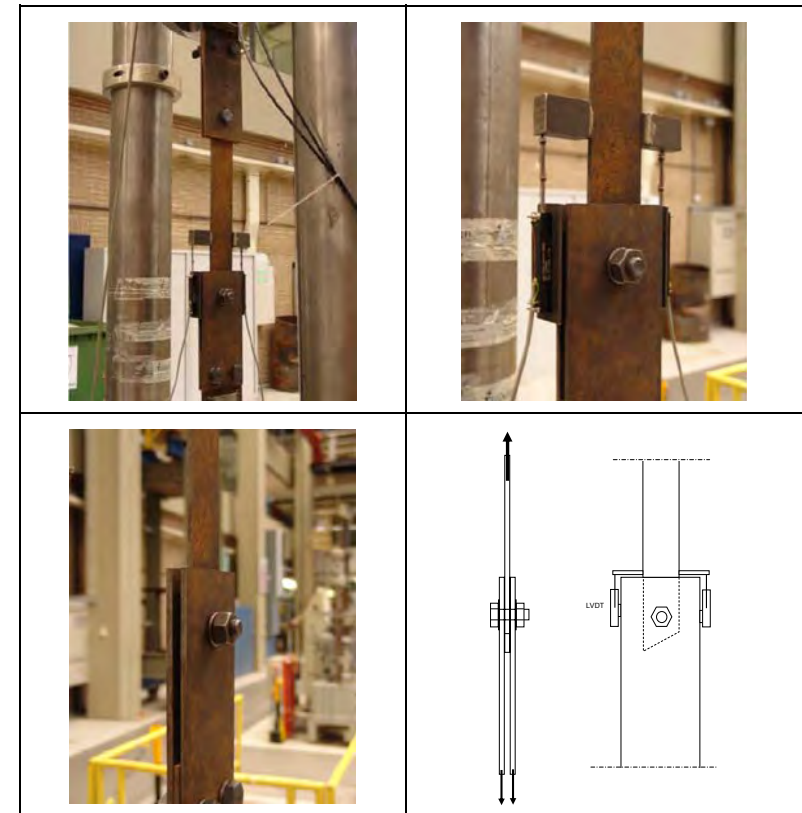


Figure 4. Test set-up
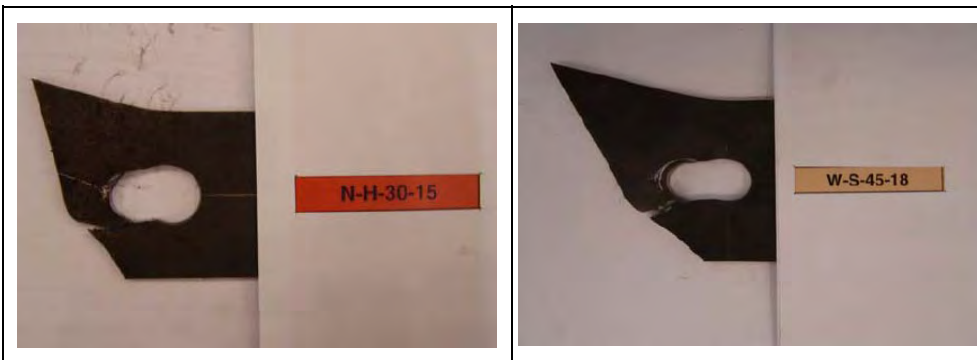
Figure 5. Typical examples of failed test pieces

## 4. ANALYSES

In Table 5 the results of the test pieces of the same geometry but made of S460 and S690 respectively are compared. From this comparison it can be seen that the ratio between the actual material strength corrected for the actual plate thickness $(f_{u(S690)}/t_{(S690)}) / f_{u(S460)}/t_{(S460)}) = (808/5,0) / (627/5,4) = 1,39$. This ratio, which should be there based on the Eurocode 3 rules, is not reached at all. That ratio, which result from the tests (see Table 5) is not larger than just 1,10. The reason for this difference finds it cause in the difference in strain at failure that is present and the fact that the mode of failure is not symmetric, which can be seen from Figure 5.

Table 5. Comparison between test results of plates made of S460 and S690 respectively.

| specimen geometry | ratio TNH/TNS | ratio TWH/TWS |
|---|---|---|
| 15-10 | 1.14 | 1.06 |
| 15-12 | 1.09 | 1.09 |
| 15-15 | 1.09 | 1.12 |
| 15-18 | 1.05 | 1.12 |
| 30-10 | 1.12 | 1.07 |
| 30-12 | 1.09 | 1.11 |
| 30-15 | 1.11 | 1.13 |
| 30-18 | 1.07 | 1.11 |
| 45-10 | 1.13 | 1.13 |
| 45-12 | 1.09 | 1.15 |
| 45-15 | 1.08 | 1.10 |
| 45-18 | 1.13 | 1.07 |
| 45-10 | 1.14 | 1.15 |
| 45-12 | 1.11 | 1.13 |
| average | **1.10** | **1.11** |

**Comparison** between test results of **S** (S460) and **H** (S690) specimens.

Left column **N**arrow specimens (T**N**H/T**N**S)

Right column **W**ide specimens (T**W**H/T**W**S)

Just using the Eurocode 3 rules as presented in Table 1 in case of non-rectangular endings and defining $e_1$ as done in Figure 1 (dimension E) and using the actual geometry and material properties the outcomes can be compared to the test results. In Table 6 the parameters for the calculation of the bearing strength for the end bolt are defined. In Table 7 these parameters, calculated on the bases of the definitions presented in Table 6, are shown. In Table 8 the Eurocode 3 predictions are compared to the test results.

Table 6. Definition of the parameters to calculate the bearing strength of the end bolt.



In the direction of the load transfer:

for end bolts: $\alpha_d = \dfrac{e_1}{3d_0}$

Applied on the force F:

$\alpha_d = \dfrac{E}{3d_0} = \dfrac{C/\cos(\alpha)}{3d_0}$

Applied on the component of F working perpendicular to the plate end:

$\alpha_d = \dfrac{C}{3d_0}$

both approaches lead to the same result for $F_b$

$$F_u = \frac{k_1 \cdot \alpha_b \cdot f_u \cdot d \cdot t}{\gamma_{M2}} = \frac{k_1 \cdot \dfrac{C/\cos(\alpha)}{3d_0} \cdot f_u \cdot d \cdot t}{\gamma_{M2}}$$

$$F_u \cdot \cos(\alpha) = \frac{k_1 \cdot \alpha_b \cdot f_u \cdot d \cdot t}{\gamma_{M2}} = \frac{k_1 \cdot \dfrac{C}{3d_0} \cdot f_u \cdot d \cdot t}{\gamma_{M2}}$$

Table 7. Calculated parameters $\alpha_d$ and $k_1$.

| **Bolts used in research:** | values of $\alpha_d$ for specimen geometries | | | |
|---|---|---|---|---|
| **M16, 10.9:** $\dfrac{f_{ub}}{f_u} > \dfrac{1000}{800}$ | angle \ C | **1.0** | **1.2** | **1.5** | **1.8** |
| | 00 | 0.33 | 0.40 | 0.50 | 0.60 |
| | 15 | 0.35 | 0.41 | 0.52 | 0.62 |
| | 30 | 0.38 | 0.46 | 0.58 | 0.69 |
| | 45 | 0.47 | 0.57 | 0.71 | 0.85 |

| values of $k_1$ | | plate width | $e_2$ | $d_o$ | |
|---|---|---|---|---|---|
| specimen plate end | | indication | [mm] | [mm] | $k_1$ |
| rectangular | | - | 60 | 30 | 18 | MIN(2.97; 2.5) =2.5 |
| non - rectangular | | N | 54 | 27 | 18 | MIN( 2.5; 2.5) = 2.5 |
| non - rectangular | | W | 72 | 36 | 18 | MIN( 3.9; 2.5) = 2.5 |

Table 8. Comparison between the EC3 prediction and the test results for S460 and S690.

| EC3 model | | | | Tests vs EC3 |
|---|---|---|---|---|
| test piece | Fb,EC3 | ratio EC3/TNS | ratio EC3/TWS | |
| | [kN] | | | **Fb,EC3:** Model value based on Eurocode 3 bearing capacity (**EC3**) |
| S-15-10 | 46.7 | 0.85 | 0.78 | |
| S-15-12 | 56.1 | 0.79 | 0.76 | |
| S-15-15 | 70.1 | 0.78 | 0.76 | **Ratio EC3/TNS:** Comparison between EC3 prediction and test results for **N**arrow specimens of steel grade **S** (S460) |
| S-15-18 | 84.1 | 0.75 | 0.77 | |
| S-30-10 | 52.1 | 0.91 | 0.85 | |
| S-30-12 | 62.6 | 0.88 | 0.83 | |
| S-30-15 | 78.2 | 0.86 | 0.82 | |
| S-30-18 | 93.8 | 0.82 | 0.83 | |
| S-45-10 | 63.8 | 1.12 | 1.01 | **Ratio EC3/TWS:** Comparison between EC3 prediction and test results for **W**ide specimens of steel grade **S** (S460) |
| S-45-12 | 76.6 | 1.02 | 1.03 | |
| S-45-15 | 95.8 | 0.98 | 0.99 | |
| S-45-18 | 114.9 | 1.01 | 0.94 | |
| S-45-10 | 63.8 | 1.13 | 1.02 | |
| S-45-12 | 76.6 | 1.03 | 0.99 | |

| EC3 model | | | | Tests vs EC3 |
|---|---|---|---|---|
| test piece | Fb,EC3 | ratio EC3/TNH | ratio EC3/TWH | |
| | [kN] | | | **Fb,EC3:** Model value based on Eurocode 3 bearing capacity (**EC3**) |
| H-15-10 | 55.8 | 0.89 | 0.88 | |
| H-15-12 | 66.9 | 0.86 | 0.83 | |
| H-15-15 | 83.7 | 0.85 | 0.81 | **Ratio EC3/TNH:** Comparison between EC3 prediction and test results for **N**arrow specimens of steel grade **H** (S690) |
| H-15-18 | 100.4 | 0.85 | 0.82 | |
| H-30-10 | 62.2 | 0.98 | 0.95 | |
| H-30-12 | 74.6 | 0.96 | 0.89 | |
| H-30-15 | 93.3 | 0.92 | 0.86 | |
| H-30-18 | 112.0 | 0.91 | 0.89 | |
| H-45-10 | 76.2 | 1.18 | 1.07 | **Ratio EC3/TWH:** Comparison between EC3 prediction and test results for **W**ide specimens of steel grade **H** (S690) |
| H-45-12 | 91.4 | 1.11 | 1.07 | |
| H-45-15 | 114.3 | 1.08 | 1.07 | |
| H-45-18 | 137.1 | 1.06 | 1.05 | |
| H-45-10 | 76.2 | 1.17 | 1.06 | |
| H-45-12 | 91.4 | 1.11 | 1.05 | |

From Table 8 it can be seen that the Eurocode 3 predictions are only safe for cases where the angle of the non-rectangular endings are not larger than 30 degrees.

The bearing strength of an end bolt can also be predicted based on the resistance calculated from the shear planes which will be formed when the end bolt will shear out of the plate in the direction of the force in the strip. This is illustrated in Table 9. In Table 10 the predictions based on the shear plane model are compared to the test results. From this comparison it can be seen that in all cases, for S460 as well as for S690 the predictions are unsafe.

Table 9. Shear plane model.

Bearing resistance based on SPM

$$F_{b,SPM} = ( e_L + e_R ) \cdot t \cdot \tau_u$$

$$F_{b,SPM-2} = MIN( e_L ; e_R ) \cdot t \cdot \tau_u = 2 \cdot e_L \cdot t \cdot \tau_u$$

Where $\tau_u = \dfrac{1}{\sqrt{3}} f_u$



Table 10. Comparison between the shear plane model predictions and the test results for S460 and S690.

| Shear Planes Model | | | | Tests vs SPM |
|---|---|---|---|---|
| test piece | Fb, SPM | ratio SPM/TNS | ratio SPM/TWS | |
| | [kN] | | | **Fb,SPM:** Model value based on **S**hear **P**lane **M**odel (**SPM**). |
| S-15-10 | 55.3 | 1.01 | 0.93 | |
| S-15-12 | 69.8 | 0.98 | 0.94 | |
| S-15-15 | 91.7 | 1.02 | 1.00 | **Ratio SPM/TNS:** Comparison between SPM prediction and test results for **N**arrow specimens of steel grade **S** (S460) |
| S-15-18 | 113.5 | 1.02 | 1.04 | |
| S-30-10 | 63.7 | 1.11 | 1.04 | |
| S-30-12 | 79.9 | 1.12 | 1.06 | |
| S-30-15 | 104.3 | 1.14 | 1.09 | |
| S-30-18 | 128.7 | 1.12 | 1.14 | |
| S-45-10 | 81.9 | 1.44 | 1.30 | **Ratio SPM/TWS:** Comparison between SPM prediction and test results for **W**ide specimens of steel grade **S** (S460) |
| S-45-12 | 101.8 | 1.35 | 1.36 | |
| S-45-15 | 131.7 | 1.34 | 1.36 | |
| S-45-18 | 161.5 | 1.42 | 1.32 | |
| S-45-10 | 81.9 | 1.45 | 1.31 | |
| S-45-12 | 101.8 | 1.37 | 1.32 | |

www.steelconstruct.com

| Shear Planes Model | | | | Tests vs SPM |
|---|---|---|---|---|
| test piece | Fb, SPM | ratio SPM/TNH | ratio SPM/TWH | |
| | [kN] | | | |
| H-15-10 | 65.9 | 1.05 | 1.04 | |
| H-15-12 | 83.3 | 1.07 | 1.03 | |
| H-15-15 | 109.4 | 1.12 | 1.07 | |
| H-15-18 | 135.5 | 1.15 | 1.11 | |
| H-30-10 | 76.0 | 1.19 | 1.16 | |
| H-30-12 | 95.4 | 1.22 | 1.14 | |
| H-30-15 | 124.4 | 1.23 | 1.15 | |
| H-30-18 | 153.5 | 1.25 | 1.22 | |
| H-45-10 | 97.8 | 1.51 | 1.37 | |
| H-45-12 | 121.5 | 1.48 | 1.42 | |
| H-45-15 | 157.1 | 1.49 | 1.48 | |
| H-45-18 | 192.8 | 1.49 | 1.47 | |
| H-45-10 | 97.8 | 1.51 | 1.36 | |
| H-45-12 | 121.5 | 1.47 | 1.39 | |

**Tests vs SPM**

$F_{b,SPM}$:
Model value based on **S**hear **P**lane **M**odel (**SPM**).

Ratio SPM/T**NH**:
Comparison between SPM prediction and test results for **N**arrow specimens of steel grade **H** (S690)

Ratio SPM/T**WH**:
Comparison between SPM prediction and test results for **W**ide specimens of steel grade **H** (S690)

This shear plane model can be made a bit more conservative by just taking for the length of the total shear plane two times the length of the shortest shear plane, the so called shear plane model 2. The results are presented in Table 11.

Table 11. Comparison between the shear plane model 2 predictions and the test results for S460 and S690.

| Shear Planes Model - 2 | | | | Tests vs SPM-2 |
|---|---|---|---|---|
| test piece | Fb, SPM-2 | ratio SPM-2/TNS | ratio SPM-2/TWS | |
| | [kN] | | | |
| S-15-10 | 46.9 | 0.85 | 0.79 | |
| S-15-12 | 61.5 | 0.86 | 0.83 | |
| S-15-15 | 83.3 | 0.92 | 0.91 | |
| S-15-18 | 105.2 | 0.94 | 0.96 | |
| S-30-10 | 45.6 | 0.80 | 0.74 | |
| S-30-12 | 61.9 | 0.87 | 0.82 | |
| S-30-15 | 86.2 | 0.94 | 0.90 | |
| S-30-18 | 110.6 | 0.96 | 0.98 | |
| S-45-10 | 50.7 | 0.89 | 0.80 | |
| S-45-12 | 70.6 | 0.94 | 0.95 | |
| S-45-15 | 100.4 | 1.02 | 1.03 | |
| S-45-18 | 130.3 | 1.14 | 1.07 | |
| S-45-10 | 50.7 | 0.89 | 0.81 | |
| S-45-12 | 70.6 | 0.95 | 0.92 | |

**Tests vs SPM-2**

$F_{b,SPM}$:
Model value based on **S**hear **P**lane **M**odel (**SPM-2**).

Ratio SPM-2/T**NS**:
Comparison between SPM prediction and test results for **N**arrow specimens of steel grade **S** (S460)

Ratio SPM-2/T**WS**:
Comparison between SPM prediction and test results for **W**ide specimens of steel grade **S** (S460)

| Shear Planes Model - 2 | | | | Tests vs SPM-2 |
|---|---|---|---|---|
| test piece | Fb, SPM-2 | ratio SPM-2/TNS | ratio SPM-2/TWS | |
| | [kN] | | | |
| H-15-10 | 55.9 | 0.89 | 0.89 | |
| H-15-12 | 73.3 | 0.94 | 0.91 | |
| H-15-15 | 99.4 | 1.02 | 0.97 | |
| H-15-18 | 125.5 | 1.07 | 1.03 | |
| H-30-10 | 54.4 | 0.85 | 0.83 | |
| H-30-12 | 73.8 | 0.95 | 0.88 | |
| H-30-15 | 102.9 | 1.01 | 0.95 | |
| H-30-18 | 132.0 | 1.08 | 1.05 | |
| H-45-10 | 60.4 | 0.94 | 0.85 | |
| H-45-12 | 84.2 | 1.02 | 0.98 | |
| H-45-15 | 119.8 | 1.13 | 1.13 | |
| H-45-18 | 155.4 | 1.21 | 1.19 | |
| H-45-10 | 60.4 | 0.93 | 0.84 | |
| H-45-12 | 84.2 | 1.02 | 0.96 | |

**Tests vs SPM-2**

$F_{b,SPM}$:
Model value based on **S**hear **P**lane **M**odel (**SPM**).

Ratio SPM-2/T**NH**:
Comparison between SPM prediction and test results for **N**arrow specimens of steel grade **H** (S690)

Ratio SPM-2/T**WH**:
Comparison between SPM prediction and test results for **W**ide specimens of steel grade **H** (S690)

From this comparison it can be seen that, for S460 and angles equal or smaller than 30 degrees, the results are safe, but for angles larger than 30 degrees the results are not consistently safe. For S690 the predictions are still unsafe in almost all cases.

## 5. CONCLUSIONS

In cases where the endings of a plate/strip in tension is not rectangular, the Eurocode 3 Part 1-8 "Design of Joints" does not provide a rule for the calculation of the bearing resistance of an end bolt. If that rule of Eurocode 3 Part 1-8 is just used in case of a non-rectangular ending, the predicted bearing resistance is only safe in cases where the non-rectangular endings are not larger than 30 degrees.

The bearing resistance can also be predicted using a shear plane model. In that case the bearing resistance of an end bolt is predicted based on the resistance calculated from the shear planes which will be formed when the end bolt will shear out of the plate in the direction of the force in the strip. From the comparison of the predictions with the test results it can be seen that in all cases, for S460 as well as for S690 the predictions are unsafe.

If the modified shear plane model 2 is used it can be seen from the comparison with test results that, for S460 and angles equal to or smaller than 30 degrees, the results are safe, but for angles larger than 30 degrees the results are not consistently safe. For S690 the predictions are still unsafe in almost all cases.

In order to further develop an adequate design rule for end bolts in plates/strips with non-rectangular endings, the research needs to be extended to evaluate more refined prediction formulae. Also, cases with more bolts in the width direction of the plate/strip need to be investigated.

# VIRTUAL TESTING OF COLD-FORMED STEEL BOLTED JOINTS IN PITCH-ROOF PORTAL FRAMES

Zsolt NAGY

*Technical University of Cluj-Napoca-400027, Romania*
E-mail: zsolt.nagy@dst.utcluj.ro

## ABSTRACT

Previous studies reported the results of a large experimental and numerical program carried out at the "Politehnica" University of Timisoara and Technical University of Cluj, in order to evaluate the performance of three different configuration of ridge (apex) and eaves knee joints of pitched roof cold-formed steel portal frames of back-to-back lipped channel sections and bolted joints under monotonic and cyclic loading [1]. The behaviour and failure mechanisms of joints were observed, to evaluate their rigidity, strength and ductility. In a second phase, considering the poor performance of joints with web bolts only, joint configurations with both web and flange bolts were used to test two full-scale double frame units under: (1) horizontal load, and (2) horizontal and gravity loadings [2]. The objective of the full-scale tests was to assess performance of pitched-roof cold-formed portal frames with moment-resisting joints under lateral loading, with particular emphasis on earthquake loading. Numerical analysis of the tested joints was performed, obtaining calibrated FE models.

A parametric study consisted of 8 ridge joint configurations with flange bolts and 6 ridge joint configurations with web bolts only was conducted using the calibrated numerical model, in order to identify the weakness of these types of joints. The failure modes of material yielding and local and distortional buckling of the joint components due to stress concentration were found in this study. The experimental joint strengths and numerical results predicted by the parametric study were compared with the design strengths calculated using the principles of component method proposed by current European specifications for steel joints.

The paper summarizes the experimental work; the numerical results of the tested ridge joints and the parametric study on the developed joint typologies are presented to determine the mechanical characteristics of the analyzed connections**.**

## 1. INTRODUCTION

The global behaviour of cold-formed steel portal frames of bolted joints were studied experimentally by Lim [3], Dundu & Kemp [4], Kwon et al. [5] and Ahamed, Hazlan & Mahendran [6]. All these studies provided evidence of the crucial importance of joint performance on the global response of frames, which are semi-rigid and in almost all cases with partial strength [3].

An extensive experimental program on ridge and eaves joints, with three alternative joint configurations, using welded bracket elements and bolts installed either on webs only or both on webs and flanges was carried out at the "Politehnica" University of Timisoara [1]. Detailed experimental results on joint behaviour are reported by Dubina et al. [1]. Based on experimental results, a calculation procedure using the component method of EN1993-1-8 [7] was adapted for cold-formed steel joints [8]. Joint stiffness and moment capacity, obtained using the component method, were used to develop a joint model for global structural analysis. In a second phase, two full-scale tests on cold-formed pitched-roof portal frames with bolted joints were performed, with the primary objective to assess their performance under horizontal (seismic) loading.

Experimental tests emphasize the bearing work of bolts associated with elastic-plastic elongation of bolt-holes is by far the most important component controlling the stiffness and capacity of such type of connections [8]. The contribution of other components, such as flanges in tension and compression due to bending action, and the web in shear due to transverse action is significantly lower.

The paper summarizes the results of the finite element analyses (FEA) done to calibrate FE models of the tested joints [9], and brings supplementary results using the parametric study on ridge joints. The comparison of the experimental and numerical results will be presented together with the ones obtained from the parametric study, for the determination of connections characteristics.

## 2. SUMMARY OF TESTING PROGRAM ON JOINTS

To define realistic specimen configurations, a simple pitched roof portal frame was first designed with the following configuration: span 12 m; bay 5 m; eaves height 4 m and roof slope of 10°. This frame was subjected to loads common in the Romanian design practice. These loads were evaluated at 10 kN/m, as uniformly distributed load on the frame. The frame was analysed and designed according to EN 1993-1-3 [10]. The size of knee and ridge specimens and testing setup were chosen to obtain in the connected members a distribution of bending moment similar to the one observed in the designed structure.

Elements of the portal frame resulted back-to-back built-up sections made of Lindab C350/3.0 profiles (nominal yield strength $f_y$=350 N/mm$^2$). Using these cross-section dimensions, three alternative joint configurations were designed (see *Figure 1. and Figure 2.*), using welded bracket elements (S235: $f_y$=235 N/mm$^2$).
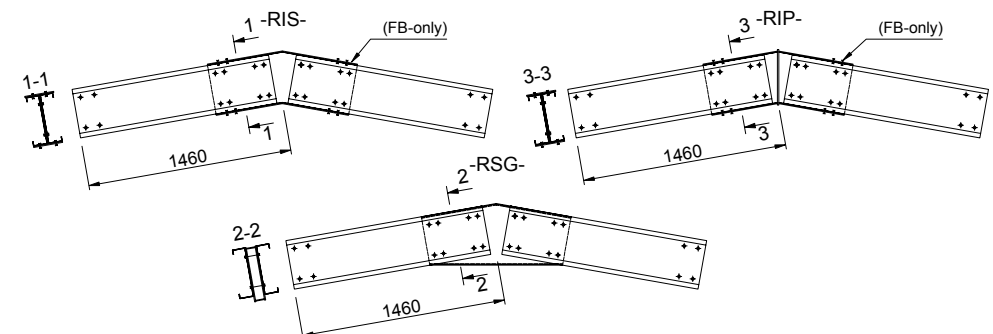


Figure 1. Configurations of ridge joints

One group of specimens (KSG and RSG) used spaced built-up gussets. In this case, bolts were provided only on the web of the C350 profile. In the other cases, where two different details were used for the connecting bracket – i.e. welded I sections only (KIS and RIS), and welded I section with plate bisector (KIP and RIP), respectively - bolts were provided on the web only, or both on the web and the flanges. Joints where bolts were provided on the web and on flanges were denoted by FB letters.

Monotonic and cyclic tests were performed for each specimen typology, all specimens being tested statically [1]. This paper will discuss only the results of the monotonic testes. The monotonic tests identified failure modes of the different joint typologies. All specimens had a failure due to local buckling of the cold-formed profiles; however two distinctive modes were identified for specimens with flange bolts and those without (see *Figure 3.* and *Figure 4.*).
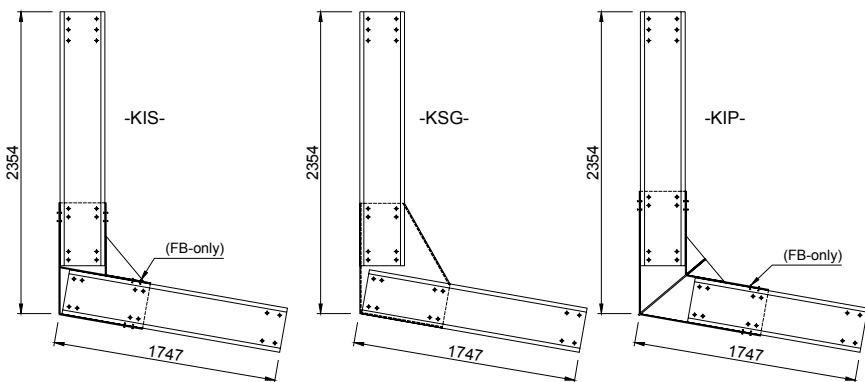


Figure 2. Configurations of knee joints



*(a) RIS-M specimen*        *(b) RIS-FB-M specimen*

Figure 3. Failure of ridge specimens

Test on joints have shown their failure occurs always at the edge of lap between connecting bracket and cold-formed sections. In case of specimens with bolts on webs only, the failure starts early by local bucking of the web, caused by the high concentration of compression stresses around bolt holes, and subsequently is extended on the flanges, to form at the end a local plastic mechanism. Specimens of bolts installed both on the flanges and webs of connected members are nearly full resistant, but still remain semi-rigid.



*(a) KIS-M knee specimen*        *(a) (b) KIS-FB-M knee specimen*

Figure 4. Failure of knee specimens

Comparative experimental curves for ridge and knee connections are presented in *Figure 5*. There are no significant differences among the specimens without flange bolts (RSG-M, RIP-M, and KSG-M, KIS-M). This could be explained by the higher stiffness and capacity of the connecting bolts compared to the other components of the joint. On the other hand, there is an important gain in load bearing capacity when bolts are installed also on the flanges, although this joint type is more difficult to fabricate (RIS-FB-M and KIS-FB-M).

Obviously, the specimens with unbolted flanges that failed prematurely by web buckling due to stress concentration around the outer bolt rows, would be the weakest part of portal frames. Consequently, this joint typology is not recommended to be used in practice.
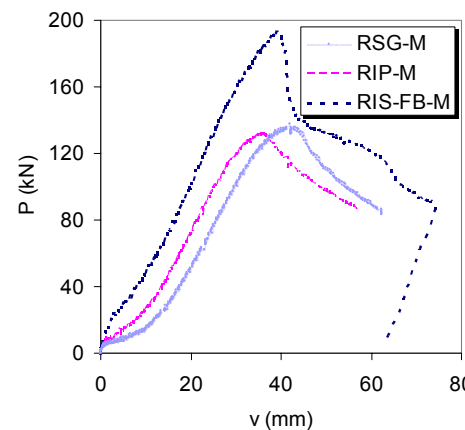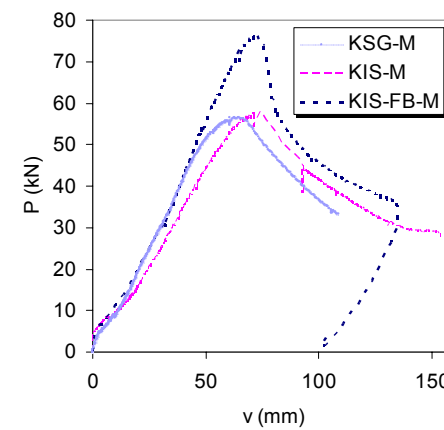


(a) ridge joints        (b) knee joints

Figure 5. Comparative results from monotonic tests

## 3. FINITE ELEMENT ANALYSIS OF RIDGE AND KNEE JOINTS – CALIBRATION PROCESS

To study the structural behaviour of the joints (RIS-FB-M; KIS-FB-M; RIS-M; KIS-M), finite element models have been developed, they are shown in *Figure 6.* and *Figure 7*. The numerical models for the tested specimens were created using the finite element analysis software package ABAQUS/CAE v.6.10 [11].

Some features about the FE model: (1) finite element type: 8-noded standard quadratic, reduced integration, homogeneous shell element (S4R) to model the cold-formed members; (2) 3D solid elements (C3D4) to model the brackets at the beam-column joints; (3) 3D elements to model the bolts between the back-to-back cold-formed lipped channels and brackets; (4) the interaction between parts was considered as hard contact behaviour for normal direction and for tangential direction was chosen tangential friction coefficient of 0.3 as penalty; (5) pre-tensioning force to model the effect of bolt tightening; (6) different mesh refinements were studied in order to find the optimum number of elements from the point of view of ultimate force accuracy and analysis time. Finally, a mesh size of 8 mm × 8 mm was considered for C-profiles and 12mm × 12mm for the bracket providing enough accuracy; (7) load and end conditions were considered as in experimental tests; (8) the material behaviour used for numerical modelling was in accordance with the recorded curves from tensile tests (multi-linear isotropic model). The material properties for thin-walled cold-formed elements, determined from coupon tests, are: yield strength of 486N/mm$^2$, ultimate tensile strength 553N/mm$^2$, Young's modulus E=210000N/mm$^2$ and a measured thickness minus zinc coating of 2.90mm.

Nonlinear analyses were performed, using dynamic explicit steps as quasi-static, choosing time parameter so that the inertial effects on the system to be insignificant (takes into account stiffness loss due to local buckling).
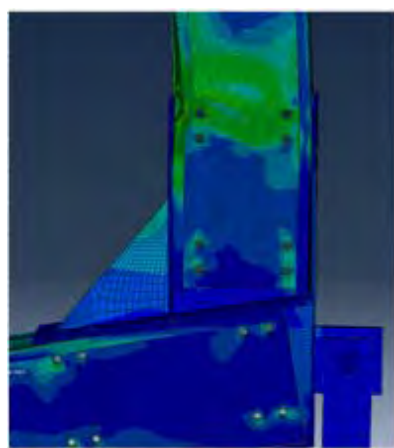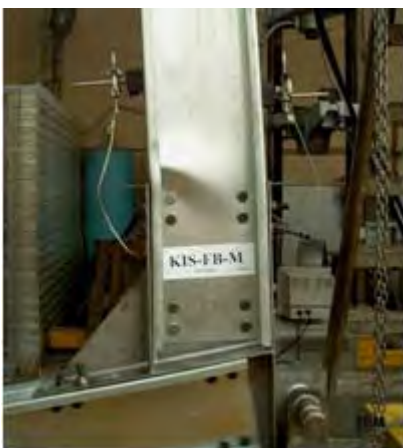


(a) Knee specimen (KIS-FB-M)experiment   (b)Knee specimen (KIS-FB-M) FEM model

Figure 6. Knee experimental test vs. ABAQUS results

The calibrated FE models reproduce the same failure mechanism in case of knee specimens (KIS-FB-M, see *Figure 6.*) as obtained experimentally. In case of ridge specimens (RIS-FB-M, see *Figure 7.*), due to the symmetry of the model, the failure was distributed between the symmetric branches, obtaining two local failure

mechanisms (see *Figure 7b.*) instead of one obtained experimentally. Due to this aspect, in case of ridge specimens, the total rotation of left and right branches was considered. *Figure 8.* presents the force-displacement curves obtained both experimentally and numerically, for all types of joints. Good agreement can be observed between groups of curves.



(a) Ridge specimen (RIS-FB-M) experiment
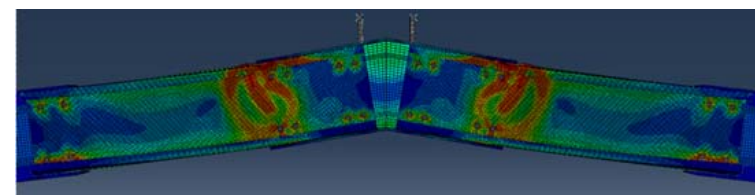


*(b)* Ridge specimen (RIS-FB-M) FEM model

Figure 7. Ridge experimental test vs. ABAQUS results

It is interesting to mention that increasing the distance between the cold formed C profile flanges and the stiff bracket on the calibrated numerical model, there is no significant differences in results in terms of stiffness neither load carrying capacity of the joint.

www.steelconstruct.com
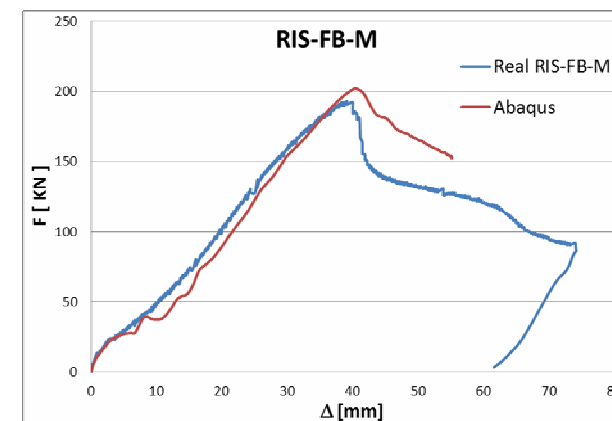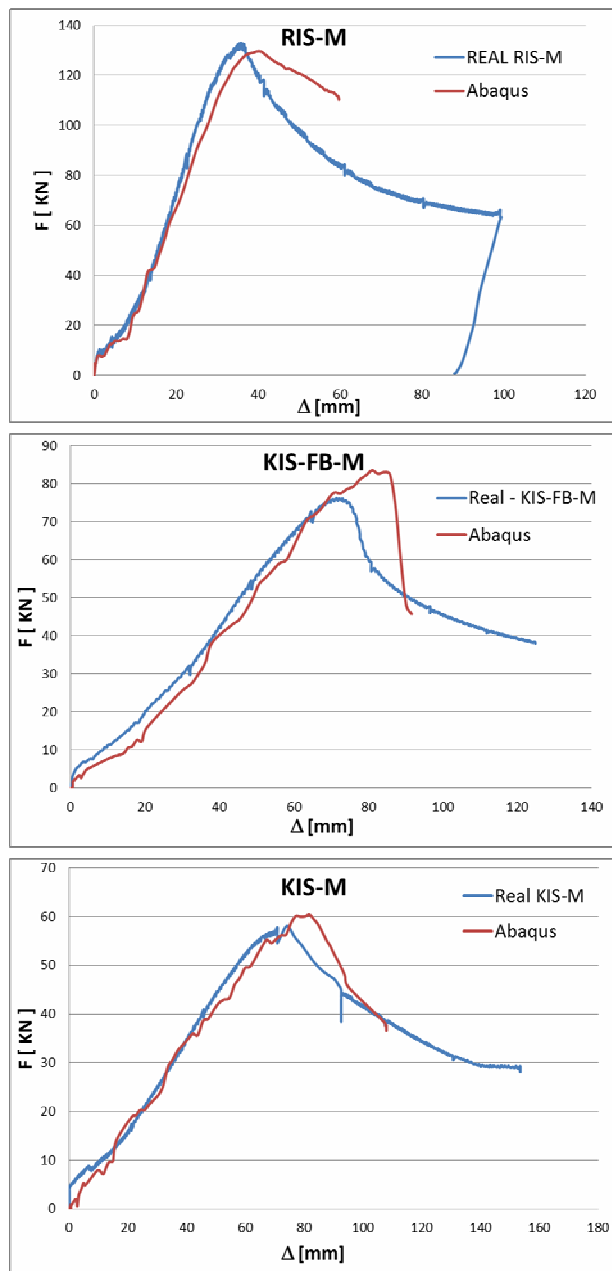
Figure 8. Knee and ridge specimens: F-Δ experimental and numerical curv

## 3.1. Parametric study of ridge joints

The calibrated FE model described in previous chapter was used in the parametric study of the ridge joints (RIS-FB-M; RIS-M). First, the influence of the

distance between the two bolt groups over global mechanical characteristics was monitored. The outer bolt group was kept on the position; the inner bolt group distance was gradually reduced, together with the length of the C profile, keeping the original end distances of the inner bolt group, till the inner and outer bolt group overlaps. Eight geometric configurations were studied, as it is presented in *Figure 9*. Configuration 1 to 4 has the same bolt numbers, in case of type 5 and 6 the number of bolts was reduced with two respectively with four bolts. Type 7 and 8 is not applicable for specimens with web bolts only. The 'yield' displacement and the corresponding conventional elastic capacities were determined according to the ECCS procedure (*Figure 10*).
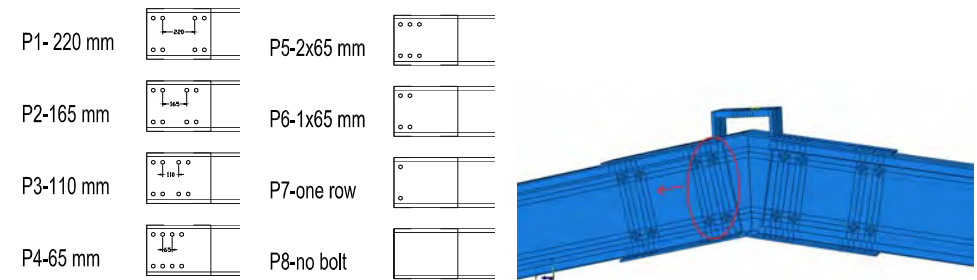


Figure 9. RIS-M ridge specimens used in parametric study
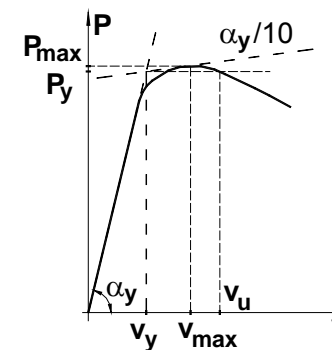


Figure 10. ECCS procedure to define the yield displacement

Model P1 corresponds to the tested specimens (RIS-FB-M; RIS-M). *Table 1* shows the variation of the computed maximum force $P_{max}$ and the corresponding displacement $v_{max}$ in the parametric study for the ridge joints (RIS-FB-M; RIS-M). According to the ECCS procedure, the yielding force $P_e$ and the corresponding yielding displacement $v_e$ was also computed. As it can be observed, in case of the specimen with flange bolts, there are insignificant differences between the specimens involved in the parametric study, since the flange bolts are present in all specimens. In case of specimens with web bolts only, there is an important capacity difference compared with the specimen with also flange bolts (in case of specimen with web bolts only $P_e$ is 35% lower), but until no any decrease in total bolts number, there is no any significant decrease in load carrying capacity of the specimen. Only in case

of specimen 5 and 6 in the load carrying capacity can be observed moderate (reducing the number of web bolts with 2) or significant decrease (reducing the number of web bolts with 4), simultaneously with moderate or significant increase in deformations of the ridge specimen.

It is also important to mention that in case of model with flange bolts, a P7 and P8 model also were analyzed. This corresponds to the situation with only two bolts on web (P7) or no any bolts on the web (P8). Moderate (P7) or significant decrease (P8) in load carrying capacity of the model with flange bolts was observed but only with moderate increase in deformations of the ridge specimen. All the computed graphs from FE analysis for RIS-FB-M and RIS-M specimens are shown in *Figure 11*.

Table 1. Parametric study results – ridge specimens

| Model | $P_e$ | $V_e$ | $P_{max}$ | $V_{max}$ |
|-------|-------|-------|-----------|-----------|
| RIS-FB-M | [kN] | [mm] | [kN] | [mm] |
| *Test* | *190.40* | *34.10* | *193.10* | *39.10* |
| P1 | 190.67 | 37.08 | 191.94 | 39.42 |
| P2 | 188.44 | 37.63 | 189.84 | 40.29 |
| P3 | 186.56 | 37.99 | 188.19 | 41.15 |
| P4 | 184.44 | 37.39 | 186.36 | 40.90 |
| P5 | 188.11 | 38.29 | 190.06 | 42.05 |
| P6 | 187.11 | 38.85 | 189.07 | 42.55 |
| P7 | 177.56 | 38.48 | 180.74 | 45.06 |
| P8 | 152.78 | 36.84 | 157.00 | 46.41 |

| Model | $P_e$ | $V_e$ | $P_{max}$ | $V_{max}$ |
|-------|-------|-------|-----------|-----------|
| RIS-M | [kN] | [mm] | [kN] | [mm] |
| *Test* | *127.30* | *26.70* | *130.50* | *31.50* |
| P1 | 127.70 | 35.83 | 129.21 | 40.02 |
| P2 | 125.10 | 37.00 | 126.07 | 39.83 |
| P3 | 121.70 | 37.57 | 122.74 | 40.70 |
| P4 | 118.20 | 38.28 | 119.66 | 42.63 |
| P5 | 112.10 | 41.76 | 113.66 | 47.07 |
| P6 | 87.56 | 48.06 | 89.22 | 57.16 |
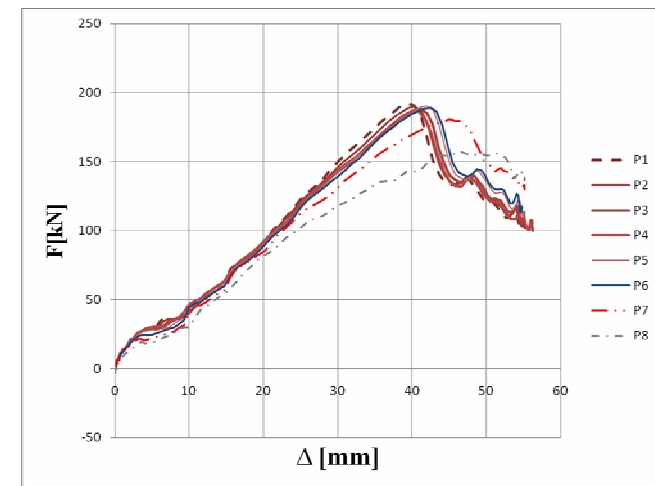


*Force – displacement graphs, ridge RIS-FB-M with flange bolts*
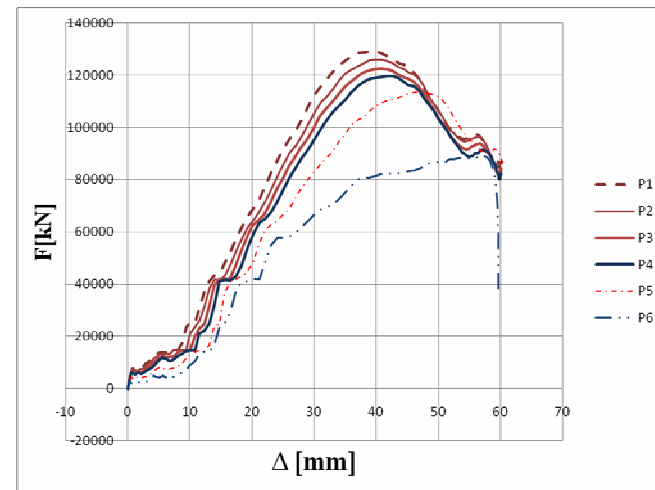


*Force – displacement graphs, ridge specimens RIS-M with web bolts only*

Figure 11. Graphs obtained in the parametric study

## 4. DISCUSSIONS

In case of the specimen with flange bolts (RIS-FB-M), the inner web bolt group contribution to the resistance and stiffness of the joints is negligible, since there are no any important differences between P1 up to P6 graphs. Reducing the number of bolts in outer group, there is a limited impact in the resistance and stiffness of the joint, which is under 25 % compared with the resistance of the tested specimens.

In case of the specimen with web bolts only (RIS-M), the inner web bolt group contribution to the resistance and stiffness of the joints is also reduced, since there are no any important differences between P1 up to P4 graphs. Reducing the number

www.steelconstruct.com

of web bolts, gives a more significant impact in the resistance and stiffness of the joint. In terms of resistance the decrease is around 30 %, compared with the resistance of the tested specimens.

The calculation model for the connection in both cases, based on the linear distribution of the force on each bolt is applicable only if the centre of gravity of the whole connection is considered on the symmetry axis of the analyzed specimen. In this particular case, the calculation model only for the bracket to C profile connection, based on the linear distribution of the force on each bolt is not correct.

The force distribution is unequal due to the flexibility of the connected members in the joint. In both cases, the force is an order of magnitude bigger in the outer bolt rows compared to inner one. All connections failed by local buckling of the compression web (in case of specimens with web bolts only) or flange (in case of specimens with flange bolts) closest to the connection bracket itself. Material yielding and local and distortional buckling of the joint components due to stress concentration were observed both in tests and developed FE models.

Further studies based on these test results will focus on the moment-rotation curves and using the component method in order to characterize the behaviour of such type of joints for frame analysis.

## 5. CONCLUSIONS

The goal of the paper was virtual testing using the previous calibrated FE model of back-to-back cold-formed steel lipped channel bolted joints. A FE model has been calibrated for ridge and knee specimens based on laboratory tests results. Using the calibrated FE model, fourteen types of different joint configurations were analyzed: 8 ridge configurations with flange and web bolts and 6 with web bolts only. According to the parametric FE analysis results, the following conclusion can be stated:

1. The calibrated knee and ridge models are able to reproduce the same failure mechanism as obtained experimentally, offering a fair force-displacement agreement between test and FE results;
2. Using the calibrated models, a quite good evaluation of the load carrying capacity of the analyzed joints can be obtained;
3. The calculation model for the connection in both cases, based on the linear distribution of the force on each bolt is applicable only if the centre of gravity of the whole connection is considered on the symmetry axis of the analyzed specimen; this imposes to account for the joint as a whole;
4. Increasing the distance between the cold formed C profile flanges and the stiff bracket on the calibrated numerical model, there is insignificant differences in results in terms of stiffness and load carrying capacity of the joint. This leads to conclude that no any significant influence of the bracket-cold formed C flange contact in the joint global behavior.

The results and conclusions of this paper have to be limited to the joint typologies and range of section dimensions used in the simulation program. The research will continue to refine the obtained results and to extend the proposed analytical procedure using the component method to evaluate the stiffness and strength, for specimens having web bolts only.

## REFERENCES

[1] Dubina D, Stratan A, Ciutina A, Fulop L, Nagy Zs. "Performance of ridge and eaves joints in cold-formed steel portal frames". *Proc. of the 17th International Specialty Conference*, Orlando, Florida, USA, 727-742, 2004.
[2] Dubina D, Stratan A, Nagy Zs. "Full – scale testing of cold-formed steel pitched-roof portal frames of back-to-back channel sections and bolted joints". *Proceedings of the Sixth International Conference on Steel and Aluminum Structures*, Oxford, UK, 931-939, 2007.
[3] Lim JBP. "Joint effects in cold-formed steel portal frames". University of Nottingham, Ph.D. Thesis, 2001.
[4] Dundu M, Kemp AR. "Strength requirements of single cold formed channels connected back-to-back". *J. of Constructional Steel Research*, Vol. 62, Issue 3: 250-261, 2006.
[5] Kwon YB, Chung HS, Kim GD. "Experiments of cold-formed steel connections and portal frames". *Journal of structural engineering*, vol. 132, no. 4: 600-607, 2006.
[6] Ahamed, Hazlan & Mahendran, Mahen. " Bolted beam-column moment connections between cold-formed steel members ". *21-st Australasian conference on the mechanics of structures and materials (acmsm 21), Victoria University, Melbourne*, 2010.
[7] EN1993-1-8. Eurocode 3: "Design of steel structures - Part 1-8: Design of joints". European Committee for Standardization, Brussels, 2005.
[8] Nagy Zs, Stratan A, Dubina D. "Application of component method for bolted cold-formed steel joints". *Proc. of the Int. Conf. on Metal Structures: "Steel – A new and traditional material for building"*, Poiana Brasov, September 20-22, 207-215, 2006.
[9] Pernes P., Nagy Zs, "Calibration of a finite element model for evaluation of cold-formed steel bolted joints in pitch-roof portal frames ". *Proc. of the 6-th International Thin Walled Structures - ICTWS 2011*, Timisoara, September 5-8, 207-215, 2011
[10] EN1993-1-3. Eurocode 3 – Part 1-3: "Supplementary rules for cold-formed thin gauge members and sheeting". European Committee for Standardization, Brussels, 2006.
[11] ABAQUS. "Theory manual", Hibbit, Karlson and Sorenson, Inc, 2007.

# FRICTION STIR WELDING IN STEEL CONSTRUCTION: RECENT ADVANCES

Ramona Gabor
*Faculty for Civil Engineering, University Politehnica of Timisoara, Romania*
*ramona.gabor@ct.upt.ro*

Jorge dos Santos
*Helmholtz-Zentrum Geesthacht, Germany*
*Jorge.dos.santos@hzg.de*

## ABSTRACT

Friction stir welding (FSW) is a solid–state, hot–shear joining process (Thomas 1991, Dawes 1996) in which a rotating tool with a shoulder and terminating in a threaded pin, moves along the butting surfaces of two rigidly clamped plates placed on a backing plate. Although FSW was invented specially to weld aluminium alloys, new developments for other materials were developed. After magnesium and titanium alloys, FSW to high strength steels opened new directions for research. This paper presents an example of FSW applied to AA5083 and AA 6082 – two aluminium alloys indicated to be used in the field of civil engineering, summaries the FSW applied to steels, and analyses residual stresses in the elements welded with FSW. Several investigations realized on different types of steels welded with FSW is presented. Future developments for the tool concepts to weld steels are discussed.

## 1. INTRODUCTION

In 1991 The Welding Institute in England invented and developed a new welding process (Thomas W.M.). Friction stir welding (FSW) is a bending procedure that takes place in solid state which is based on the heating of the materials through friction and plastic deformation realized at the interaction between the non-consumable pin tools which is rotating at surface of the joined elements as shown in Figure 1.
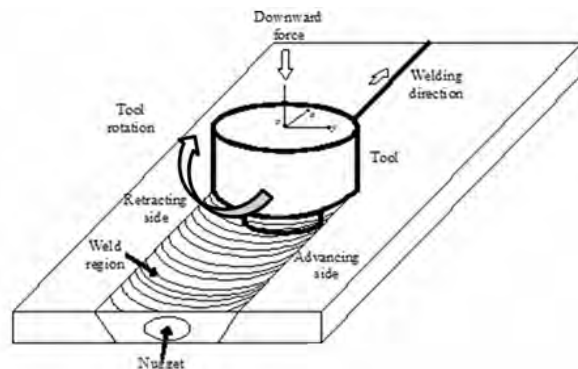


Figure 1. Schematic of the friction stir welding process

The shoulder makes firm contact with the top surface of the work–piece. Heat generated by friction at the shoulder and to a lesser extent at the pin surface, softens the material being welded. Severe plastic deformation and flow of this plasticized metal occurs as the tool is translated along the welding direction. Material is transported from the front of the tool to the trailing edge where it is forged into a joint. Although Figure 1 shows a butt joint for illustration, other types of joints such as lap joints and fillet joints can also be fabricated by FSW.

FSW is considered to be the most significant development in metal joining in a decade and is a ''green'' technology due to its energy efficiency, environment friendliness, and versatility. As compared to the conventional welding methods, FSW consumes considerably less energy. No cover gas or flux is used, thereby making the process environmentally friendly. The joining does not involve any use of filler metal and therefore any aluminum alloy can be joined without concern for the compatibility of composition, which is an issue in fusion welding (dos Santos, J).

## 2. EXPERIMENTAL PROCEDURE

The experimental program was realized for two of the most indicated aluminium alloys - AA 6082 and AA5083 - to be used in the field of civil engineering, especially to bridge constructions, where one of the biggest enemy is the corrosion. The 6082 aluminium series alloys are very frequently used for many fatigue-critical parts of structures, mainly due to the fact of allying a relatively high strength, good corrosion resistance and high toughness to a good formability and weldability. Aluminium 5083 is known for exceptional performance in extreme environments. This alloy is highly resistant to attack by both seawater and industrial chemical environments.

In order to evaluate the behavior of the two alloys welded with FSW, a series of characterizations on butt welded plates, 6 mm thick, have been realized. For this bending tests, hardness measurements, macrostructure analysis, tensile tests and fatigue analysis were carried out.

It is known that two of the welding parameters, i.e. welding speed and rotational speed play an important role in realizing weld seams without defects. In order to establish a proper pair of these two parameters, several calibrations welds were carried out. For all welded samples bending tests were performed to investigate if there are surface or root defects. In the following are presented the test results of the samples without any root or surface defects.
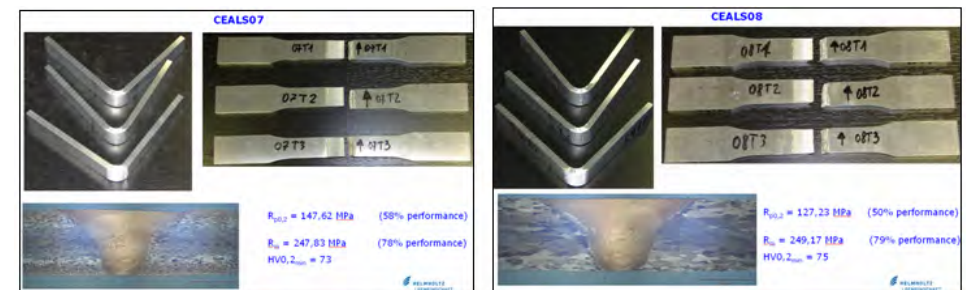


(a)                                              (b)

Figure 2. Results on AA 6082 (a) and AA 5083 (b) FS welded specimens

Figure 2 (a) presents the results and the performances for the 60820 AA and Figure 2. (b) presents the results for 5083 AA. It can be observed from the macrographs that no defect was present in the weld seam. Still, the failure of the tensile specimens took place right near the weld seam, zone which is named the heat affected zone (HAZ).
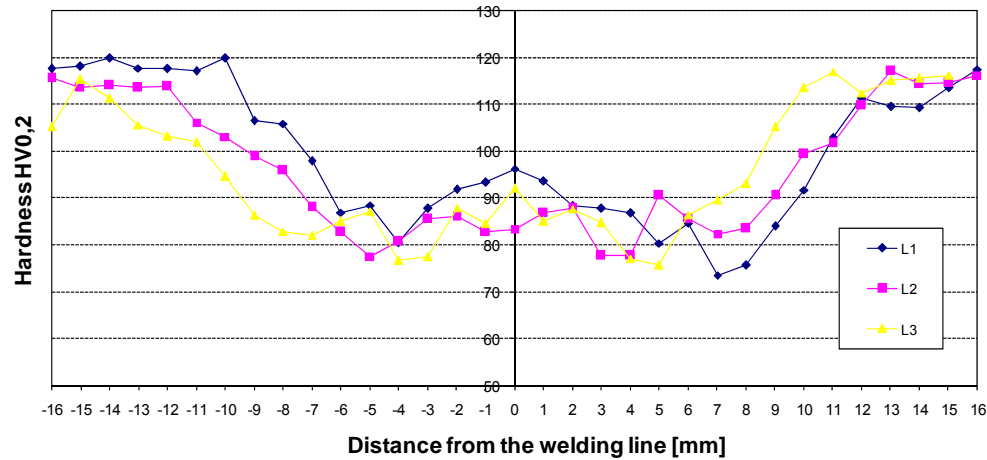


(a)
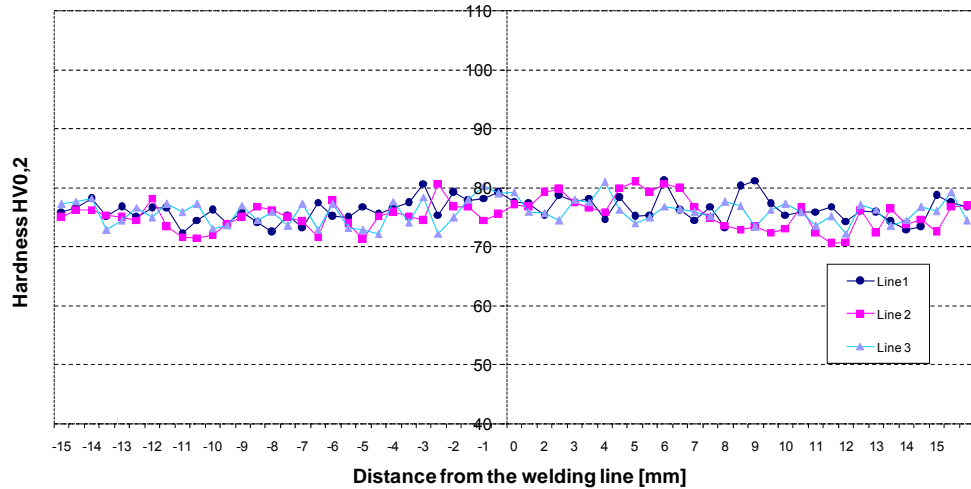


(b)

Figure 3. Hardness measurements on AA 6082 (a) and AA 5083 (b)

Significant hardness drop can be observed especially to the welds of AA6082 (Figure 3 (a)). In the case of the other alloy, the variations are not quite significant, but they exist in HAZ. These softening caused the collapse in the HAZ of the specimens. Also in this area is situated the end of the shoulder contact zone with the elements, and it may be considered as a defects concentration area. It was found that hardness drastically decreases in the thermomechanically affected zone and the yield stress

and rupture stress of friction stir welded specimens presented lower values than un-welded specimens.

The results presented by Zhou regarding the fatigue life of 5083 AA welded with FSW indicated a significant improvement of the fatigue behavior of the AA connection, in comparison with MIG connections fatigue life and the predicted design curves of IIW for this alloy.
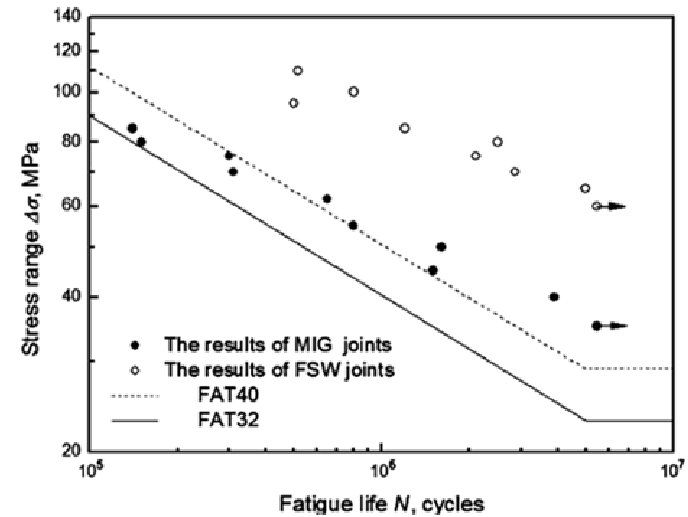


Figure 4. Comparison of fatigue test results and IIW design curves. (Zhou)

For the AA 6082 the results for fatigue life also presented improvements. Ericsson concluded that the fatigue strength of FS welded Al–Mg–Si alloy 6082 is higher than that of MIG-pulse and TIG welds of the same material.
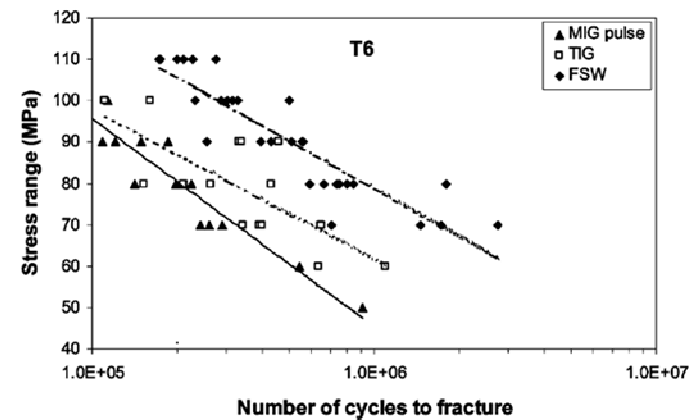


Figure 5. Results of fatigue testing for FSW, MIG-pulse and TIG specimens (Ericsson)

From the presented experimental program and from other studies for these two alloys, results that FSW produces qualitative weld seams, without defects and with a higher fatigue life.

## 3. RESIDUAL STRESSES

An important issue of the welded connections is represented by residual stresses. These may affect the fatigue life and other structural failures. It is important to have a quantitative estimation of such stresses for the safe performance of the structural components.

The presence of residual stress in a weld plate affects its distortion behaviour and ability to sustain applied loads while maintaining structural integrity (Withers (2001), Francis (2007)). While compressive stresses can in some circumstances be beneficial (Ohta (1999)), tensile stresses can cause crack initiation and aid its propagation leading to catastrophic failure.
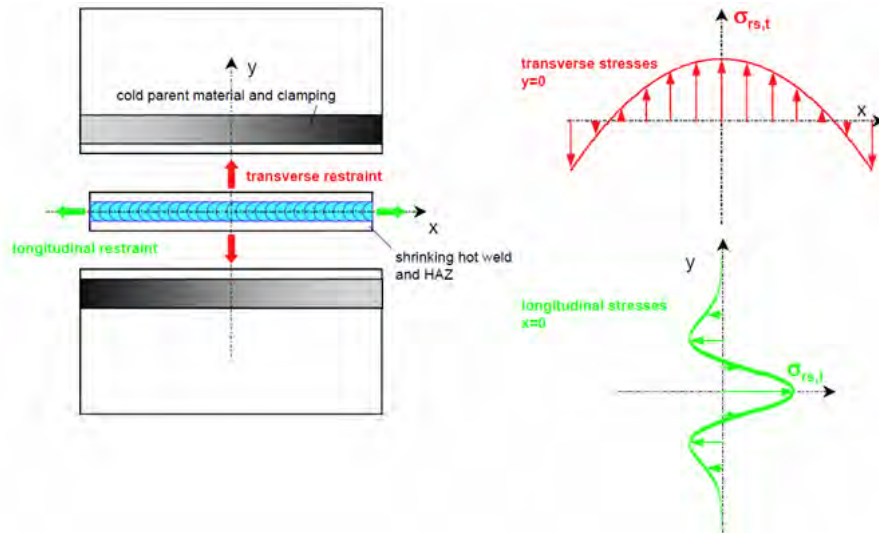


Figure 6. Schematic of the restraint exerted by the cooler parts of the plates and the clamping on the HAZ and the weld (Dalle Donne, C)

As in ordinary welds, residual stresses develop in constrained assemblies during FSW due to expansion during heating and contraction during cooling; a feature unique to FSW is the additional stress caused by the rotational and translational components of the tool so that the welding parameters of FSW must affect the final state of stress (Chen (2006)). The stirring action of the tool is believed to relieve some of the stresses within the thermomechanically affected zone (Khandkar (2006)).

A higher welding speed enhances the longitudinal resid ual stress but reduces it along the lateral direction. The analysis also showed that the maximum temperature gradients in the sample are located just beyond the edge of the tool-shoulder (Peel).

For the steel HSLA-65 the peak tensile residual stresses were measured in the region of 400 MPa (compared to a nominal yield stress of ~450 MPa).Tthe largest residual stresses were observed for the higher traverse speed welds (Steuwer). It is then important a good correlation between the welding parameters, i.e. welding speed, rotational speed, welding tool, force and base material characteristics and the temperatures that are introduced during the welding process.

In order to quantify the temperature distribution close to the weld seam during the weld of the samples, the temperatures in the backing bar were measured. If the

temperature is higher, also the residual stresses may increase because of the more pronounced shrinkage.
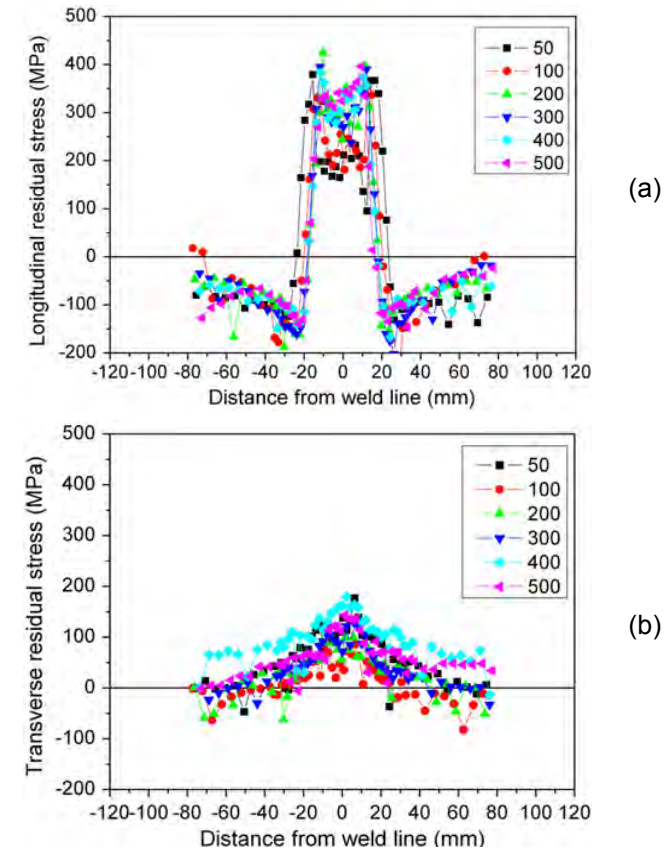


Figure 7. (a) Longitudinal and (b) transverse residual stresses as a function of distance from the weld line for different traverse speeds (mm/min) for a W-Re tool, 25 mm shoulder diameter (Steuwer)
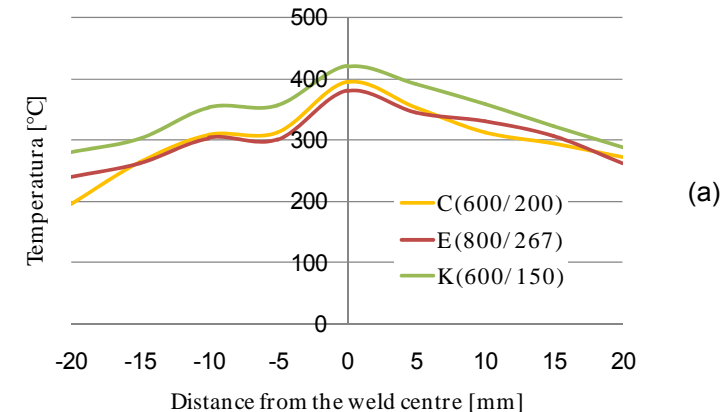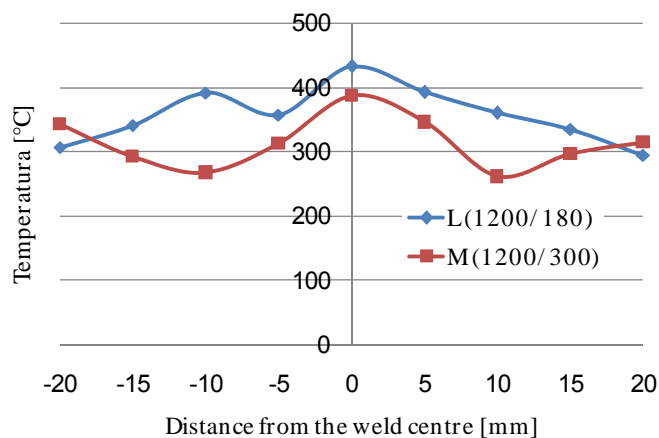
Figure 8. Temperature measurements during the welding process (Gabor (2010))

In Figure 8 can be observed that to a lower welding speed, a higher temperature occurs close to the weld seam. This allows a better fusion between the materials to be weld, but also increases the cooling time, which can produce additional residual stresses.

A higher welding speed enhances the longitudinal residual stress but reduces it along the lateral direction. As might be expected, the residual stress distribution is dramatically altered on unclamping the samples after friction stir welding and this must be taken into account in any modeling effort.

The role of plasticity during the friction stir welding process is known to be important in the calculation of residual stress; a large overestimation of the magnitudes of the residual stress (Khandkar (2006)) can result when this effect is ignored. Nevertheless, the outcome that the longitudinal stress along the weld centre line is tensile and (Reynolds (2003)) larger than all the other component stresses is believed to be correct (Bhadeshia (2008)).

## 4. APPLICATION OF FSW TO STEELS

The friction–stir welding of steels has not progressed as rapidly as for aluminium for important reasons. First, the material from which the tool is made has to survive much more strenuous conditions (Bhadeshia (2008)) because of the strength of steel. Second, there are also numerous ways in which steel can be satisfactorily and reliably welded. Third, the consequences of phase transformations accompanying FSW have not been studied in sufficient depth. Finally, the variety of steels available is much larger than for any other alloy system, requiring considerable experiments to optimise the weld for a required set of properties.

Early optimism (Thomas (1999), Threadgill (2004)) that FSW will become a commercially attractive method for the fabrication of ships, pipes, trucks, railway wagons and hot plate has not yet come to fruition. That the application of FSW to steels is premature is emphasised by the fact that with few exceptions, only elementary mechanical properties have been characterised; most reports are limited to simple

bend, tensile and hardness tests. For serious structural applications of the type proposed above it would be necessary to assess fracture toughness and other complex properties in greater depth. There are indications that elongation suffers following FSW (Sanders).
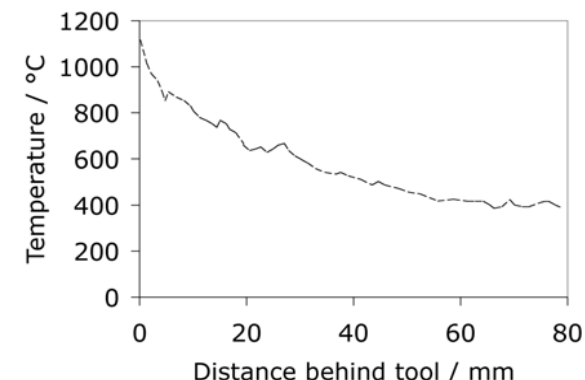


Figure 9. Temperature as a function of distance behind a tool after 250 mm of welding with the tool advancing at 3mms−1 (Thomas (1999))

In most studies, the steel being friction stir welded becomes locally red hot; the maximum temperature reached is less than 1200°C (Thomas (1999), Lienert (2003)) and the time Dt8–5 taken to cool over the range 800–500°C is ~11 s. Austenite will therefore form during the heating cycle and will subsequently transform during the cooling cycle. With few exceptions, only elementary mechanical properties have been characterized in studies of the FSW of steels; (Bhadeshia) most reports are limited to simple bend, tensile and hardness tests. For serious structural applications, it would be necessary to assess fracture toughness and other complex properties in much greater depth.
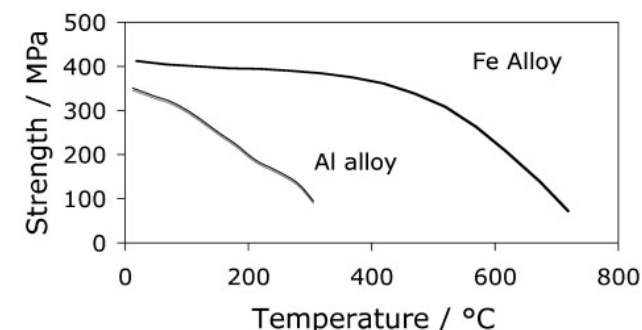


Figure 10. Typical temperature dependence of hot strength of aluminium alloys and steels (Bhadeshia (2008))

An experimental program on S355J2G3 plates of 12 mm thickness, welded by using polycrystalline cubic boron nitride (PCBN) tool, was realized to HZG (Muller (2004)). The analyzed weld seams are presented in Table 1.

Table 1. Welded plates investigated

| Identification Code | Material | Dimensions [mm] | | Weld Length [mm] | Comments | |
|---|---|---|---|---|---|---|
| ST_EB_10 | C-Mn steel S355J2G3 | Length | 342 | 332 | Single-Pass | - |
| | | Width | 390 | | | |
| | | Thickness | 12 | | | |
| ST_EB_3AB | C-Mn steel S355J2G3 | Length | 320 | 310 | Double-Pass | Same Direction of travel speed |
| | | Width | 390 | | | |
| | | Thickness | 12 | | | |
| ST_EB_7AB | C-Mn steel S355J2G3 | Length | 338 | 300 | Double-Pass | Opposite Direction of travel speed |
| | | Width | 390 | | | |
| | | Thickness | 12 | | | |

S355J2G3 is classified as non-alloy Carbon-Manganese steel for structural applications. A nominal characteristic of this steel is its relatively high percentage in weight of manganese. The presence of manganese facilitates the deoxidising of the melt and favors hot working.

To investigate the performance of the welds, a series of microstructural analysis and mechanical testing have been performed.



(a)                                                    (b)
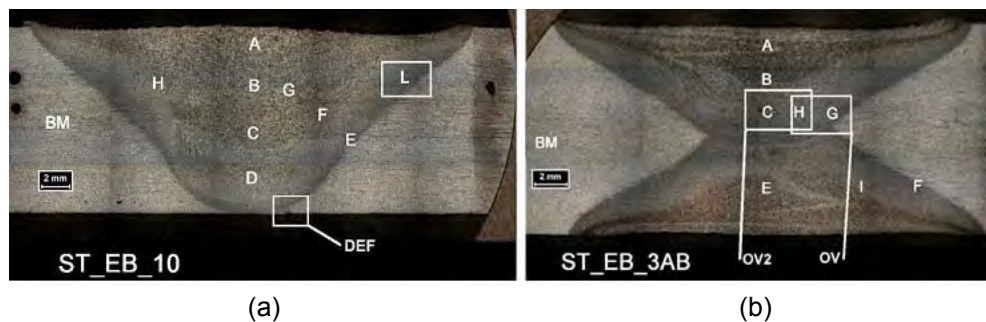
Figure 11. Macrograph of a single pass weld (a) and a double pass weld (b)

Table 2. Welded specimens, results of the tensile testing

| Specimen | ST_EB-10 | | ST_EB_3AB | | ST_EB_7AB | |
|---|---|---|---|---|---|---|
| **Stress** | | | | | | |
| Yield strength | 390 | [MPa] | 381 | [MPa] | 380 | [MPa] |
| Tensile strength | 557 | [MPa] | 556 | [MPa] | 548 | [MPa] |
| Rupture strength | 398 | [MPa] | 391 | [MPa] | 368 | [MPa] |
| | | | | | | |
| **Elongation** | | | | | | |
| Total elongation | 14.9 | [%] | 11.2 | [%] | 11.2 | [%] |

The conclusions of the experimental work above presented were:

- The microstructure of friction stir welded S355J2G3 consists basically of bainitic structure in the nugget and bainitic (single pass weld) and recrystallised acicular structure (double-pass weld) in the HAZ, especially next to the nugget. In the double-pass weld a limited effect of the second thermal cycle, originating from the second pass, on the microstructure could be observed.
- The tensile test shows that for all specimens necking and failure occurred out of the welded region, in the base material. (Figure 12). For all three investigated specimens, the yield strength is higher than the nominal yield strength of the base material (Table 2).
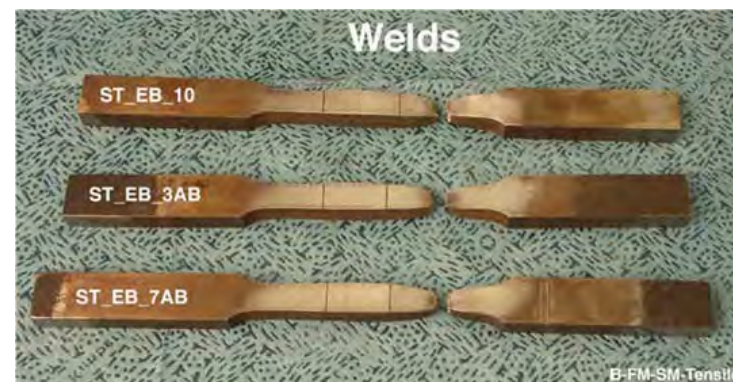


Figure 12. Tested tensile specimens

The procedure was applied to S235 JR+N steel to the National Research and Development Institute for Welding and Material Testing – ISIM Timisoara in order to characterize the behavior of this steel with various industrial fields, in conjunction with FSW. The weld seams were realized with a welding tool made of high-alloy steel and hardened to 52-56 HRC, with sharp-edged pin that ensure easier deployment of welding material from front of the tool and translating it into the back of it. The results indicated that FSW to S235 JR+N steel is very good, when optimized welding parameters are used (Figure 13).



(a)                                                    (b)
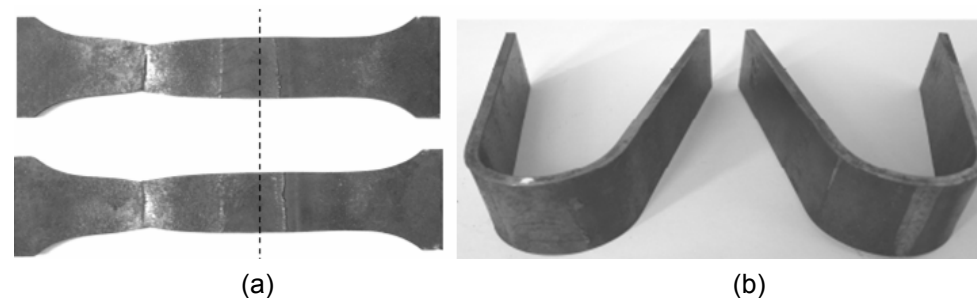
Figure 13. Welded joints for S235 JR+N –statical tensile tests (a) and the welded samples after static bending test (b) (Cojocaru, 2011)

For steels, many researches has as subject the stainless steels or the new developed steels, that are hard or unweldable steels by using the usual welding procedure. Very recent (2012) an extensive research program was developed for the HSLA-65 steel, a high strength, low-alloy steel with 448-MPa specified minimum yield strength, relatively high level of toughness due to the low carbon content. The results conducted to good defect-free welds. The weld nugget microstructure was found to be a mixture of martensite, bainite, and proeutectoid ferrite in all the welds examined. The proportions of the different phases, and thus the weld nugget hardness, were influenced by the weld tool traverse speed, rotation speed, and material (Barnes). The maximum residual stresses were located just outside the HAZ of the weld in the parent metal. The weld residual stress profile was very similar to that observed for aluminum alloys despite the presence of transformation products near the weld line (Steuwer). For the both studies the authors used two types of weld tools – a tungsten rhenium (W-Re) tool and a polycrystalline boron nitride (PCBN) tool.

The tools that are usual used to weld steels have not a long life and also there very few tool producers around the world. These facts have led the researchers to look for new possibilities to build up a new tool with a longer life, easy to replace and also to produce different weld geometries. As known, due to its main operational features, FSW process is suited to butt and overlap joints. This is not the case for fillet welds where some material must be available at the junction between the vertical and the horizontal member. HZG has recently developed a concept to produce fillet welds in which minor modifications to joint design are required to allow for defect free, high performance joints (Figure 13). The fillet weld FSW process variant allows for complete bonding of the area to be welded. This concept can in principle be also considered for a possible transportable FSW machine for field application.
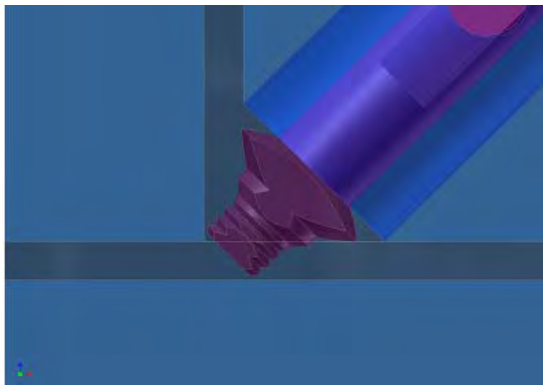


Figure 13. FSW-Tool concept newly developed at HZG for welding of fillet joints

A double tool concept can also be used for fillet joints in production. Hence, with recently developed FSW process technology it is possible to produce fillet welds without any major modification of the joint geometry or expensive machining of the base material before welding and to provide advantages for sustainability.

This new geometry opens new directions, especially for the structural application of FSW to structural steels. Still, detailed analysis of the connections must be realized, in order to have proper characteristics of them.

## 5. CONCLUSIONS AND GENERAL RECOMMENDATIONS

Friction stir welding was mainly developed to weld "unweldable" alloys, especially the aluminium alloy. The benefits of this technology include low distortion, greater weld strength, and no need for consumables, all position capability and energy efficiency. The absence of fusion leads to absence of fume or spatter, and there is no arc to give ultraviolet or electromagnetic radiation, reasons that we can say about FSW that is an environmental friendly welding process.

To illustrate the characteristics of the FS welds, an experimental work on two aluminium alloys is presented. The free of defects macrostructures of the welds offer good characteristics in comparison with one for the MIG weld.

A discussion about the residual stresses that appears in the elements due to the welding process in general and also in case of FSW is presented. Due to the rigid clamping during the process, the welded elements are affected by these stresses, even if the welding does not involve the melting process, as for the usual welding processes. By using the proper FS welding parameters i.e. welding speed and rotational speed, the residual stresses can be minimized.

FSW of S355 C-Mn steel plates of 12mm thick using a double-pass welding technique has also been investigated and revealed a positive effect of the second pass by tempering the first weld.

Currently, a number of different high temperature materials (ceramic and metallic) are being investigated aiming at a reduction of tool costs and increased tool life.

Future work can be led in the direction of new tools for steel welding; also new movable welding machines can increase the interest for FSW in structural engineering. For a better understanding of the phenomena, more detailed analyses and characterizations of the produced welds on the structural components are needed.

## ACKNOWLEDGMENTS

## REFERENCES

[1] Bhadeshia, H. K. D. H., DebRoy, T., Nandan, R., (2008), "Recent Advances in Friction Stir Welding – Process, Weldment Structure and Properties", Progress in Materials Science 53 (2008) 980-1023.

[2] Barnes S.J., Bhatti A.R., Steuwer A., Johnson R., Altenkirch J., Withers P.J., (2012), "Friction Stir Welding in HSLA-65 Steel: Part I. Influence of Weld Speed and Tool Material on Microstructural Development", Metallurgical and Materials Transactions Volume 43A, July 2012—2355

[3] Chen C. M. and Kovacevic. R., (2006), "Parametric finite element analysis of stress evolution during friction stir welding", Journal of Engineering Manufacture, 220: 1359–1371.

[4] Cojocaru R., Botila L., Ciuca C (2011), "Friction Stir Welding of S235 Steel", Modern Technologies, Quality and Innovation - New face of TMCR, ModTech 2011

[5] Dalle Donne, C., Lima, E., Wegener, J. Pyzalla, A, (2001), "Investigations on Residual Stresses in Friction Stir Welds", 3nd International Symposium on Friction Stir Welding, Kobe, Japan, 27 and 28 September.

[6] Dawes C.J. and Thomas W.M, (1996),"Friction stir process welds aluminum alloys", Welding Journal, 75(3):41 – 45.

[7] dos Santos J.F., v. Strombeck A., Schilling C., (2002), „Reibrührschweißen", 2. GKSS Workshop, 22.-23.01.2002, GKSS-Forschungszentrum, Geesthacht.

[8] Ericsson M., Sandstroäm R., (2003), "Influence of welding speed on the fatigue of friction stir welds, and comparison with MIG and TIG", International Journal of Fatigue 25, pg 1379–1387

[9] Francis J.A., Stone H.J., Kundu S., Rogge R. B., Bhadeshia H.K.D.H., Withers P.J., and Karlsson L., (2007), "Transformation temperatures and welding residual stresses in ferritic steels", In Proceedings of PVP2007, ASME Pressure Vessels and Piping Division Conference, pages 1–8, San Antonio, Texas, American Society of Mechanical Engineers, ASME.

[10] Gabor R.F., (2010), "Application of Friction Stir Welding in Civil Engineering", Phd Thesis.

[11] Khandkar M. Z. H., Khan J. A., Reynolds A. P., and Sutton M. A., (2006), "Predicting residual thermal stresses in friction stir welded metals", Journal of Materials Processing Technology, 174:195–203.

[12] Lienert, Jr, T. J., Stellwag W. L., Grimmett B. B. and Warke R. W., (2003), „Weld. J.", 82, 1s–9s.

[13] Moreira, P., (2008), "Lightweight stiffened panels: mechanical characterization of emerging fabrication technologies", Phd Thesys.

[14] Muller, S., (2004), "Friction stir welding of steel", Diplomarbeit

[15] Ohta A., Suzuki N., Maeda Y., Hiraoka K., and Nakamura T., (1999), "Superior fatigue crack growth properties in newly developed weld metal", International Journal of Fatigue, 21:S113–S118.

[16] Peel, M., A. Steuwer, M. Preuss, and P. J. Withers, (2003), "Microstructure, mechanical properties and residual stresses as a function of welding speed in aluminium AA5083 friction stir welds," Acta Materialia, 51(16), pp. 4791-4801.

[17] Reynolds A. P., Wei Tang, Gnaupel-Herold T., and Prask H., (2003), "Structure, properties, and residual stress of 304L stainless steel friction stir welds". Scripta Materialia, 48(9):1289–1294.

[18] Sanders D.G., Ramulu M., Klock-McCook E.J., Edwards P. D., Reynolds A.P., and Trapp T., "Characterization of superplastically formed friction stir weld in titanium 6Al-4V: Preliminary results", 17:187–192, Journal of Materials Engineering and Performance.

[19] Steuwer A., Barnes S.J., Alternkirch J., Johnson R., Withers P.J., (2012), "Friction Stir Welding of HSLA-65 Steel: Part II. The Influence of Weld Speed and Tool Material on the Residual Stress Distribution and Tool Wear", Metallurgical and Materials Transactions Volume 43A, July 2012—2365

[20] Thomas W.M., Nicholas E. D., Needham J. C., Murch G. M., Temple-Smith P. and Dawes C. J., (1991), "Friction stir butt welding, International Patent Application no. PCT/GB92/02203", December

[21] Thomas W. M., Threadgill P. L., and Nicholas E. D., (1999), "Feasibility of friction stir welding steel", Science and Technology of Welding and Joining, 4:365–372.

[22] Thomas W. M. and Dolby R. E., (2003), "Friction stir welding developments". In S. A. David, T. DebRoy, J. C. Lippold, H. B. Smartt, and J. M. Vitek, editors, 6th Int. Trends in Welding Research, pages 203–211, Materials Park, Ohio, USA, ASM International.

[23] Threadgill P.L. and Johnson R., (2004), "Progress in friction stir welding of steels", Technical Report 815/2004, TWI (The Welding Institute), Great Abington, Cambridge, U.K.

[24] Withers P.J. and Bhadeshia H.K.D.H., (2001), "Residual stress part 1 - measurement techniques", Materials Science and Technology, 17:355–365.

[25] Withers P. J. and Bhadeshia H. K. D. H., (2001), "Residual stress part 2 - nature and origins", Materials Science and Technology, 17:366–375.

[26] www.hzg.de

[27] Zhou C., Yang X., Luan G., (2005), "Fatigue properties of friction stir welds in Al 5083 alloy", Scripta Materialia 53 (2005) 1187–1191

# STEEL BRACE-TO- RC FRAME POST-TENSIONED BOLTED CONNECTION

Adrian Dogariu[1]; Sorin Bordea[1]; Dan Dubina[1,2]

[1] "Politehnica" University of Timisoara, Romania
[2] Romanian Academy, Timisoara Branch, Romania
adrian.dogariu@ct.upt.ro; dan.dubina@ct.upt.ro

## ABSTRACT

The paper presents and evaluates the technical solution for a post-tensioned bolted connection applied to inserting infill steel braces in order to improve seismic behavior of reinforced concrete frames; in present case, buckling restrained braces (BRB) have been considered. In order to validate a simple design approach that establishes the connection behavior, a complete finite element model was build. The proposed connection technique was validated through experimental tests, conducted on the entire RC frame.

## 1. INTRODUCTION

Many of contemporary buildings located in seismic zones were erected more than 50 years ago and being designed without a proper consideration of the seismic action present a high seismic vulnerability.

The resistant structure of these buildings is either masonry or RC frames. In case of RC frames, it is well known that 50 years ago, in the early period of seismic engineering design codification, the reinforcing details of the joints and plastic zones did not appropiately satisfy the seismic demand, and unfortunately, the subsequent important earthquakes proved that. From this reason, it is important to provide a better resistance and ductility of these structures, by appropriate consolidation measures. One of the most efficient retrofitting measures, from the structural and technological point of view, is based on inserting dissipative steel braces. This technique improves both the global resistance and stiffness of the structure, and the ductility. To obtain a higher capacity in terms of energy dissipation and resistance, buckling restrained braces (BRB) may be used. Even if, theoretically, the retrofitting solution itself, seems to be very efficient, the proper connection between the RC frame and the new steel elements plays a very important role. In fact, without a full interaction, the new elements cannot bring their positive effect in the global behavior. Usually, the connection between the existing RC elements and the new steel elements is made by post-installed mechanical or chemical anchors. A good behavior of this type of connection is highly dependent on the quality of the concrete, which generally, at that time was poor. The failure, if occurs in the concrete members can be fragile. It is possible to provide a local strengthening of concrete members using FRP but, in some way, this solution might disturb the installation of anchors. Present paper proposes a connection solution which uses post-tensioned ties and a steel detailing, which also enables for a local confinement of concrete.

# 2. CONNECTION SYSTEM

## 2.1. Technical solution

The steel brace – to - RC frame connection is realized with post-tension high strength steel ties, which together with the steel plates, act like a metallic clamp. Figure 1(a) and (b) presents the solutions sketch of the upper connection between the RC beam, respectively the bottom connections between the RC columns and the inserted steel braces (BRBs). The technology is rather simple and did not require highly qualified workers or special devices other than a torch control wrench. Another important technological aspect is the possibility to remove the connection.
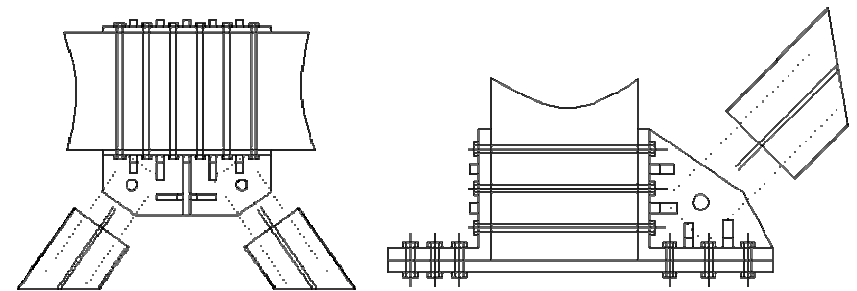


Figure 1. (a) Upper connection between RC beam and BRB (b) Bottom connection between RC column and BRB.

The high strength steel ties introduce controlled a normal pressure, at the interface level between RC elements and steel plates, and activates frictional forces when relative slippage tends to occur. To obtain a good behavior of the connection, a proper post-tension level must be calibrated and introduced. In order to provide a high frictional force it would be desirable to avoid completely any relative slippage through high post-tension level. In the same time, the prestressing level, which basically ensure the grip between the RC members and steel brace, also introduces a biaxial state of stress in the concrete elements, thus improving the material behavior by node confinement.

There are two limitations for increasing the pre-stress level, i.e. the steel elastic resistance and crushing strength on concrete.

In order to avoid any plastic deformation in the connection, tick plates are recommended to be used. Even so, in case of base plate failure, the connection will exhibit a ductile behavior. A large contact area between steel plates and RC elements is desired, so strongly stiffened plates are to be used, because their bending must be limited. A flexible plate would bend excessive and the contact area between steel plate and RC beam might reduced. This will increase the local pressure, which might induce crushing of concrete.

The present paper shows the application of the proposed connecting system for inserting inverted V BRB as a seismic retrofitting technique to upgrade an existing RC frame building which was initially designed considering only the gravity loads (Nardini, 2008). The geometry and main dimensions of RC frame members are presented in Figure 2, and all the details regarding the number and diameters of rebars in element cross section, the distance between stirrups are given in Figure 3.
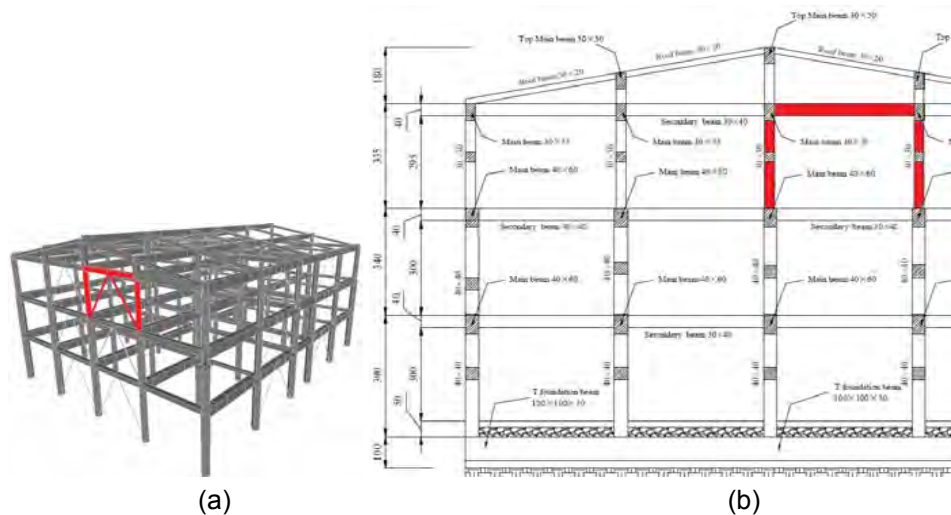
(a)           (b)

Figure 2. (a) Axonometric view of RC frame (b) Geometry of the planar frame (Nardini, 2008).



Figure 3. Reinforcement details for the studied RC frame members

To validate the proposed technique, an isolated portal RC frame extracted from the second floor of the previous presented RC building (see Figure 2), was experimentally tested in CEMSIG laboratory. The RC frame was tested with and without BRB devices. The following characteristics of BRBs were obtained from the pre-experimental numerical simulations: an 1.7 m length rectangular cross section active zone (yielding segment) of 30x10 mm and a 0.4 m length transition zone of 60x10 mm. A S235 steel quality has been ordered for the BRBs, but a 335 N/mm$^2$ yield limit has been experimentally determined. A C20/25 concrete ($R_c$ = 20.5 N/mm$^2$) was intended to be obtain, but material tests have revealed a higher characteristic resistance of $R_c$ = 35.5 N/mm$^2$.

First, a Performance Based Seismic Evaluation (PBSE) of initial r.c. building frame was done in order to define the intervention objectives. After that the PBSE of the frame strengthened with BRBs was performed to quantify the demands for braces and design them accordingly.

## 2.2. Design procedure: simplified method

Using simple assumptions and considering the full prestressed ties, an initial dimension of steel plates and of the number of steel ties was determined. Based on the application principles stated above the connection have been made by a 25 mm tick steel plates S235 steel grade and 10.9 grade for the post-tensioned M16 ties. Considering a very stiff steel plate, with a contact area of 300x504 mm with the concrete element, the maximum force applied to all bolts, corresponding to a full pretension level of the ties ($F_t$ = 109.9 kN per bolt, equivalent to a torque moment of Ms = 200Nm) creates in the concrete element at the interface with the steel plate, a normal pressure σ of approximate 8.75 MPa (see Figure 4(a)) at the interface with the RC beam, which is much smaller than the compressive strength of the RC beam, i.e. 35 MPa.

Consequently, the friction force ($F_f$) between the steel plate and the concrete element should be higher than the cumulated two horizontal components of BRB forces (see Figure 4(b)). Using a static friction coefficient of 0.45 between concrete and steel, a maximum shear force of 595 kN can be considered without any relative slippage, corresponding to a number of 12 prestressed ties.
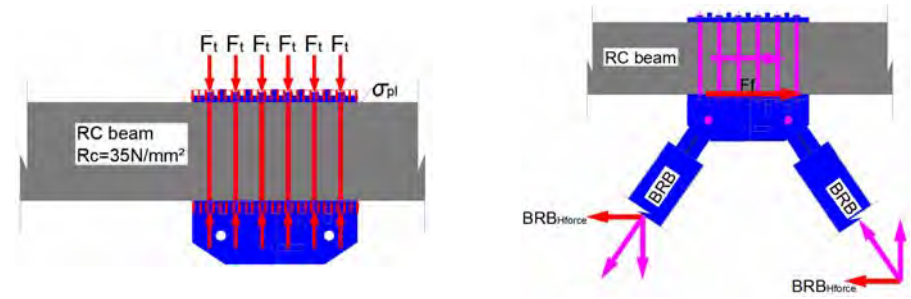


Figure 4. (a) RC beam – BRB connection: pressure under the steel plate due to bolts pre-stressing (b) Load transfer and forces on the upper connection.

The connection slip capacity depend on the number of prestressed ties, and the total slip force that must be withstand depend on the rigidity of the bracing system and on the imposed transient interstorey drift of the reinforced concrete frame for a certain level of performance, i.e. 1% - Immediate Occupancy, 2% Life Safety and 4% Collapse Prevention (FEMA 356).

In a simple manner the designer have two options to determine the required shear force for which the connection must withstand. According to the first one, the designer must establish the desired performance level and the corresponding interstorey drift. At this level of displacement at interface between RC beam and the connection steel plate a shear force will appear. Second option asks the designer to determine the maximum shear force that can be induced into connection when the BRB attains tension capacity. Both of these approaches must give the same results because the BRB cross section should be chosen according with the same imposed

interstorey drift limitation. Depending on this shear force the designer can determine the necessary connecting force (ΣFt, see Figure 4(a)) and obtain consequently the diameter, quality and number of prestressed ties.

The connection between the RC beam and the steel elements can be considered as fully rigid, without any slippage, until the shear capacity is reached (attainment of ultimate friction force).

For the base-column connection, the dimension of the bolts have been computed in order to resist the BRB forces (both vertical and horizontal components) and the prestressing level was calibrated to avoid the slippage of the column (see Figure 5).
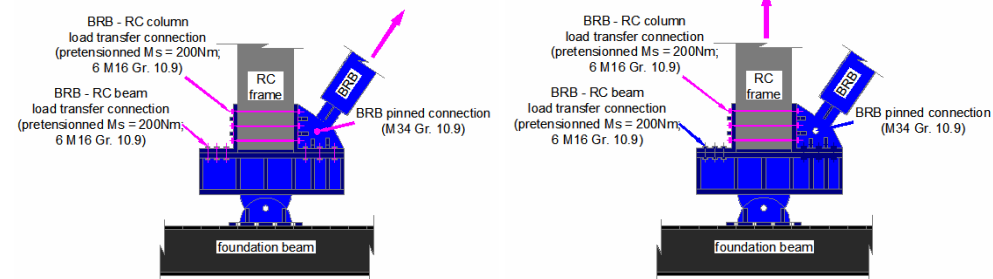


Figure 5. Load transfer and forces on the bottom connection.

## 3. EXPERIMENTAL BEHAVIOR OF THE CONNECTIONS

### 3.1. Experimental specimens and set-up

The testing set-up includes the entire RC frames together with the BRB (see Figure 6(a)). The connection between RC column and steel BRB was introduced in a simple manner, using a very stiff steel element, in order to simulate a real RC joint (see Figure 6(b)).



(a)                                    (b)
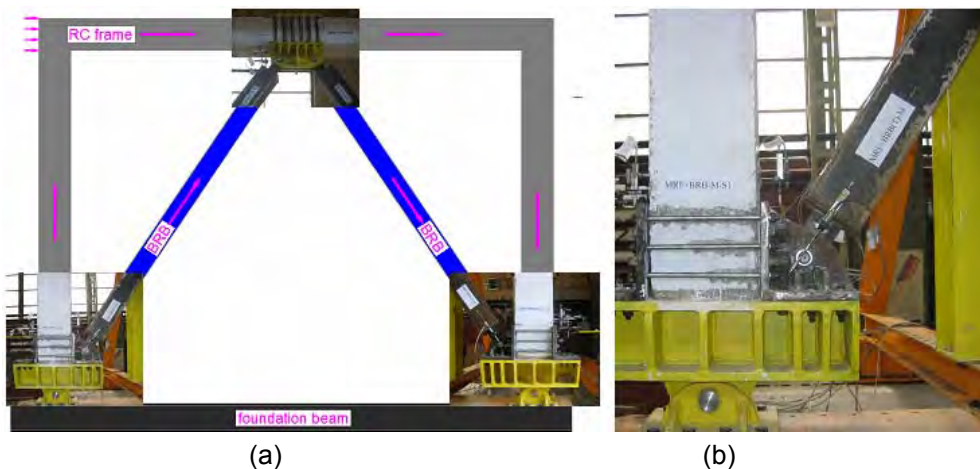
Figure 6. (a) Experimental frame (b) experimental connection between RC column and BRB.

Displacement transducers have been used to determine all the relative displacements and rotations that can appear in the connections. Four displacement transducers were used on the bottom of each column, to measure the vertical displacement (see Figure 7) the horizontal displacement of the connection and the load transfer from the connection to the column and bottom part (see Figure 8).
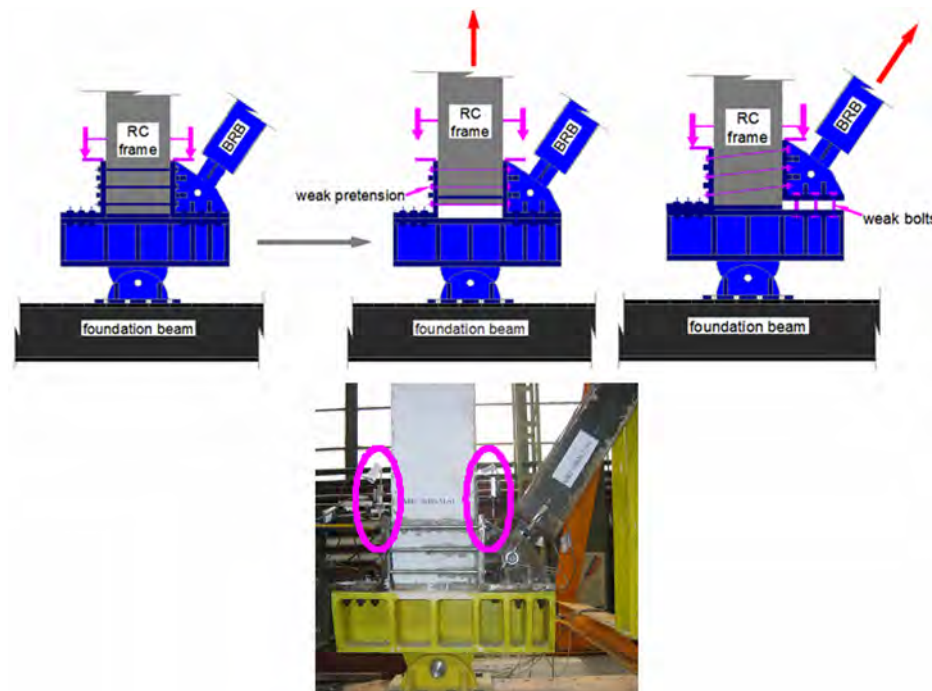


Figure 7. Measurement of the vertical displacement of the connection between the BRB and the column.
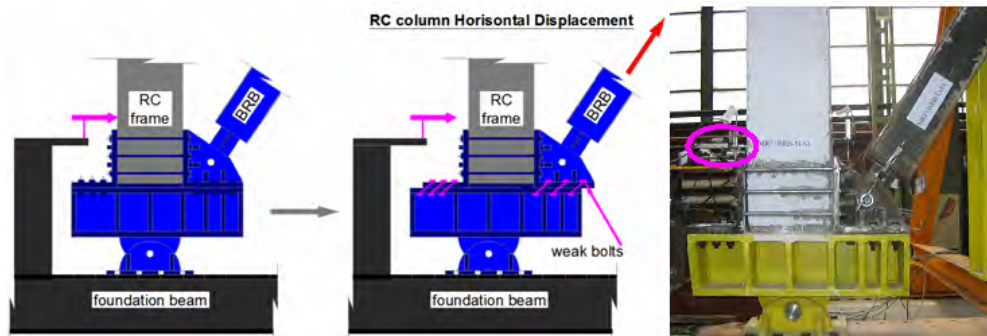


Figure 8. Measurement of the horizontal displacement of the connection between the BRB and the column.

Two displacement transducers have been placed on the RC beam for monitoring the slippage of the upper connection (see Figure 9).
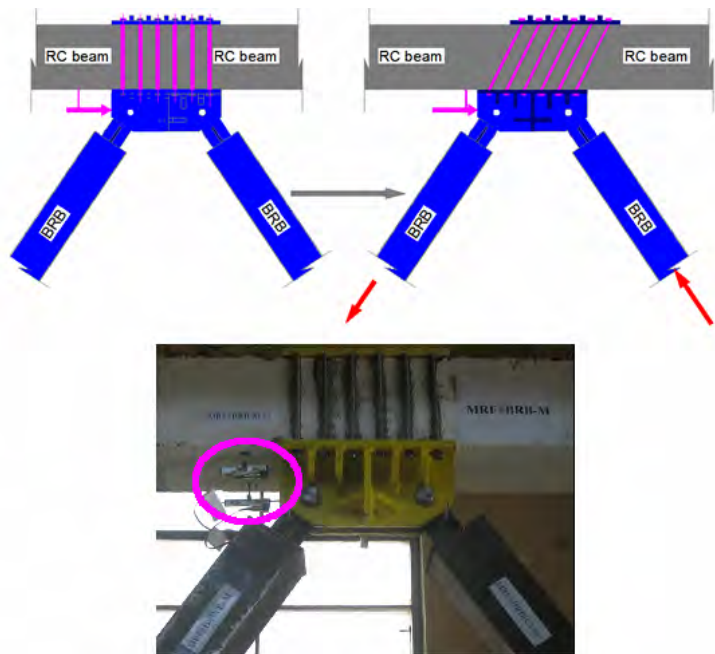
Figure 9. Measurement devices distribution: horizontal on the RC beam.

Monotonic and cyclic tests were considered. A modified ECCS cyclic loading protocol was applied in the cyclic tests (ECCS, 1986).

## 3.2. Experimental results

All the connections between BRB system and RC frame (BRB to column and BRB to beam) showed a very good behavior and no slippage was recorded.

No important slippage between steel plates and concrete columns was emphasized (see Figure 10).



Horizontal displacement [mm]



Vertical displacement [mm]
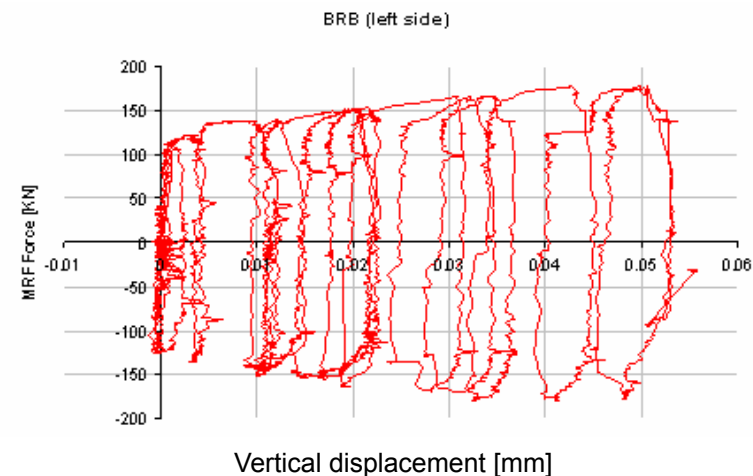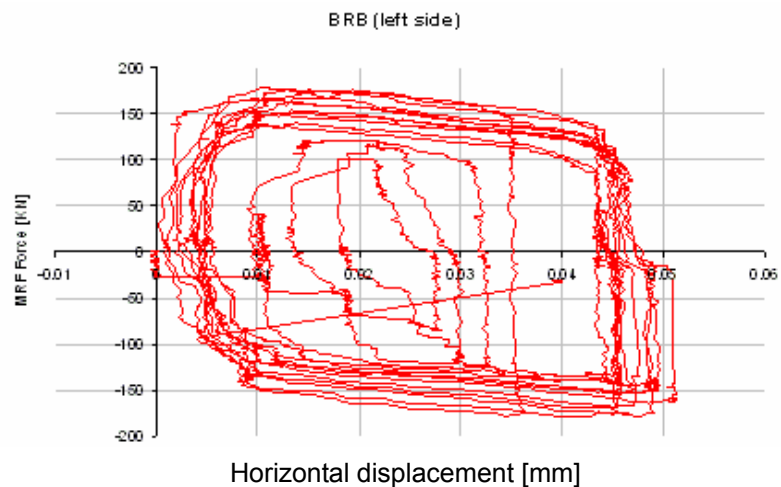
Figure 10. Behavior of connection between BRB and left RC column during cyclic test.

When the left side BRB failed in tension, the horizontal displacement recorded at the connection between BRB and the RC was limited to 5 mm (see Figure 11)
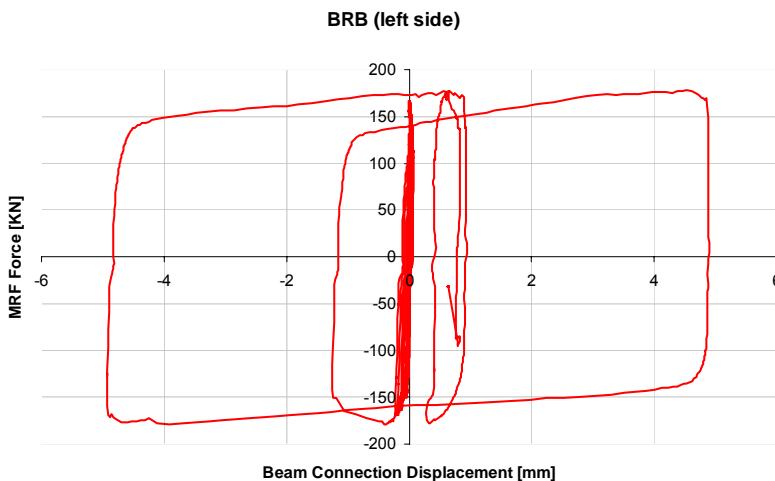


Figure 11. Connection between the BRB and the beam during cyclic test – hysteretic curve.

## 4. FINITE ELEMENT MODELS OF CONNECTIONS

### 4.1. Description of finite element models

Considering the number of contact zones of the specimens (between RC frame, steel ties and steel plates), ABAQUS Explicit product has been preferred. This product has the advantage of an explicit formulation of the equilibrium, which is well-suited to simulate and to effectively handle severely nonlinear behavior, such as contact. This product was build mainly for dynamic events, but using proper amplitude

and mass scaling of the model, quasi-static loading response can be obtain with very good accuracy and in a shorter computing time.

For the preliminary verification of the connecting systems prior to the experimental tests, two numerical models of the both connections have been made.

Using ABAQUS software, two detailed models have been made. Due to the symmetry of the model and to the load conditions, for the base-column connection between the RC column and BRB only half of the specimens have been made; with respect to the symmetry boundary conditions (see Figure 12). 3D deformable finite elements (C3D8R) have been used. No prestressing of ties have been applied.
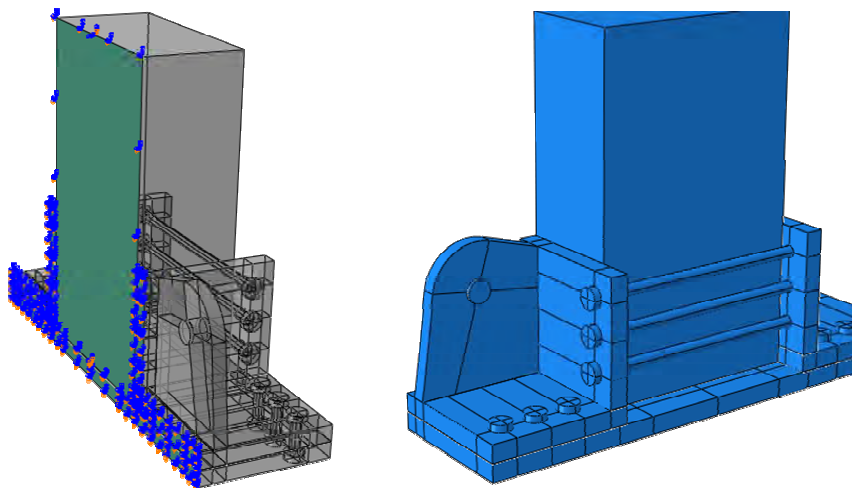
Figure 12. Finite Element Model of the connection between BRB and RC column.

In the case of upper connection between BRBs and RC beam a more complex numeric model was used. To replicate with higher accuracy the behavior of the connection and the loading conditions, the entire RC frame model was build (see Figure 13). The tested frame has a 4.5m span and 3.2m total height, with rectangular cross section of 30 by 30 cm for beam and column. 3D wire elements (B31) for RC columns and RC beam corners, and 3D solid elements (C3D8R) for the middle part of the beam in the connection area for introducing the contact properties at their interface, to allow development of frictional forces, have been applied. The BRB members were modeled also as wire having only axial properties (k = 28000N/mm). The supports were considered pinned, the behavior of the hinge connection between RC column and BRB being considered perfect-ideal without any significant slip or deformation. The experimental tests confirmed these assumptions.

The bolt prestressing load cannot be introduce in the model as a load option in case of explicit procedure, instead connecting elements loaded with connector force to simulate the prestressing, can be used (Montgomery, 2002). Considering the small bending rigidity of steel ties, an axial type connector was chosen to model the bolt rod. These types of connector provide a translational connection between two nodes that acts along the line connection the nodes. Elastic behavior only was considered (k = 145000N/mm), no plasticity or damage behavior options were define, because during the desire behavior mode, i.e. no relative slip occurs, the elongation

in the connector element must be almost zero so the load level in the connector must remain almost constant. The bolt head and the nut were model using solid elements (C3D8R) to allow the occurrence of local forces between bolt head and steel plates and bolt rod and plates holes. All the steel plates from the connection were modeled as solid elements (C3D8R).

The contact behavior was define as "hard" contact with the possibility of separation after contact in case of normal behavior and for the tangential behavior a penalty friction formulation with a 0.45 static friction coefficient was used.

Because the purpose of this paper was only the study of the slip-resistant connection behavior, the plastic behavior of the reinforced concrete elements was neglected. However, the level of interface stress was monitored to avoid the normal pressure to exceed the concrete compressive resistance value of 35 Mpa, and the equivalent von Misses stress in the steel plates.

The analysis was conducted in two steps. First the pretensioning load was applied in the connectors, and secondly a linear horizontal displacement of RC frame corner was imposed (see Figure 13).

First step: connector pretensioning load
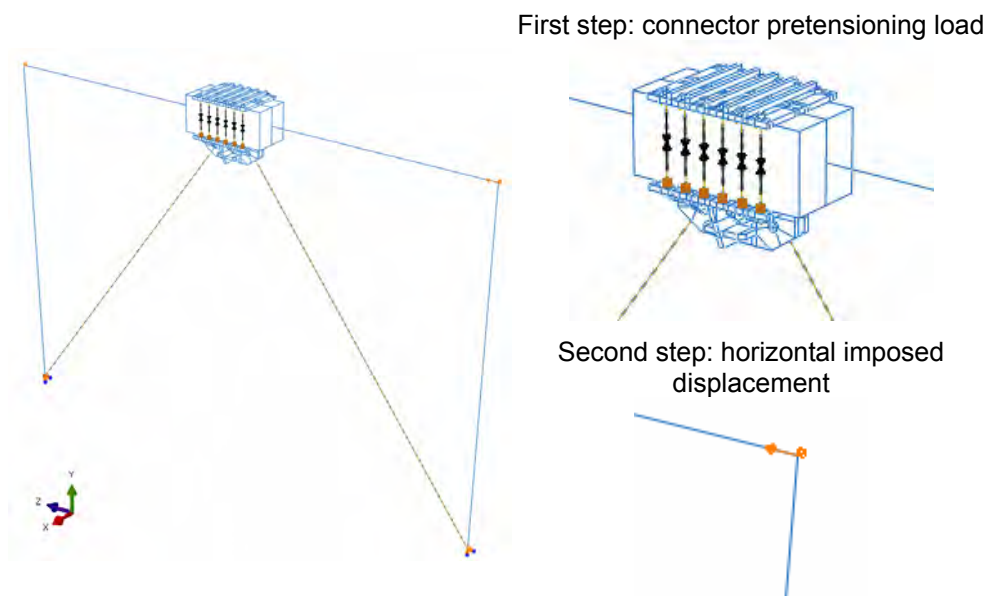
Second step: horizontal imposed displacement

Figure 13. Finite Element Model of the entire experimental frame with the boundary and load conditions.

## 4.2. FE results

The numerical simultation enabled to observe the effectiveness of friction contact inbetween the concrete and steel plates. Both normal and tangential stresses have been considered.

At the end of the first step a tension stress $\sigma$ of 700 MPa was obtained in the bolts, while the total clamping force $\Sigma F_t$ was 1300 kN,this corresponds to approx 110 kN in each connector see figure 14(a). A slight bending only of the steel plate was observed (see figure 14(b).
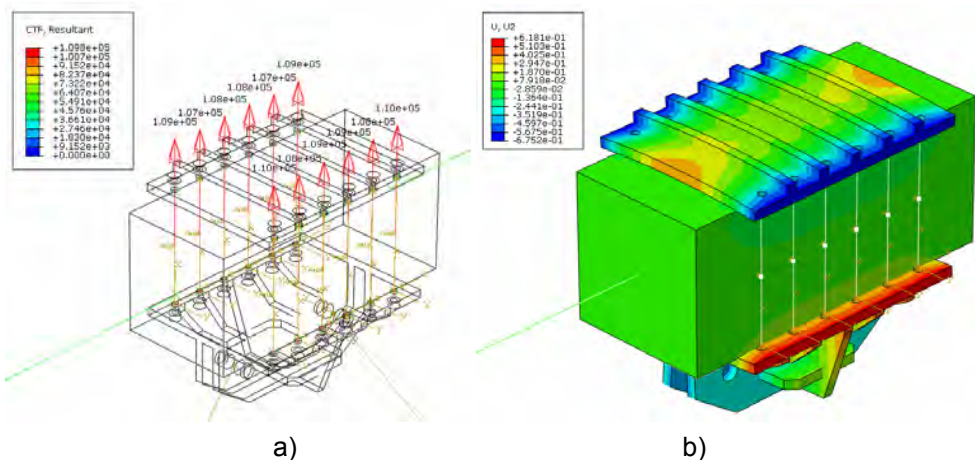
a)

b)

Figure 14. (a) Pretension forces in steel ties and (b) vertical deformation and bend shape of the steel plate.

The numerical simulation shows the steel plate does bend in such way to introduce to high pressure on the concrete beam corners and cause excesive local damages (see Figure 15). The upper steel plate stress level (see Figure 16) slightly exceeds the yield limit value in limited area.

It was also checked the relative slippage at the steel-concrete interface (see Figure 18) at the expected level of force in order to observe if the connection works as a full shear joint. The slip (see Figure 17) occurs at a 37.48 mm horizontal displacement, corresponding to a total applied force of 757 kN. The numerical analysis showed that the global force at which the friction resistance is exceeded, which represents the failure criteria of the upper connection, is much higher that the capacity of retrofitted RC frame.



a)

b)
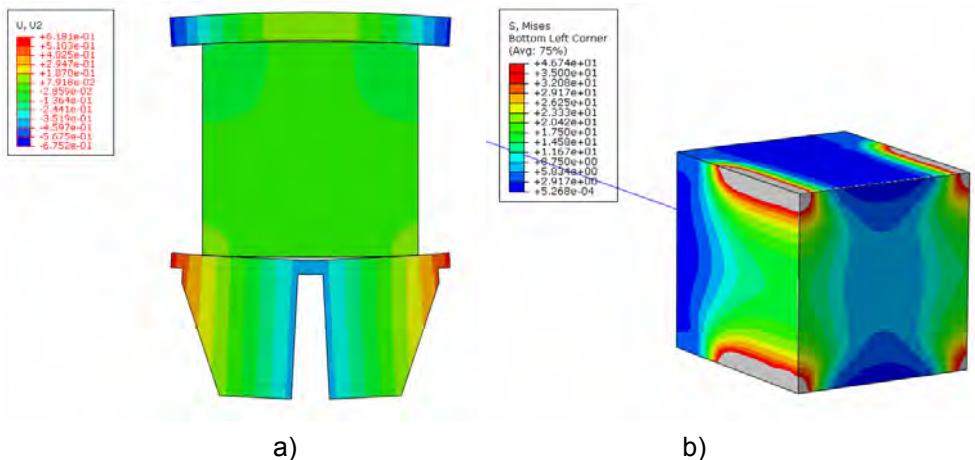
Figure 15. The bending of the upper steel plate (a) (10x) and the crush zones in concrete beam (b).
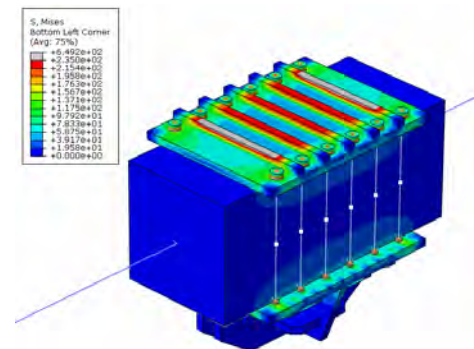


Figure 16. Von Misses stress on the upper connection after the application of the pretension in ties (deformation scale factor of 10).
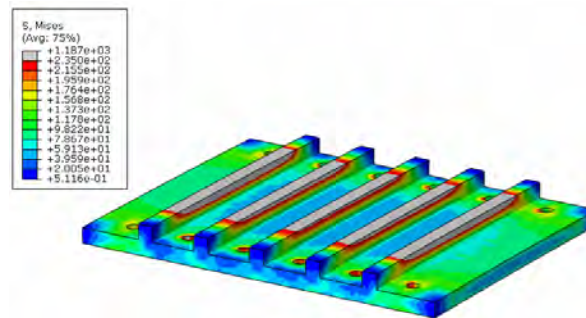


(a)
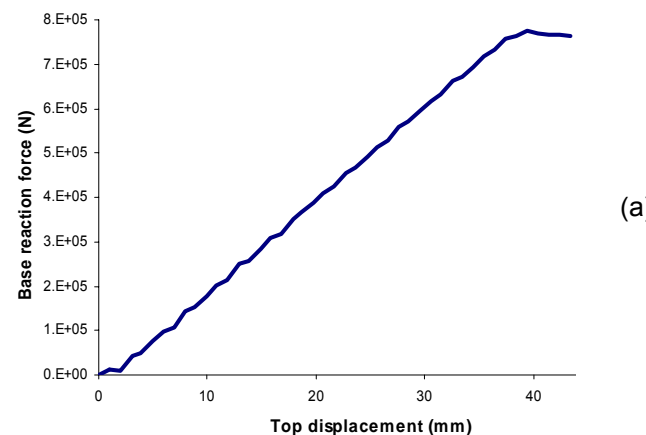
(b)

Figure 17. Behavior curves of RC frame (a) and friction connection (b)
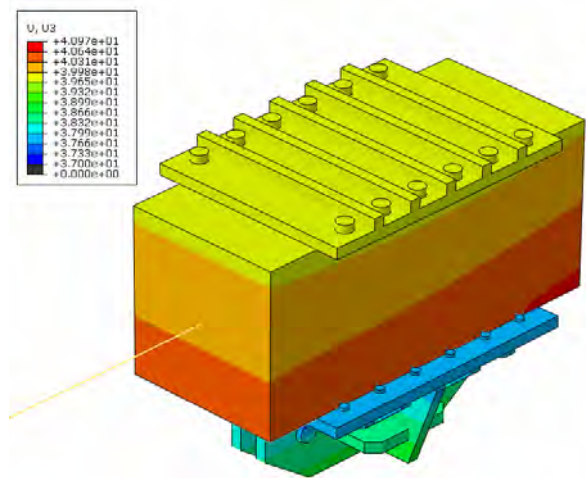
(a)
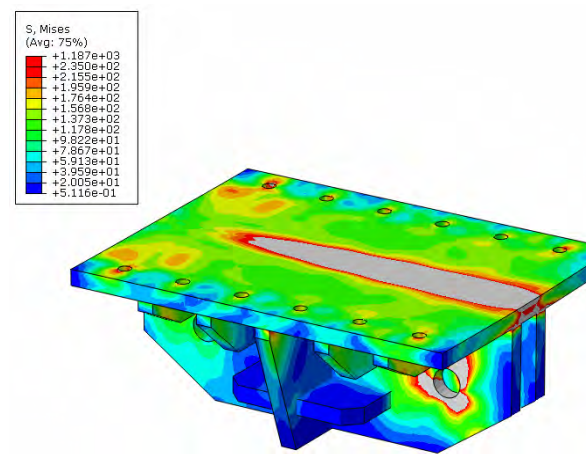


(b)

Figure 18. (a) Relative slippage of the RC beam (b) von Mises stress in steel plates when the friction force is exceeded

The higher friction force can be explained by the higher force in the connectors and the slight clamping of connection plates around concrete beam (see Figure 19). The induced force in the BRB is 640 kN, and taking into account that its plastic capacity is 105 kN, and the ultimate resistance is 135 kN, it means, at this level the BRB core is already broken.
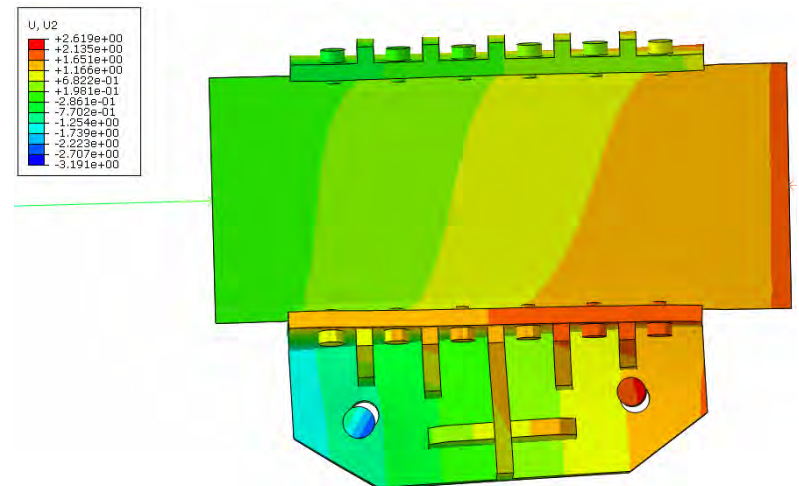


Figure 19. Vertical displacement and the clamp of upper connection at the slip (10x)

For the bottom connection (with the RC column), the stress level in the ties, bolts and in the concrete elements was also analyzed (see Figure 20).
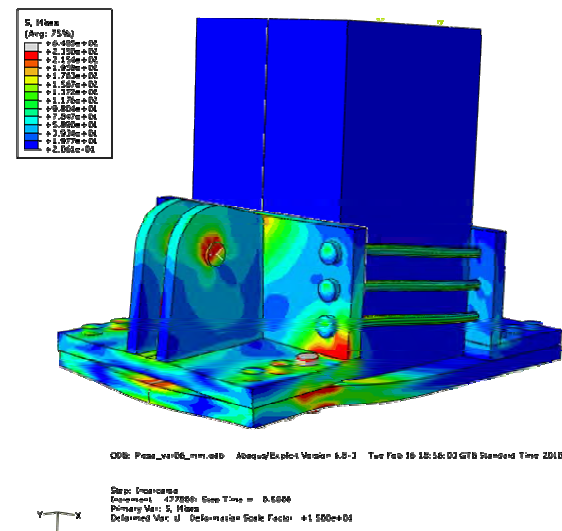


Figure 20. Von Misses stress on the bottom connection (15x).

The results of the numerical simulations have been used to validate the geometry of the specimens, obtained considering the simplified assumptions.

## 5. CONCLUSION AND FURTHER DEVELOPMENT

The connections between the steel braces and the RC members performed very well under both monotonic and cyclic loading.

The connection devices used for installing BRB's within the frame took benefit from the friction resistant forces induced by the post-tensioned ties and showed a very good behavior. However, related to the moment when the BRB internal stress are transferred to the ties, these are, in fact, pre-stressed. Very reduced slippage only was observed, with very small influence on the hysteretic loops of BRB system. The experimental results recommend the application of this connecting system for such interventions. Moreover, in the case of multi-storey frames (see Figure 21), such connecting systems provide also a beneficial confining effect at the frame joints, enhancing both strength and ductility of the MRF+BRB system. The portal frame tested experimentally could not take such benefit.
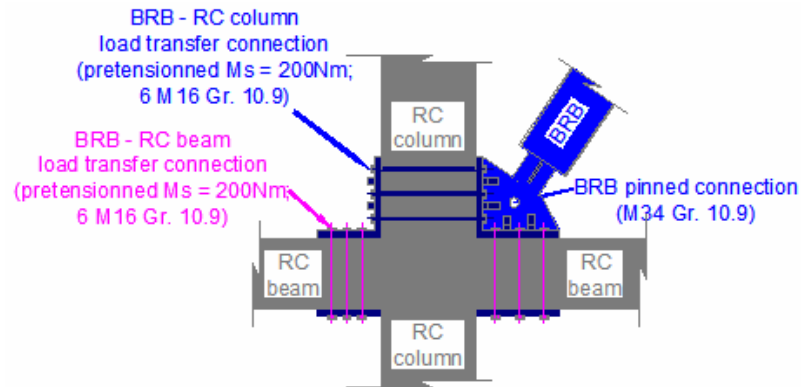


Figure 21. Bottom connection in case of multi-storey frames.

This type of connection may be used successfully for all types of retrofitting techniques for RC moment resisting frames based on inserting dissipative steel bracings.

For a global analysis, both connections can be considered fully rigid. It is on interest to develop a more complex nonlinear model based on calibrated FE models in agreement with the experimental results. This model should consider not only the behavior until the attainment of the bearing capacity, but also the real rigidity of the connections and the post-slippage behavior. As a further study, the behavior of the connections on dynamic loading conditions should be considered.

## ACKNOWLEDGMENT

## REFERENCES

[1] Bordea, S. (2010), "Dual frame systems of buckling restrained braces", PhD Theses, Ed. Politehnica, Timisoara, ISBN 978-606-554-059-0

[2] ABAQUS Version 6.8 Documentation (2008) © Dassault Systems Simula

[3] Montgomery (2002), "Methods for modeling bolts in the bolted joint", ANSYS User Conference, 2002

[4] FEMA 356 (2002), Guidelines for Seismic Rehabilitation of Buildings, Vol 1, Washington DC, 2002

[5] Nardini L., Braconi A., Osta A., Salvatore W. (2008), "Definition of the reinforced concrete benchmark building for the execution of comparative performance analysis between steel intervention techniques", STEELRETRO benchmark

[6] ECCS (1986), "Recommended testing procedures for assessing the behaviour of structural steel elements under cyclic loads", ECCS Publication N.45, 1986

[7] PROHITECH (2003), FP 6 INCO-CT-2004-509119/2004 „Earthquake Protection of Historical Buildings by Reversible Mixted Technologies 2003

[8] STEELRETRO (2006), RFSR-CT-2007-00050 Steel solutions for seismic retrofit and upgrade of existing constructions, 2006

# EXPERIMENTAL SEISMIC RESPONSE OF SLOTTED CONNECTIONS AT THE INTERSECTION OF HSS BRACES IN X-BRACING SYSTEMS

Ali Davaran, Alexandre Gélinas, and Robert Tremblay

*Dept. of Civil Engineering, École Polytechnique of Montréal, Montréal, Canada*
*ali.davaran@polymtl.ca; alexandre.gelinas@polymtl.ca;*
*robert.tremblay@polymtl.ca*

## ABSTRACT

This paper discusses an ongoing experimental study evaluating the seismic performance of bolted connections used in steel X-braced frames. Ten full-scale specimens with one continuous and one discontinuous tubular (HSS) diagonal bracing members connected at the intersection points are studied. The frames are of the conventional construction (Type CC) and moderately ductile (Type MD) categories of CSA S16-09. Two types of slotted brace connections are examined: single shear splices exhibiting inherent out-of-plane eccentricity and symmetrical double shear splice plates. The influence of the brace size, connection geometrical parameters such as plate thickness, plate width, length of overlapped plates, and the presence of stiffeners are also examined. The tests show that instability of the connections is a common behaviour for all the studied cases. Local stability effects must therefore be accounted for in the design and response of this type of X-bracing systems.

## 1. INTRODUCTION

Steel braced frames are among the seismic force resisting systems commonly preferred by design engineers for building and industrial structures in Canada. These frames must be designed and detailed in accordance with the provisions of the 2010 National Building Code of Canada (NBCC) (NRCC, 2010) and the special seismic requirements contained in the CSA S16-09 standard for the design of steel structures (CSA 2009). According to NBCC 2010, the design seismic loads are obtained using ductility-related and overstrength-related force modification factors, $R_d$ and $R_o$, respectively. While the former is related to the ability of the structure to dissipate the induced seismic energy through inelastic response, the $R_o$ factor reflects the dependable lateral overstrength offered by the system (Mitchell *et al.*, 2003).

In CSA S16-09, steel concentrically braced frames (CBFs) are categorized into three categories: Type CC (conventional construction) with $R_d = 1.5$, Type LD (limited ductility) with $R_d = 2.0$, and Type MD (moderately ductile) with $R_d = 3.0$. A factor $R_o = 1.3$ is assigned to all three systems. The seismic response of Type CC CBFs is expected to be essentially elastic with limited ductility demand. The system relies on the inherent ductility of steel and other sources of energy dissipation that normally exists in ordinary steel frames (e.g., friction) to dissipate the seismic energy

input. In moderate and high seismic regions, the connections along the structure lateral load path must be either detailed to exhibit a ductile failure mode or designed for seismic induced forces magnified by 1.5. This amplified seismic force level corresponds to elastic seismic response level ($R_d = 1.0$). Amplified seismic design loads also apply to member design for Type CC CBFs used in structures taller than 15 m. Nonetheless, the seismic design of these frames remains easier in comparison to the comprehensive and lengthy capacity design procedure applicable to the more ductile Type LD and Type MD CBF systems. For these two CBF categories, brace connections as well as beams and columns, must be designed for seismic effects based on the probable brace axial resistances.

For all CBF categories, hollow structural sections (HSS) bracing members are often preferred in design as they exhibit superior compressive resistance per unit weight compared to W sections or double angle braces. The X-bracing configuration with bracing members intersecting at a middle connection is also commonly used to take advantage of the shorter effective length for the compression brace resulting from the lateral support provided by the tension-acting brace, either in the plane or out of the plane of the frame, as demonstrated in past studies (e.g., El-Tayem and Goel, 1986; Picard and Beaulieu, 1987).

Due to the mid-connection, X-bracing typically have one continuous brace member and one discontinuous brace member, and various details are employed to transfer the load between the two disconnected brace segments at the middle connection. Satisfactory cyclic inelastic performance was observed experimentally in X-braced frames with HSS members when tubes were directly welded to each other and continuity plates were used at the mid-connections (Tremblay *et al.*, 2003). Bolted connections with splice plates are also typically used in X-bracing, as illustrated in Figure 1. In both cases, a plate known as through plate passes through the continuous brace and single shear lap (SS) joints (Figure 1a) or double shear (DS) lap joints (Figure 1b) are used. For this type of connections, numerical studies by Davaran (2001) and Davaran and Hovaidae (2009) showed that the bending stiffness of the connecting plates at the mid-connection may affect the buckling compression capacity of the bracing members. Concerns have also been raised regarding the possibility that single shear (SS) lap joints with inherent eccentricity could lead to local instability of the connection when loaded in compression.



a)                             b)

Figure 1. Bolted connections at brace intersection in X-bracing:
a) Single shear lap splices; b) Double shear lap splices.

A full-scale cyclic quasi-static test program has been initiated to investigate the stability response of X-bracing built with HSS members. Type CC and Type MD braced frames designed with single shear splices exhibiting out-of-plane eccentricity and symmetrical double shear splice plates are studied. Preliminary results from 4 tests revealed that buckling of the mid-connection can precede buckling of the diagonal members, leading to reduced brace compression resistance and localized inelastic demand on the connections (Gélinas *et al.*, 2012). This paper describes the behaviour of 10 specimens as obtained in that test program.

## 2. TEST PROGRAM

X-bracing specimens are tested in a 4.087 m tall x 7.5 m wide test frame vertically mounted in the Structural Engineering Laboratory at Ecole Polytechnique of Montreal (Figure 2). The focus of the test program is on the effect of the mid-connection design on frame response. Hence, the beams and columns of the frame are sized to remain elastic when inelastic response develops in the braces and their connections. At the frame base, the columns are connected to the strong floor through true pins fastened for vertical reactions. The beams are connected to the columns with bolted web clip angles with horizontal slotted holes to prevent the development of bending moments in the frame connections. Two high-performance 1000 kN actuators are employed to apply a predefined horizontal cyclic displacement protocol to the specimens.



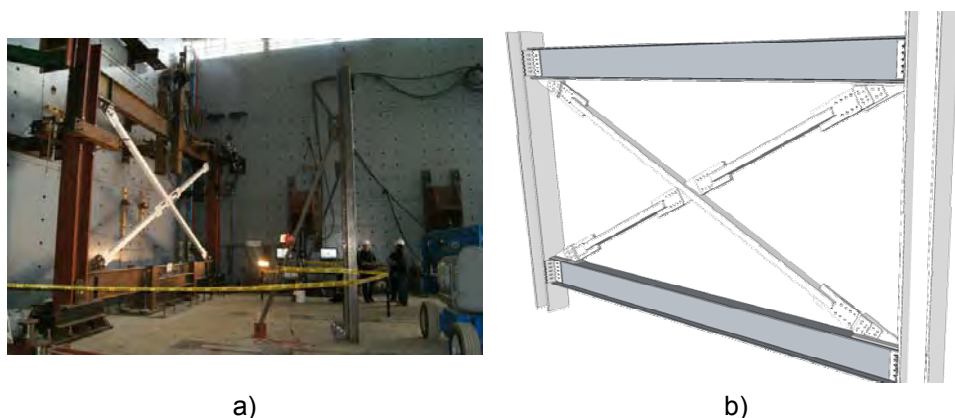a)                                         b)

Figure 2. Experimental setup: a) Laboratory; b) Frame illustration.

The properties of the test specimens are given in Table 1. Details of the mid-connection are given in Table 2 and illustrated in Figure 3. The specimen ID indicates the type of splice connections (DS *vs* SS), the thickness and width of the splice plates, and the CBF type (Type CC *vs* Type MD). Through plates passing in the continuous braces had the same width and thickness as the splice plates for the SS connections. Through plates were two times thicker than the splice plates for DS specimens. In Test 4, angles were used to connect the discontinuous brace segments to the through plate, without slotted holes, as shown in Figure 3b. All braces are made of ASTM A500, gr. C, HSS members with nominal yield strength, $F_y$ = 345 MPa, ultimate tensile stress, $F_u$ = 427 MPa, and nominal section properties: $A$ = 3400 mm² and $r$ = 48.3

mm for HSS 127x127x8, and $A$ = 2170 mm² and $r$ = 38.6 mm for HSS 102x102x6. Table 1 also gives the brace length between the hinge location in the corner gusset plates, $L_h$, as well as the measured brace section properties.

The brace connections were designed for brace axial forces, $S_f$, determined assuming the nominal brace section properties. For Type CC CBF specimens, the specimen labels with CCS and CCM extensions in Tables 1 & 2 indicate that the connections were designed for magnified seismic loads, $S_f = 1.5 \times C_r$, and non-magnified seismic loads, $S_f = C_r$, respectively, where $C_r$ is the factored brace axial compression resistance determined assuming a brace effective length $KL = 0.5\ L_h$. For Type MD specimens, the connections were designed for the brace probable resistance in tension, $S_f = A \times R_y \times F_y$, and the brace where $R_y F_y$ = 460 MPa, as prescribed in CSA S16-09 for HSS braces. The connection design forces are given in Table 2. Stability of the connections was not verified in the design, except for the unsupported segments of the splice plates between the HSS and last row of bolts.



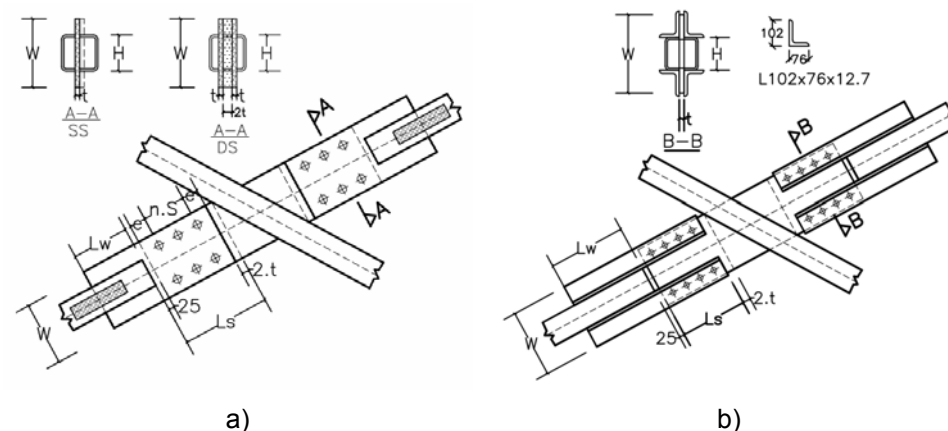a)                                         b)

Figure 3. Middle connection geometrical parameters for single shear (SS) lap and double shear (DS) lap configurations with: a) splice plates; and b) angles.

Table 1. Specimen properties.

| Test | Specimen | HSS brace | Brace length | Continuous member | | $F_y$ (MPa) | Discontinuous member | |
|------|----------|-----------|--------------|------|------|------|------|------|
| No | ID | d x b x t (mm) | $L_h$ (mm) | $A$ (mm²) | $r$ (mm) | | $A$ (mm²) | $r$ (mm) |
| 4 | DS-L4x3-MD | 127x127x8 | 6502 | 3592 | 48.2 | 439 | 3408 | 48.3 |
| 6 | DS-9.5x220-CCS | 127x127x8 | 6510 | 3583 | 48.2 | 439 | 3487 | 48.3 |
| 7 | SS-16x280-CCS | 127x127x8 | 6507 | 3639 | 48.1 | 392 | 3552 | 48.2 |
| 8 | SS-25x200-CCS | 127x127x8 | 6491 | 3661 | 48.1 | 392 | 3529 | 48.2 |
| 9 | SS-16x280(S)-CC | 127x127x8 | 6510 | 3474 | 48.3 | 392 | 3677 | 48.1 |
| 10 | DS-8x180-CCM | 127x127x8 | 6510 | 3587 | 48.2 | 392 | 3547 | 48.2 |
| 11 | DS-9.5x300-CCM | 127x127x8 | 6502 | 3574 | 48.2 | 392 | 3477 | 48.2 |
| 12 | DS-8x240-MD | 102x102x6 | 6510 | 2364 | 38.5 | 512 | 2436 | 38.4 |
| 13 | DS-8x150-CCM | 102x102x6 | 6510 | 2412 | 38.5 | 512 | 2393 | 38.5 |
| 14 | SS-16x150-CCM | 102x102x6 | 6507 | 2340 | 38.5 | 512 | 2340 | 38.5 |

Table 2. Details of mid-connections.

| Test No | Specimen ID | W (mm) | t (mm) | e (mm) | S (mm) | $L_s$ (mm) | Bolts n x $d_b$ (mm) | $S_f$ (kN) |
|---|---|---|---|---|---|---|---|---|
| 4 | DS-L4x3-MD | 304 | 19.05 | 50 | 75 | 325 | 8 x 22.225 | 1564 |
| 6 | DS-9.5x220-CCS | 220 | 9.525 | 50 | 75 | 307 | 6 x 22.225 | 1050 |
| 7 | SS-16x280-CCS | 280 | 15.875 | 71 | 95 | 389 | 6 x 31.75 | 1050 |
| 8 | SS-25x200-CCS | 203 | 25.4 | 71 | 95 | 406 | 6 x 31.75 | 1050 |
| 9 | SS-16x280(S)-CCS | 280 | 15.875 | 71 | 95 | 389 | 6 x 31.75 | 1050 |
| 10 | DS-8x180-CCM | 180 | 7.9375 | 50 | 75 | 232 | 4 x 22.225 | 700 |
| 11 | DS-9.5x300-CCM | 320 | 9.525 | 50 | 75 | 240 | 4 x 19.05 | 700 |
| 12 | DS-8x240-MD | 240 | 7.9375 | 50 | 75 | 307 | 6 x 22.225 | 998 |
| 13 | DS-8x150-CCM | 152.4 | 7.9375 | 36 | 75 | 203 | 4 x 15.875 | 357 |
| 14 | SS-16x150-CCM | 152.4 | 15.875 | 50 | 75 | 232 | 4 x 22.225 | 357 |

Specimens 7 and 9 were identical specimens with single shear lap joints, except that one stiffener was added to one side of the splice plates at the mid-connection to improve the connection compression strength for Specimen 9. The angle connection used for specimen DS-L4x3-MD (Figure 3b) can be distinguished from the rest of connections regarding its increased stiffness at junction of HSS to gusset plate. This connection is built without any slot in the discontinuous HSS members and is suggested as an alternative detail to prevent buckling of the mid-connection. Except for Specimen No.13, the space left between the double splice plates of the discontinuous HSS members in all DS specimens was filled with a shim (filler) plate. In Specimens Nos. 10 and 12, the shim plate was connected to the splice plates using tack welds. In Specimens Nos. 6 and 11, the shim plate was entirely welded to the splice plates along its edges.

## 3. OBSERVED BEHAVIOUR

All specimens were subjected to a symmetrical displacement protocol with stepwise increasing amplitudes (Gélinas *et al.*, 2012). The storey drifts when storey shear decreased to 80% of the peak storey shear and the observed failure modes are described in Table 3. Failure occurred in tension for all specimens. For 5 specimens, failure took place at the location where plastic hinging developed upon buckling. For these cases, low-cycle fatigue (LCF) contributed to failure. Except for Specimen No. 4, all specimens experienced buckling in the connections, as shown in Figures 4 and 5 for Specimens Nos. 7 (SS) and 6 (DS), respectively. For 8 of these 9 specimens, buckling occurred first in the mid-connection of the discontinuous HSS members. In Specimen No. 11, buckling was observed first in the corner connection of the discontinuous member. Hence, discontinuous brace members in X-configuration with traditional single or double shear lap slotted connections could not develop the conventional buckling mode in the member, as expected in design. Buckling of the discontinuous bracing member was observed in Test No. 4. Buckling of the continuous bracing member was observed for all SS specimens as well as for DS Specimen No. 4. For all other DS specimens, buckling occurred first at the end connections. Further detail on the observed behaviour of SS and DS connections are discussed in sections 3.2 and 3.3. The measured hysteretic responses for the diagonals for some of specimens are given in Figure 6.

Table 3. Maximum storey drift and failure modes.

| Test No. | Storey Drift[1] (%$h_s$) | Failure mode |
|---|---|---|
| 4 | 1.4 | Tension - net area (slot) of continuous HSS at mid-connection |
| 6 | 1.0 | Tension - net area (bolt holes) of splice plate of continuous HSS at end connection (LCF) |
| 7 | 0.8 | Tension - net area (weld end) of splice plate of discontinuous HSS at mid-connection (LCF) |
| 8 | 1.5 | Tension - net area (slot) of continuous HSS at mid-connection slot |
| 9 | 1.0 | Tension - net area (weld end) of splice plate of discontinuous HSS at mid-connection (LCF) |
| 10 | 0.8 | Tension - through plate, after tearing at mid-connection |
| 11 | 1.4 | Tension - gusset plate of discontinuous HSS at end connection (LCF) |
| 12 | 1.1 | Tension - net area (slot) of continuous HSS at end connection, after tearing |
| 13 | 0.8 | Tension - net area (slot) of continuous HSS at end connection, after tearing |
| 14 | 0.5 | Tension - net area (weld) of splice plate of discontinuous HSS at mid-connection (LCF) |

[1] Storey drift when storey shear reduces to 80% of peak storey shear ($h_s$ = storey height)

### 3.1. Brace compressive strengths and effective lengths

Maximum recorded brace axial compression forces ($C_{max}$) and tension forces ($T_{max}$) forces are given in Table 4. The $C_{max}$ values are compared to the predicted brace compressive resistances, $C_{u,pred}$, as determined with the measured brace cross-section and material properties of Table 1 and assuming $KL = 0.5L_h$. Except for Specimen No. 4, the test-to-predicted ratios for all discontinuous members are lower than 1.0, with an average value of 0.79, which resulted in effective length factors, $K_{eff}$ higher than 0.5 (average value = 0.63). These low compressive resistances

Table 4. Brace axial strengths and effective length factors.

| Test No. | Discontinuous Bracing Member | | | Continuous Bracing Member | | | Tensile Strength | |
|---|---|---|---|---|---|---|---|---|
| | $C_{max}$ (kN) | $C_{max}$ /$C_{u, pred}$ | $K_{eff}$ | $C_{max}$ (kN) | $C_{max}$ /$C_{u, pred}$ | $K_{eff}$ | $T_{max}$ (kN) | $T_{max}$ /$S_f$ |
| 4 | 1125 | 1.27 | 0.37 | 984 | 1.05 | 0.47 | 1627 | 1.04 |
| 6 | 847 | 0.93 | 0.53 | 948 | 1.02 | 0.49 | 1541 | 1.47 |
| 7 | 454 | 0.52 | 0.84 | 808 | 0.91 | 0.55 | 1426 | 1.36 |
| 8 | 535 | 0.62 | 0.75 | 763 | 0.85 | 0.59 | 1431 | 1.36 |
| 9 | 829 | 0.92 | 0.54 | 871 | 1.02 | 0.49 | 1420 | 1.35 |
| 10 | 586 | 0.67 | 0.70 | 629 | 0.72 | 0.67 | 867 | 1.24 |
| 11 | 474 | 0.56 | 0.80 | 550 | 0.63 | 0.74 | 1015 | 1.45 |
| 12 | 477 | 0.93 | 0.53 | 604 | 1.21 | 0.43 | 1199 | 1.20 |
| 13 | 433 | 0.86 | 0.56 | 474 | 0.93 | 0.53 | 715 | 2.00 |
| 14 | 284 | 0.58 | 0.71 | 483 | 0.98 | 0.51 | 585 | 1.64 |
| Average = | | 0.79 | 0.63 | | 0.93 | 0.55 | | 1.41 |

www.steelconstruct.com

are due to instability in the connections of the discontinuous braces. The differences are less important for the continuous braces, with an average $K_{eff}$ equal to 0.55, indicating that the discontinuous members, when loaded in tension, can still restrain out-of-plane buckling of the continuous member under compression. All connections could develop in tension the design connection forces.

### 3.2. Specimens with single shear (SS) lap connections

Specimens Nos. 7 and 8, 9, and 14 are in this group. The first nonlinear event was buckling of the connecting plates at the mid-connection in a two-hinge mechanism (Figure 4b). Except for Specimen No. 8, the specimens in this group failed by net section rupture of the splice plate at mid-connection, with pronounced low cycle fatigue effects due to cyclic plastic rotation in the hinge located near the end of the discontinuous HSS. The behaviour of Specimen No. 7 is illustrated in Figure 4. Specimens Nos. 7 and 8 were identical except that thicker splice plates were used at the mid-connection of Specimen No. 8 (25 mm $vs$ 16 mm). This increased plate thickness resulted in a higher buckling resistance ($C_{max}$ = 454 kN $vs$ 535 kN for Specimens Nos. 7 and 8) and instability occurring later in the test, at storey drifts of 0.2% and 0.3% $h_s$, respectively, for Specimens Nos. 7 and 8 (see Table 3). Specimen No. 9 was a duplicate of Specimen No. 7 except that a stiffening plate was welded over the splice plates at mid-connection. This also resulted in higher compressive
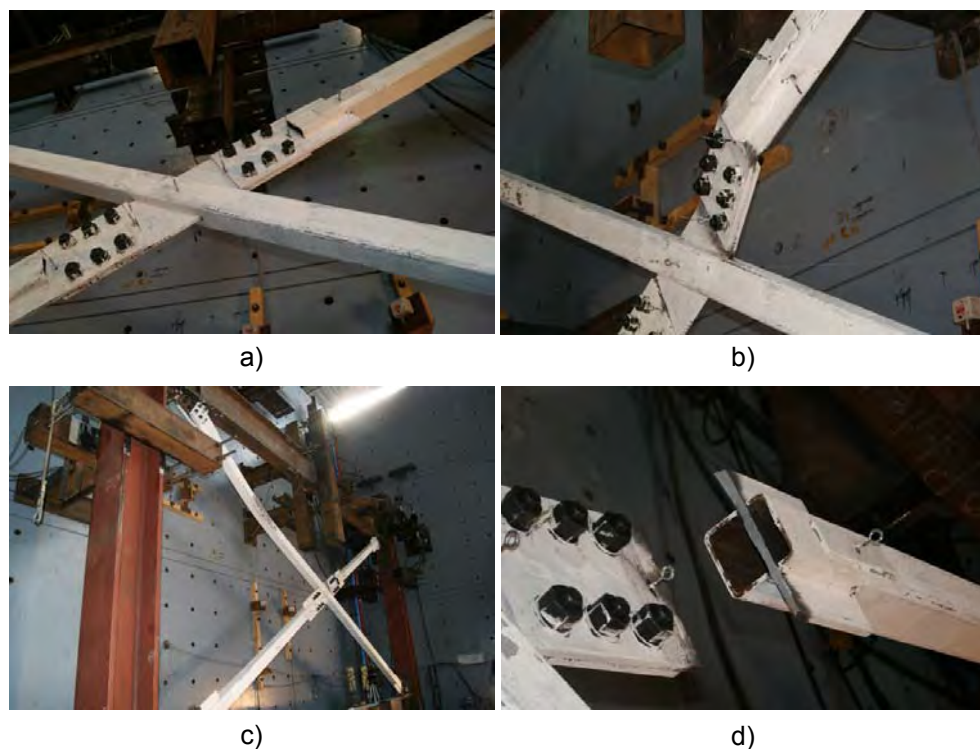
resistance (829 $vs$ 454 kN). For these three specimens, buckling of the continuous brace took place at a storey drift of 0.5% $h_s$. In Table 4, the average $K_{eff}$ factors for this group are 0.71 and 0.54 for the discontinuous and continuous members, respectively. For the SS specimens, the maximum and minimum storey drifts at failure, when storey shears reduced to 80% of peak storey shear, belong to Specimens Nos. 8 and 14 (1.5% $h_s$ and 0.5% $h_s$, respectively). Though the addition of stiffeners in Specimen No. 9 successfully improved the buckling load of the discontinuous member compared to Specimen No. 8, the ductility of the latter was higher (1.5% $h_s$ $vs$ 1.0% $h_s$).

### 3.3. Specimens with double shear (DS) lap connections

This group comprised Specimens Nos. 6, 10, 11, 12, and 13. For all these specimens, connection buckling was the first non linear event: at the mid-connection for Specimens Nos. 6, 10, 12 and 13, and at the end connection for Specimen No. 11. Later in the displacement protocol, global buckling of the continuous HSS occurred in a single curvature pattern which gradually changed to double curvature as the discontinuous brace straightened upon increasing further the imposed displacement. In most of the specimens, global buckling of the continuous HSS was observed in the first few cycles only, as buckling at its corner connections eventually developed at larger frame displacements. Repeated buckling of the mid-connections of the discontinuous HSS and of the end connections of the continuous braces were observed until failure of the specimens. The behaviour of Specimen No. 6 is illustrated in Figure 5.



a)

b)

c)

d)

Figure 4. Behaviour of single shear connection (Specimen No. 7): a) Connection; b) Buckling of connection in the discontinuous HSS; c) Buckling of the continuous HSS; and d) Failure at mid-connection.
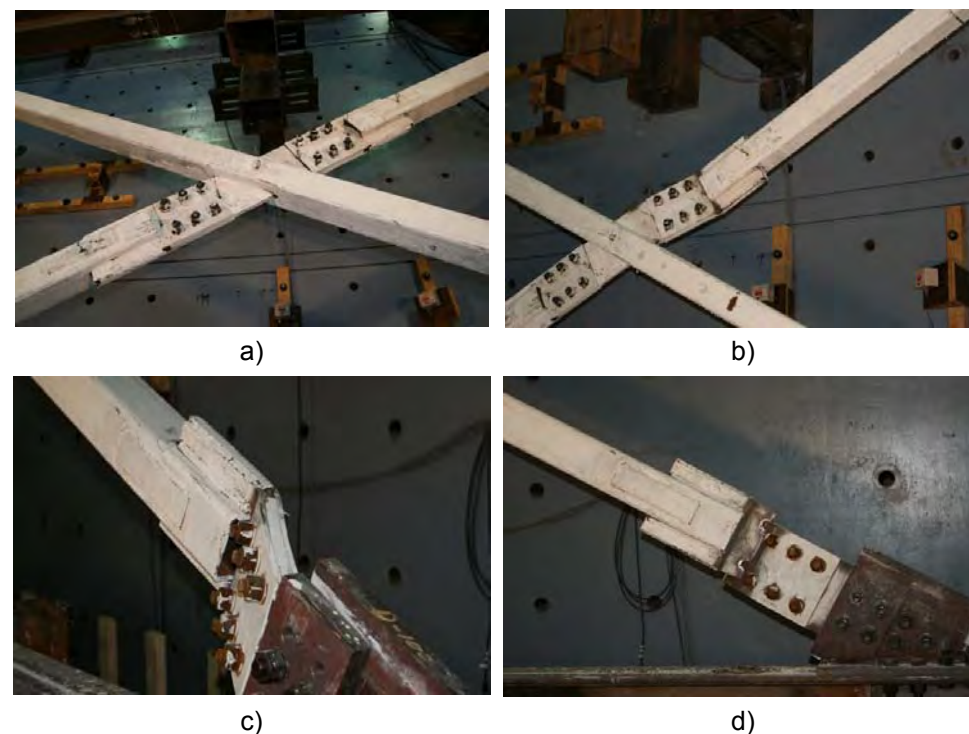


a)

b)

c)

d)

Figure 5. Behaviour of a double shear connection (Specimen No. 6): a) Connection; b) Buckling of the connection in the discontinuous HSS; c) Buckling of the connection in the continuous HSS; and d) Failure at end connection
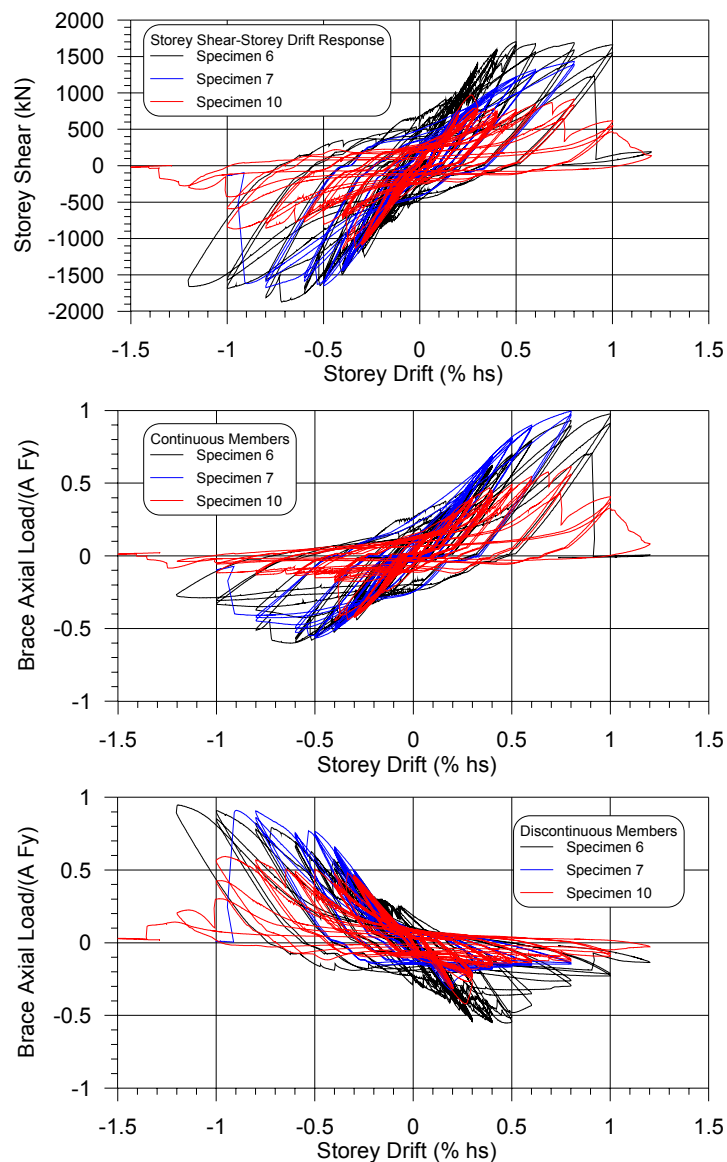
Figure 6. Hysteresis behavior for specimen 6, 7 and 10. 1) Total storey shear; 2) Continuous diagonal; 3) Discontinuous diagonal.

The other studied parameters in the DS group were the presence of the shim (filler) plate within the HSS slots (between the double splice plates) and the welding technique used to connect these plates. No shim plate was used in Specimen No. 13. In Specimens Nos. 10 and 12, shim plates were tack welded whereas continuous welds were used over the entire shim plate length for Specimens Nos. 6 and 11. The results show that inserting shim plates can improve the behaviour of DS connections, especially when the shim plates are fully welded.

## 3.4. Connection tension strength and ductility demand

Failure of Specimens Nos. 4 and 8 took place in the continuous brace at the reduced (net) section created to insert the through plate (see Table 3). The remaining 8 specimens failed at the connections transferring axial brace loads at the ends of the HSS segments. In Table 4, the maximum recorded brace tension forces, $T_{max}$, exceeded the design connection forces, $S_f$, in all cases, with an average test-to-design ($T_{max}/S_f$) load ratio of 1.41. For Type MD Specimen No. 4, however, the observed failure of the continuous brace at the net section is not acceptable as brace gross yielding in tension must be achieved. Net section reinforcement plates must be provided as necessary at the through plate location, similar to reinforcement used at the brace end connections. Failure at net section in the other Type MD specimen (No. 12) is also undesirable. This failure was likely due to local connection instability and could probably be avoided by stiffening the brace connection.

In Table 3, the average storey drifts for the 9 specimens with slotted SS or SD configuration is 1.0% $h_s$, varying from 1.5% $h_s$ for (No. 8) to 0.5% $h_s$ (No. 14). In Specimen No. 8, the thick (25 mm) splice plates designed for magnified seismic loads exhibited good ductility under repeated bending in compression followed by straightening in tension. Conversely, Specimen No. 14 had the smallest splice plates (16 mm x 150 mm) for an SS connection. This specimen exhibited the smallest deformation capacity together with pronounced strength degradation. Figure 6 shows the hysteresis behavior of specimens 6, 7 and 10. All specimens are Type CC CBFs with HSS 127x127x8 members. Specimens Nos. 6 and 10 differ by the design load and the technique used for connecting the shim plates to the splice plates: CCS and continuous welds in Specimen No. 6 *vs* CCM and tack welds in Specimen No. 10. The former exhibited a better hysteretic response in Figure 6. Type CC Specimens Nos. 6 and 7 respectively have DS and SS connections. Connections of both specimens were designed for magnified seismic loads. The frame with DS connections (No. 6) showed higher ductility compared to the frame with SS connections.

## 4. CONCLUSIONS AND RECOMMENDATIONS

Cyclic quasi-static testing has been performed on 10 full-scale X-braced frame specimens with HSS bracing members and common bolted-slotted connections to study the effect of mid-connection design on the frame seismic inelastic response. Type MD and Type CC braced frame categories were examined, and two different connection design loads were used for the Type CC CBFs. The other main parameter investigated in this study was the splice connection configuration: single shear (SS) and double shear (DS) lap joints. The main conclusions from this test program can be summarized as follows:

1) X-braced frames built with commonly used slotted-bolted brace connections developed local instability in the mid-connections and end (corner) connections, instead of global buckling of the diagonal bracing members.

2) As a result of mid-connection buckling, the discontinuous braces exhibited a reduced compressive resistance compared to the continuous member. For both braces, the effective brace length was longer than half the total brace length between the hinges in the corner gusset plates.

3) The behaviour of single shear overlapping plate connections (SS) was improved by using thicker splice plates or adding stiffener plates on one side of the overlapped plates.

4) Adding shim plates to fill the slots in DS lap joints can improve the strength of the connection and lead to better performance of the whole frame, especially when the shim plates are fully welded to the splice plates.

5) All brace connections could resist the tension force intended in design. The storey drift capacity of the frames was limited, however, varying between 0.5 and 1.5% of the storey height. For Type MD CBFs, the observed storey drift capacity (1.4% and 1.1% $h_s$ for Specimens Nos. 4 and 12, respectively) may not be sufficient. Moreover, non ductile failure occurred on net section, prior to brace gross yielding, which is unsatisfactory.

In view of the observed buckling response of the connections in X-bracing specimens with slotted connections that reflect current construction practice, it is recommended that further research be performed to better characterize the different possible connection buckling modes and develop methods to accurately predict their related compression resistances under cyclic loading conditions. Additional research is also needed to propose connection details that will eliminate connection buckling in X-braced frame structures for which ductile seismic response is required.

## ACKNOWLEDGMENTS

## REFERENCES

[1] CSA. (2009), *CSA-S16-09, Design of Steel Structures,* Canadian Standards Association, Willowdale, ON.

[2] Davaran, A. (2001), "Effective Length Factor for Discontinuous X-Bracing Systems". *Journal of Engineering Mechanics,* ASCE, vol. 127(106) (pp. 106-112).

[3] Davaran, A., and Hoveidae, N. (2009), "Effect of mid-connection detail on the behavior of cross-bracing systems." *Journal of Constructional Steel Research*, vol. 65(4) (pp. 985-990).

[4] El-Tayem, A.A., and Goel, S.C. (1986). "Effective length factor for the design of X-bracing systems". *Engineering Journal*, AISC, vol. 23(1) (pp. 41-45).

[5] Gélinas, A., Tremblay, R. and Davaran A. (2012), "Seismic Behaviour of Steel HSS X-Bracing of the Conventional Construction Category". ASCE/SEI Structures 2012 Congress, Chicago, IL, March 29-31.

[6] Mitchell, D., Tremblay, R., Karacabeyli, E., Paultre, P., Saatcioglu, M., and Anderson, D. L. (2003), "Seismic force modification factors for the proposed 2005 edtion of the National Building Code of Canada". *Canadian Journal of Civil Engineering*, vol. 30(2), (pp. 308-327).

[7] NRCC. (2010), *National Building Code of Canada*, 13th ed., National Research Council of Canada, Ottawa, ON.

[8] Picard, A., and Beaulieu, D. (1987), "Design of diagonal cross bracings. Part 1: Theoretical study". Engineering Journal, AISC, vol. 24(3) (pp. 122–126).

[9] Tremblay, R., Archambault, M.H., and Filiatrault, A. (2003), "Seismic Performance of Concentrically Braced Steel Frames made with Rectangular Hollow Bracing Members". *Journal of Structural Engineering*, ASCE, vol. 129(12) (pp. 1626-1636).

# MODELLING AND DESIGN OF DISSIPATIVE CONNECTIONS FOR BRACE-TO-COLUMN JOINTS

Lucia Tirca; Cristina Caprarelli; Nicolae Danila
*Department of Building, Civil and Environmental Engineering, Concordia University, Montreal, Canada*
tirca@encs.concordia.ca; c_caprarelli@encs.concordia.ca;
n_danila@encs.concordia.ca

Luis Calado
*IST - Department of Civil Engineering, Instituto Superior Tecnico Lisbon, Portugal*
calado@civil.ist.utl.pt

## ABSTRACT

In this paper, the behaviour of a dissipative brace-to-column connection device is emphasized. The computation is carried out for a single- and double-pin connection by using the theoretical beam model and the OpenSees beam model under monotonic and cyclic quasi-static displacement loading. The proposed model was calibrated against experimental test results and the validation was completed when both the experimental and simulated models provided a good match in terms of force-displacement hysteresis loops and cumulative dissipated energy.

## 1. INTRODUCTION

Concentrically braced frames (CBF) are effective systems, able to provide strength and stiffness to building structures subjected to earthquake loading. The system dissipates energy through tension yielding and inelastic buckling of bracing members, while the remaining framing components behave elastically. In spite of its efficient stiffness, the behaviour of bracing system is non-symmetrical. Thus, the amount of dissipated energy in compression is lower than that in tension and the compression resistance degrades in the post-buckling range with the number of cycles. To overcome the drawbacks and to preserve the ability of the CBF system to respond in elastic range, researchers have proposed alternative solutions consisting of adding ductile seismic fuses in bracing members and/or their connections (Tremblay *et al.,* 2011). In addition, the Canadian Design of Steel Structures standard (CSA/S16, 2009) states that for primary framing members forming the seismic-force-resisting system of conventional constructions, connections should be "designed and detailed such that the governing failure mode is ductile when the member strength does not control the connection design loads". Meanwhile, the European seismic code (Eurocode 8, 2005) states: "the overstrength condition for connections (brace-to-frame) need not apply if the connections are designed to contribute significantly to the energy dissipation capability" of the system. In this light, authors have carried

out research in the field of dissipative connections placed at each end of CBFs braces (Tirca *et al.,* 2012). These dissipative connections that may consist of single-pin or double-pin devices, as illustrated in Figure 1, are designed and detailed to yield, while braces behave in elastic range. The single-pin device is composed of two outer-plates welded or bolted to column flanges, two inner-plates welded to the brace and a rectangular pin member with rounded corners running through the four plates. If the single-pin device does not have sufficient capacity to carry the axial load developed in the brace member, the double-pin connection should be used. The single-pin device was initially proposed and experimentally tested in the frame of the European INERD project (Plumier *et al.*, 2006).
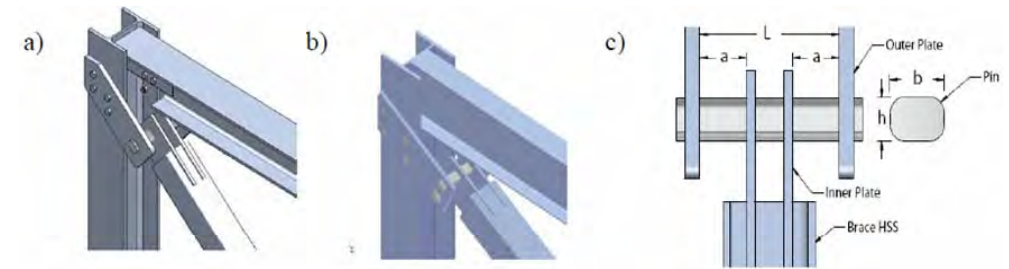


Figure 1. Dissipative connections: a) single-pin; b) double-pin; c) detail.

To simulate the behaviour of pin device, a numerical model was developed in the OpenSees framework version 2.2.0 (McKena *et al.,* 2009). Thus, in this paper, the OpenSees model for a single-pin device is calibrated against results obtained from experimental tests conducted at Instituto Superior Tecnico of Lisbon (IST), Portugal. In addition, a numerical model of a double-pin device with pins displaced in parallel is developed with the aim of preparing for upcoming experimental tests.

## 2. BEHAVIOUR OF SINGLE-PIN AND DOUBLE-PIN DEVICES

To validate the design method for the single-pin connection device, two numerical models are employed and defined as follows: the simple beam model and the OpenSees beam model. Regarding the simple beam model, the same approach considered by Vayas and Thanopoulos (2005) and slightly modified by authors is used to size the pin cross-section and the connection's components. By using data from both models studied under static loading, the authors replicate two experimental tests conducted at IST Lisbon under quasi-static displacement loading. The calibration of the model is validated when both the experimental and simulated models match in terms of hysteresis loops generated from plotting the force versus displacement, the energy dissipated per cycle and the cumulative dissipated energy.

### 2.1. Simple beam model

The behaviour of the single-pin device in terms of its capacity to dissipate energy under cyclic loading is influenced by the length of the pin, *L*, its cross-sectional shape and size, as well as the distance between the inner-plates (*L-2a*), as is illustrated in Figure 1c. Regarding the shape of the pin, the rectangular cross-section with rounded corners was chosen instead of a rounded shape due to its larger moment of inertia.

However, the configuration of pin device depends on the size and depth of the column's cross-section, which governs the pin's length. Herein, the axial force developed in the brace, $P$, is transferred to the pin through the two inner-plates as uniformly distributed loads that have the resultant P/2. For simplicity, the pin is considered to behave as a four-point loaded beam, as is shown in Figure 2. When the yielding moment $M_y = W_y F_y$ is reached, the pin starts to yield in bending under the point load $P_y/2 = M_y/a$. At this stage, the static deflection of the pin is:

$$\delta_y = (M_y/6EI)aL(3 - 4a/L) \tag{1}$$

where $EI$ is the flexural stiffness, $W_y$ is the section modulus and $F_y$ is the yield strength of the pin. In Eurocode provisions, the corresponding $F_y$ symbol is $f_y$.
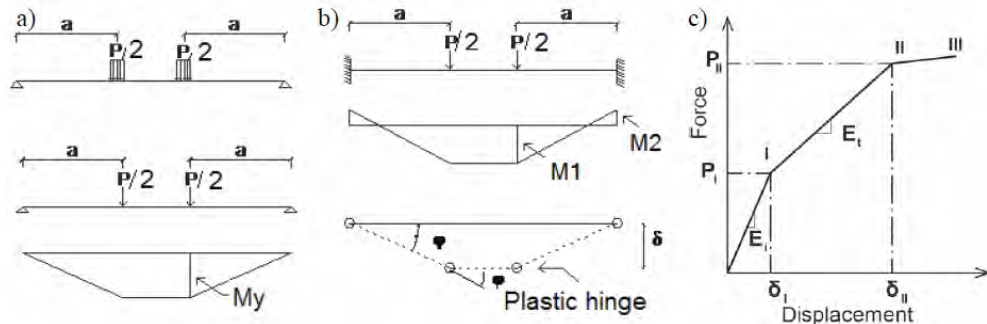


Figure 2. Behaviour of simple beam model: a) elastic; b) plastic; c) tri-linear curve.

By definition, the pin's rotation at yield, $\varphi_I$ is $k_I l_p$, where $k_I$ is the curvature at yield. Herein, $k_I = 1/r = 2\varepsilon_I/h$, where r is the radius of curvature and $l_p$ is the length of the plastic hinge. Under the applied $P_y/2$ loads, the simply supported beam deflects in single curvature and the mid-span deflection of pin device is $\delta_y = r(1 - cos(L/2r)$. The strain corresponding to the static yield stress may be two to five times the yield strain $\varepsilon_y$ (Ziemian, 2010). In this study, $\varepsilon_I$ is expressed as: $\varepsilon_I = 1.5\varepsilon_y$ and the corresponding radius of curvature becomes $r_I = h/(2x1.5\varepsilon_y)$. The magnitude of $P_y/2$ loads that generate the yielding moment $M_y = W_y F_y$ is expressed in Eq. (2) and the corresponding pin's mid-span deflection is given in Eq. (3). After the attainment of $M_p$, some clamping starts developing at the pin's ends and end bending moment is generated (Figure 2b). By equating the external work, $P\delta/2 = P(\varphi a)/2$, with the internal work $(M_1 + M_2)\varphi$, the magnitude of the ultimate load carried by the beam, $P_{II}$, is given in Eq. (4). It is estimated that the ultimate flexural capacity of the pin, $M_u$, is $M_u = W_p F_u$, where $F_u$ is the steel ultimate strength. Under the two-point loads $P_u/2$, the ultimate strain $\varepsilon_u$ is approximated as being equal to $\varepsilon_u = 50\varepsilon_y = 0.1$ and the corresponding value of the ultimate plastic rotation, $\varphi_u$, becomes $\varphi_u = k_{II} l_p = 0.2$ radians, while the ultimate deflection, $\delta_{II}$ is given in Eq. (5).

$$P_I = P_y = 2M_y/a \tag{2}$$

$$\delta_I = \delta_y = (h/3\ \varepsilon_y)(1 - cos(1.5L\varepsilon_y/h)) \tag{3}$$

$$P_{II} = P_u = 2(M_1 + M_2)/a \sim 4M_u/a \tag{4}$$

$$\delta_{II} = \delta u = 1.25(0.2a) \tag{5}$$

The numerical coefficient 1.25, given in Eq. (5) symbolizes the ratio between the length of the plastic hinge $l_p$ and the cross-sectional height, $h$. When the pin device undergoes incursions in the strain hardening range, the magnitude of load $P_{II}$ may slightly increase to a value $P_{III}$, while the maximum deflection of pin at failure is estimated to be $\delta_{III} = 0.4a$. By employing Eqs. (2) to (5) and the parameters at failure: $P_{III}$ and $\delta_{III}$, the pin response follows a tri-linear curve (Figure 2c).

### 2.2. OpenSees beam model for single-pin device

The purpose of developing the OpenSees beam model is to simulate the behaviour of the pin in its outer-plate supports. Thus, until the yielding moment is reached, the pin behaves as a simply supported beam. Then, during the plastic response, the deformed pin member causes bearing pressure to the contact surface of the outer-plate hole which is the pin's support. In this stage, bending moment is generated at both pin ends and its magnitude is incremented until the pin reaches its failure mechanism. Therefore, the OpenSees beam model was built to simulate the behaviour of the pin member acting as a four-point loaded beam, as previously described. The model shown in Figure 3 consists of eight nonlinear beam-column elements with distributed plasticity and four integration points per element. The pin's cross-section is made up of 60 fibers. Among them, 12 fibers were assigned along the height of the cross-section, $h$, and 5 along its width, $b$, as illustrated in Figure 3. The length of the pin, $L$, is the clear span between the outer-plates, which act as supports. Herein, the pin's supports (outer-plates) are modelled as rigid links of length $H$, which represents the free length. To allow rotation between the pin member and the support (rigid link), a zero-length element is added at both pin ends. The material assigned to the pin and rigid link is *Steel02*, which is also known as Giuffre-Menegotto-Pinto material. To simulate the deformation of the pin in the outer-plate supports, a calibrated *Pinching4* material, explained below, is assigned to both zero-length elements. The length and thickness of the outer-plates influence the behaviour of the connection and the deflection of the pin controls the deflection of outer-plates. When the pin member behaves elastically, both links act as cantilever members with a stiffness $K_I = 3E_l I_l/H^3$, where $E_l I_l$ is the flexural stiffness of the link. The *Pinching4* material represents a pinched force-deformation response and it allows users to simulate the transition phase from a shear connection to a semi-rigid connection when the beam is loaded below its elastic bending capacity.
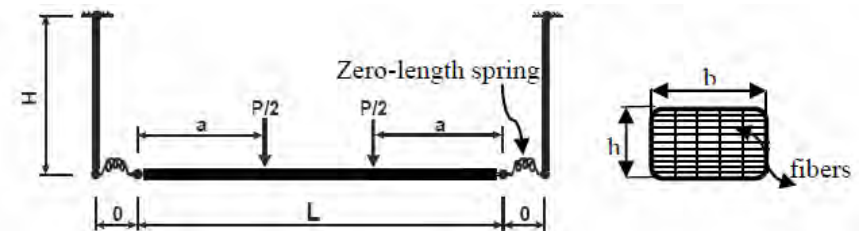


Figure 3. OpenSees beam model for single-pin device

The *Pinching4* material is calibrating by using data from two experimental tests conducted at IST Lisbon, and the involving specimens, shown in Figure 4, are P-A9 and P-3. The difference between them is the distance between the inner-plates.

www.steelconstruct.com

In both cases, the pin is made of steel with the following characteristics: $F_y = 396$ MPa and $F_u = 558$ MPa, while the pin's cross-sectional dimensions are 60x40 mm. The tri-linear curve of specimen P-A9 is built by using the theoretical values computed with Eqs (2) to (5) and is plotted in Figure 5a. To investigate the correlation between the theoretical tri-linear curve and that resulted from the OpenSees beam model, an incremental analysis is performed. Pairs of applied forces and deflections recorded at the beam's mid-span are plotted and shown in Figure 5b together with the theoretical tri-linear curve. In addition, at each incremental loading application, the stress and strain corresponding to each one of the 12 fibers recorded at beam's mid-span are plotted (Figure 6). Thus, when the force $P_y = 145$ kN, computed with Eq. (2), is applied to the OpenSees beam model, the strain recorded in the extreme fiber of the cross-section is $\varepsilon_y$ and the corresponding stress is $F_y$. The maximum strain developed in the fibers is approximately $60\varepsilon_y$ and is reached under the applied force, $P_{II} = 612$ kN, as computed with Eq.(3). The corresponding stress recorded in the same fibers is $F_u$. Thus, the theoretical and the OpenSees beam model show a good correlation and the stress and strain diagrams validate the theoretical equations previously devised.
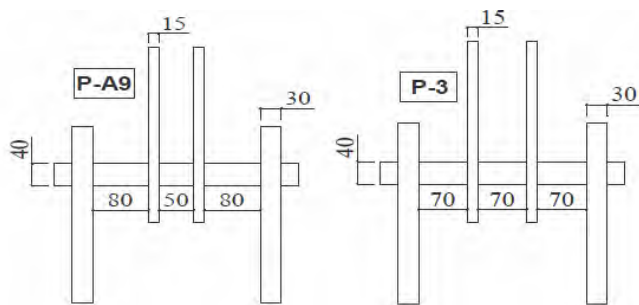


Figure 4. The geometry of specimens P-A9 and P-3.
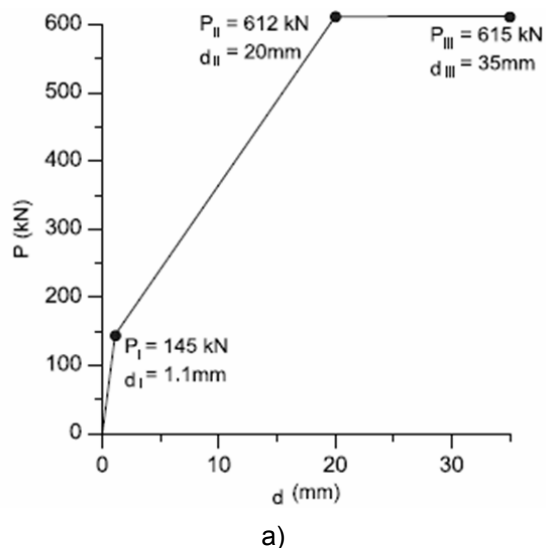


a)
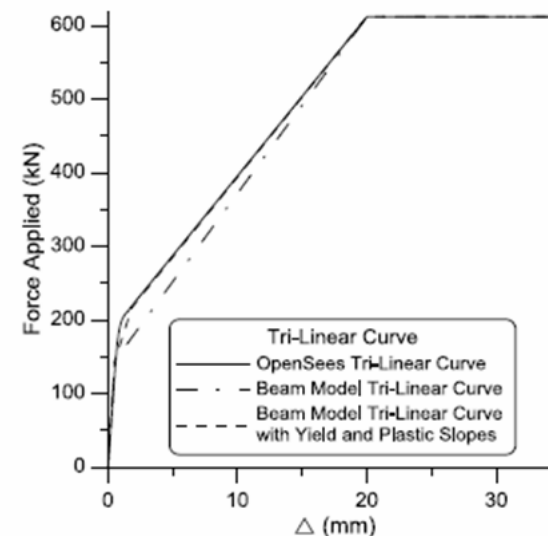


b)

Figure 5. Tri-linear curve of P-A9 device: a) theoretical, b) OpenSees model.
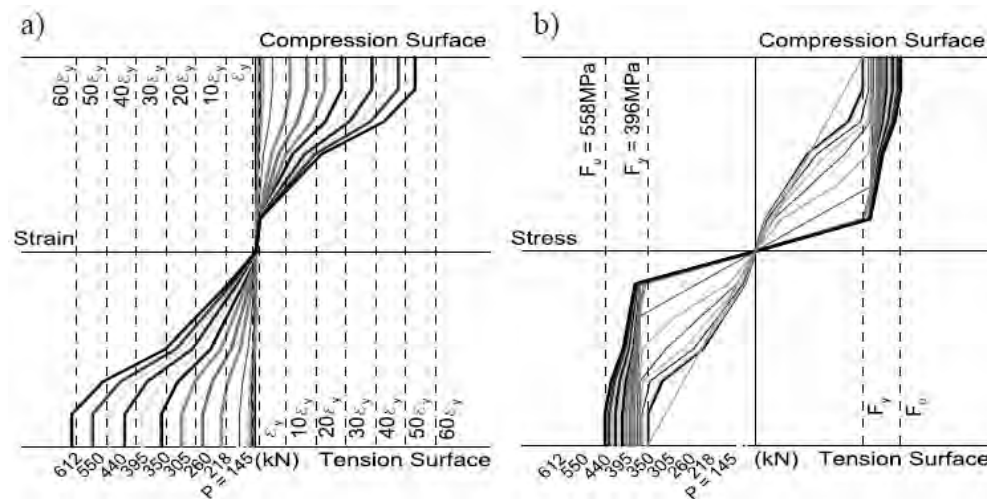


Figure 6. Strain and stress diagram of modeled P-A9 connection device

### 2.3. Validation of the numerical model against experimental test results

The two selected specimens P-A9 and P-3 were tested on a box stand under the ECCS cyclic quasi-static loading protocol. The displacement loading applied to the P-A9 sample has 25 cycles with a rate of loading of 0.45 mm/s and a maximum displacement in the last cycle of 40 mm. The displacement loading protocol applied to the P-3 sample has 21 cycles, a rate of loading 0.33 mm/s and a maximum displacement of 45 mm. In both cases, three consecutive cycles reach the same

displacement amplitude. The force-displacement hysteresis loops that characterize the behaviour of samples P-A9 and P-3 are shown in Figure 7. In both cases, the failure of the pin occurred in the compression side at one of the two points of load application, as shown in Figure 8. Thus, in the case of specimen P-A9, when the distance between the outer-plate and the inner-plate is larger than the distance between the inner-plates, the failure occurs in the longer pin segment at the external face of the inner-plate. In the case of specimen P-3, the failure occurred in the middle segment at the internal face of the inner-plate. For both specimens, same stiffness degradation occurred during reloading. Although both specimens reached the same deformation in bending of 35 mm, the corresponding ultimate tensile forces (615kN for P-A9 and 670kN for P-3) differ by 10%. On the other hand, for both specimens, the capacity in tension is larger than that in compression by 12%. This difference in strength is due to out-of-plane bending of outer-plates which implies an increased distance between the pin's supports in the outer-plate hole. In this case, the outer-plates deflect toward exterior as is shown in Figure 8b. Thus, the thickness of outer-plates influences the behaviour of the connection.
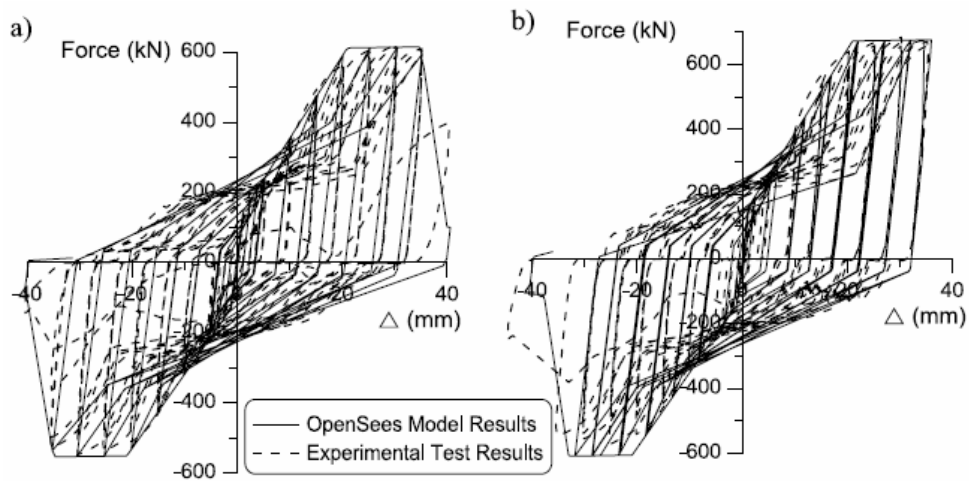
For modelling of connections, the *Pinching4* uniaxial material defined in the OpenSees library (Mazzoni *et al.,* 2007) is employed. This material model is able to simulate the cyclic degradation of stiffness during unloading or reloading and the degradation of strength. Meanwhile, it could be defined for a hardening-type or softening-type load-deformation response envelope. Thus, by analyzing the hysteretic response of specimens P-3 and P-A9, the unloading stiffness degradation model for a hardening-type response envelope is used and calibrated against the aforementioned experimental results. For *Pinching4* material calibration, three floating points are required to be defined in tension and three in compression. Floating point values (*1*) and (*2*) are 0.5 and 0.35 respectively. The first floating point (*1*) represents the ratio of the force at which pinching begins, 301 kN, to the total hysteretic force demand, 615 kN. Similarly, the second (*2*) represents the ratio of displacement where pinching begins, 12 mm, to the total hysteretic displacement demand, 35 mm. The third (*3*) floating point value is the value of force at negative unloading, 17 kN, to the total load during monotonic testing, 615 kN, resulting in a value of 0.03. Therefore, as shown above, the pinching curve is built by multiplying certain values of the skeleton curve, better known as the tri-linear curve, with the above floating point values defined for the tension side. For the compressive side, the floating points corresponding to (*1*) and (*3*) are reported to a total compressive force of 549 kN. Thus, the three floating points in tension and compression are shown in Figure 9.



Figure 7. Hysteresis loops recorded from the OpenSees model vs. experimental test results: a) P- A9, b) P- 3.



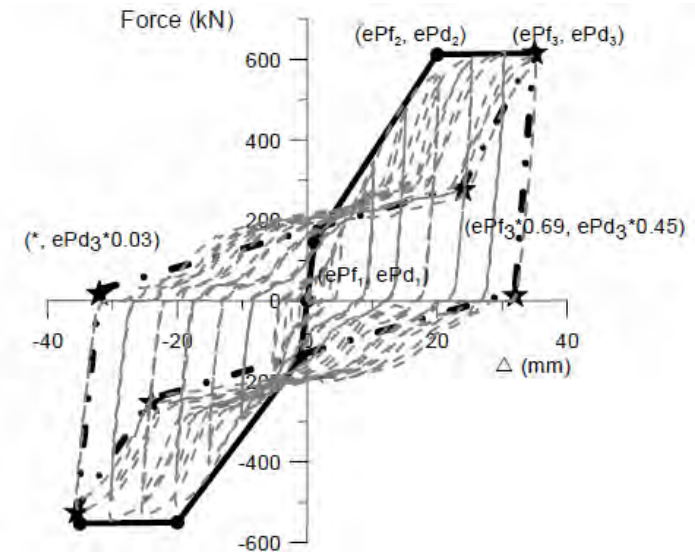Figure 8. Failure mechanism of specimens P-A9 and P-3.



Figure 9. *Pinching4* material definition.

The validation of the OpenSees model against the experimental results recorded for specimens P-A9 and P-3 is expressed in terms of normalized energy dissipated per cycle and the normalized cumulative energy, as shown in Figures 10 and 11. The hysteresis response of the specimen P-A9 during the last cycle shows failure in compression after a tentative failure in tension before reloading. As illustrated in Figure 10a, the proposed computer model is not able to simulate this type of softening that occurred during the last cycle and shows a large discrepancy in terms of
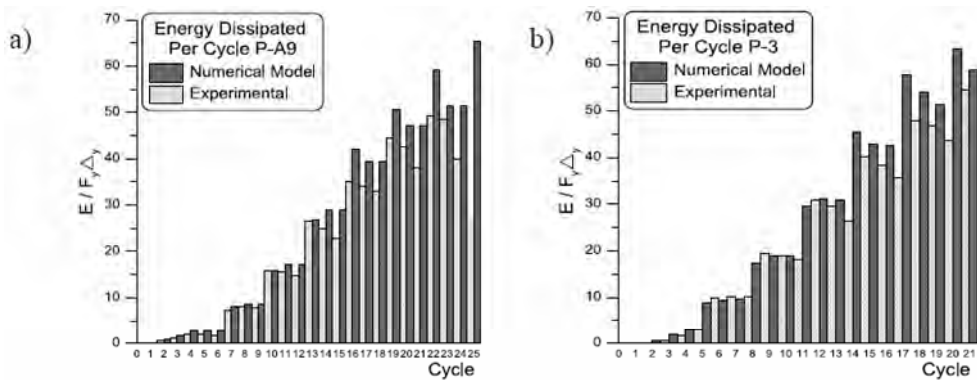
Figure 10. Energy dissipated per cycle for specimens: a) P-A9 and b) P-3.

energy dissipated. However, in the case of specimen P-3, a close correlation was observed (Figure 10b). Overall, the OpenSees model is able to replicate the pin's response. Regarding the cumulative energy dissipated by both samples, the P-3 pin was subjected to 21 cycles, while the P-A9 pin to 25 cycles. Under similar conditions it is expected that the connection device with a larger distance between inner-plates posses a larger dissipative energy capacity. The OpenSees model may be improved by wrapping the *Fatigue* material to the pin device material. The *Fatigue* material accounts for the effect of low-cyclic fatigue and does not influence the force-deformation relation of the initial material. The algorithm is based on the Coffin-Manson relationship in the log–log domain and the damage value is accumulated into the material in accordance with Miner's rule.
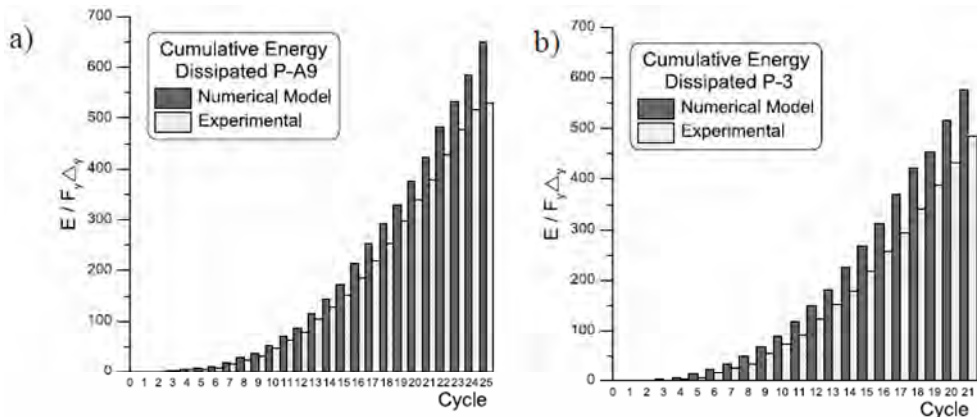


Figure 11. Cumulative energy dissipated by specimens: a) P-A9 and b) P-3.

## 2.4. Numerical modelling of the double-pin device with pins in parallel

When a larger axial force is required in brace members and the capacity of single-pin device cannot satisfy the demand, the connection with two pins acting in parallel is proposed and is illustrated in Figure 12. Due to the symmetry of a double-pin connection, the study can be conducted on half of the device and its behavior is

reduced by the single-pin OpenSees beam model as is shown in Figure 3. For simplicity, two small pins of rectangular shape 40x35 mm are used herein and the flexural stiffness is similar with that of an equivalent single-pin 60x40 mm. By employing two pins in the same connection, each pin is able to carry half of the force transferred by the brace, while undergoing the same deflection as per the equivalent single-pin device. In this example, the same connection device geometry as that considered for the sample P-A9 is selected. The theoretical curve proposed for the double-pin model is an equivalent tri-linear curve shown in Figure 13a. It is obtained by doubling the forces $P_I$, $P_{II}$, and $P_{III}$ which characterize the behavior of one of the two pins placed in parallel, while experienced the same deformation as per an equivalent single-pin. The strain corresponding to one pin belonging to the double-pin device is shown in Figure 13b.
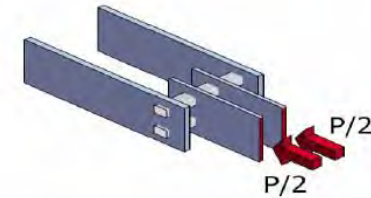


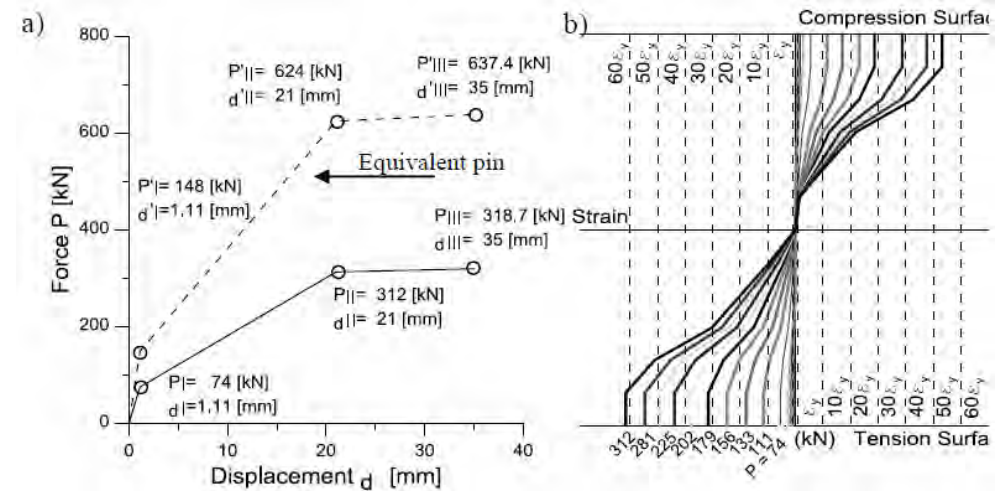Figure 12. Double-pin connection device with pins placed in parallel.



Figure 13. Double-pin connection device: a) theoretical tri-linear curve; b) strain experienced by one pin.

Thus, by doubling pins, the connection load-carrying capacity doubles, while the deflection remains the same due to the increasing of the flexural stiffness.

## 2.5. Fatigue of pin connection devices

The method applied to summarize data as recorded from testing P-3 and P-A9 under cyclic loading (Plumier *et al.,* 2006) was based on S-N line approach which is in agreement with Eurocode 3 provisions. In Figure 14, the collected test data of

P-3 and P-A9 specimens are plotted in the fatigue resistance curves obtained according with Eurocode 3. These fatigue resistance curves adopted in Eurocode 3, are built using a statistical analysis of constant amplitude fatigue test data. In the case of the P-3 and P-A9 samples, a variable amplitude loading history (ECCS) was used. However, the direct assessment of the fatigue resistance in not possible and reference should be made to the cycle-counting method (rainflow) and to a suitable damage accumulation rule. Thus, the linear damage accumulation rule proposed by Minner was employed for calculation of an effective value, $Seq$, which was adopted instead of $S$, as an argument in the fatigue failure prediction function. From Figure 14 it is possible to see that the P-3 device is on line 90 of EC3 while P-A9 is on line 80 of EC3. It seems that fatigue behaviour of the pins increases with larger distances between the inner-plates. This evidence agrees with the dissipated energy of the pins illustrated above.
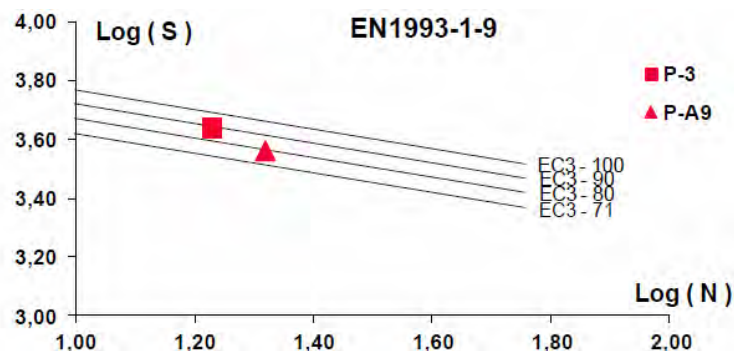


Figure 14. Fatigue resistance curves according to Eurocode 3 with detail category.

## 3. CONCLUSIONS AND GENERAL RECOMMENDATIONS

In this paper, the behaviour of a dissipative brace-to-column connection device is emphasized. The computation is carried out for single- and double-pin connection devices by using the simple beam model and the OpenSees beam model under monotonic and cyclic quasi-static displacement loading. The proposed model was calibrated against experimental test results. From this study, the following recommendations are proposed:

i. The simple beam model can be used for preliminary design applications.
ii. The dissipative energy capacity of connection devices increase if larger distance between the inner-plates is provided.
iii. Fatigue strength curves like the ones of Eurocode 3 allow predicting the stress range and number of stress cycles to fatigue failure. Low-cyclic fatigue failure is not the typical failure mode for these devices.
iv. An OpenSees model calibrated against experimental test results is developed and may be used for analyzing CBFs with dissipative pin connection devices.

## ACKNOWLEDGMENTS

## REFERENCES

[1] CAN/CSA 2009. Canadian Standard Association. CSA/S16-2009: Design of Steel Structures. Toronto, Ontario.
[2] EN 1998-1-2005. European Committee for Standardization – CEN. Eurocode 8: Design of structures for earthquake resistance. Brussels.
[3] EN1993-1-9-2005: European Committee for Standardization – CEN. Eurocode 3: Design of steel structures, Part 1.9: Fatigue. Brussels.
[4] Mazzoni, S., McKenna, F., Scott, M.H. and Fenves, G.L. et al. (2007), "OpenSees comand language manual", Pacific Eathquake Engineering Research Center, University of California, Berkeley.
[5] McKenna, F., Scott, M.H. and Fenves, G.L. et al. (2009), "Open system for earthquake engineering simulation", OpenSees software version 2.2.0.
[6] Plumier, A., Doneux, C., Castiglioni, C., Brescianini, J., Crespi, A., Dell'Anna, S., Lazzarotto, L., Calado, L., Ferreira, L., Feligioni, S., Bursi, O., Ferrario, F., Sommavilla, M., Vayas, I., Thanopoulos, P., and Demarco, T. (2006), "Two innovations for earthquake resistant design". *European Commission, Technical Steel Research, Report EUR 22044 EN,* ISBN 92-79-01694-6.
[7] Tirca, L., Caprarelli, C., and Danila, N. (2012), "Seismic simulation and design of low-rise CBF buildings with and without dissipative connections using OpenSees". *STESSA conference,* Santiago, Chile (pp. 365-371).
[8] Tremblay, R., St-Onge, E., Rogers, C., Morrison, T., Legeron, F., Desjardins, E., Tirca, L., Gray, M., Christopoulos, C., and Packer, J. (2011), "Overview of ductile seimic brace fuse systems in Canada". *EURO*Steel *conference, Budapest,* (pp. 939-945).
[9] Vayas, I. and Thanopoulos, P. (2005), "Innovative dissipative (INERD) pin connections for seismic resistant braced frames". *Int. Journal of Steel Struct.*, vol. 5.
[10] Ziemian, R. (2010), "Guide to stability design criteria for metal structures". J. Wiley & Sons.

# BEHAVIOUR OF STEEL TRUSS FRAME WITH LASER SHAPED DOUBLE SIDE NON-WELDED RHS JOINTS

Jerzy K. Szlendak
*Department of Civil & Environmental Engineering,*
*Bialystok University of Technology, Poland*
*szlendak@stal-projekt.com.pl*

## ABSTRACT

Push-pull type non-welded joints in application to steel truss made with RHS are the base to this research. Up to now, it is no experimental evidence of such joint behaviour (Wardenier, 1982, EN 1993-1-8-2005, Packer, 1992 & 1996). Laser shaped truss RHS joints tested in natural scale are described and axial-deflection curves obtained are presented. Yield line local push mechanism on front wall and, what is new, on bottom wall chord section is used to the theoretical estimation of joints failure load (Szlendak *et al*., 2010 & 2011). Theoretical and experimental results of joints resistance are compared. Experimental verification of truss behaviour with such joints are presented as the results of natural scale tests of half truss specimen. As the last step of research proposed estimations are verified from a natural scale experimental programme of full frame truss with such joints undertaken at the Bialystok University of Technology, Bialystok, Poland (Szlendak, 2012). Finally, some conclusions with regard to the implementation of double side non-welded laser shaped joint solution are given.

## 1. INTRODUCTION

Laser technology, Figure 1, is used to create such contact area between the chord and branch RHS member who could transfer the joint local stresses only by squash and shear. The socket has been developed in the shape (Figure 1), which make possible transfer not only normal but also moment load from branch to the chord (Szlendak, 2012). Welds are not used what is a new idea for such type plug & play type joints. In this research experimental results of T & N RHS joints resistance are referred. The theoretical models and design formulas are presented by (Szlendak *et al*., 2010 & 2011).

## 2. BEHAVIOUR OF ISOLATED T & N JOINTS

### 2.1. T joints

In a research project developed at the Bialystok University of Technology (Szlendak, 2010, 2012), eleven T RHS laser made joints tests, in natural scale, were carried out up to failure (Figure 2). Three of them (Figure 3, WTLi, i=1,2,3) have been one side lock joints, where only top face wall of RHS chord has been loaded by branch member but bottom wall has been unloaded. The other ones have the two side lock (WT2Li, i=1-8), where also bottom wall of chord member take part in the resistance of joint (Figure 4). In several steps the branch was loaded up to the

reach the failure load. After each loading step, the joint was unloaded to measure the permanent deformations of the tested specimen. Typical joint failure was the inelastic deformation of the loaded top and top & bottom flange of chord. In Table 1 the geometry of the specimens and their mechanical properties are given. LVDT gauges were used to measure the displacements.



Figure 1. Laser cut of lock & concept of T joint



Figure 2. Experimental tests of T & N isolated joints

Table 1. Geometrical dimensions and mechanical properties.

| No specimen | RHS chord $b_0$x$h_0$ mm | RHS branch $b_n$x$h_n$ mm | chord wall thick $t_0$ mm | branch wall thick $t_n$ mm | chord $f_{y0}$ MPa | $\beta = b_n/b_0$ | $\eta = h_n/b_0$ | $\lambda_0 = b_0/t_0$ |
|---|---|---|---|---|---|---|---|---|
| WTL1 | 100x100 | 40x40 | 3.0 | 3.0 | 334 | 0.40 | 0.40 | 33.3 |
| WTL2 | 100x100 | 60x60 | 3.0 | 3.0 | 343 | 0.60 | 0.60 | 33.3 |
| WTL3 | 100x100 | 80x80 | 3.0 | 3.0 | 335 | 0.80 | 0.80 | 33.3 |
| WT2L1 | 100x100 | 40x40 | 3.0 | 3.0 | 335 | 0.40 | 0.40 | 33.3 |
| WT2L2 | 100x100 | 60x60 | 3.0 | 3.0 | 335 | 0.60 | 0.60 | 33.3 |
| WT2L3 | 100x100 | 80x80 | 3.0 | 3.0 | 335 | 0.80 | 0.80 | 33.3 |
| WT2L4 | 100x100 | 40x40 | 4.0 | 3.0 | 335 | 0.40 | 0.40 | 25.0 |
| WT2L5 | 100x100 | 60x60 | 4.0 | 3.0 | 335 | 0.60 | 0.60 | 25.0 |
| WT2L6 | 100x100 | 80x80 | 4.0 | 3.0 | 335 | 0.80 | 0.80 | 25.0 |
| WT2L7 | 100x100 | 40x40 | 5.0 | 3.0 | 335 | 0.40 | 0.40 | 20.0 |
| WT2L8 | 100x100 | 60x60 | 5.0 | 3.0 | 335 | 0.60 | 0.60 | 20.0 |

where: WTLi – one side, WT2Li – two side joint



Figure 3. Chord upper wall failure (WTL1) & chord side walls failure (WTL3).



Figure 4. Joint WT2L1 after test (detail of branch in right corner); Joint WT2L2 (bottom wall failure).

Above research have been referred in (Szlendak *et al.*, 2011), where following conclusions have been presented: - shape and dimensions of the lock should be such design then net section of branch will be at least as strong as the face plate or face wall & bottom wall of chord, - for the presented lock shear of face plate has not be decisive, - permanent deformations of the loaded face of chord arise very quickly,

$$N = f_0 \cdot t_0^2 \cdot \left[ \frac{2 \cdot \eta \cdot (1 - 2k) + 2 \cdot \sqrt{1 - \frac{3}{2}\beta + \frac{\beta^2}{2}}}{1 - \beta} + \frac{2 - \beta}{\sqrt{1 - \frac{3}{2}\beta + \frac{\beta^2}{2}}} \right] \quad (1)$$

$$N = f_0 \cdot t_0^2 \cdot \left[ 2 \cdot \frac{\eta + \sqrt{1 - \beta \cdot \left(p - \frac{3}{2}\right) + \beta^2 \cdot \left(p - \frac{1}{2}\right)}}{1 - \beta} + \frac{2 + 2p\beta - \beta}{\sqrt{1 - \beta \cdot \left(p - \frac{3}{2}\right) + \beta^2 \cdot \left(p - \frac{1}{2}\right)}} \right] \quad (2)$$

- formulas (1 & 2) developed (Szlendak *et al.*, 2011-coeficients k and p is given there) sufficiently predict the resistance of such joints. For the design load coefficient $\gamma_{M5} = 1.25$, is proposed to be used, - two side joints are almost three time as strong as the one side for the ($\beta$=0.4 and 0.6). For the stronger joints ($\beta$ = 0.8) their resistance is about two times larger.

### 2.1. N joints

Second step in this research project has been estimation of strength eight N RHS laser made joints tests in natural scale, which have been loaded up to failure (Figure 2). Geometrical dimensions and mechanical properties are given in Table 2.

Table 2. Geometrical dimensions and mechanical properties.

| No specimen | RHS chord $b_0$x$h_0$ mm | RHS branch $b_n$x$h_n$ mm | chord wall thick $t_0$ mm | branch wall thick $t_n$ mm | chord $f_{y0}$ MPa | $\beta = b_n/b_0$ | $\eta = h_n/b_0$ | $\lambda_0 = b_0/t_0$ |
|---|---|---|---|---|---|---|---|---|
| WTLN1* | 100x100 | 4,0 | 60x60 | 3,0 | 334 | 0,60 | 0,60 | 25,0 |
| WTLN2 | 100x100 | 4,0 | 60x60 | 3,0 | 343 | 0,60 | 0,60 | 25,0 |
| WTLN3 | 100x100 | 5,0 | 40x40 | 3,0 | 335 | 0,40 | 0,40 | 20,0 |
| WTLN4 | 100x100 | 3,0 | 80x80 | 3,0 | 335 | 0,80 | 0,80 | 33,3 |
| WTLN5 | 100x100 | 3,0 | 60x60 | 3,0 | 335 | 0,60 | 0,60 | 33,3 |
| WTLN6 | 100x100 | 3,0 | 40x40 | 3,0 | 335 | 0,40 | 0,40 | 33,3 |
| WTLN7 | 100x100 | 5,0 | 60x60 | 3,0 | 335 | 0,60 | 0,60 | 20,0 |
| WTLN8 | 100x100 | 5,0 | 80x80 | 3,0 | 335 | 0,80 | 0,80 | 20,0 |
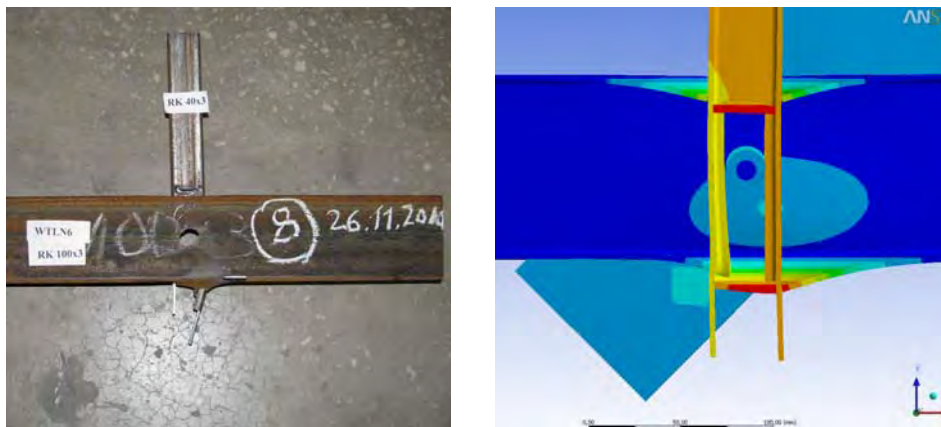
Figure 5. Joint WTLN6 (*β* = *η* =0,40; *λ₀* = 33,0)after test - mode of failure & numerical analysis of stresses (ANSYS)



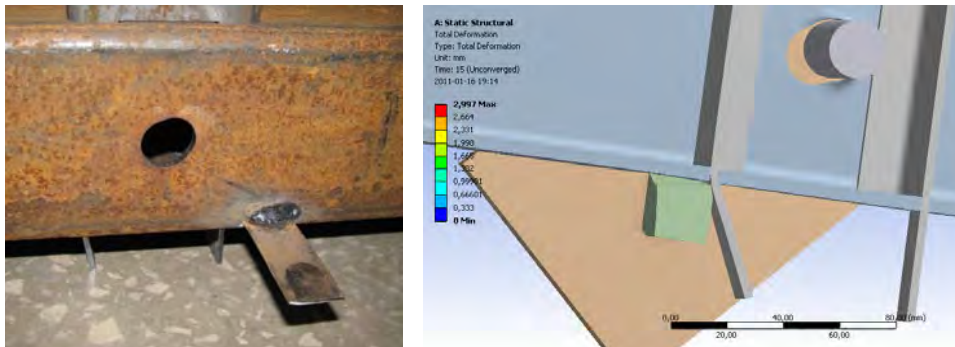Figure 6. Joint WTLN4 (*β* = *η* =0,80; *λ₀* = 33,0): after test & numerical model



Figure 7. Joint WTLN8 (*β* = *η* =0,80; *λ₀* = 20,0) after test & numerical model

Above research have been referred in (Szlendak, 2012), where following conclusions have been presented: - vertical member of N joints could transfer loads very similar as it is observed for T-joints, - tension diagonals bearing failure of thin walls (Figure 6), specially when thickness of chord member wall is small, - bearing

failure could be when decreased when additional square strut (or U member) could transfer tension directly to bottom chord wall and it is blocked by outside plate of vertical member (Figure 7)

## 3. BEHAVIOUR OF JOINTS IN TRUSS MEMBER

Third step in this research project has been two tests in natural scale of the truss member with double side non-welded laser shaped N joints (Figure 8). Half of the truss has the geometry similar to that shown in Figure 9. Two tests generally confirmed proper behaviour of joints and finally truss member failed by buckling.
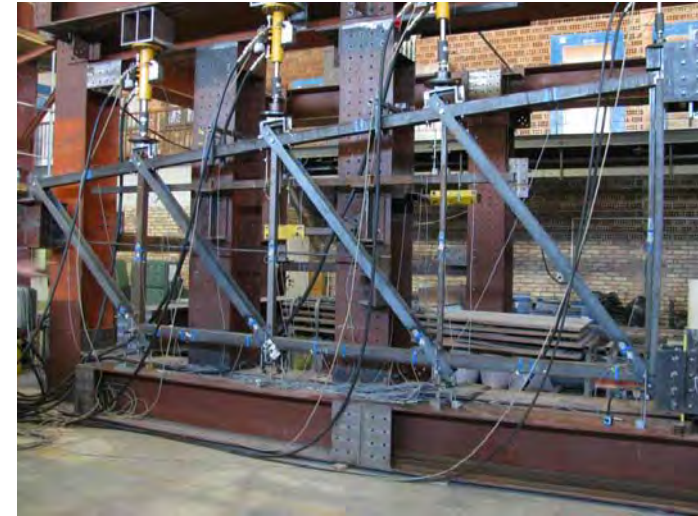


Figure 8. Truss element (half) during test
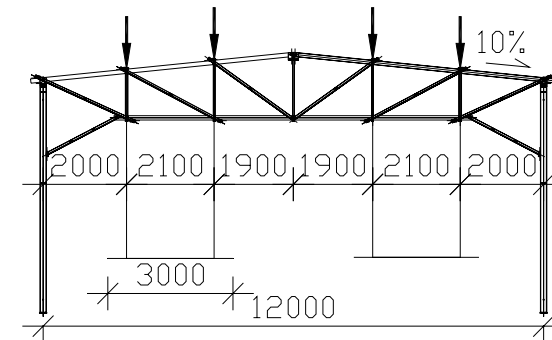


Figure 9. Inner frame of industrial hall

## 4. BEHAVIOUR OF TRUSS FRAME HALL

In the previous sections, a methodology for the evaluation of the response of steel T & N RHS joints under static loads was developed. Finally, such full truss is tested in natural scale as the inner frame of the industrial hall (Figure 9, 10 & 11).

Geometry of frame is shown in Figure 9, where points of applied loads are also given. Trusses have been assembly in fabrication hall to check their proper geometry and tolerances (Figure 10). After erection of full industrial hall the beams-roads hanging system has been assembly on the inner truss to applied to truss vertical loads in five step: 1) concrete plate by one side, 2) concrete plate by second side, 3) first concrete block by one side, 4) second concrete block by second side, 5) third concrete block by one side and finally 6) forth concrete block by second side.



Figure 10. Inner frame after assembly.

However after full vertical load the horizontal load (45deg) has been also applied to inner truss (Figure 11). Significant horizontal displacement of frame has been noticed (Figure 16).



Figure 11. Testing truss frame of industrial hall

Test results for inner frame obtained from two experiments are shown on diagrams bellow (Figure 12-16).
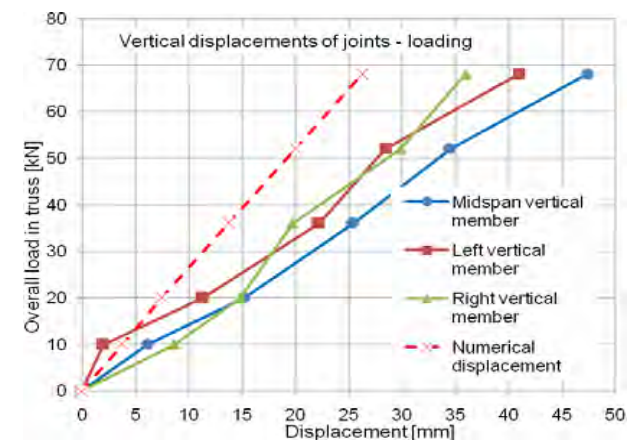


Figure 12. Test 1 – vertical loading
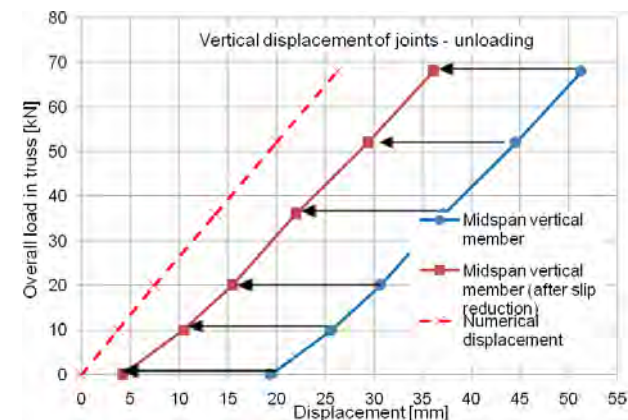


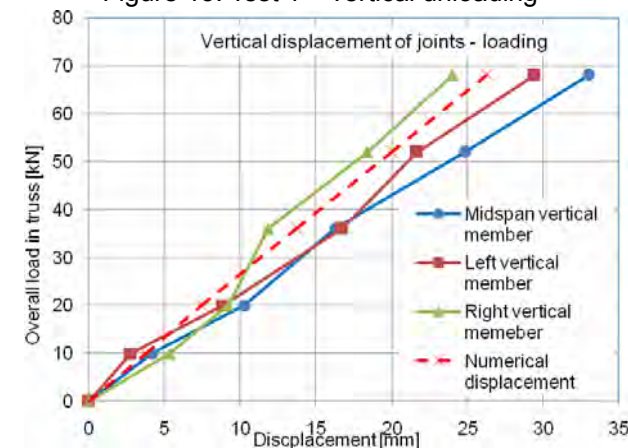Figure 13. Test 1 – vertical unloading
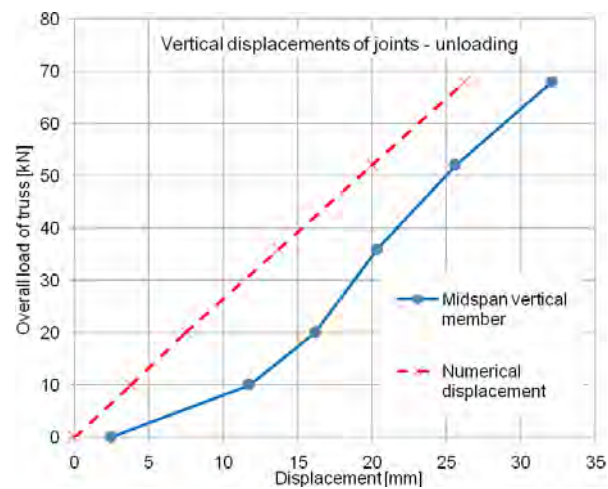


Figure14. Test 2 – vertical loading

Figure 15. Test 2 – vertical unloading



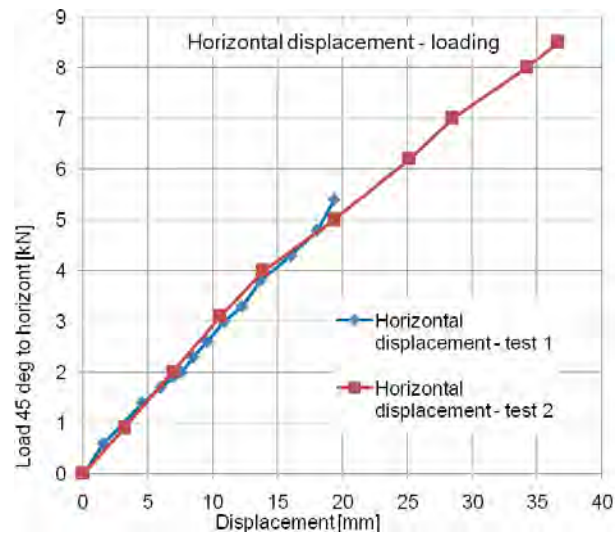Figure 16. Test 1 & 2 – horizontal loading

## 5. CONCLUSIONS AND GENERAL RECOMMENDATIONS

In this paper, new one and double side non-welded laser shaped T & N RHS joint were studied. Theoretical strength prediction is proposed and compared with experimental tests. Moreover joints behaviour and strength have been verified by full scale tests of half truss (two tests) and truss frame in industrial hall (two tests). Based on the results and considerations achieved during this research work, some design suggestions were proposed:

i) formulas (1 & 2) developed (Szlendak et al., 2011) sufficiently predict the resistance of such joints.

ii) behaviour of truss frame in industrial hall shows that double side non-welded laser shaped RHS T & N connections have no smaller failure load then welded ones. However additional elements are needed for proper transfer the bearing loads.

iii) significant slip in loading system and also in connections could be observed in Figure 13.

### REFERENCES

[1] EN 1993-1-8-2005. European Committee for Standardization – CEN. Eurocode 3: Design of steel structures. Part 1.8: Design of joints, Brussels.

[2] Szlendak, J.K. (2012),” RHS trusses and frames completed without welding with branch-chord clock laser made joints”, *National Centre for Research and Development (NCBiR),* 2011 Annual report of research project N R04 0008 06, PR/WBiIŚ/1/09/NCBR, Poland

[3] Szlendak, J.K.(2010), ” Resistance of laser made T RHS joints under compression load, *SDSS'Rio 2010 Stability and Ductility of Steel Structures,* E. Batista, P. Vellasco, L. de Lima (Eds.), Rio de Janeiro, Brazil (pp.311-318).

[4] Szlendak, J.K. and Oponowicz, P.A. (2011) “Compression resistance of non-welded T RHS truss joints making by laser cutting”, *ICMS 2011, 12th International Conference on Metal Structures, Wroclaw, Poland*.

[5] Szlendak J. K. (2007), “Design models of beam-column welded joints in steel structures made with rectangular hollow sections”, (in polish), *DSc Thesis, Scientific Treatises of Bialystok University of Technology, nr 148,* Bialystok, Poland (pp.212).

[6] Packer, J. A., Wardenier J., Kurobane Y., Dutta D. and Yeomans N.(1996),” *Design guide for rectangular hollow section (RHS) joints under predominantly static loading (No 3)”*. Comité International pour le Développement et l'Étude de la Construction Tubulaire (CIDECT) and Verlag TÜV Rheinland GmbH, Koln, Germany, 2 edition

[7] Packer J. A. and Henderson J. E. (1992), ” *Design guide for hollow structural section connections*. Canadian Institute of steel Construction, Toronto, Canada.

[8] Wardenier, J.(1982), “ Hollow section joints.” *Delft University Press,* Delft, the Netherlans.

# FINITE ELEMENT EVALUATION OF THE "MODIFIED-HIDDEN-GAP" HSS SLOTTED TUBE-TO-PLATE CONNECTION

Rolando Moreau; Colin A. Rogers
*Department of Civil Engineering & Applied Mechanics, McGill University, Canada*
*rolando.moreau@mail.mcgill.ca; colin.rogers@mcgill.ca*

Robert Tremblay
*Department of Civil, Geological & Mining Engineering, École Polytechnique, Canada*
*robert.tremblay@polymtl.ca*

Jeffrey A. Packer
*Department of Civil Engineering, University of Toronto, Canada*
*jeffrey.packer@utoronto.ca*

## ABSTRACT

This paper describes a finite element study of Modified-Hidden-Gap (MHG) connections of tubular brace members when subjected to monotonic tensile loading. The parameters varied included the overlap length, weld length and material strengths. The MHG connection has shown the potential to allow the tube's gross cross-sectional area to yield, as well as to distribute inelastic demand along the tube and away from the connection region. The overlap length, the weld length and material properties were found to influence the inelastic response of the connection.

## 1. INTRODUCTION

In Canada, concentrically braced frames (CBFs) are utilised to dissipate seismic energy for the majority of low- to medium- rise steel buildings. Hollow structural sections (HSS), or tubular members, are commonly selected for the lateral braces of these CBF structures. The seismic behaviour of HSS braces has been well-researched and documented over the past 30 years. However, HSS brace connections have been investigated to a lesser extent. Past research programs and the response of real buildings during earthquakes have shown that the conventional slotted tube-to-plate connection (Figure 1a) is susceptible to brittle net-section fracture under tensile loading. Due to this potential failure mode the connection is often detailed with net-section reinforcement plates (Figure 1b) or wrapped-around welds (Figure 1c). However, reinforcement plates are expensive, especially for circular HSS (CHS) braces, and wrapped-around welds are unreliable.

Therefore, to circumvent brace net-section fracture and to enhance brace ductility, a connection detail termed Modified-Hidden-Gap (MHG) was developed.

However, design and detailing rules have not yet been established for this connection. Thus, a finite element (FE) parametric study was carried out using ABAQUS to understand the geometric and material properties that influence the MHG connection response. This paper describes the FE model, the parametric study and the preliminary findings.
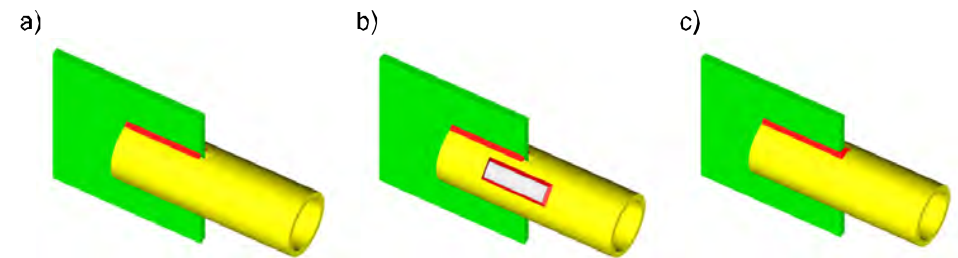


Figure 1. a) Conventional slotted tube-to-plate connection, b) Connection reinforced with plate, c) Wrapped-around welds

## 2. LITERATURE REVIEW

### 2.1. Conventional Slotted Tube-to-Plate Connection

The conventional slotted tube-to-plate connection detail is popular among designers and fabricators. However, in North America the typical open slot in front of the gusset plate leaves a net-cross-sectional area which can lead to circumferential fracture when the brace is loaded in tension. Furthermore, the brace's tensile resistance is often reduced by shear lag which occurs because the entire cross-section is not connected to the gusset plate. This leads to an uneven strain distribution which tends to concentrate inelastic demand at the beginning of the weld, and subsequently may trigger circumferential fracture.

The net-section resistance of a brace is given by $A_{ne}F_u$, where $F_u$ is the ultimate tensile stress. Shear lag is accounted for in the CSA S16 Standard (2009) through use of an effective net area, $A_{ne}$. The area $A_{ne}$ is a fraction of the net area, $A_n$, varying with the ratio of the weld length ($L_w$) to the circumferential distance between welds ($w$) in consideration of the gusset plate thickness (Figure 2). Martinez-Saucedo and Packer (2009) have also suggested net-section and block shear design equations for conventional slotted tube-to-plate connections loaded in monotonic tension as a function of $L_w/w$.
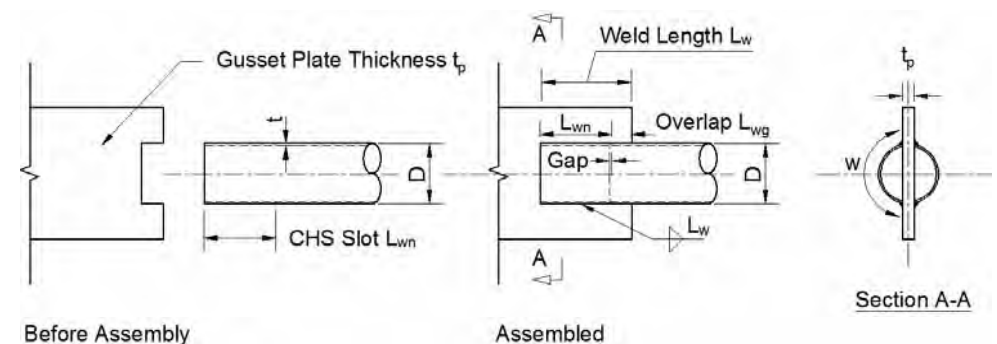


Figure 2. MHG Connection Detail

The CSA S16 Standard requires that the net-section resistance of a brace be greater than the probable brace yield capacity in tension ($R_yA_gF_y$), where $R_y$ is the ratio of the expected yield to nominal stress $F_y$, and $A_g$ is the brace gross cross-section area. However, the requirement $A_{ne}F_u > R_yA_gF_y$ often cannot be satisfied. Therefore, reinforcement plates are commonly welded to the tube to increase the net cross-sectional area (Figure 1b). This detail, however, is expensive to fabricate for CHS braces due to the curved surface. The use of "wrapped-around" welds to eliminate the gross area is not recommended due to possible weld defects, hot-spots and reduced ductility (AISC, 2010).

Additionally, HSS steel grades exhibit considerable material variability due to the cold working process (Packer et al., 2010). Therefore, $F_u$ and $F_y$ values may be difficult to determine in the absence of coupon tests. For conventional slotted tube-to-plate connections, a low $F_u/F_y$ ratio tends to result in a concentration of inelastic demand in the connection region

## 2.2. Modified-Hidden-Gap Connection

The Modified-Hidden-Gap (MHG) connection was developed to avoid net-section fracture without having to reinforce the connection (Figure 2). It was adopted from AIJ (2002) recommendations based on work by Mitsui et al. (1985) and was studied by Martinez-Saucedo et al. (2008) and Packer et al. (2010). The MHG connection consists of creating a slot in the gusset plate and inserting the plate into the brace slot. A hidden tolerance gap is left between the brace end wall and the slot in the gusset plate. Welds are applied from the gusset plate end towards the tube end covering the hidden gap. Thus, strain concentrations due to shear lag at the beginning of the weld will occur over the gross cross-sectional area.

Martinez-Saucedo et al. (2008) conducted experimental and FE simulation of two CHS braces with MHG connections subjected to reversed cyclic (tension dominated) loading. No parametric studies were conducted. Packer et al. (2010) conducted reversed cyclic testing of four CHS braces using the MHG connection. The MHG connection has shown the potential to distribute inelastic demand away from the connection region and along the tube leading to tube yielding and subsequent fracture at the tube's mid-length.

These tests were limited to 168 mm diameter CHS with gap sizes of 6 and 30 mm. Design and detailing rules have not yet been developed from these past research projects. Thus, a research program was initiated to develop codified design and detailing rules for the MHG connection.

A FE parametric study was carried out to gain a better understanding of the MHG connection. The work of Martinez-Saucedo et al. was expanded to incorporate the effects of geometric and material changes to the MHG connection. This was done to gain a better understanding of the stress-strain distribution around the connection, as well as to assist in the designing and testing of braces in the future.

# 3. FINITE ELEMENT MODEL

## 3.1. Overview

A FE parametric study was conducted to better understand the material and geometric properties that influence the MHG connection response. Monotonic tensile loading of the connection was adopted for this parametric study because the conventional connection often fails in tension through the net-sectional area of the brace. Thus, monotonic loading represents an extreme loading case, as well as allowing the opportunity to study the stress-strain distribution of the connection before proceeding into the reversed cyclic loading regime.

## 3.2. Methodology

The brace configuration from Martinez-Saucedo et al. (2008) was adopted as a starting point for the parametric study (Figure 3). In all the FE models the tube diameter, weld size and gusset plate thickness were kept constant. The overlap length, $L_{wg}$, weld length, $L_w$, (Figure 2) and material strength properties, $F_y$ and $F_u$, were varied; their effects on the connection response are described in Section 4. The global load-displacement response and stress-strain distribution at critical points were extracted.

The overlap length, $L_{wg}$, is defined as the length of weld on the gross cross-sectional area of the tube (Figure 3). It is believed to be one of the most important parameters influencing the MHG connection response. Thus, in the first part of the study, various $L_{wg}/L_w$ values ranging from 0 to 0.36 were considered, where $L_{wg}/L_w$ of 0 represents a conventional connection. The weld length, $L_w$, was held equal to 250 mm, leading to $L_w/w = 1.07$. All other dimensions as shown in Figure 3 were also held constant. Additionally, two steel grades for tube materials were used in this study: ASTM A500 Gr.C (2010) (Material 1) and CSA G40.21 Class C (2009) (Material 2). The actual material properties used in the modelling were those obtained through measurement in the test program by Martinez-Saucedo (2007) and Martinez-Saucedo et al. (2008) (Table 1). These two grades result in a range of $F_u/F_y$ values (1.08 to 1.27) that are encountered in practice. CSA G40.21 300W grade steel was used for the gusset plate.

The effects of varying the weld length is examined by comparing the responses obtained with $L_w = 250$ mm ($L_w/w = 1.07$) and 175 mm ($L_w/w = 0.75$). The comparison is performed for the extreme values of $L_{wg}/L_w$ (0.08 and 0.36) and for both materials.
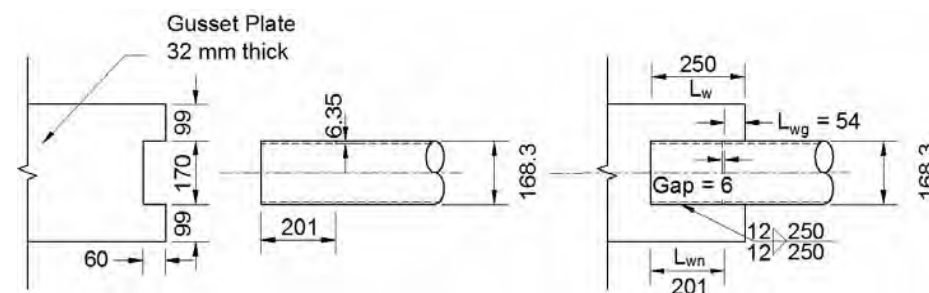


Figure 3. MHG Connection used in FE studies (Dimensions in mm)

Table 1. Summary of Material Properties

| Properties | CHS | | Gusset Plate | Weld Metal |
|---|---|---|---|---|
| | Material 1 | Material 2 | | |
| E (MPa) | 235 | 200 | 200 | 235 |
| $F_y$ (MPa) | 382 | 498 | 351 | 382 |
| $F_u$ (MPa) | 484 | 540 | 530 | 484 |
| $F_u/F_y$ | 1.27 | 1.08 | ------- | |

    www.steelconstruct.com

### 3.3. Finite Element Model

The parametric study was conducted using ABAQUS 6.10 EF1. Symmetry was utilised to model one-quarter of the geometry as shown in Figure 4. This is acceptable since buckling is not expected. Displacement loading was applied at the gusset end and reaction forces were measured at the other end of the tube. A tube length of 750 mm was used to minimize computational time (Martinez-Saucedo, 2007). Longer tube lengths were investigated but resulted in no change in the strain distribution along the brace. A tolerance gap of 1.25 mm between the gusset plate and the tube slot was modelled ensuring load is transferred through the welds alone.
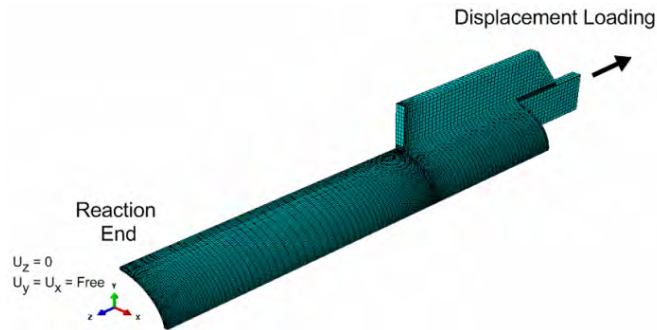


Figure 4. FE Model showing Boundary Conditions and Meshing

First-order reduced-integrated hexahedral 8-noded solid elements with hourglass control (C3D8R) were used to model the tube, welds and gusset plate. The authors modelled the CHS braces that were tested by Martinez-Saucedo and Packer (2009) in monotonic tension, and found that the C3D8R element type accurately reproduced the experimental results. However, this calibration study is not presented here since several connection configurations were modelled. A fine mesh was chosen near the weld region at the overlap length where large-strain gradients are expected. The mesh size was reduced at this location until the plastic strains remained relatively constant. Three elements were used through the thickness of the gusset plate and tube to control hour-glassing.

A non-linear isotropic von-Mises hardening module was used to model all materials. True stress-strain curves for the materials (Martinez-Saucedo, 2007; Martinez-Saucedo et al., 2008) are shown in Figures 5a and 5b. Fracture models were not implemented in this study; the equivalent plastic strains (PEEQ) in the model were used as a relative indicator for fracture potential. Fracture PEEQ values between 0.8 – 1.0 have been reported in the literature (Zhao et al., 2009). The measured tube material properties were used for the weld metal since true stress-strain curves for welds are difficult to obtain.

## 4. PARAMETRIC STUDY RESULTS

### 4.1. Influence of Overlap Length and Material Properties

The global load-displacement response for Materials 1 and 2 is shown in Figures 6a and 6b, respectively. For each material, there is no difference between the ultimate strengths over the overlap range. The MHG connection allows the entire
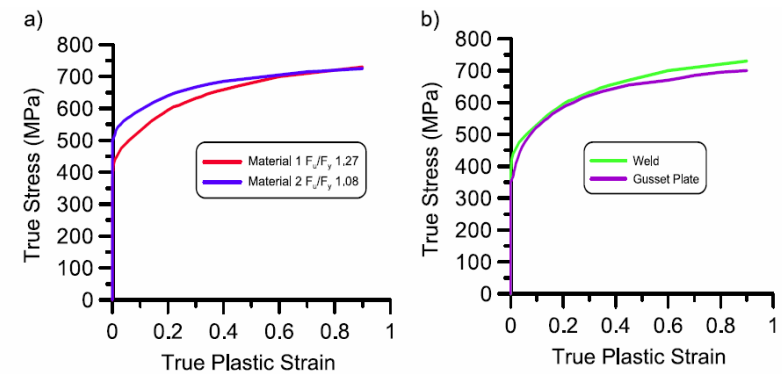


Figure 5. True Stress vs. True Plastic Strain: a) Tube, b) Gusset Plate & Weld (Martinez-Saucedo, 2007; Martinez-Saucedo et al., 2008)
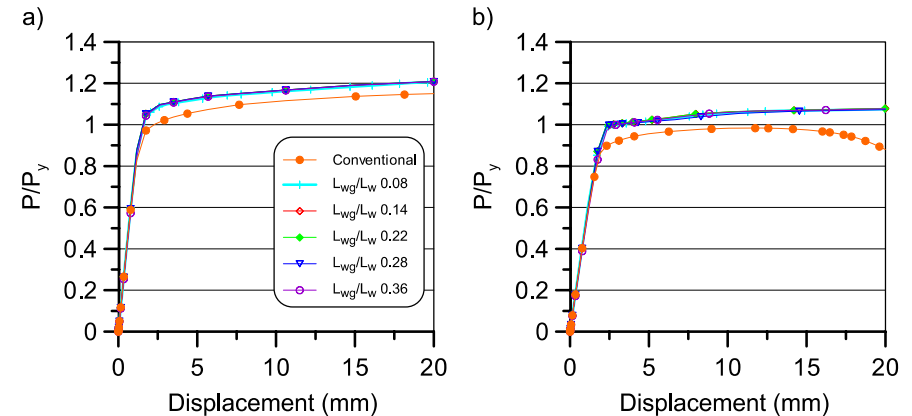


Figure 6. Global Load-Displacement for Tube $L_w/w$ = 1.07:a) Material 1, b) Material 2

tube to yield on the gross area for both materials. The conventional connection is unable to reach the same ultimate load as the MHG connections due to yielding on the net cross-sectional area. The tube with the conventional connection is able to yield for Material 1 due to a favourable $F_u/F_y$, but unable to yield for Material 2.

The local PEEQ-displacement response at location 1 in front of the weld for Materials 1 and 2 is shown in Figures 7a and 7b, respectively. As expected, the PEEQ is the highest for the conventional connection for both materials. An increase in the $L_{wg}/L_w$ ratio leads to a decrease in plastic strains for both materials. However, there is little reduction in plastic strains for $L_{wg}/L_w$ values between 0.14 – 0.28 for both connections. The plastic strains for $L_{wg}/L_w$ of 0.36 begin to increase for both materials. This is attributed to local flexural demand at the gusset plate, as discussed later.

The local PEEQ-displacement response at location 2 along the tube for Materials 1 and 2 is shown in Figures 8a and 8b, respectively. Location 3 at the tube reaction end has the same PEEQ as location 2 for the same overlap length within each material and thus is not shown here. For both materials, there is an increase in the plastic strains along the tube with increasing overlap length. This behaviour is desirable

since yielding occurs over the gross cross-sectional area and not in the connection region. There is no improvement in behaviour between overlap ratios of 0.14-0.28 for both materials. The connection performance decreases for an overlap ratio of 0.36 as seen by a decrease in the tube`s plastic strains. This decrease is discussed later. The conventional connection is unable to develop tube yielding for Material 2 and inelastic demand is concentrated in the weld region which may trigger early fracture.
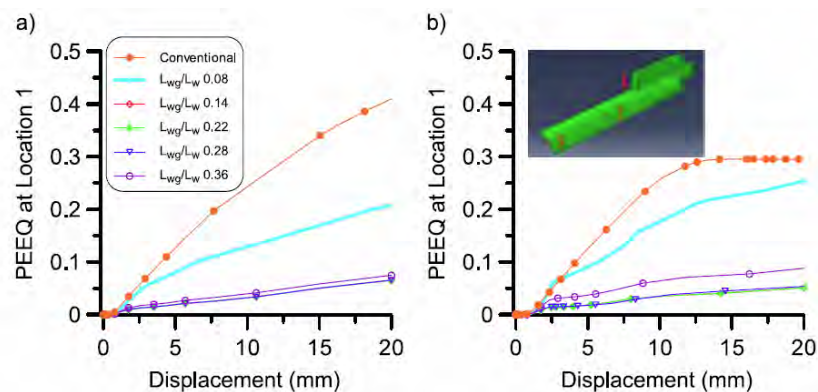


Figure 7. PEEQ at Location 1 vs. Displacement for Tube $L_w/w = 1.07$: a) Material 1, b) Material 2



Figure 8. PEEQ at Location 2 vs. Displacement for Tube $L_w/w = 1.07$: a) Material 1, b) Material 2

Figure 9a shows how flexural demand is created in the gusset plate due to the overlap length. This demand arises due to the eccentricity between the force at the weld and the centroid of the part of the gusset plate that extends outside the tube diameter. As the overlap length is increased, the load that is transferred from the tube to the weld increases, subsequently leading to an increase in flexural demand.

Figure 9b shows the PEEQ at location 4 where the weld begins on the gross cross-sectional area of the tube for Material 2. The PEEQ is approximately the same for overlap ratios between 0.08-0.28. However, the PEEQ increases by 250% for an overlap ratio of 0.36. It is assumed that the flexural demand is responsible for an

increase in plastic strains at location 1 (Figure 7b) and a decrease in plastic strains at location 2 (Figure 8b). The gusset plate was widened in the FE model and the plastic strains decreased by 35% at location 4, but the plastic strains at locations 1 and 2 remain relatively unchanged. This behaviour is undesirable since gusset bowing may occur which may result in reduced brace ductility. Similar behaviour was observed for the connection with a brace of Material 1. Further studies are required to quantitatively assess the influence of the geometry on this behaviour.
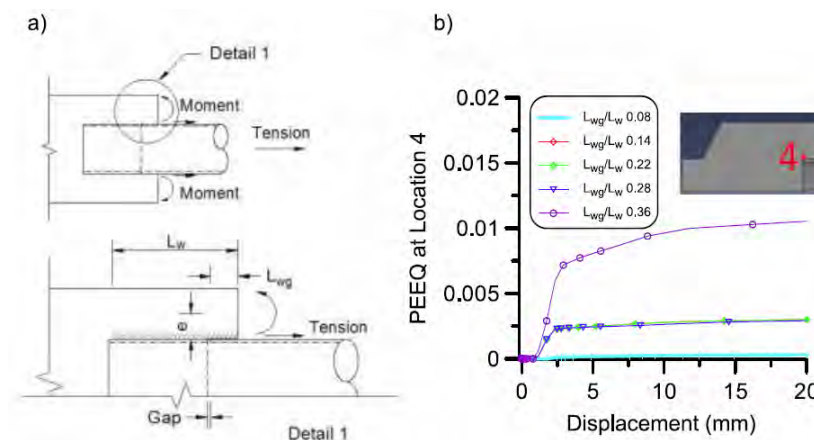


Figure 9. a) MHG Connection Detail showing Flexural Demand, b) PEEQ at Location 4 for Tube $L_w/w = 1.07$ Material 2
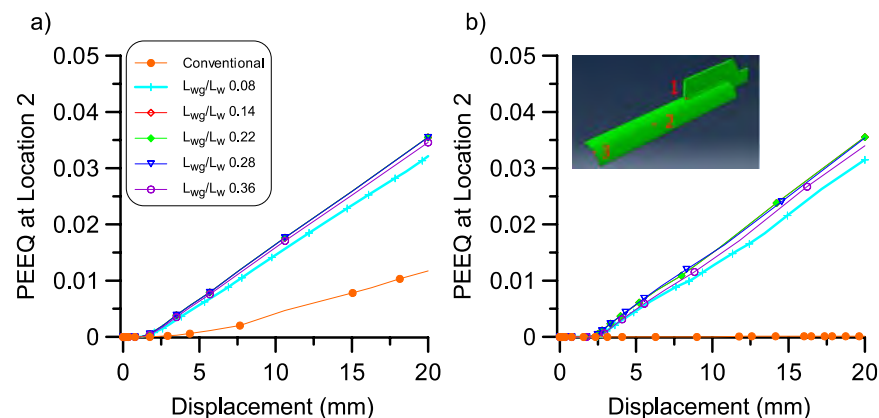
### 4.2. Influence of Weld Length

Shear lag reduces a brace`s tensile resistance by concentrating plastic strains at the weld region. Therefore, shear lag effects were investigated by reducing the weld length to a practical limit while preventing any other tensile failures such as block shear in the tube and gusset plate, and weld fracture. Martinez-Saucedo and Packer (2009) suggested that net-section tube fracture with shear lag will occur for $L_w/w$ between 0.7 – 1.0. A value of 0.75 was therefore chosen for comparison with the previous case of $L_w/w = 1.07$.

Figure 10a shows the global load-displacement response for Material 1 for two $L_w/w$ ratios. Only the extreme overlap ratios, $L_{wg}/L_w$, of 0.08 to 0.36 are provided since the other overlap lengths lie between these extremes. Figure 10c shows the corresponding PEEQ at location 1 in front of the weld. When little shear lag exists ($L_w/w = 1.07$), the maximum brace load is the same for all overlap lengths (Figure 10a). However, there is a gradual increase in the maximum brace load with increasing overlap lengths for $L_w/w$ of 0.75. This can be explained by examining Figure 10c which shows that there is significant connection deformation for an overlap ratio of 0.08 compared to 0.36 (dotted lines) for $L_w/w$ of 0.75.

Furthermore, shear lag leads to a drop in connection stiffness due to early yielding near the weld region and thus higher displacements are required to achieve the brace yield load for a low overlap ratio. Similar behaviour was observed for Material 2 (Figure 10b). However, the reduction in connection stiffness is more evident as larger displacements are required to achieve yield load. Figure 10d suggests that these

www.steelconstruct.com

displacements are concentrated in the connection region as opposed to along the tube when $L_w/w$ is high. Thus, a material with lower ductility ($F_u/F_y = 1.08$) coupled with shear lag ($L_w/w = 0.75$) leads to poor connection behaviour.
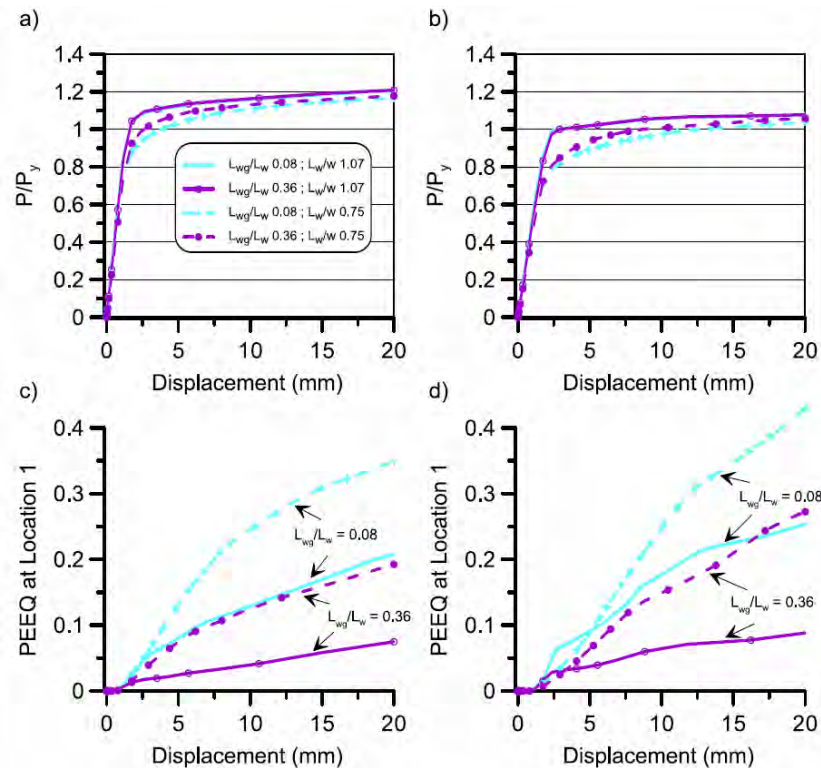


Figure 10. Global Load-Displacement for Overlaps 0.08 & 0.36 for Tubes $L_w/w$ 0.75 & 1.07: a) Material 1, b) Material 2. Corresponding PEEQ at Location 1: c) Material 1, d) Material 2.

## 5. CONCLUSIONS

This parametric study has provided insight into the parameters affecting the MHG connection. Results have shown that the overlap length ratio, weld length and material properties contribute significantly to the performance of the MHG connection. In particular, the welding of the gusset plate to the gross area of the tube allows the tube to attain its yield strength on the gross area. Furthermore, the stiffness of the connection allows inelastic demand to be distributed along the tube and away from the connection region, compared to the conventional connection which concentrates inelastic demand into the weld region. A higher $F_u/F_y$ ratio leads to overall better connection performance especially for low $L_w/w$ where shear lag is dominant. Moreover, there is a range of overlap lengths when the brace ultimate loads, as well as the plastic strains along the tube remain constant. High overlap lengths lead to gusset plate yielding due to the flexural demand and an increase in the plastic strains at the weld region.

## 6. FUTURE WORKS

This parametric study was limited to CHS brace member connections; similar studies of rectangular (RHS) brace member connections are planned. These parametric studies will provide an invaluable tool in the decision-making process when selecting members and connection details for testing. At least two monotonic and two reversed cyclic tests are planned for RHS members using the MHG connection. These tests will be incorporated in further calibration of the FE model. The calibrated FE model will be used to investigate additional overlap lengths, welds length, as well as other geometric parameters such as gap size, gusset plate widths, tube size, etc.

## ACKNOWLEDGEMENTS

## REFERENCES

[1] AIJ, Recommendations for the design and fabrication of tubular truss structures in steel. Architectural Institute of Japan: Tokyo Japan, 2002.

[2] AISC, Seismic provisions for structural steel buildings, ANSI/AISC 341-10. American Institute of Steel Construction: Chicago, IL, USA, 2010.

[3] ASTM, Standard specification for cold-formed welded and seamless carbon steel structural tubing in rounds and shapes. American Society for Testing and Materials, West Conshohocken, PA, USA, 2010.

[4] CSA, General requirements for rolled or welded structural quality steel / structural quality steel G40.20/G40.21. Canadian Standards Assocation: Mississauga, ON, Canada, 2009.

[5] CSA, Design of Steel Structures S16. Canadian Standards Assocation: Mississauga, ON, Canada, 2009.

[6] Martinez-Saucedo, G. Slotted End Connections to Hollow Sections. PhD Thesis, University of Toronto, 2007.

[7] Martinez-Saucedo, G.; Packer, J. A., Static Design Recommendations for Slotted End HSS Connections in Tension. *Journal of Structural Engineering* 2009, *135* (7), 797-805.

[8] Martinez-Saucedo, G.; Packer, J. A.; Christopoulos, C., Gusset Plate Connections to Circular Hollow Section Braces under Inelastic Cyclic Loading. *Journal of Structural Engineering* 2008, *134* (7), 1252-1258.

[9] Mitsui, Y.; Kurobane, Y.; Endoh, K., Experimental study on ultimate strength and deformation capacity of welded tube-to-through gusset plate joints. *Journal of Structural Engineering* 1985, *31* (B), 145-156.

[10] Packer, J.A.; Chiew, S.P.; Tremblay, R.; Martinez-Saucedo, G., Effects of material properties on hollow section performance. *Proceedings of the Institution of Civil Engineers* 2010, *Structures and Buildings 163* (SB6), 375-390.

[11] Zhao, R.; Huang, R.; Khoo, H.A.; Cheng, J.J.R., Parametric finite element study on slotted rectangular and square HSS tension connections *Journal of Constructional Steel Research* 2009, *65*, 611-621.

www.steelconstruct.com

# EXPERIMENTAL VALIDATION OF A BRACE WITH TRUE PIN CONNECTIONS

Aurel Stratan[1], Dan Dubina[1,2], Ramona Gabor[1], Cristian Vulcu[1], Ioan Mărginean[1]
[1] *Department of Steel Structures and Structural Mechanics,*
*"Politehnica" University of Timisoara, Romania*
[2] *Romanian Academy, Timisoara Branch, Romania*
*aurel.stratan@ct.upt.ro, dan.dubina@ct.upt.ro, ramona.gabor@ct.upt.ro,*
*cristian.vulcu@ct.upt.ro, ioan.marginean@ct.upt.ro*

## ABSTRACT

Circular hollow section braces with "true pin" connections were adopted in the design of a 29 storey building located in Bucharest, Romania. The brace uses connections with gusset plates and pin. One of the brace connections has an eccentric pin, allowing for variation of the pin-to-pin length, which facilitates erection on one hand, and allows compensation for axial forces in braces due to gravity loads on the other hand. High strength steel was used for gussets and pin, in order to keep connection dimensions to a minimum. Finite element analyses and cyclic experimental tests were performed in order to validate the seismic performance of the brace and its connection. Four tests were performed on a scaled model of the brace, for two different pin-to-pin lengths.

## 1. INTRODUCTION

A multi-storey building with two underground and 29 levels above ground is under design in Bucharest, Romania by SC Popp & Asociatii SRL. In-plan dimensions of a typical floor are 52.0x25.6 m, while the total height amounts to 117.6 m. The structure uses steel framing for resisting gravity forces. In the transversal direction the main lateral force resisting system is composed of two reinforced concrete cores, while in the longitudinal one the cores are supplemented by steel braces located in the facade of the building. The braces are placed in X configuration developed over two storeys. This reduces the number of brace connections and helps in complying with code limitations on slenderness. Braces are realised from hot-finished Circular Hollow Sections (CHS) and have connections with pins. The structure was designed according to EN 1993-1-1 (2005) and P100-1 (2006) – the Romanian seismic design code, which is very similar to EN 1998-1 (2004). The connections were designed according to EN 1993-1-8 (2005).

There two brace configurations: developed over two storeys, of 9300 mm pin to pin length (see Figure 1a), and developed over one storey, with an additional connection at the beam from the intermediate storey, of 4200 mm pin to pin length (see Figure 1b). The initial design used the following cross-sections: D244.5x25, D244.5x20, D219.1x20, D219.1x16 and D219.1x10, all in S355 steel. One of the pins of each of the brace features an eccentricity of 5 mm, allowing a +/- 5 mm

adjustment of the pin to pin length of the brace. This allows for more relaxed erection tolerances on one hand, and reduces gravity-induced axial forces in the brace on the other hand, as the eccentric pin is mounted after casting of reinforced concrete floors.



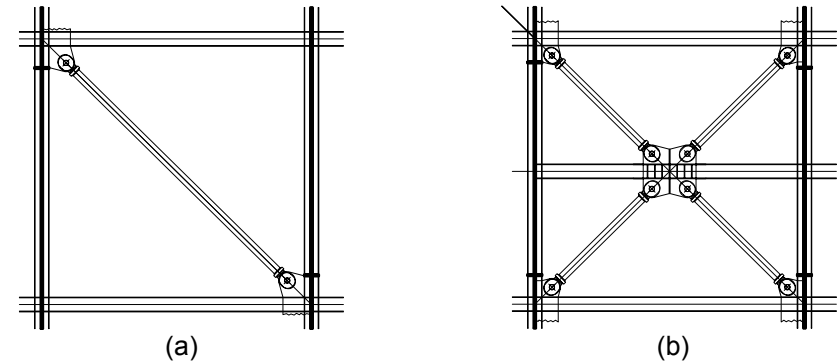(a)                                    (b)

Figure 1. Brace configurations in the analysed structure:
developed over two storeys (a) and one storey (b).

In order to have a validation of the seismic performance of the braces, a series of numerical simulations and experimental tests were performed, which are described in the following sections.

The non-dimensional slenderness $\bar{\lambda}$ of braces used in the structure varied between 1.53 and 1.72 for long braces (9300 mm), and between 0.69 and 0.78 for short braces (4200 mm). The buckling length as considered to be the distance between the pins. All braces were of class 1 according to EN 1993-1-1 (2005). Due to constraints imposed by the size of the testing platform and actuator stroke and capacity, reduced scale experimental models were adopted. The experimental specimens were chosen so as to reproduce the non-dimensional slenderness and cross-section class of braces used in the designed structure. As a result, a class 1 cross section of 139.7x6.3 was adopted, with the pin to pin brace length of 5900 mm and 2700 mm, having $\bar{\lambda}$ values of 1.64 and 0.75 respectively. The same steel grade as in the braces from the structure was used – S355J0H.

## 2. PRE-TEST FINITE ELEMENT ANALYSES

Pre-test finite element analyses were performed with the general purpose finite element code Abaqus. Firstly a connection model was analysed, followed by a complete model of the brace assembly.

### 2.1. Connection modelling

The connection of the 219.1x10 brace size was used for a detailed analysis. It consists of a central gusset connected through a pin to two external gussets, which are welded to the end plate using full-penetration welds. The initial connection design used S690Q grade steel for the pin, and S460N grade steel for the end plate and gussets. A tolerance of 1 mm on diameter was used between the pin and the gussets. Due to bearing resistance requirements, the central gusset resulted quite thick (68 mm). In order to reduce the weight of the structural steelwork and avoid disproportionate thicknesses at the welded connection between the central gusset and the beam/column,

the central gusset was locally reinforced with two welded plates (see Figure 2a). An alternative solution aiming at reducing both the thickness and the workmanship was also analysed, by adopting S690Q grade steel for the gussets. In this way, the central gusset could be realised using a single piece, without reinforcements (see Figure 2b).
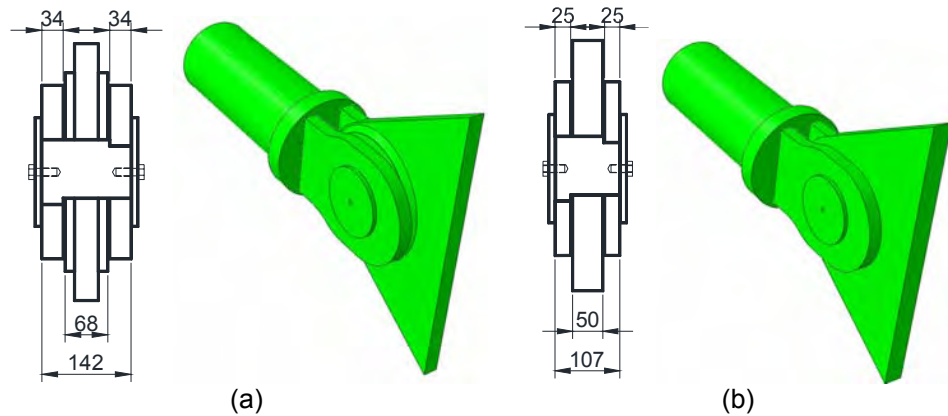


Figure 2. Connection geometry: initial design (a) and modified one (b).
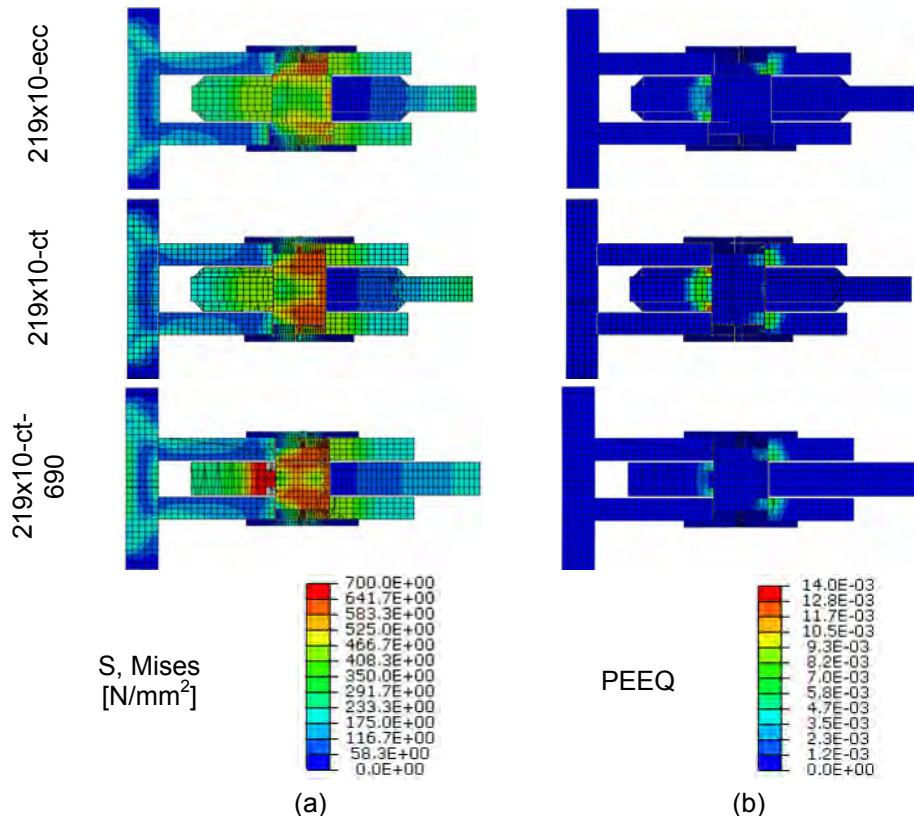


Figure 1. Distribution of von Mises stresses (a) and equivalent plastic strains (b).

The numerical model of the connection consisted of the central gusset, pin, washers, external gussets, end plate and a short portion of the CHS brace. It was discretized using three-dimensional continuum linear hexahedral elements with reduced integration and hourglass control – type C3D8R. Normal and tangential (with a coefficient of friction of 0.3) behaviour was defined at all surfaces in contact. Stress-strain relationships based on nominal material characteristics were used for all components, with the exception of the brace, for which an overstrength $\gamma_{ov}$=1.25 was applied to the yield strength. The model was subjected to tensile force equal to the design force according to EN 1998-1 (2004): plastic resistance of the brace amplified by overstrength and strain hardening (1.1·$\gamma_{ov}$ $N_{pl,Rd}$). The explicit solution method was used in all cases.

Table 1. Maximum values of von Mises stresses and equivalent plastic stains in connection models.

| Model | Pin | | External gusset | | Central gusset and reinforcements | |
|---|---|---|---|---|---|---|
| | $\sigma_{VM}$ [N/mm$^2$] | $\varepsilon_p$ | $\sigma_{VM}$ [N/mm$^2$] | $\varepsilon_p$ | $\sigma_{VM}$ [N/mm$^2$] | $\varepsilon_p$ |
| 219x10-ecc | 646.4 | 0.00527 | 464.0 | 0.00720 | 465.2 | 0.00938 |
| 219x10-ct | 639.5 | 0.00399 | 464.7 | 0.00800 | 471.2 | 0.01402 |
| 219x10-ct-690 | 638.9 | 0.00304 | 464.6 | 0.00772 | 706.2 | 0.00430 |

Three models were analysed: the initial one (S460N gussets and reinforced central gusset), with eccentric pin (model 219x10-ecc) and constant pin (219x10-ct), and the modified one (S690Q gussets and unreinforced central gusset) with constant pin (model 219x10-ct-690) – see Figure 1.

Minor plastic strains were observed in the pin and in the gusset plates of all models (see Figure 1 and Table 1). However plastic strains are local only, as they do not extend over the full cross-section. Thus, there is always a large portion of the pin or gusset that stays in the elastic range, providing the necessary strength of the connection. This behaviour is in agreement with the design followed, as the pin was designed as non-replaceable according to EN 1993-1-8 (2005).

The initial model with eccentric pin (219x10-ecc) showed slightly larger plastic strains in the pin, close ones in the external gussets and smaller ones in the central gusset and reinforcements, in comparison with the corresponding model with constant pin (219x10-ct). On the other hand, the model that used a single-thickness central gusset and higher strength steel in gussets (219x10-ct-690) showed slightly smaller plastic strains in the pin and in the external gussets, and considerably smaller ones in the central gusset, in comparison with the initial design (219x10-ct). This is attributed to the beneficial effect of reduced bending in the shorter pin of the modified model (219x10-ct-690). Considering the above observations, the modified model using S690Q gussets was adopted for the brace.

## 2.2. Assembly modelling

Full-size numerical models of the experimental specimens described in section 3 were analysed. Each brace assembly consisted of a connection with constant pin,

www.steelconstruct.com

the CHS brace and a connection with eccentric pin. The same parameters as in the connection modelling were adopted, with the exception of the brace, which was meshed using shell linear quadrilateral elements with reduced integration and hourglass control of type S4R. Considering the fact that behaviour in tension is not much different than the on observed on connection model, in the following the behaviour in compression is described. Residual stresses in the brace member were ignored, as they are very low in hot-finished tubes (Ziemian, 2010). An initial imperfection of the member equal to 1/500 of the pin to pin length (the maximum delivery tolerance allowed per EN 10210-2, 2006) was considered, in the form of a circular arc. During preliminary numerical simulations, it became clear that the brace assembly is susceptible to out-of-plane buckling (out of plane of the connection). In this particular case out of plane deformations are detrimental mainly due to two reasons: (1) the rotation in the connections is perpendicular to the intended one, leading to stress concentrations and possible failure not accounted for in its design, and (2) large out of plane deformations of the brace would damage non-structural components (building facade). In order to account for the worst situation, member imperfection was oriented predominantly out-of-plane (7.5° with respect to the direction perpendicular to the plane of the gussets).

Several models of brace assemblies were subjected to compression in displacement control, up to a displacement of 30 mm, well into the post-buckling range. Figure 2a shows the deformed shape at the maximum displacement of the brace assembly with a pin to pin distance of 2700 mm, with nominal geometry and initial imperfections as described above (SP27N-C model). Lateral deformations follow the initial member imperfection and are predominantly out of plane. In an effort to understand the causes of this behaviour, two other models were derived from the reference one: with lateral deformations forced in plane (SP27N-CI) and out of plane (SP27N-CO), through some rigid frictionless surfaces. As can be seen from Figure 2b, the buckling strength of the SP27N-CI model is larger than of the SP27N-CO, the response of the reference model (SP27N-C) being basically identical to the one of the latter.

The reason for out of plane buckling of the brace, apart from the quite unfavourable orientation of the initial imperfections, is the connection itself and the circular shape of the cross-section. The in-plane connection rotation is not totally free due to friction between its components (pin and gussets). On the other hand, out of plane behaviour of the connection is very close to a perfect pin at small rotations, due to the clearance between the pin and the holes in the gussets (1 mm on diameter), as well as between the central and lateral gussets (1.5 mm). In the conditions described above, at initial stages of loading lateral deformations develop mainly in the direction of initial imperfections (out of plane). Once the wedging of the gussets and the pin occurs, out of plane rotation of the connection is not free any more, though its in-plane rotations is also restrained to some extent due to additional friction between the gussets and the pin. With reference to the SP27N-C series of models (see Figure 2b), even if the post-buckling strength of the SP27N-CI model is smaller than the one of the SP27N-CO one, "switching" to in-plane buckling at large deformations is restrained by the friction developed between the gussets and the pin, as a result of out of plane rotations of the connection.

A possible solution was sought in the form of a design initial connection eccentricity specified in the plane of the connection (SP27NE-C series of models, see Figure 6a). The magnitude of the eccentricity (4 mm) was chosen close to the maximum initial bow imperfection of the member (L/500 = 5.4 mm). As can be seen in Figure 3a, the behaviour of the brace improved somehow, lateral deformations of the brace in the post-buckling range being predominantly in the plane of the connection, though with important component in the out of plane direction. The in-plane buckling strength (model SP27NE-CI, see Figure 3b) is now only slightly higher than the out of plane one (model SP27NE-CO). Though the reference model (SP27NE-C) buckles initially out of plane, in the post-buckling range lateral deformations develop predominantly in-plane.

A further improvement of the response of the assembly was obtained by welding two 14x14 squares along the tube perpendicular to the plane of the connection (see Figure 4a). It increases the out of plane stiffness of the tube, decreasing the out of plane lateral deformation of the brace in favour of the in-plane ones. The buckling strength of the model with lateral deformations forced in plane (SP27NES-CI) is now very close to the one of the model with lateral deformations forced out of plane (SP27NES-CO), see Figure 4b. Furthermore, the post-buckling strength of the reference model (SP27NES-C) is now very close to the one of SP27NES-CI. Additionally, this in following model used strengthened washers securing the pin (see Figure 6b).
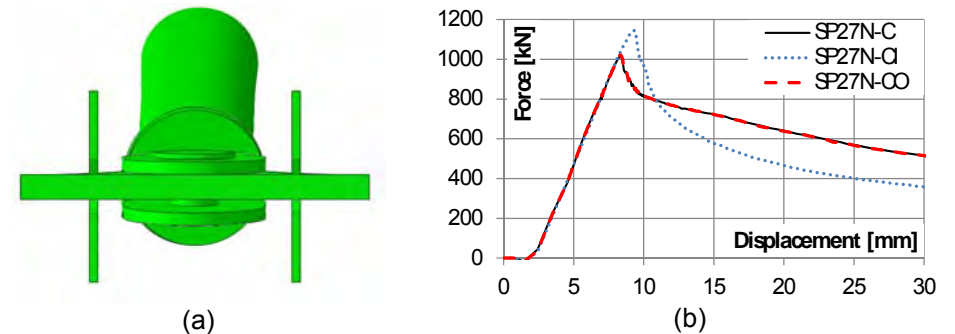


(a)　　　　　　　　(b)

Figure 2. Deformed shape of the SP27N-C model at the maximum displacement (a) and the force-displacement relationship for SP27N-C series of models (b).
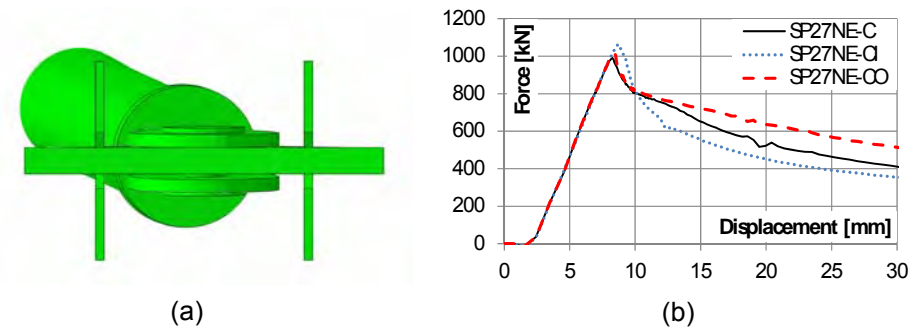


(a)　　　　　　　　(b)

Figure 3. Deformed shape of the SP27NE-C model at the maximum displacement (a) and the force-displacement relationship for SP27NE-C series of models (b).
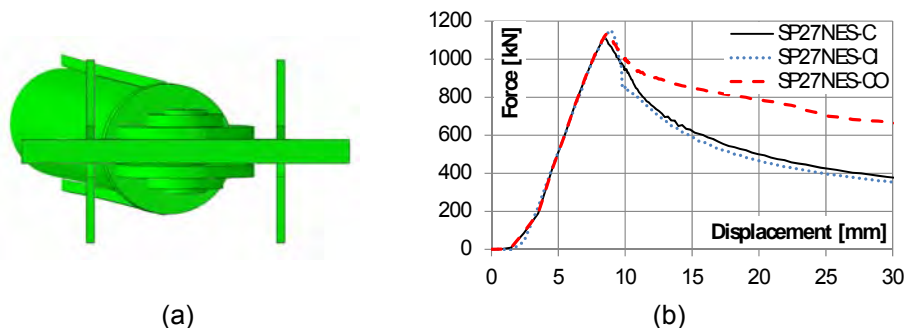
　　　www.steelconstruct.com

(a)

(b)

Figure 4. Deformed shape of the SP27NES-C model at the maximum displacement (a) and the force-displacement relationship for SP27NES-C series of models (b).
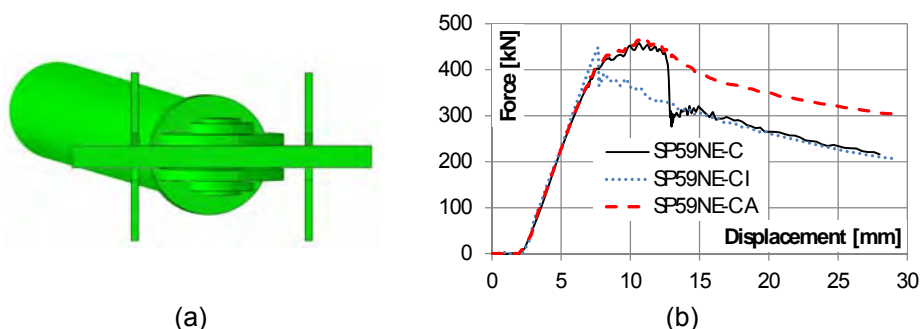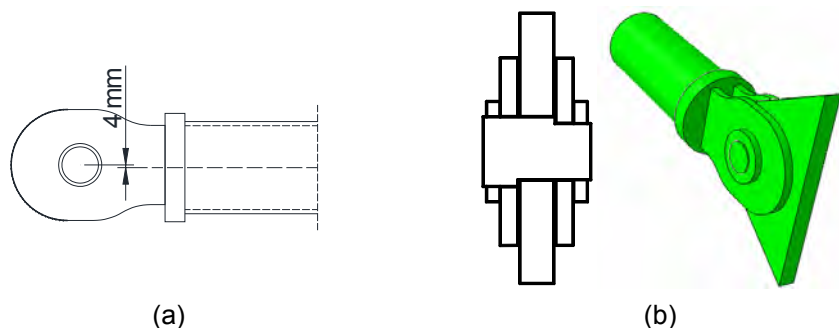


(a)

(b)

Figure 5. Deformed shape of the SP59NE-C model at the maximum displacement (a) and the force-displacement relationship for SP59NE-C series of models (b).s



(a)

(b)

Figure 8. Connection eccentricity (a) and improved connection detailing (b).

The model of the longer brace (5900 pin to pin length) used the same connection eccentricity (4 mm), but no longitudinal stiffeners. In the post-buckling range lateral deformations are predominantly in the plane of the connection (see Figure 7a), though the in-plane buckling strength is slightly larger than the out of plane one (see Figure 7b). The SP59NE-C model initially develops mainly out of plane lateral deformations, but, at about 12 mm axial deformation, when the in-plane moment imposed on the connection becomes larger than the resisting one due to friction, a sudden switching to in-plane buckling takes place, which becomes the governing post-buckling behaviour.

## 3. EXPERIMENTAL PROGRAM

The experimental program included 4 braces subjected to cyclic loading, overviewed in Table 1. Specimen SP27-1 used the connection configuration shown in Figure 2b, with weak washers. All other specimens used longer pins with strong washers securing the pins (see Figure 8b). The SP27-2 specimen had two 14x14 squares welded along the tube in a plane perpendicular to the one of the connection. A design connection eccentricity of 4 mm in the plane of the connection was required for all specimens. After fabrication of specimens, imperfections were measured. They revealed that initial member imperfections were quite small: 1.19, 0.91, 2.28, 2.21 mm for SP27-1, SP27-2, SP59-1 and SP59-2 respectively. However, measured connection eccentricities were large: between -1.58 mm and +2.41 mm in the out of plane direction (+/-0.0 specified), and between -5.67 mm and +4.07 mm in the plane of the connection (+4.0 specified). This did not allow full experimental assessment of the effectiveness of design connection eccentricity. All 4 specimens were subjected to cyclic loading according to ECCS (1985) protocol. The cyclic tests consisted of four cycles in the elastic range (±0.25Dy, ±0.5Dy, ±0.75Dy and ±1.0Dy), followed by groups of three cycles at amplitudes multiple of 2Dy (3x±2Dy, 3x±4Dy, 3x±6Dy, etc.). The yield displacement Dy was determined from numerical simulations using mechanical properties of materials obtained from tensile tests. The loading was applied quasi-statically, in displacement control.

Table 2. Experimental program.

| Specimen | Pin to pin length [mm] | Cross-section | Cross section class | $\bar{\lambda}$ | Loading protocol |
|---|---|---|---|---|---|
| SP27-1 | 2700 | D139.7x6.3 | 1 | 0.75 | Cyclic, first cycle in tension |
| SP27-2 | 2700 | D139.7x6.3 with reinforcements | 1 | 0.68 | Cyclic, first cycle in compression |
| SP59-1 | 5900 | D139.7x6.3 | 1 | 1.64 | Cyclic, first cycle in tension |
| SP59-2 | 5900 | D139.7x6.3 | 1 | 1.64 | Cyclic, first cycle in compression |

The SP27-1 specimen buckled out of plane (see Figure 9) in the first cycle of 2Dy. The washers used to keep the pins into position where fixed to the pin using M6 screws. Due to out of plane buckling, the screws broke, the washers fell off, letting exterior gusset plates bend out of plane. This caused partial loss of contact between the pin and the outer gusset plates, with rapid loss of load bearing capacity of the specimen (see Figure 12).

Due to favourable initial imperfections and connection eccentricities, as well as due to the improved connection design (strong washers securing the pin) and the two 14x14 squares welded along the tube, the SP27-2 specimen buckled in the plane of the connection (see Figure 10a). Failure took place during the first tension cycle at 6Dy due to fracture of the cross section which experienced local buckling in previous compression cycles (see Figure 12).

The SP59-1 specimen buckled in the plane of the connection, failure taking place at significant plastic deformations – 16Dy (see Figure 12). Failure was caused by fracture in tension due to progressive local buckling of the brace in compression (see Figure 10b). The SP59-2 specimen experienced similar level of plastic deformations – 16Dy (see FGigure 12). However, it first buckled out of plane (see Figure 11a). However, starting with the 4Dy cycles, the buckling changed progressively to in-plane one (see Figure 11b), failure taking place similar to the previous specimen (see Figure 11c).



Figure 9. Failure mode of the SP27-1 specimen.



(a)                                    (b)

Figure 10. Failure mode of the SP27-2 (a) and SP59-1 (b) specimens.
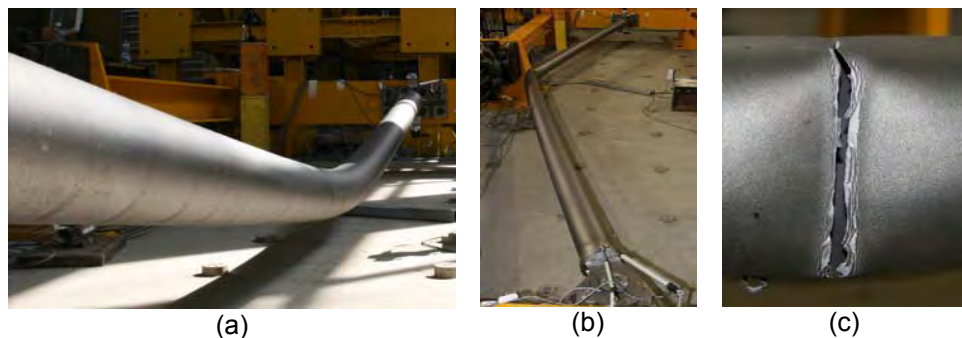


(a)                    (b)                    (c)

Figure 11. Specimen SP59-2: out of plane bucking (a), followed by in-plane buckling (b), and rupture of the cross-section (c).
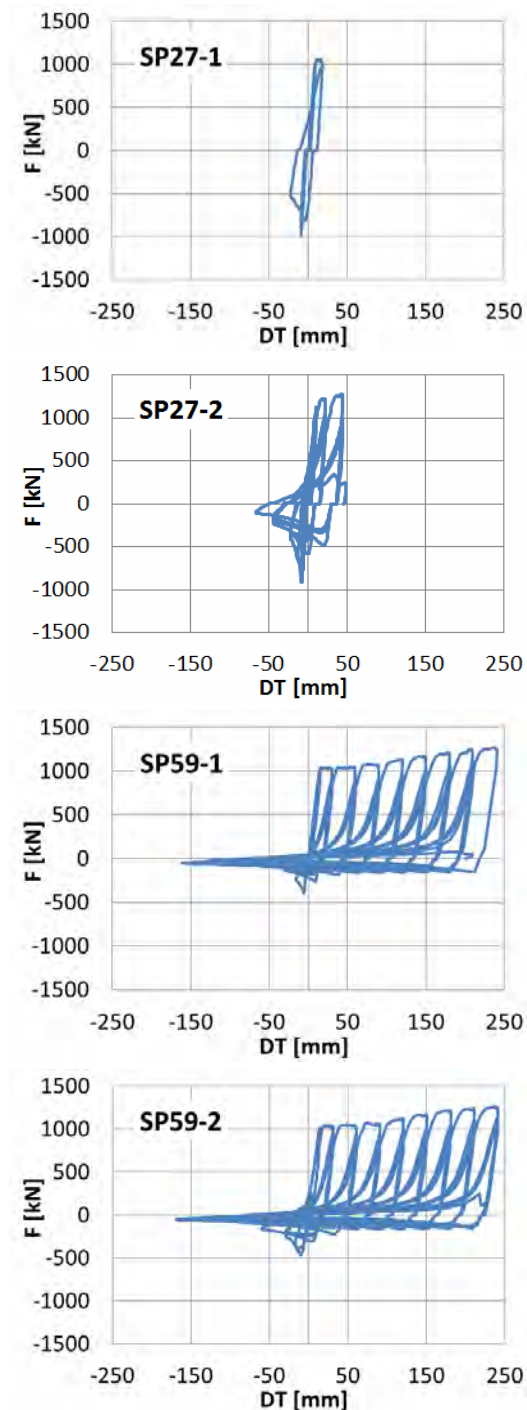


Figure 12. Force – axial deformation curves of the experimental specimens.

Welds between the tube and end plate, as well between end plate and gussets performed adequately in all cases. The cyclic response of the tubular member was similar to the one characteristic for structural hollow sections. The total ductility at fracture, $\mu_F$ (Tremblay, 2002) was considerably larger for longer braces (amounting to 4.3 for SP27-1, 9.6 for SP27-2, 26.6 for SP59-1, and 28.3 for SP59-2 specimens). Some pinching was caused by slip in the connection with pins and rotation of the eccentric pin, additionally to the one experienced due to brace buckling. Connection deformation amounted roughly to 17% and 6% of the total one for short and long specimens respectively.

## 4. CONCLUSIONS

Numerical simulations and experimental testing were performed in order to validate the design of pinned brace for a seismic resistant multi-storey building. Based on finite element numerical simulations, a more compact solution was proposed and adopted, using high-strength steel components.

Due to connection detailing and tubular shape of the cross-section, the brace assembly was shown to be sensitive to out of plane buckling, leading to failure of the connection in a brittle way. Firmly fixing the washers to the pin helps preventing brittle failure of the connection, even when buckling takes place out of the plane of the connection.

The main causes of out of plane buckling are (1) the free out of plane rotations of the connection at small deformations due to the tolerance between the pin and the hole in gussets, (2) friction that restrains to some extent in-plane rotations of the connection and (3) initial member and connection imperfections. In-plane buckling of the brace assembly is favoured by the following: (1) design in-plane connection eccentricity, (2) reduction of out of plane rotation of the connection through smaller tolerances at the pin or larger spacing between gussets, (3) lower friction at the pin – gussets interface, (4) slender braces, and (5) brace cross section with different moments of inertia about the two principal axes (elliptical, RHS, wide flange).

## ACKNOWLEDGMENTS

## REFERENCES

[1] Abaqus. Analysis User's Manual. Version 6.8. Dassault Systèmes Simulia Corp., Providence, Rhode Island, U.S.A.

[2] ECCS (1985). Recommended Testing Procedures for Assessing the Behaviour of Structural Elements under Cyclic Loads. European Convention for Constructional Steelwork, Technical Committee 1, TWG 1.3-Seismic Design, No. 45.

[3] EN 10210-2 (2006). European Committee for Standardization – CEN. Hot finished structural hollow sections of non-alloy and fine grain steels - Part 2: Tolerances, dimensions and sectional properties, Brussels.

[4] EN 1993-1-8 (2005). European Committee for Standardization – CEN. Eurocode 3: Design of steel structures - Part 1-8: Design of joints, Brussels.

[5] EN 1993-1-1 (2005). European Committee for Standardization – CEN. Eurocode 3, Design of steel structures - Part 1-1. General rules and rules for buildings, Brussels.

[6] EN 1998-1 (2004). European Committee for Standardization – CEN. Eurocode 8: Design of structures for earthquake resistance - Part 1: General rules, seismic actions and rules for buildings, Brussels.

[7] P100-1 (2006). Seismic design code P100: Part I: Design rules for buildings (in Romanian).

[8] Tremblay, R. (2002). "Inelastic seismic response of steel bracing members." Journal of Constructional Steel Research, 58, 665–701.

[9] Ziemian, R.D. (2010). "Guide to Stability Design Criteria for Metal Structures". Sixth edition. John Wiley & Sons, Inc., USA.

# CONNECTION STUDIES AND RESEARCH NEEDS

**Reidar Bjorhovde**
The Bjorhovde Group, Tucson, Arizona, USA
rbj@bjorhovde.com

**Riccardo Zandonini**
University of Trento, Trento, Italy
riccardo.zandonini@unitn.it

## ABSTRACT

The paper summarizes the research needs that have been identified by the workshop authors. The subjects include the items that have been discussed in the various technical sessions, as follows: (1) Structural design and design codes; (2) Methods of analysis; (3) Connections for seismic effects; (4) Connections with hollow structural sections (HSS); (5) Bolting and special connection topics; and (6) Bracing and truss connections.

## 1. INTRODUCTION

The Seventh International Workshop on Connections in Steel Structures has presented a range of subjects that address the state-of-the-art. Based on advanced analytical and experimental studies, the subjects incorporate a variety of issues. Specifically, the topics are related to serviceability and ultimate limit states, deformation demands and capacities, and suitable design code requirements. The material that is presented in the following sections is by necessity only brief descriptions of each subject, given in the form of bullet points, and identifying the sources (*authors or other contributors*) of the recommendations.

## 2. STRUCTURAL DESIGN AND DESIGN CODES

- Code requirements for structural robustness and structural integrity, considering local and overall limit states (*Carter and Duncan*)
- Assessment of American and European connection design requirements, with a view towards harmonization (*Marinopouloulou, Kardaras and Palamas*)
- Solutions for the limit states of thin-walled members that incorporate realistic distortional failure modes (*Weynand, Oerder and Demonceau*)
- Comprehensive examination of the bearing resistance limit states of bolted connections (*Moze and Beg*)
- Strength and practical design models for column base connections under monotonic loads (*Latour, Piluso and Rizzano*)

- Models of behavior and strength of trapezoidal shear panels in connections (*Bayo, Loureiro, Lopez and Gil*)
- Re-assessment of the tensile strength of connections with staggered bolt in various steel grades (*dos Santos, A.T. da Silva, de Lima, da Silva Vellasco, de Andrade and J.G.S. da Silva*)
- Block shear strength model for bolted connections in stainless steel (*Teh and Clements*)

## 3. METHODS OF ANALYSIS

- Theoretical and physical evaluation of the rotation capacity of partial strength steel connections (*Girao Coelho and Bijlaard*)
- Development of simplified expressions for the flexibility characteristics of connections (*Kozlowski and Sleczka*)
- Influence of the stiffness of realistic base connections on the computed drift of metal building portal frames (*Charney, Verma, Bajwa and Moen*)
- Influence of the types of connections on the seismic behavior of moment-resistant frames (*Montuori, Piluso and Troisi*)
- Influence of steel-to-concrete beam-to-column connections on the flexural and shear strength of beams in seismically loaded frames (*Ciutina, Danku and Dubina*)
- Low-cycle performance of T-stub components in bolted beam-to-column moment connections (*Pop, Grecea and Ciutina*)

## 4. CONNECTIONS FOR SEISMIC EFFECTS

- Seismic design procedures for bolted top-and-seat angle connections (*Schippers, Ruffley, Rassati and Swanson*)
- Modeling for finite element analysis to develop moment-rotation curves for shear tab connections (*Schroeder, Barber, Rassati and Swanson*)
- Development of innovative bolted beam-to-column connections for seismically resistant building frames (*Comeliau, Demonceau and Jaspart*)
- Advanced behavior and design criteria for post-tensioned column bases for self-centering moment-resisting frames (*Chi and Liu*)
- Damage behavior and modeling of welded connections in frames subjected to severe earthquakes (*Y. Shi, Weng, G. Shi, Xiong and Wang*)
- Behavior and strength of T-stub friction beam-to-column connections subjected to cyclic loads (*Latour, Piluso and Rizzano*)
- Non-linear behavior and strength of shear lugs and their effect on the response of steel buildings (*Aguirre*)
- Effect of reduced beam section (RBS) coupling beams on the seismic response of moment-resistant frames (*Dinu, Dubina, Vulcu, Neagu and Both*)
- Seismically resistant welded connections for concrete-filled tubular columns and wide-flange beams (*Vulcu, Stratan and Dubina*)

## 5. CONNECTIONS WITH HOLLOW STRUCTURAL SECTIONS (HSS)

- Experimental validation of the outcomes of FE analyses of I-beam to CHS column moment connections with external diaphragms for use in seismic design (Sabbagh and Chan)
- Development of design guidelines and models of flange continuity joints between RHS under biaxial bending under ambient and fire conditions (Perttola and Heinisuo)
- Evaluation of the accuracy of formulae to weld design for RHS connections, applicable to branch bending loads. (McFadden, Sun and Packer)
- Assessment of the need for a ultimate deformation limit in the design of tubular joints (da Silva, de Lima, da Silva Vellasco and da Silva)
- Calibration of the component method applied to base plate joints of tubular columns (Horova, Tomsu and Wald)
- Enhancement of the proposed model of bolted flange joints of CHS to better incorporate prying forces and to extend it to base plate conditions (Couchaux, Hjiaj and Ryan)

## 6. BOLTING AND SPECIAL CONNECTION TOPICS

- Technological enhancement of the friction stir welding tools to ensure economic viability in practical applications for steel structures (Surovek, Jasthi and Widener, and Gabor and dos Santos)
- Assessment of the fire robustness of sub-frames in composite structural systems (Haremza, Santiago and da Silva)
- Validation of design models for joints between composite beams and concrete walls (Henriques, da Silva and Valente)
- Comprehensive models for endplate joints subject to combined actions (Baldassino, Mancini and Zandonini)
- Reliability and design of welded stud connectors in high strength steel grades (Ungermann and Trillmich)
- Comprehensive design criteria for injection bolts in serviceability and ultimate conditions (Gresnigt, Beg and Bijlaard)
- Design models for the bearing resistance of bolted joints with non-rectangular plate endings (de Vries, Bijlaard and Gresnigt)
- Validation and extension of simplified models of joints in pitch-roof cold formed portal frames (Nagy)
- Innovative solutions for use of steel braces in seismic retrofitting of r.c. frames (Dogariu, Bordea and Dubina)

### BRACING AND TRUSS CONNECTIONS

- Characterization of different possible connection buckling modes in X-braced frames for ductile seismic response (Davaran, Gelinas and Tremblay)
- Enhanced seismic behavior of CBF by dissipative devices (Tirca, Caprarelli, Danila and Calado)

- Mechanical joints without connecting devices (Szlendak)
- Connection detailing in CBF with tubular bracings (Moreau, Rogers, Tremblay and Packer)
- Design and fabrication of 'true' pinned bracing's connections (Stratan, Dubina, Gabor and Vulcu)

## 7. CONCLUSIONS AND ACKNOWLEDGEMENTS

A very large number of studies of connections and structural systems have been identified. Sincere appreciation is extended to the participants in the workshop for their work in preparing the written contributions and their active participation in all technical discussions.

This is the hallmark of a leading research community, providing continuing advances towards improved understanding of behavior and strength, as well as the development of innovative tools for design and fabrication. The efforts towards the international design code community are very useful and highly regarded.

Particular appreciation and thanks are extended to the Polytechnic University of Timisoara for the extensive efforts in the arrangements of the connections workshop. Significant support was provided by the American Institute of Steel Construction (AISC) and the European Convention for Constructional Steelwork (ECCS), which sponsored the Seventh International Workshop on Connections in Steel Structures together with the Polytechnic University of Timisoara and the Romanian Academy. Special thanks are warmly extended to professors Dan Dubina and Daniel Grecea and their colleagues and staff for very fine arrangements and staff work.
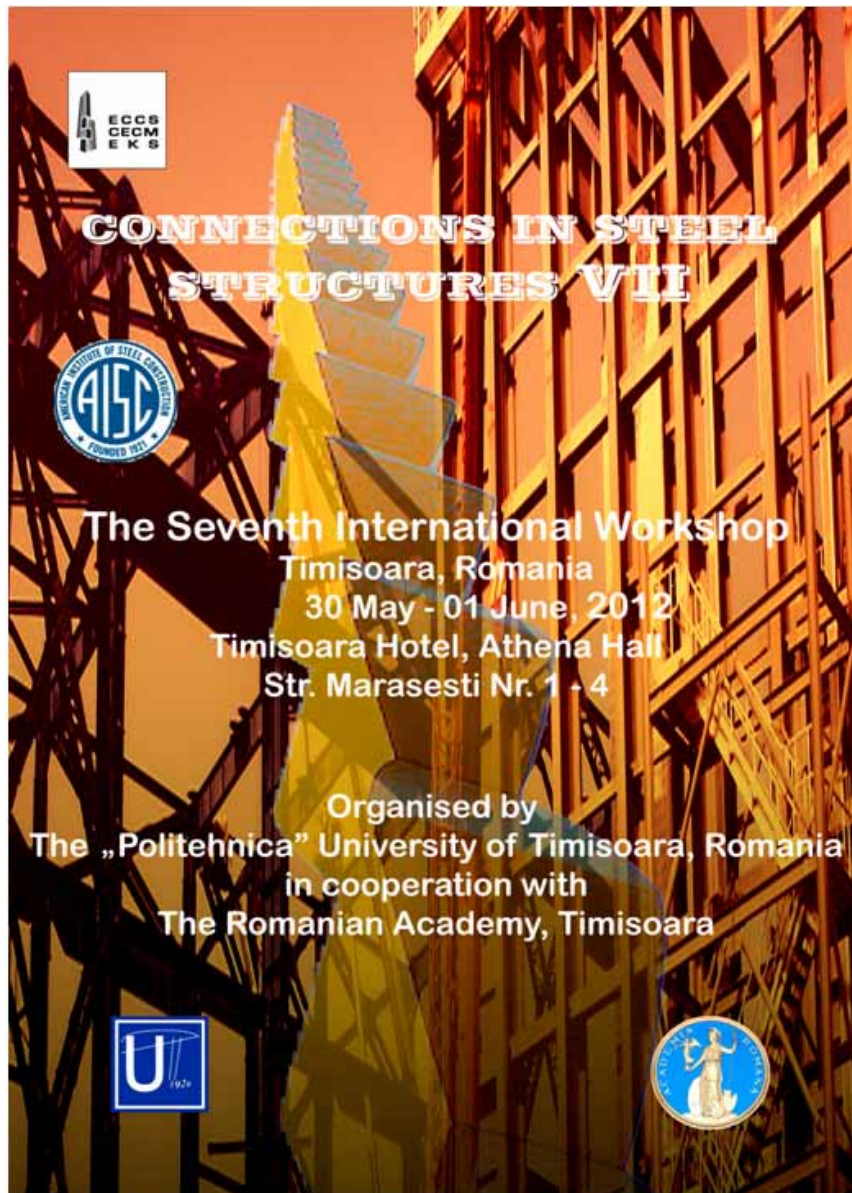
# PARTICIPANTS – CONNECTIONS VII WORKSHOP

Bjorn Aasen .............................. Norconsult AS, Norway

Carlos Aguirre ........................... Technical University Federico Santa Maria, Chile

Eduardo Bayo ............................ University of Navarra, Spain

Edwin Belder ............................. Iv- Consult b.v., The Netherlands

Frans Bijlaard ............................ Delft University of Technology, The Netherlands

Reidar Bjorhovde ..................... The Bjorhovde Group, USA

Ioan Both ................................... Politehnica University of Timisoara, Romania

Charles J. Carter ....................... American Institute of Steel Construction, USA

Tak Ming Chan .......................... University of Warwick, UK

Finley Charney ......................... Virginia Polytechnic Institute, USA

Adrian Ciutina ........................... Politehnica University of Timisoara, Romania

Maël Couchaux ........................ CTICM, France

Jean-Francois Demonceau ....... University of Liège, Belgium

Florea Dinu ............................... Politehnica University of Timisoara, Romania

Adrian Dogariu ......................... Politehnica University of Timisoara, Romania

Dan Dubina ............................... Politehnica University of Timisoara, Romania

Norin Filip-Vacarescu .............. Politehnica University of Timisoara, Romania

Ramona Gabor ........................... Politehnica University of Timisoara, Romania

Mircea Georgescu .................... Politehnica University of Timisoara, Romania

Ana Girao Coelho ................... Institute of Computers and Systems Engineering of Coimbra (INESCC), Portugal

Daniel Grecea ........................... Politehnica University of Timisoara, Romania

A.M. (Nol) Gresnigt ................. Delft University of Technology, The Netherlands

Gorka Iglesias .......................... GRUPO CONDESA, Spain

Adriana Ioan ............................. Politehnica University of Timisoara, Romania

Jean-Pierre Jaspart .................... University of Liège, Belgium

Helmuth Kober ......................... Technical University of Construction Bucharest, Romania

Aleksander Kozlowski ............. Rzeszów University of Technology, Poland

Luciano Lima ........................... State University of Rio de Janeiro, Brazil

Judy Liu ................................... Purdue University, USA

Abdul Malik ............................. The Steel Construction Institute, UK

Ionel Marginean ...................... Politehnica University of Timisoara, Romania

David Moore ............................ British Constructional Steel Association, UK

Primoz Moze ........................... University of Ljubljana, Slovenia

Zsolt Nagy ............................... Technical University of Cluj-Napoca, Romania

Calin Neagu ............................. Politehnica University of Timisoara, Romania

Rene Oly ................................. LINDAB S.A., Luxembourg

Jeffrey A. Packer ..................... University of Toronto, Canada

Henri Perttola .......................... Tampere University of Technology, Finland

Vincenzo Piluso ...................... University of Salerno, Italy

Dan Pintea ............................... Politehnica University of Timisoara, Romania

Anamaria Pop .......................... Politehnica University of Timisoara, Romania

Gian Andrea Rassati ................. University of Cincinnati, USA

Gianvittorio Rizzano ................ University of Salerno, Italy

Colin Rogers ........................... McGill University, Canada

Aldina Santiago ...................... University of Coimbra, Portugal

Marcel Schneider .................... V&M Deutschland GmbH, Germany

Luis Simoes da Silva ............... University of Coimbra, Portugal

Lucjan Sleczka ........................ Rzeszów University of Technology, Poland

Bogdan Stefanescu ................... Technical University of Construction Bucharest, Romania

Aurel Stratan ........................... Politehnica University of Timisoara, Romania

Andrea Surovek ...................... South Dakota School of Mines & Technology, USA

James Swanson ....................... University of Cincinnati, USA

Jerzy Szlendak ........................ Bialystok Technical University, Poland

Lip Teh .................................... University of Wollongong, Australia

Lucia Tirca .............................. Concordia University of Montreal, Canada

Ian Tomsu ...................................Czech Technical University, Czech Republic

Robert Tremblay ..................... École Polytechnique of Montréal, Canada

Viorel Ungureanu .................... Politehnica University of Timisoara, Romania

Pedro Vellasco ........................ State University of Rio de Janeiro, Brazil

Cristian Vulcu ......................... Politehnica University of Timisoara, Romania

Frantisek Wald ........................ Czech Technical University, Czech Republic

Klaus Weynand ....................... Feldmann + Weynand GmbH, Germany

Raul Zaharia ............................ Politehnica University of Timisoara, Romania

Riccardo Zandonini ................. University of Trento, Italy

# AUTHOR INDEX

# CONNECTIONS VII WORKSHOP – 2012





*Openning ceremony (from left): L. Simoes da Silva, C.J. Carter, D. Dubina, F.S.K. Bijlaard, R. Bjorhovde*



*F.S.K. Bijlaard (r), receiving the Silver medal of ECCS from L. Simoes da Silva*



*Openning ceremony*

*Openning ceremony*



*Welcome Reception: The Rector of Politehnica University of Timisoara is awarding the representative of ECCS (F.S.K. Bijlaard) with the Honnorary Plaquette of PUT*



*Session 2 chaired by L.S. da Silva and R. Trambley*



*Welcome Reception: The Rector of Politehnica University of Timisoara is awarding the representative of AISC (R. Bjorhovde) with the Honnorary Plaquette of PUT*



*Concluding pannel composed by R. Bjorhovde and R. Zandonini presenting (and disputing) their Report*



*Conference Dinner (Recas Winery)*

*Conference Dinner (Recas Winery)*



*Post conference tour: visiting the fortress of Alba Iulia, the first capital in 1600*
*of the unified three Romanian Lands – Valahia, Moldavia and Transilvania*



*Post conference tour: visiting the fortress of Alba Iulia, the first capital in 1600*
*of the unified three Romanian Lands – Valahia, Moldavia and Transilvania*

The Series of International Workshops on Connections in Steel Structures was initiated as a cooperation between ECCS - The European Convention on Constructional Steelwork , the Technical Committee No. 10, Connections , and AISC - The American Institute of Steel Construction . The 1st edition was organized in Paris (1987), and the following ones in Pittsburgh (1991); Trento (1995); Roanoke (2000); Amsterdam (2004) and in Chicago (2008). The 7th edition , held in 2012, was organised in Timisoara, Romania. The present volume contains the Proceedings of this Workshop, presenting the recent research advances on structural connections in steel, innovative technical solutions and latest design code development in the field. These papers are grouped in the following topics:

> Structural design and design codes;
> Method of analysis;
> Connections for seismic effects;
> Connections with hollow structural sections;
> Bolting and special connections topics;
> Bracing and truss connections.

Dan DUBINA "Professor" of Steel Structures at "Politehnica" University of Timisoara, Romania, and Corresponding Member of Romanian Academy "the Head" of Department of Steel Structures and Structural Mechanics at Faculty of Civil Engineering. He is Member of ECCS TC 10- Connection in Steel Structures, and Member of ECCS TC 13- Seismic Design

Daniel Mihai GRECEA is Professor of Structural Mechanics at " Politehnica " University of Timisoara , within the Department of Steel Structures and Structural Mechanics at Faculty of Civil Engineering, being Member of ECCS TC 10- Connection in Steel Structures, and Corresponding Member of ECCS TC 13- Seismic Design.

**ECCS**
**CECM**
**EKS**

EUROPEAN CONVENTION FOR CONSTRUCTIONAL STEELWORK
CONVENTION EUROPÉENNE DE LA CONSTRUCTION MÉTALLIQUE
EUROPÄISCHE KONVENTION FÜR STAHLBAU

publications@steelconstruct.com | www.steelconstruct.com

TC10 is the Technical Committee within ECCS for Structural Connections. The committee is a forum which brings together academics, reserchers, designers and industry engineers aiming to investigate and debate problems of structural steel connections . The outputs of this activity consists in recommendations and consulting for design and execution of steel connections , drafting design guidelines and providing support for design codification in the field.